The University Of Sheffield.

Experimental and Numerical Study of the Shear Strength of Unsaturated Sand

By:

Bestun Jumaa Shwan

A thesis submitted in partial fulfilment of the requirements for the degree of Doctor of Philosophy

The University of Sheffield
Faculty of Engineering
Department of Civil and Structural Engineering

October 2015

Declaration of Authorship

I, Bestun Jumaa Shwan, hereby confirm that all work presented here is my own. Where information has been used from other sources, I confirm that this has been clearly stated within the thesis.

Signed: _____

Date: _____

Abstract

In the last few decades there have been extensive studies conducted into the mechanical and hydraulic behaviour of unsaturated soils. To date most attention has been focused on fine grained soils where the effects of partial saturation are expected to be more significant. Coarser grained soils have been under-represented in the literature. This study, therefore, focuses on the behaviour and modelling of an unsaturated sand and is divided into two main parts, governing experimental and numerical studies.

The experimental work involved two key parametric studies: (i) a laboratory based study of the relationship between shear strength and suction using a specially designed direct shear box where the suction was controlled using the hanging column technique (HCT). (ii) a laboratory study into the bearing capacity of a strip footing placed on the surface and at depth.

The numerical part in this study extended the upper bound discontinuity layout optimization (DLO) method to account for the effects of partial saturation on strength. The modified DLO method was then calibrated and incorporated into the commercial LimitState:GEO software. The software was then utilised to perform parametric studies into the effect of suction profile, and soil strength for passive earth pressure and bearing capacity problems, comparing the latter results with the experimental part.

The experimental drained direct shear and bearing capacity tests indicated an increase in the shear resistance of unsaturated samples compared to the fully dry or saturated cases. An existing shear strength equation showed poor agreement with the experimental data found in the literature as well as the direct shear results conducted in this study. A reformulated shear strength equation was then suggested, evaluated and showed good agreement with the experimental results. Furthermore, an existing SWCC equation was modified and evaluated. Although the direct shear test aimed to evaluate the existing shear strength equation for unsaturated soils, the results showed several additional interesting findings such as (i) increase of both ϕ and c parameters for unsaturated samples, (ii) high shear resistance for fully saturated samples compared to the fully dry case, (ii) wetting collapse behaviour at a high degree of saturation, (iii) oscillation of the shear resistance with shear displacement, (iv) drying behaviour during loading and shearing. Simple hypotheses of these behaviours are proposed throughout this thesis.

The DLO analysis of the passive earth pressure and bearing capacity problems demonstrated a non-linear relationship for passive earth pressure and bearing capacity with water table depth. The passive resistance and bearing capacity was seen to initially increase with increasing suction in the soil and then this increase levelled off as the saturation of the soil fell. Changes in capacity were significant, e.g. up to factors of 10 for bearing capacity despite the small magnitude of suctions involved (0 - 6 kPa).

Acknowledgements

Firstly, I would like to thank my supervisors, Dr. Colin C. Smith and Prof. Matthew Gilbert. Special appreciation to my first supervisor Dr. Colin C. Smith whom steer me through his wise counsel and guidance during this study.

My deep gratitude and appreciation to Prof. Alessandro Tarantino for his recommendations and suggestions with regards to modifications of the experimental apparatus.

Many thanks to Ministry of Higher Education and Scientific Research in Kurdistan (Iraq) for their PhD grant and their infinite support and encouragement during my study.

My heartfelt thanks to all aspects of Mr. Paul Osbourne, Mr. Mark Foster, Mr. David Callaghan and Dr. Paul Bentley who helped me in building the required equipments to complete this work.

I would like also to thank the Geotechnical Engineering Research Group for their friendship during my study.

Finally, I wish to bring my love and gratitude to my dear parents and family for which I have worked hard to get this certificate. They were inspiring source, strength and support to me during my studies.

Contents

List of Figures

List of Tables

List of Symbols

ξ_c and ξ_γ	Shape factors from Vesic (1973)
$(\dot{u}_a - \dot{u}_w)\delta_{hk}$	Suction increment
$(u_a - u_w)_{AVR}$	Average between matric suction directly beneath the stress bulb and a specific depth
$(u_a - u_w)_b$	Air entry value
α	Material parameter
α_β	Scaling factor for phase β
α_w	Porosity
$\bar{U}_f$	Desired degree of pressure dissipation
β	Fitting parameter
χ	Weighting factor which ranges from 0 to 1 for fully dry and saturated cases
Δh	Horizontal displacement of the shear box
δ	Block displacement
δ_{ij}	Kronecker's delta
$\dot{\sigma}'_{hk}$	Increment of Terzaghi saturated effective stress
η	Parameter accounting for fluid flow impeded by the ceramic disk
$\frac{\partial h_w}{\partial y}$	Hydraulic head gradient
$\frac{A_a}{A_{total}}$	Part of the pore area occupied by air
$\frac{A_w}{A_{total}}$	Part of the pore area that is occupied by water
γ	Unit weight of soil
γ'	Buoyant unit weight of soil
γ_t	Total unit weight
γ_w	Unit weight of water

$\hat{c}$	Amount of increase in cohesion due to the saturated or unsaturated condition
$\hat{C}$	Apparent cohesion force
λ	Impedance factor
$\phi^{'}$	Effective internal friction angle
ϕ^{*}	Internal friction angle at peak or parameter at the state under conditions
ϕ^{a}	Internal friction angle with respect to the net normal stress at constant suction
ϕ^{b}	Internal friction angle with respect to the matric suction at constant net normal stress
π	Osmotic suction
ψ	Total suction
ψ_{r}	Suction corresponding to the residual suction
ρ_{w}	Water density
ρ_{dry}	Dry unit weight of the soil
ρ_{sat}	Saturated unit weight of the soil
σ	Total stress
$\sigma^{'}$	Effective stress
$\sigma^{'}_{ij}$	Unified effective stress averaged over a total volume scheme
σ_{1}	Vertical stress at failure
σ_{h}	Horizontal stress
$\sigma^{'}_{h}$	Effective horizontal stress
σ_{v}	Vertical stress
$\sigma^{'}_{v}$	Effective vertical stress
σ_{ij}	Total exterior stress
τ	Shear strength
θ	Volumetric water content
θ_{s}	Saturated volumetric water content
θ_{i}	Angle of interface
$\varepsilon^{'}_{ij}$	Strain rate

A	Corrected area of the shear box
a	Fitting parameter
A_o	Initial area
B	Footing width
b_m	Slope of the SWCC in terms of gravimetric water content versus matric suction
C	Drained compressibility of the granular skeleton
c	Cohesion
$C(\psi)$	Correction factor
$c^{''}$	Cohesion intercept when the two stress variables are zero
C'^{e}_{ijhk}	Drained elastic compliance matrix
$c^{'}$	Effective cohesion
C'_s	Elastic proportionality coefficient for the hydraulic behaviouR
c^*	Cohesion at peak or parameter at the state under conditions
C^{ep}_{ijhk}	Tangent elasto-plastic matrix in saturated conditions
C^{s}_{ijhk}	Coefficient of proportionality between strain increments and suction increments
C_s	Finite grains compressibility
c_u	Unconfined compressive strength of the soil
C_v	Soil coefficient of consolidation
D	Diameter of the shear box
d	Diameter of capillary
$d\dot{h}$	Shear rate
dh_f	Lateral displacement at failure
E	Energy dissipation
e	Void ratio
e_o	Initial void ratio before the drainage
F	Collapse load
F_o	Correction factor
g	Gravitational acceleration

G_s	Specific gravity
H	Height of the retaining wall
H_c	Capillary rise height
h_c	Capillary rise height
H_w	Water table depth (positive downward)
h_w	Hydraulic head
k_p	Passive earth pressure coefficient
k_s	Saturated hydraulic conductivity
k_w	Coefficient of permeability
L	Thickness of the specimen
L_d	Thickness of the high air entry disk
L_s	Drainage path length
L_i	Length of interface
m	Number of interface
n	Porosity
N_{γ_w} and N_{H_w}	Factors that account for the pore-water pressure and the position of the water table
N_c, N_q and N_γ	Bearing capacity factors
n_i	Normal displacement jumps
p^*	Equivalent pore pressure
P_p	Total passive earth pressure
p_w	Pore water pressure
P_1, P_2, P_3 and P_n	Pressure of different fluid
p_β	Pressure of fluid
q	Surcharge
q_{lim}	Bearing capacity
q_o	Overburden pressure
$q_{ult(unsat)}$	Ultimate bearing capacity of unsaturated soil
q_{ult}	Ultimate bearing capacity of soil

s	Suction
s^*	Suction at peak or parameter at the state under conditions
S_e	Effective degree of saturation
S_o	Residual degree of saturation
s_o	Air entry value
S_r	Degree of saturation
S_r^*	Degree of saturation at peak or parameter at the state under conditions
s_i	Relative shear jumps
S_r^e	Effective degree of saturation
S_r^m	Microscopic degree of saturation
T	Surface tension of water
t_f	Failure time
u	Pore water pressure
u_a	Pore air pressure
U_w	Pore water pressure
U_i	Pore water force
V_s	Volume of solid
V_t	Total volume
V_v	Volume of voids
V_w	Volume of water
v_w	Rate of water flow through a soil mass
w	Water content
W_B	Weight of a block above the discontinuity
W_t	Total weight of the sample
W_i	Weight of the strip above interface
y	Gravitational head
y_1	Distance from the water table to the capillary rise line
y_{max}	Distance from the domain base to the soil surface
Y_w	Water table height from origin (positive upward)
z	Vertical coordinate (positive downward)

Chapter 1

Introduction

1.1 Introduction

Many historical geotechnical structures such as railway embankments and cuttings were designed before the modern science of soil mechanics was developed. In many cases these structures only stand up due to the strength imparted to them through partial saturation and the effects of surface tension (water suction) acting in the soil pores which holds the soil particles together. Generally, soil above the water table considered to be in an unsaturated condition, where the degree of saturation is influenced by several factors such as capillary rise effect, infiltration, evaporation and transpiration near soil surface as shown in Fig. 1.1.

In modern geotechnical design, the risk of rainfall eliminating the suctions in such structures would lead to alternative, much more conservative designs. However while most of the historical structures remain viable and around the world there are many natural slopes that are only stable due to partial saturation. In addition, many modern engineering applications can benefit from the application of unsaturated soil mechanics such as earth dams, embankments, natural slopes and foundations subjected to heave due to swelling.

The effect of climate change, i.e. high intensity rainfall events or reduced snowfall, has a significant influence on the stability of geotechnical structures (e.g. slopes) in which variations in matric suction can lead to major landslides following a heavy rainfall event or increased stability for cases when a hot and humid climate occurs. Toll (2001) stated that rainfall is the main triggering event for landslides in which major and minor slope failures can result due to the intensity of the rainfall, e.g. major failures have occurred when rainfall events exceed 100 mm/day.

With improved understanding of unsaturated soil mechanics and soil-structure interaction in such conditions, it may be possible to utilise the additional strength due to partial saturation (which can be very significant) in conventional design e.g. with engineered controls on the saturation, under a risk based framework, in temporary works, or in assessing cumulative cyclic loading effects through the seasons.

Significant efforts during the last two decades have been focused in this field and this has led to the formulation of a theoretical framework for understanding unsaturated soil mechanics. At the present, 20% of geotechnical publications in recent years have been either directly or indirectly related to field of unsaturated soil mechanism, Vanapalli et al. (2008).

Several constitutive models have been proposed in the field of unsaturated soil mechanics. Toll (1990) proposed a framework for unsaturated soil based on the extended critical state model for saturated soil in which additional variables for unsaturated soil were incorporated. Alonso et al. (1990) proposed a constitutive model for describing the stress-strain

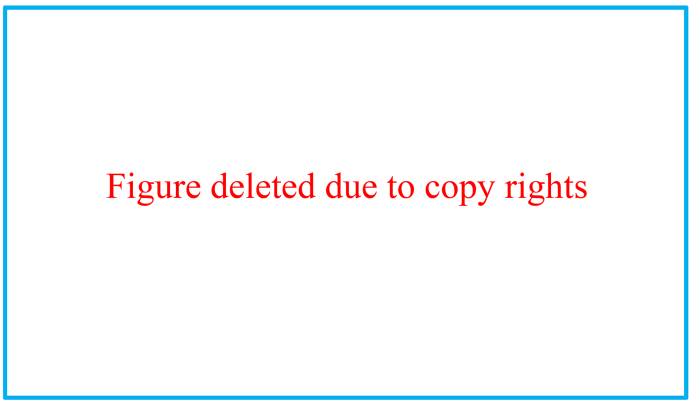

Figure 1.1: Role of climate change on unsaturated soil, after Likos & Lu (2004).

behaviour of partially saturated soil based on the framework of hardening plasticity using two independent sets of stress variables. Wheeler (1991) proposed an alternative framework for unsaturated soil behaviour based on a critical state model. Wheeler & Sivakumar (1995) also proposed an elasto-plastic state framework for unsaturated soil. More recently, Tarantino (2007) proposed a critical state framework for unsaturated compacted clay.

In contrast, the application of unsaturated soil mechanics to unsaturated sand examining behaviours such as shear strength within a small suction profile, dilation, capillarity, hydro-mechanical effects and water migration due to applied loads is limited. Physical modelling studies (e.g. bearing capacity problems) of unsaturated sand are also limited and few studies into the unsaturated bearing capacity problem can be found in the literature, e.g. Fathi & Vanapalli (2006).

There has been little previous work applying unsaturated soil mechanics to computational limit analysis (CLA). Typically work has either involved the incorporation of unsaturated mechanics into modified numerical models (e.g. finite element, slip circle and finite difference), or into conventional hand type calculations (either using limit analysis or limit equilibrium methods). In terms of the latter, Zhao et al. (2009) proposed an approach to calculate passive earth pressure based on the upper bound theorem and the shear strength of unsaturated soils. More recently, Stanier & Tarantino (2010) proposed equations based on the lower and upper bound theorems for the active earth pressure exerted by partially saturated soils. There is a significant scope, therefore, to further investigate the above stated behaviours for unsaturated sand that can be used to extend the application of unsaturated soil behaviour into CLA.

1.2 Objectives and contributions of the thesis

The aim of the research is to study the stress-strain, hydro-mechanical and capillarity phenomena of unsaturated sand and to investigate and extend the application of the CLA method to unsaturated geotechnical problems. Specifically an upper bound approach, known as discontinuity layout optimization (DLO) which was proposed by Smith & Gilbert (2007*a*) will be extended to model the effects of partial saturation. The extended numerical model will be validated against an analytical retaining wall case study and applied to laboratory scale models of bearing capacity. Specific objectives are as follows:

1.2.1 Experimental studies

1. Investigate the effect of suction on the shear strength of an unsaturated sand using a modified direct shear box that allows control of suction using the hanging column technique (HCT).

2. Investigate the effect of suction on the bearing capacity of sands through the physical modelling of a scaled strip footing. Both surface and buried strip footings will be investigated. In addition to load-displacement data, the failure mechanism for the footing will be studied using the particle image velocimetry (PIV) technique.

3. Propose and/or modify a shear strength equation for a fine-grained unsaturated sand based on existing work and the direct shear data from 1.2.1 (1). This work will also aim to evaluate and/or modify an existing soil water characteristic curve (SWCC) equation.

1.2.2 Numerical studies

1. Develop a formulation for predicting the shear strength of unsaturated soil for a variety of water table locations suitable for incorporation in the DLO method and validate these formulations. This development will be based on the modified shear strength and SWCC equations from 1.2.1 (3). Use these formulations to first extend, modify and validate an existing MATLAB DLO code developed by Smith & Gilbert (2007*a*) such that it can be applied to a variety of problems in the field of unsaturated soils. Subsequently these equations will be incorporated into a research version of the commercial DLO software LimitState:GEO.

2. Use the modified version of the LimitState:GEO software to undertake parametric studies into:

   (a) the bearing capacity of a strip footing placed on the surface and buried to a specific depth into saturated and unsaturated sand. These will be validated against the experimental results mentioned in 1.2.1 (2); and

   (b) the total passive earth pressure for a variety of water table positions, a range of applied suctions and different backfill materials. This study will also include the effect of internal friction angle and wall friction on the total passive earth pressure exerted by the wall.

1.3 Thesis structure

This thesis is organised into 8 chapters that cover the theoretical background, literature review and experimental and theoretical developments carried out during the PhD research. A review of relevant literature is presented in Chapter 2.

Chapter 3 describes the experimental methodology developed in this study. This includes choice of the material, design of the apparatus, sample preparation techniques, suction control using the HCT, the basis of the experimental programme, the principles of image particle velocimetry (PIV) and repeatabilty of the tests.

Chapter 4 presents the results of the experimental works for both the direct shear and bearing capacity tests. The evaluation and reformulation of an existing shear strength equation based on the laboratory data found in the literature and conducted in this study is presented in Chapter 5.

The incorporation of the proposed shear strength equation into the DLO procedure and the numerical modelling aspect is presented in Chapter 6 which includes a parametric study of a retaining wall and a comparative analysis of the bearing capacity problem. This includes the study of total passive thrust exerting by a retaining wall across a wide range of applied suctions using two simulated backfill materials and bearing capacity of a footing placing on the surface and buried to a specific depth into the saturated and unsaturated sand. Chapter 7 discusses the experimental and numerical results, while Chapter 8 includes the conclusions and proposes additional work for research. The appendices include published, submitted (or to be submitted) papers, validation of equations derived for the numerical modelling conducted in this research, general validation procedure for the apparatus used in the experimental study, derivation of the equations for the total passive earth pressure using the Rankine method and calculation procedure for determination of the SWCC using the HCT.

Chapter 2

A Review of Unsaturated Soil Mechanics

2.1 Introduction

The state of knowledge of unsaturated soil mechanics covering experimental and computational viewpoints is addressed in this chapter. This chapter is divided into two main parts: first: definitions, physics of unsaturated soils and methods of controlling and measuring suction, second: the shear strength of partially saturated soils based on recent works found in the literature as well as a summary of limit analysis theory.

2.2 Definition of unsaturated soil

Soil whose voids are filled with water and air is widely identified in the literature as "unsaturated soil". Fredlund & Rahardjo (1993) defined unsaturated soil as a soil whose pore water has a negative pressure. Unsaturated soil contains three distinct phases: solid, water and air. The solid phase comprises the soil grain. The liquid phase comprises of liquid water and dissolved air. The last phase comprises air and water vapour. Accordingly, water and air are identified as the only two species for the liquid part of the problem. The degree of saturation of the soil (S_r) is defined as a ratio between the volume of water (V_w) and the volume of voids (V_v) as follows:

$$S_r = \frac{V_w}{V_v} \tag{2.1}$$

2.3 Suctions in unsaturated soils

Unsaturated soils have more than two phases and the existence of air along with water in the voids gives rise to two types of pore pressures: pore air pressure and pore water pressure. The latter is normally negative relative to pore air pressure due to surface tension effects. The theory of suction was mainly developed within the theory of soil-water plant systems, Fredlund & Rahardjo (1993). In general, soil total suction has two components: matric suction (s) and osmotic suction (π). According to Aitchison (1965), the total suction ψ is given by:

$$\psi = s + \pi \tag{2.2}$$

Matric suction is the difference between pore air (u_a) and pore water (u_w) pressures as shown in Eq. 2.3.

$$s = u_a - u_w \tag{2.3}$$

Matric suction is a function of several soil properties such as grain size, voids geometry constrained between the soil particles, soil density and degree of saturation. Soil suction is significantly associated with degree of saturation.

Pore water pressure in unsaturated soil is normally less than the pore air pressure, hence a concave contractile skin forms at the interface between air and water which is called "meniscus". The contact between water and solid surface is at an angle called the contact angle (θ) (see Fig. 2.1a). This angle arises when a balance between the cohesive forces in the liquid and the adhesive forces between the solid and liquid happens, Marinho et al. (2008). The contact angle values range between zero (perfect wetting liquid) to 90^o (imperfect wetting liquid). For water, the contact angle is noticeably less than 90^o and naturally approaches zero, Marinho et al. (2008). Capillarity in a fluid surface system occurs when the contact angle is less than 90^o, Marinho et al. (2008), and for this case concavity of the water-air interface occurs when water rises in small diameter pores as shown in Fig. 2.1b. The water

[a] Figure deleted due to copy rights

[b] Figure deleted due to copy rights

Figure 2.1: (a)Contact angle for an ideal smooth, homogenous and non-deformable surface (γ = surface tension, sl = solid liquid, sg = solid gas, lg = liquid gas) (b) Capillary rise of wetting fluid, after Marinho et al. (2008).

pressure at the back of the meniscus can be calculated by the equation below:

$$u_w = u_a - \frac{4\ T \cos\theta}{d} \tag{2.4}$$

where T is the surface tension of water and d is diameter of the capillary. Since cos θ is greater than zero, the water pressure u_w is less than u_a and hence, the water meniscus rises in the capillary tube until hydrostatic conditions are achieved. When air pressure is atmospheric (101.6 kPa), water surface tension at 20 ^{o}C is equal to 0.072 N/m and angle of contact θ is zero, the pore pressure becomes negative and a higher negative value can be observed as the radius of the interface decreases.

The relationship between matric suction and capillary rise (h_c) can be written as:

$$h_c = \frac{s}{\gamma_w} \tag{2.5}$$

where γ_w is unit weight of water. Referring to Eq. 2.4 and Fig. 2.1a, it is clear that matric suction is related to the surface tension and it is linked to the capillary rise of the

partially saturated soil. Considering Eq. 2.4 and Fig. 2.1b, the capillary rise of the small diameter capillary of diameter (d) shown in Fig. 2.1b can be given by:

$$h_c = \frac{4\ T \cos\theta}{d\ \gamma_w} \tag{2.6}$$

2.4 Soil water characteristic curve (SWCC) for unsaturated soil

The relationship between soil suction and volumetric water content is widely used in unsaturated soil mechanics and it is called soil water characteristics curve (SWCC) or soil water retention curve (SWRC). The volumetric water content is often replaced by gravimetric water content or degree of saturation and the relationship between them is given by:

$$\theta\ (1 + e) = S_r\ e = w\ G_s \tag{2.7}$$

where θ is volumetric water content, e is void ratio, w is gravimetric water content and G_s is specific gravity. In Eq. 2.7, water content and degree of saturation can be considered as counterpart variables to the void ratio. Both these two variables can be used to express the amount or volume of water in the pore space.

The SWCC is usually determined from laboratory tests by applying a constant or null level of net stress. Another feature that is widely established in the literature about the SWCC is its original position can be shifted during shearing due water flowing in or out of the pore voids, Nuth (2009). This shifting is widely called as hydraulic behaviour. Also, the mechanical straining can be established due to the applied load. Such two behaviours; hydraulic and mechanical are related each to other, hence coupling between them is intrinsic to address several significant phenomena in unsaturated soil such as drying and wetting and plastic collapse. The coupling between hydraulic and mechanical behaviours is called hydro-mechanical behaviour.

Figure 2.2 shows a typical SWCC illustrating some useful features. Air entry value is the matric suction where air starts to enter the largest pores in the soil, while residual suction is the suction where a large change in suction is required to remove additional water from the soil, Fredlund & Xing (1994).

The SWCC is one of the most important physical properties of unsaturated soil, since there is a relationship between the SWCC and the shear strength of unsaturated soil, Fredlund & Rahardjo (1993). The SWCC is affected by several factors such as particle structures, void size distribution, soil texture, soil compaction and mineral type. The SWCC can be produced in two modes: wetting (adsorption) and drying (desorption) curve (see Fig. 2.2). These two curves are different due to hysteresis and this phenomenon means that at a known matric suction, many different gravimetric water contents or degree of saturation values can be obtained in the wetting and drying curves. The reasons for this hysteresis may relate to non-uniform pore size distribution (different passages can be interconnected by the different voids in shape) as well as existence of entrapped air in the pore water voids, Hillel (1980).

2.5 Methods of controlling and measuring suction

The theoretical developments in unsaturated soil mechanics are due to the ability to measure the suction in unsaturated soils confidently. In the past, several methods have been developed

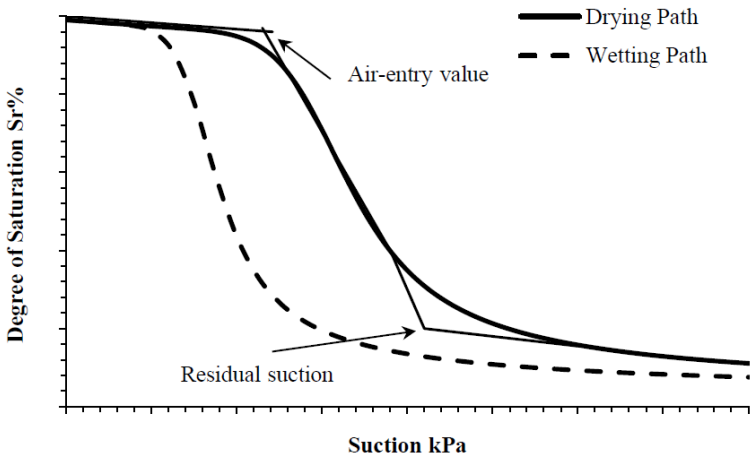

Figure 2.2: Typical soil water characteristic curve (SWCC).

to measure the suction both in the field and in the laboratory, Fredlund & Rahardjo (1993). Matric suction has been considered as an important variable in defining the state of stress in an unsaturated soil and several researchers have suggested matric suction as an independent variable such as Bishop (1960), Toll (1990), Fredlund & Rahardjo (1993) and Tarantino (2007). Consequently, significant efforts have been made to control and measure matric suction precisely.

In this section, therefore, the working principle and application of some of the methods of controlling and measuring suction are discussed.

2.5.1 Methods of controlling suction

2.5.1.1 Axis translation technique

Hilf (1956) introduced this technique to control matric suction in which the origin of the reference of the pore water pressure was translated from the standard atmospheric condition to the final air pressure in the chamber. This technique has been used successfully by many researchers such as Ho & Fredlund (1982), Escario & Saez (1986), Wheeler & Sivakumar (1995), Toll & Ong (2003) and Toll et al. (2008). The basic principle of this technique which is based on the capillary pore model can be described by Figs. 2.3a and b. In Fig. 2.3a the air pore pressure is atmospheric (zero gauge pressure) since the tube is open-ended and the pore water pressure is negative. The contact angle between the solid and the liquid is (θ_o) since the water is ascending in the tube. However, the pore air pressure can be raised above atmospheric (101.6 kPa) pressure when the capillary tube is close-ended and the air in the tube subjected to a pressure as shown in Fig. 2.3b. Olson & Langfelder (1965) assumed that water and solid boundaries are incompressible and the contact angle and hence the curvature do not significantly change ($\theta_o = \theta_{AT}$). Accordingly, matric suction does not changed.

Figure 2.4 shows a schematic diagram explaining the axis translation technique. Pore water pressure in the sample has been raised to become positive by elevating pore air pressure. Elevating pore air pressure in the system has led to an increase in the total stress and the pore water pressure in the sample with the same value and this means the net suction ($u_w - u_a$) does not change.

The sample is set on a fine porous disk, known as high air entry disk (HAED), which

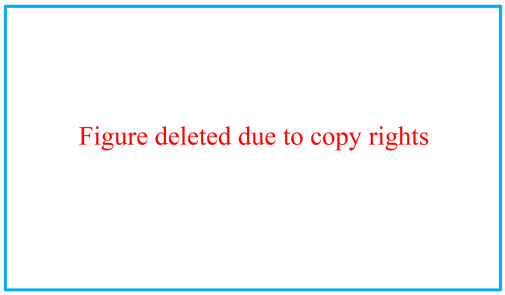

Figure 2.3: Principle of the axis translation technique, after Marinho et al. (2008).

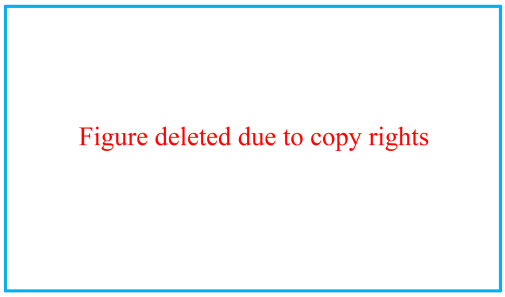

Figure 2.4: A schematic diagram showing the axis translation technique, after Ng et al. (2007).

provides a connection between soil pore water pressure and pore water measuring system and prevents air from getting into the pore water measurement system. The difference between air pressure and water pressure gives the suction in the sample. The air entry value of the HAED must be higher than the applied suction else air can easily enter the measuring system.

This technique can be used in the laboratory environment without any problems associated with cavitation, Hilf (1956). Another advantage of this method is no chemical is used in the system, therefore, the chemistry of the pore fluid does not change. Nevertheless, disadvantages of this method are as follows:

1. It is not representative of the field conditions where air pressure is under atmospheric conditions.

2. Air could diffuse (due to applying air pressure) into the HAED which then affects the suction measurement.

3. This technique is valid only for soils with completely inter-connected pore-air pressure voids, for soil particles that are incompressible and for continuous air-water interphases, Vanapalli et al. (2008).

2.5.1.2 Osmotic suction

This method was first developed by biologists Lagerwerff et al. (1961) and then adopted by Williams & Shaykewich (1969) and geotechnical researchers Cui & Delage (1996), Delage et al. (1998) and Ng et al. (2007).

In this technique, a semi-permeable membrane in contact with soil specimen as shown in Fig. 2.5 is used to control the negative water pore pressure along which a polyethylene glycol (PEG) solution is circulating in the other side of the membrane. Water molecules can

cross the membrane; while PEG molecules cannot. An osmotic suction that increases with the PEG concentration is then applied to the soil through the semi-permeable membrane. The pore air pressure in the soil is atmospheric. High suctions up to 10 MPa can be applied using this method, Delage et al. (1998). This method has been effectively adapted to a wide range of geotechnical tests such as in a modified triaxial device (Cui & Delage (1996) and Ng et al. (2007)) and in an oedometer apparatus (Kassif & Ben Shalom (1971) and Dineen & Burland (1995)).

This method overcomes the limitation of the axis translation technique that is relates to measure suction at high degrees of saturation (occluded air). On the other hand, the drawbacks of this method are:

1. Weakness of the membrane and its sensitivity to microbial attack.
2. An equilibrium time up to 2 months is required, Murray & Sivakumar (2010).

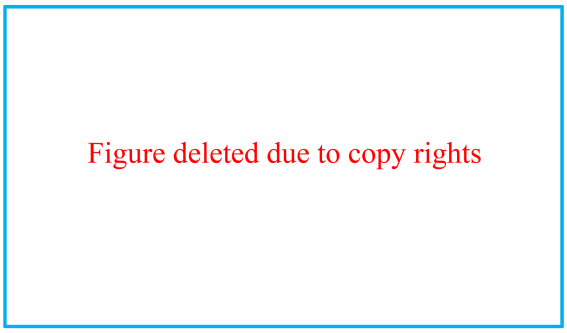

Figure 2.5: Schematic diagram showing the osmotic technique, after Ng et al. (2007).

2.5.1.3 Hanging column technique (HCT)

The relation between capillary potential and water content (SWCC) was first measured by Buckingham (1907). The capillary potential was defined as the gravitational potential energy within the water at any elevation above the reference reservoir elevation after attaining equilibrium conditions, Vanapalli et al. (2008). The technique was simplified and improved by several researchers such as Richards (1928), Haines (1930), Romano et al. (2002) and Sharma & Mohamed (2003) and recently Vanapalli et al. (2008) provided details of the historical development of measuring matric suction using the HCT.

The apparatus consists of a funnel connected to a burette (water column) via a rubber tube. The layout of the apparatus is shown in Fig. 2.6. The specimen can be prepared by pouring sand from a specific height into the funnel which is previously filled with water.

The pressure in the bulk water can be reduced to subatmospheric by lowering the burette (see Fig. 2.6), while the soil sample has a gas pressure at atmosphere pressure. This subsequent reduction in hydraulic head causes the water to flow from the sample to the burette. At static equilibrium, there is a linear relationship between water pressure head and the elevations of the burette. Once the negative pressure is applied to the sample, water migrates towards the burette. Therefore, outflow volume and pressure can be measured at each step. The measured suction head is the distance from water level in the burette to any specified point (e.g. surface of the sample) when flow of water ceases from or to the sample. Time required for the sample to achieve equilibrium with the system is ranges from several hours to days.

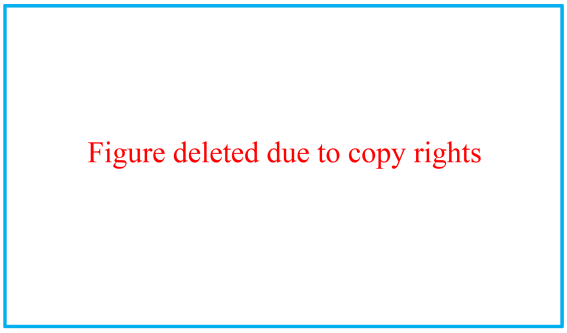

Figure 2.6: Buchner funnel for obtaining SWCC, after Sharma & Mohamed (2003).

Although the hanging column technique is a method of controlling suction in unsaturated soils, it has not been utilised broadly to address stress-strain, hydro-mechanical, compressibility and dilation phenomena for coarse unsaturated soils. This study, therefore, aimed to use this method with a modified direct shear device that account for water flow change and suction variations. Apart from the advantages (simplicity) of this method, this technique has the following limitations:

1. The suction that can be applied ranges from 0 to 30 kPa, Vanapalli et al. (2008). In fact the absolute limit would be 101.6 kPa (before cavitation occurs) with the likely practical limit at 80 - 90 kPa.

2. This technique is limited to use with coarse grained soils with little fines due to the small range of suctions which can be applied by this method, Vanapalli et al. (2008).

2.5.2 Methods of measuring suction

2.5.2.1 Filter paper method

The filter paper method is an indirect method for measuring matric suction which is economical, simple to use and allows a large range of suctions to be measured. The approach is based on the assumption that equilibrium (either by liquid or vapour) can be attained after a period of time between the filter paper and the soil (see Fig. 2.7). The water absorbed by the filter paper is related to soil suction through a pre-determined calibration curve. The accuracy of the filter paper method depends on the accuracy of the filter paper water content and the calibration curve. This method can be used to measure both total (using the non-contacted method) and matric suction (using the contacted method) as shown in Fig. 2.7, Fredlund & Rahardjo (1993). Furthermore, it could be used to measure suction ranges from 0 to 10 MPa, Murray & Sivakumar (2010).

Regardless of the simplicity of the method, this technique suffers from these limitations:

1. Not useful for in situ measurement.

2. Great attention should be taken when measuring small masses, Fredlund & Rahardjo (1993).

2.5.2.2 Tensiometer

A tensiometer can be utilised to measure negative pore pressure in the laboratory using the same conditions as the field, Murray & Sivakumar (2010). Figure 2.8 shows an electronic

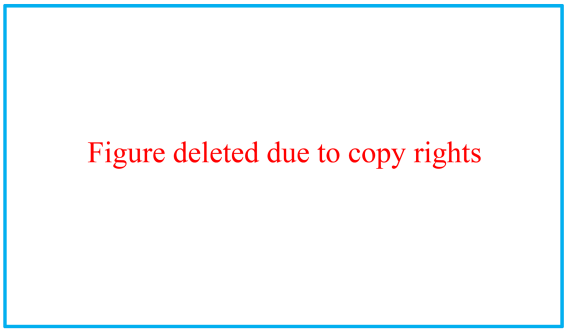

Figure 2.7: Schematic diagram of matric suction measurement using the filter paper method, after Bulut & Leong (2008).

pressure transducer tensiometer with its components. The water compartment is to keep the HAED fully saturated during the tensiometer operation and to apply suction to the diaphragm. The way of applying suction is based on extracting water from the reservoir in the tensiometer through the HAED (ceramic disk). So that, the water pressure equalises between the instrument and the soil. The main advantage of the tensiometer is that a direct

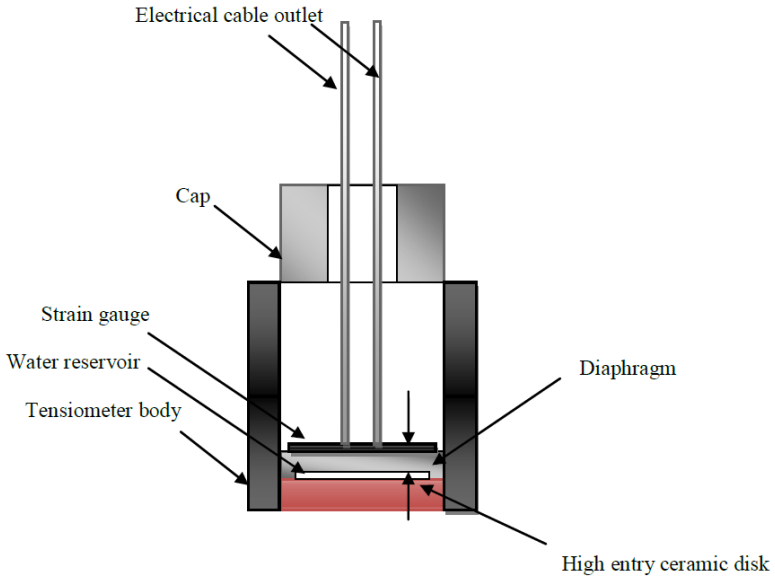

Figure 2.8: Electronic pressure transducer tensiometer.

measurement of the suction can be extended up to 1500 kPa, Murray & Sivakumar (2010).

On the other hand, the tensiometer suffers from these disadvantages:

1. Care required while applying tensile stress to water due to risk of creating air bubbles.
2. Expensive.

2.6 Effective stress principle

Effective stress is expressed as a function of externally applied stresses and internal pore fluid pressures. The lexicon of "effective stress" was first used by Terzaghi (1936) and is

given by:

$$\sigma_{ij}^{'} = \sigma_{ij} \; - \sum_{\beta=1}^{n} \alpha_{\beta} \; p_{\beta} \; \delta_{ij} \tag{2.8}$$

where $\sigma_{ij}^{'}$ is unified effective stress averaged over a total volume scheme (see Fig. 2.9), σ_{ij} is total exterior stress, α_{β} is the scaling factor for phase β and p_{β} is the pressure of fluid. In Fig. 2.9, P_1, P_2, P_3 and P_n designate the pressures of different fluids.

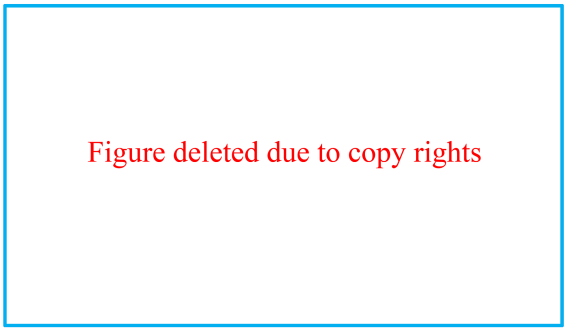

Figure 2.9: Conversion of multiphase and multi stress medium into single continuum, after Nuth & Laloui (2008*b*).

For soils saturated with water, Eq. 2.8 can be simplified to Eq. 2.9 as suggested by Terzaghi (1936):

$$\sigma_{ij}^{'} = \sigma_{ij} \; - p_w.\delta_{ij} \tag{2.9}$$

where p_w is pore water pressure and δ_{ij} is Kronecker's delta ($\delta_{i=j} = 1$,$\delta_{i\neq j} = 0$). Equation 2.9 was derived on the assumption that effective stress controls all measurable effects of the stress change such as change in shearing resistance and compression. Note that Eq. 2.9 is valid for a fully dry case as the second term turns to zero. Equation 2.9 represents a very particular case which assumes incompressible grains and the pore space is filled with incompressible fluid. The shortcoming of Eq. 2.9 (if the above assumption is not valid) led to further investigations for more formulations, so Eq. 2.10 was proposed for a single fluid phase as:

$$\sigma_{ij}^{'} = \sigma_{ij} \; - \alpha_w \; p_w.\delta_{ij} \tag{2.10}$$

where α_w is equal to porosity n, (as first suggested by Terzaghi and then he assumed α_w = 1 and this led to Eq. 2.9).

Hereafter, Biot (1955) included porosity (n) in the second term of Eq. 2.9 as:

$$\sigma_{ij}^{'} = \sigma_{ij} \; - n \; p_w.\delta_{ij} \tag{2.11}$$

Porosity inclusion again raised the problem of non-constant void ratio. Skempton (1960) then suggested α_w as a function of finite grains compressibility Cs leading to a new formula for effective stress as:

$$\sigma_{ij}^{'} = \sigma_{ij} \; - (1 - \frac{Cs}{C}) \; p_w.\delta_{ij} \tag{2.12}$$

where C is drained compressibility of the granular skeleton. Finally, Suklje & Sûklje (1969) proposed a formula which combined porosity and the compressibility coefficient as follows:

$$\sigma_{ij}^{'} = \sigma_{ij} \ - (1 - (1 - n)\frac{Cs}{C}) \ p_w.\delta_{ij} \tag{2.13}$$

In an unsaturated soil mechanism, the situation is more complex than fully dry or saturated cases due to the presence of two fluids (air and water). In the next section, therefore, current thinking about using stress state variables for unsaturated soil is detailed.

2.7 Stress frameworks for unsaturated soils

Unsaturated frameworks witnessed comprehensive development in which several frameworks were suggested (e.g. Toll (1990), Alonso et al. (1990), Gens (1995) and Jardine et al. (2004)). These advanced constitutive frameworks present several level of complexity and seemingly were inherited from Bishop's single effective stress equation. It is proposed in the next sections, therefore, to have an overview to the Bishop's effective stress equation as well as the latest development on the shear strength for unsaturated soils.

2.7.1 Effective stresses in unsaturated soils

As an early attempt, Bishop (1960) used single independent stress state variables as a function of net stress $(\sigma - u_a)$ and suction $(u_a - u_w)$ and he suggested a tentative equation that required more experimental works to validate it as follows:

$$\sigma^{'} = (\sigma - u_a) \ + \chi(u_a - u_w) \tag{2.14}$$

where χ is a weighting factor which ranges from 0 to 1 for fully dry and saturated cases, respectively. Equation 2.14 is an extension of Terzaghi's effective stress equation assuming that effective stress controls the measurable effect of a change of stress and effective stress in unsaturated soils is excess of total stress over equivalent pore pressure.

$$\sigma_{ij}^{'} = \sigma_{ij} \ - p^*.\delta_{ij} \tag{2.15}$$

where p^* is equivalent pore pressure (a portion of the effective stress induced by the pressures of all fluids in the voids). Equation 2.14 was presented as a function of total stress and the pore water pressure in which any mechanical effect of the stress change is controlled by the pore water pressure. The basis behind Eq. 2.14 was built on conversion of a multiphase and a multi stress medium into single continuum shown in Fig. 2.9.

To validate Eq. 2.14, tests on unsaturated soils were conducted. Bishop & Donald (1961) performed a series of triaxial tests on an unsaturated soil and they suggested:

$$\chi = \chi^{'} S_r \tag{2.16}$$

Then, Jennings & Burland (1962), Bishop & Blight (1963), Burland (1964) and Burland (1965) verified Eq. 2.14 experimentally. They came to the conclusion that using two stress variables for unsaturated soils is inevitable.

Equation 2.14 is limited due to its inability to predict volume change in unsaturated collapsible soils (Jennings & Burland (1962), Burland (1965) and Matyas & Radhakrishna

(1968)). During the wetting (suction decrease), swelling or collapse was observed. Experimental evidence from Sivakumar (1993) for clay soils to support the idea is shown in Fig. 2.10.

The local value of the effective stress within the saturated microstructure of the clay packets is decreased during wetting due to increase of the water pressure (u_w). Therefore, the wetting always produced swelling of the individual packets. However, slippage at the inter-packet contact points can cause collapse of the micro-structural arrangement of particles due to the softening of the packets into the large, partially air-filled inter-packet voids.

On the other hand, at low values of $(\sigma - u_a)$, the soil is able to endure the load even after softening, so collapse does not occur. It is not the effective stress, therefore, that controls behaviour of unsaturated soils but the two stress state variables $(\sigma - u_a)$ and $(u_a - u_w)$ this was also supported by Jennings & Burland (1962). Similarly, Matyas & Radhakrishna (1968) concluded that the collapse behaviour due to decreasing suction at high values of $(\sigma - u_a)$ can not be explained by the equation suggested by Bishop (1960).

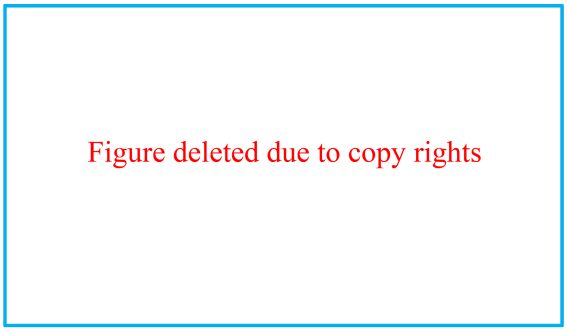

Figure 2.10: Swelling and collapse phenomena in kaolin, after Sivakumar (1993).

The weakness in Bishop's equation motivated researchers to propose two independent stress state variables (e.g. Coleman (1962), Bishop & Blight (1963) and Matyas & Radhakrishna (1968)). Coleman (1962) suggested an elasto-plastic model for an unsaturated soil using two stress variables as:

$$\dot{\varepsilon}_{ij}^{'} = C_{ijhk}^{ep} \ (\dot{\sigma}_{hk} - \dot{u}_a \ \delta_{hk}) + C_{ijhk}^{s} \ (\dot{u}_a - \dot{u}_w)\delta_{hk} \tag{2.17}$$

where $\dot{\varepsilon}_{ij}^{'}$ is the strain rate, C_{ijhk}^{ep} is the tangent elasto-plastic matrix in saturated conditions, C_{ijhk}^{s} is the coefficient of proportionality between strain increments and suction increments $(\dot{u}_a - \dot{u}_w)\delta_{hk}$.

The stress state in Eq. 2.17 is described by the net stress and the matric suction. Fredlund & Morgenstem (1977) stated that any two of the three stress variables shown below can be used:

1. $(\sigma - u_a)$ and $(u_a - u_w)$.
2. $(\sigma - u_w)$ and $(u_a - u_w)$.
3. $(\sigma - u_a)$ and $(\sigma - u_w)$.

The first and the second pairs of variables were used by Toll (1990), Alonso et al. (1990) and Geiser et al. (2006). The use of the first combination of the stress state variables was

verified by Fredlund & Morgenstem (1977) by performing a series of null tests on silts and kaolin. The null test was conducted by increasing each stress state variables by the same amount; therefore, there was no volume change and change in degree of saturation.

The second combination of stresses was used by Geiser et al. (2006) leading to a modified constitutive equation as follows:

$$\dot{\varepsilon}^{e}_{ij} = C'^{e}_{ijhk}\ \dot{\sigma}'_{hk} + C'_{s}\ \dot{s}\ \delta_{ij} \tag{2.18}$$

where C'^{e}_{ijhk} is the drained elastic compliance matrix, $\dot{\sigma}'_{hk}$ is the increment of Terzaghi saturated effective stress, C'_{s} is the elastic proportionality coefficient for the hydraulic behaviour, both of which assumed independent each with respect to the other. Reviewing the evolution in stress state variables shown above is a useful precursor to describing the development in shear strength for unsaturated soils which is presented in the next section.

2.8 Shear strength of unsaturated soils

Based on the Bishop (1960) equation, a tentative shear strength equation was suggested by Bishop et al. (1960) as follows:

$$\tau = c' + [(\sigma - u_a) + \chi\ (u_a - u_w)] \tan \phi' \tag{2.19}$$

where τ is the shear strength, c' is the effective cohesion and ϕ' is the effective internal friction angle. Equation 2.19 was based on Terzaghi's shear strength equation for the fully saturated case. Equation 2.19, however, did not overcome the disadvantages of the stress state variable equation proposed by Bishop (1960). The need to propose an equation based on two independent variables was then necessary. The shear strength of unsaturated soils, therefore, has been investigated by many researchers such as Fredlund et al. (1978), Escario & Saez (1986), Gan et al. (1988), Toll (1990), Öberg & Sällfors (1997), Toll & Ong (2003), Tarantino & Tombolato (2005) and Likos et al. (2010).

Fredlund et al. (1978) introduced an equation for shear strength of unsaturated soils which is an extension of Mohr-Coulomb failure envelope as follows:

$$\tau_f = c'' + (\sigma - u_a) \tan \phi^a + (u_a - u_w) \tan \phi^b \tag{2.20}$$

where c'' is the cohesion intercept when the two stress variables are zero, ϕ^a is the internal friction angle with respect to the net normal stress at constant suction, ϕ^b is the internal friction angle with respect to the matric suction at constant net normal stress.

Fredlund et al. (1978) defined the shear strength equation in terms of ϕ^a and then made the simplifying assumption that the net normal stress $(\sigma - u_a)$ contribution was controlled by ϕ' and also that c'' is the same as saturated cohesion intercept c'. Therefore, they simplified the shear strength equation as below:

$$\tau_f = c' + (\sigma - u_a) \tan \phi' + (u_a - u_w) \tan \phi^b \tag{2.21}$$

The failure envelope in Eq. 2.21 was assumed planar with ϕ' and ϕ^b as shown in Fig. 2.11. Data of Bishop et al. (1960), which was obtained for a compacted shale clay, were

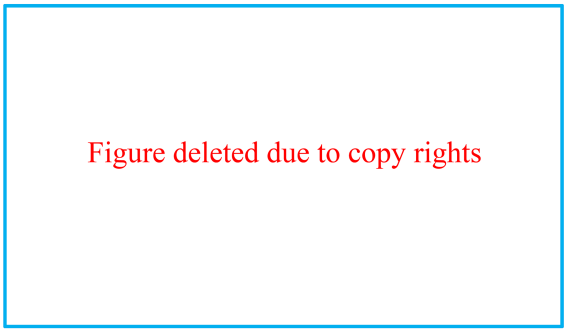

Figure 2.11: Failure envelope surface for an unsaturated soil, after Fredlund & Rahardjo (1993).

used to evaluate the above assumption and they found that the failure envelope is planar. Similarly, Ho & Fredlund (1982) found the same conclusions for sandy soils.

Escario & Saez (1986) studied clay and sand soils using a modified direct shear apparatus. A non-linear planar failure envelope between shear strength and suction was found from their study. This showed the inability of Eq. 2.21 to capture the behaviour as shown in Figs. 2.12b, 2.13b and 2.14b. The results for a Madrid grey clay and red clay (Guadalix de la Sierra) exhibited no linearity and variation of ϕ^b with suction. However, the results for the Madrid clayey sand showed that ϕ^b is constant at high values of suction (see Fig. 2.14b). Also at low suction values in Fig. 2.14b, the results showed variation of ϕ^b with suction (inverse relationship between suction and ϕ^b).

[a] 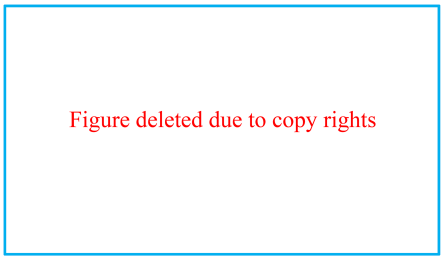

[b] 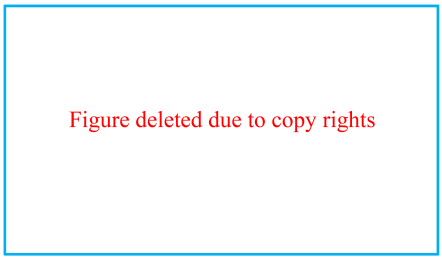

Figure 2.12: Direct shear results for Madrid grey clay (a) Shear strength versus net normal stress (b) Shear strength versus suction, after Escario & Saez (1986).

[a] 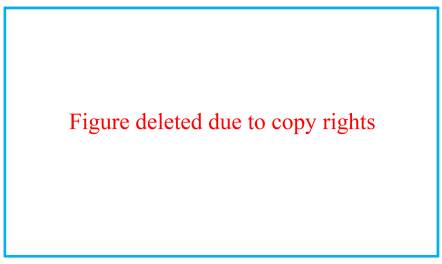

[b] 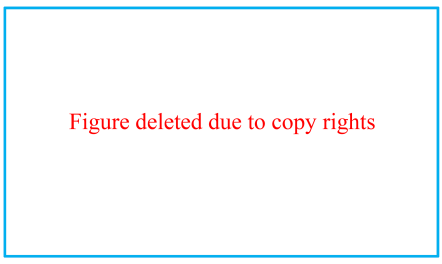

Figure 2.13: Direct shear results for red clay (Guadalix de la Sierra) (a) Shear strength versus net normal stress (b) Shear strength versus suction, after Escario & Saez (1986).

Vanapalli et al. (1996) suggested an empirical, analytical model to predict shear strength

[a] 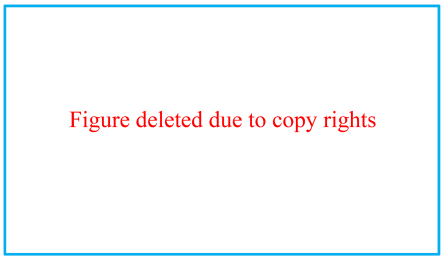

[b] 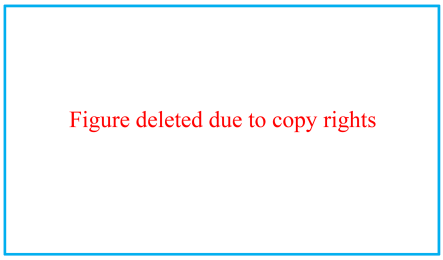

Figure 2.14: Direct shear results for Madrid clayey sand (Arena de miga) (a) Shear strength versus net normal stress (b) Shear strength versus suction, after Escario & Saez (1986).

in which Eq. 2.21 was modified to take into consideration the SWCC of the soil as below.

$$\tau_f = c^{'} + (\sigma - u_a)\tan\phi^{'} + (u_a - u_w)\left[\tan\phi^{'}(\frac{S - S_r}{100 - S_r})\right] \tag{2.22}$$

where S is degree of saturation and S_r is degree of saturation at residual suction which can be obtained based on the SWCC. The prediction of Eq. 2.22 showed a nonlinear relationship between shear strength and suction. However, the equation was applied only to tills and clays soils and as Vanapalli et al. (1996) pointed out an accurate measurement of SWCCs in simulated field condition (same void ratio) is required .

Khalili & Khabbaz (1998) modified the Bishop (1960) single effective stress equation (Eq. 2.14) in which a relationship between parameter χ and suction ratio was suggested as follow:

$$\chi = \left[\frac{(u_a - u_w)}{(u_a - u_w)_b}\right]^{-0.55} \tag{2.23}$$

where $(u_a - u_w)_b$ is the air entry value. The equation was then validated using different types of soils with a range of suction values from 40 to $\approx$ 1000 kPa and showed good agreement. However, it did not overcome the limitations of a single stress variable equation (2.14) and also was not validated for sandy soils with suction values less than 40 kPa.

More recently, Alonso et al. (2010) proposed two shear strength equations based on the effective stress equation as follows:

$$\tau = c^{'} + (\sigma - u_a)\tan\phi^{'} + s\ S_r^e \tan\phi^{'} \tag{2.24}$$

where S_r^e is effective degree of saturation and is given by:

$$S_r^e = \left[\frac{S_r - S_r^m}{1 - S_r^m}\right] \tag{2.25}$$

while the second shear strength equation is as same as Eq. 2.24, however with replacing S_r^e as follows:

$$S_r^e = S_r^\alpha \tag{2.26}$$

where S_r^m is a microscopic degree of saturation and α is a material parameter ($\alpha \geqslant 1$). The proposed equations were analysed using a few different soils from granular to high-plasticity clay materials. Validation of the proposed equations with the experimental data showed consistent results.

Limitations of the Fredlund et al. (1978) equation led others to propose alternative shear strength equations, however, the one suggested by Öberg & Sällfors (1997) is presented in the next section in more detail as it is accepted broadly and overcomes the limitation of ϕ^b variation.

2.8.1 Shear strength equation due to Öberg & Sällfors (1997)

Referring back to the Terzaghi (1936) equation for the effective stress for the fully saturated case:

$$\sigma^{'} = \sigma - u_w \tag{2.27}$$

The pore water pressure in Eq. 2.27 acts over the total surface area of the soil and the shear strength for the fully saturated case can be given by:

$$\tau_f = c^{'} + \sigma^{'} \tan \phi^{'} \tag{2.28}$$

The above two Eqs. 2.27 and 2.28 are no longer valid for unsaturated soils because water is not covering the entire total surface area (A_{total}) of the soil skeleton as shown in Fig. 2.15. The rest of the area which is occupied by air has a significant effect on the shear strength of unsaturated soils.

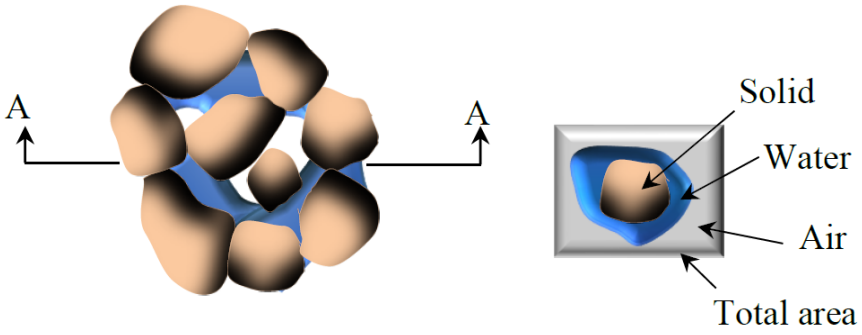

Figure 2.15: Soil skeleton structure.

The factor χ in Bishop's equation (see Eq. 2.14) is difficult to determine experimentally. Therefore, Öberg & Sällfors (1997) proposed an alternative of it as (A_w/A_{total}). Where (A_w/A_{total}) is the fraction of the pore area that is occupied by water. For simplicity, throughout this manuscript the shear strength equation that proposed by Öberg & Sällfors (1997) is called the (sS_r) equation. Hence, the proposed (sS_r) equation for the shear strength of unsaturated soils becomes:

$$\tau = c^{'} + (\sigma - \frac{A_w}{A_{total}} u_w - \frac{A_a}{A_{total}} u_a) \tan \phi^{'} \tag{2.29}$$

where $\frac{A_a}{A_{total}}$ is the part of the pore area occupied by air. Once more, the area ratios $\frac{A_w}{A_{total}}$ and $\frac{A_a}{A_{total}}$ are difficult to determine experimentally. Hence, Öberg & Sällfors (1997) replaced the area ratios by terms volume ratios S_r and $(1 - S_r)$, respectively. Therefore, the shear strength of the unsaturated soils can be re-written as:

$$\tau = c^{'} + (\sigma - S_r \; u_w - (1 - S_r) \; u_a) \tan \phi^{'} \tag{2.30}$$

where S_r is the degree of saturation. The proposed Eq. 2.30 used $\phi^{'}$ rather than ϕ^b (see Eq. 2.21) even for matric suctions lower than the air entry value. Equation 2.30 has the

advantage of simplicity. In other words, knowing the SWCC and shear parameters $c^{'}$ and $\phi^{'}$ for the soil, it would be possible to determine shear strength using Eq. 2.30 by assuming that the soil is under the atmospheric condition and therefore the equation will become:

$$\tau = c^{'} + (\sigma - S_r \; u_w) \tan \phi^{'} \tag{2.31}$$

where u_w has a negative value. Among others, Öberg & Sällfors (1997) were pioneers in using the S_r term in the calculation of the shear resistance of unsaturated soils. They proposed the equation based on the SWCC for the unsaturated soil. Comparisons between shear resistance of the proposed equation and that obtained from the experimental tests for different types of soils were undertaken in their study. For most of the soils that were used in their evaluations, the SWCCs were unavailable. Therefore, they assumed that the SWCC can be obtained by matching the grain size distribution curve to a similar grain size distribution curve of another soil for which an SWCC had been determined.

The range of suction values in which their equation was evaluated was from 0 to $\approx$ 1000 kPa. The agreements were good as shown in Figs. 2.16 and 2.17 (evaluations of only two soils are presented). The proposed equation also showed good match for the other soils, however, they proposed further testing and verifications to show how reliable the proposed equation actually is.

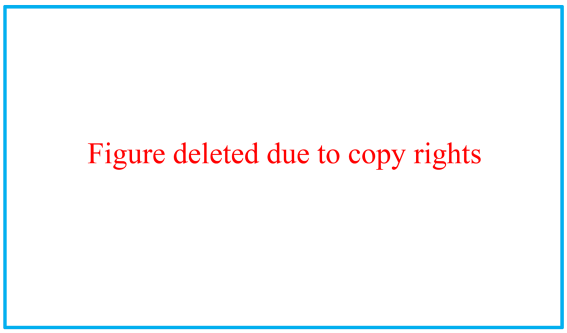

Figure 2.16: Shear strength versus matric suction for the Madrid grey clay, after Öberg & Sällfors (1997).

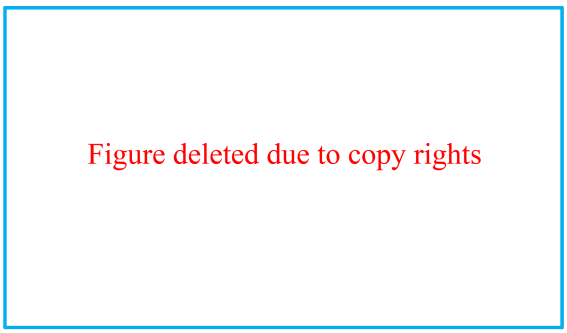

Figure 2.17: Total cohesion versus matric suction for the residual material from Sirerra do Mar., after Öberg & Sällfors (1997).

Due to its overcoming of the limitation of the Fredlund et al. (1978) equation that assumed a linear relationship between the internal friction angle and suction, a good match with experimental data, simplicity and the wide use of the equation by other researchers, the Öberg & Sällfors (1997) equation is, therefore, selected for evaluation with the experimental

results that will be conducted in this study. Since the work of the Öberg & Sällfors (1997), a number of studies have been available in which the actual measured SWCCs for the soils were obtained. Therefore, re-evaluation of the Öberg & Sällfors (1997) equation will be performed again in this study based on the actual measured SWCCs for the variety of the soil types and suction ranges.

2.9 General considerations about the direct shear test

The direct shear test is consider one of the oldest tests and the earliest attempt to measure shear strength was made by a French engineer Alexandre Collin in 1946, Head (1994). The equipment consists of a shear box which is a horizontally split container in which the lower half of the box can be slid horizontally along the other fixed top half due to steadily increasing horizontal forces. Therefore, shear forces can be developed along the horizontal surface. Serrated or grooved metal plates (see Fig. 2.18a) are placed at the top and bottom faces of the soil with the grooves perpendicular to the movement to generate shear forces as shown in Fig. 2.18b. The bottom plate is perforated to allow a free drainage of water during the test.

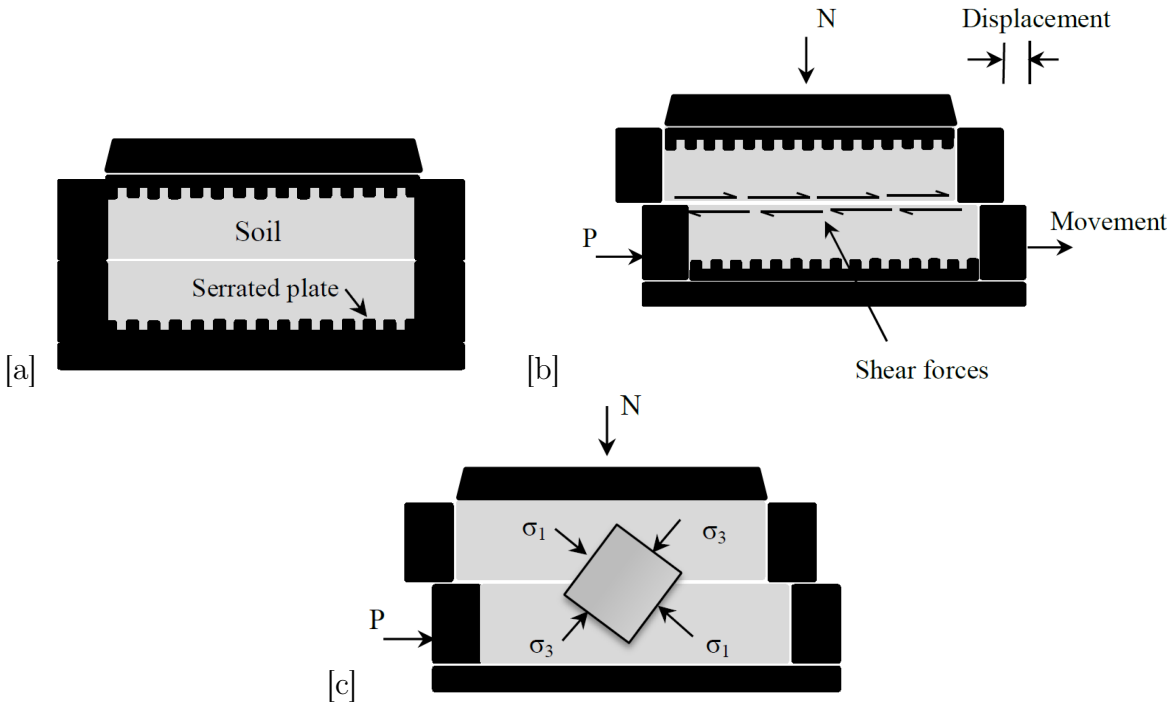

Figure 2.18: (a) Shear box showing serrated plates (b) Shear forces along the shear surface (c) Orientation of the principles stresses.

The normal stresses on the vertical and horizontal surfaces can be assumed constant with no shear stresses on these planes at a zero horizontal displacement value. However, rotation of the stresses happens once the test starts (see Fig. 2.18c). Additionally, the only stress variables available from the direct shear test are the normal and nominal shear stresses. Also, deformations throughout the sample are non-uniform and complex, therefore, the horizontal and vertical displacements cannot be easily used to determine the strains. This provides difficulties in understanding the direct shear test variables comparing to other laboratory tests, Liu (2006).

However, the recent development of the distinct element method (DEM) have provided better understanding of deformations and particle orientation in the direct shear test (e.g. Masson & Martinez (2001) and Liu (2006)). Figures 2.19a and b, for example, give an instantaneous velocity field obtained using DEM for dense and loose samples (after, Masson & Martinez (2001)). For both cases, particles in the lower half of the box displaced horizontally. However, the difference can be seen in the top half of the box as the dilation for the dense sample caused an upward movement. No relative movement at the top and bottom faces can be observed, therefore, the shear band (which is a thin layer localized along the shear surface) is not affected.

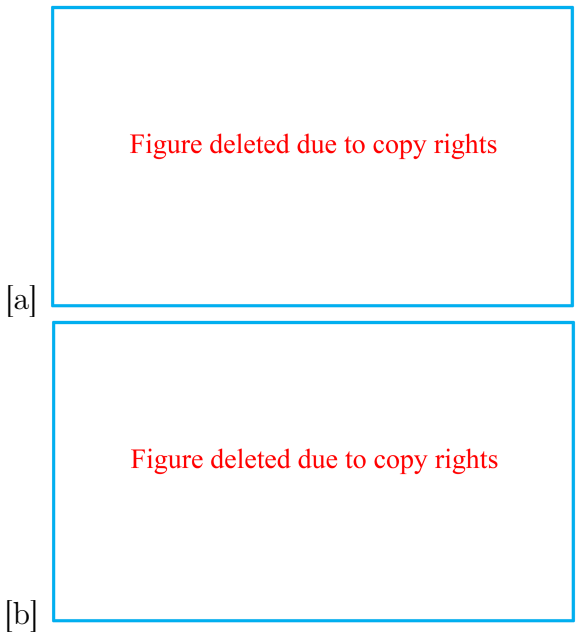

Figure 2.19: Velocity field obtained using DEM for (a) Dense sample(b) Loose sample, after Masson & Martinez (2001).

Another disadvantage of the direct shear test is that the box provides no control of water drainage; therefore, the test is unsuitable for undrained conditions. The thickness of the shear band depends on the particle size and for a sand soil the shear band is 10-20 or about 15 the particle size according to Yoshida (1994) and Vermeer (1990), respectively. Excess pore water pressures can be concentrated in the shearing zone but not the entire thickness of the sample. Therefore, water can migrate out or into the shearing zone and hence the test is not truly undrained.

The short duration of the test, however, has an advantage that the test can be considered suitable for general engineering practice and therefore can be used for unsaturated soils when it is compared to a drained triaxial test (long period of drainage), Carsuso & Tarantino (2004).

Over the last few decades, many investigations were conducted on unsaturated soils using the direct shear test where the bottom serrated plate has been replaced by a high air entry disk (HAED) (e.g. Escario (1980), Escario & Saez (1986) and Likos et al. (2010)). These studies gave no concern about the smoothness of the HAED.

Recently, Lings & Dietz (2004) conducted two types of tests on a dense coarse virgin Leighton Buzzard sand using a modified direct shear box. The serrated plates were used for the first set of the tests, while for the second set were excluded. They found very similar peak

friction angles between these two set of tests however dilative behaviour was underestimated when using the plates due to an inadequate initial bedding between the sand and the plates.

2.10 Water flow in unsaturated soils

Air can be configured between the voids in different arrangements depending on the degree of saturation. Two phases of air, occluded and continuous air, can be observed at high and at low degrees of saturation, respectively. The movement of air through the water phase and therefore flow law might be varied for each phases, Fredlund & Rahardjo (1993). Throughout this section, the fundamental concepts of flow characterization, Darcy's law and relationship between the coefficient of permeability and degree of saturation is presented.

Flow of water in unsaturated soils has been studied broadly and several concepts such as hydraulic head gradient, matric suction gradient and water content gradient have been suggested. In reverse order, the water content gradient definition is based on the premise that water can move from higher to lower water content zones. Water from lower water content zones, however, can also flow to higher water content zones in unsaturated soils. Thus this concept failed to signify hysteresis effects and stress history, Fredlund (1981). Flow of water once more cannot be characterized by the matric suction gradient since flow can happen from one region to another at different gradients of matric suction (increase or decrease of matric suction). The hydraulic head gradient can more properly describe water flow in unsaturated soils, Fredlund & Rahardjo (1993). The simple derived equation to express the hydraulic head is given by:

$$h_w = y + \frac{u_w}{\rho_w \, g} \tag{2.32}$$

where h_w is the hydraulic head, y is the gravitational head, u_w is the pore water pressure, ρ_w is the water density and g the gravitational acceleration.

Darcy's law which is given in Eq. 2.32 was applied to the field of unsaturated soils by several researchers such as Buckingham (1907) and Richards (1931). Application of Darcy's law in unsaturated soils was suggested by assuming that air filled pores are similar to the solid part, therefore, unsaturated soil can be considered similar to the saturated case with reduced water content, Childs (1969).

$$v_w = -k_w \frac{\partial h_w}{\partial y} \tag{2.33}$$

where v_w is the rate of water flow through a soil mass, k_w is the coefficient of permeability and $\frac{\partial h_w}{\partial y}$ is the hydraulic head gradient.

Apart from saturated soils, the coefficient of permeability in unsaturated soils is not constant and it is significantly affected by the water content or the matric suction, Fredlund & Rahardjo (1993). Once soil becomes unsaturated, air enters the large pores causing water to flow to smaller pores. Pore volume of water continues to decrease for further increase of suction. The coefficient of permeability, hence, decreases. Figure 2.20 illustrates the air-water interface for different stages of matric suction and degree of saturation.

2.11 Bulk and meniscus water in unsaturated soils

The arrangement of water within the voids has a significant effect on inter-granular forces and hence on the shear strength of the soil and has an inverse relationship with suction,

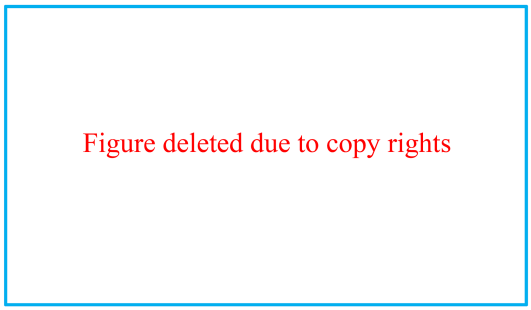

Figure 2.20: Air-water interface at different suctions, after Childs (1969).

Vasallo & Mancuso (2000). Wheeler & Karube (1995) and Wheeler (2006) defined two different forms of liquid water in unsaturated soil: bulk and meniscus water as shown in Fig. 2.21a. Accordingly; at high degrees of saturation (low suction), soil follows the bulk water form. As long as the air entry value of the sample is not exceeded, there is bulk water form between the particles. At low degrees of saturation (high suction), the meniscus water form is more pronounced when the applied suction is greater than the air entry value, Vasallo & Mancuso (2000).

Understanding these two liquid forms during the test (at shearing) and their effect on shear strength of the soil is significant. Romero & Vaunat (2000) studied the soil water retention curve (SWRC) for deformable clays and delimiting zones in the water retention curve were defined, which is controlled by water ratio (volume of water to volume of solids). Two zones: intra-aggregate water (adsorbed water) and inter-aggregate water were recognized. In the latter zone, air is occluded and the water ratio is highly sensitive to loading. The above short overview of water forms will be referenced throughout this thesis to explain water migration behaviour that happened in the experimental tests conducted in this study.

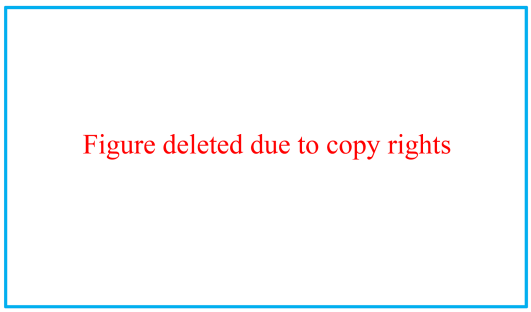

Figure 2.21: (a) Bulk and menisci water forms (b) Water-air meniscus between two solid spheres, after Fisher (1926) (c) Distribution of forces between two solid spheres.

2.12 Increase of shear strength parameters $c^{'}$ and $\phi^{'}$ for unsaturated soils

Early works in field of unsaturated soil mechanics make the assumption that $c^{'}$ and $\phi^{'}$ are constant and independent of suction. However, a number of studies have reported an increase in internal friction angle for unsaturated soils. Röhm & Vilar (1995) established a

maximum difference of friction angle of about 2.5 degrees for suction ranges between 0 to 400 kPa for a sandy soil using Eq. 2.21. Wheeler & Sivakumar (1995) found an increase in internal friction angle of about 3.5 degrees in the range of suctions between 0 to 200 kPa for compacted Speswhite kaolin for triaxial compression tests.

Toll (2000) studied the influence of fabric on the shear behaviour of clayey soils compacted dry of optimum. The internal friction angle with respect to the net stress ϕ^a (see Eq. 2.20) was found to be greater than the saturated internal friction angle $\phi^{'}$ due to aggregation of the particles. Also the internal friction angle with respect to the matric suction ϕ^b was found to be less than $\phi^{'}$ and equal to zero when the soil approached the dry condition.

Feuerharmel et al. (2005) conducted a series of direct shear tests on saturated and unsaturated colluvium soils (named as AV and RO). Suction was applied using the axis translation method. The applied suction values were 0, 50, 100 and 200 kPa and the net normal stresses (in relation with water phase) $(\sigma - u_w)$ were 50, 100 and 200 kPa.
For the AV soil, they found $\phi^b > \phi'$ by 7.6^o where $\phi' = 32^o$. While for the RO soil, ϕ^b was greater than ϕ' $(= 27.1^o)$ by 9.8^o. Where ϕ^b was taken as an average value since it varied at different $(\sigma - u_w)$ values. The increase of internal friction angle with suction was attributed to the change in the soil structure due to the suction elevation.

Toll et al. (2008) conducted a series of triaxial tests on artificially bonded sand for unsaturated samples at constant water content while suction was applied using the axis translation technique. The sample was prepared by mixing 87% sand and 13% kaolin, then the mixture was fired in a furnace at 500 ^{o}C. Three radial net stresses: 50, 100 and 300 kPa and a range of suctions from 0 to 560 kPa were used. The data were presented at the critical state using Eq. 2.20. Three different internal friction angles were stated according to the water retention curve. For suctions less than the air entry value, ϕ^a and ϕ^b were found to be equal to $\phi^{'}$ $(\phi^a = \phi^b = \phi^{'})$. For the range between the air entry value and the residual suction, $\phi^a > \phi^{'}$ and $\phi^b = \phi^{'}$ were observed. Finally at the residual suction, ϕ^a remained constant and ϕ^b started to reduce. To put this into context, a difference of 4 degrees between ϕ^a and $\phi^{'}$ was observed. This behaviour was explained due to a change in fabric of the soil.

Kim et al. (2011) conducted a series of direct shear tests for both unsaturated and saturated samples of weathered granite soil called "Yeonki" with sand content of 78.9%. An increase in internal friction angle of 5.4^o and cohesion of about 10.9 kPa were found when the undisturbed-unsaturated (U-U) sample was compared to the disturbed saturated (D-S) sample. No explanation for this increase of shear strength parameters was given by the authors.

Although the above investigations showed the possibility of increase the internal friction angle and cohesion with the suction (moisture content change), no clear explanation had been proposed by the researchers. This change of shear strength parameters significantly affects the shear resistance of the soil under different moisture contents.

2.13 Shear strength in fully saturated conditions

Horn & Deere (1962) conducted a series of direct shear tests on sands using different minerals such as calcite, quartz and microcline feldspar. These tests were performed to study the frictional characteristics of these minerals. The tests were carried out using four different surface moistures: "oven-dried", "oven-dried/air-equilibrated", "saturated/air-equilibrated" and "saturated" conditions. Samples for the "oven-dried" condition were prepared by placing soil into oven for several hours at temperature of 105 ^{o}C then cooling down in a laboratory

environment under a relative humidity (RH) less than 7%. The second condition "oven dried/air-equilibrated" samples were prepared in the same manner as "oven dried" condition samples however they allowed to cool down under a known RH ranging from 17% to 97%. Samples of "dried/air-equilibrated" were initially saturated and then stored in a room of RH between 30% and 40% for several days. At the time when the samples were tested, the visible surface moisture evaporated. Finally, the "saturated" tests were prepared in fully saturated conditions where had water slightly covered the sliding surfaces. A slow shear rate of 17.7 mm/min (0.7 inch/min) was used for most of the tests, while a number of tests were performed under a faster shear rate of 152.4 mm/min (6 inch/min).

Figure 2.22a shows the frictional resistance (shear resistance) versus normal load in which a higher frictional resistance of the "saturated" sample when compared to the "oven-dried/air-equilibrated" and "saturate/air equilibrated" was obtained, where μ in Fig. 2.22 denotes the frictional coefficient. Samples which where initially saturated then air-dried were able to retain more moisture than those samples which were oven dried and allowed to adsorb moisture from the air under a RH value of 28%.

Figure 2.22b shows the effect of surface roughness on the frictional resistance of quartz with two different surfaces: roughened and polished for "oven dried/air-equilibrated" and "saturated" samples. These tests were conducted at a slow shear rate. The roughened surfaces were prepared by grinding them with No. 240 carborundum grit. Higher frictional resistance was obtained for the samples with roughened surfaces than those with polished surfaces.

The above findings of high shear resistance for saturated sands (using different minerals) will be referenced throughout this thesis to explain high shear strength behaviour that was obtained for saturated samples conducted in this study.

2.14 Plastic (wetting) collapse in unsaturated soils

Reduction in suction upon inundation is the major cause of the collapse of unsaturated soils, Matyas & Radhakrishna (1968), Escario & Saez (1986), Cox (1978), Lloret & Alonso (1980), Maswoswe (1985) and Blanchfield & Anderson (2000). Near to full saturation, a large volume change can occur and this is the case for clay soils, Alonso et al. (1990), and for coarse-grained soils, Blanchfield & Anderson (2000).

The reduction in suction causes a decrease of effective stress in the soil. As suction decreases upon wetting, the friction between the particles reduces and then the overburden pressure will mobilize the movement. After collapse, a closer packing of the soil particles can be produced as the particles are interlocking after the failure.

The degree of collapse significantly depends on the availability of the space between the particles. At the fully interlocking position for coarse-grained soils, the collapse is limited due to small space accessibility. The two stress state variables of $(\sigma - u_a)$ and $(u_a - u_w)$ are best to analyse the volume change of the unsaturated soils, Barden et al. (1969).

When the water table is lowered, the effective stress of the soil will increase causing a reduction in volume (settlement). However, if the soils are then inundated, the effective stress will decrease and collapse will happen. According to this wetting behaviour, the effective stress equation such as proposed by Bishop (1960) fails to explain wetting and collapse behaviours near saturation.

Plastic collapse also can be observed when the sample is wetted by adding water during shearing. This observation which is due to wetting behaviour during shearing was also found by several researchers such as Nicotera (2000) and Casini et al. (2011). In terms of the

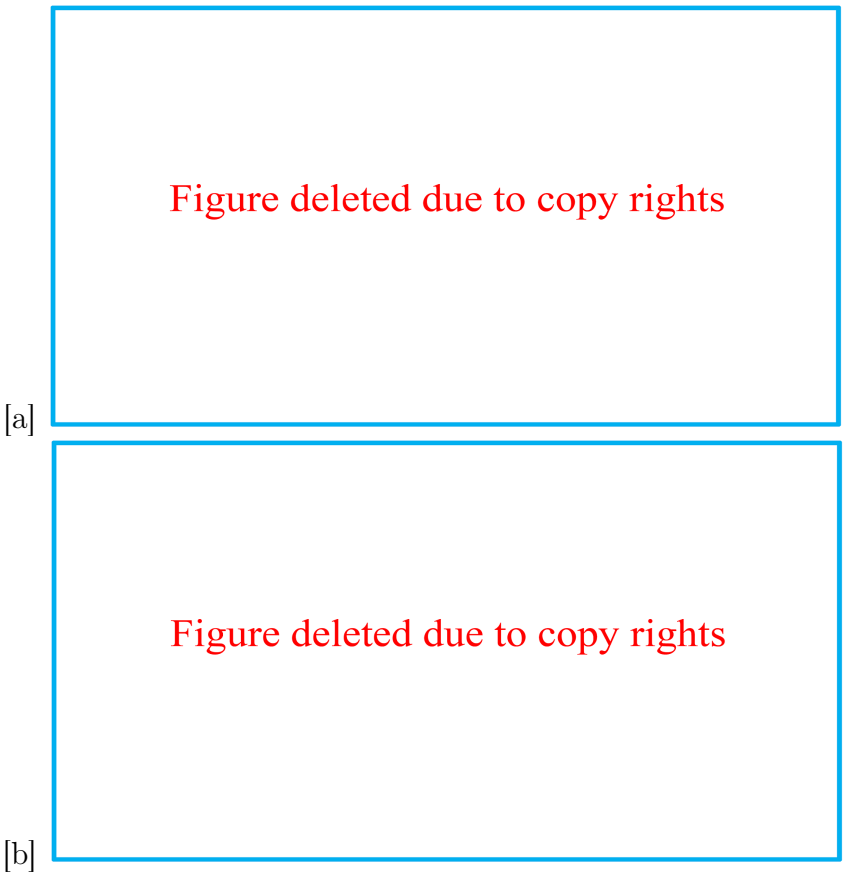

Figure 2.22: Frictional characteristics for the (a) surface moisture history samples- polished surfaces of microcline feldspar (b) polished and roughened surfaces of milky quartz, after Horn & Deere (1962).

latter, a series of direct shear tests were performed on a silty sand soil at three different water contents. The samples were then wetted at peak during the shearing stage. Wetting collapse (as they called it) happened and caused reduction in volume and shear resistance of the sample.

2.15 Incorporation of unsaturated soil mechanics in analytical and numerical models

Application of unsaturated soil mechanics theory to computational methods has been studied by many researchers and works have involved the incorporation of the unsaturated soil mechanics into modified numerical models. Quasilinear based procedures to study the flow of water for both saturated and unsaturated soils have been studied by Connell (1999). Based on the finite element (FE) method, Xie et al. (1998) studied flow in unsaturated soils. Recently, Lu et al. (2006) conducted a study of the climate change effect on slope stability for partially saturated expansive soil using the FE method.

A number of analytical studies were found in the literature that studied active and passive thrust of unsaturated soils. Stanier & Tarantino (2010) used Eq. 2.31 to make a prediction of active thrust for a retaining wall supporting unsaturated soil based on the upper and lower bound theorems.

In terms of a numerical bearing capacity analysis, Balzano et al. (2012) proposed an equation for the bearing capacity of partially saturated granular soil based on the upper bound theorem (see Eq. 2.38). The proposed equation was restricted to a two block failure mechanism. Such a study is limited by the nature of what can be dealt with using hand calculations. More complicated cases (more than three blocks failure mechanism) might be impractical due to the difficulty in using the Balzano et al. (2012) equation.

2.16 Bearing capacity for unsaturated soils

The bearing capacity for dry and fully saturated soils has been explored broadly by many researchers. Terzaghi (1943) was the first to propose a theory for assessment of the ultimate bearing capacity for a rough, strip footing as:

$$q_{ult} = c\ N_c + q\ N_q + \ 0.5\ B\ \gamma\ N_\gamma \tag{2.34}$$

where q_{ult} is the ultimate bearing capacity of the soil (kPa), q is the surcharge (kPa), B is the footing width (m), γ is the unit weight of soil (kN/m^3) and N_c, N_q and N_γ are the bearing capacity factors. For a cohesionless soil ($c = 0$) and a footing placed on the surface, Eq. 2.34 can be rewritten as:

$$q_{ult} = 0.5\ B\ \gamma\ N_\gamma \tag{2.35}$$

Equations 2.34 and 2.35, however, underestimated bearing capacity for unsaturated soil. Investigations to study the bearing capacity of unsaturated soils were, therefore, carried out by several researchers such as Steensen-Bech et al. (1987), Fredlund & Rahardjo (1993), Costa et al. (2003), Vanapalli & Mohamed (2007) and Oh & Vanapalli (2011).

Shallow footings generally are placed above the water table in soil in which the pore water pressure is negative. Therefore, bearing capacity for unsaturated soils can be considered to have a cohesion that consists of two components: effective cohesion and matric suction. As a result, the conventional bearing capacity concept can be applied to unsaturated soil mechanics, Fredlund & Rahardjo (1993).

From this point of view, Fredlund & Rahardjo (1993) extended Terzaghi's bearing capacity theory which is based on effective stress concepts to the unsaturated field. This modification of bearing capacity equation added another stress state variable to the equation derived from the shear strength equation (Eq. 2.21). The proposed equation, however, suffered from the same limitations as Eq. 2.21.

Oloo et al. (1997) proposed an equation to estimate bearing capacity of unsaturated fine-grained soils based on Terzaghi's effective stress approach as follows:

$$q_{ult(unsat)} = \Big[[c^{'} + (u_a - u_w)_b \tan\phi^{'}] + [(u_a - u_w) - (u_a - u_w)_b] \tan\phi^b]\Big]\ N_c + \ 0.5\ B\ \gamma\ N_\gamma \tag{2.36}$$

where $q_{ult(unsat)}$ is the ultimate bearing capacity of unsaturated soil, $c^{'}$ is the effective cohesion, $(u_a - u_w)_b$ is the air-entry value, $(u_a - u_w)$ is the matric suction, $\phi^{'}$ is the internal friction angle, ϕ^b is the internal friction angle with respect to matric suction. N_c and N_γ are based on ϕ' $(= \phi^b)$ for matric suctions less than the air entry value and ϕ^b for matric suctions greater than the air entry value. Equation 2.36 is based on assumptions that the failure envelope is bilinear and a delimited zone was defined according to value of ϕ^b as shown in Fig. 2.23. It could be argued that at higher suctions after residual suction, the

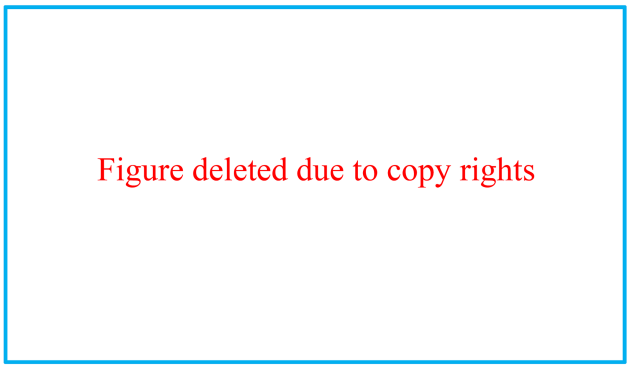

Figure 2.23: Variation of bearing capacity with respect to suction for different types of soils, after Oh & Vanapalli (2011).

shear strength of unsaturated soil decreases and hence bearing capacity. Equation 2.36, therefore, leads to an overestimated bearing capacity value for matric suctions greater than the residual suction.

Fathi & Vanapalli (2006) proposed a semi-empirical equation for the bearing capacity of a surface footing for coarse-grained soils based on their experimental results as follows:

$$q_{ult(unsat)} = [c^{'} + (u_a - u_w)_b \ (1 - S^{\psi} \tan \phi^{'}) + (u_a - u_w)_{AVR} \ S^{\psi} \tan \phi^{'}] \ N_c \ \xi_c + \ 0.5 \ B \ \gamma \ N_\gamma \ \xi_\gamma \tag{2.37}$$

where $(u_a - u_w)_b$ is the air entry value, S is the degree of saturation, $(u_a - u_w)_{AVR}$ is the average between matric suction directly beneath the stress bulb and a specific depth, ψ is a fitting parameter and ξ_c and ξ_γ are the shape factors from Vesic (1973). Equation 2.37 did not, however, overcome the limitations of Eq. 2.21 and it could not be applied for fine-grained soils, Oh & Vanapalli (2011).

Following on from the Balzano et al. (2012) study (Section 2.15), they proposed an equation for bearing capacity as follows:

$$q_{lim} = q_o \ N_q + \ 0.5 \ B \ \gamma \ N_\gamma + 0.5 \ N_{\gamma_w} \ \gamma_w \ B \ + N_{H_w} \ \gamma_w \ H_w \tag{2.38}$$

where q_{lim} is the bearing capacity, q_o is the overburden pressure, N_{γ_w} and N_{H_w} are the factors that account for the pore-water pressure and the position of the water table H_w, respectively. For unsaturated soil, the pore water pressure was related to the degree of saturation via a water retention function shown below:

$$S_r = \begin{cases} (1+ \ (-\alpha \ u_w)^n)^{-m} & when \ (u_w \leq 0) \\ 1 & when \ (u_w > 0) \end{cases} \tag{2.39}$$

where α, n and m are soil parameters.

The results obtained from Eq. 2.38 for a two block failure mechanism overestimated the bearing capacity values. This study was recorded by Balzano et al. (2012) as a comparative approach for investigating the bearing capacity of unsaturated soils.

The above short overview on the bearing capacity for unsaturated problems raised several issues. The emphasis of this study will be, therefore, to understand the influence of several factors on the bearing capacity of surface and buried footings for an unsaturated sand. These factors include matric suction, overburden stress and variation of internal friction angle and cohesion on the bearing capacity for unsaturated soils. Investigating the bearing capacity by using a physical model will also provide results that can be used to evaluate the modified numerical DLO method (as mentioned previously in Chapter 1).

2.17 Limit analysis

Stability problems in soil mechanics can be analysed through several methods such as limit equilibrium and limit analysis. Limit analysis, which is more rigorous than limit equilibrium method, is a direct method that can determine the maximum load sustainable by a body or structure, which is assumed:

1. not to deform prior to collapse;

2. to deform at a constant load subsequently (e.g. a rigid-plastic idealization).

In the limit analysis method, regardless of the complexity of the geometry or loading condition, it is possible to have a reasonable and realistic value of collapse load, Chen (1975). In contrast to limit equilibrium method, limit analysis takes the stress-strain relationship of the soil into consideration via the flow rule. As long as the direction of the plastic strain increment vector is perpendicular to the failure surface, the normal or associative flow rule is valid.

The stress-strain relationship of most soils can be defined by a simple straight line and a peak or failure stress followed by softening to a critical stress as shown in Fig. 2.24a. In limit analysis, the stress-strain curve is idealized as two straight lines as shown in Fig. 2.24b. The simplification of the stress-strain relationship serves to reduce the required parameters for modelling. However, this is based on the assumption that full shear strength is mobilized everywhere with deforming soil.

In limit analysis, lower bounds are obtained in which the equilibrium is preserved, stress boundary conditions satisfied and the yield criterion not exceeded by the stress within the problem domain, whereas using energy balance or kinematic methods, upper bounds for the problem are obtained, Chen (1975). The concept of normality used by Drucker et al. (1952) allowed development of the upper and lower bound theorems of plasticity.

[a] Figure deleted due to copy rights

[b] Figure deleted due to copy rights

Figure 2.24: Stress-strain relationship for (a) Elastic perfectly-plastic, after Chen (1975) (b) Rigid-plastic.

2.17.1 Yield surface

The yield surface can be defined as the stress state that initiates plastic flow, Chen & Liu (2012). Many yield surfaces to describe the strength of the soil have been developed such as Tresca, von Mises, Drucker-Prager and Mohr-Coulomb. The yield criterion is the mathematical relationship between the peak shear stress and the shear strength of the material, Aysen (2002). The most broadly and common yield criteria used in soils is Mohr-Coulomb, Griffiths (1990).

The yield criterion in the Mohr-Coulomb theory is based on an internal friction angle in which stresses at failure can be defined. Vermeer & Borst (1984) stated that the Mohr-Coulomb criterion can be used to describe frictional and granular materials. For frictional materials, the yield surface can be produced using the Mohr-Coulomb model as shown in Fig. 2.25. where $c^{'}$ is the intercept of the yield surface with the y-axis that present cohesion of the soil.

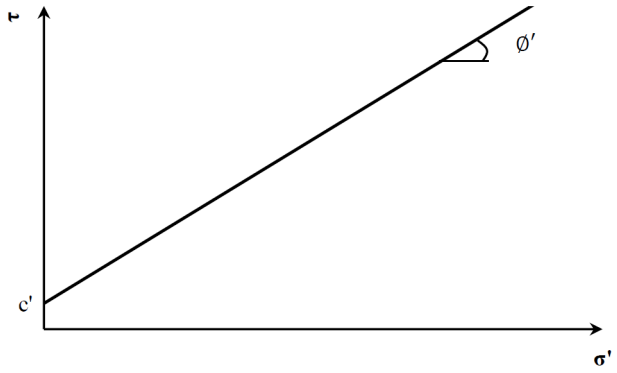

Figure 2.25: Linear Mohr-Coulomb yield surface.

2.17.2 Upper bound

The upper bound theorem determines a load that is greater than or equal to the actual failure load (assuming fully plastic behaviour). By equating the internal energy dissipated to the work done by the external forces in a collapse mechanism, the upper bound can be found, Chen (1975). The failure mechanism can be produced by determining a kinematically admissible failure mechanism or velocity field which means the deformations associated with the assumed mechanism can actually physically occur, Powrie (2013). The failure mechanism should satisfy compatibility, the flow rule, and velocity boundary conditions, Lyamin et al. (2005). The kinematics of the mechanism are determined by the flow rule.

Figures 2.26a and b illustrate the relation of the strain vector to the failure surface for frictionless and frictional soils. A Mohr-Coulomb yield criterion is applicable in the case of

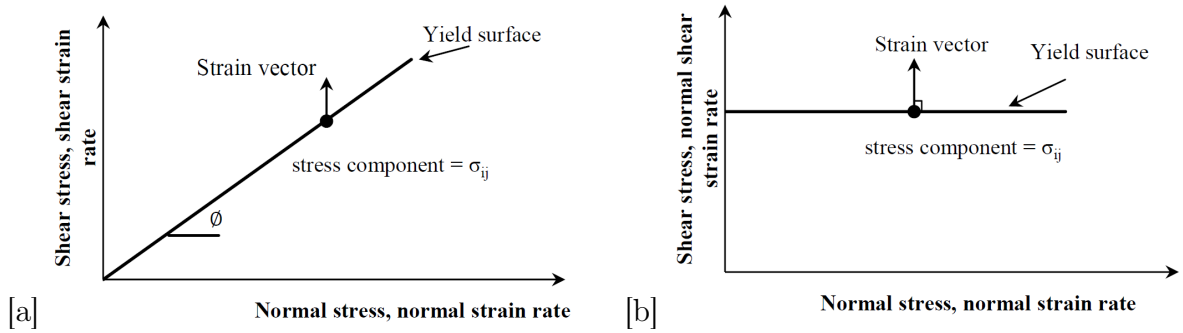

Figure 2.26: Relation of the strain vector to the failure surface (a) Not normal for idealized fiction model (b) Normal for idealized non-frictional (dilational) model.

frictional soil and the shear strength depends on both shear stress and normal stress due to friction. For instance, if a block of soil is sheared horizontally by a horizontal force of (T) and a normal force of (N) on a horizontal plane, there is no vertical motion and the direction

of displacement vector will be as shown in Fig. 2.26a. This is a non-associative plastic flow case as the displacement vector is not normal to the yield surface. In a frictionless soil, on the other hand, the shear strength of soil is unrelated to the normal stress and it is constant. In such soils, the displacement vector is logically associative as it is normal both on yield surface and in the direction of the shear stresses as shown in Fig. 2.26b. A Tresca yield criterion is applicable and no volume change or dilation is provided.

2.17.3 Non-associativity

The effect of the flow rule on bearing capacity has been studied by several researchers. Loukidis et al. (2008) performed finite element analyses of a rigid strip footing placed on frictional soil. The analyses were based on both associative and non-associative flow rules and the results for the non-associative flow rule showed a $15-30\%$ reduction in the N_γ term when compared to the associated flow rule (pure plasticity model). To put this into context, this is equivalent to utilising an internal friction angle 3% less than the actual angle.

Loukidis & Salgado (2009) studied the effect of the flow rule on both strip and circular bearing capacity footings using the elastic-perfectly plastic Mohr-Coulomb finite element method. A difference of 11.75% for a rough strip footing (with $c^{'} = 0.002$ kPa, $\gamma = 20$ kPa and surcharge q = 0 kPa) in N_γ value between use of an associative ($\phi^{'} = \psi = 45^o$) and a non-associative ($\phi^{'} = 45^o,\ \psi = 25^o$) flow rule was reported. To put this into context, this is equivalent to a 0.48^o change in the value of $\phi^{'}$. Here Loukidis & Salgado (2009) obtained 239.9 and 211.7 for N_γ values for associative and non-associative cases, respectively.

2.18 Discontinuity Layout Optimization (DLO) procedure

The DLO procedure is a computational limit analysis method that directly identifies the collapse load for stability problems. The procedure allows either the determination of load or strength for any stability problem. Failure mechanisms involving several blocks also can be displayed as shown in Fig. 2.27d. The procedure was first described by Smith & Gilbert (2007*a*).

The basic principle of the DLO is based on recognizing a critical layout of lines of discontinuity to create failure mechanism. These lines are the slip-boundaries between the rigid blocks due to the applied loads. A wide range of different failure mechanisms can be produced by utilising high numbers of nodes, then discretizing these nodes by connecting them each to another as shown in Fig. 2.27 a-d.

2.19 Energy dissipation

Following Smith & Gilbert (2007*a*) and Smith & Gilbert (2007*b*) in the presence of static water, the rate of internal energy dissipation and work done against body forces for the problem of a Mohr-Coulomb material with self-weight γ, cohesion c and angle of friction ϕ collapsing as a set of sliding blocks where each discontinuity (or interface) i between adjacent sliding blocks which have relative shear and normal displacement jumps of s_i and n_i can be written as:

$$E = \sum_{i=1}^{m} (c_i\ L_i\ s_i + U_i\ n_i + W_i\ s_i \sin\theta_i\ + W_i\ n_i \cos\theta_i) \tag{2.40}$$

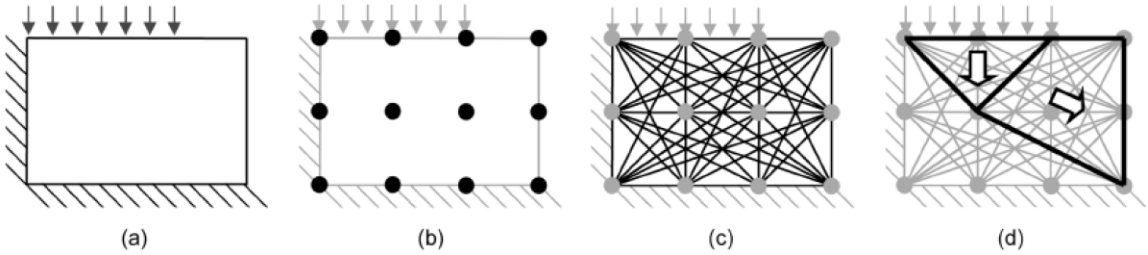

Figure 2.27: Example DLO procedure: (a) Starting problem (surcharge applied to block of soil close to vertical cut) (b) Discretization of soil using nodes (c) Interconnection of nodes with potential discontinuities (d) Identification of critical subset of potential discontinuities using optimization (giving the layout of the slip-lines in the critical failure mechanism), after Gillbert et al. (2010).

where m is the number of interfaces, U_i and W_i are respectively the pore water force and weight of the strip of soil above interface i and L_i and θ_i are the length of interface i and the angle of interface i to the horizontal, respectively. For a limit analysis approach, $n_i = |s_i| \tan \phi'$. This equation applies equally to saturated and unsaturated conditions. For saturated conditions, the following equation is used:

$$U_i = \int_0^L u.dl \tag{2.41}$$

where u is the pore water pressure. The strip weight of the soil W above a discontinuity (see Fig. 2.28) can be obtained by double integration of the unit weight over the strip area. By matching the internal energy to the external work done, it is possible to determine the critical collapse load and mechanism.

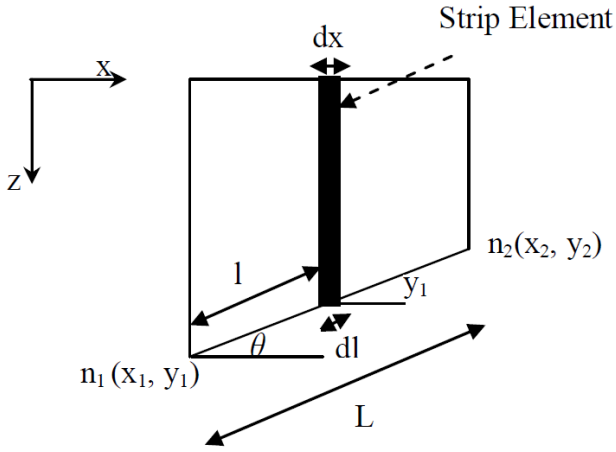

Figure 2.28: Strip weight above the discontinuity showing nodes and strip element.

2.20 Summary of the chapter

This chapter discussed the definition, overview and principles of unsaturated soil mechanics, methods of controlling and measuring the suction, experimental studies found in the

literature and the most relevant phenomena to this PhD study. The objectives were first to assess the requirements to modify the experimental apparatus and the numerical modelling that meet with the aims of this study and second to characterize the list of behaviours of unsaturated soil to be addressed in this research. Several shear strength equations for unsaturated soils were presented. An overview of the limit state analysis generally and upper bound theorem specially was also presented. This was essential as the numerical part of this study is based on the upper bound theorem.

Chapter 3

Experimental Setup and Test Procedure

3.1 Introduction

The experimental works performed in this research aimed to investigate the effect of suction on the shear strength of unsaturated sand using a modified direct shear test, and on bearing capacity through the modelling of a scaled strip footing. This chapter discusses the materials used, design of the direct shear and bearing capacity apparatuses, sample preparation techniques, suction measurement using the filter paper method, suction application using the HCT and a short review of the particle image velocimetry (PIV) technique. A test schedule including numbers of tests performed and repeatability is also presented in this chapter.

3.2 Choice of test material

At the beginning of the experimental programme, four different Leighton Buzzard sand fractions: A, B, C and D supplied by the David Ball Company, UK, were assessed for suitability in the test programme.

The grain size distribution curves for the selected materials obtained using sieve analysis are shown in Fig. 3.1. Table 3.1 shows the preliminary physical parameters obtained for these sands. Matric suctions for fractions B and D were obtained using the filter paper method. Measurement of suction was extended beyond the residual suction of the two selected fractions and the results showed suction ranges of 0 to 1.5 and 0 to 8 kPa for fraction B and D, respectively.

The suction range for fraction D was found compatible with the range of the suctions that can be applied using the HCT for both direct shear and bearing capacity rigs, therefore, no attempts were performed for suction measurements for fractions A and C. Fraction D was, therefore, selected as the research material. The wider range of suction for fraction D has another advantage in that air entry and residual suctions can be distinguished easily allowing investigation of shear resistance and bearing capacity at these two specific suctions.

A magnified image of fraction D particles is shown in Fig. 3.2a and shows rounded to sub-rounded particles. In addition to sieve analysis, particle size distribution was also to be measured using a MasterSizer apparatus. However problems were encountered. Figures 3.2b, c, d and e show photos of the oven dry fraction D sand poured into de-ionized water in the MasterSizer dispersion chamber in which no deflocculant was used. Surprisingly, sticking behaviour and aggregation of the finer fraction particles was observed even the machine was stirred to separate the particles. Repeat tests confirmed the stick behaviour and aggregation. Two other different materials were tested: a kaolin and a sand (63 - 75 μm in particle size)

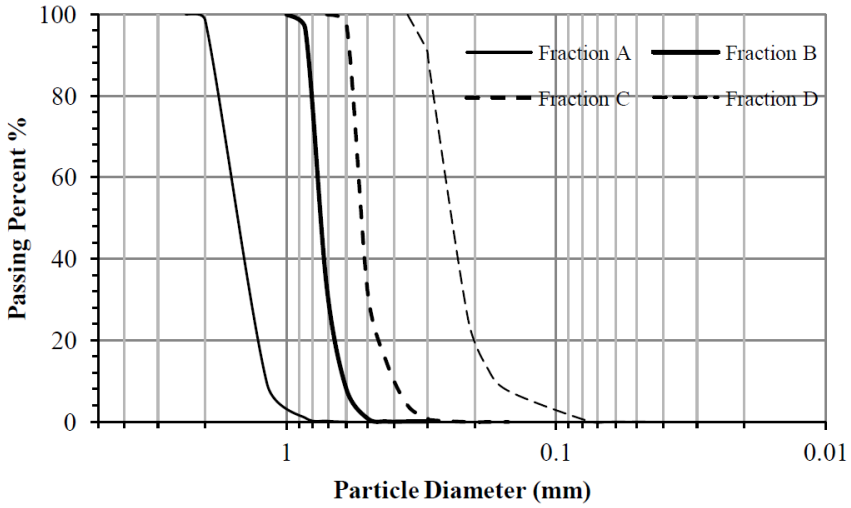

Figure 3.1: Particle size distribution curves for four different sands (fractions A, B, C and D).

in order to eliminate any anomalies that may arise due to the machine, in both cases the results showed no sticking behaviour.

Table 3.1: Physical properties for the selected sands.

Soil properties	Fraction A	Fraction B	Fraction C	Fraction D
G_s	2.65	2.65	2.65	2.65
D_{10}, (mm)	1.225	0.625	0.4	0.17
D_{30}, (mm)	1.375	0.715	0.49	0.22
D_{60}, (mm)	1.63	0.795	0.577	0.26
Coefficient of uniformity, cu	1.33	1.27	1.44	1.529
Coefficient of curvature, cv	0.94	1.02	1.04	1.095
Particle size range, (mm)	0.8-2.4	0.475-1.0	0.285-0.725	0.075-0.3
Internal friction angle, ϕ (degrees)	—	—	—	44.1
Cohesion, c (kPa)	—	—	—	13.45
γ_{dry}, (kN/m^3)	—	—	—	15.30
γ_{sat}, (kN/m^3)	—	—	—	19.33

3.3 Sample preparation and experimental procedure for the filter paper test

In the filter paper method, soil suction is a function of the water absorbed by the filter paper and is measured using a pre-determined calibration curve. Accordingly, the SWCC can be established including the air entry value and residual suction. The procedure for measuring matric suction using the filter paper method in this study was as follows:

1. The soil was poured into a small container of height 20 mm and diameter of 158 mm (volume of 3.921×10^{-4} m^3) to obtain a pre-specified unit weight (15.30 kN/m^3).

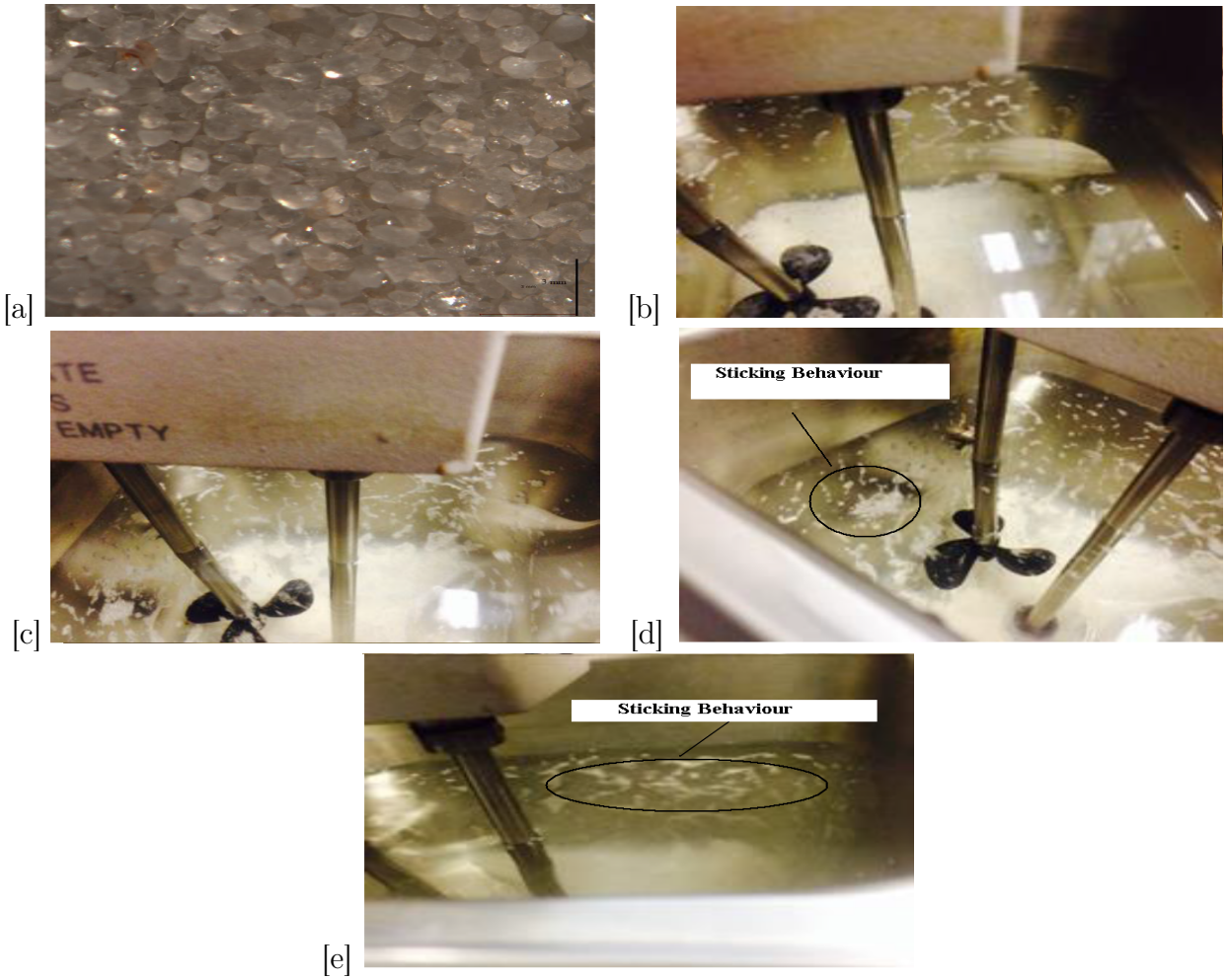

Figure 3.2: (a) Microscopic image for the fraction D sand used in this study. Photos of fraction D sand in the Matersizer device showing aggregation (b) the first test (c) the first test (d) the second repeat test (e) the second repeat test.

2. The container was fully submerged in a tray filled previously with de-aired water and then the tray was subject to a small vibration using a hammer until no air bubbles were observed to come out of the sample.

3. After saturation, the sample was taken out from the tray and left in the laboratory to air-dry to the desired water content which was determined by weighing the sample until it reached the required weight as shown in Fig. 3.3a.

4. Two samples of the same water content were sandwiched together using electrical tape and put in sealed plastic bags for 3 days to achieve equilibrium.

5. After reaching equilibrium, the containers were opened carefully and 3 filter papers of Whatman No.42 with a diameter of 55 mm were placed between them and again the two half containers were taped, waxed and positioned in a sealed plastic bag (see Fig. 3.3b). To ensure good contact between the sample and the filter papers, care was taken to ensure a flat surface for the samples.

6. The plastic bags were arranged in a Styrofoam box and the lid of the box was taped to prevent any humidity change (Fig. 3.3c). The samples were left in a temperature

controlled room (20 ^{o}C) for at least 7 days to achieve equilibrium.

7. After the required period of equalization, the water content of the middle filter paper was determined and the suction corresponding to the water content value was determined from a standard calibration curve.

More details in relation to sample preparation and the calibration curves are provided by Bulut & Leong (2008). The calibration equations, proposed by Chandler et al. (1992) for Whatman filter paper No.42, were used in this study as these showed better agreement with the results of the HCT (see Fig. 4.1) among other equations proposed by (for example) Van Genuchten (1980), Hamblin (1981) and Leong et al. (2002) and are as shown in Eqs. 3.1 and 3.2. Results of the filter paper were fitted using the Fredlund & Xing (1994) procedure. Equations relating to this procedure are shown in Chapter 4 (Eqs. 4.1 and 4.2).

Figure 3.3: (a) Air-drying the samples (b) Taping, waxing and placing samples in the plastic bag (c) Placing samples in the Styrofoam box for equilibrium.

1. For matric suction and $w \leqslant 47$ %:

$$Log_{10}\ s = 4.84 - 0.0622\ w \tag{3.1}$$

2. For matric suction and $w > 47$ %:

$$Log_{10}\ s = 6.05 - 2.48\ Log_{10}\ w \tag{3.2}$$

where w is the filter paper water content.

3.4 Test equipment

3.4.1 Design of direct shear and bearing capacity rigs

3.4.1.1 Design of direct shear box

The conventional square direct shear box is unsuitable for unsaturated studies. A new circular direct shear box, therefore, built of Perspex was designed with the following additional features over standard laboratory shear boxes:

1. Inclusion of a high air entry disk (HAED) of 1 bar in the bottom half of the shear box (80.3 mm in diameter). The HAED works as an interface between the unsaturated soil and the negative pore water pressure (suction) applied (in this study, suction was applied by using a burette). Water in the HAED provides a connection between pore water in the soil and the water in the burette, however air cannot pass through the HAED from the soil. Therefore, the negative pore water pressure can be measured easily from the level in the burette.

2. Provision of grooves of the bottom half of the shear box to form a water reservoir underneath the HAED as shown in Figs. 3.4a and b. This groove also enables flushing of air below the HAED by circulating water prior to the test.

3. Provision of influent and effluent ports in the bottom half of the box which allow saturation of the groove channels during test initialization and connection to the burette. This led to an increase in height of the box to 86 mm which is higher than the height of a conventional direct shear box (50 mm). This caused problem of driving the box in the compression direction due to a restriction in the apparatus. Therefore, the box was driven in the tension direction and the load cell was calibrated in the tension direction. The valve of the influent port is closed after flushing and (hence during shearing), while the effluent port is connected to the burette.

4. Provision of a burette to allow application of a hanging water column for applying and controlling suction (further details are given in Section 3.6). The applied suction head is the distance from water level in the burette to the point of interest in the soil.

5. Provision of a camera installed in front of the burette to capture the water level in the burette during shearing. Hence the water content of the sample at different stages of the test can be calculated accordingly. This has advantage of tracking any change of degree of saturation at different stages of the test and hence the sample path on the SWCC can be followed.

In addition; to minimize friction between the two halves of the box and to prevent water flowing out from the sample, the gap between the two halves is sealed before the test by applying a layer of silicon grease. Since this may have an influence on the measured shear strength, its effect was thoroughly investigated and is reported in Chapter 4 (see Subsection 4.6.2).

3.4.1.2 Bearing capacity rig

To study the effect of the behaviour of unsaturated soil on bearing capacity, a container of 400 mm length, 140 mm width and 400 mm height equipped with base drainage was constructed (see Fig. 3.5).

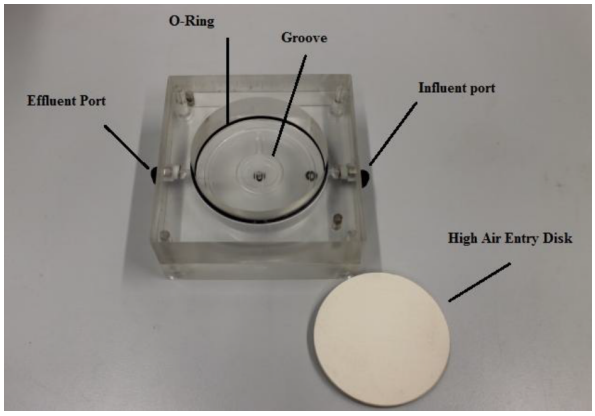

[a]

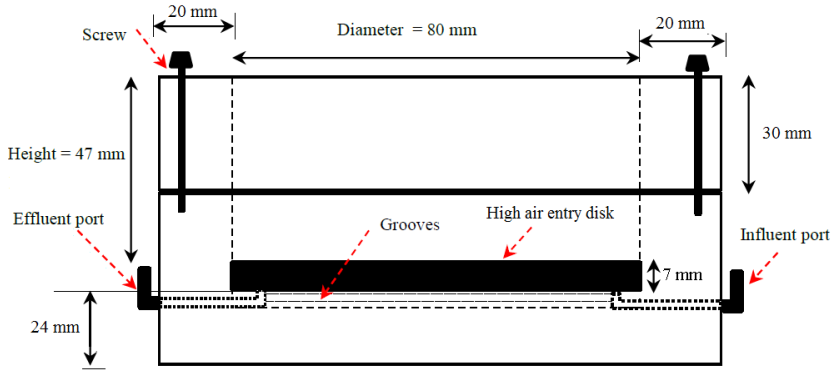

[b]

Figure 3.4: (a) A modified direct shear box (b) cross-sectional view of the modified direct shear box.

To minimize the effect of friction between the container walls and the soil, a glass sheet of 4 mm thickness covered both front and back faces of the container. The outer frame of the container was constructed to prevent lateral displacement during the loading stage to ensure plane-strain conditions. To transmit a specific suction, a filter layer was prepared and placed in the base of the rig, detailed in Subsection 3.4.1.3. A camera was installed in front of the rig (see Fig. 3.11b) to capture an image every 1 minute during the test to be used for PIV analysis.

An appropriate width of the footing can be chosen according to the dimensions of the rig and the anticipated failure mechanism developed. Rankine's method and the Limit-State:GEO software were used to calculate a suitable width for the strip footing. The Rankine method is based on a simplified failure mechanism as shown in Fig. 3.6 where $\beta = 45 - \frac{\phi}{2}$ and $\alpha = 45 + \frac{\phi}{2}$, while the software can model the full failure mechanism.

Equations 3.3 and 3.4 were used to find depth (y) and length (x) of the slip line (see Fig. 3.6) using several assumed widths of the footing based on the shear strength parameters for fraction D in dry conditions shown in Table 3.1. The dry internal friction angle was obtained using a direct shear test at a displacement rate of 0.0096 mm/min.

$$y = \frac{W}{2} \times \tan \alpha \tag{3.3}$$

$$x = \frac{y}{\tan\ \beta} \tag{3.4}$$

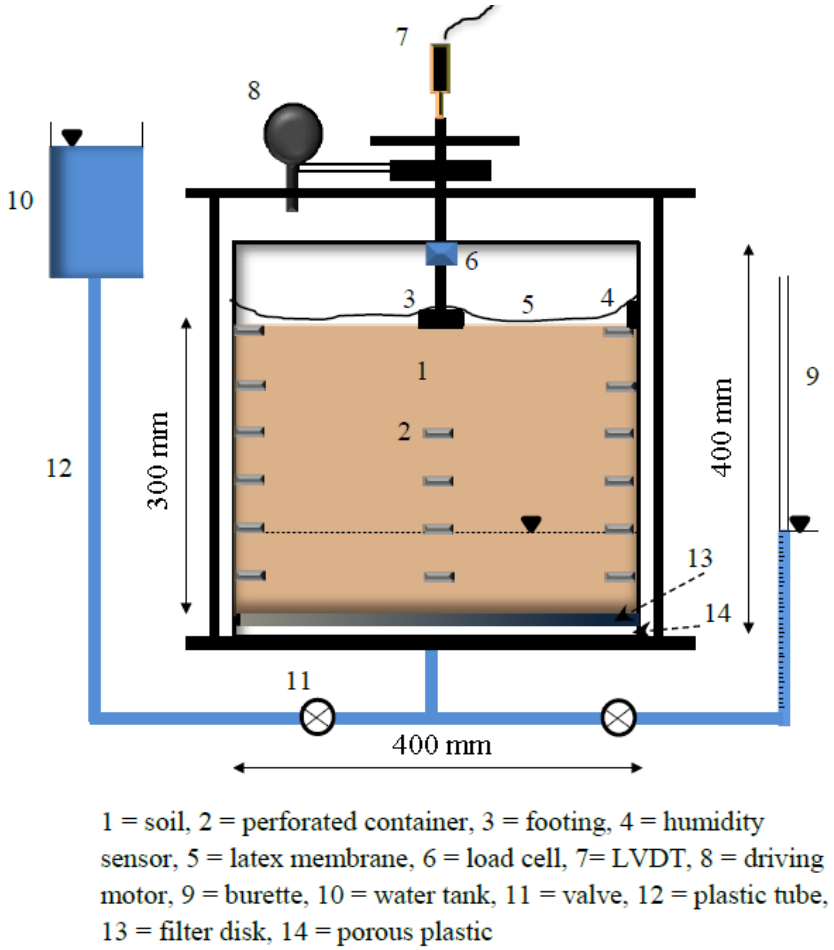

Figure 3.5: Modified bearing capacity rig showing filter layer.

where W is footing width.

The estimation of the failure zone for a strip footing of 10 cm width using Rankine's method showed that the mechanism failure extends to a width of about 28 cm and the depth of soil required is about 12 cm. While the other widths show smaller failure zone boundaries.

Figures 3.7a, b, c and d show the failure mechanisms obtained using the LimitState:GEO software for different widths of the footing and different soil conditions: dry and unsaturated cases. For Fig. 3.7d, a suction of 3.72 kPa was applied to show the effect of apparent (artificial) cohesion on the failure mechanism boundary for a 2.5 cm footing width. The water table height was assigned to be 38 cm below the surface (8 cm below the base). This can be compared with the fully dry case (e.g. Fig. 3.7c). The failure zone for a 10 cm footing width is constrained by the rig boundary (Fig. 3.7a). While, 5 cm footing width shows failure zone close to the edge of the container (Fig. 3.7b) and a smaller failure mechanism can be seen for the 2.5 cm footing width (Fig. 3.7c and d). It can be seen that the Rankine approach underestimates failure width.

The experimental depth of soil used in this study was 300 mm which extends beyond both the Rankine and Limit State:GEO results (see Figs. 4.7a, b and c). This can be considered as a conservative depth; however, the range of applied suction within the soil can be increased using a higher depth of the soil.

As a double check for the above calculations based on both the Rankine and Limit State:GEO results, an initial laboratory bearing capacity test was performed using a 5 cm

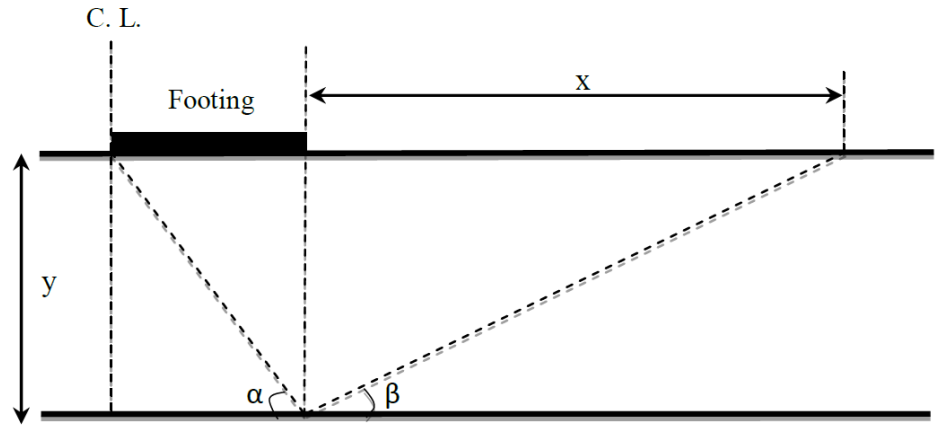

Figure 3.6: Failure mechanism using the Rankine method

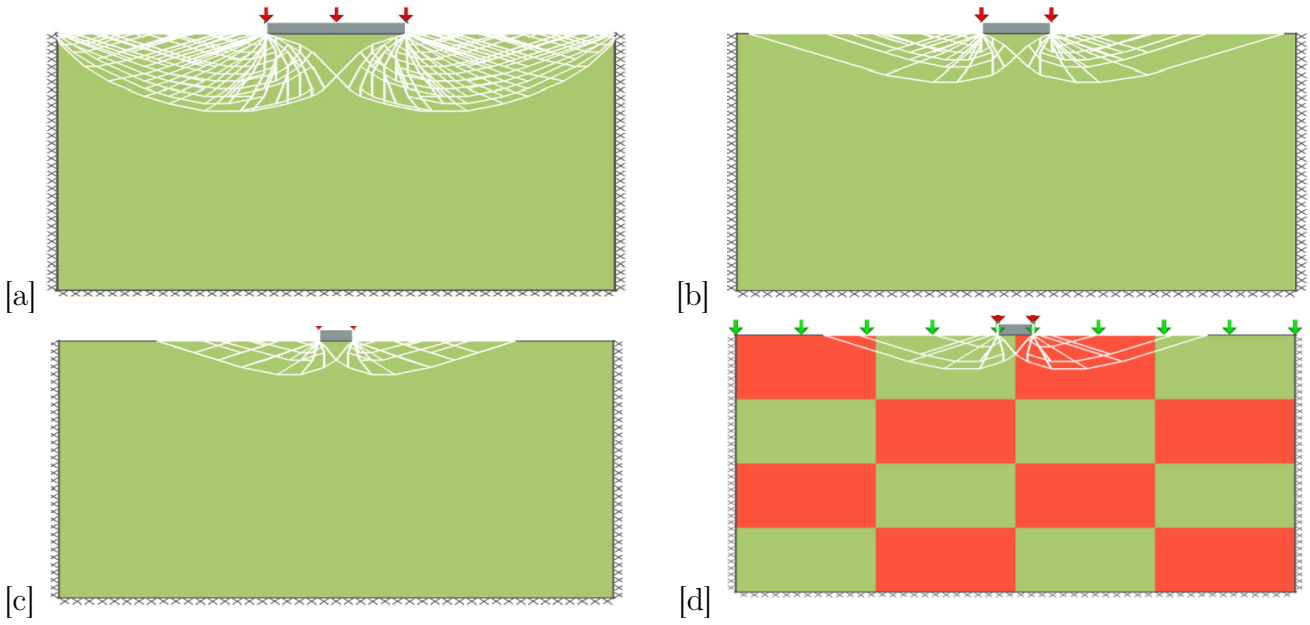

Figure 3.7: Failure mechanism hitting edge of the rig for footing width = 10 cm (b) Failure mechanism close to edge of the rig for footing width = 5 cm (c) Failure mechanism for footing width = 2.5 cm (d) Failure mechanism for footing width = 2.5 cm at an applied suction of 3.72 kPa.

footing width and an applied suction of 2 kPa. Figure 3.8 shows that the failure mechanism hits the edge of the rig.

As it is confirmed both numerically and physically that a footing of 5 cm width was unsuitable for performing bearing capacity problems for the existing rig, a footing of 2.5 cm width was selected to be used in this study. The results both physically and numerically are presented in Chapter 4 and 6, respectively. The footing/particle size ratio was $\sim$ 134 which should ensure particle size effects are negligible, Ovesen (1979). This is based on an average particle size range between (0.075 and 0.3) for fraction D (see Table 3.1).

Figure 3.8: Failure mechanism for a footing width of 5 cm reaching edge of the rig boundary.

3.4.1.3 Filter layer preparation for bearing capacity test

Although commercial HAEDs are used widely in the field of unsaturated soil, it is difficult to fit a large HAED into the rig. An alternative simple filter layer was prepared by placing a piece of porous plastic in the base of the rig. Then a weight of a fine sand to target a height of 1 cm (fraction F- available from the David Ball Group, UK) was rained over the porous plastic. The surface of the filter layer was levelled and then the rig was connected to the water tank through a plastic tube. Once the water valve was opened, water flowed into the rig saturating the filter. Experimental trials showed that the height of the water tank should be low to prevent piping (boiling) due to the small weight of the filter soil layer (1 cm height). The water valve was then closed and water from the filter layer was removed by another plastic tube connected to bottom of the rig. Clear water removed from the filter layer indicated successful preparation of the filter layer as shown in Fig. 3.9. Following filter layer generation, several cyclic applications of drainage (saturating and desaturating the filter layer) were applied to the filter layer by applying 6.5 kPa suction. This was to expose the filter layer to air and to ensure no air can be observed in the plastic tube. This procedure was repeated several times until a successful filter layer was prepared.

The SWCC for the filter sand (fraction F) is shown in Fig. 3.10 and it can be seen that the filter layer has an air entry value of about 7 kPa which is greater than the maximum applied suction used in this study (5.93 kPa). This is to prevent breaking of the filter layer (air transfer) when applying suction higher than 7 kPa.

The chosen filter layer has the advantage of providing a comparatively higher hydraulic conductivity leading to shorter equilibrium times. Also, proper contact between it and the main test soil can be achieved that ensures full transfer of the suction to the sample, Stanier & Tarantino (2013).

3.4.1.4 Humidity and temperature control for bearing capacity test

To monitor the humidity and temperature of the bearing capacity sample during equilibrium and testing, a commercially data logger device (LE-USB-2) was installed on the wall side of the rig prior to covering the rig (see Fig.3.5 - item No.4). The device was able to acquire up to 16,382 readings for the temperature and humidity at different intervals. The accuracy of the temperature and the humidity readings were 1^oC and 3%, respectively. In this study,

Figure 3.9: Comparison between clean water and water extracted from the sample.

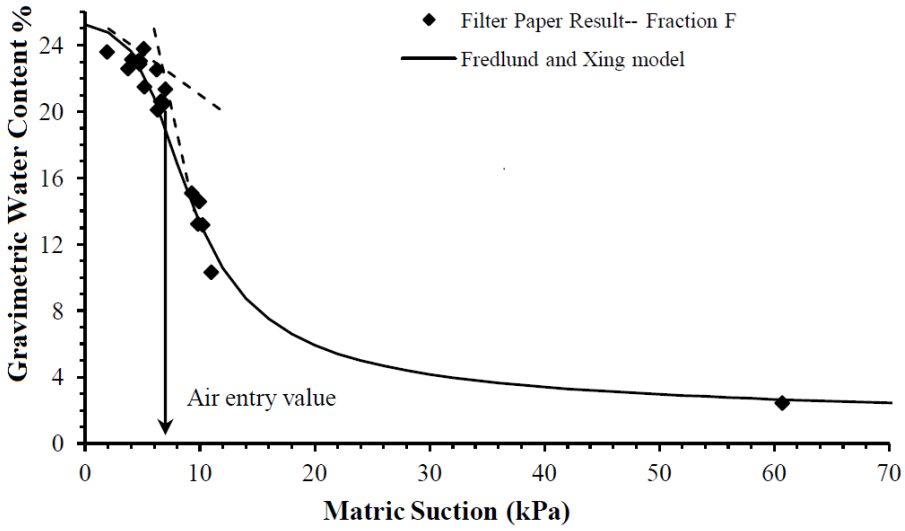

Figure 3.10: SWCC for the filter sand (fraction F) obtained using the filter paper method.

the interval time for acquiring a reading for the temperature and the humidity was set to 1 minute.

3.5 Sample preparation and experimental procedure

3.5.1 Experimental procedure for SWCC using the HCT

The modified direct shear box of diameter 80.3 mm was used to prepare the sample to determine the SWCC. Prior to the test, the HAED of 1 bar capacity and thickness of 7 mm was placed under water in a desiccator under a vacuum pressure of -80 kPa. The disk was subjected to several cyclic applications of the vacuum for several hours to ensure that no air bubbles could be observed. At this stage, the HAED was deemed to be fully saturated as no air could be observed being extracted from the HAED.

The saturated HAED was, then, encircled with the O-ring and pushed into the bottom

half of the shear box. The two halves of the box were fixed together by screws. The gap between the two halves was sealed by a layer of silicon grease to prevent water leakage from the sample. A burette was then connected to the influent port (named as burette No. 1- see Fig. 3.11a) to flush 10 gm of de-aired water beneath the HAED in order to remove the air, while the effluent port was connected to another burette (named as burette No. 2) with a capacity of 10 cm^3. At this stage, a continuous path of water was ensured since both of the burettes were connected to each other through the influent and effluent ports. At the beginning, several trials for flushing were performed using different amounts of de-aired water to obtain the volume of water required to remove the total air beneath the HAED and it was found that 10 cm^3 of water was suitable. This amount of water filled the grooves and the plastic tube that connects the box to the burette No. 2. This 10 cm^3 of water was excluded from the total amount of water used to saturate the sample.

Water flushing was performed by raising the elevation of burette No. 1 so that water moved towards the box, filled the grooves beneath the HAED and air was removed and moved towards burette No. 2. Since burette No. 2 was subjected to atmospheric conditions (open end), air escape from the burette No. 2 was allowed. The system was subject to several circulations of flushing to ensure no air can exit beneath the HAED. After the successful flushing procedure, the influent port was disconnected from burette No. 1 and closed. No excess water was seen above the HAED at this stage and the amount of water required to saturate the sample, (95 gm calculated by mass of dry soil prior to sample preparation) was poured into the box. A mass of dry soil (364 gm provides a void ratio of 0.70 and a dry unit weight of 15.3 kN/m^3) was then poured into the box using the water pluviation technique. With the water pluviation technique, an initially saturated sample can be obtained, no precise drop height is required and less effort and time comparing to the air pluviation technique can be achieved, Vaid & Negussey (1988). After pouring, the soil surface was levelled off to give the final height of the sample of 47 mm and then the box was covered by a piece of latex membrane to avoid evaporation prior and during the test. A small opening in the latex membrane was made using a needle to ensure atmospheric pressure in the sample air. At this stage, the water level in the burette coincided with the water level at the surface of the sample. The sample was then left for two hours to ensure full saturation. No change of water level in the burette indicated full saturation case and the water level was recorded (zero suction).

3.5.2 Sample preparation and experimental procedure for direct shear test

The same procedure as that used to obtain the SWCC in terms of flushing and sample preparation was adopted for the direct shear test. During application of the desired suction (see Section 3.6), if any air was observed in the plastic tube that connects the box to the burette, the system was flushed again via burette No. 1 (see Fig. 3.11a).

After the desired suction was obtained, the sample was left at least for 15 hrs for equalization purposes. The vertical and horizontal LVDTs were then set up and a small normal stress (the loading plate) of 0.97 kPa (0.5 kg - using area of the direct shear box) was placed on the sample and left for 1 hr. The first reading of suction was taken prior to the test and an appropriate displacement rate was selected (see Section 3.7). The data logging (LabVIEW) software was set to capture a reading every 1 minute for the load cell and the horizontal and vertical LVDTs. A Canon EOD1100 camera with 7 MB resolution was utilised to capture the water level in the burette every 30 minutes during the test for the unsaturated samples.

[a]

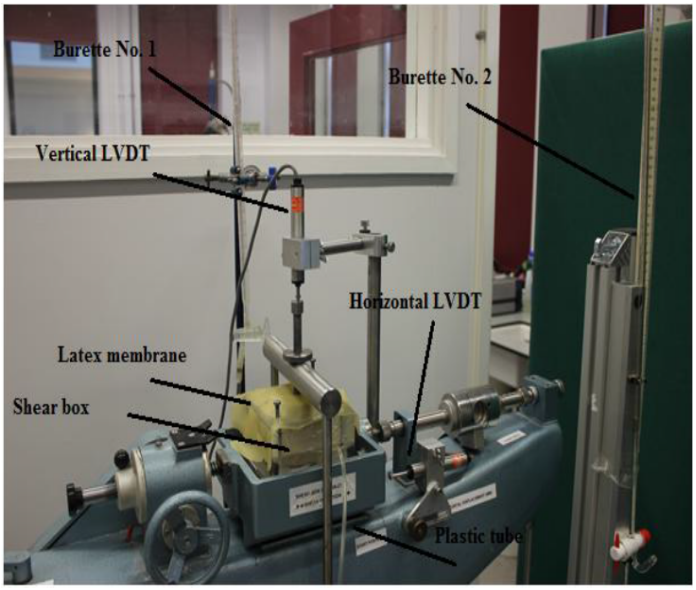

[b]

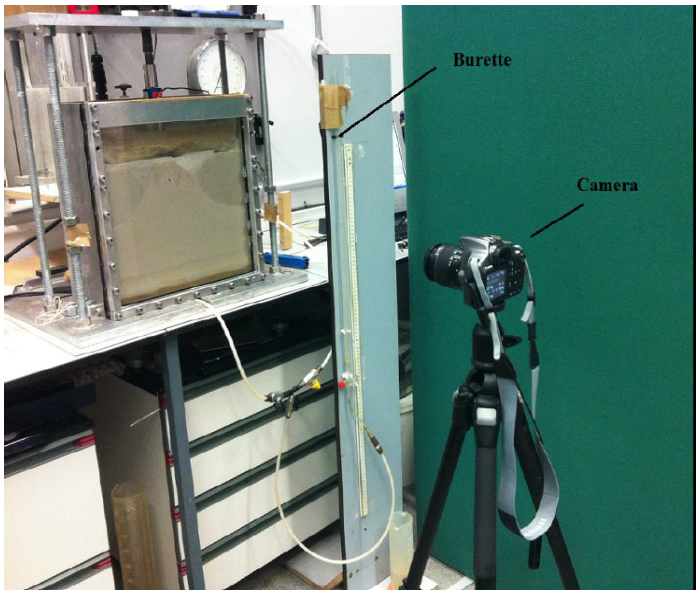

Figure 3.11: (a) Modified direct shear device showing application of suction using the HCT (b) Bearing capacity rig showing burette and installed camera.

For fully saturated samples, a time of 10 minutes was used due to the short period of the test for the fully saturated samples. Figure 3.12 shows a water level in the burette captured by the camera during the test.

The camera was used to observe any change of water level in the burette during the test and hence the degree of saturation of the sample can be calculated accordingly. This change in water content might be difficult to calculate using other methods of applying and controlling suctions such as using a tensiometer, the axis translation technique or the osmotic method. It is useful for determining the scanning path (drying and wetting paths) on the SWCC if the change in water content at different stages of the test is known. This is discussed further in Subsection 4.9.1. Also it would be possible to model unsaturated soil when both suction and degree of saturation are known at different stages during the test. At the end of the test, five samples were taken along the height of the box to calculate the water content.

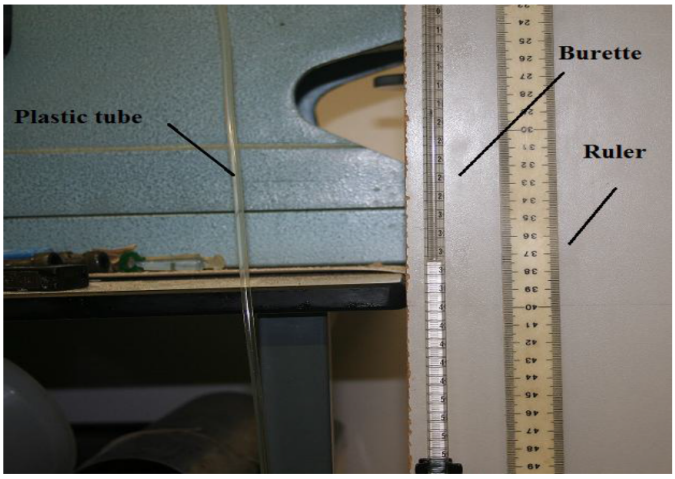

Figure 3.12: An image of the water level captured during the test.

3.5.3 Sample preparation and experimental procedure for bearing capacity test

Uniform, homogeneous and fully saturated samples of large size require a precise procedure for sample preparation. This was attained using the water pluviation technique. Sample preparation for the bearing capacity test was as follows:

1. After a successful filter disk preparation (described in Subsection 3.4.1.3), an elevated water tank was filled with the required de-aired water and was connected to the rig and to the burette by flexible plastic tube (see Fig. 3.5). The water tank valve was opened and allowed de-aired water to flow into the box and the burette. At this stage, air expulsion is ensured from the bottom of the box, and the burette and water level in the box and the burette are at the same height. Since the air pressure in both of the box and the burette was maintained at atmospheric pressure, no effect of air diffusion was noticed on the burette measurement during the test. The amount of water (pre-calculated by mass of dry soil) to saturate a 30 cm height of soil was 7103 gm. The water tank valve was closed after the desired amount of water had flowed into the box.

2. The sample then was prepared by pouring oven dry fine sand (below the water level) into the box at zero distance from the bottom of the box while keeping the water level above the soil surface to avoid air blocking. Due to the large scale of the bearing capacity box, the height of the specimen was divided to six equal layers of 50 mm and the mass of dry sand poured into the box was controlled every fifth centimeter. The soil sample obtained from this procedure had a dry unit weight of 15.30 kN/m^3 and a void ratio of 0.70. This is to coincide with the direct shear test sample which were within 1% of the overall average required dry unit weight (15.30 kN/m^3) which corresponds to a void ratio 0.70.
   During the soil pouring, perforated sample containers were placed each 5 cm depth in both sides of the rig as well as beneath the footing (Fig. 3.5). To avoid any restriction of the failure zone by the containers (soil reinforcement), the 10 cm beneath the footing was left without placing containers and samples for this 10 cm were taken directly after the test.

3. After obtaining the desired height of the sample (30 cm), the sample surface was levelled

using a T-shaped scraper and the humidity and temperature meter was installed on the wall of the rig (see item 4 in Fig. 3.5).

4. The strip footing was then placed gently in the middle of the rig and levelled in both x and y directions using a spirit level. For a footing placed at 5 cm depth, the 5^{th} layer (targeting 25 cm depth of soil) was levelled using a T-scraper and then footing was placed. The last 5^{th} cm depth of the soil then was poured to present a surcharge above the footing. The water level was slightly higher than the soil surface to ensure a fully saturated case. The footing was free to rotate to either side due to application of the load. However, the rotation was small or negligible for the fully dry and saturated cases due to even resistance of the soil on both sides of the footing as will be shown in Chapter 4 (i.e. see Fig. 4.63)

5. The rig was covered by a piece of latex membrane to avoid evaporation of water from the sample during the test (see item 5 in Fig. 3.5). The latex membrane was placed as close as to the soil surface to ensure shorter equilibrium time for the space that was left between the soil and the membrane.

6. The sample was left for 2 hrs to ensure a fully saturated case (no change in water level in the burette was observed). Then, the water level in the burette was recorded (which is at the same level in the box). At this stage, the sample preparation was completed and for unsaturated samples, suction was applied using the HCT (see Section 3.6).

3.6 Suction application using the HCT

The burette, which was fixed to a board as shown in Figs. 3.11a and b was lowered to a desired level to generate a known suction. After lowering, water started to flow from the box through the HAED for the direct shear tests or the filter disk for the bearing capacity tests, towards the burette. The system reached equilibrium after a period of time when water ceased to flow from the box and the water level in the burette stabilized. The stabilized water level in the burette was a good indication that application of suction was completed. The stated suction head measured at the soil surface was the distance from the water level in the burette to the soil surface for both the shear box and the bearing capacity rigs as shown in Figs. 3.13a and b. Although for the direct shear tests, suction was measured to the surface not to the shear plane, it was thought that such small variation in suction should not have a large effect on the behaviour of the soil. For the bearing capacity test, suction was assumed to vary linearly with depth below the top surface, so that suction changed within the zone of shearing.

Consistency of suction application using the HCT for small samples (such as the direct shear sample) was achieved by checking the amount of water that was removed from the sample for each repeat test. For example, for a direct shear sample with a suction of 2 kPa, the amount of water removed (after the lowering of the burette) from the sample was very close for each repeated test (see Subsection 4.4.3- Chapter 4). This gives an indication that degree of saturation can be maintained constant at the same applied suction and also demonstrates the applicability of the HCT as a suction controlling technique for coarse-grained soils. However, for a bigger sample size (e.g. the bearing capacity rig), it was difficult to obtain the same amount of expelled water each time at the same suction, so a range of suctions were obtained. In other words, for an initial applied suction of 2 kPa, difficulty of obtaining the same final equilibrium suction led to a resulting range of suctions

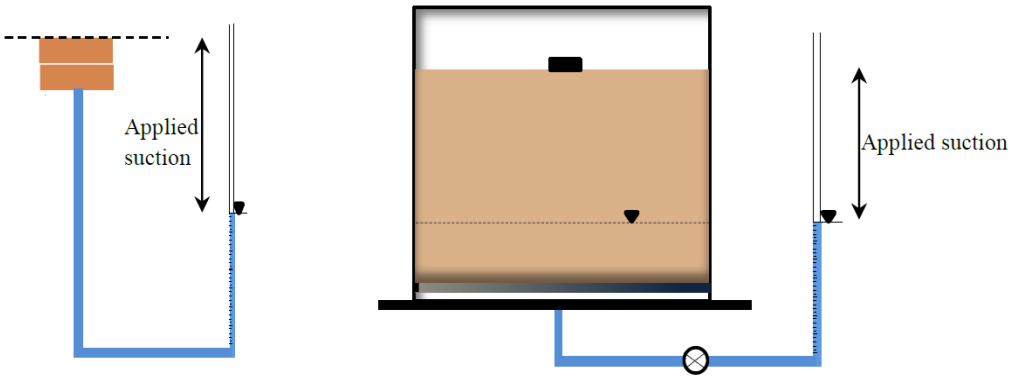

Figure 3.13: Applied suction in (a) The direct shear test (b) The bearing capacity test.

less or more than 2 kPa. This is why the bearing capacity results are separated to a range of applied suctions not to a specific suction (see Subsection 4.10.1.2- Chapter 4).

3.6.1 Equilibrium time

Care is required in selecting an appropriate equilibrium time. ASTM-D6836-02 (2008) standards propose that the equilibrium time should be determined according to the applied suction level. After the burette lowering, the water level was checked every 30 minutes. It was found that an equilibrium time of 15 hrs and 1 day was suitable for the direct shear and bearing capacity tests respectively for the sand used in this study since the water level in the burette did not change. After the equalization, a suction reading was taken. The amount of water removed from the sample at each lowering was the difference between the water levels in the burette.

3.7 Displacement rate

3.7.1 Displacement rate selection for direct shear test

To avoid rate effects a maximum shear displacement rate for unsaturated soils must be determined. Different soil types require different displacement rates. Due to the low permeability of clay, for example, dissipation of excess pore water pressure must be ensured during shearing by selecting an appropriate displacement rate. Within the context of the above short discussion, the following paragraphs deal with an overview of the displacement rates found in the literature and an approach of estimating displacement rate.

Tarantino & Tombolato (2005) used a displacement rate of 0.005 mm/min for Speswhite kaolin unsaturated samples using a direct shear test with specimen dimensions of 60×60 mm and height of 10 mm. Nishimura et al. (2008) used 0.25 mm/min as a horizontal displacement rate for direct shear tests conducted on both saturated and compacted unsaturated silty soil. Sun & Xu (2007) used displacement rates of 0.0096 mm/min for a sandy silt soil. Nam et al. (2011) used displacement rate of 0.005 mm/min for silt and clay soils and 0.008 mm/min for sand.

Bishop & Gibson (1964) proposed an equation to calculate the failure time (t_f) of the specimen as follows:

$$t_f = \frac{(\frac{L}{2})^2}{\eta\ C_v\ (1 - \bar{U}_f)} \tag{3.5}$$

where L is thickness of the specimen, C_v is soil coefficient of consolidation, $\bar{U}_f$ is desired degree of pressure dissipation and η is a parameter accounting for fluid flow impeded by the ceramic disk, given by:

$$\eta = \frac{0.75}{1 + (\frac{3}{\lambda})} \tag{3.6}$$

where λ is an impedance factor (see Eq. 3.13). The coefficient C_v can be obtained from:

$$C_v(\psi) = \frac{k_w\ (1 + e_o)}{\rho_w\ g\ b_m\ G_s} \tag{3.7}$$

where k_w is hydraulic conductivity of soil, e_o is initial void ratio before the drainage, ρ_w is density of water, g is gravitational acceleration, b_m is the slope of the SWCC in terms of gravimetric water content versus matric suction and G_s is the specific gravity of soil.
Then a proper shear rate ($d\dot{h}$) can be determined by:

$$(d\dot{h}) = \frac{dh_f}{t_f} \tag{3.8}$$

where dh_f being lateral displacement at failure that can be estimated.

Estimation of an appropriate displacement rate to bracket more sands was presented by Likos et al. (2010) and they provided a sequence of relationships as shown in Figs. 3.14 and 3.15 in case SWCC and hydrologic properties are not known. Figure 3.14a was determined using Eqs. 3.9 and 3.10 from the Van Genuchten (1980) model. While Fig. 3.14b was modelled using the Van Genuchten (1980) approach and Eq. 3.11.

$$S_e = \left[\frac{1}{1 + [\alpha(\psi)]^n]}\right]^m \tag{3.9}$$

$$S_e = \frac{S - S_r}{1 - S_r} \tag{3.10}$$

where S_e is effective degree of saturation, α is a fitting parameter (kPa^{-1}), ψ is suction (kPa), n and m are fitting parameters and S_r is residual saturation.

$$k_w = k_s \left[S_e^{0.5}[1 - (1 - S_e^{1/m})^m]^2\right] \tag{3.11}$$

$$m = 1 - \frac{1}{n} \tag{3.12}$$

where k_s is the saturated hydraulic conductivity for poorly graded coarse sand and well graded fine sands. Figure 3.14c shows the impedance factor (λ) versus the matric suction obtained using Eq. 3.13.

$$\lambda = \frac{k_d\ L_s}{k_w\ L_d} \tag{3.13}$$

where k_d is the saturated hydraulic conductivity of the HAED, L_s is the drainage path length and L_d is the thickness of the disk. Finally, Figs. 3.15a and b were obtained using Eqs. 3.8 and 3.10, respectively. These were based on an assumption that 95% dissipation of excess pore water pressure can be attained and dh_f is estimated at 2 mm horizontal displacement.

[a]

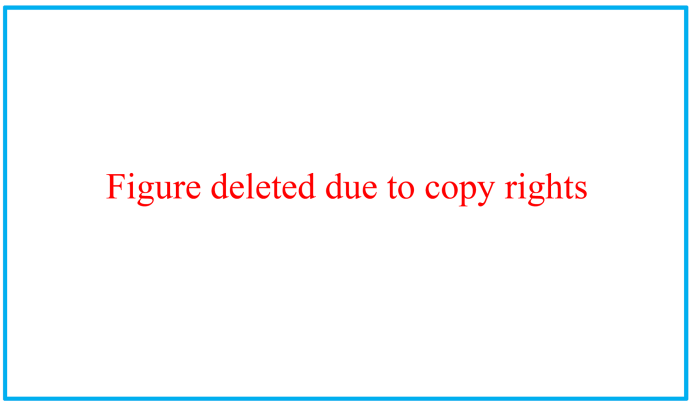

[b]

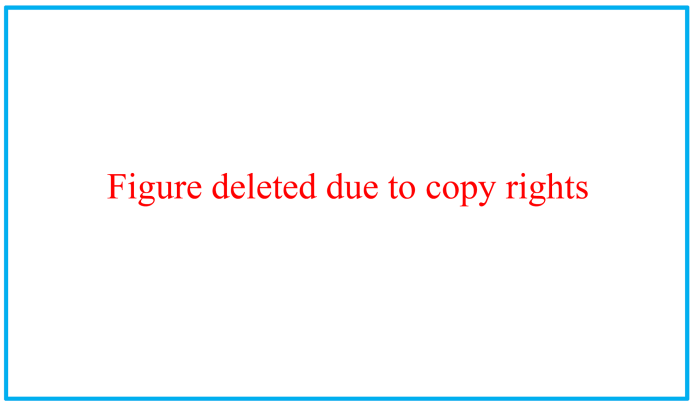

[c]

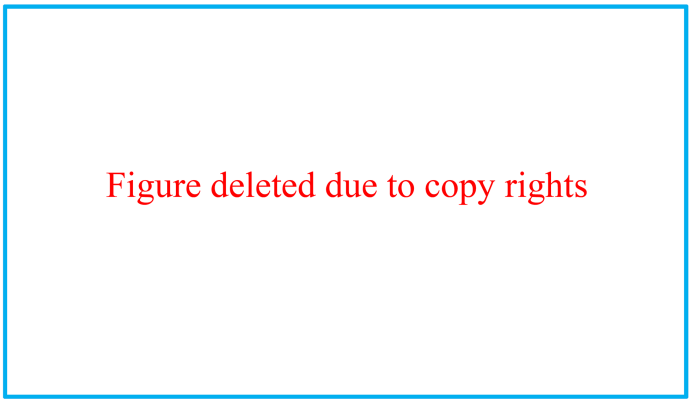

Figure 3.14: (a) Saturation versus matric suction (b) Hydraulic conductivity versus matric suction (c) Impedance factor versus matric suction, after Likos et al. (2010).

Based on Eqs. 3.5 to 3.9 and sequences Figs. 3.14 and 3.15, Likos et al. (2010) suggested several displacement rates for sands at different degree of saturation (S_r). They suggested 1×10^{-4} mm/sec for S_r between 100-60%, 1×10^{-5} mm/sec for S_r between 60-30%, and for S_r less than 30% the above equations are not recommended.

Using the above equations and figures for estimating displacement rate for the sand used in this study, a suitable displacement rate was estimated as 1×10^{-4} mm/sec (6×10^{-3} mm/min - 8.64 mm/day) for poorly graded soil. The sand used in this study was

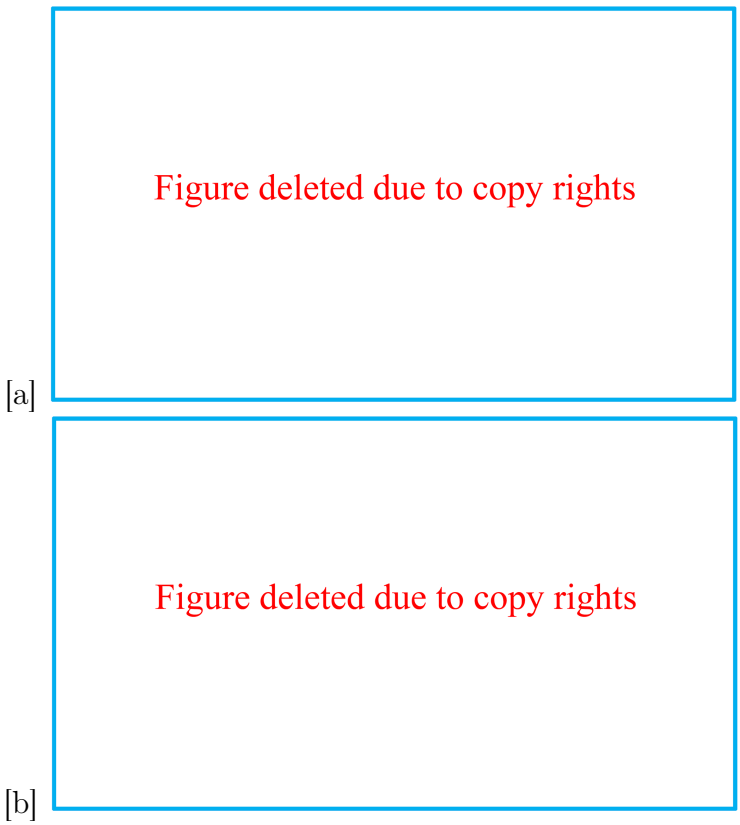

Figure 3.15: (a) Required displacement rate versus matric suction (b) Required displacement rate versus saturation, after Likos et al. (2010).

classified as a poorly-graded sand (SP) according to the unified soil classification system (ASTM) and accordingly, the shear displacement rate used in this study was set as 9.6×10^{-3} mm/min (13.82 mm/day) for unsaturated samples. The slight difference between the estimated displacement rate using the above equations and the actual used rate of about 5.18 mm/day is because for rate 8.64 mm/day, there was necessity to extend the test for more than 24 hrs to target 10 mm horizontal displacement (direct shear tests were terminated when reached 10 mm horizontal displacement). Based on the preceding equations and the previous literature, therefore, the displacement rate of 13.82 mm/day was used. The test was not extended to more than 24 hrs to save time due to the large numbers of the direct shear tests (see Table 3.4).

The rate utilised in this study for saturated samples was 4.8 $\times 10^{-2}$ mm/min. A higher displacement rate was used for the saturated samples compared to the unsaturated samples due to higher effective permeability of the former.

3.7.2 Loading rate selection for bearing capacity test

Due to the large settlement to be targeted in the bearing capacity tests (most of the tests were terminated at 20 mm settlement), it was impossible to use a low displacement rate to be compatible with the direct shear displacement rate (0.0096 mm/min). This is because it would require about 35 hrs to aim 20 mm settlement. Due to the large numbers of the bearing capacity tests (see Table 3.5), an appropriate loading rate was therefore chosen accordingly. The selected rate was also supported by the other work found in the literature,

although such kind of studies on unsaturated soils unfortunately are limited in a very few investigations.

Alabdullah (2010) used 0.12 mm/min as a loading speed for a bearing capacity study on Hostun unsaturated sand. This rate was utilised to coincide with biaxial tests conducted in his study. A rig with dimensions of 1000 mm long, 500 mm high and 500 mm wide was used. The study was conducted using a strip footing with dimensions of 477 mm length, 79 mm width and 45 mm depth was used.

Variation of ultimate bearing capacity with matric suction was investigated by Uchaipichat & Man-Koksung (2011). They used compacted kaolin specimens (101.6 mm in diameter - 4 inches) with different initial matric suction values. The tests were performed by penetrating a rod with a diameter of 1.5 cm into the specimen surface and the loading rate used was 1 mm/minute (personal communication).

Mohamed et al. (2011) conducted bearing capacity tests on unsaturated sand. They used two different displacement rates of 1.2 mm/min and 2.5 mm/min. A square footing with dimensions of 150×150 mm was placed on surface and depth. They assumed that the different strain rates had no influence on the load capacity.

Oh & Vanapalli (2012) conducted bearing capacity study on statically compacted fine grained soil (Indian HAED Till) using a square footing of 50 mm width. The test was performed in a cylindrical high-strength plastic tank (300 mm diameter, 300 mm height and 127 mm thickness) and a loading rate of 1.14 mm/min was utilised.

Based on the above investigations, therefore, the bearing capacity test in this study was subjected to a displacement controlled procedure and the displacement rate was selected as 0.6 mm/min. This was the minimum rate using an existing motor drive (see Fig. 3.16) as the motor was unable to drive the soil for any rate less than 0.6 mm/min (motor displacement rate decreased significantly, especially for unsaturated samples, as the soil gained strength). This displacement rate was believed to be sufficient as higher speed rates were found in the literature as stated in the previous paragraphs. The test was ended when failure was observed at the soil surface or when soil settlement reached 20 mm.

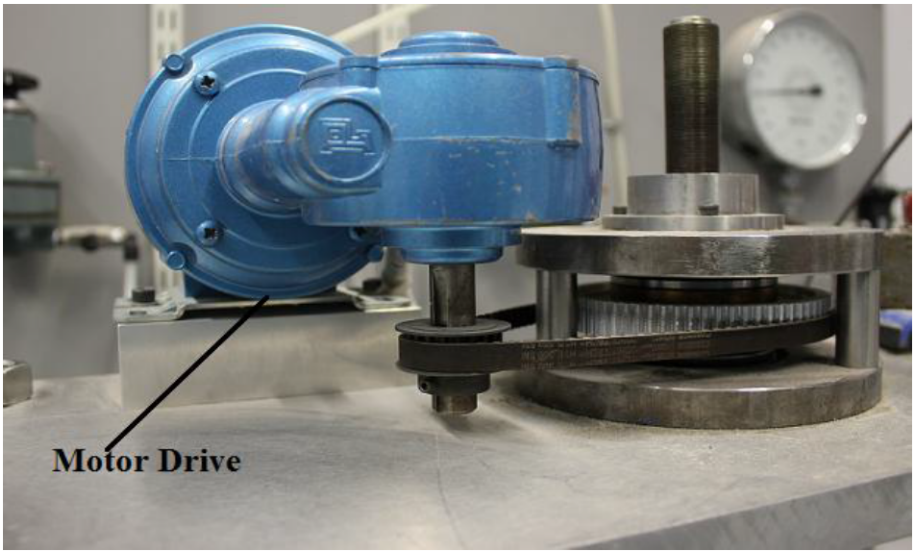

Figure 3.16: Motor-drive used for the bearing capacity test.

3.8 Particle image velocimetry (PIV)

Particle image velocimetry (PIV) is a velocity-measuring procedure which was first developed in the field of experimental fluid mechanics, Adrian (1991). The velocity of the fluid flows was determined by means of tracking seeding particles which were illuminated using light sheets. A camera was used to capture images of the seeding particles during the test. Two different methods were utilised for presenting the velocity fields, namely "Particle Tracking Velocity" (PTV) and "High Image Density" (PIV). In terms of the former, the individual particles within the image were tracked, while within the PIV approach interrogation patches which contained multiple particles were used. Correlation algorithms were used for tracking the particles for both the PTV and PIV. Due to the vast development in the computer and camera technology, interest in using the PIV has exploded. PIV has been used widely in several engineering fields such as chemical, nuclear, building and environment and geotechnical engineering, Stanier (2011).

Implementation of the PIV technique in geotechnical engineering has been reported by several researchers such as Guler et al. (1999), White (2002), Liu & Iskander (2004) and Sadek et al. (2005). Displacement in soil during pile installation was tracked using the PIV by White (2002). This led to further development of the PIV and the release of the GeoPIV Matlab code.

In this study, the PIVlab software version 1.32 which is a Matlab module that implements PIV in a manner suited to water and geotechnical engineering testing was used to obtain displacement data from sequences of digital images captured during the geotechnical model test. The principle of the PIV is beyond the scope of this study and more details can be found by White et al. (2003), Liu & Iskander (2004), Sadek et al. (2005) and Stanier (2011).

3.9 Photogrammetry and digital camera

Photogrammetry is defined as the process of converting the displacement from image space to object space. This can be undertaken by using trackers which are a series of the black markers dots on the transparent window. Figure 3.17 shows the black markers fixed on a movable Perspex window for calibration purposes.

The camera was set on a tripod which was previously installed at height 111 cm and distance of 82 cm away from the front view of the chamber. To obtain consistency during the entire test regarding to the position of the tripod, three markers were marked on the ground indicating coordinates of the tripod in the x-y plane. The digital camera was fitted with an 18mm-25mm zoom lens. Only minimum 18 mm and maximum 55 mm zoom lens were allowed in the test. This is because of impossibility of obtaining consistency for all the tests within the intermediate zoom lens.

The maximum zoom lens which was used in this study has the benefit of reducing the maximum angle between the plane of intersection and the CCD of the digital camera. As a result, both radial and tangential lens distortions can be reduced. By adjusting the optical zoom facility, it was possible to capture almost the whole chamber view. This is to ensure that the whole failure mechanism and soil displacement can be captured, although the failure mechanism did not extend to cover the entire rig's width as was found in preliminary testing. Table 3.2 shows the parameters used in the PIV analysis. The images were captured at 1 min intervals during the test.

The exposure time (shutter speed) and the aperture are important features in obtaining high quality clear images. Special care was required to select these two parameters under

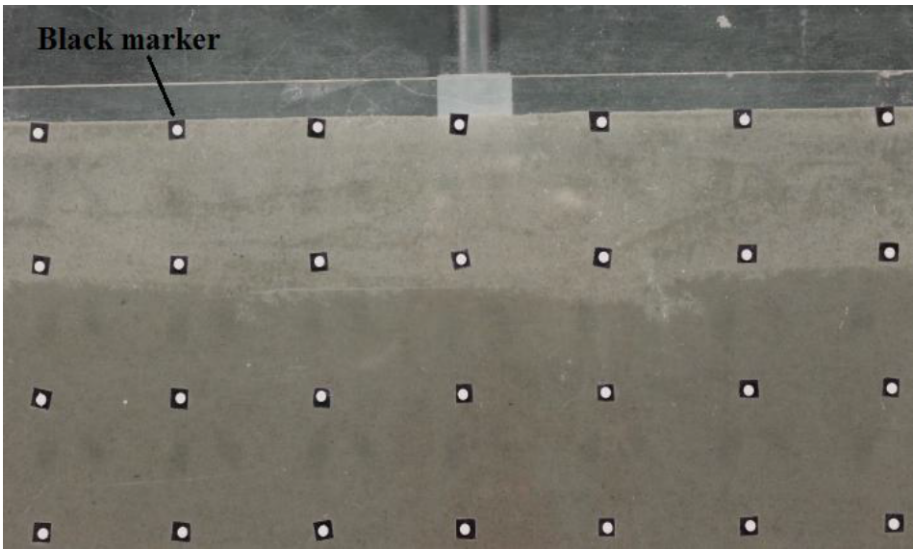

Figure 3.17: Black markers used for the calibration for the bearing capacity test.

the lighting conditions in the laboratory. Throughout several trials, the exposure time and aperture were set as shown in Table 3.2. Due to the high reflection from the window, the built-in-flash facility of the camera was not utilised. The white balance facility was used to overcome the effect of the fluorescent tube lamps used in the laboratory. The ISO feature was set up as 100. The set up remained constant throughout all tests. The resolution of the images were taken was (4272× 2848) pixels which corresponds to a scale of (0.0082) mm per pixel.

Table 3.2: Camera setup for the PIV analysis.

Image sensor	
Type	CCD
Effective pixels	12.5 M
Dimensions	4272×2848
Lens	
Focal length	55 mm
(Aperture) f/number	f/5.6
Exposure time	1/4 sec
Recording control	
ISO speed equivalent	100
Flash mode	No flash, compulsory

3.10 Test Programme

3.10.1 SWCC tests

Table 3.3 details the SWCC tests. No repeats of the filter paper tests were scheduled since they were used as a secondary check on the moisture content-suction data obtained during the course of the direct shear tests.

Table 3.3: The SWCC test details using the filter paper technique and the HCT.

Soil Type	**No. of tests using the filter paper**	**No. of tests using the HCT**
Fraction D	1	1
Fraction F	1	–
$\sum$ **No. of Tests**	2	1

3.10.2 Direct shear tests

Four different nominal suctions: 0, 2, 4 and 6 kPa were studied where the nominal suction was defined as that at the sample surface. However, the actual obtained suction values are slightly different due to difficulty of obtaining the nominal values using the HCT. For each suction, three normal stresses: 50, 100 and 200 kPa were used.

Table 3.4 summarises the direct shear test programme for fully saturated, unsaturated and dry cases. As a result of observations made during these tests, additional tests were undertaken as follows (also see Table 3.4): effect of displacement rate and geometry of shear box on oscillation[1], effect of drained and undrained[2] conditions on shear strength for fully saturated sample, multi-stage tests[3] for drained and undrained conditions, tests which conducted on empty box to identify friction between the two halves of the Perspex box, tests conducted for empty box where the clearance between the two halves of the box was sealed by silicon grease, tests performed on fully saturated samples at low normal stresses and tests which conducted to obtain friction angle between soil and the footing (soil-footing interface). These tests to be explained later in Chapter 4 in more details. Table 3.4 is presented in the same order that the tests are presented in Chapter 4.

3.10.3 Bearing capacity tests

The bearing capacity testing programme is summarized in Table 3.5 in which two main types of tests (for dry, saturated and unsaturated cases) were conducted for a strip footing placed on surface and buried at 5 cm depth. Four different nominal suctions were used: 0, 2, 4 and 6 kPa. The muti-stage dry to fully saturated test was performed for a footing placed on surface. The aim of this test was to compare bearing capacity results between fully dry and saturated samples (detailed in Section 4.11- Chapter 4). Table 3.5 also shows the total tests performed for all cases in this study.

[1]A sudden loss of strength followed by rapid recovery of strength which was observed for the sand tested in this study.

[2]A case when the effluent port was closed during the test to not allow water in or out of the specimen from the burette.

[3]Tests where dry samples were saturated after a specific horizontal displacement during shearing.

Table 3.4: Direct shear programme testing.

															Total tests
Saturated and unsaturated tests-drained condition															
Normal stress kPa	50				100				200						
Suction kPa	0	2	4	6	0	2	4	6	0	2	4	6			
No. of tests	3	3	3	3	3	3	3	3	3	3	3	3			36
Dry tests															
Displacement rate (0.0096 mm/min)							Displacement rate (0.48 mm/min)								
Normal stress kPa	50		100		200		50		100		200				
No. of tests	3		3		3		3		3		3				18
Dry tests-effect of displacement rate on oscillation-0.048 (mm/min)															
Normal stress kPa	50				100				200						
No. of tests	1				-				-						1
Dry tests-effect of geometry (square box) on oscillation-0.048 (mm/min)															
Square box-porous plastic							Square box-Serrated plate								
Normal stress kPa	26.5						26.5								
No. of tests	1		-		-		1		-		-				2
Saturated tests-undrained condition-0.0096 (mm/min)															
	HAED				porous plastic		drained and undrained-0.048 mm/min								
Normal stress kPa	50				50		50								
No. of tests	1				1		2								4
Multi-stage tests-dry to fully saturated-drained and undrained conditions															
Normal stress kPa	50				100		200								
No. of tests	2				-		-								2
Empty box															
	No grease-no water				Grease-no water		Grease-water added								
							begining of test				3mm displacement				
No. of tests	3				3		2				1				9
Saturated tests-low normal stresses-0.048 (mm/min)															
	HAED				HAED		porous plastic-0.048 mm/min								
Normal stress kPa	6.25				12.5		25								
No. of tests	1				1		1								3
Soil-footing interface-0.48 (mm/min)															
Normal stress kPa	44.4				83		166				332				
No. of tests	3				3		3				3				12
$\sum$ **No. of tests**															87

Table 3.5: Bearing capacity programme testing.

Unsaturated tests										Total tests
	Footing placed on surface				Footing buried at 5 cm depth					
Suction kPa	0	2	4	6	0	2	4	6		
No. of tests	5	5	6	6	4	4	4	4		38
Dry tests										Total tests
	Footing placed on surface				Footing buried at 5 cm depth					
No. of Tests	7				6					13
Multi-stage test- dry to fully saturated										
Footing placed on surface										
No. of tests					2					2
Total No. of tests										53

Chapter 4

Experimental Results

4.1 Introduction

This chapter reports results of the experimental programme and highlights the most important and interesting findings. Highlighted results include comparison of the SWCC using two different methods, direct shear results for dry, saturated and unsaturated samples, dilatancy behaviour, the observed oscillation phenomenon of the shear resistance for dry, saturated and unsaturated samples, shear resistance under fully saturated conditions, increase in internal friction angle and cohesion due to unsaturated conditions, plastic collapse at high degrees of saturation and hydro-mechanical behaviour of unsaturated samples. Following the direct shear tests, the bearing capacity results for both strip footings placed on the surface and buried at 5 cm depth are presented. The most important observations of the bearing capacity test results are presented in this chapter supported by displacement vectors using PIV analysis.

4.2 Physical and shear strength parameters for the fraction D sand

The shear strength parameters and physical properties for the fraction D sand are shown in Table 4.1. The minimum and maximum values for the internal friction angle using the direct shear test on dry sand were obtained at displacement rates of 0.48 and 0.0096 mm/min, respectively and they are based on the average values of three repeated tests at three different normal stresses. The latter displacement rate was used to be compatible with the rate which was utilised for the unsaturated samples, while the former was selected to study the oscillation behaviour (see Section 4.5). The quick tilt test was used to find maximum void ratio, while minimum void ratio was obtained using ASTM-D4253 (1989) method.

4.3 Results of SWCC using the HCT and filter paper technique

The procedure explained in Chapter 3 for SWCC determination using the HCT and filter paper method (Sections 3.3 and 3.5) were performed and results are shown in Fig. 4.1. The main drying curve of the SWCC by the HCT (upper red solid square) was obtained by lowering the burette to a known depth, and then a reading of suction was taken after the

Table 4.1: Shear strength parameters and physical properties for the test sand.

Soil properties	
Shear strength parameters	
c, (kPa)	12.43 - 13.45
$\phi_{peak-\ dry}$, (degrees)	39.15 - 44.1
Physical properties	
G_s	2.65
γ_{dry}, (kN/m^3)	15.30
γ_{sat}, (kN/m^3)	19.33
Void ratio, e	0.70
Coefficient of uniformity, cu	1.53
Coefficient of curvature, cv	1.09
Particle size range, (mm)	0.075-0.3
e_{min}	0.54
e_{max}	0.87
Relative density %	52

period of equalization. As stated before, the stated applied suction head was the distance from the water level in the burette to the top of the sample. The calculation procedure for the main drying and wetting curves for the SWCC using the HCT is given in Appendix M.

The gravimetric water content in Fig. 4.1 was calculated as follows: the weight of the saturated sample at the beginning of the test was calculated and the volume of water extracted was measured at each burette lowering. Consequently, the wet unit weight of the sample was calculated by dividing the weight of the sample by volume (see Eq. 4.3 - Section 4.9). It was assumed that the void ratio and hence volume of the sample was constant and unaffected by suction change (after lowering the burette).

The main wetting curve of the SWCC was also determined experimentally using the HCT and it corresponds to the lower bound of the region that can be attained as shown in Fig. 4.1 (lower red solid square). It was obtained by adding water to the burette and as a result increasing water content of the sample. The suction reading was taken after an adequate equilibrium time. Several trial equilibrium times were conducted for the main wetting curve over 1, 2, 3 and 4 hrs. The equilibrium time of 4 hrs was used for the main wetting curve since the water level in the burette had stabilized after that time.

At the end of the HCT test, 2 samples were taken, the gravimetric water content was measured and plotted on the SWCC (see Fig. 4.1 - open circle). At this stage, since the water level in the burette was close to the sample surface, suction was almost zero. Good agreement between the measured (open circle) and calculated water content (red solid square - based on weight volume relationships) can be seen as shown in Fig. 4.1.

Using the filter paper method for fine-grained soil with very small range of suction is always controversial due to high sensitivity of the procedure required. However, it can be seen that good agreement between the filter paper technique and the HCT was obtained apart from two results at around 6 kPa suction.

The experimental results were fitted using the Fredlund & Xing (1994) model for both the drying and main wetting curves. The fitting parameters used in this model for both paths are shown in Table 4.2. The Fredlund & Xing (1994) equations are given by:

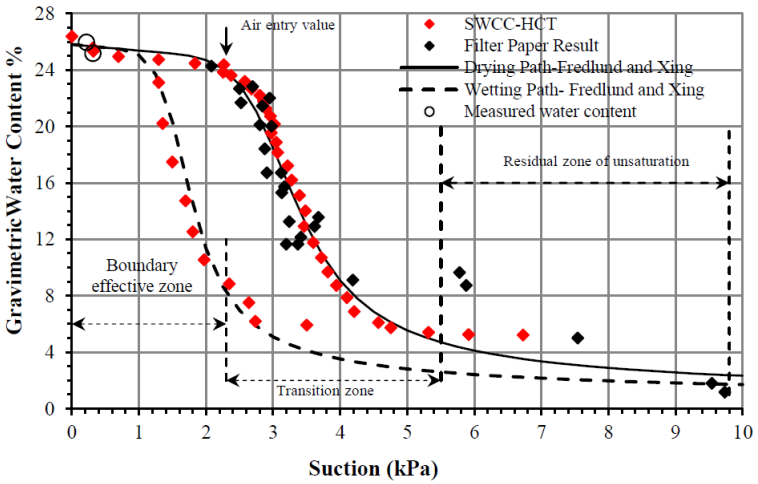

Figure 4.1: SWCC for the model sand using two different methods.

Table 4.2: Parameters used with Fredlund & Xing (1994) model.

	θ_s	a	n	m	ψ_r
Drying path	26.377	2.95	8.4	1	5.5
Wetting path	26.377	1.55	7.5	1	5.5

$$\theta = C(\psi)\ \theta_s \left[\frac{1}{ln[e + (\frac{\psi}{a})^n]}\right]^m \tag{4.1}$$

$$C(\psi) = \left[1 - \frac{ln[1 + \frac{\psi}{\psi_r}]}{ln[1 + (\frac{10^6}{\psi_r})]}\right] \tag{4.2}$$

where θ is volumetric water content, θ_s is saturated volumetric water content, $e = 2.718$, ψ is suction, a, n and m are fitting parameters, $C(\psi)$ is a correction factor and ψ_r is suction corresponding to the residual water content.

For the obtained SWCC, the air entry value and residual suction were determined by plotting tangents as shown in Fig. 4.2. Values of 2.3 and 5.5 kPa were found for the air entry and residual suctions, respectively.

As stated before in Chapter 3; a time of 2 hrs was used for each suction reading after lowering the burette for the main drying curve (for obtaining the SWCC using the HCT), however for the direct shear tests, 15 hrs was allowed for equalisation of suction following the application of the final suction value. This was a conservative estimate of the adequate equilibrium time after each lowering according to the observation of water table stabilization in the burette. Figure 4.2 shows good agreement between these two samples in which suctions were taken at two different times and confirms the suitability of the 2 hrs time as an equilibrium time for the drying path. This is also a good indication of consistency of the sample preparation.

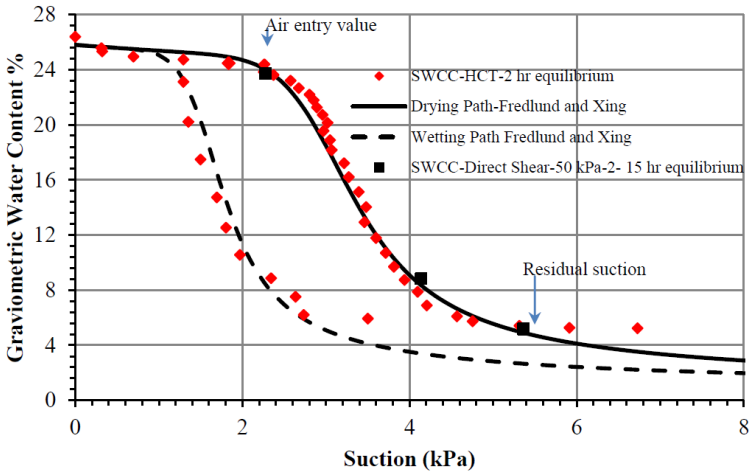

Figure 4.2: SWCC using two different equilibrium times.

4.4 Direct shear results

4.4.1 Unsaturated shear resistance

The direct shear test was conducted using the procedure that was explained in detail in Sections 3.5.2 and 3.6. A series of 36 water-drained tests (including repeat tests) were conducted at different vertical stresses and at a range of nominal suctions (0, 2, 4 and 6 kPa). The suction is achieved on a drying path. The programme also included direct shear tests on fully dry samples. Values of 2 and 6 kPa nominal suction were selected since they are close to the air entry suction (2.3 kPa) and residual suction (5.5 kPa) for the sand used. A nominal suction of 0 kPa was set as the benchmark for comparison to the other applied suctions. Finally, to investigate the behaviour of unsaturated sand at the transition zone (zone between air entry and residual suctions - see Fig. 4.1), a value of 4 kPa nominal suction was also utilised.

Due to the difficultly in obtaining an exact suction value (e.g. $s = 2$ kPa) using the HCT, slightly different values of suction are obtained. Also; after application of the normal load (before shearing), the water level in the burette increased for most of the samples due to water migration (to be explained later in this chapter). Table 4.3, therefore, presents suction values before and after the normal load application. The difference between the nominal suction and suction value after the normal load application can be considered small except for a few cases (e.g. $\sigma = 200$ - 2 at nominal $s = 4$ kPa). The negative values for $s = 0$ kPa denote the water table level above the soil surface. The term suction will be used to refer to the suction achieved at the sample surface based on the height difference between burette water level and sample surface in the context of this thesis and in the figure's legends. Otherwise; other suctions, obtained before or after application of the normal load, will be stated clearly whenever it is required.

Figures 4.3 to 4.5 plot the shear resistance versus horizontal displacement conducted at five different suctions and at three normal stresses 50, 100 and 200 kPa. The shear resistance values are based on the corrected area of the samples. For each normal stress, three tests were performed and labelled as 1, 2 and 3 denoting first, second and third repeat test, respectively as shown in Figs. 4.3a, b and c. The tests were terminated when the horizontal displacement reached 10 mm, apart from some tests (e.g. see Fig. 4.3a - $s = 4$ kPa - 1), where the test was terminated due to data logging problems. For those tests that did not reach 10

Table 4.3: Suction values for nominal, before and after application of the normal load.

σ^1	$s_{nominal}{}^1$	s before normal load application^1	s after normal load application^1
50-1	0	0	-0.12
50-2	0	0	-0.06
50-3	0	0	-0.07
100-1	0	0	-0.14
100-2	0	0	-0.08
100-3	0	0	-0.12
200-1	0	0	-0.28
200-2	0	0	-0.24
200-3	0	0	-0.64
50-1	2	2.17	2.06
50-2	2	2.06	2.04
50-3	2	2.19	2.18
100-1	2	1.87	1.86
100-2	2	2.15	1.96
100-3	2	2.02	2.00
200-1	2	2.25	1.89
200-2	2	2.1	1.86
200-3	2	2.06	1.77
50-1	4	4.35	4.27
50-2	4	4.1	4.1
50-3	4	3.95	3.89
100-1	4	4.06	4.05
100-2	4	4.08	3.94
100-3	4	3.97	3.91
200-1	4	4.16	3.93
200-2	4	4.21	3.82
200-3	4	4.08	3.77
50-1	6	5.33	5.32
50-2	6	5.88	5.79
50-3	6	6.02	5.92
100-1	6	6.12	5.95
100-2	6	5.92	5.71
100-3	6	5.77	5.54
200-1	6	6.17	5.62
200-2	6	5.88	5.52
200-3	6	5.56	5.56

1 suction and normal stress values in the Table are in kPa.

mm horizontal displacement, the samples had already passed the peak shear resistance and levelled off to critical state hence the peak shear resistance and critical state resistance can be identified easily.

All saturated and unsaturated specimens exhibited a peak strength followed by a shear resistance reduction to critical state. The peak-phenomenon for unsaturated soils also was observed by other researchers such as Alonso et al. (1990), Wheeler & Sivakumar (1995), Chiu & Ng (2003) and Tarantino & Tombolato (2005). In general, over consolidated clay and

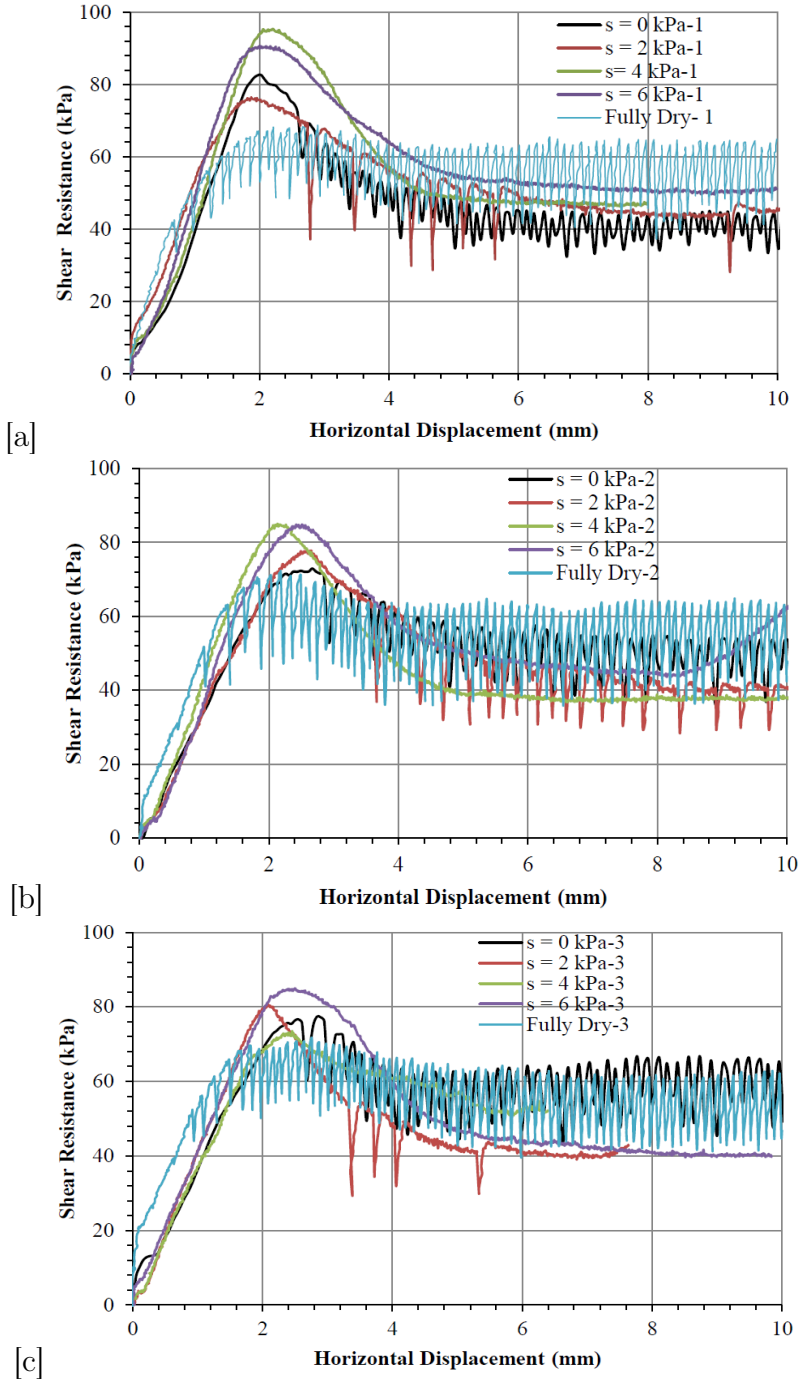

Figure 4.3: Shear resistance versus horizontal displacement at $\sigma = 50$ kPa for (a) the first test (b) the second repeat test (c) the third repeat test.

dense sand show a peak strength and strain softening behaviour, while normally consolidated clay and loose sand follow a strain hardening behaviour. Although the samples were prepared as loose (relative density = 52%), strain softening was obtained. This is attributed to the unsaturated conditions and dilative behaviour which is discussed in detail in Subsection 4.4.5.

Different patterns of behaviour prior to and at peak can be observed due to the applied suction. There is a significant increase in the shear resistance for unsaturated cases when compared to the fully dry case. For example, the shear resistance at peak for $s = 4$ kPa

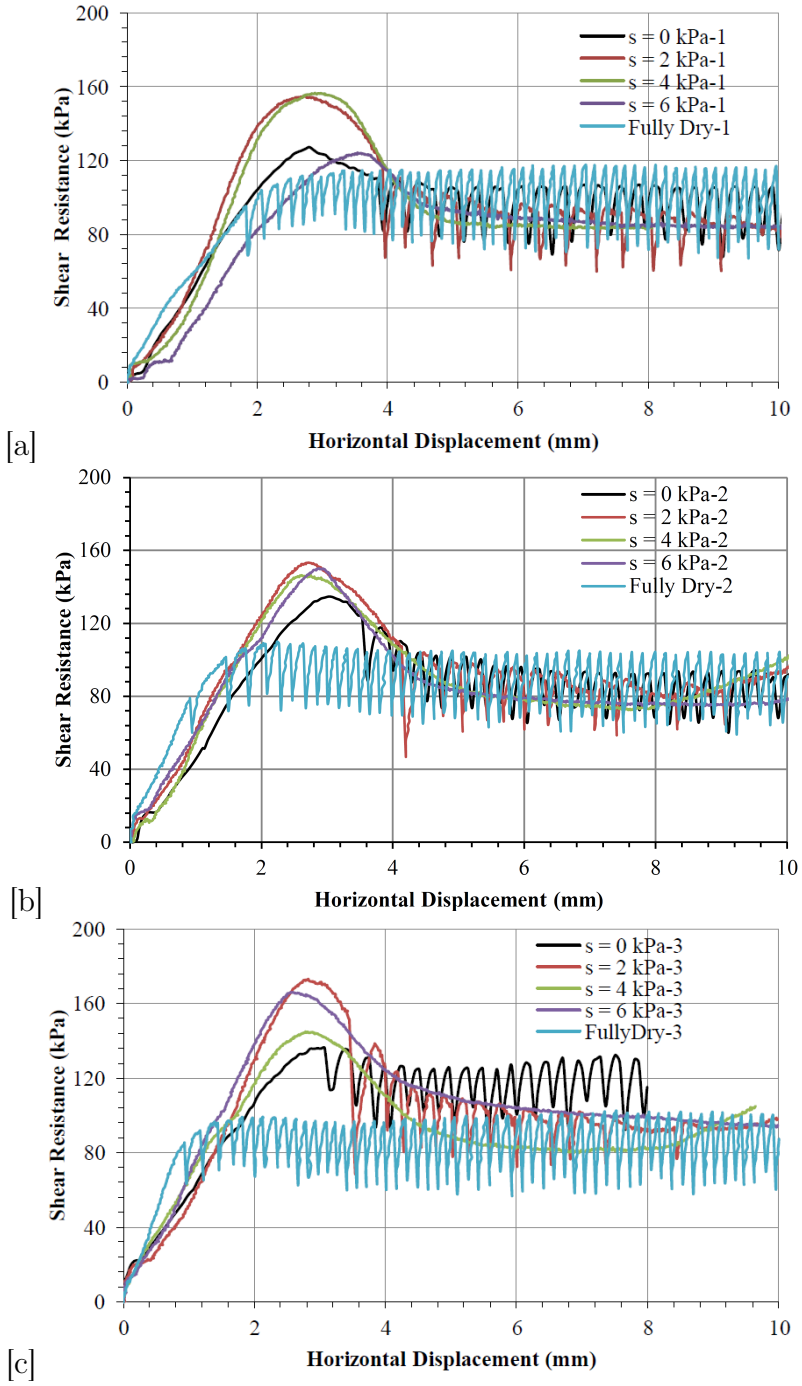

Figure 4.4: Shear resistance versus horizontal displacement at $\sigma = 100$ kPa for (a) the first test (b) the second repeat test(c) the third repeat test.

increased about 1.45 fold compared to the fully dry case (see Fig. 4.3a).

Peak shear resistance within the range of suctions of 2 (close to the air entry value) to 4 kPa (in the transition zone between the air entry value and the residual suction) is achieved (see Figs. 4.3, 4.4 and 4.5). Md. Noor (2005) performed a series of triaxial tests on unsaturated granular soil. In his study, the peak shear resistance was obtained at the residual suction. Likos et al. (2010) performed direct shear tests on a poorly graded fine sand at relatively low net normal stress. A range of suctions 0 to 10 kPa was applied using the HCT. The peak shear resistance was obtained near the air entry suction of the soil.

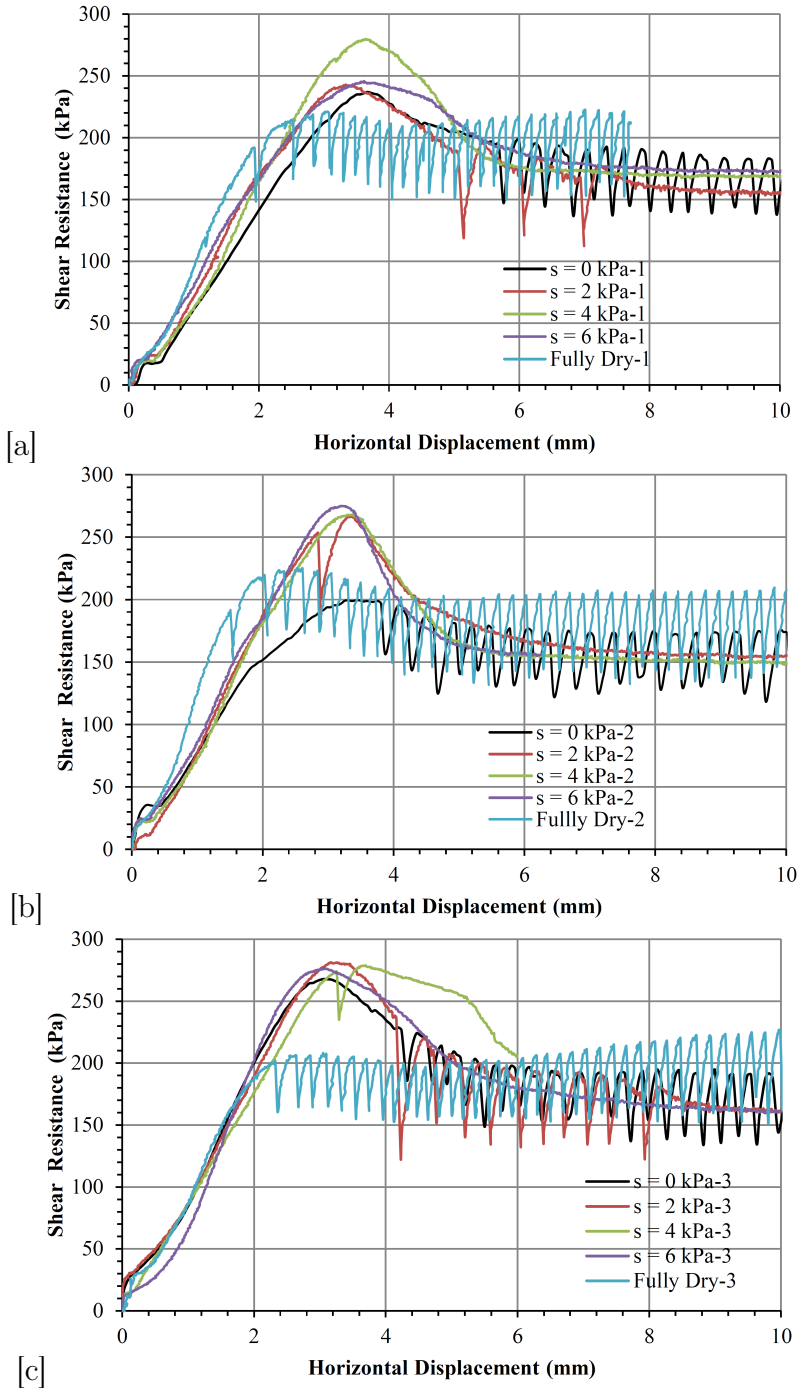

Figure 4.5: Shear resistance versus horizontal displacement at σ = 200 kPa for (a) the first test (b) the second repeat test (c) the third repeat test.

Figure 4.6 shows the scatter in the peak shear resistance for the three repeat tests for a range of suctions as well as for the dry tests (displacement rate = 0.0096 mm/min). The data for the dry cases were fitted at s = 0 kPa.

Oscillation of the shear resistance for samples prepared at high degrees of saturation (s = 0 and 2 kPa) as well as for the fully dry case can also be observed. More details regarding to this behaviour are presented in Section 4.5. Also, the effect of oscillation on apparent cohesion and internal friction angle at peak and critical state is presented in Section 4.7. This oscillation can be filtered using a Matlab code and presented in terms of two bounds

(upper and lower) as shown in Fig. 4.6b.

Fully saturated samples ($s = 0$ kPa) exhibit high shear resistance (close to shear resistance of $s = 2$ kPa - see Figs. 4.3) compared to the dry case. As this behaviour is not consistent with the common findings in the basic soil mechanics, it was thought that the higher shear resistance of fully saturated samples might be attributed either to a decrease in the degree of saturation due to application of normal stress (water was expelled from the sample after applying the normal stress-drained condition), displacement rate or low permeability of the HAED. A series of tests, therefore, were conducted to investigate the above mentioned factors and more details are presented in Section 4.6.

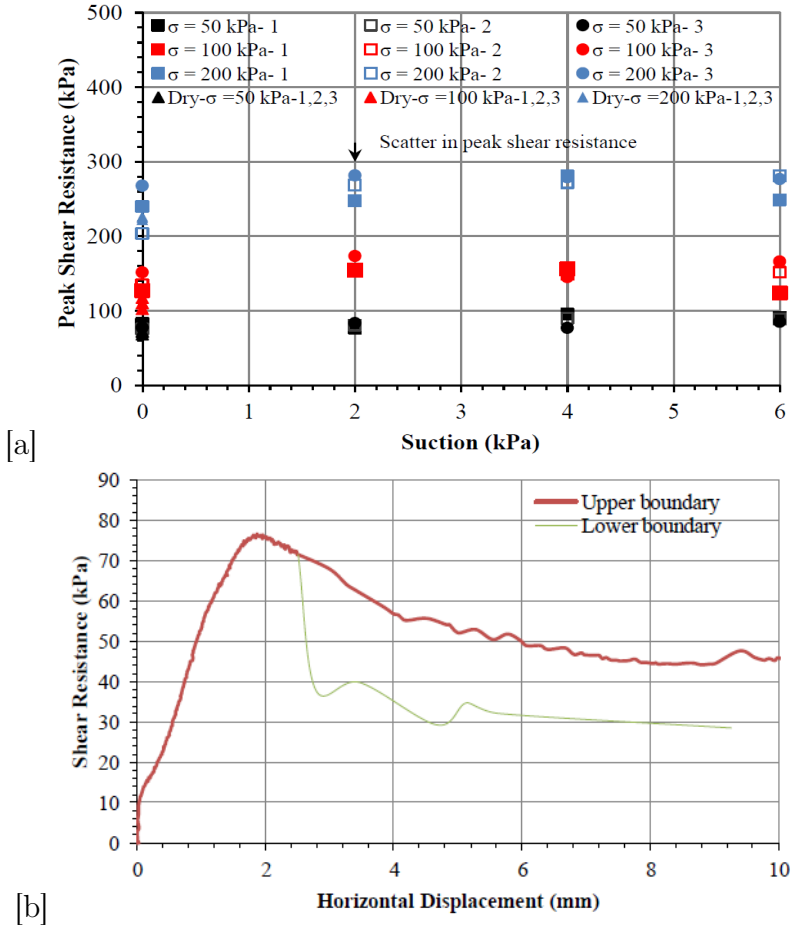

Figure 4.6: (a) Scatter of peak shear resistance for three repeat tests at different suction values (b) Upper and lower boundaries of the oscillation for $\sigma = 50$ kPa-1 and $s = 2$ kPa.

4.4.2 Repeatability of the tests

For each normal stress and suction, three tests were conducted. The average values of shear resistance (red lines) were taken for the repeat tests as shown in Figs. 4.7 to 4.9 with error bars. The error bars show a range of the shear resistance for the repeat tests with more widely spaced data for the fully saturated case due to the higher displacement rate for this test. For the $s = 0$, 2 kPa and dry cases, there are some discrepancies in the average shear resistance which is caused by the oscillations. As before, for samples were terminated before 10 mm horizontal displacement, the error bars also ended before the targeted displacement.

The average peak shear resistance values are used to determine shear strength parameters c and ϕ. This is presented in Section 4.7.

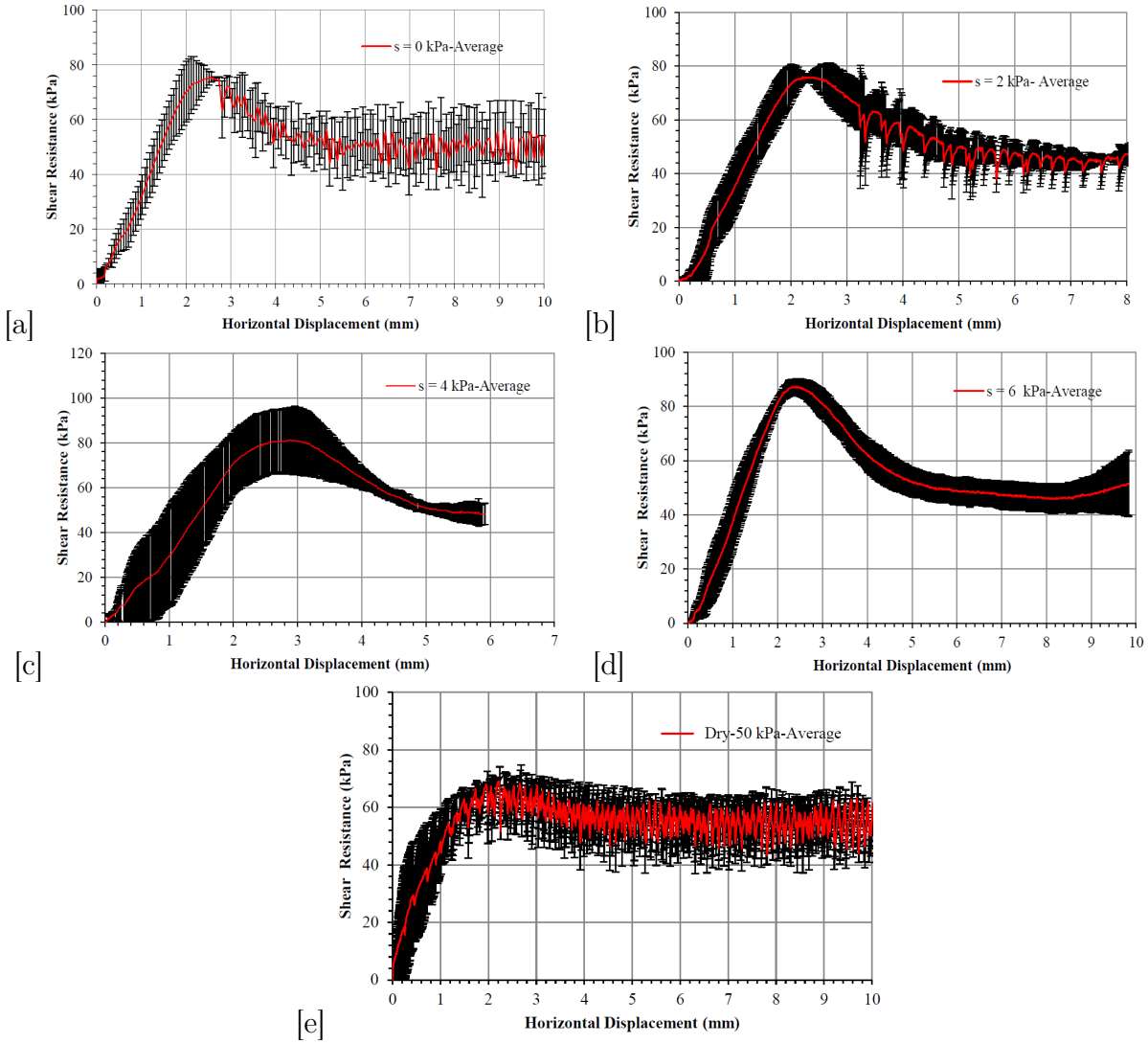

Figure 4.7: Average shear resistance of three repeat tests showing error bars for $\sigma = 50$ kPa for (a) $s = 0$ kPa (b) $s = 2$ kPa (c) $s = 4$ kPa (d) $s = 6$ kPa (e) the dry case.

4.4.3 Water effluent mass

The amount of water drained from the sample due to application of the suction and during shearing can be measured at any stage by observing the water level in the burette. This allows any change of degree of saturation and hence suction to be tracked. Figures 4.10a, b and c show the water effluent mass versus suction before and to the end of the test for suction $s = 2$, 4 and 6 kPa and at different normal stresses 50, 100 and 200 kPa. The straight line represents the amount of water removed from the sample (by lowering the burette) before the test until the suction was applied. While the line after the kink defines the amount of water extracted from the sample (after applying the normal stress and shearing) induced by shearing which is presented separately in Subsection 4.4.4. The begining of the kink does not necessarily mean the begining of the test as for some cases suction further increased during shearing (water imbibed).

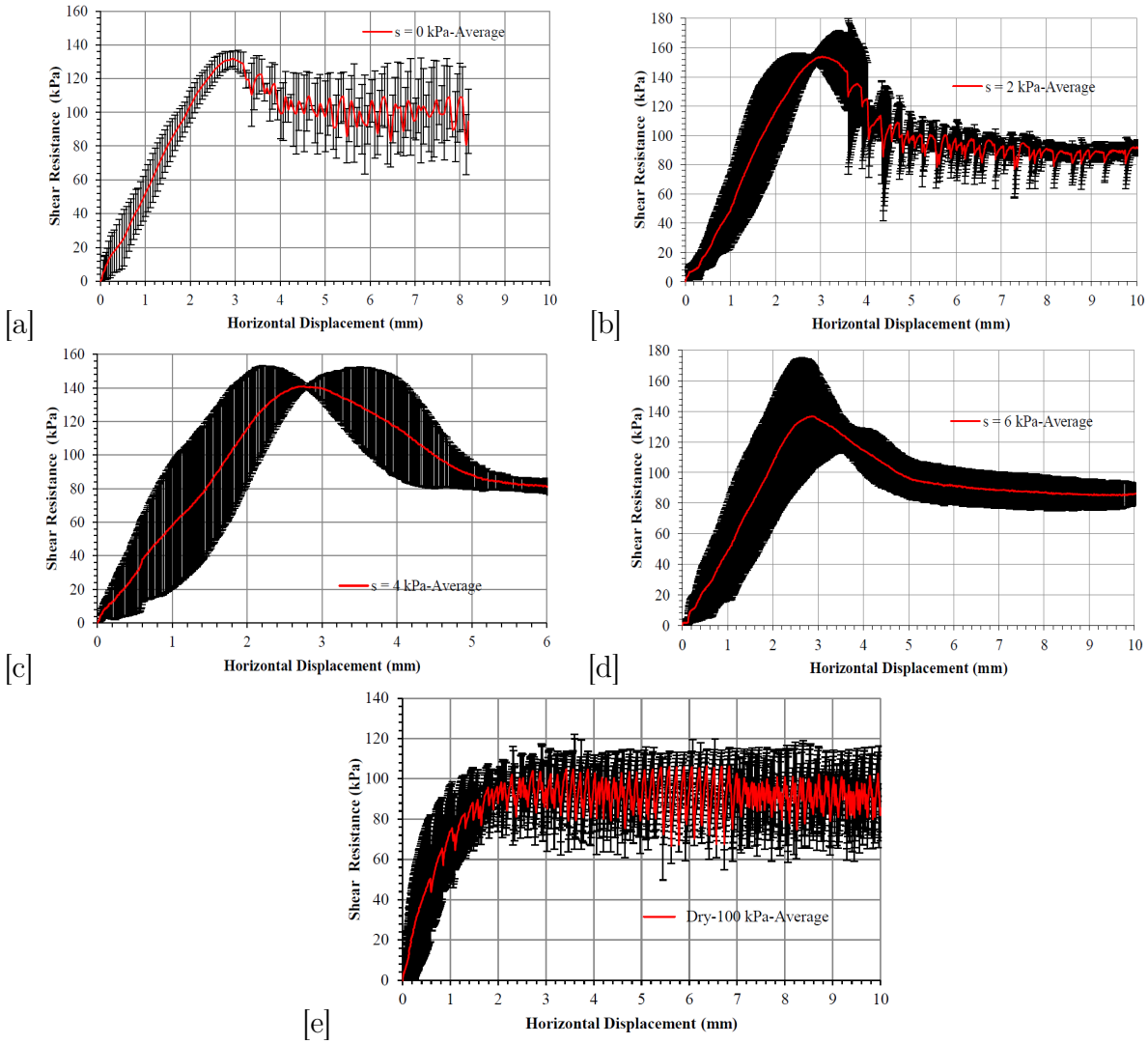

Figure 4.8: Average shear resistance of three repeat tests showing error bars for $\sigma = 100$ kPa for (a) $s = 0$ kPa (b) $s = 2$ kPa (c) $s = 4$ kPa (d) $s = 6$ kPa (e) the dry case.

For $s = 2$ kPa in which the sample is near full saturation, one lowering attempt of the burette was sufficient to achieve the obtained suction. In other words; to achieve $s = 2$ kPa, it was required to lower the burette to a specific depth only one time. However, to target higher suctions such as $s = 4$ and 6 kPa, almost (9 to 12) and (11 to 13) lowering stages of the burette, respectively were required due to the larger amount of expelled water (see Figs. 4.10b and c).

In Fig. 4.10b, apart from Fig. 4.10a for $s = 2$ kPa, the sample for normal stress of 50 kPa-1 (during sample preparation) at nearly 2.6 kPa suction showed smaller amount of water extracted. Nevertheless; at the end of the sample preparation (at the kink point), nearly all samples showed good consistency in amount of water extracted. The same observations also can be seen for the $s = 6$ kPa at normal stress of 200 kPa-3 as shown in Fig. 4.10c.

4.4.4 Water effluent mass during the shearing stage

Figures 4.11a, b and c show the water effluent mass versus suction during the test. These figures magnify the post kink part from Figs. 4.10a, b and c. The amount of water removed

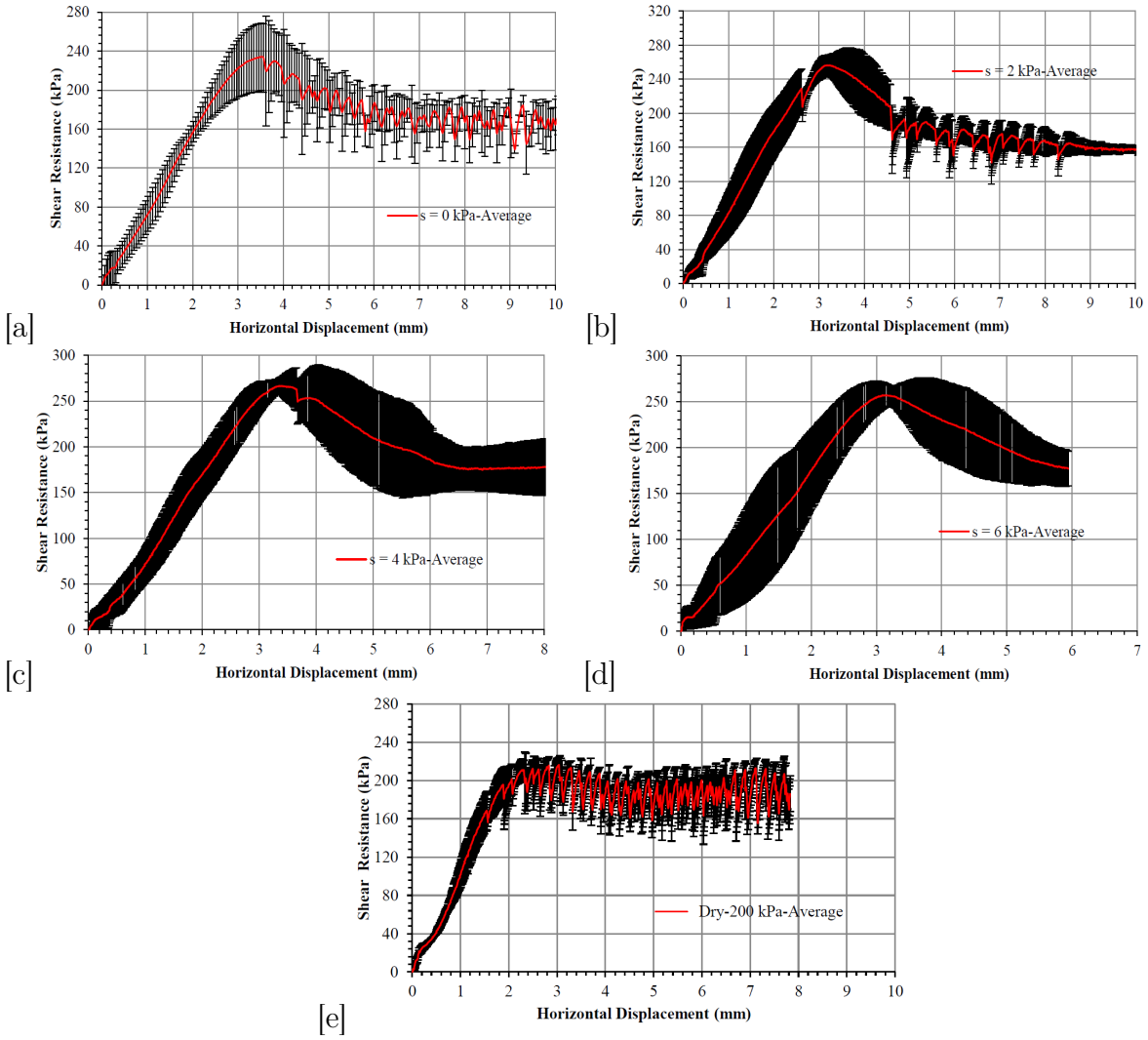

Figure 4.9: Average shear resistance of three repeat tests showing error bars for $\sigma = 200$ kPa for (a) $s = 0$ kPa (b) $s = 2$ kPa (c) $s = 4$ kPa (d) $s = 6$ kPa (e) the dry case.

due to shearing was used to track change in suction and degree of saturation and to model behaviour of the soil under any change of void ratio. In all cases, it can be seen that water was expelled or imbibed by the sample during shearing, leading to a rise or a drop in burette level and thus a change in suction. However, it would be expected that loss of water would lead to a gain in suction and vice versa. Section 4.9 presents an analysis of hydro-mechanical behaviour in more detail.

4.4.5 Dilatancy behaviour

Dilatancy can be defined as the rate of volume change of the soil when it is shearing, Powrie (2013). Soil behaviour is significantly affected by the dilatancy and in saturated soils it is well understood. In contrast, understanding the phenomena of dilatancy in unsaturated soils is restricted due to the long experimental time and complexity, Ng & Zhou (2005).

Within the next paragraphs, results of the drained direct shear test in terms of vertical displacement are presented. The reason for presenting them in terms of vertical displacement is because a wetting (plastic) collapse was observed for almost all cases at $s = 2$ kPa (see e.g. Fig. 4.12b at 4 mm displacement - circled in the figure) and this could be lost if the

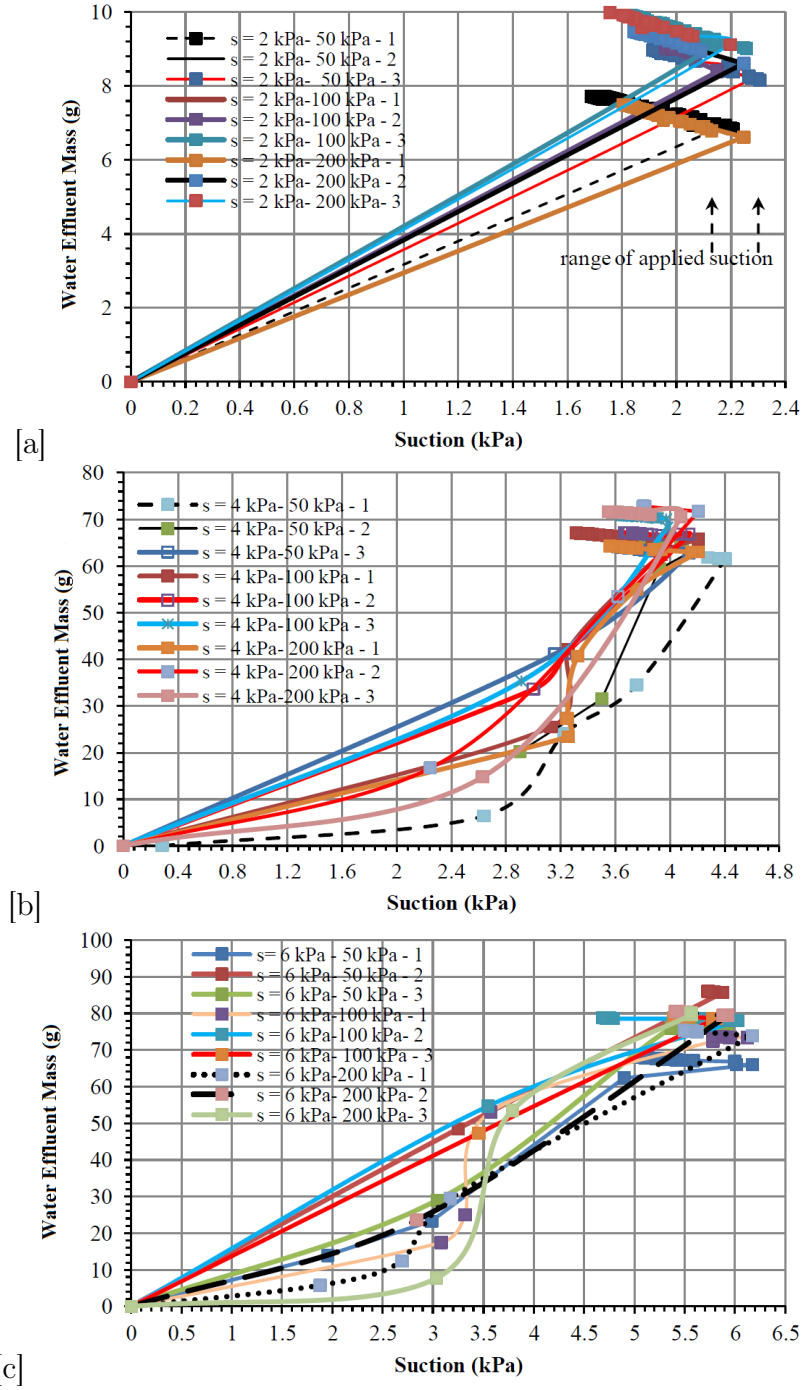

Figure 4.10: Water effluent mass versus suction for repeat tests at different normal stresses for (a) $s = 2$ kPa (b) $s = 4$ kPa (c) $s = 6$ kPa.

data was presented in terms of dilatancy = (-volumetric strain/shear strain).

Figures 4.12 to 4.14 show the vertical displacement versus horizontal displacement for all suctions at the three normal stresses of 50, 100 and 200 kPa as well as for the dry sample. The figures are plotted with the negative vertical displacement (dilation) axis pointing downwards. For almost all the three normal stresses, the fully dry case shows less dilation compared with the other applied suctions. Also, the fully saturated case showed less volume change compared to the unsaturated samples. This was consistent for almost all the saturated samples. Steeper curves can be seen for the unsaturated cases indicating increase

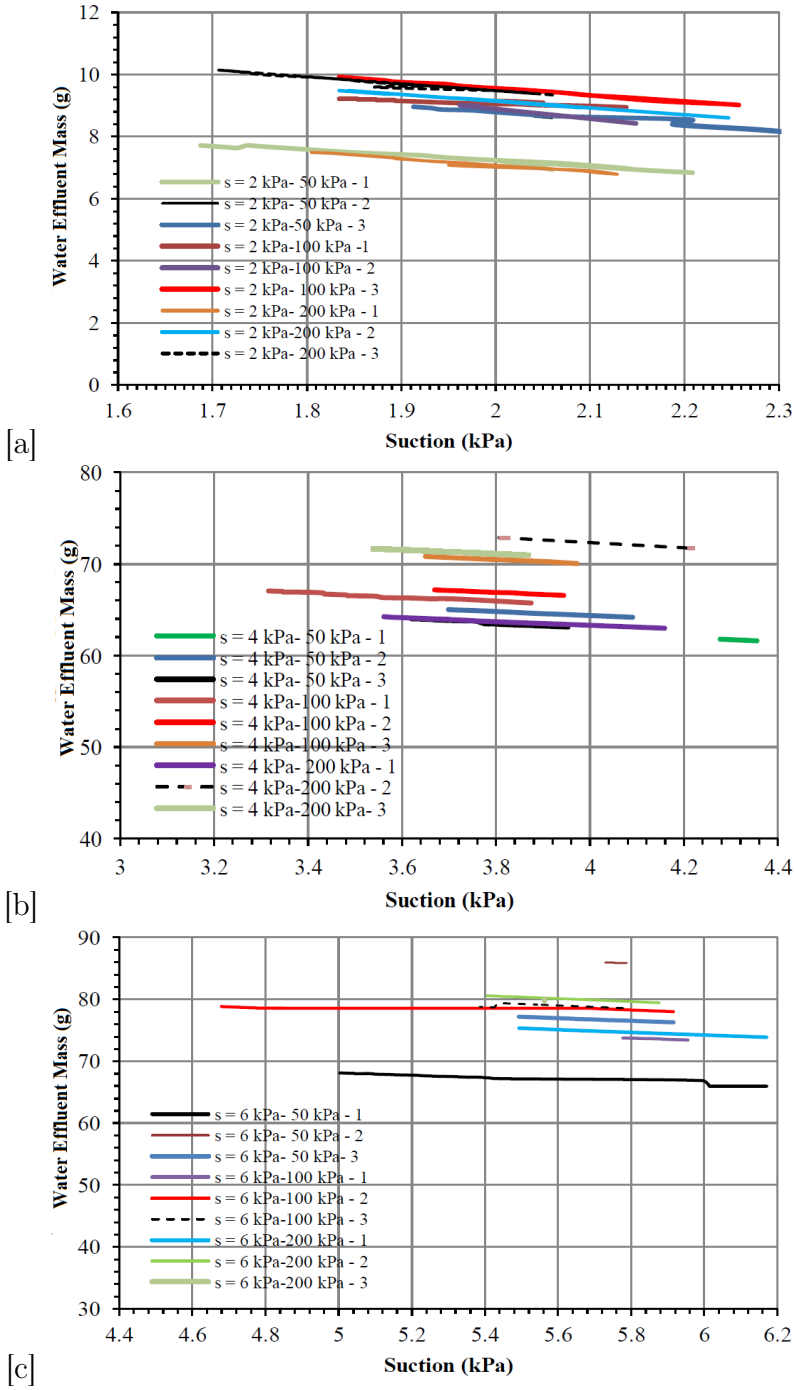

Figure 4.11: Water effluent mass versus suction during the shearing stage for repeat tests at different normal stresses for (a) $s = 2$ kPa (b) $s = 4$ kPa (c) $s = 6$ kPa.

in dilation rate which coincides with the maximum shear resistance (e.g. see Fig. 4.3a - near 2 mm horizontal displacement), then followed by less steep curves until critical state is reached. Once more, the maximum value of volume change (dilatancy) does not match with the higher value of the applied suction (e.g. in Fig. 4.12c maximum dilation happened at $s = 4$ kPa not at $s = 6$ kPa). The unsaturated samples (especially for cases $s = 4$ and 6 kPa) showed higher dilation than the fully dry and saturated cases.

All samples exhibited contractive behaviour initially, but then dilation behaviour as horizontal displacement continued to increase. In other words, the samples were packed to a

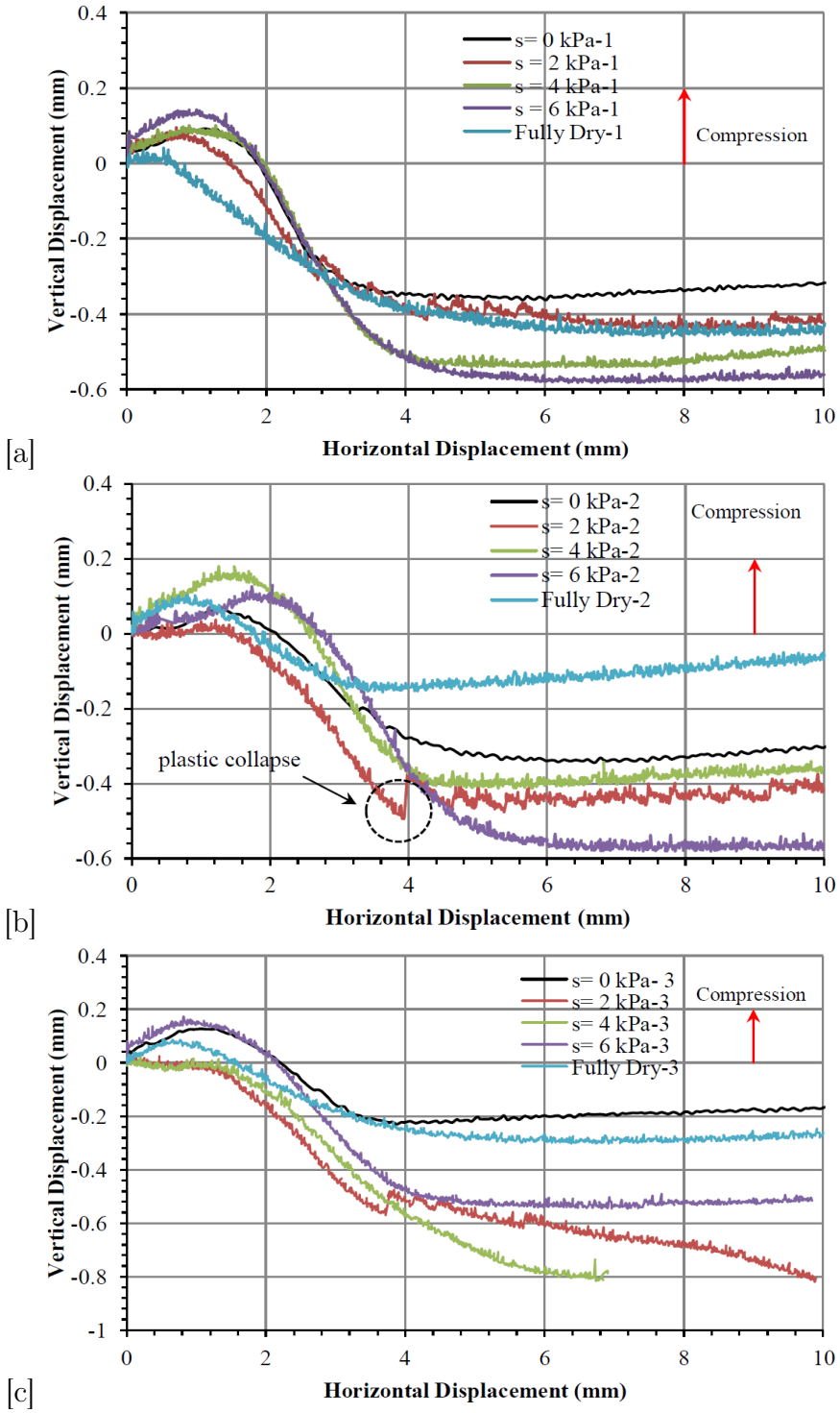

Figure 4.12: Vertical displacement versus horizontal displacement for a range of applied suctions at $\sigma = 50$ kPa for (a) the first test (b) the second repeat test (c) the third repeat test.

denser condition at the initial stages of the test (until about 2 mm displacement) and this served to decrease void ratio and densify the packing. Then, the samples were loosened (increase in volume) until the critical void ratio was reached.

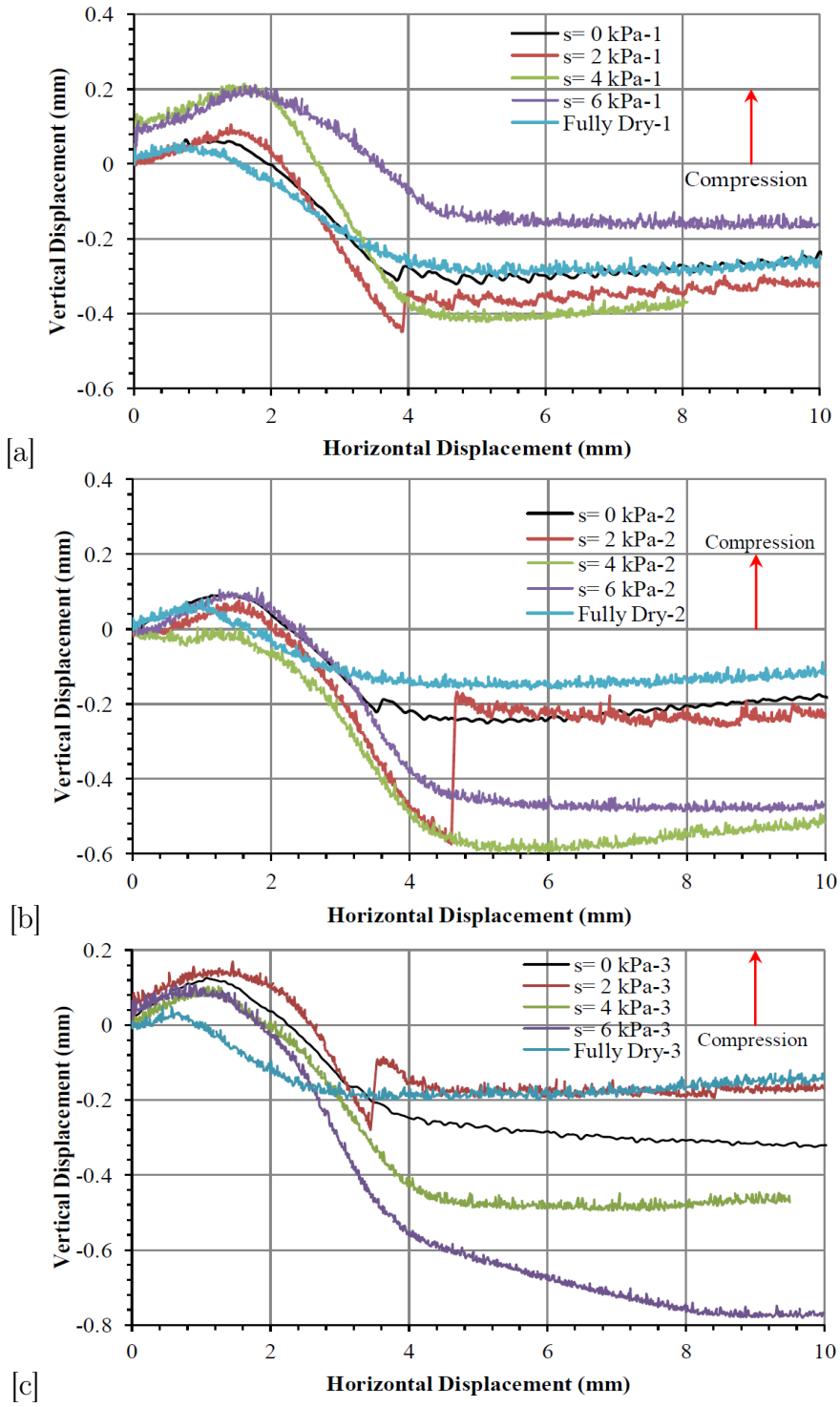

Figure 4.13: Vertical displacement versus horizontal displacement for a range of applied suctions at $\sigma = 100$ kPa for (a) the first test (b) the second repeat test (c) the third repeat test.

4.5 Oscillation of the shear resistance

Oscillation or stick - slip behaviour for the shear resistance of the direct shear results was observed for values of $s = 0$ and 2 kPa as well as for fully dry samples (e.g. see Fig. 4.3a). The oscillatory behaviour is attributed to periodic instability in which slippage of the particles

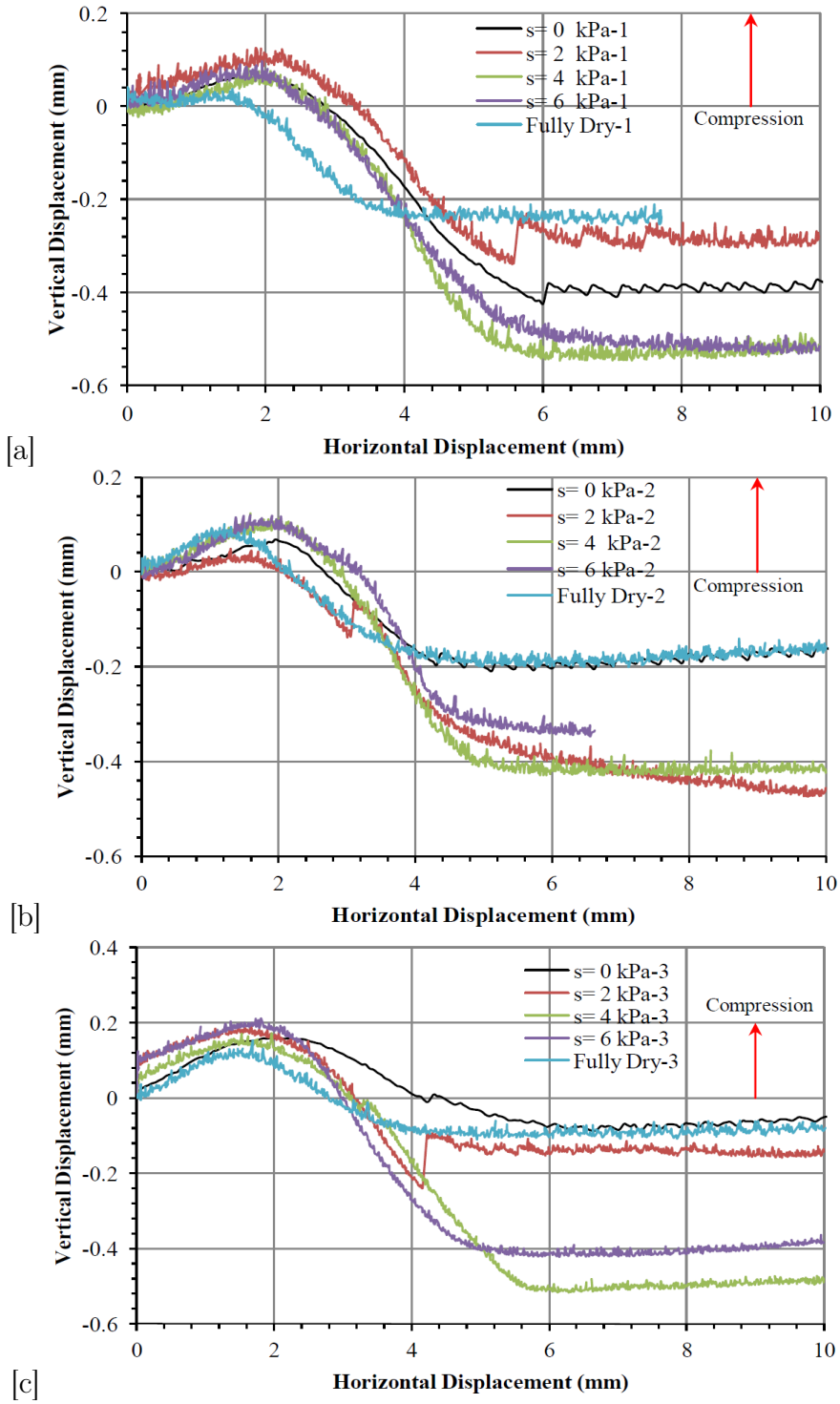

Figure 4.14: Vertical displacement versus horizontal displacement for a range of applied suctions at $\sigma = 200$ kPa for (a) the first test (b) the second repeat test (c) the third repeat test.

that caused plastic collapse happened. This behaviour occurs after the soil passed its peak shear resistance and continues until the critical state. The upper and lower boundaries of the oscillation cause difference in shear resistance and hence in internal friction angle. The oscillation displacement period (time between one oscillation to another) is shorter for the fully saturated case than for $s = 2$ kPa, however higher reduction in shear resistance can be

observed at each oscillation for $s = 2$ kPa. In contrast, no oscillation in shear resistance can be observed for $s = 4$ and 6 kPa (except for $s = 4$ kPa-3 - see Fig. 4.5c).

At first glance, it seemed that water content and displacement rate caused the observed behaviour. This behaviour was unexpected for the fully dry case (eliminating the effect of water as it was thought the slippage happened due to water) and further investigation considering the following different factors: displacement rate, geometry of the box and effect of the HAED on shear band were performed. Also, the possibility of sand entering the space between the box halves, which may have caused oscillation, was monitored before and during the test (this was done visually as the box was transparent). Inspection after the test confirmed that sand was not present on the interface between the two halves of the box.

Throughout the next subsections, several tests on dry soil are presented. Firstly, three different displacement rates were used to examine the effect of displacement rate on oscillation of the shear resistance. Secondly, changing the geometry of the box from circular to the conventional square direct shear box 100×100 mm examines any effect of the shape of the box.

4.5.1 Effect of displacement rate

The effect of displacement rate on the oscillation of the shear resistance for a fully dry case at a normal stress of 50 kPa was investigated. Three different displacement rates were selected at 0.48, 0.048 and 0.0096 mm/min. For the former displacement rate, the data logging LabVIEW software was set to take reading every 1 second rather than 1 minute as for the other two displacement rates. This is to ensure that any change (oscillation) of the shear resistance can be picked up quickly by the data logger at the higher displacement rate. Figures 4.15a and b show the results of three tests in which oscillation of the data and different dilation behaviour can be readily seen.

4.5.2 Effect of shear box geometry on the oscillation

A conventional direct shear box of size 100×100 mm was used to investigate the effect of shape and size of the box on the oscillation. A piece of porous plastic was placed in the bottom of the box instead of the HAED due to difficulty of fitting a square HAED in the box. The sample was subjected to a normal load of 26.5 kPa and sheared at a displacement rate of 0.048 mm/min. Figure 4.16a shows the shear resistance versus horizontal displacement of the conventional shear box in which oscillation of the dry sand can be observed.

A further test was conducted using the conventional shear box by replacing the porous plastic by a serrated plate placed perpendicular to the box movement. This was to eliminate slippage of the particles that might happen between the porous plastic and soil particles (although studies can be found in the literature that used a HAED instead of the serrated plates - see Section 2.9). The result, once more, shows oscillation as shown in Fig. 4.16b. However, more oscillation can be seen in case when porous plastic was placed as shown in Fig. 4.16a.

One of the interesting behaviours observed (e.g. see Fig. 4.3a) is that no oscillation can be observed for both $s = 4$ and 6 kPa suctions (except for Fig. 4.5c). In other words, in spite of dilative behaviour after the peak shear resistance and increase in void ratio no oscillation can be observed. This is discussed in more detail in Subsection 7.3.4.

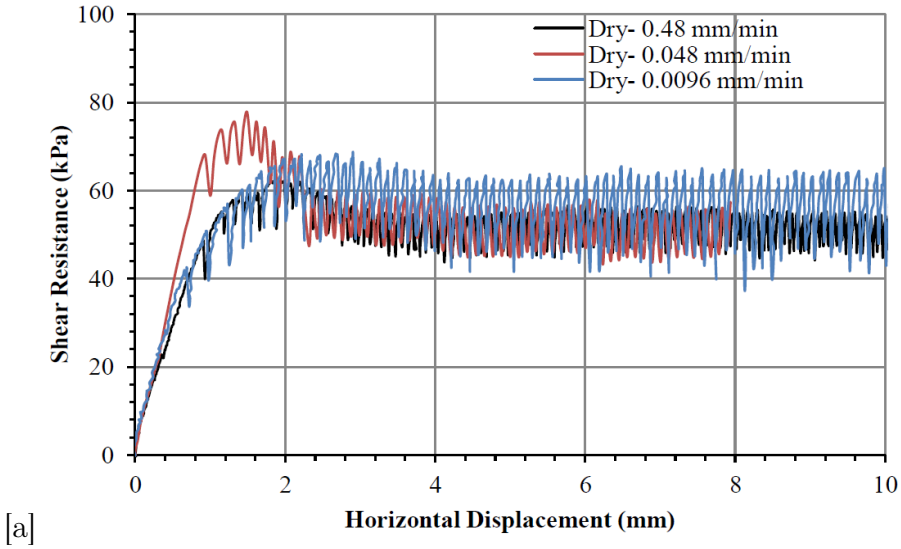

[a]

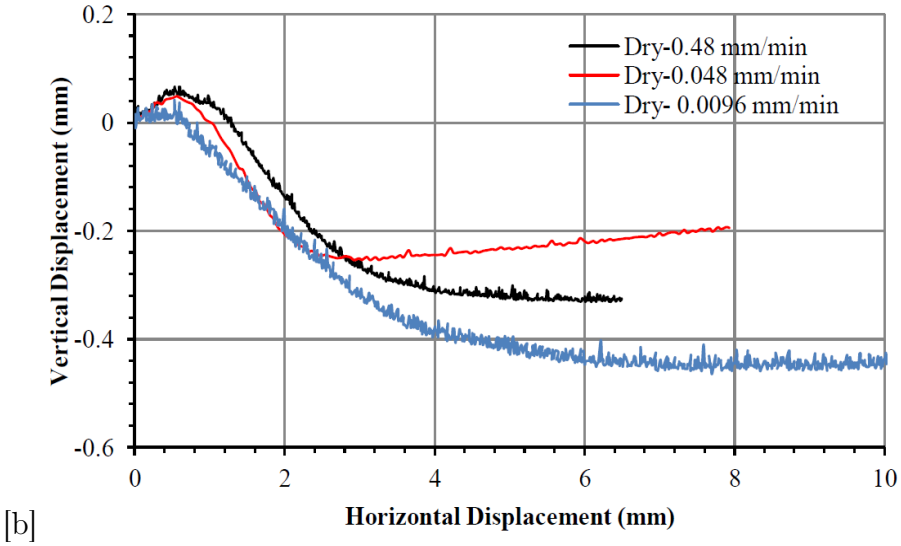

[b]

Figure 4.15: (a) Effect of displacement rate on the oscillation for the dry sand (b) Effect of different displacement rate on dilation for the dry sand.

4.6 Shear resistance in fully saturated conditions

An additional unexpected result was the high values of shear resistance obtained in fully saturated cases compared to the dry case. Since the tests were conducted under drained conditions and following application of normal stress on the samples; water flowed out from the sample to the burette, this may have an effect on the shear resistance (shear resistance increases as degree of saturation decreases). A series of tests was set up to explore this in more detail (see Table 3.4). Two series of tests were conducted as follows:

1. Undrained conditions.
2. Drained multi stage: dry to fully saturated case.
3. Undrained multi stage: dry to fully saturated case.

The "undrained" condition was achieved when the effluent port, burette No.2 in Fig. 3.11a, was closed during the test to not allow any water in or out of the specimen from the burette. However, water could freely drain upwards around the loading plate.

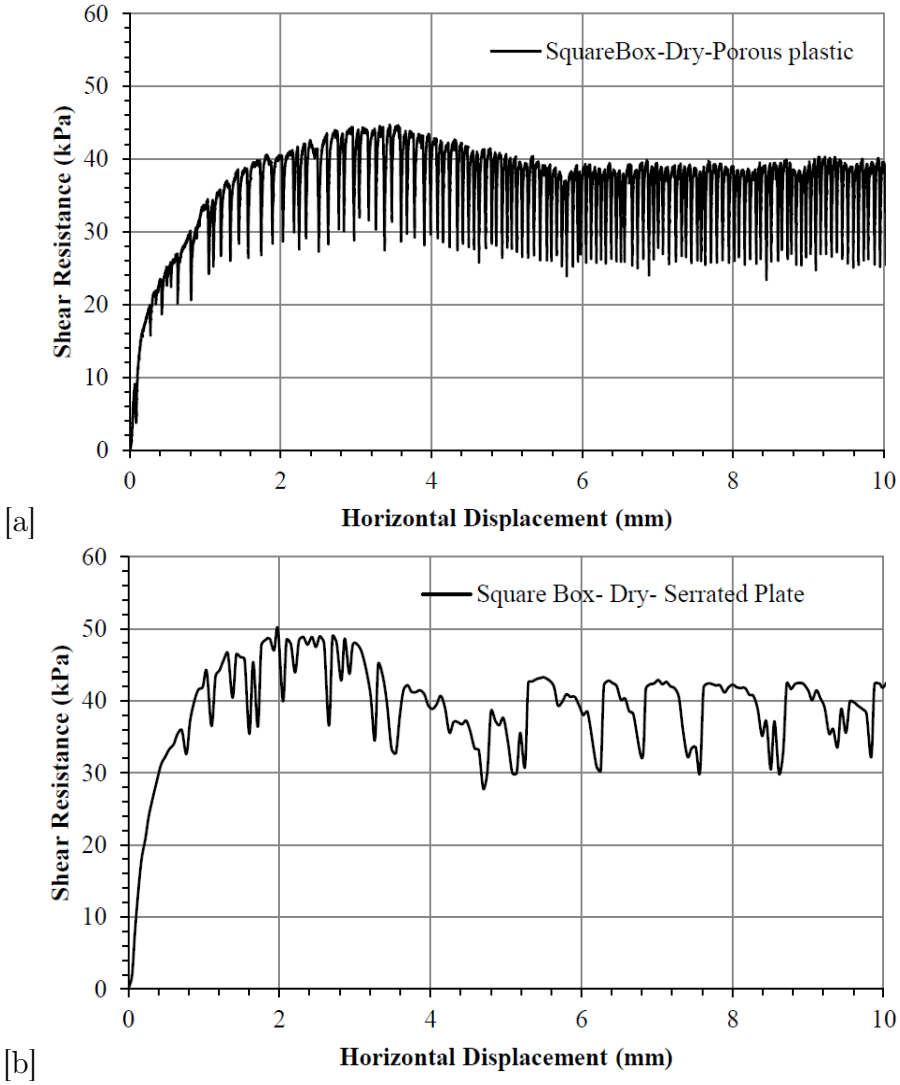

Figure 4.16: Oscillation of the conventional square shear box (100×100 mm) at displacement rate of 0.048 mm/min using at the bottom of the box (a) porous plastic (b) serrated plate.

4.6.1 Shear resistance of fully saturated soil under "undrained" conditions

The tests were conducted at 50 kPa normal stress and at two different displacement rates of 0.048 and 0.0096 mm/min. For the case of the 0.0096 mm/min displacement rate, the test took nearly 17.4 hr to achieve 10 mm horizontal displacement. Another test was conducted by replacing the HAED with a piece of porous plastic fitted to the bottom half of the box. The porous plastic was previously saturated by putting it in a desiccator under (-80 kPa) vacuum pressure for several hours and for several circulations of vacuum. Using the porous plastic was to double check that the high shear resistance is not due to the HAED, since it was thought possible that shear band extended to hit the HAED.

Results of the tests are shown in Fig. 4.17 and compared with one of the direct shear results for the drained case at 50 kPa. All samples showed almost same shear resistance under different displacement rates, different drainage disks and at different conditions (drained and undrained). Sample of "Drained-0.048 mm/min-HAED" offset horizontally, otherwise closely matches the undrained tests. The degree of saturation after the test was calculated for all

the cases based on the measured water content (samples were taken) and it was about 99% showing that the soil was close to fully saturated conditions.

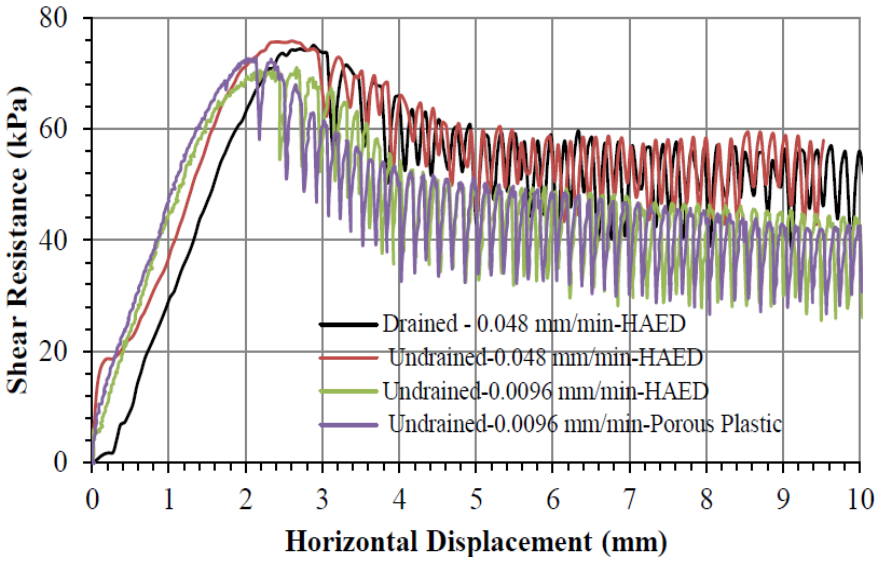

Figure 4.17: Shear resistance test for fully saturated case for $\sigma = 50$ kPa at different displacement rate, drained and undrained conditions, and with HAED or porous plastic drain.

4.6.2 Shear resistance of fully saturated soil in multi stage tests

As stated before, the fully saturated direct shear tests (and bearing capacity tests, shown later in this chapter) showed higher values of shear strength than dry cases. However, the shear strength and bearing capacity values for the fully saturated case should be less or equal to the fully dry case according to standard soil mechanics. A comprehensive programme, therefore, was set up to investigate this behaviour in which a multi stage dry to fully saturated test was carried out for both the direct shear and bearing capacity tests. The multi stage direct shear test involved shearing in fully dry conditions to a target horizontal displacement (i.e. ~ 3.2 mm- see Fig. 4.18a and b). The sample was then saturated using dry pluviation technique and was covered by a piece of latex membrane to prevent evaporation. After saturation, the sample was left for 24 hrs to equilibrate and the test was restarted. At the end of the test, samples were taken for water content measurements. The multi-stage direct shear test was conducted under two different conditions, drained and undrained at a displacement rate of 0.0096 mm/min.

Figs. 4.18a and b show the shear resistance versus horizontal displacement for both drained and undrained conditions in which shear resistance increased due to adding water. Here the dilatancy rate (see Figs. 4.18c and d) was observed to rise after saturation in line with the currently reported tests.

As stated before, the box was greased on the outside faces to prevent leakage of the water due to the high permeability of the sand. It was thought that grease may provide an additional strength to the box. Also, contact between soil, water and the grease may happen. Therefore, this may also increase the shear resistance of the soil. To investigate this effect, two types of tests were conducted as follows:

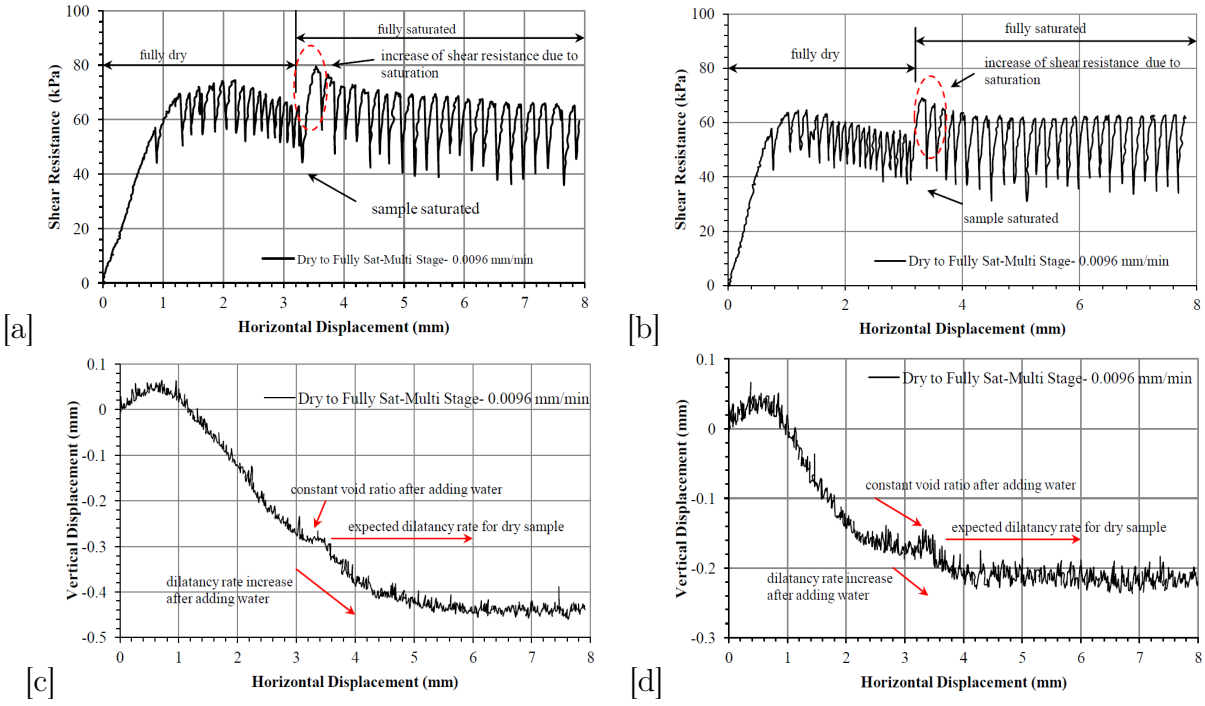

Figure 4.18: Multi-stage direct shear test at displacement rate of 0.0096 mm/min for $\sigma = 50$ kPa for (a) drained condition (b) undrained condition. Dilatancy rate behaviour for (c) drained condition (d) undrained condition.

1. **Em**pty box
   (a) with **N**o **G**rease and **N**o **W**ater (**EM-NG-NW**).
   (b) with **G**rease and **N**o **W**ater (**EM-G-NW**).
2. **Em**pty box
   (a) **G**rease with **W**ater (**EM-G-W**).
   (b) **G**rease and **W**ater added after 3 mm of horizontal displacement (**EM-G-W-M**).

Figure 4.19a shows the average for three repeat tests for both (**EM-NG-NW**) and (**EM-G-NW**) series in which the difference between the results is small and it is within the noise of the data acquisition system (LabVIEW software).

The second series of tests (**EM-G-W**) and (**EM-G-W-M**) investigated the effect of water-grease on the shear resistance. Figure 4.19b shows the results of two repeat tests of (**EM-G-W**) in which a small increase of shear load was observed of about 7 and 15 N. This provides an increase of 1.382 and 2.96 kPa in shear resistance, respectively. An interesting observation from Fig. 4.19b is that only at very earlier stage of the test (~ 0.2 mm horizontal displacement) the shear load increased then decreased. This small increase in shear resistance can be considered marginal since the difference between peak shear resistance for dry and fully saturated soil samples was more than 30 kPa (see Figs. 4.3, 4.4 and 4.5).

It was possible that this early increase of 15 N of the shear load is due to water-grease contact. To investigate further, the (**EM-G-W-M**) test was conducted in which the empty box was sealed with grease and sheared until 3 mm horizontal displacement. Then at 3 mm horizontal displacement, water was added (poured into the box) then the test restarted. However, no further increase in shear load was observed as shown in Fig. 4.19c.

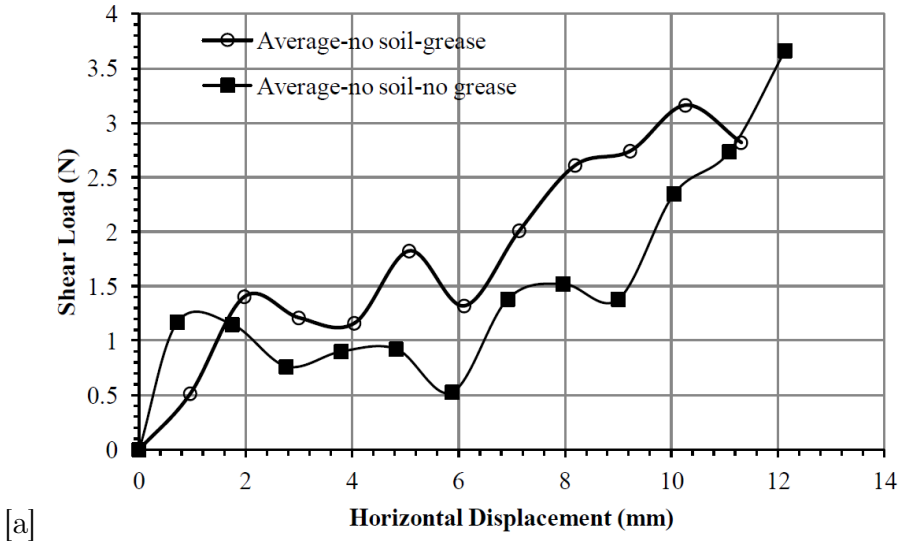

[a]

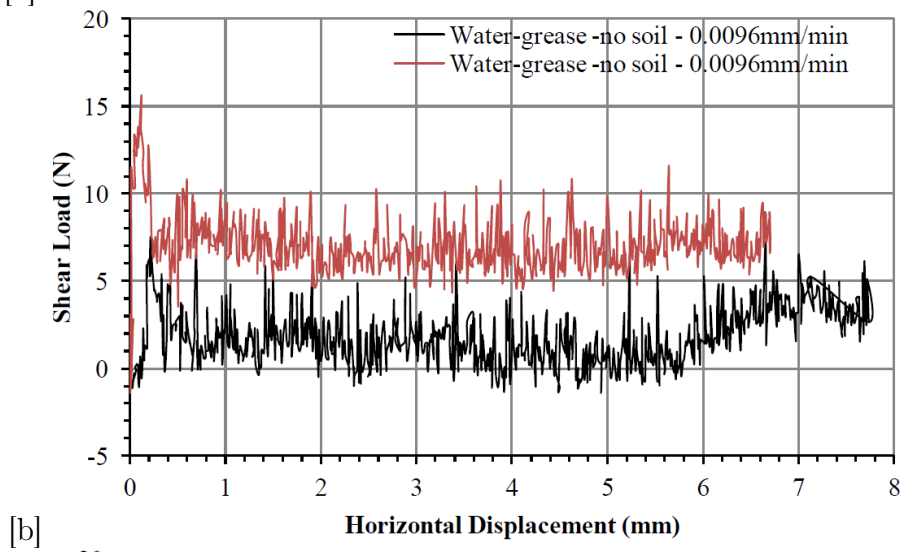

[b]

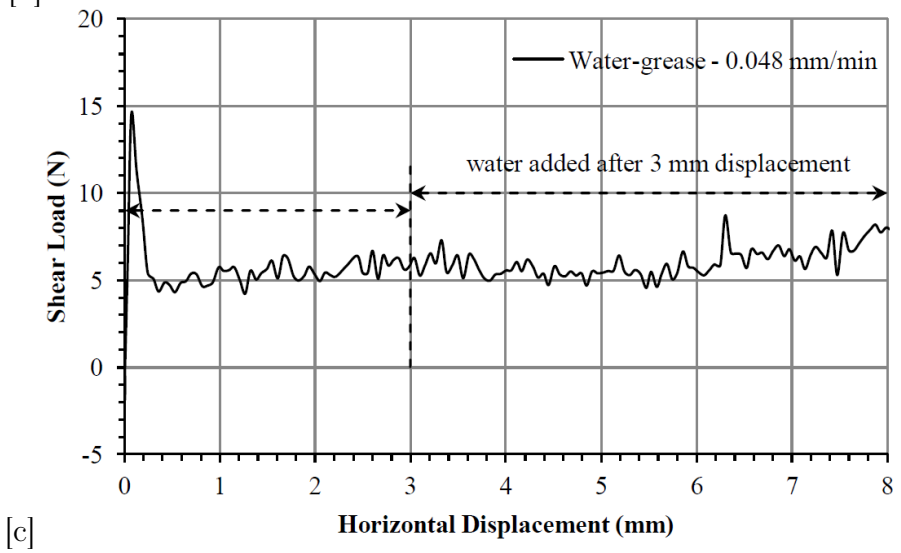

[c]

Figure 4.19: shows two direct shear tests for (a) (**EM-NG-NW**) and (**EM-G-NW**) (b) (**EM-G-W**) (c) (**EM-G-W-M**).

From the results of tests (**EM-NG-NW**), (**EM-G-NW**), (**EM-G-W**) and (**EM-G-W-M**), it can be concluded that the effect of grease and water is marginal and that the high

shear resistance of the samples at fully saturated cases is not due to the grease. A high shear resistance of fully saturated soils compared to the dry condition was also observed by Horn & Deere (1962) which was attributed to the effect of surface moisture history and surface roughness, see Section 2.13.

4.7 Internal friction angle and cohesion at peak, critical state and oscillatory stage

In light of the experimental results of the direct shear test, the following sections derive the internal friction angle ϕ at peak, critical state and oscillatory stages for saturated, unsaturated and dry conditions. The peak internal friction angle is based on the maximum shear resistance experienced by the sample, while the critical state friction angle was determined based on the shear resistance value at the end of the test (10 mm horizontal displacement). For those tests terminated before 10 mm horizontal displacement, ϕ at critical state was determined from the last measured value of shear resistance. If oscillation happened at the end of the test, the value before last oscillation was selected to determine the internal friction angle at critical state (see Fig. 4.3a, $s = 0$ kPa).

The variation of ϕ for the unsaturated cases provides information to explore its effect on shear resistance. Tables 4.4, 4.5 and 4.6 give values of ϕ and c at peak, critical state and oscillation conditions for saturated, unsaturated and dry samples obtained using direct shear results. Values of ϕ and c in Tables 4.4, 4.5 and 4.6 are obtained based on Figs. 4.20 to 4.22.

Table 4.4: ϕ and c at peak for dry, saturated and unsaturated samples.

	Test 1	Test 1	Test 2	Test 2	Test 3	Test 3	Average ϕ	Average c
s (kPa)	ϕ†	c†	ϕ	c	ϕ	c	(degrees)	(kPa)
0	46.3	26.25	40.4	41.17	51.8	19.20	46.6	28.86
2	48.7	30.23	51.4	24.02	52.9	29.12	51	28.45
4	51	33.17	50.5	28.38	53.4	9.76	51.7	23.77
6	46.5	28.30	52	23.88	51.9	29.85	50.2	27.34
Dry Case	45.5	16.02	43.9	14.70	43	9.62	44.1	13.45

† The symbols c and ϕ ($= \phi^a$ in Eq. 2.20 - see Chapter 2) were used in Tables 4.4 to 4.7 for unsaturated samples for the direct shear results, rather than c^* and ϕ^* to avoid confusion. However, c^* and ϕ^* for unsaturated samples will be used in Chapter 5 (e.g. see Eq. 5.12).

The average ϕ is determined by fitting Mohr-Coulomb failure envelope through the average values of peak shear resistance versus normal stresses of 50, 100 and 200 kPa. Where Test 1 and Test 2 and Test 3 in Tables 4.4, 4.5 and 4.6 denote to first, second and third repeat tests, respectively and the average ϕ is based on the average peak shear resistance values for the all three conducted tests. For the dry case, the range of ϕ given in Tables 4.4, 4.5 and 4.6 is based on the displacement rate of 0.0096 mm/min. Values of ϕ at oscillation were determined based on the minimum (less conservative case) shear resistance experienced by the sample after the peak. For tests when no oscillation happened, the minimum value of shear resistance was taken as the critical state value (see case $s = 4$ and 6 kPa in Tables 4.5 and 4.6 - highlighted in bold).

For Test 3 at 4 kPa suction shown in Table 4.6, a high value of ϕ (45.6^o) at oscillation was obtained. This is because this test halted after 6 mm horizontal displacement (Fig. 4.5c)

Table 4.5: ϕ and c at critical state for dry, saturated and unsaturated samples.

	Test 1	Test 1	Test 2	Test 2	Test 3	Test 3	Average ϕ	Average c
s (kPa)	ϕ	c	ϕ	c	ϕ	c	(degrees)	(kPa)
0	43.3	0.53	37.9	15.33	40.3	41.21	40.6	19.02
2	37.6	6.55	36.7	11.31	37.3	14.70	37.2	10.85
4	39.1	4.38	36.3	14.49	45.6	0†	**40.3**	6.29
6	39.6	5.73	35.8	10.88	39	6.08	**38.2**	7.56
Dry Case	45.9	11.74	43.6	9.58	45.9	0	45.1	7.10

† For any negative value of cohesion (e.g. see Fig. 4.22b - $s = 2$ kPa -2 - oscillation), $c = 0$ kPa was assumed.

and $\phi = 45.6^o$ is based on a high shear resistance value at critical state. However, it would have more reduction in shear resistance if the test had continued to 10 mm displacement as observed for other tests at 10 mm displacement. If this value being discarded, the value of 37.7 (see Table 4.6) for averaged ϕ can be obtained.

It can be seen from Table 4.6 that there is a reduction in ϕ at oscillation for $s = 0$ and 2 kPa when its compared with ϕ at critical state. This reduction significantly affects the shear resistance and this behaviour is addressed to model a bearing capacity problem using a range of ϕ values including ϕ at oscillation which is presented in Chapter 6.

To investigate the variation in internal friction angle and cohesion for the three different cases stated above, Figs. 4.23 and 4.24 also are plotted based on Tables 4.4, 4.5 and 4.6. For the dry sample, the data were fitted at $s = 0$ kPa. The observed variation in internal friction angle and cohesion was attributed to differences in soil fabric for each sample. Finally, Figs. 4.25a, b and c are presented which show the averaged shear resistance versus normal stress. The data are fitted using the least square method. For simplicity, Table 4.7 is presented based on Figs. 4.25a, b and c showing the average values of ϕ and c at peak, critical and oscillation.

Table 4.6: ϕ and c at oscillation for dry, saturated and unsaturated samples.

	Test 1	Test 1	Test 2	Test 2	Test 3	Test 3	Average ϕ	Average c
s (kPa)	ϕ	c	ϕ	c	ϕ	c	(degrees)	(kPa)
0	35.6	0	30.2	5.90	31.4	6.28	32.4	4.06
2	30.6	0.27	39.3	0	31.3	5.15	33.9	1.81
4	39.1	4.37	36.3	14.89	**45.6**	0	**40.3**/37.7	6.42
6	39.6	5.73	35.8	10.88	39	6.08	**38.2**	7.56
Dry Case	36	0	31	0	33.3	0	33.4	0

4.8 Wetting collapse for unsaturated soils at high degree of saturation

Previous investigations in the literature with regards to wetting collapse are detailed in Section 2.14. This section discusses the wetting collapse that was observed in the direct shear test results and is based in part of a conference paper accepted in the 6^{th} Asia-Pacific

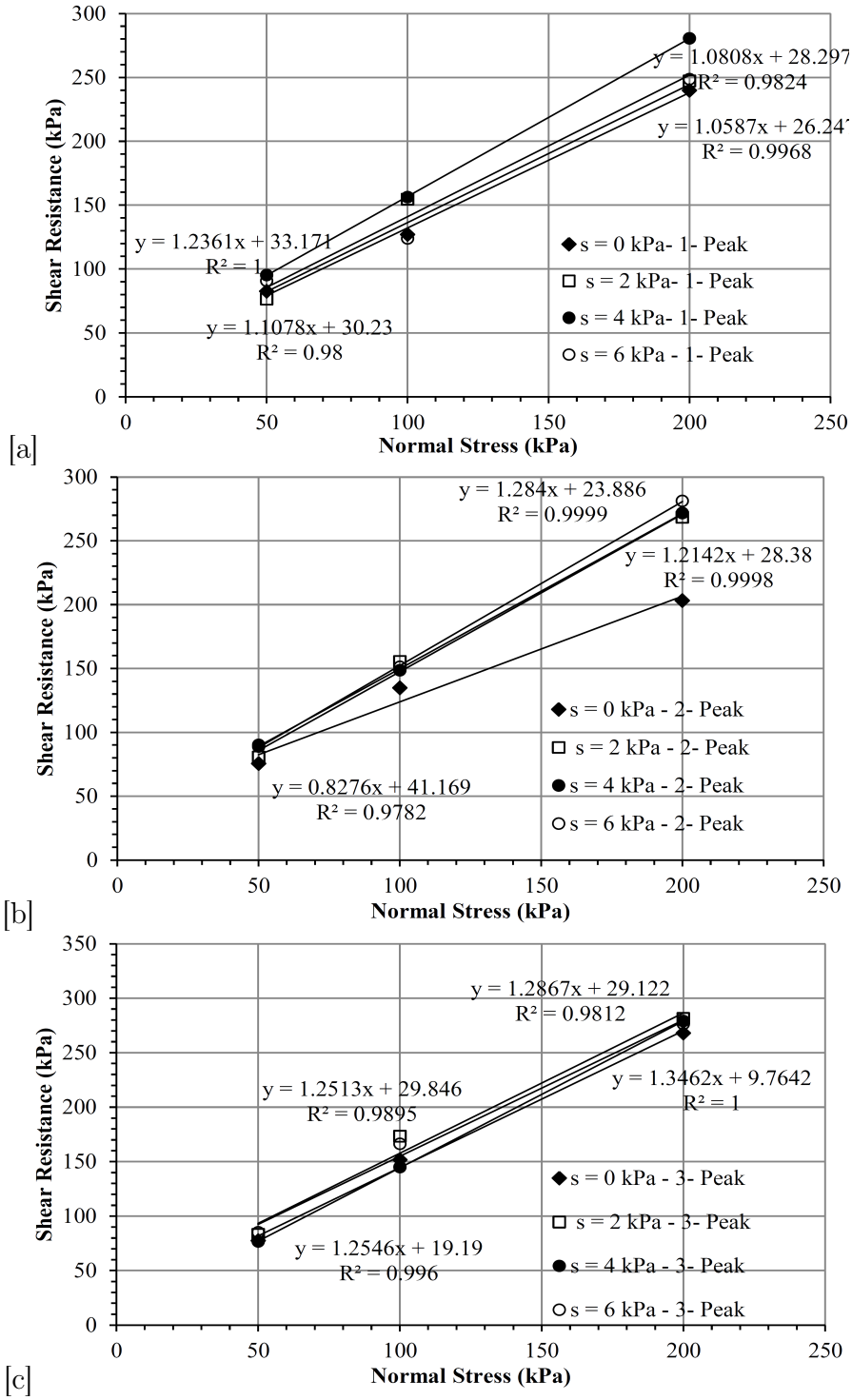

Figure 4.20: Shear resistance versus normal stress at peak for Test 1, 2 and 3 for different values of suction.

conference on unsaturated soils - China (AP-UNSAT-2015). The full paper is given in Appendix E.

Wetting collapse was observed in the direct shear test results where the response was punctuated by a sudden loss of strength and volume followed by rapid recovery of strength and slower dilation. After this, further repeated sudden losses of strength were observed but without significant loss of volume as shown in Figs. 4.26a and b. This plastic volumetric

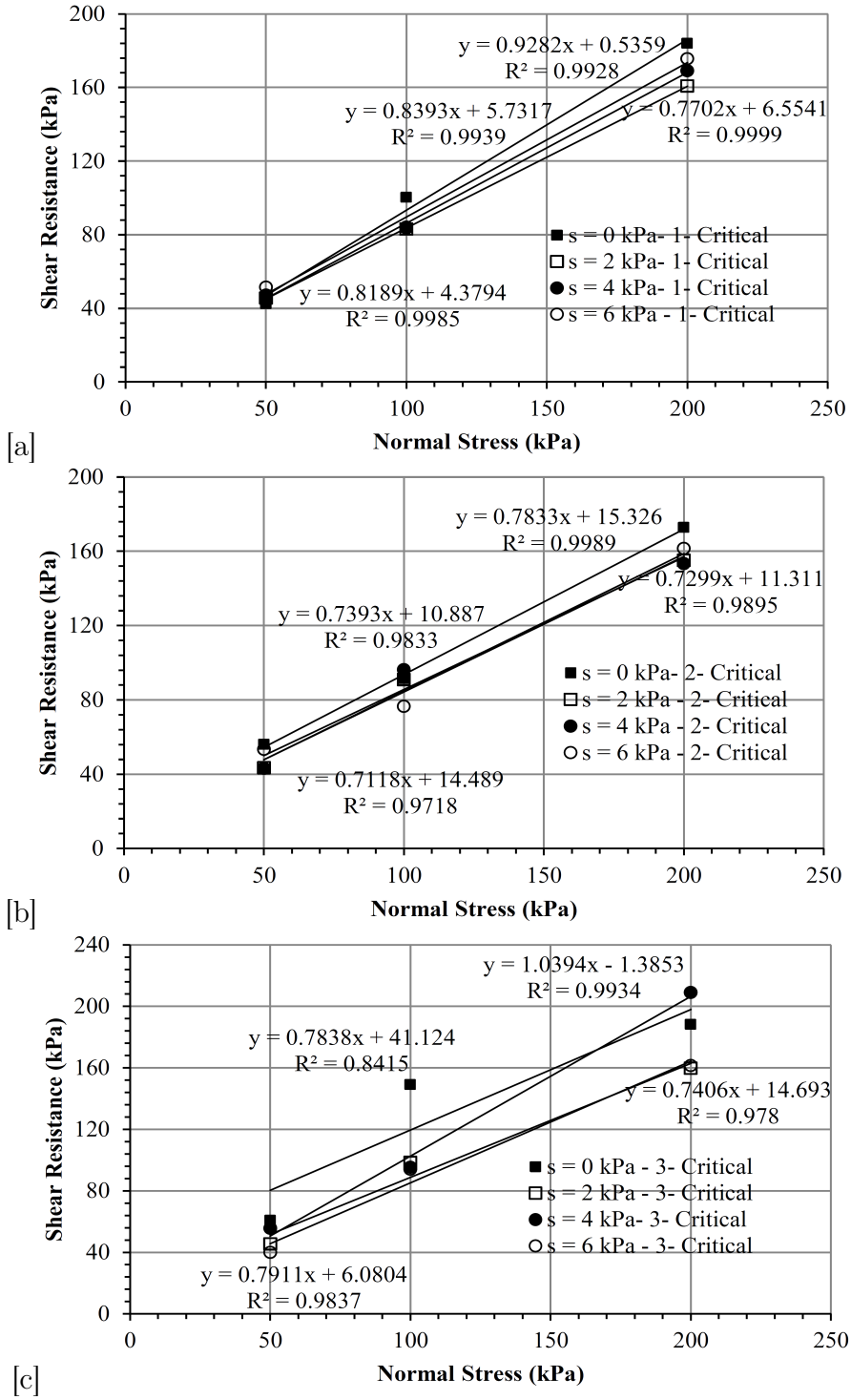

Figure 4.21: Shear resistance versus normal stress at critical state for Test 1, 2 and 3 for different values of suction.

contraction was at its maximum value in the first oscillation then decreased for the other oscillations as shown in Fig. 4.26b.

The sudden volume loss was most evident for the samples with highest saturation (s = 2 kPa). The plastic collapse was seen in all samples at s = 2 kPa and at different normal stresses (see Figs. 4.12 to 4.14). This suction is close to the air-entry value of the sand tested (2.3 kPa - see Fig. 4.1) and the saturation at s = 2 kPa is S_r = 88.9 - 91.5%. Figure

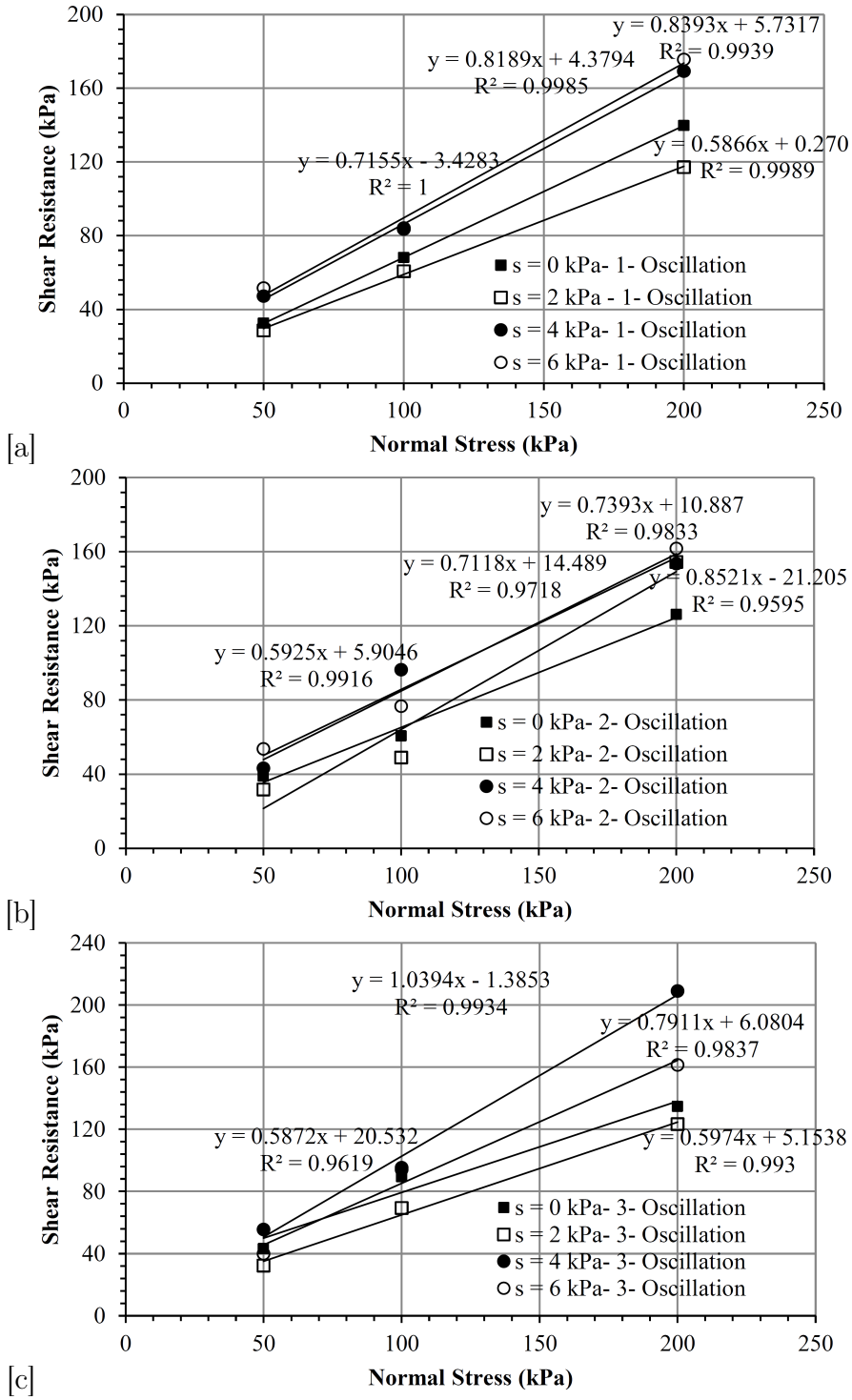

Figure 4.22: Shear resistance versus normal stress at oscillation for Test 1, 2 and 3 for different values of suction.

4.26c plots the degree of saturation versus horizontal displacement at different stages of the test for $s = 2$ kPa - $\sigma = 50$ kPa -2. The degree of saturation at $s = 2$ kPa increased due to the contractive behaviour for first 1.6 mm horizontal displacement. During oscillation, the sample was not fully saturated ($S_r \approx 96\%$) and it was possible that the voids had occluded air. Therefore, the plastic collapse may be associated with a high degree of saturation and occluded air. For case $s = 0$ kPa (e.g. see Figs. 4.3 and 4.12), plastic collapse did not occur.

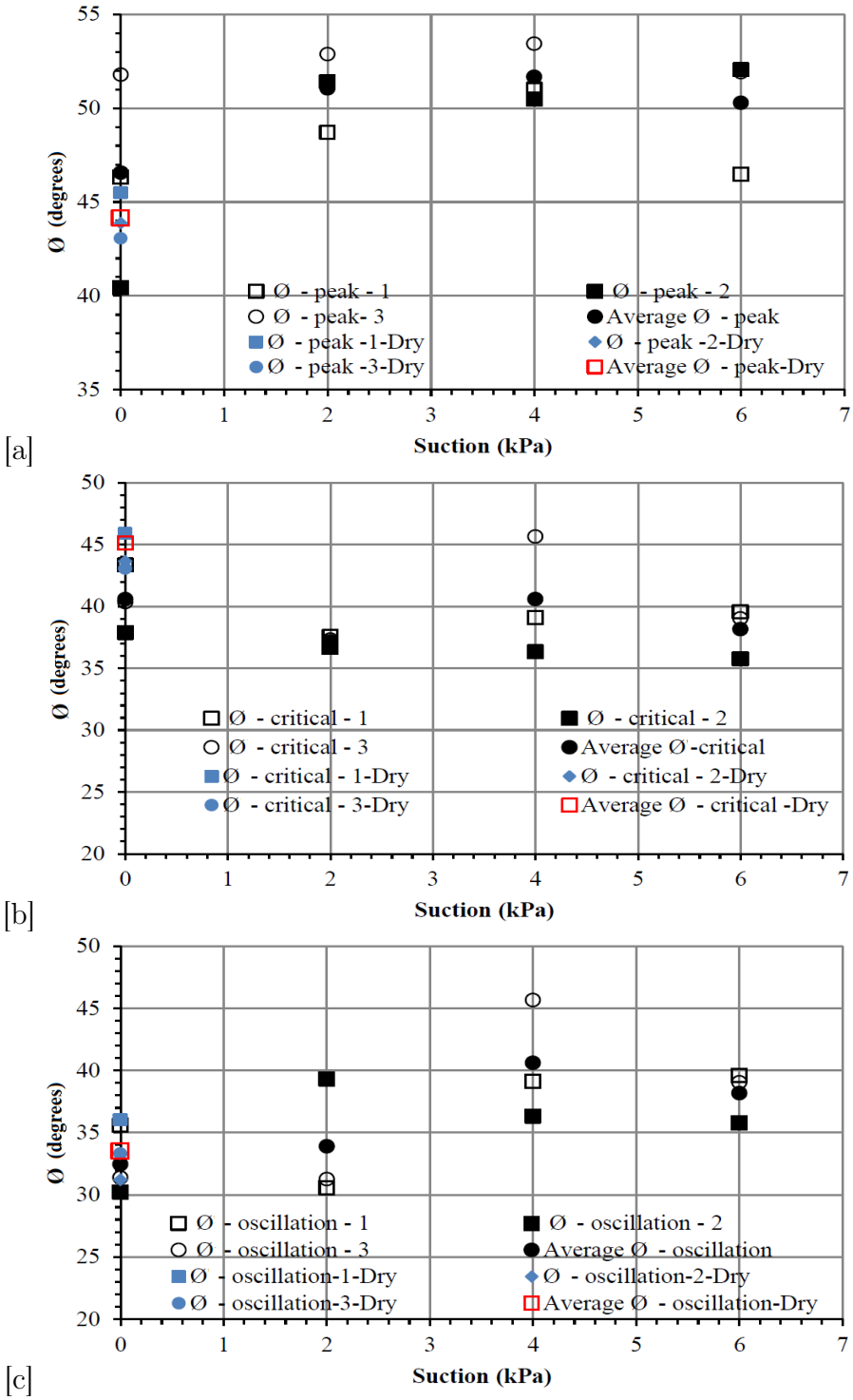

Figure 4.23: Variation of ϕ versus suction for the three repeat tests at normal stresses of 50, 100 and 200 kPa for (a) the peak (b) the critical state (c) the oscillation.

This may be due to the absence of occluded air.

Unsaturated samples prepared at $s = 4$ (S_r = 24-36%) and $s = 6$ kPa (S_r = 15-22%) did not show wetting collapse (see Figs. 4.12 to 4.14) indicating the effect of a high degree of saturation on this behaviour. Dry samples generally displayed continuous oscillations in strength, with no sudden changes in volume (e.g. see Figs. 4.3 and 4.12).

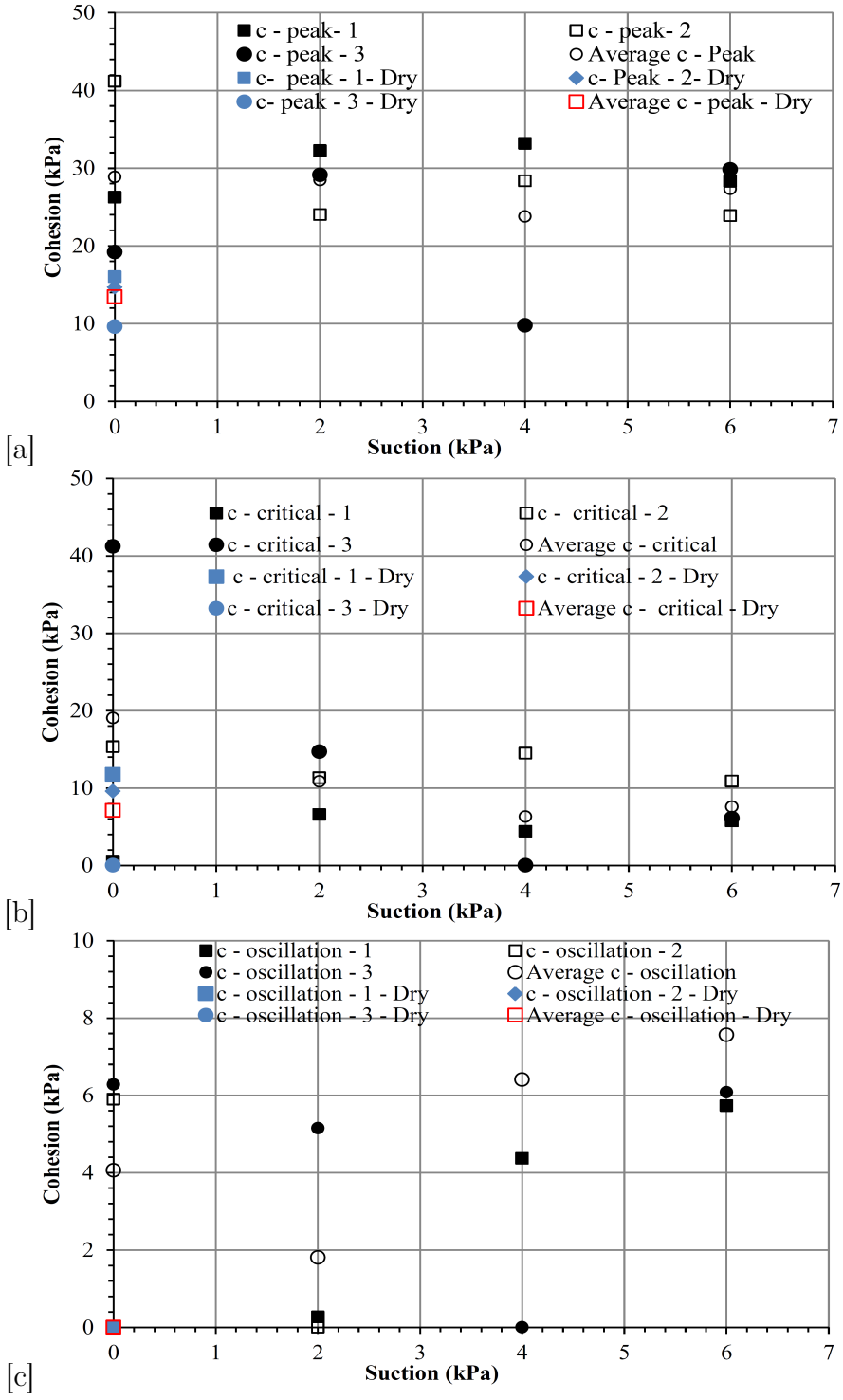

Figure 4.24: Variation of cohesion versus suction for the three repeat tests at normal stresses of 50, 100 and 200 kPa for (a) the peak (b) the critical state (c) the oscillation.

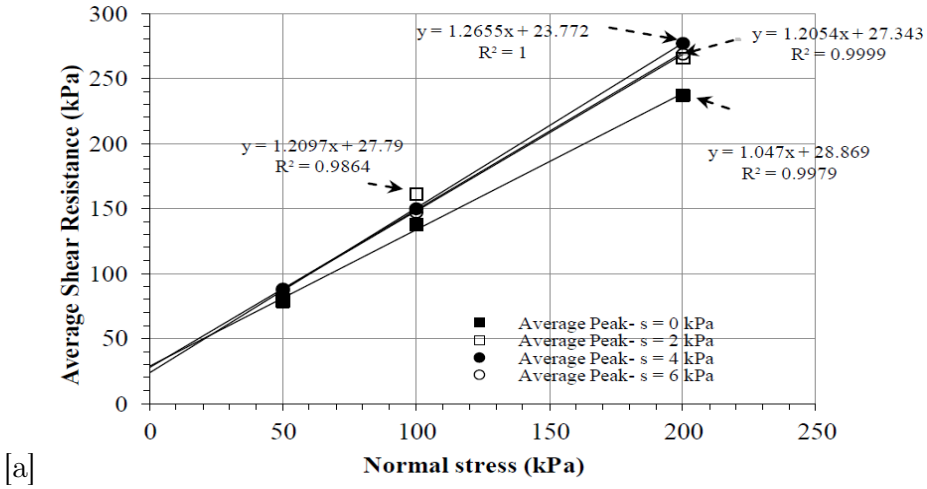

[a]

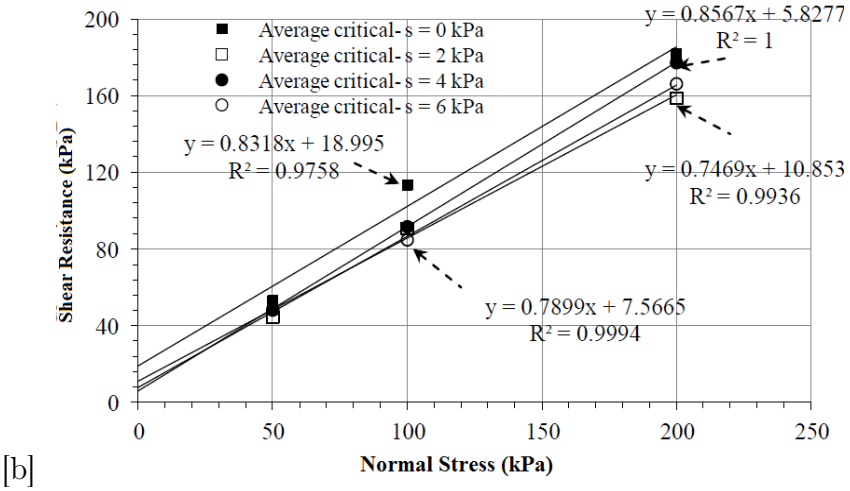

[b]

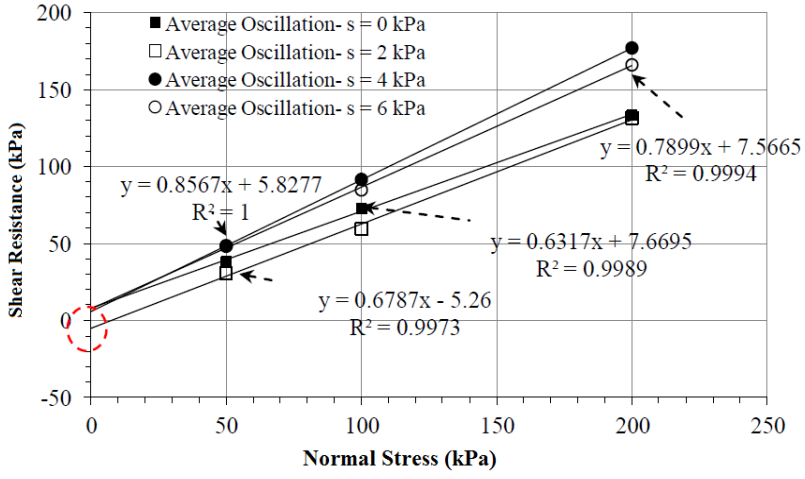

[c]

Figure 4.25: Average shear resistance versus normal stress for four applied suctions at (a) the peak (b) the critical state (c) the oscillation.

4.9 Hydro-mechanical behaviour of soil at shearing

As stated before, the SWCC was determined when zero load (null load case) was applied. For the direct shear tests, however, movement of the water was observed immediately after applying the load and during shearing. This behaviour caused drying of the sample and to track moisture-suction on the SWCC, 5 samples were taken after the end of the direct

Table 4.7: Variation of ϕ and c for the averaged values of peak, critical state and oscillation for saturated and unsaturated samples.

	Averaged peak		Averaged critical state		Averaged oscillation	
s (kPa)	ϕ (degrees)	c (kPa)	ϕ (degrees)	c (kPa)	ϕ (degrees)	c (kPa)
0	46.6	28.86	40.6	18.99†	32.4	7.66
2	51	27.79	37.2	10.85	33.9	**-5.26**
4	51.7	23.77	40.3	5.82	40.3/37.7	5.82
6	50.2	27.34	38.2	7.56	38.2	7.56
Dry	44.1	13.45	45.1	10.66	33.4	0

† The data here should not necessarily match Tables 4.4, 4.5 and 4.6 as they based on the average values of shear resistance.

shear test. The height of the sample (47 mm) was divided into five parts and samples were taken accordingly as shown in Fig. 4.27. The suction head for sample No.1 was calculated according to the last water level in the burette captured by the camera, while suction head for sample No.2 was less than suction head of sample No.1 by (47/5) mm and so on. Due to the application of normal stress and the shearing, water migrated (in the downwards direction) and this was detected by observing a change in water level in the burette. To determine the sample scanning path after shearing, water contents were calculated for the samples and suction head was determined as the distance between sample locations and the last water level in the burette captured by the camera. The scanning path is any intermediate point between drying and wetting curves, Nuth & Laloui (2008*a*).

Based on weight volume relationships and prior to the direct shear test, the unit weight of the sample was calculated at each step after lowering the burette. First, the total volume of the sample was calculated. Then the amount of water extracted from the sample was collected in a small container (by opening the burette's valve), measured to a scale of three decimal place accuracy and total weight was adjusted. The total unit weight of the sample was calculated using Eq. 4.3:

$$\gamma_t = \frac{W_t}{V_t} \tag{4.3}$$

where γ_t is total unit weight of the sample (kN/m^3), W_t is total weight (kN) and V_t is total volume (m^3). The total volume of the sample was assumed constant (no void ratio change was observed due to lowering the burette prior to the test) and degree of saturation (S_r) and water content (w) were calculated using the equations below:

$$S_r = \frac{\gamma_t\ (1+e) - G_s\ \gamma_w}{e\ \gamma_w} \tag{4.4}$$

$$w = \frac{S_r\ e}{G_s} \tag{4.5}$$

where e is void ratio, G_s is specific gravity and γ_w is unit weight of water (kN/m^3). By knowing water content and the applied suction prior to the test, the start point of the scanning path on the SWCC (described later) can be located. Then the measured water content (based on the 5 samples taken after the test) was paired with the suction and plotted at the end of the scanning path on the SWCC (e.g. see Fig. 4.28a).

During the test, the same procedure and equations mentioned above can be used to calculate water content (see Fig. 4.28a). The total volume of the sample is changeable due

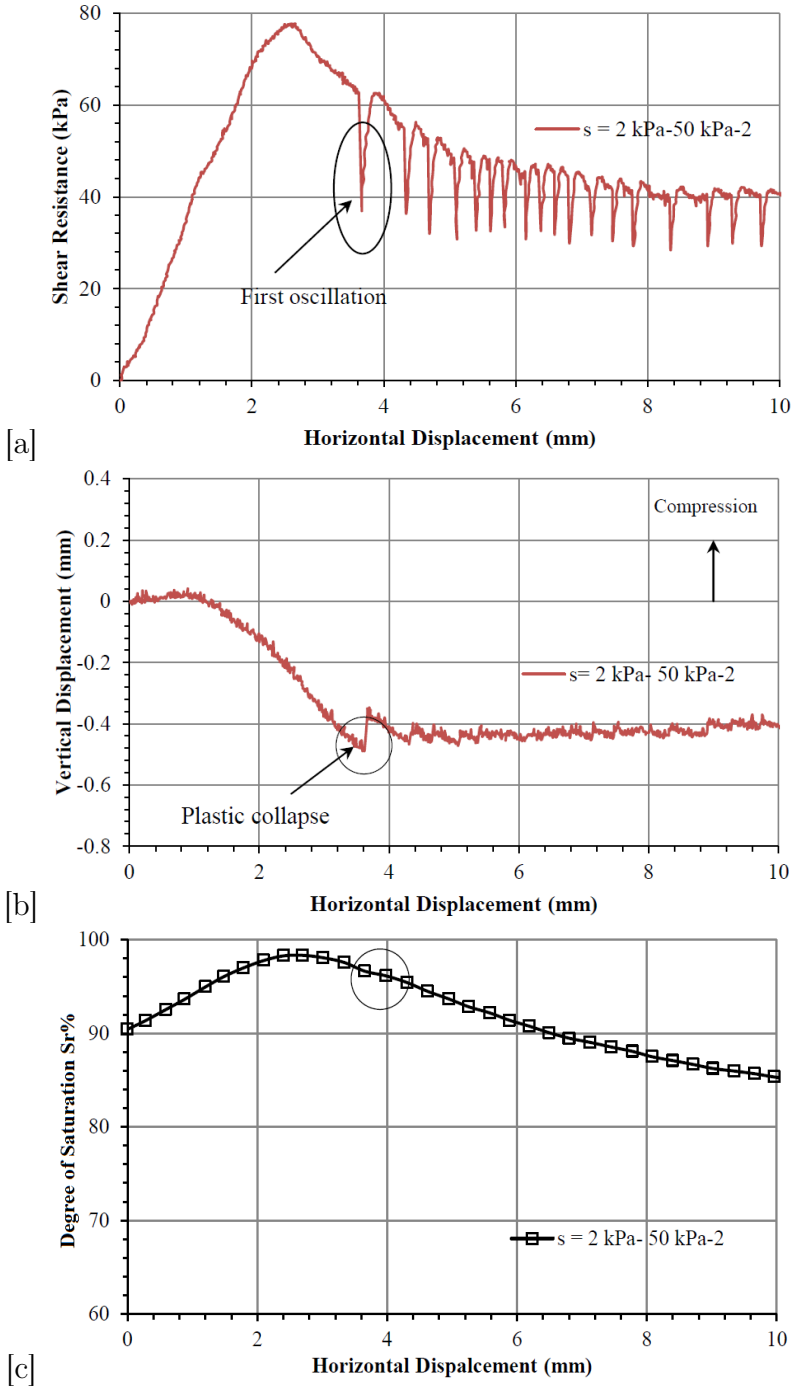

Figure 4.26: Results of $s = 2$ kPa-$\sigma = 50$ kPa-2 (a) shear resistance versus horizontal displacement showing oscillatory behaviour (b) vertical displacement versus horizontal displacement showing plastic collapse (c) degree of saturation versus horizontal displacement.

to change of height of the sample during the test (dilation and compressibility behaviours) and cross-sectional area of the sample. Consequently, the height of the sample was adjusted at each step during the shearing by tracking the change in reading of the vertical LVDT. Also the area of the sample was corrected using Eq. 4.6. The change in height of the specimen was monitored every 10 and 30 minutes during the test for fully saturated and unsaturated cases, respectively (because suction values were available at these times - water level in the burette was captured by the camera every 10 and 30 minutes). Therefore, both total volume

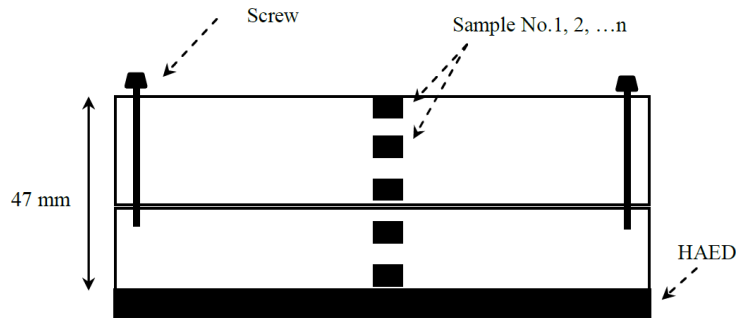

Figure 4.27: Different positions of the samples were taken after the test for moisture content measurement.

and the volume of void can be adjusted at each step since the height of the sample is known.

$$A = A_o \; F_o \tag{4.6}$$

where A is corrected area, A_o is initial area and F_o is correction factor is given by Eq. 4.7 for a circular shear box, Bardet (1997):

$$F = \frac{2}{\pi}\left[\cos^{-1}(\frac{\Delta h}{D}) - (\frac{\Delta h}{D})\sqrt{1-(\frac{\Delta h}{D})^2}\right] \tag{4.7}$$

where D is diameter of the box and Δh is horizontal displacement.

The amount of water (removed from the sample before the test to apply suction and expelled or imbibed during the test) and the adjusted total volume provide an opportunity to amend the total unit weight of the sample at each 10 and 30 minutes using Eq. 4.3.

The void ratio was calculated using Eq. 4.8. The volume of voids (V_v) at the beginning of the test was assumed to be equal to the amount of water added to the sample (95 gm) to obtain a fully saturated case (soil is fully saturated) and here it was assumed that no air exist.

$$e = \frac{V_v}{V_s} \tag{4.8}$$

where V_s is volume of solid.

To double check the assumption that V_v is equal to 95 gm, the volume of voids was calculated using:

$$V_v = V_t - V_s \tag{4.9}$$

The void ratio at the beginning of the test was 0.7 calculated using weight-volume relationships (see Table 4.1). Using Eqs. 4.8 and 4.9 and by knowing both the initial void ratio e and V_t (2.38×10^{-4} m^3), the calculated V_v showed a value of (9.8032×10^{-5} m^3) which is close to the amount of water added to the sample (9.5×10^{-5} m^3). It is assumed that such difference in volume of voids might be because of sample preparation in which the specimens experienced a small change in void ratio. Note that V_s is constant and V_v changed during the test due to a change of height and cross-sectional area of the sample. The void ratio, therefore, was calculated at different stages and then, S_r and w were calculated using Eqs. 4.2 and 4.3 accordingly. The calculated water content was paired with the suction (obtained

based on the last water level in the burette taken by the camera and samples locations - e.g. sample No.2 in Fig. 4.27) and plotted on the SWCC (see Fig. 4.28a). The calculated water content is based on the overall sample depth. The specimen was subjected to drying prior to the test to target the desired suction (see point A - Fig. 4.28a) and this was achieved by lowering the burette. The scanning path, then, can be identified by linking point A with the last state after the test. For the five samples shown in Fig. 4.28a, the legends put in order from top to bottom as they were sampled in the direct shear box (see Fig. 4.27). In other words, the solid circle symbol denotes to sample No.1 and hollow circle symbol to sample No. 2 and so on.

4.9.1 Drying behaviour during shearing at different suctions and constant normal stress

The drying behaviour for the unsaturated samples by tracking moisture-suction is studied in this section in the context of the SWCC. The drying behaviour appeared to be associated with a decrease in suction. This is due to the constraints of the HCT as used in this study (the column was not adjusted to maintain constant suction during the test), where the flow of water out of the specimen produced a change in head (loss of suction). Figures 4.28, 4.29 and 4.30 plot the gravimetric water content versus suction at constant $\sigma = 50$ kPa and different suctions of 2, 4 and 6 kPa showing the scanning paths. The beginning of the scanning path (point A in Fig. 4.28a) is plotted based on the adjusted values of the suction after the application of the load (see Table 4.3). The beginning of the scanning path (point A) for a few cases was observed either above or below the drying path of SWCC-HCT. This is attributed to the effect of void ratio in which the sample initially was prepared denser (below the SWCC-HCT curve) or looser (above the SWCC-HCT curve). The denser sample provided less void ratio and hence less water was retained between the particles.

In Figs. 4.28, 4.29 and 4.30, the most significant drying behaviour (water migration) happened to the sample No.1 (solid circle). The overall trend showed the drying behaviour at the different suctions with a few cases of the wetting near the failure plane for most of the samples (e.g. see solid square - Fig. 4.28b). The drying behaviour is attributed to (i) the effect of the normal load application which caused water movement downwards and (ii) due to concentration of the suction in the shearing zone but not the entire thickness of the sample (see Section 2.9). This caused water migration into or out of the shearing zone. This may indicate why the wetting behaviour for most of the cases was observed near the failure plane. Concentration of suction is due to the dilative behaviour in which dilation created bigger voids between the particles near the shear band for water to move into. The drying and wetting behaviours can be explained by the soil fabric that suggests an increase of the volume due to riding the packets (assemblages of particles) over each other. However, the individual packets themselves were subjected to compression leading to a reduction in suction (wetting behaviour). Variations of suction at constant water content were also stated by Toll (1990) in which dilation and compression behaviours were observed during shearing simultaneously.

4.9.2 Drying behaviour during shearing at different normal stresses and different suctions

The effect of the normal stress on the drying behaviour at different suctions is presented in Figs. 4.31a, b and c for three repeat tests. The data plotted in Figs. 4.31 are for the sample

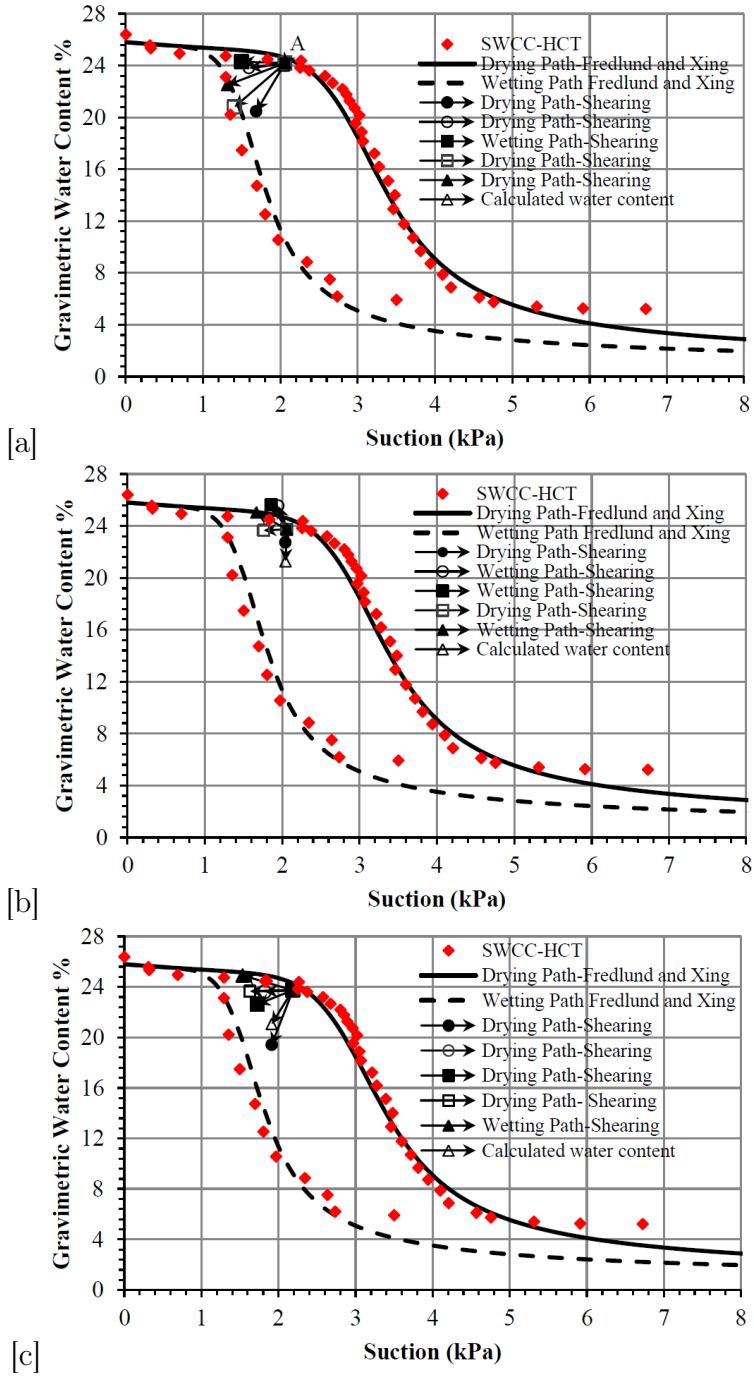

Figure 4.28: Drying and wetting paths for $s = 2$ kPa at $\sigma = 50$ kPa for (a) the first test (b) the second repeat test (c) the third repeat test.

No.1 (see Fig. 4.27). The amount of water loss at the smaller applied suction (e.g. $s = 2$ kPa) is greater due to higher degree of saturation and free water for the sample. Also the final state of the scanning path at the same suction and different normal stresses are almost same (same amount of water loss- see Figs. 4.31a, b and c at $s = 2$ kPa). This indicates that the smallest applied normal stress, 50 kPa, was enough to cause water migration.

The implication of Figs. 4.28, 4.29, 4.30 and 4.31 is important as the applied suction, using the HCT, is no longer constant during shearing due to the effect of the drying phenomenon and this affects the behaviour of the soil. The results of the bearing capacity tests

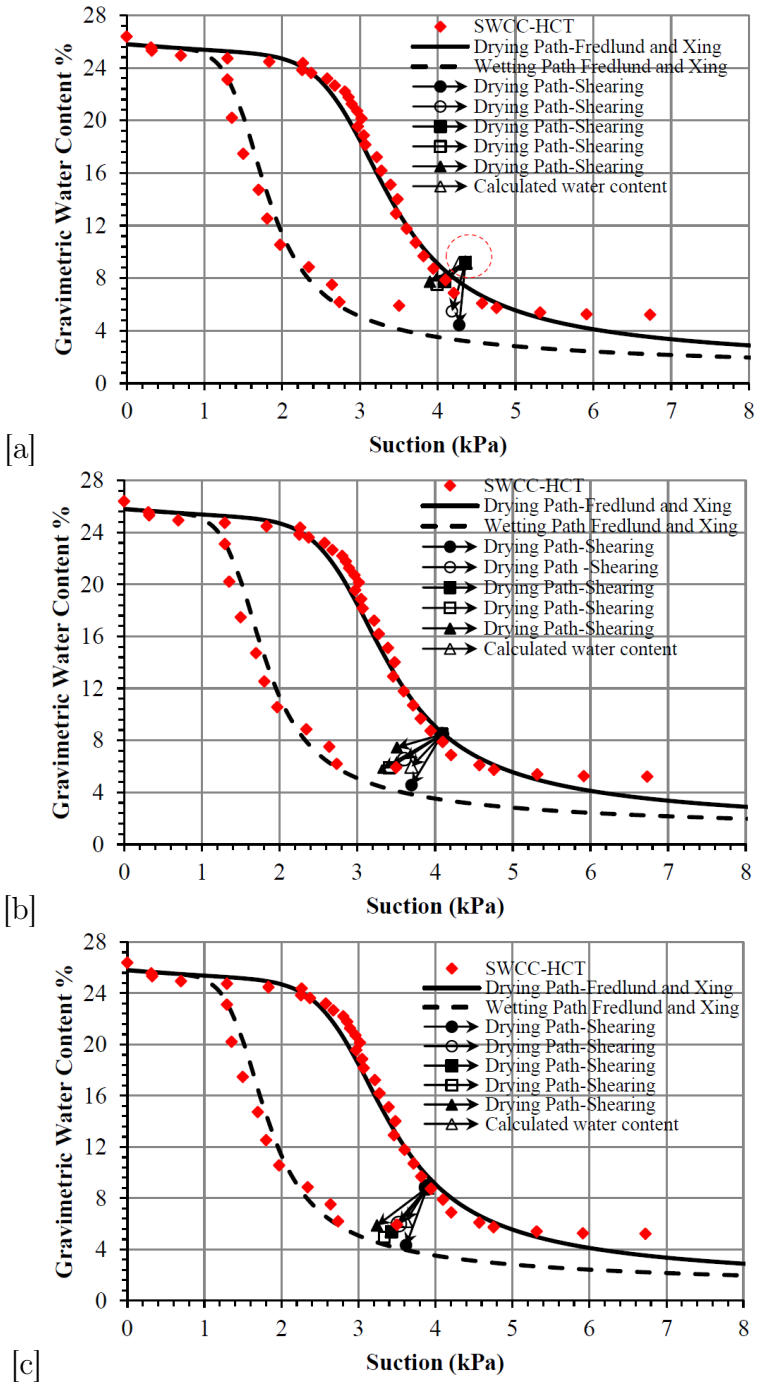

Figure 4.29: Drying and wetting paths for $s = 4$ kPa at $\sigma = 50$ kPa for (a) the first test (b) the second repeat test (c) the third repeat test.

also showed water movement around the footing due to application of the normal load and is discussed further in Subsection 4.10.1.2 (see Fig. 4.38b).

4.10 Bearing capacity results

This section addresses the results of the bearing capacity tests which were performed for strip footings placed on the surface and at 5 cm below the soil surface. Test details are shown in Table 3.5. The bearing capacity test was performed before the direct shear tests

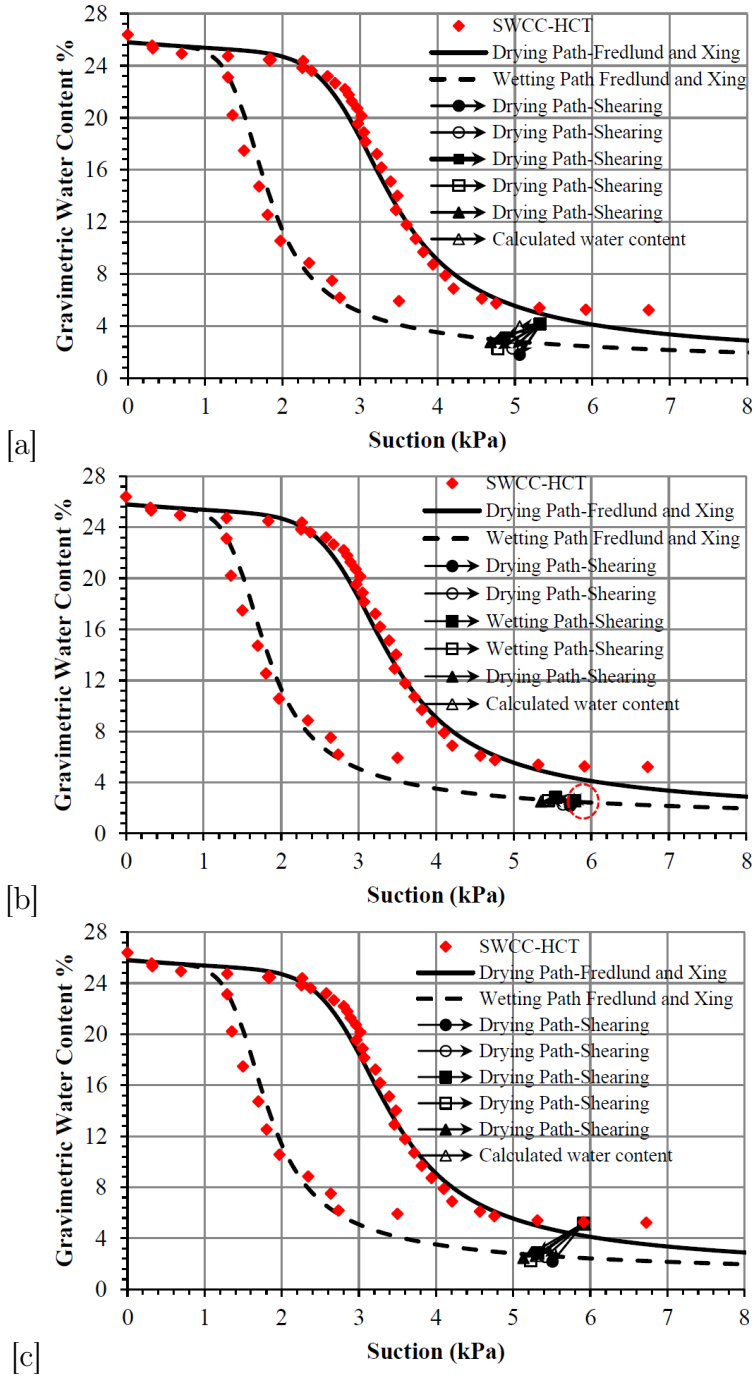

Figure 4.30: Drying and wetting paths for $s = 6$ kPa at $\sigma = 50$ kPa for (a) the first test (b) the second repeat test (c) the third repeat test.

due to availability of the rig. Hence, the equilibrium time for the larger sample used for the bearing capacity test was not yet established. At the beginning of the bearing capacity test programme, therefore, a range of different equilibrium times were used.

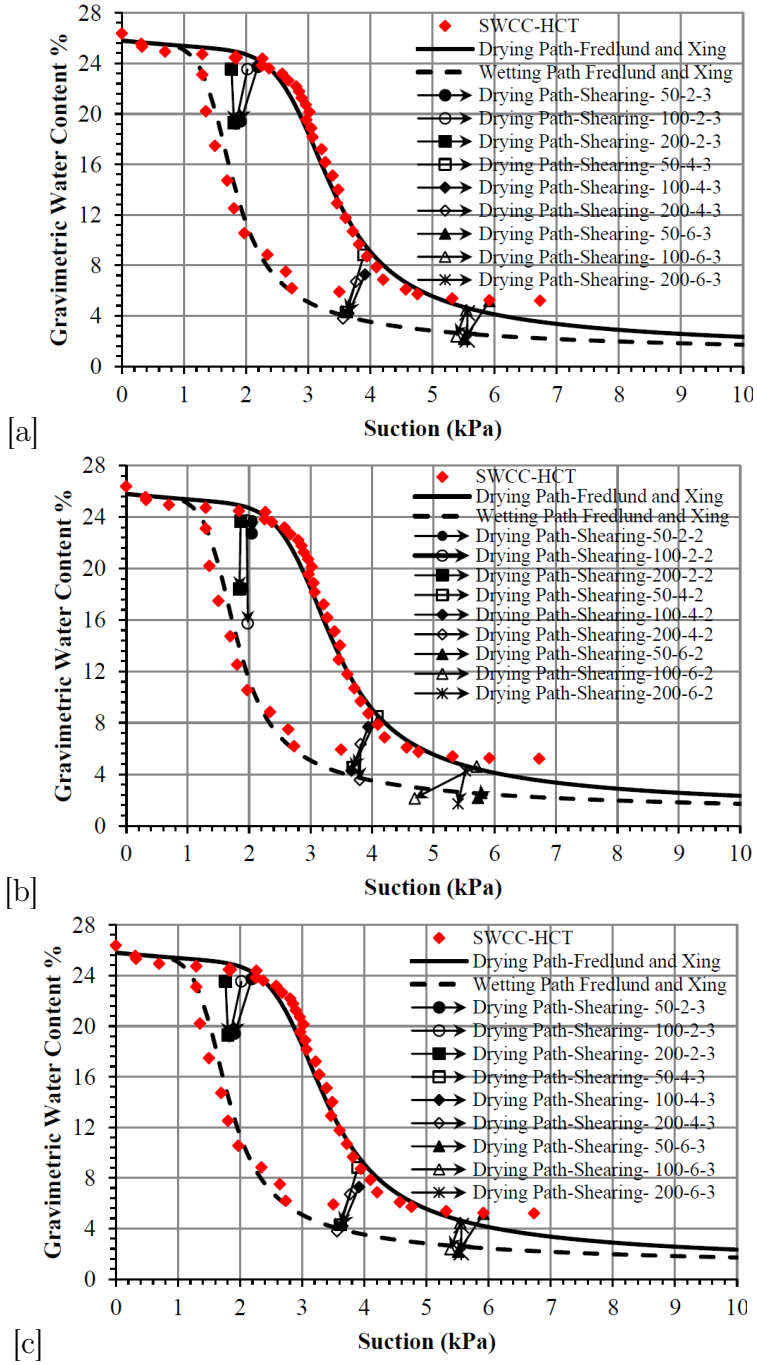

Figure 4.31: Effect of normal stress (σ) on the drying behaviour for (a) the first test (b) the second repeat test (c) the third repeat test.

4.10.1 Surface footing tests

4.10.1.1 Fully saturated case $s = 0$ kPa-Series (S-I)

Figure 4.32 shows the results of five tests conducted at the same surface suction, $s = 0$ kPa, and at different equilibrium times. The legend in Fig. 4.32 is presented as a suction value ($s = 0$ kPa), then followed by the test number. The standard equilibrium time was 1 day. Cases where the equilibrium time was less than 1 day (e.g. 3hr equilibrium time) are shown in the legend. In the remainder of this chapter, the term bearing capacity is defined as the maximum bearing resistance at peak or at the end of the test for those tests when no distinct

peak can be observed and when the bearing resistance is still increasing.

Tests $s = 0$ kPa-2-0.5 hr and $s = 0$ kPa-3 showed higher bearing capacity values compared to the others. It was observed as the test continued, soil on both sides of the footing bulged and this caused soil to be raised above the water table (the soil then lost moisture and was subjected to a suction) as shown in Fig. 4.33a and b. The application of the load caused

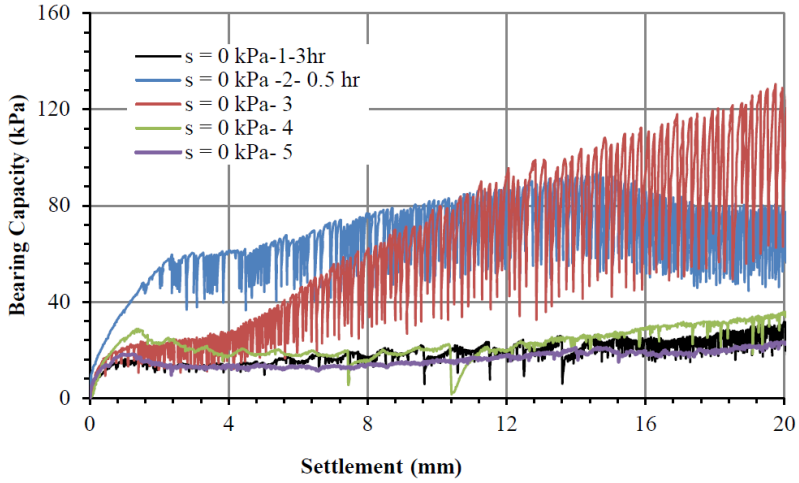

Figure 4.32: Bearing capacity versus settlement for the surface footing for $s = 0$ kPa.

the water level to rise in the burette as was also observed in the direct shear tests as shown in Fig. 4.33c and d. To avoid the soil rising above the water table again during tests, the water table level at the beginning of the test was escalated slightly. For the other three tests shown in Fig. 4.32, the results are consistent. Also a significant oscillatory behaviour can be seen for $s = 0$ kPa-3hr and $s = 0$ kPa-2-0.5hr.

Figure 4.34a shows the water content measurement versus depth for $s = 0$ kPa-5 from 15 samples that were obtained using perforated containers which were placed in the rig at each 5 cm depth during sample preparation (see Fig. 3.5). The idiom "left" in the figure's legend denotes the containers placed in the left hand side of the rig as it is explained by the small graph in Fig. 4.34a and so on. Surface samples were collected at the surface and slightly at deeper depth (i.e. 5 mm below the surface), however, depth = 0 cm was assigned in the water content measurement figures.

Samples at the surface showed a higher water content than the saturated water content of the sample (26%). This is because the containers had excess water when sampled. For the tests shown in Fig. 4.32, only water content data was measured for $s = 0$ kPa-5. This is because with the water pluviation technique, initially saturated samples can be obtained, Vaid & Negussey (1988), and the difference in water content at different depths showed small variations (see Fig. 4.34a). Water content measurements, therefore, are not available for the other repeat tests. For those tests at fully saturated cases which have more than two or three water content measurements, they were used to double check that water content values are consistent with the depth.

Figures 4.34b and c show the humidity and temperature measurements for $s = 0$ kPa for tests 4 and 5. The humidity started from almost 75% and stabilized at about 103%. This is a good indication that can also be used to support a sufficient equilibrium time. The temperature variation was $\pm$ 0.5 ^{o}C due to accuracy of the thermal probe ($\pm$1 ^{o}C), however, during the test stable temperature can be seen. The humidity and temperature meter was installed to measure water vapour in the space between the soil surface and latex membrane

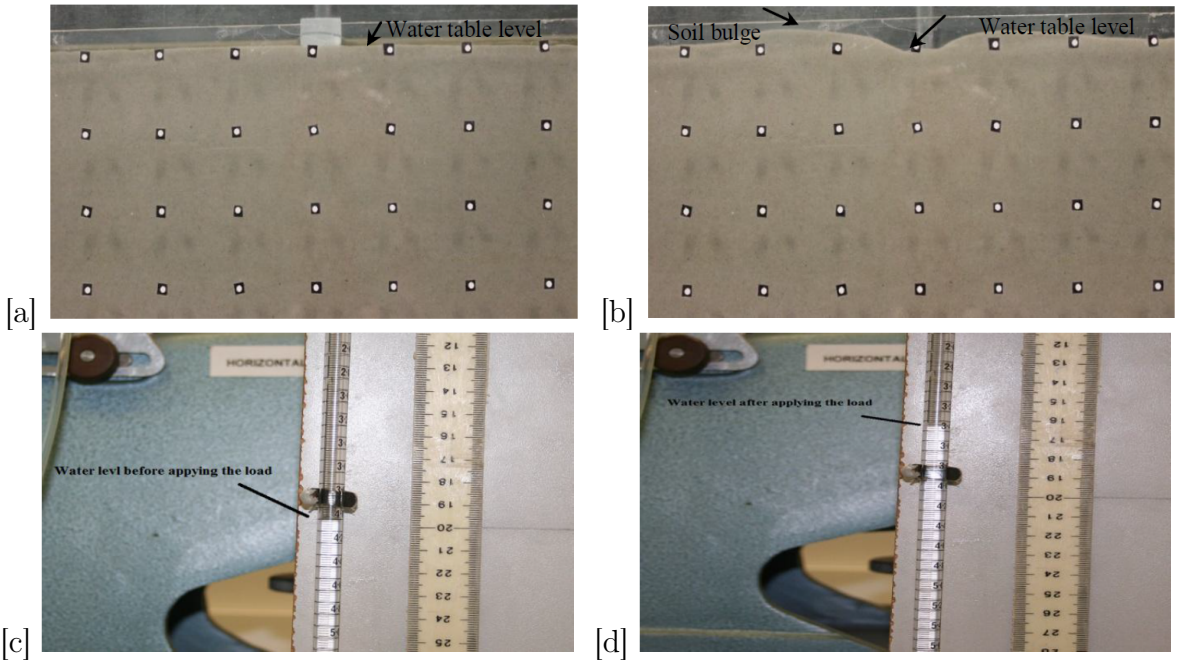

Figure 4.33: Fully saturated sample for $s = 0$ kPa-2-0.5 hr (a) showing water table at the surface (b) showing soil bulges above water table. Water level in the burette for the direct shear test (c) before applying normal load (d) after applying normal load.

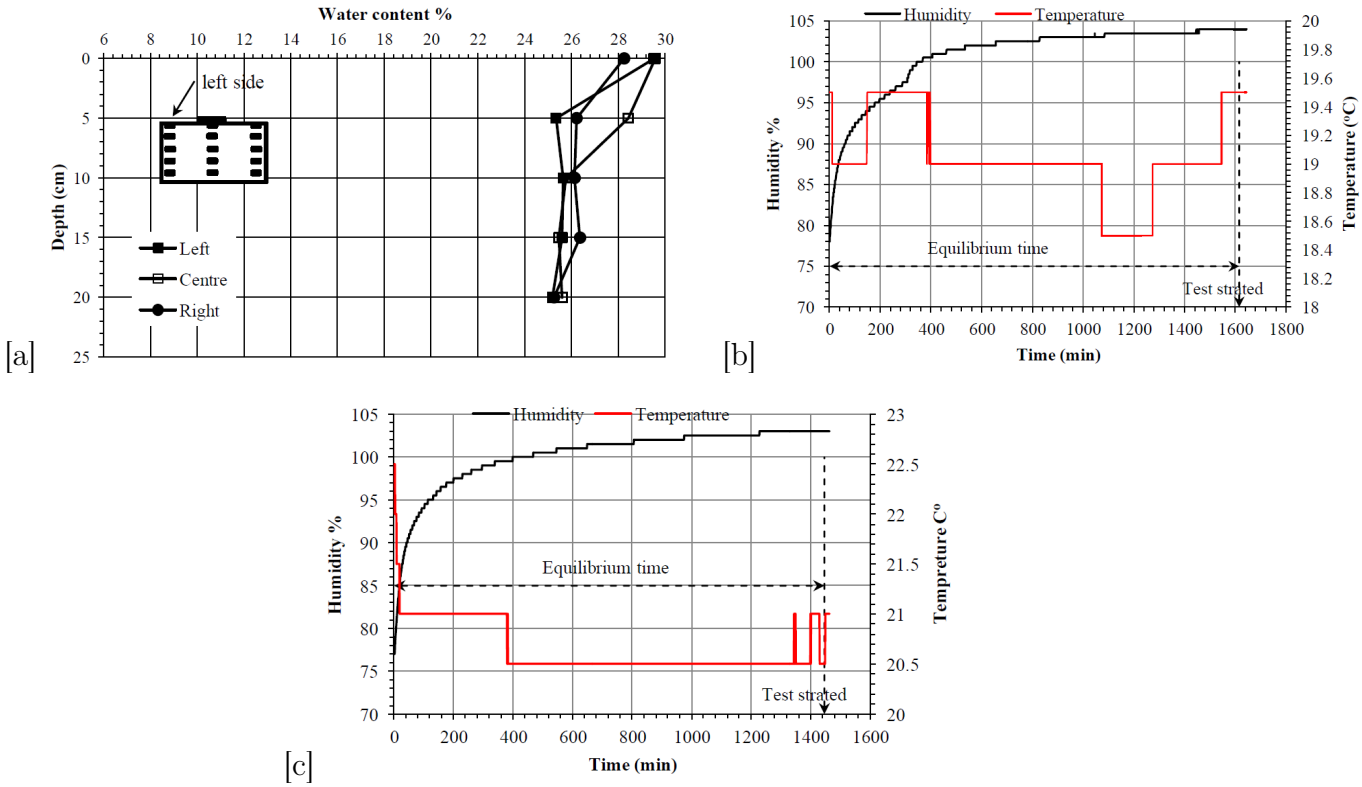

Figure 4.34: (a) Water content measurement versus depth for the surface footing for $s = 0$ kPa-5 at end of the test (b) Humidity and temperature measurement for the surface footing for $s = 0$ kPa-4 (c) Humidity and temperature measurement for the surface footing for $s = 0$ kPa-5.

(see Fig. 3.5) in which the equilibrium time is the time required for the water vapour to be in equilibrium with the soil. Values higher than 100% indicate supersaturated air in the space in which they are a feature of the meter (accuracy of ± 3%) and are not related to the real measurement of behaviour.

The humidity and temperature probe (LE-USB-2) was set to take the readings five minutes after covering the rig with a latex membrane and to the end of the test. This explains why the temperature readings started at high or low values at the beginning of some of the tests and then stabilized. The slight variation of the humidity and temperature readings at the beginning of the test for the whole figures presented in the rest of this chapter is because tests were performed during the whole year (high value of temperature in summer and low value in winter- see Figs. 4.39a and b), despite temperature control in the laboratory.

For any other bearing capacity tests presented in the rest of this chapter when water content measurement or humidity and temperature data are not available, either the measurement was lost (for the water content measurement) or not taken (for the humidity and temperature). For the non-taken data for humidity and temperature, some of the tests were conducted before deciding to install the LE -USB-2 probe in the rig. This was the case for most bearing capacity tests for the footing placed on the surface in which test 1, 2 and 3 (especially for the surface footing) were performed before installing the probe. The lost samples of the water content measurements were due to damage to the samples during moving them to the oven or after taking them out from the oven.

4.10.1.2 Results for s = 1.962 to 2.47 kPa-Series (S-II)

Figure 4.35 shows the bearing capacity results for five tests conducted at a suction range of 1.962 to 2.47 kPa and at two different equilibrium times: 3 hr and 1 day. As stated before in Section 3.6 in Chapter 3, due to the difficulty in obtaining the same suction for each test, different variations of applied suction can be seen in Fig. 4.35. Test s = 1.962 kPa-1-3 hr shows a smaller bearing capacity value compared to the other tests. This may be attributed to the shorter equilibrium time utilised for this test resulting in lower suction in the sand bed. For the rest of the tests, the same equilibrium time was used, however scattering of data can be easily seen. It can be seen from Fig. 4.35 that the bearing capacity increases by about 4 to 10 fold (typically peak) when compared to the fully saturated models in Fig. 4.32 (e.g. see s = 0 kPa-4). Nabil (1985), Steensen-Bech et al. (1987) and Fathi & Vanapalli (2006) also observed similar differences for similar ranges of suctions in the partially saturated zone. The former stated that the bearing capacity of unsaturated soil is higher by a factor of 3 to 5 fold compared to fully saturated soil. Steensen-Bech et al. (1987) established a 4 to 6 fold increase in bearing capacity, while Fathi & Vanapalli (2006) showed in their study a 5 to 7 fold increase in bearing capacity.

Oscillation of the data can be seen after the soil experienced its peak bearing capacity for most of the tests. The peak bearing capacity was attained between 2.8 to 5.6 mm vertical displacement. Some of the tests experienced an increase of bearing capacity after the peak. This may be due to additional tangential forces developing along the footing sides as the footing penetrated further into the soil.

Figure 4.36 shows the consistency of the motor drive (see Fig. 3.16) to apply the loading (displacement) rate (strain control) in which a small difference in the speed rate can be seen. The speed rates in Fig. 4.36 are 0.609, 0.587, 0.642, 0.64 and 0.613 mm/min for the tests shown with the same order in Fig. 4.35. Water content measurements after the test were obtained as shown in Figs. 4.37a and b for the cases of s-2 kPa-4 and s-2.4 kPa-5. Surprisingly, the left surface sample (circled in Fig. 4.37a) showed a significantly lower water

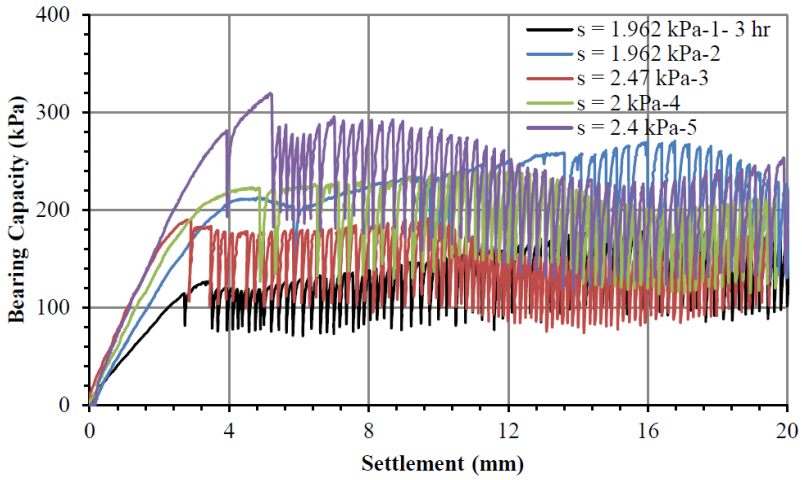

Figure 4.35: Bearing capacity versus settlement for the surface footing for the suction range between 1.962 - 2.47 kPa.

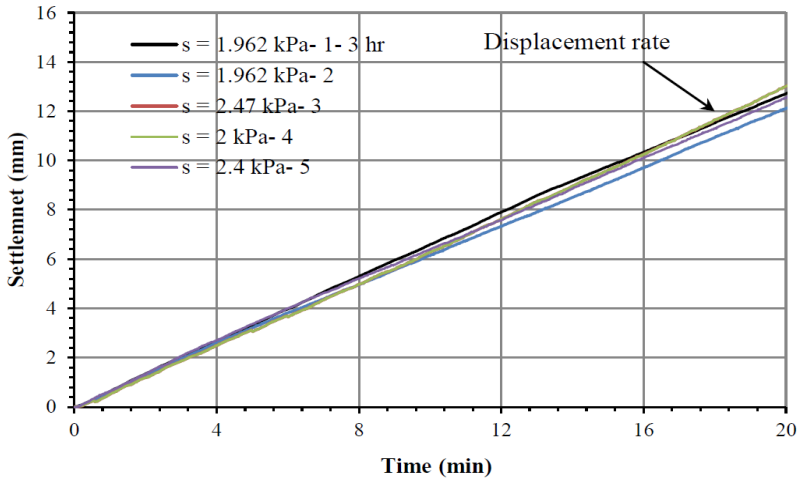

Figure 4.36: Settlement versus time for the suction range between 1.962 - 2.47 kPa.

content of about 14% (the initial water content may be estimated from the original SWCC from Fig. 4.1 at $s = 2$ kPa - initial $w \approx 25\%$) when compared to the other two samples. It was believed that water movement occurred due to the applied pressure. To investigate this behaviour further, a pair of images which were taken for the PIV analysis are shown in Figs. 4.38a and b. This qualitatively indicates drying behaviour due to application of the load as well as dilation. These two images were taken at the beginning and at the end of the test and water migration can clearly be seen in the left and right hand side as well as beneath the footing. The failure mechanism is also clear with dilation of the soil around the footing and along the failure mechanism in which the footing rotated to the left hand side. As the soil dilates, the void ratio increases leading to a decrease in degree of saturation and subsequently an increase in suction.

Figures 4.39a and b show the humidity and temperature results versus time for tests $s = 2$ kPa-4 and $s = 2.4$ kPa-5, respectively. The figures show also time for saturation (from time = 0 to the line of sample desaturated- see Fig. 4.39a) and equilibrium time. Again, the data are satisfactory in terms of equilibrium time.

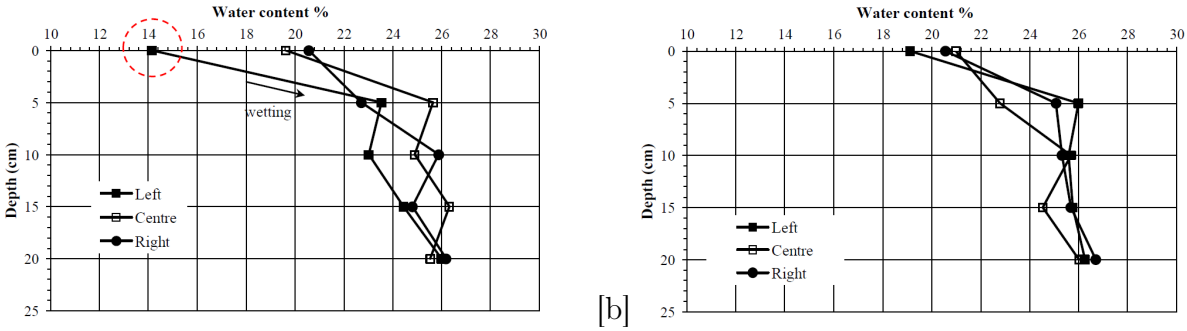

Figure 4.37: Water content measurement versus depth at end of the test for the surface footing for (a) $s = 2$ kPa-4 (b) $s = 2.4$ kPa–5.

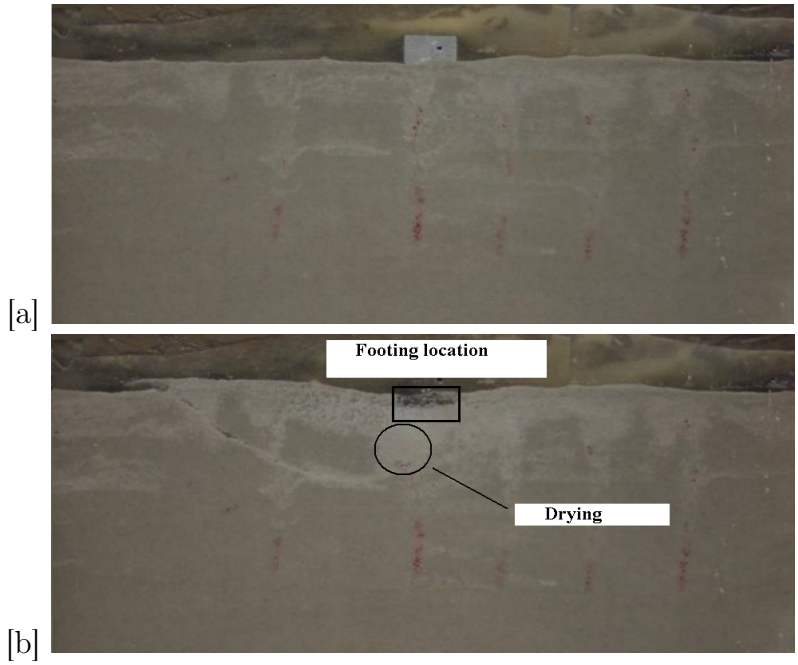

Figure 4.38: Image at the (a) beginning of the test (b) end of the test showing water movement and dilation.

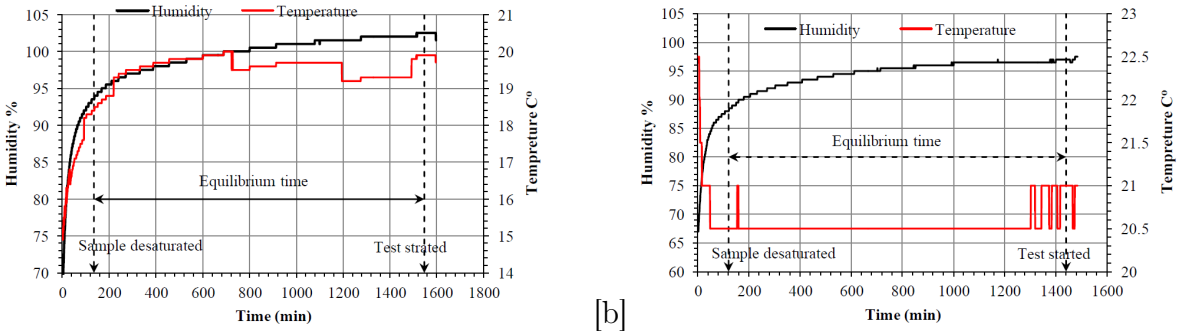

Figure 4.39: Humidity and temperature measurement for the surface footing for (a) $s = 2$ kPa-4 (b) $s = 2.4$ kPa-5.

4.10.1.3 Results for $s = 3.50$ to 4.54 kPa-Series (S-III)

Results of a bearing capacity test which was aimed to apply suction in the range of the transition zone of the SWCC is shown in Fig. 4.40. Apart from the $s = 3.72$ kPa-1 test

in which a 2 hr equilibrium time was set, 1 day was utilised for the rest of the other tests. Oscillation of data also can be seen for most of the tests which happened after the samples experienced peak (except s = 3.72 kPa-2). Variation of the bearing capacity values at peak can be seen and surprisingly the test of s = 3.63 kPa-5 showed a high bearing capacity value of about 450 kPa. However, at the end of the tests, all samples showed nearly same bearing capacity at the critical state void ratio.

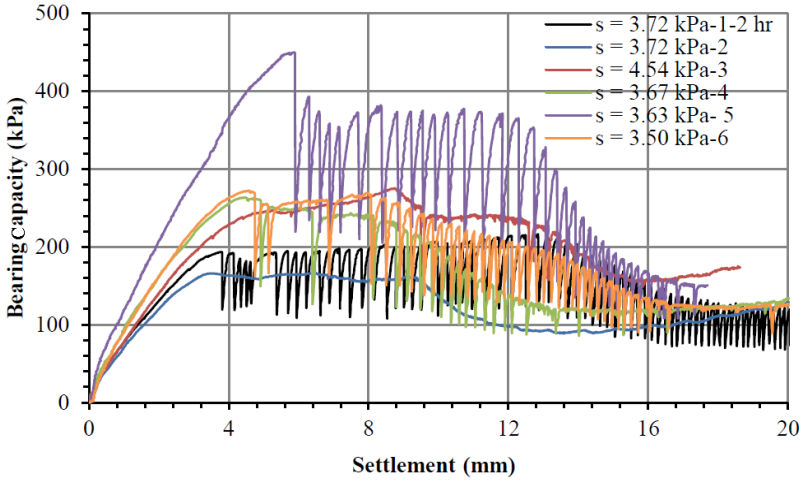

Figure 4.40: Bearing capacity versus settlement for the surface footing for the suction range between 3.50 - 4.54 kPa.

Figures 4.41a, b, c, d and e show the water content measurements in which variation in water content at the surface can be seen. For tests of s = 3.72 kPa-2 and s = 4.54 kPa-3, water content measurement data behind 10 cm depth were lost. Figures 4.42a and b show the humidity and temperature results for two applied suction values from the beginning of the sample preparation to the end of the test.

4.10.1.4 Results for s = 5.38 to 5.93 kPa-Series (S-IV)

Figure 4.43 shows the bearing capacity versus settlement for a range of applied suctions near residual suction. Again, variation of bearing capacity can be seen, however, the most interesting behaviour that can be observed in the figure is that the oscillation vanished (except for s = 5.4 kPa-1 and s = 5.8 kPa-5) as the water content of the samples decreased when comparing to the case of series shown in Subsections 4.10.1.2 and 4.10.1.3. For these two samples when oscillation happened, the period of the oscillation is longer compared to the results for the previous suction ranges. It can also be seen that the soil has gained more strength compared to the two previous cases. The high value of bearing capacity for test s = 5.8 kPa-5 is because that the footing did not rotate until about 6 mm penetration into the soil, then, at the end of the test bearing capacity values were close to the other tests. The water content measurement showed that almost all the samples started at the same water content (with difference 3%) at the surface as shown in Figs. 4.44a, b, c and d. Figures 4.45a and b show the humidity and temperature results versus time for two applied suctions.

4.10.2 Results for footing buried at 5 cm depth

This section addresses bearing capacity results for the footing buried at 5 cm depth for a range of applied suctions. The aim of this study was to investigate the effect of surcharge

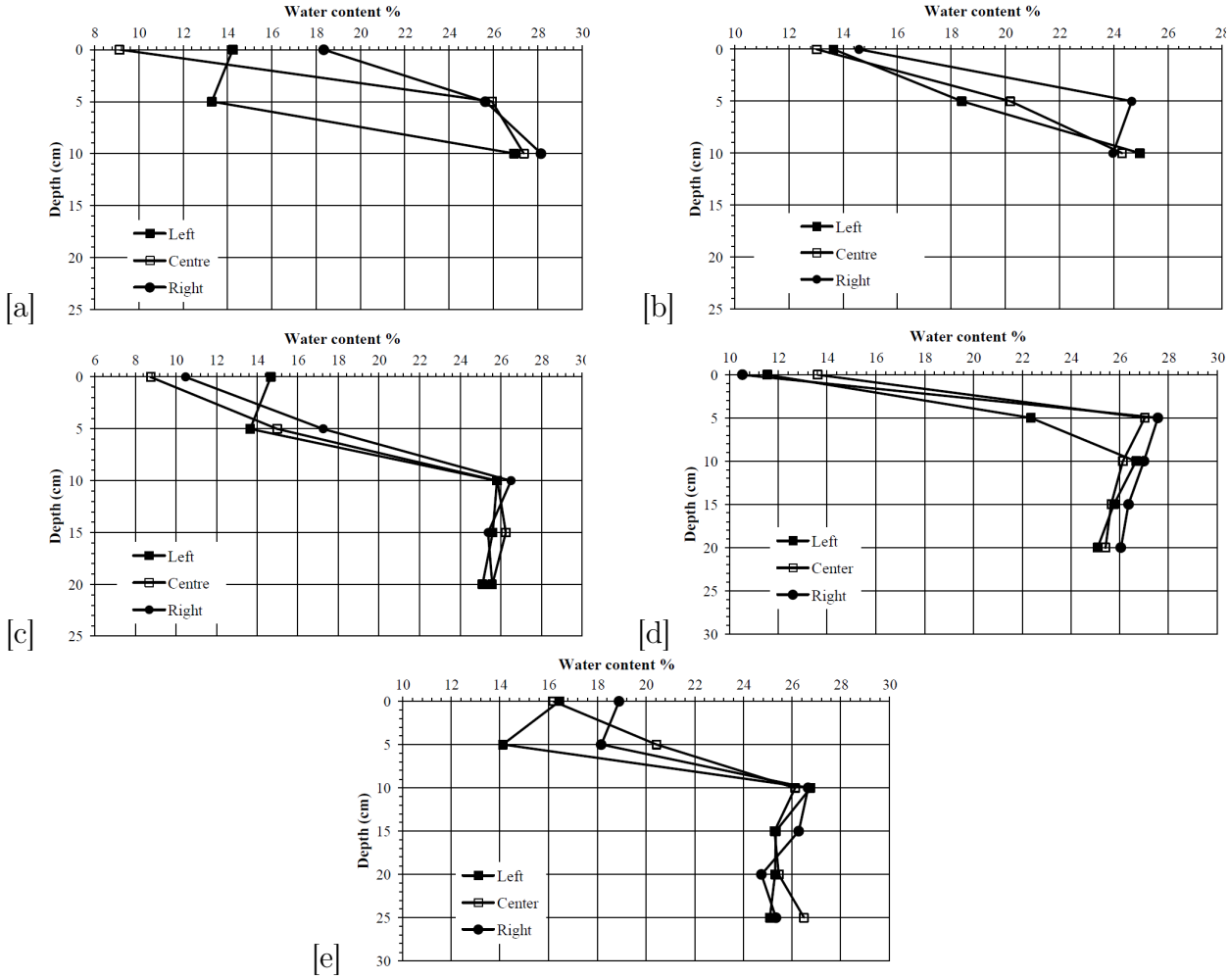

Figure 4.41: Water content measurement versus depth at end of the test for the surface footing for (a) $s = 3.72$ kPa-2 (b) $s = 4.54$ kPa-3 (c) $s = 3.67$ kPa-4 (d) $s = 3.63$ kPa-5 (e) $s = 3.50$ kPa-6.

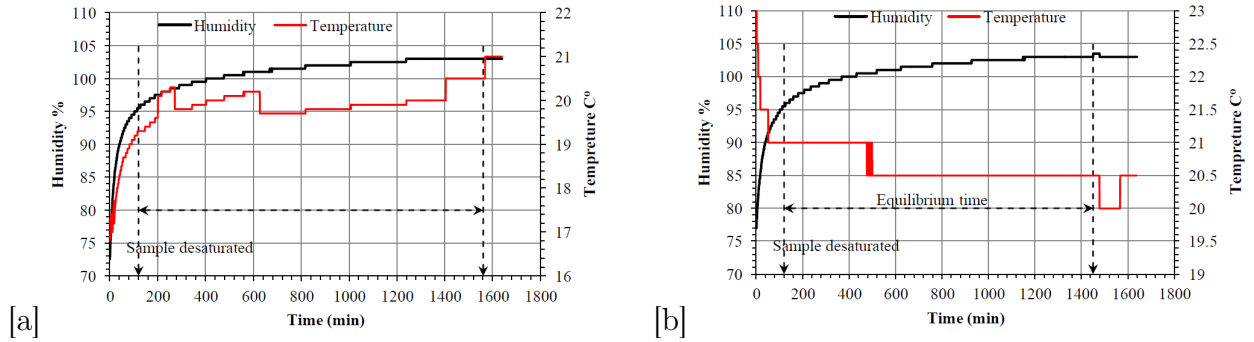

Figure 4.42: Humidity and temperature versus time for the surface footing for (a) $s = 3.63$ kPa-5 (b) $s = 3.50$ kPa-6.

both experimentally and numerically (presented in Chapter 6) at different applied suctions. For most of the cases, four repeat tests were performed with availability of water content measurement and humidity and temperature data for most of the tests. For this case study, the suction head is calculated using the distance from the water table to the soil surface.

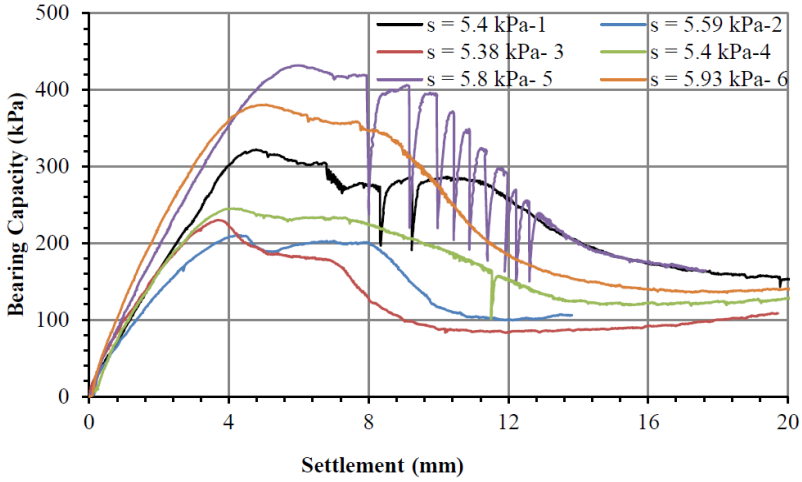

Figure 4.43: Bearing capacity versus settlement for the surface footing for the suction range between 5.38 - 5.93 kPa.

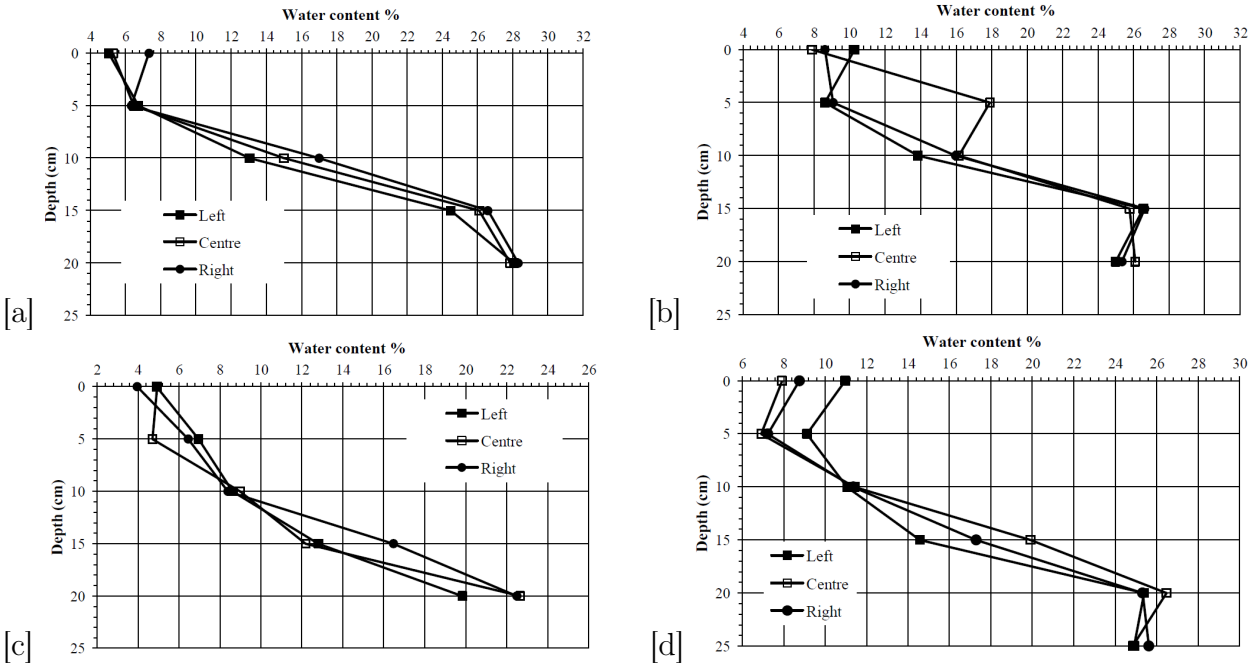

Figure 4.44: Water content measurement versus depth at end of the test for the surface footing for (a) $s = 5.59$ kPa-2 (b) $s = 5.38$ kPa-3 (c) $s = 5.4$ kPa-4 (d) $s = 5.93$ kPa-6.

4.10.2.1 Fully saturated case $s = 0$ kPa-Series (D-I)

Figure 4.46 shows the bearing capacity versus settlement for four tests at $s = 0$ kPa. The letter "D" in the bearing capacity legend figures indicates footing placed at depth. As before, two of the test results show high bearing capacity since soil was raised above the water table. Other test results reveal the same bearing capacity values especially at the end of the test. Figures 4.47a and b show the water content measurement versus depth for two of the tests, while Fig. 4.48a, b, c and d show the humidity and temperature results versus time. For tests $s = 0$ kPa-D-1 and $s = 0$ kPa-D-2, equilibrium times were 2.36 and 2.83 hrs, respectively.

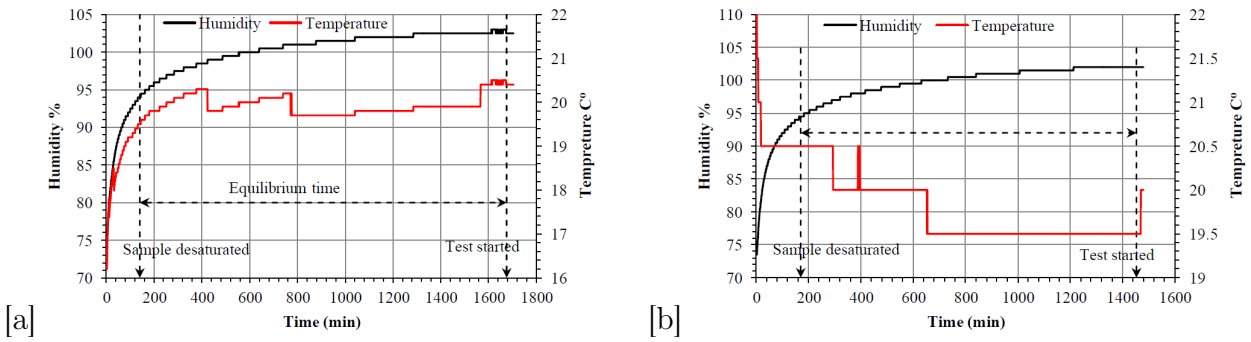

Figure 4.45: Water content measurement versus time for the surface footing for (a) $s = 5.8$ kPa-5 (b) $s = 5.93$ kPa-6.

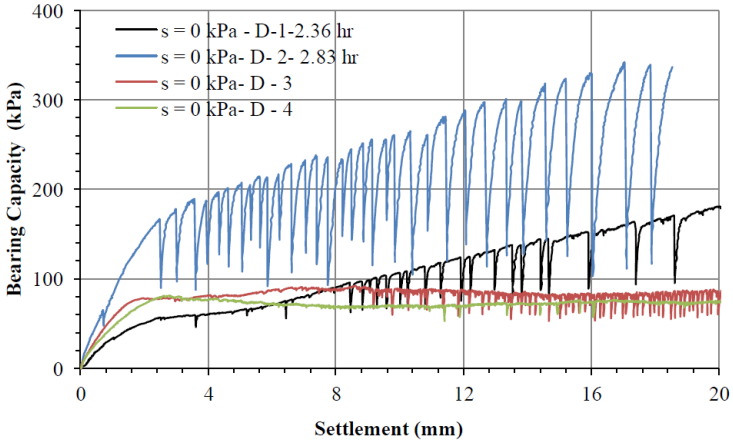

Figure 4.46: Bearing capacity versus settlement for the buried footing for $s = 0$ kPa.

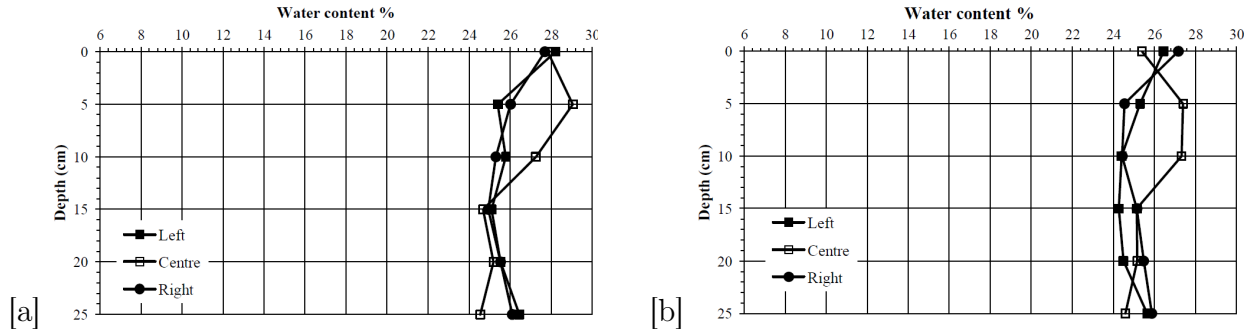

Figure 4.47: Water content measurement versus depth for the buried footing at end of the test for (a) $s = 0$ kPa-D-3 (b) $s = 0$ kPa-D-4.

4.10.2.2 Results for $s = 1.962$ to 2.99 kPa-Series (D-II)

Figure 4.49 shows the bearing capacity results for four applied suctions between 1.962 to 2.99 kPa. Non-consistency in bearing capacity values and oscillation phenomenon are the most noticeable behaviours in the figure. Figures 4.50a, b, c and d show the water content measurement versus depth for the tests. In Figs. 4.50a and b, one water content measurement at depth 10 cm and 5 cm for each test was lost, respectively.

The most interesting phenomenon observed in this series of tests and shown in Fig. 4.50

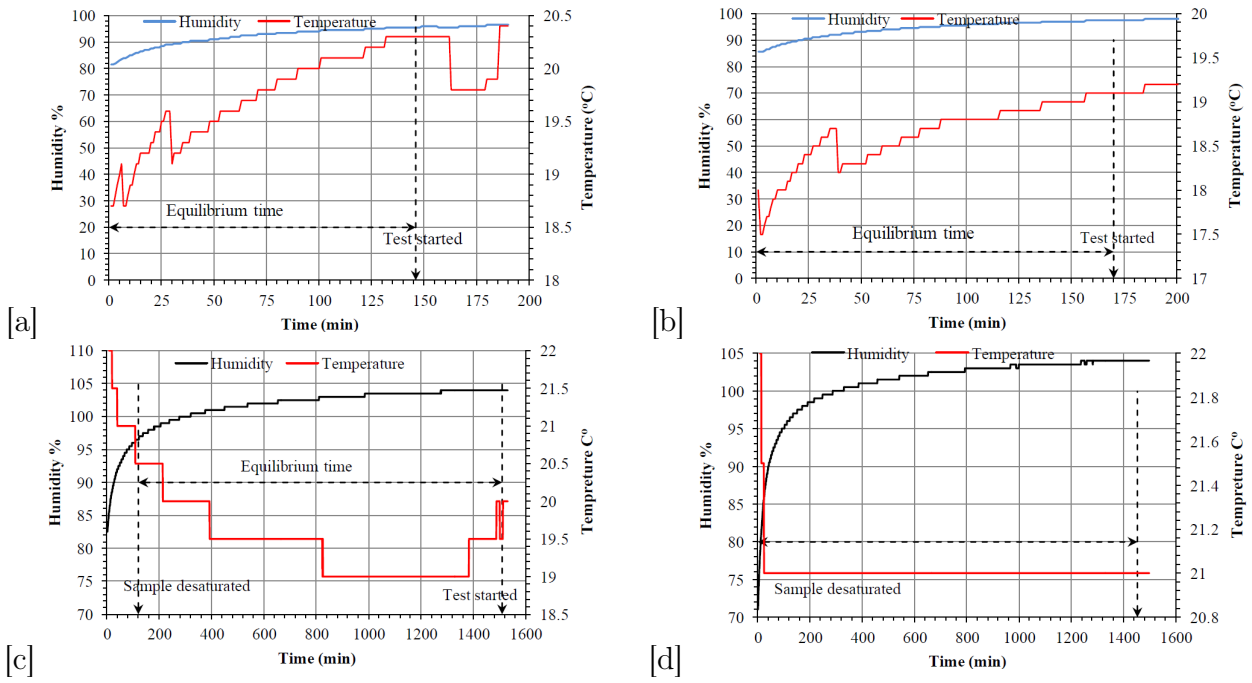

Figure 4.48: Humidity and temperature versus time for the buried footing for (a) $s = 0$ kPa-D-1 (b) $s = 0$ kPa-D-2 (c) $s = 0$ kPa-D-3 (d) $s = 0$ kPa-D-4.

where the footing was buried at 5 cm depth, is that soil at the surface dried out as the footing was pushed into the soil. Further evidence for this behaviour, can be seen in the images as shown in Figs. 4.51a and b. It is clear from Figs. 4.51a and b that water movement at the surface (probably downwards) for the left and right hand sides as well as at the centre had occurred. Another interesting behaviour which can be observed from Fig. 4.51b is that a crack happened at the surface and above the footing. This is an evidence that soil gained cohesion due to the unsaturated conditions. Figures 4.52a, b and c show the humidity and temperature data for three applied suction values where data for the $s = 2.99$ kPa-D-1 were lost.

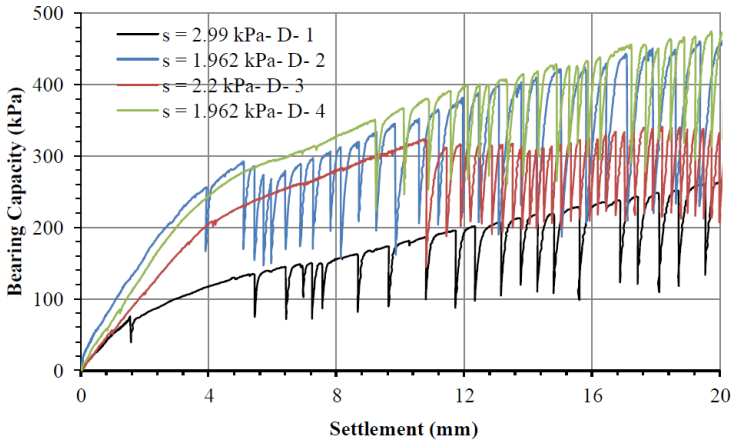

Figure 4.49: Bearing capacity versus settlement for the buried footing for the suction range between 1.962 - 2.99 kPa.

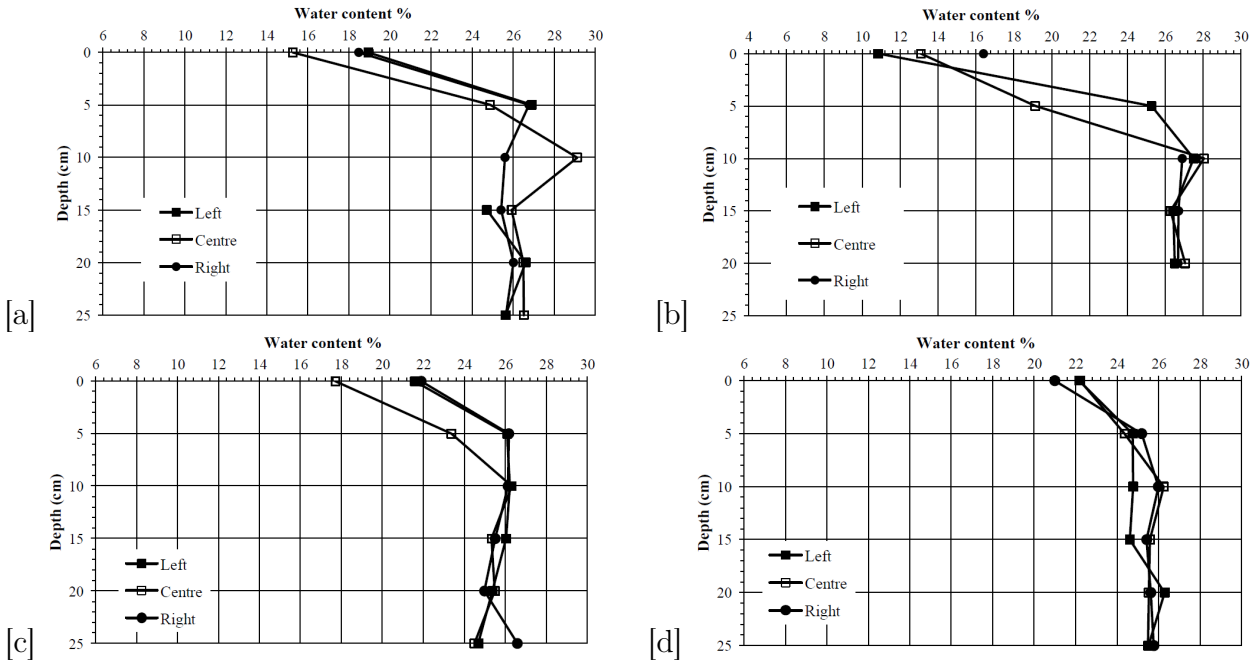

Figure 4.50: Water content measurement versus depth for the buried footing at end of the test for (a) $s = 2.99$ kPa-D-1 (b) $s = 1.962$ kPa-D-2 (c) $s = 2.2$ kPa-D-3 (d) $s = 1.962$ kPa-D-4.

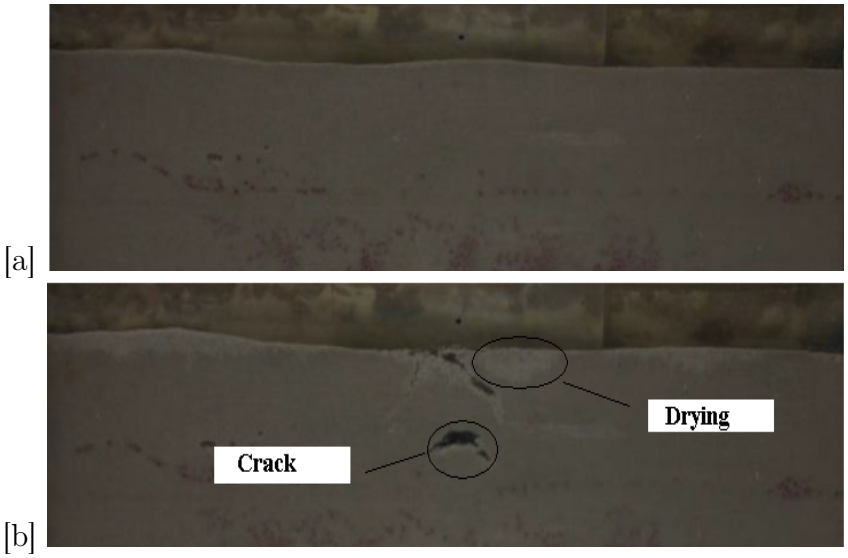

Figure 4.51: Image for buried footing for $s = 1.962$ kPa-D-4 at (a) the beginning of the test (b) the end of the test showing drying at the surface and the crack behaviours.

4.10.2.3 Results for $s = 3.4$ to 3.92 kPa-Series (D-III)

The third range of the applied suction between 3.4 to 3.92 kPa is shown in Fig. 4.53. The bearing capacity results, to some extent, showed higher values at the end of the test compared to the two previous cases. Oscillation happened for all the tests; however the interval between one oscillation to another is longer compared to the two cases discussed previously. Also it started after 10 mm settlement (except for case $s = 3.92$ kPa-D-2). The longer interval of the oscillation is attributed to the effect of suction in turn which gave rise

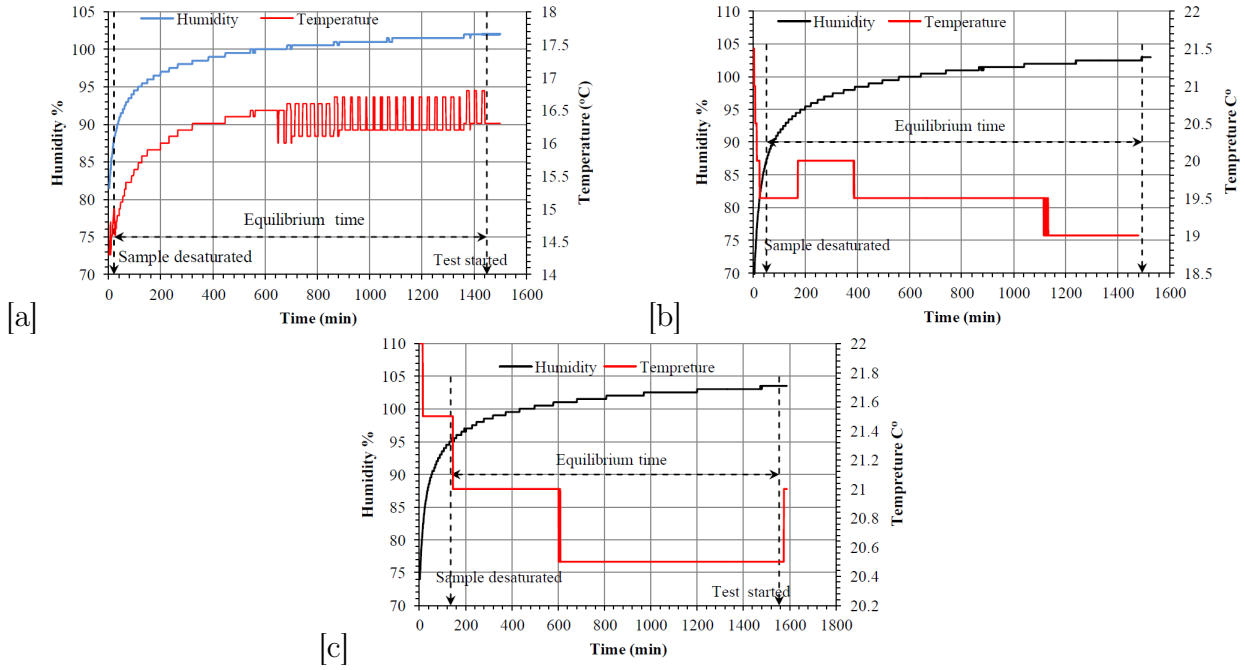

Figure 4.52: Humidity and temperature versus time for the buried footing for (a) $s = 1.962$ kPa -D-2 (b) $s = 2.2$ kPa-D-3 (c) $s = 1.962$ kPa-D-4.

to a gain in strength. The water content and humidity and temperature measurements are shown in Figs. 4.54 to 4.55.

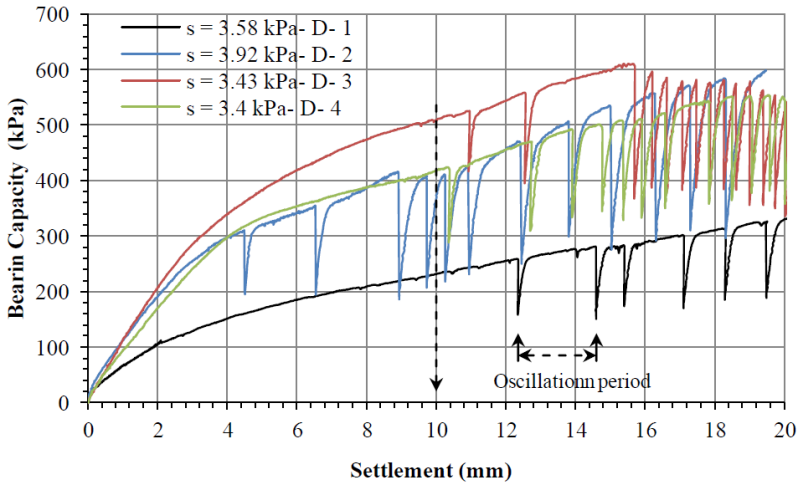

Figure 4.53: Bearing capacity versus settlement for the buried footing for the suction range between 3.4 - 3.92 kPa.

4.10.2.4 Results for $s = 5.68$ to 5.88 kPa-Series (D-IV)

Finally, Fig. 4.56 shows the bearing capacity results versus settlement for the last applied suction range. The results of this series show a distinct peak and oscillatory behaviour for most of the tests. The case of $s = 5.88$ kPa-D-1 shows less bearing capacity, however, at critical state it merged with other cases. The $s = 5.72$ kPa-D-3 sample shows a high bearing capacity of about 560 kPa at a nearly vertical displacement of 15.5 mm. Once again, this is

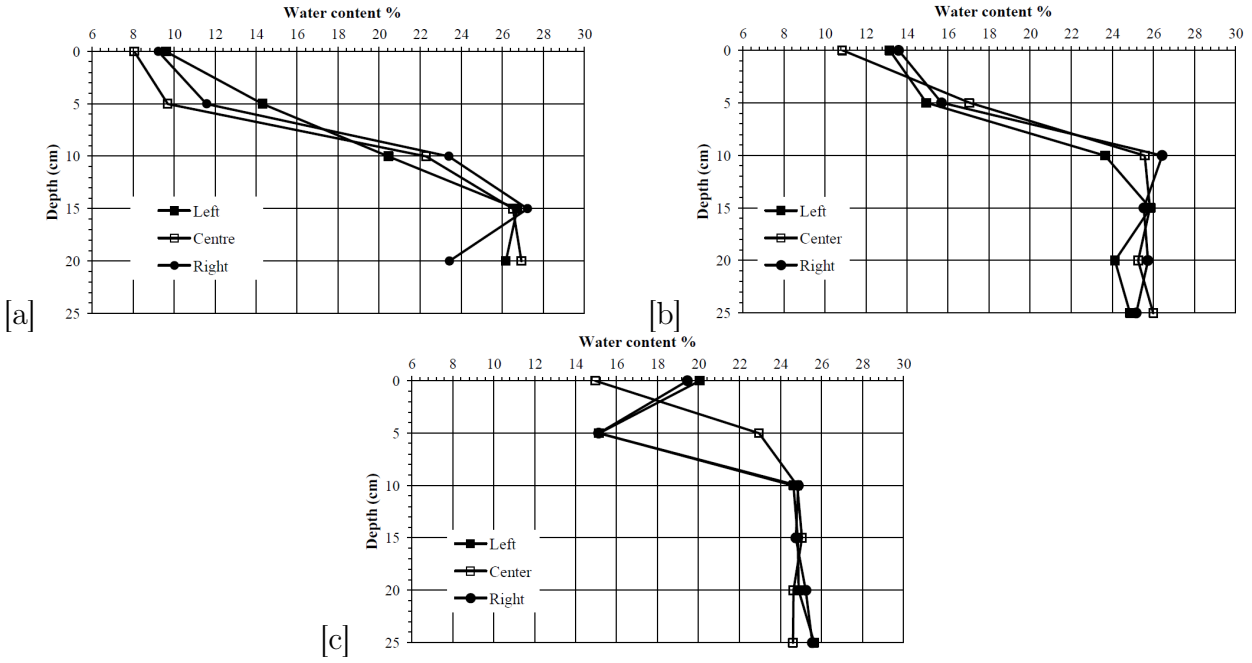

Figure 4.54: Water content measurement versus depth for the buried footing at end of the test for (a) $s = 3.58$ kPa-D-1 (b) $s = 3.43$ kPa-D-3 (c) $s = 3.4$ kPa-D-4.

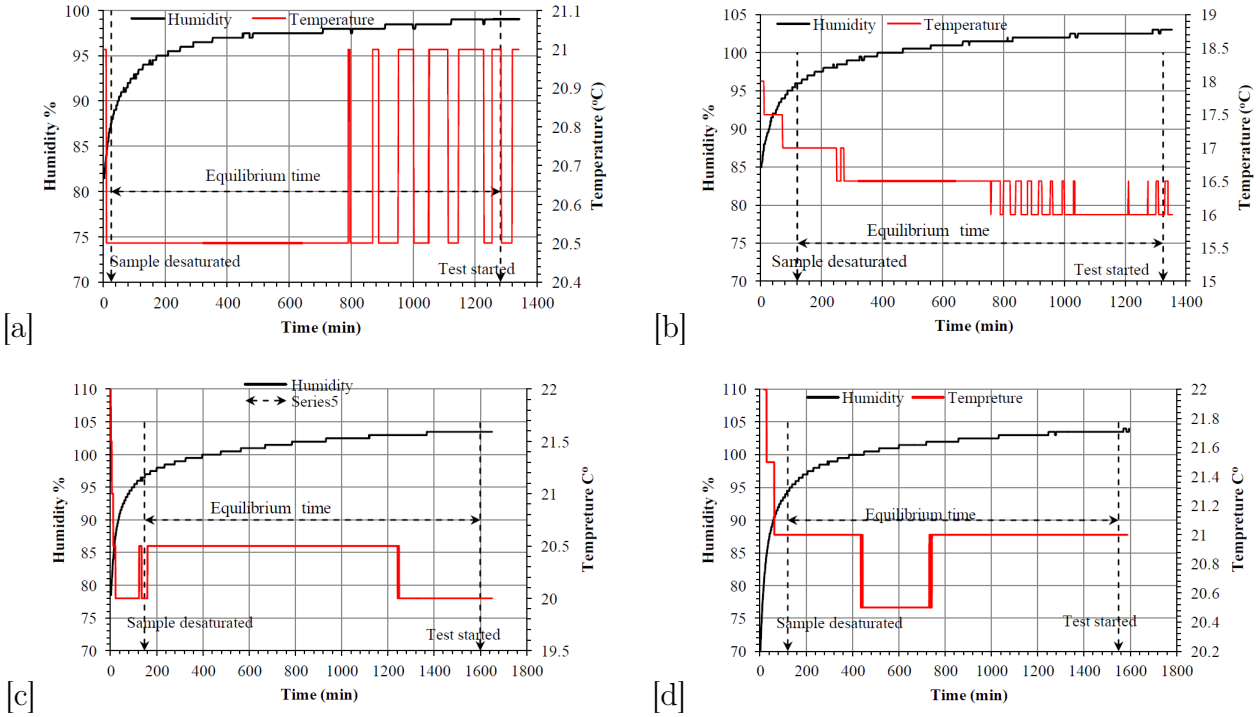

Figure 4.55: Humidity and temperature versus time for the buried footing for (a) $s = 3.58$ kPa-D-1 (b) $s = 3.92$ kPa-D-2 (c) $s = 3.43$ kPa-D-3 (d) $s = 3.4$ kPa-D-4.

attributed to a small angle of rotation of the footing. Figures 4.57a, b and c and 4.58a, b, c and d show the water content and humidity and temperature measurements for this series, respectively.

Finally, variations of the peak bearing capacity with suction for both surface and buried

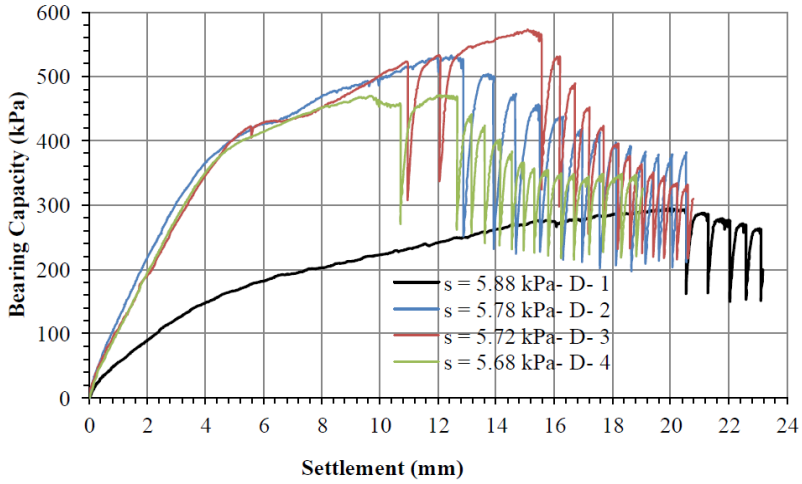

Figure 4.56: Bearing capacity versus settlement for the buried footing for the suction range between 5.68 - 5.88 kPa.

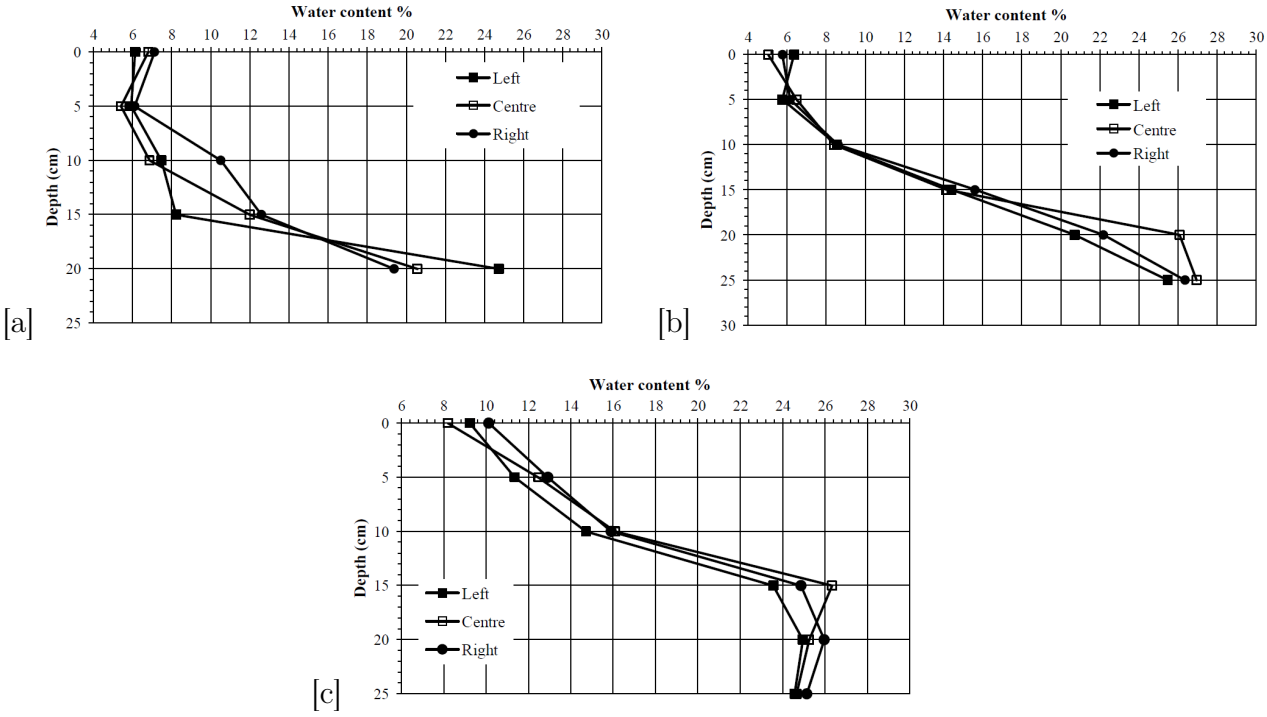

Figure 4.57: Water content measurement versus depth for the buried footing at end of the test for (a) $s = 5.88$ kPa-D-1 (b) $s = 5.78$ kPa-D-2 (c) $s = 5.72$ kPa-D-3.

footings are shown in Figs. 4.59a and b in which the scatter in the bearing capacity values for the repeat tests for a range of suctions can be seen easily. A non-linear peak relationship for bearing capacity with water table depth within the range of suctions of 2 to 6 kPa was observed.

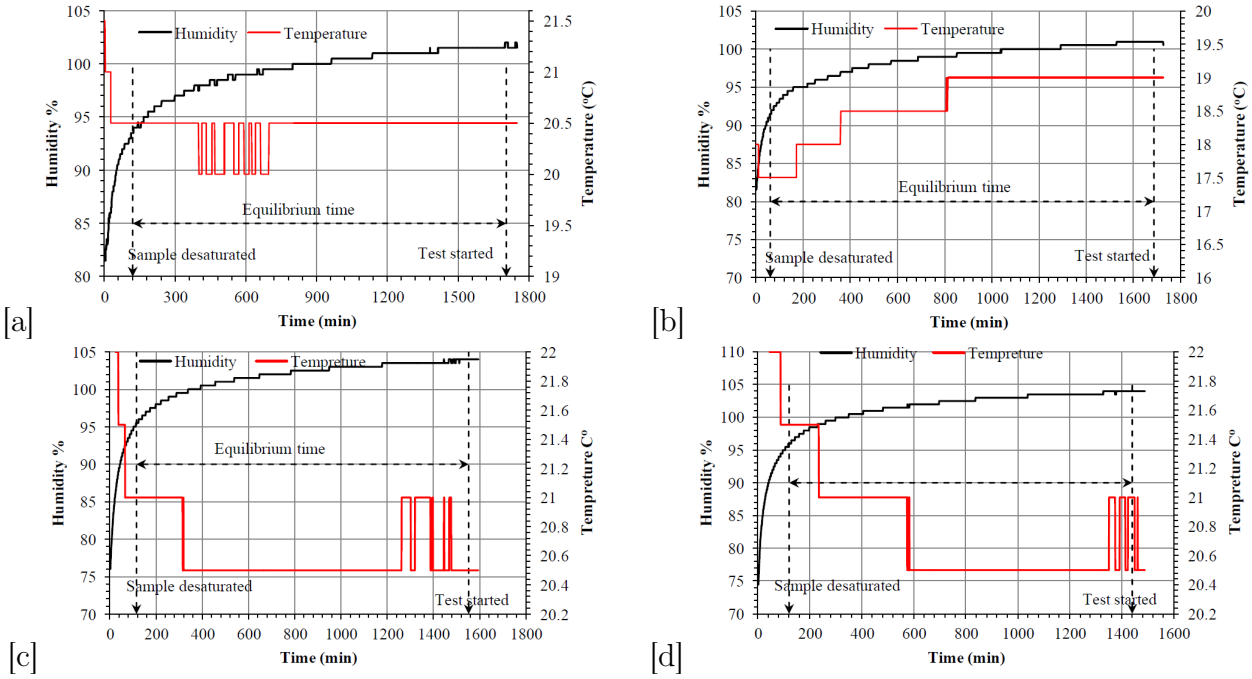

Figure 4.58: Humidity and temperature versus time for the buried footing for (a) $s = 5.88$ kPa-D-1 (b) $s = 5.78$ kPa-D-2 (c) $s = 5.72$ kPa-D-3 (d) $s = 5.68$ kPa-D-4.

4.11 Multi stage bearing capacity test from dry to fully saturated case

The strength of the fully saturated samples observed in the direct shear and bearing capacity tests, compared to the fully dry case, led to further investigation into the effect of water on the shear resistance in fully saturated conditions. A series of multi stage dry-fully saturated tests was therefore conducted for a surface footing. The bearing capacity test was performed by pouring oven-dry soil, at zero distance from the bottom of the box, into the rig to a target height of 30 cm. A dry unit weight of 14.66 kN/m^3 was obtained which is less than that obtained for the fully saturated sample using the water pluviation technique, 15.30 kN/m^3. This happened because for the fully saturated sample, soil consolidated more with the water pluviation technique hence the void ratio was smaller.

The multi stage test involved shearing in fully dry conditions to a target vertical displacement (i.e. ~ 6 or ~ 8 mm-see Fig. 4.60a and e). The ~ 6 or ~ 8 mm vertical displacement of the footing was conducted at two stages, 3 or 4 mm each, respectively leaving about 20 minutes between each stage loading. Then, the rig was connected to a water tank filled previously with de-aired water to saturate the sample. The time for achieving a fully saturated sample using the dry pluviation technique was recorded as 30 minutes for a tank set about 40 cm higher than the soil surface. Then the humidity and temperature meter was installed on the wall of the rig to record readings during the equilibruim time and the test. The rig was then covered by a piece of latex membrane to prevent evaporation. The sample was left about 24 hrs to achieve equilibrium. During this stage, there was about 2 mm consolidation of the soil (see Fig. 4.60a). This gave a final height of 29.8 cm for the sample. Therefore, the dry unit weight changed from 14.66 kN/m^3 ($e = 0.773$) to 14.76 kN/m^3 ($e = 0.761$). It is believed that this small change had an insignificant effect on the bearing capacity results.

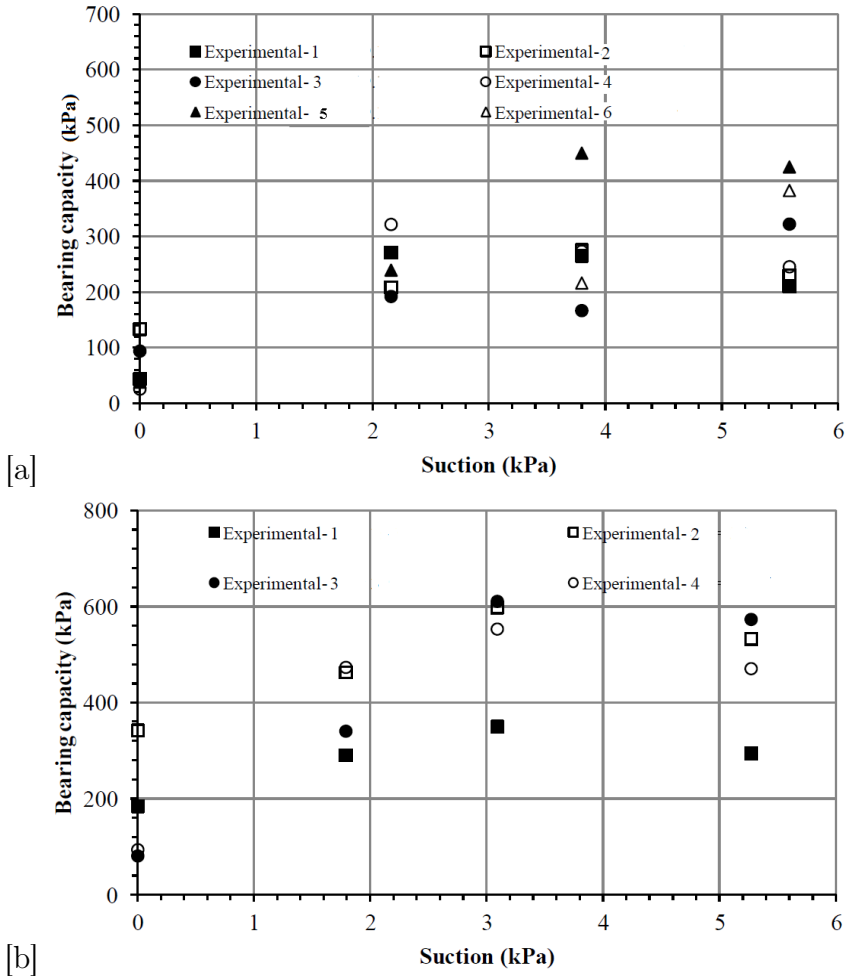

Figure 4.59: Experimental peak bearing capacity for a range of applied suction for (a) the surface footing (b) the buried footing.

During sample preparation, perforated containers were placed at different depth (each 5 cm) from left, centre and right of the rig for water content measurements. The test was then started in two stages as shown in Fig. 4.60a. As the contact between the soil and the loading ram was lost due to the consolidation of the sample after the saturation, the data logging recorded almost no increase in bearing capacity to about 2 mm settlement (see Fig. 4.60a from settlement of about 6.2 to 8.2 mm).

The humidity and temperature readings after saturation of the sample to the end of the test, shown in Fig. 4.60b, were steady in spite of a few fluctuations before the test. The water content measurements confirmed the fully saturated condition as shown in Fig. 4.60c.

Figure 4.60d shows a comparison between three dry tests conducted with Fig. 4.60a. The multi-stage case showed almost same bearing capacity when compared to the dry cases, especially for Fully Dry-2 and Fully-Dry-3. Figure 4.60e shows the multi-stage repeat test (red line) which was compared with Fig. 4.60a in which the results exhibited almost the same bearing capacity. Figure 4.60e also compares the peak bearing capacity results for 7 dry samples, three of which are shown in Figure 4.60d, as shown in Fig. 4.60f. The comparison confirmed that water content gave rise to strength as the fully saturated cases showed almost the same or higher bearing capacities when compared to the fully dry samples. The peak values of the dry samples were selected at near 20 mm settlement.

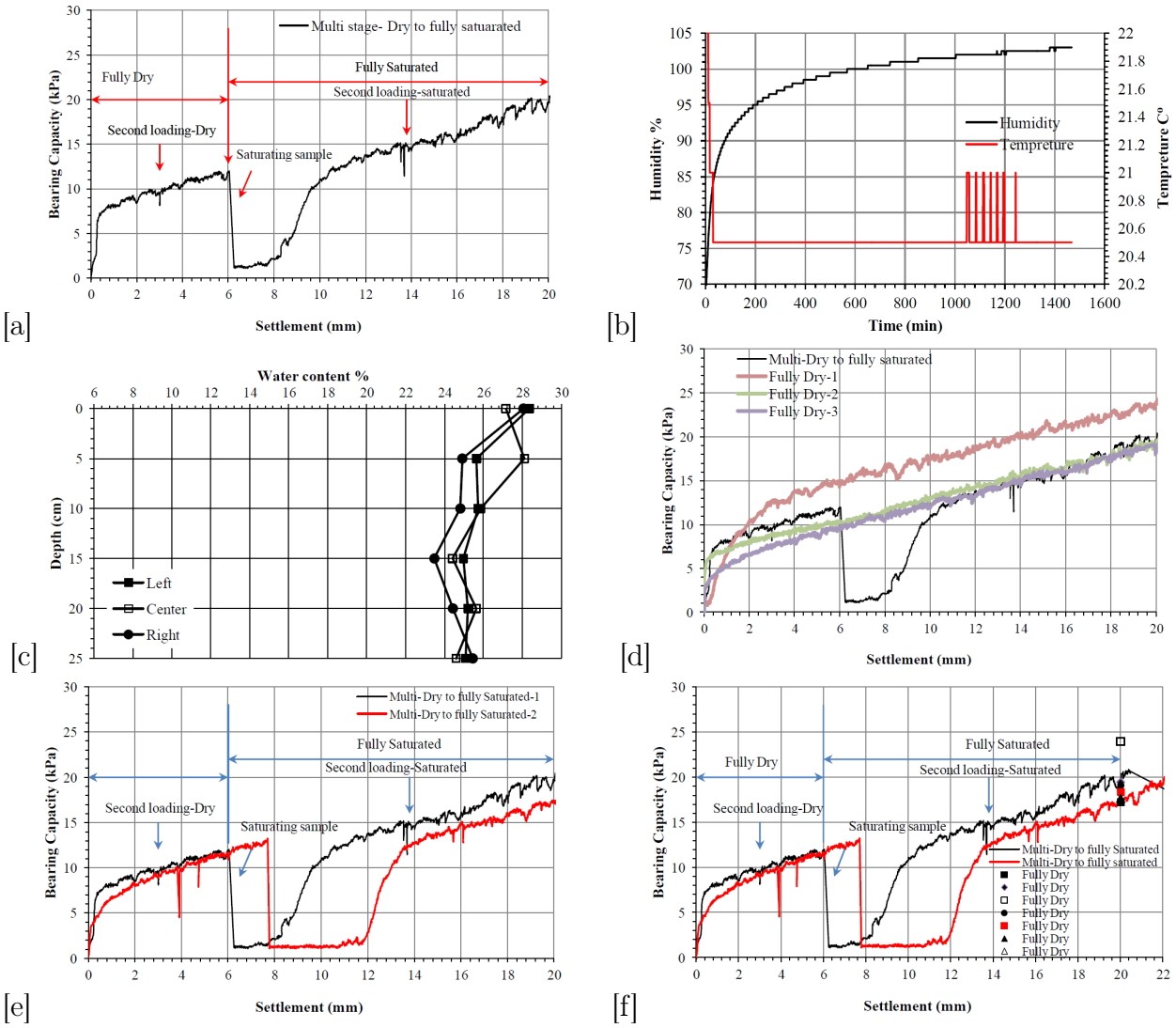

Figure 4.60: (a) multi-stage dry to fully saturated test for the surface footing (b) humidity and temperature after the saturation stage for the sample shown in Fig. 4.60a (c) water content with depth after the saturation stage for sample shown in Fig. 4.60a (d) comparison between multi-stage test with the fully dry cases (e) comparison of two repeat tests for the multi-stage cases (f) comparison between the multi-stage tests with the fully dry cases.

4.12 Effect of low normal stress on the internal friction angle

Although comprehensive direct shear tests were conducted at three different normal stresses: 50, 100 and 200 kPa, a set of tests were also undertaken at low normal stresses for the fully saturated case. The aim of this test was to determine ϕ at low normal stresses and hence to provide an idea about mobilized ϕ in the bearing capacity tests for fully saturated and dry samples that will be used in the numerical bearing capacity study, presented in Subsection 6.6.1.1 in Chapter 6. Normal stresses of 6.25, 12.5 and 25 kPa were therefore selected according to the experimental peak bearing capacity results obtained for the fully dry and saturated cases (e.g. see Fig. 4.60f). A displacement rate of 0.048 mm/min was selected.

To ensure drained conditions, and to be consistent with the drained condition that was

achieved for the bearing capacity tests, burette No.2 (see Fig. 3.11a) was connected to the effluent port. The water level in the burette was kept at the same level as the soil surface to ensure a fully saturated case. At the end of the test, five samples were taken for water content measurements and the average degrees of saturation were 104, 100 and 101% for the three normal stresses: 6.25, 12.5 and 25 kPa, respectively. Figures 4.61a, b and c show the results of the test.

An internal friction angle and cohesion intercept of 43.64^o and 14.2 kPa at peak were obtained, respectively. The value of $\phi = 43.64^o$ is close to the average saturated ϕ value, 46.6^o, obtained at the high normal stresses of 50, 100 and 200 kPa (see Table 4.4).

4.13 Internal friction angle at soil-footing interface

The aim of this series of direct shear tests was to determine the mobilized ϕ at the soil-footing interface which will be used in the numerical part of the bearing capacity (see Subsection 6.6.1).

The test was conducted by placing a piece of steel (as used for the footing material) to fit the bottom half of the direct shear box, while the top half of the box was filled by pouring oven-dry sand to a target unit weight of 15.30 kN/m^3 and a void ratio of 0.7. The soil was then sheared at a displacement rate of 0.48 mm/min which is of the same order of magnitude as the loading rate used for the bearing capacity tests, 0.6 mm/min.

Figure 4.62 shows the average shear resistance versus normal stress at both peak and critical state for three tests at the same normal stresses: 41.44, 83, 166 and 332 kPa. The average shear strength parameters, c and ϕ, obtained at the peak and critical state were (13.6 kPa, 21.59^o) and (9.6 kPa, 21.54^o), respectively.

4.14 PIV Results

In this section, displacement vectors using the PIV technique for both the surface and buried footings are presented. The aim is to investigate the effect of suction on the failure mechanisms of the strip footing and in addition, to compare qualitatively the results with the failure mechanisms which are obtained using the numerical DLO method (explained in Chapter 6). The results are presented in terms of displacement vectors.

4.14.1 Results of displacement vectors for the surface footing

Figures 4.63a, b, c, d and e show the displacement vectors of five samples: dry-4, fully saturated $s = 0$ kPa-4, $s = 2.4$ kPa-5, $s = 3.63$ kPa-5 and $s = 5.93$ kPa-6, respectively. The results were obtained using all the images from the beginning of the test to an image corresponds to 14 mm vertical settlement to produce the final cumulative plot. This is because for most of the tests, samples experienced peak load before 14 mm vertical displacement; therefore, only images until this displacement were selected for the PIV analysis. This gives the advantage of decreasing the analysis time by using fewer images. For cases when no distinct peak for the bearing capacity can be seen (especially for the buried footing results) images were analysed also until 14 mm vertical displacement and the results showed reasonable failure mechanisms. Thus, no attempt was carried out to extend the PIV analysis behind the 14 mm vertical displacement. A patch size of 150×75 was used in the PIV analysis for all the tests.

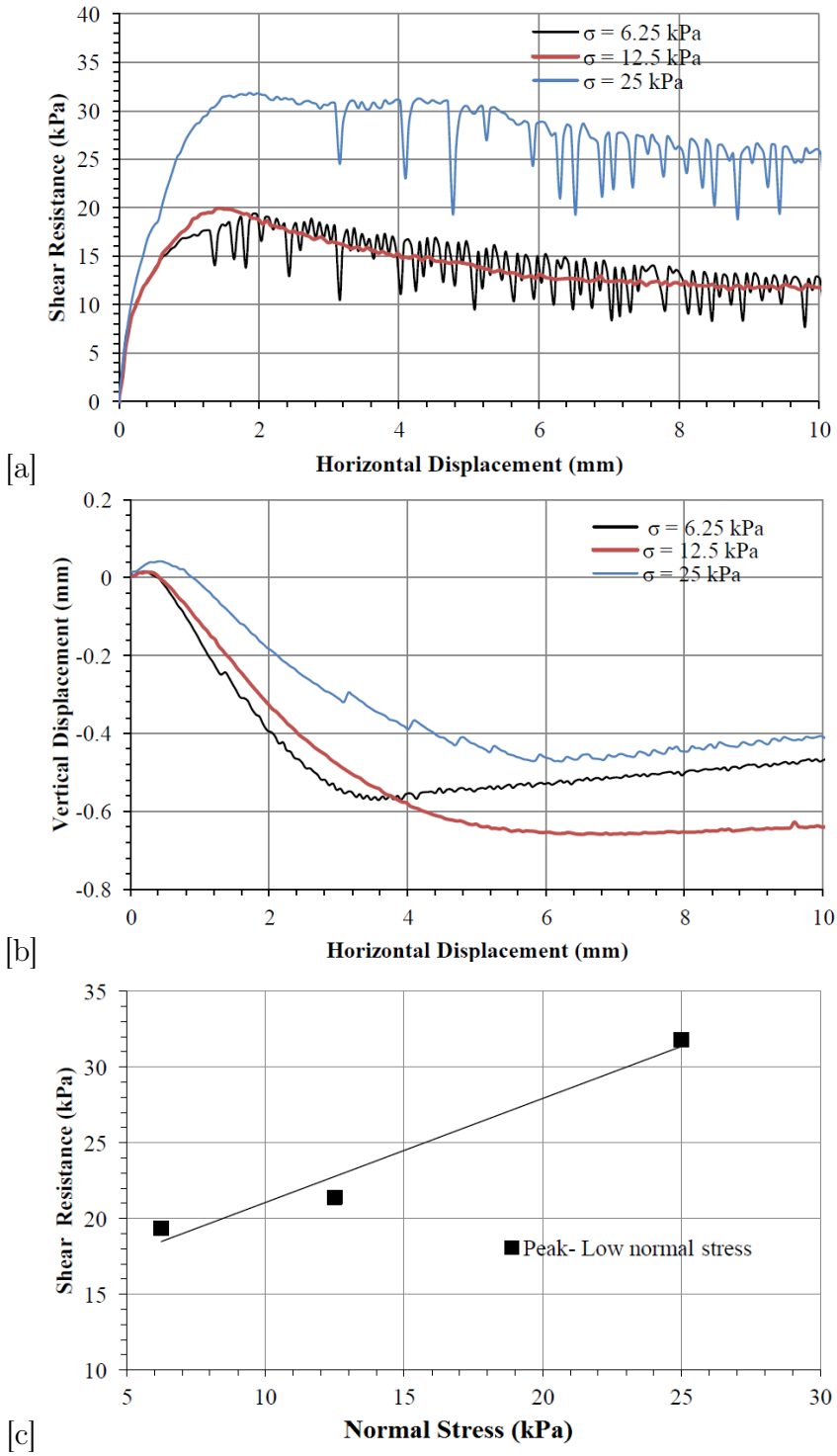

Figure 4.61: Direct shear results for the fully saturated case at different low normal stresses: 6.25, 12.5 and 25 kPa and displacement rate of 0.048 mm/min (a) shear resistance versus horizontal displacement (b) vertical displacement versus horizontal displacement (c) shear strength versus normal stress at peak.

The fully dry and saturated samples showed displacement vectors on both sides of the footing with less settlement for the fully saturated case. This is because of the effect of water on the soil which gave rise to strength for the fully saturated sample as was observed also for the direct shear tests (fully saturated samples showed higher shear strength than the dry

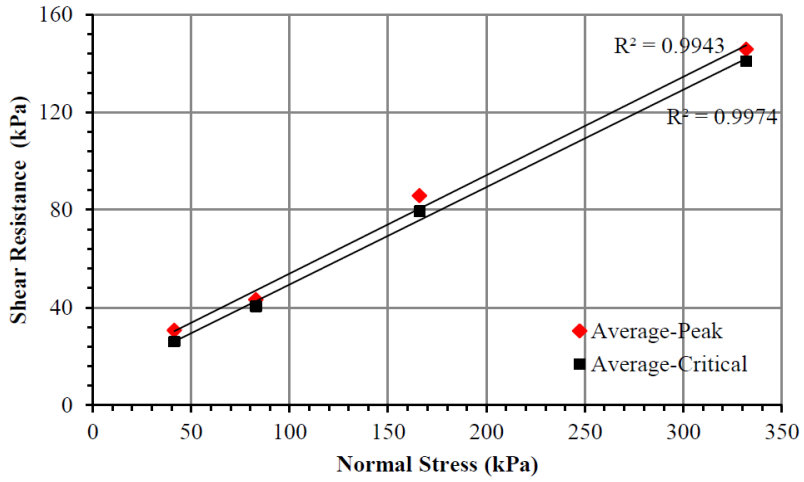

Figure 4.62: Shear resistance versus normal stress at soil-footing interface using the direct shear test for the fully dry sand.

samples - see Figs. 4.3).

The unsaturated samples, however, showed one sided-shallower failure mechanisms, when compared to the fully dry or fully saturated samples, due to rotation of the footing. The rotation of the footing was attributed to uneven increase of strength due to the unsaturated conditions. This could be attributed to either (i) increased peak strength and strain softening effects in the unsaturated samples leading to shear localisation on one or other side of the footing or (ii) due to differences in menisci arrangements on both sides of the footing, leading to differences in strength on each side leading to rotation of the footing towards the weaker side. The difference in the menisci arrangements, even at the same depth, and water migration would cause differences in water content and hence degree of saturation (see. Figs. 4.37a and b). The implication is important as this difference caused a higher degree of rotation for the unsaturated samples.

The most interesting observation from Figs. 4.63a, b, c, d and e is that the pattern indicates more dilation and a wider failure mechanism for the unsaturated samples. The finding here is identical with the direct shear test results in which the unsaturated samples showed higher dilation than the fully dry and saturated samples (see Figs. 4.13). This further confirms the high bearing capacity for the unsaturated samples and hence the possibility of increase of shear strength parameters due to higher dilative behaviour for the unsaturated samples in the bearing capacity test.

4.14.2 Results of displacement vectors for the buried footing

Figures 4.64a, b, c, d and e show the PIV results for the buried footing for the fully dry-4, s = 0 kPa-D-4, s = 2.2 kPa-D-3, s = 3.4 kPa-D-4 and s = 5.68 kPa-D-4 samples, respectively. Once again, the fully dry case shows a deeper and relatively symmetrical failure mechanisms, while the other cases exhibit wider failure mechanisms. This is attributed to the effect of the unsaturated condition as was observed for the surface footing. Interestingly, soil above the footing for the unsaturated samples shows a very small settlement compared to the fully dry and saturated samples.

In conclusion, the qualitative analysis of the PIV results for the surface and buried footings performed in this study enabled study of the effect of degree of saturation and hence suction through the displacement vectors and the failure mechanisms. The effect of

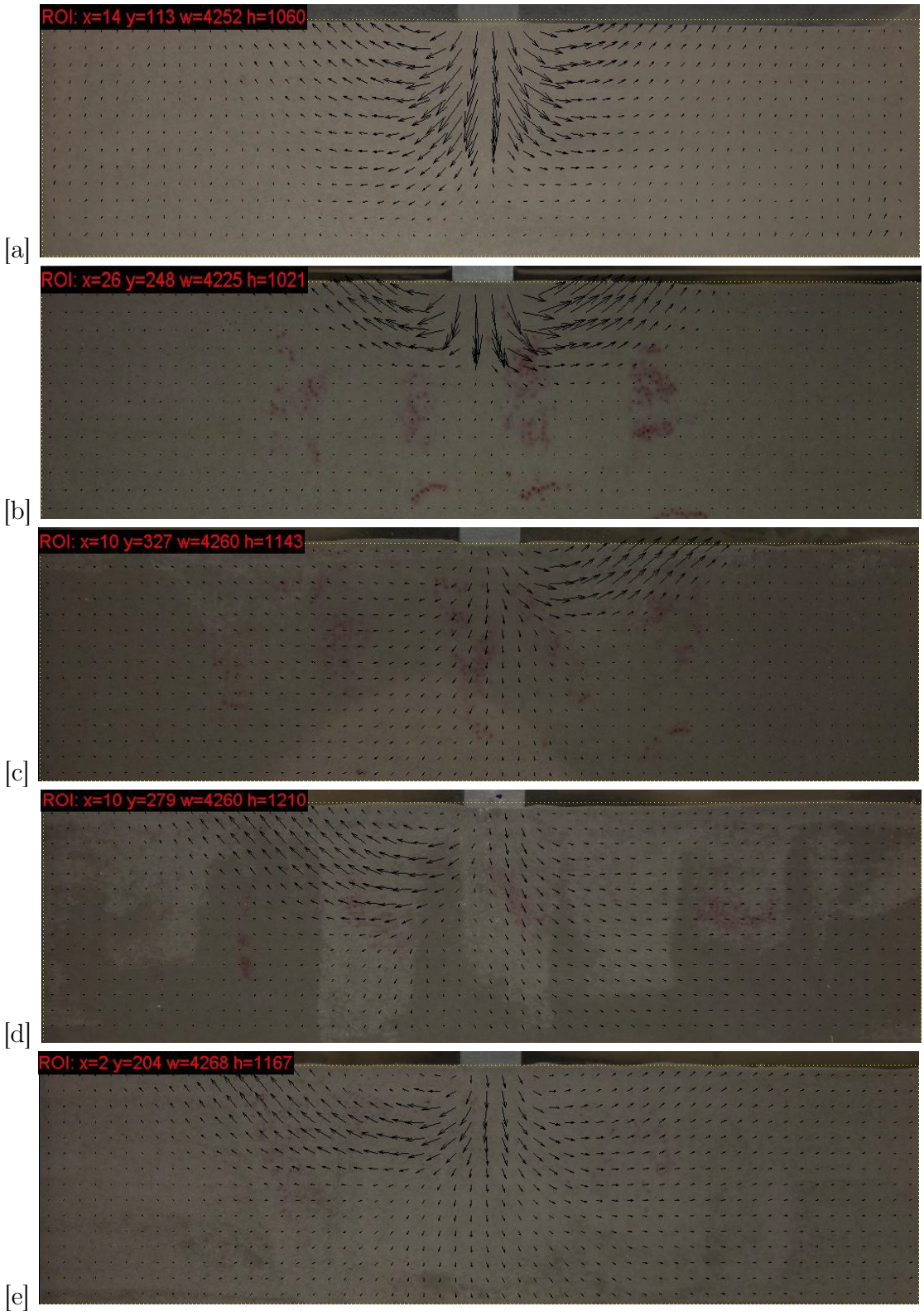

Figure 4.63: Displacement vectors for the surface footing for (a) the fully dry case-4 (b) $s =$ 0 kPa-4 (c) $s = 2.4$ kPa-5 (d) $s = 3.63$ kPa-5 (e) $s = 5.93$ kPa-6.

dilative behaviour which was observed in the failure mechanisms for the surface and buried footings provides supporting evidence of the possibility of the increase in shear strength

parameters in the unsaturated tests.

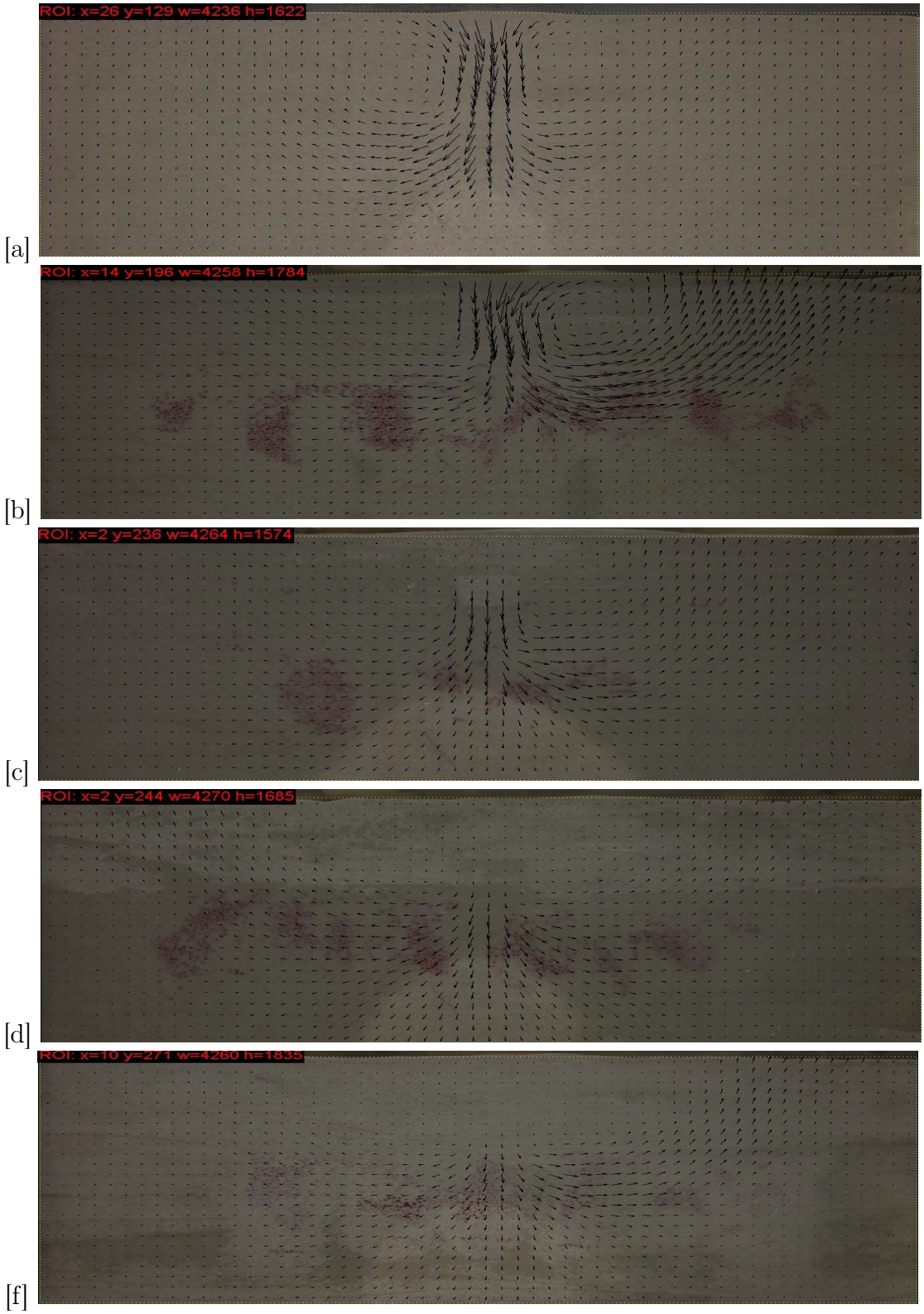

Figure 4.64: Displacement vectors for the buried footing for (a) the fully dry case-4 (b) $s =$ 0 kPa-D-4 (c) $s = 2.2$ kPa-D-3 (d) $s = 3.4$ kPa-D-4 (e) $s = 5.68$ kPa-D-4.

4.15 Summary of the chapter

This chapter reported the experimental results conducted in this study for the SWCC using the filter paper method and HCT, the direct shear and the bearing capacity tests.

The direct shear results displayed interesting behaviours such as the dilative phenomenon of the unsaturated samples, the oscillation of shear resistance, the high shear resistance for the fully saturated and unsaturated cases, the variation of the internal friction angle and cohesion values at peak, critical and oscillation, states wetting collapse and the hydro-mechanical behaviour during shearing.

Higher shear resistance and dilative behaviour were observed for the unsaturated samples. An increase in the internal friction angle and cohesion intercept was also observed for the fully saturated and unsaturated samples. Oscillatory behaviour was most evident for the fully dry, saturated and unsaturated samples prepared at a high degree of saturation ($s = 2$ kPa). Also samples prepared at high degrees of saturation showed a sudden wetting collapse.

The bearing capacity results for the surface and buried footings involved a study on strength for a series of applied suction profiles for the fully saturated and unsaturated samples. Behaviours such as drying due to load application, load-displacement, oscillation and increase of bearing capacity values of the unsaturated samples were observed. High bearing capacity values observed for the fully saturated case were investigated further through performing a series of multi-stage bearing capacity tests. The effect of the soil-footing interface was also studied by conducting a series of direct shear tests. Finally, results of the displacement vectors and the failure mechanisms using the PIV analysis were presented.

Unsaturated samples gave rise to strength due to unsaturated conditions. For the surface footing, for example, a 4-10 fold increase in bearing capacity was observed when unsaturated models were compared to a fully saturated model. The PIV results showed that the dilative behaviour was most evident for the unsaturated samples due to gain in strength.

The direct shear results presented in this chapter are to be utilised in evaluation of the shear strength equation (Eq. 2.31) in Chapter 5. The bearing capacity results, on the other hand, are used to perform a comparative study against DLO analyses presented in Chapter 6.

Chapter 5

Shear Strength Model

5.1 Introduction

In this chapter a detailed evaluation of Eq. 2.31 presented in Chapter 2 and proposed by Öberg & Sällfors (1997) is carried out against several types of the soils for a wide range of suctions. Although, Öberg & Sällfors (1997) evaluated their equation based on an assumed SWCC as explained previously in Subsection 2.8.1, the equation is evaluated again in this study based on the original measured SWCC or actual developed degree of saturation and suction at peak for some of the data found in the literature.

As will be shown the evaluation of the equation showed poor agreement with the experimental results, therefore, a reformulation of the equation is proposed for an unsaturated sand. The reformulation is based on the increase of the shear strength parameters behaviour observed in the direct shear test. Also an existing equation that predicts the degree of saturation for unsaturated soils is proposed which takes the effect of air entry value of the soil into consideration.

Following the reformulation, the proposed shear strength equation is further evaluated against the direct shear test results conducted in this study. The effects of the suction and degree of saturation (s S_r) and ϕ, c (at peak and critical state) on the shear strength are studied.

5.2 Evaluation of the Öberg & Sällfors (1997) equation

In this section, the equation which was proposed by Öberg & Sällfors (1997) (Subsection 2.8.1) is evaluated using several studies found in the literature. Different types of soil with various methods for measuring and controlling suction were used. The Öberg & Sällfors (1997) equation is repeated below.

$$\tau = c^{'} + [\sigma - S_r \; u_w \,] \tan \phi^{'} \tag{5.1}$$

The reason for re-evaluating Eq. 5.1 is that since the work of Öberg & Sällfors (1997), a number of studies have become available in which the actual measured SWCC for the soils were obtained as stated previously in Subsection 2.8.1. The same procedure as conducted by Öberg & Sällfors (1997) for evaluation of Eq. 5.1 was, therefore, repeated based on the actual measured SWCC (rather than one based on grain-size distribution curve). The following evaluations are either based on the original SWCC to determine S_r from suction or on the actual values of S_r and s at peak or critical state. Evaluation of Eq. 5.1 based on

measured suction at peak and critical state is important as it takes into consideration effect of void ratio during shearing. In other words; as shearing process continues, both suction and degree of saturation change.

5.2.1 Comparison with Vanapalli et al. (1998)

Vanapalli et al. (1998) studied the shear resistance of a Botkin silt using a conventional unconfined compressive test over a range of suctions from 0 to 100,000 kPa (see Table 5.1). The saturated shear resistance parameters $c^{'}$ and $\phi^{'}$ were given as 14.2 kPa and 36.5^{o}, respectively. The SWCC was utilised to obtain the degree of saturation by knowing the suction. Given the unconfined compressive strength of the soil, c_u, the vertical stress at failure σ_1 is determined as:

$$\sigma_1 = 2\ c_u \tag{5.2}$$

Since the soil in the laboratory was exposed to the atmosphere, u_a in Eq. 5.1 was set to zero and the normal stress on the critical shear plane σ was assumed to be equal to $(\sigma_1/2)$. Table 5.1 shows the range of suction values selected to obtain degree of saturation based on the available SWCC (see Fig. 5.1a) and corresponding values of σ_1 at the same selected suctions were obtained according to the unconfined compressive strength figure available in the paper.

It is clear from Table 5.1 (see column 5 and 6) and Fig. 5.1b that Eq. 5.1 overestimates the experimental values. The enormous difference at the high suctions may not be an issue because of difficulties of attained such suction values in the practical life, however, is still affecting the evaluation of Eq. 5.1.

Table 5.1: Evaluation of Eq. 5.1 against Vanapalli et al. (1998).

s kPa	S_r%	sS_r kPa	σ_1 kPa	c_u kPa = τ_f kPa Experimental	τ kPa Eq. 5.1
1	100	1	27.74	13.87	25.204
10	96	9.6	51.06	25.53	40.198
100	85	85	242.02	121.01	166.639
1,000	53	530	620.78	310.39	636.058
10,000	28	2800	1591.7	795.85	2674.990
100,000	12	12000	3544.06	1772.03	10204.966

5.2.2 Comparison with Nishimura et al. (2008)

Evaluation of Eq. 5.1 can also be carried out for small net normal stresses $(\sigma_1 - u_a)$ of 3.5 kPa based on the study of Nishimura et al. (2008). The shear resistance of an unsaturated silty soil was obtained using a direct shear test. The SWCC was obtained using two different approaches namely, the pressure plate and vapour pressure techniques. In the latter technique, Lord Kelvin's equation was used based on the relative humidity of the samples as follows:

$$\psi = -135022\ ln(RH) \tag{5.3}$$

where ψ is the soil suction or total suction in kPa and RH is the relative humidity (%). The sample preparation procedure can be found in Nishimura et al. (2008). The degree of saturation was calculated using a weight-volume relationship in which the water content was

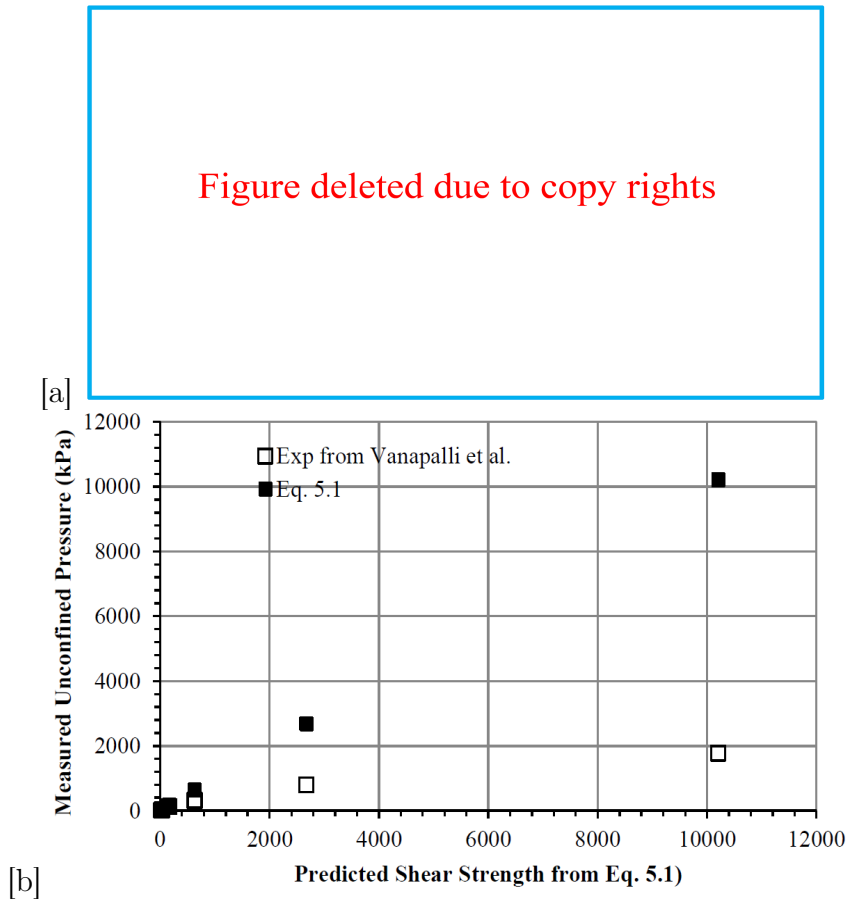

Figure 5.1: (a) The SWCC for the tested Botkin silt, after Vanapalli et al. (1998) (b) Evaluation of Eq. 5.1 against Vanapalli et al. (1998) work.

obtained from the SWCC for any known suction. However, the hysteresis of the SWCC is neglected due to unavailability of the degree of saturation and suction at the peak or critical state. Table 5.2 shows the soil properties used in the study. Table 5.3 shows the suction values obtained using the two methods and a comparison between the experimental and the obtained shear resistance based on Eq. 5.1. Again, the agreement is rather poor as shown in Fig. 5.2 with Eq. 5.1 underestimating the experimental data.

Table 5.2: Soil properties used in the evaluation, after Nishimura et al. (2008).

Initial void ratio, e	0.89
Specific gravity, G_s	2.65
Effective cohesion, $c^{'}$ (kPa)	0
Internal friction angle, $\phi^{'}$(degrees)	32.3

The prediction for the high applied suctions are overestimated as shown in Fig. 5.3. No attempt was made by Öberg & Sällfors (1997) to evaluate the equation at suctions greater than 1000 kPa.

5.2.3 Comparison with Tarantino & Tombolato (2005)

Tarantino & Tombolato (2005) conducted a series of direct shear test on a non-active clay (Speswhite kaolin) soil in which three normal stresses were used: 300, 600 and 1200 kPa.

Table 5.3: Evaluation of Eq. 5.1 against Nishimura et al. (2008).

s kPa	S_r%	$(\sigma_1 - u_a)$ kPa	τ_f Experimental kPa	τ Eq. 5.1 kPa
20[1]	76.82	3.5	26.1	11.92
40[1]	44.66	3.5	56.2	13.50
80[1]	26.20	3.5	77.3	15.46
120[1]	19.94	3.5	87.7	17.34
180[1]	14.88	3.5	73.4	19.15
2830[2]	7.44	3.5	32.9	135.38
6940[2]	6.25	3.5	39.1	276.54
9800[2]	3.57	3.5	38.1	223.57
39000[2]	2.67	3.5	37.8	662.90
83400[2]	1.48	3.5	37.1	787.13

*1*suction obtained using the pressure plate technique
*2*suction obtained using the vapour technique. This is total suction (not matric suction) and explains the apparent discrepancies in Fig. 5.3.

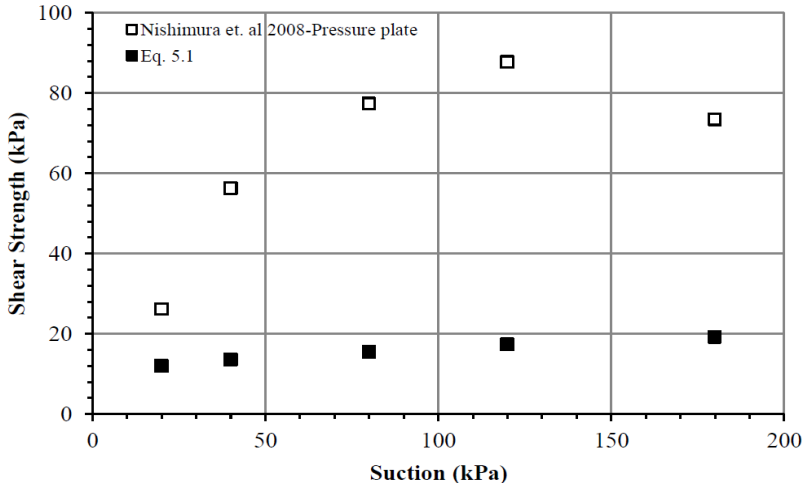

Figure 5.2: Evaluation of Eq. 5.1 against Nishimura et al. (2008) work for suction $<$ 200 kPa.

The evaluation was carried out by selecting s and S_r at peak shear resistance for two normal stresses 300 and 600 kPa since the measured suction, using tensiometer, during the test at peak were available for these two normal stresses. Samples at these two normal stresses were first prepared at almost the same water content by compacting them at 600 kPa compaction pressure. Table 5.4 shows the suction, degree of saturation and shear resistance at peak for the two normal stresses 300 and 600 kPa. As can be seen the prediction of Eq. 5.1 in comparison with the experimental data is rather poor as shown in Fig. 5.4. The shear strength parameters values of the soil, $c^{'}$ and $\phi^{'}$, were 186.9 kPa and 3.5^o, respectively.

Table 5.4: Evaluation of Eq. 5.1 against Tarantino & Tombolato (2005).

σ kPa	s kPa	S_r%	τ_f kPa	τ kPa Eq. 5.1
300	555	74	206.6	230.4
600	600	76	329.3	251.5

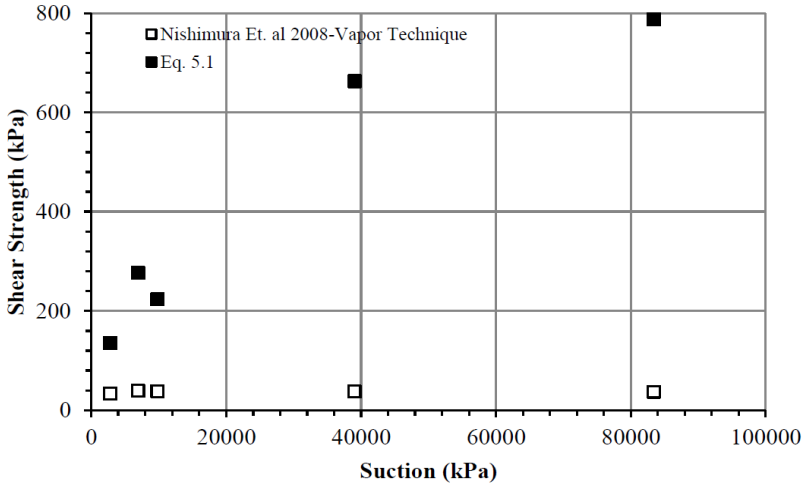

Figure 5.3: Evaluation of Eq. 5.1 against Nishimura et al. (2008) work at high suctions.

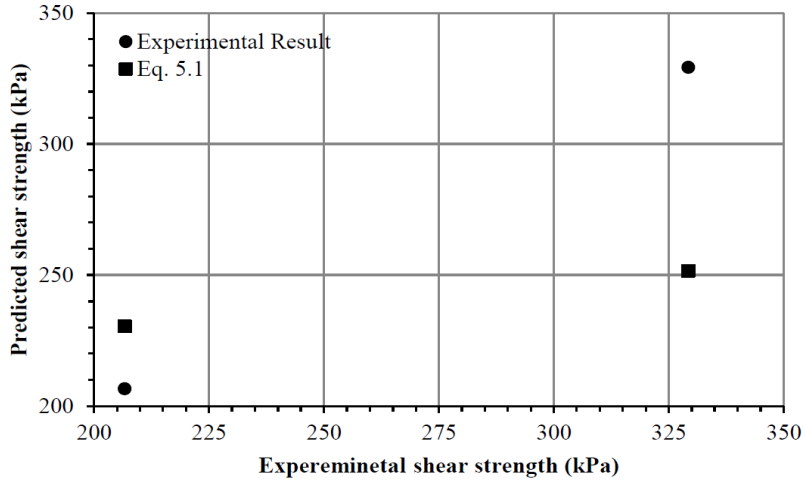

Figure 5.4: Evaluation of Eq. 5.1 against Tarantino & Tombolato (2005) work for normal stresses of 300 and 600 kPa.

5.2.4 Comparison with Boso (2005)

Boso (2005) conducted direct shear tests at three different normal stresses: 100, 300 and 500 kPa for a reconstituted clayey silt. As with the Tarantino & Tombolato (2005) work, s and S_r at critical state were available. Table 5.5 shows the parameters and the calculated values used in this evaluation.

Figure 5.5 shows modest agreement of Eq. 5.1 against Boso (2005). Although Eq. 5.1

Table 5.5: Evaluation of Eq. 5.1 against Boso (2005).

$c^{'}$ kPa	$\phi^{'}$ degrees	σ kPa	s kPa	S_r%	sS_r kPa	τ_f kPa	τ kPa Eq. 5.1
190	29.72	100	1000	45	450	185.1	503.96
190	29.72	300	500	75	375	317.46	575.32
190	29.72	500	270	85	229.5	413.38	606.43

is able to follow the decrease trend as the experimental results when suction increasing, however the comparison again is rather poor.

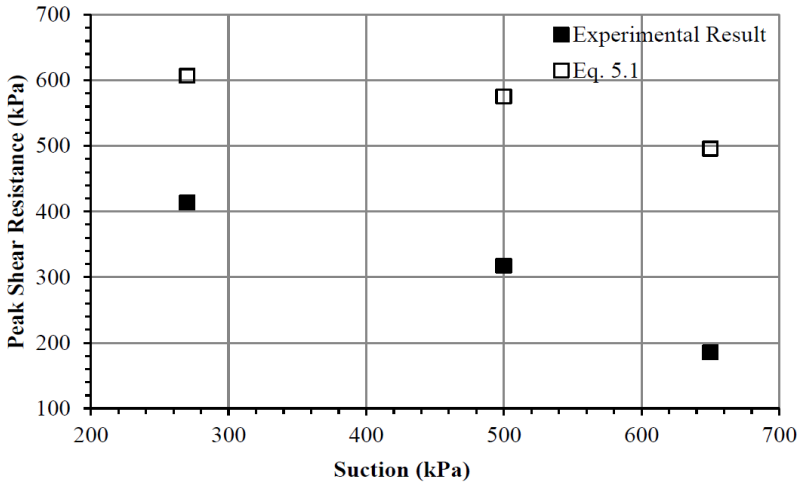

Figure 5.5: Evaluation of Eq. 5.1 against Boso (2005) work.

5.2.5 Comparison with Likos et al. (2010)

Likos et al. (2010) conducted direct shear tests at three low normal stresses (denoted as A, B and C in Table 5.6 and in Fig. 5.6) using the HCT. The shear strength parameters values of the soil, $c^{'}$ and $\phi^{'}$, were 0 kPa and 40.1^{o}, respectively. Table 5.6 shows the parameters obtained from the Likos et al. (2010) study. Reasonable fits were obtained for series A, however not for series B and C.

Table 5.6: Evaluation of Eq. 5.1 against Likos et al. (2010).

	σ kPa	s kPa	S_r%	sS_r kPa	τ_f kPa	τ kPa Eq. 5.1
A	0.30	1.12	97	1.0864	4	1.16
	0.37	2.09	84	1.7556	5.01	1.78
	0.34	2.72	80	2.176	4.96	2.12
	0.32	5.11	60	3.066	5	2.85
	0.32	7.85	48	3.768	4.73	3.44
B	1.93	1.12	94	1.0528	5.5	2.51
	1.91	2.7	84	2.268	7.57	3.52
	1.89	5.11	31	1.5841	6.53	2.92
	1.87	7.8	18	1.404	6.95	2.75
C	9.13	1.12	93	1.0416	11.26	8.56
	9.14	2.1	86	1.806	16.91	9.22
	9.12	2.7	77	2.079	17.67	9.43
	9.11	5.11	41	2.0951	12.44	9.43
	9.1	7.8	24	1.872	10.07	9.24

5.2.6 Comparison with current work

The experimental direct shear work in this study was conducted at normal stresses of 50, 100 and 200 kPa and a range of applied suctions (at peak) between 0 to 5.5 kPa. The evaluation is shown in Figs. 5.7a, b and c. For the experimental results shown in Figs. 5.7a, b and c, each value of shear resistance at the same suction is the average of three conducted tests. Based on the experimental results of the shear strength parameters for the dry soil showed

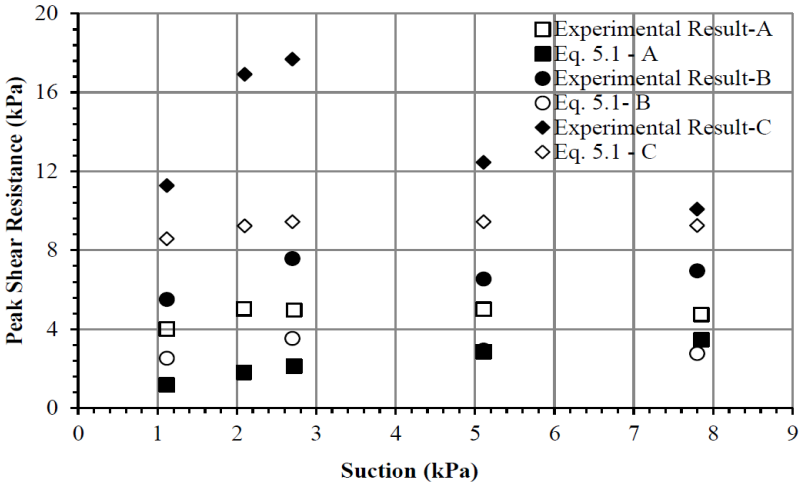

Figure 5.6: Evaluation of Eq. 5.1 against Likos et al. (2010) work.

previously in Table 4.1, two pairs of (c, ϕ): (12.43 kPa, 39.15^o) and (13.45 kPa, 44.1^o) are used in Eq. 5.1.

The results of shear resistance for both the peak and Eq. 5.1 are obtained according to measured suctions (s^*) and calculated degree of saturation (S_r^*) at the peak. This provides the advantage of taking the scanning path of the SWCC and void dependency into consideration. For these tests, u_a = 0 kPa since the soil is exposed to the atmosphere. As it is clear from Figs. 5.7a, b and c, the difference between the experimental and calculated shear resistance is large for the three conducted normal stresses.

The variation of the (sS_r) term for the sand used in this study is minor due to the small capillarity of the soil (from 0 to 6 kPa - see Fig. 4.1) and, therefore, the effect of the (sS_r) term in Eq. 5.1 on the shear resistance for the sand used is marginal. In other words, at s = 2 kPa (S_r = 88.9 - 91.5%), the additional shear resistance which can be provided by the term $sS_r \tan\phi$ using $\phi = 44.1^o$ is small (1.72 - 1.77 kPa). At a higher suction of 6 kPa ($S_r \approx 15 - 22\%$), the additional shear resistance giving by $sS_r \tan\phi$ is ranges between (0.87 - 1.28 kPa). Although the term $(\sigma - u_a)$ is more dominant than the (sS_r) term, Eq. 5.1 shows poor agreement.

To summarize, the preceding sections evaluated Eq. 5.1 for different types of soils (sand, silt and clay) and at a wide range of suctions. The evaluations generally showed poor agreement. Reformulation to Eq. 5.1 is; therefore, proposed and presented in the next section. The equation is then evaluated against the direct shear results conducted in the current work.

5.3 Reformulation and evaluation of the Öberg & Sällfors (1997) equation for unsaturated sand

5.3.1 Modelling of strength and suction

Stanier & Tarantino (2010) used the Öberg & Sällfors (1997) equation to propose an equation for compacted aggregated soils in partially saturated conditions as follows:

$$\tau = (\sigma + s\ S_r) \tan\phi' \tag{5.4}$$

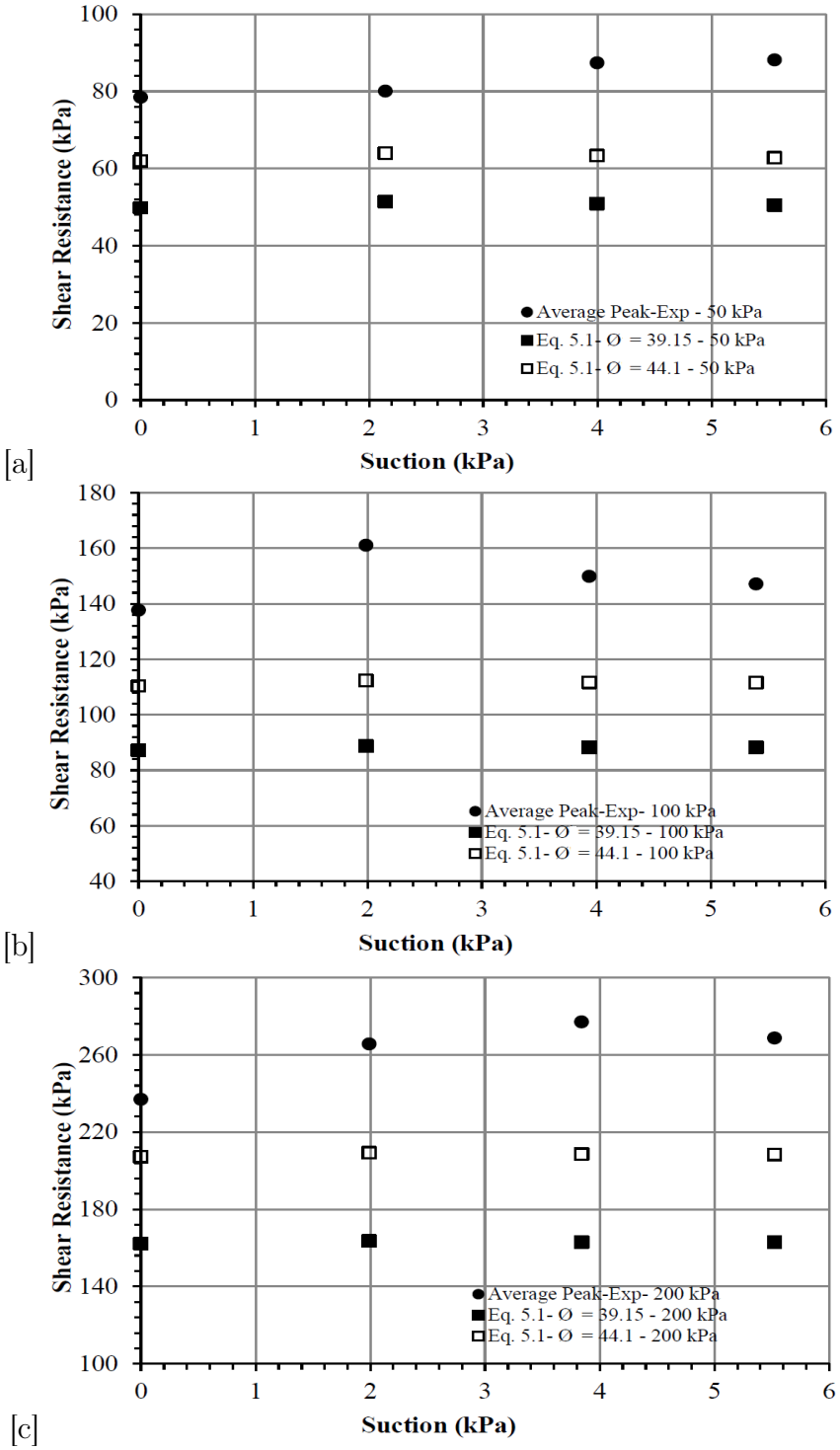

Figure 5.7: Evaluation of Eq. 5.1 against the current work for two different $\phi^{'}$ values at (a) σ = 50 kPa (b) σ = 100 kPa (c) σ = 200 kPa.

where s is the hydrostatic suction (kN/m^2), S_r is the degree of saturation (they assumed to be equal to effective degree of saturation S_{re} due to the simplicity). Equation 5.4 is exactly same as the Öberg & Sällfors (1997) equation (see Eq. 5.1), without the cohesion term $c^{'}$ and u_w being replaced by s. The second term in the brackets in Eq. 5.4 represents the effect of water pressure (suction) while also allowing for the reduced effective area of action due to the reduction of water content. A linear relationship with S_r is assumed here. Stanier

& Tarantino (2010) proposed equations for suction, degree of saturation and unit weight for unsaturated soil as follows:

$$s = \gamma_w \ (H_w - z) \tag{5.5}$$

$$S_r = e^{-as} \tag{5.6}$$

$$\gamma \ = \rho_{dry} + (\rho_{sat} - \rho_{dry}) \ S_r \tag{5.7}$$

where γ_w is unit weight of water (kN/m^3), H_w is water table depth (positive downward) (m), z is vertical coordinate (positive downward), e is exponential constant (2.718), a is fitting parameter (kPa^{-1}), γ is unit weight of the soil (kN/m^3), ρ_{dry} is dry unit weight of the soil (kN/m^3) and ρ_{sat} is saturated unit weight of the soil (kN/m^3). Equation 5.5 assumes full water continuity within the soil.

It is proposed that the preceding equations may be used to represent the unsaturated behaviour of fine sand. Implicit in this is the assumption that the water distribution is continuous, dominated by gravimetric effects and unaffected by deformation. Following Shwan & Smith (2014) (full paper is presented in Appendix C), additional variations of Eqs. 5.4 and 5.6 are proposed which allow more flexible modelling of the unsaturated conditions as follows:

$$\tau = (\sigma + s \ S_r^{\beta}) \tan \phi \tag{5.8}$$

where β is a fitting parameter and

$$S_r = 1.0 \ldots\ldots\ldots\ldots\ldots\ldots\ldots\ldots\ldots \ s \leq s_o \tag{5.9}$$

$$S_r = e^{-a(s-s_o)} \ldots\ldots\ldots\ldots\ldots\ldots\ldots\ldots \ s > s_o \tag{5.10}$$

where s_o (kPa) is the air entry value of the soil and it is related to the depth of capillary rise (full saturation) H_c as follows:

$$H_c = H_w + \frac{s_o}{\gamma_w} \tag{5.11}$$

The data of the SWCC for the sand test (Fig. 4.1) is fitted to Eqs. 5.9 and 5.10 and plotted in Fig. 5.8 (and also in Fig. 5.9a). It can be seen that a reasonable fit to the data is obtained over the range of suctions 0 - 5 kPa using a value of $s_o = 2.3$ kPa and $a = 0.7$.

5.3.1.1 Reformulation of shear strength equation based on the current experimental parameters

In light of the experimental direct shear results conducted in this study, further reformulations to Eq. 5.8 are proposed. The reformulations are based on the experimental behaviours observed for the sand used in which internal friction angle and cohesion increased (explained in details in Section 4.7). Hence, further variations to the equation are applied as follows:

$$\tau = f(c^*, s^*, S_r^*, \phi^*, \beta) \tag{5.12}$$

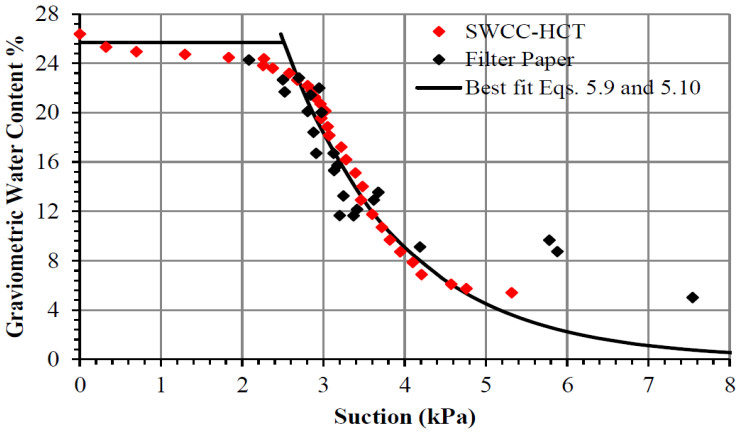

Figure 5.8: SWCC for model sand fit using Eqs. 5.9 and 5.10.

where c^* is cohesion at peak and it is given by Eq. 5.13, s^* is the suction measured at peak, S_r^* is the degree of saturation at peak and ϕ^* is the internal friction angle at peak. In Chapter 4, the symbols c and ϕ were used for saturated and unsaturated samples for the direct shear results, rather than c^* and ϕ^* to avoid confusion. In Chapter 4, the symbols c and ϕ were used for saturated and unsaturated samples for the direct shear results, rather than c and ? to avoid confusion. For the rest of this thesis, however, c^* and ϕ^* will be used to represent cohesion and internal friction angle at the peak strength condition for the saturated and unsaturated samples (or parameters at the state under conditions, i.e. at the critical state or oscillation). The value of c^* is given by:

$$c^* = c + \hat{c} \tag{5.13}$$

where c is soil cohesion in (kPa) (at fully dry condition) and $\hat{c}$ is the amount of increase in cohesion due to the saturated or unsaturated condition (kPa). The values of s^* and S_r^* can be determined by observing the water level in the burette and using weight-volume relationships, respectively (explained in Section 4.9). By combining Eqs. 5.12 and 5.13 in Eq. 5.8, the following can be obtained:

$$\tau = c^* + [(\sigma + s^* \ S_r^{*\ \beta})] \tan \phi^* \tag{5.14}$$

Equation 5.14 represents a simple formula for unsaturated sand and it is valid for all the cases (e.g. dry, fully and unsaturated conditions). Essentially the equation is acknowledging that for any given suction, the sand obeys a Mohr-Coulomb friction law, but that the Mohr-Coulomb friction parameters c and ϕ are strong functions of the suction/water content level.

5.3.2 Comparison of the reformulated SWCC equations with the experimental data

The reformulated SWCC equations (Eqs. 5.9 and 5.10) were compared using a wide range of suctions and different types of soils. Table 5.7 shows the derived parameters used in the SWCC equations. Figures 5.9a and b show the comparison in which the data fitted well with the SWCC equations for the most soils until the residual suction. The most important advantages of the reformulated SWCC equations compared to the Fredlund & Xing (1994) equation (see Eq. 4.1) is that it is easy to integrate and need only two single parameters: a and s_o, while the Fredlund & Xing (1994) equation needs five parameters (see Table 4.2).

Table 5.7: Parameters in the modified SWCC equations.

Soil Type	s_o (kPa)	parameter a (kPa^{-1})
Sand-Fredlund & Xing (1994)	0.4	0.83
Fraction D-This study	2.3	0.70
Pyroclastic silty sand-Stanier & Tarantino (2010)	3.25	0.20
Sandy soil- Krishnapillai & Ravichandran (2012)	5	0.10
Silt Loam-Krishnapillai & Ravichandran (2012)	7	0.01
Madrid clay sand-Krishnapillai & Ravichandran (2012)	17	0.0033
UPC[1]-Axis translation-Tarantino et al. (2011)	130	0.0040
EPFL[1]-Pressure plate-Tarantino et al. (2011)	150	0.0010

1 soil used: 70% sand, 20% active clay and 10% non-active clay.

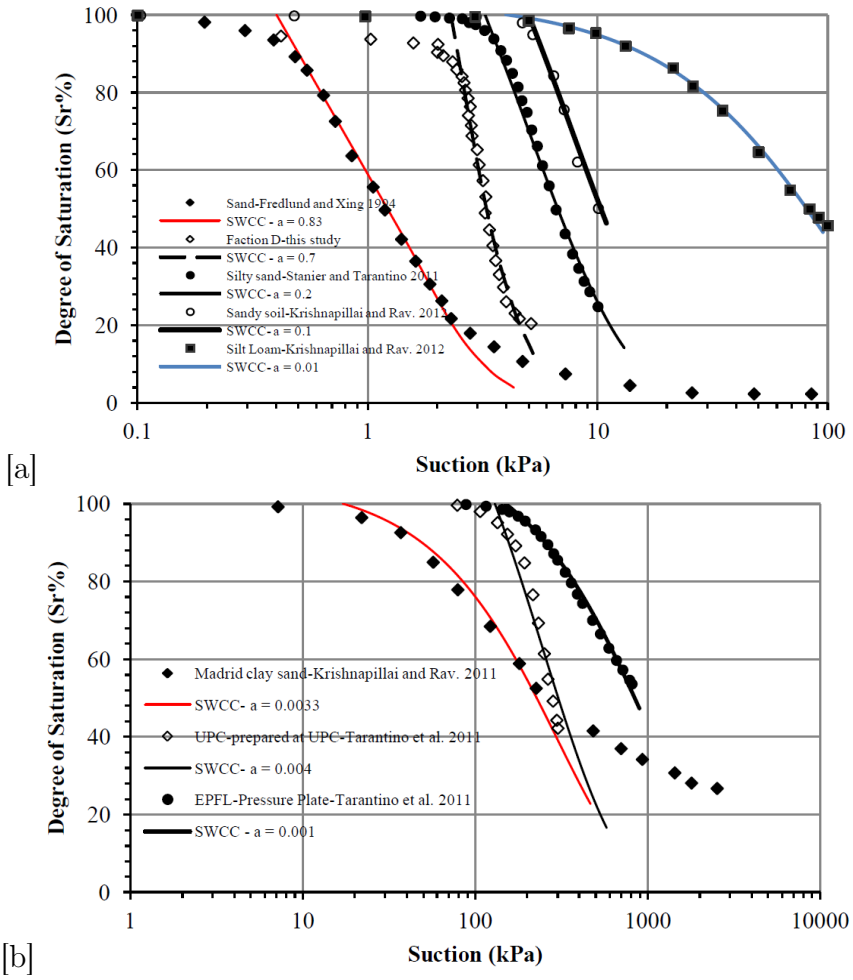

Figure 5.9: Comparison of the formulated SWCC equations with the experimental data over a range of the suction values (typically from fully saturated to the residual suction).

5.3.3 Evaluation of the reformulated shear strength equation against experimental results for dry sand at peak

A series of direct shear tests on dry soil were conducted using the same modified direct shear box which was used for the unsaturated samples (e.g. see Fig. 4.3). Figure 5.10 shows the average peak data for three tests conducted at three normal stresses: 50, 100 and 200 kPa showing error bars. The regression line was obtained using the least square method. In the

evaluation, $\phi = 39.15^o$ and $c = 12.43$ kPa were used. The experimental data were, then, evaluated as shown in Fig. 5.10 using Eq. 5.14 for the dry case.

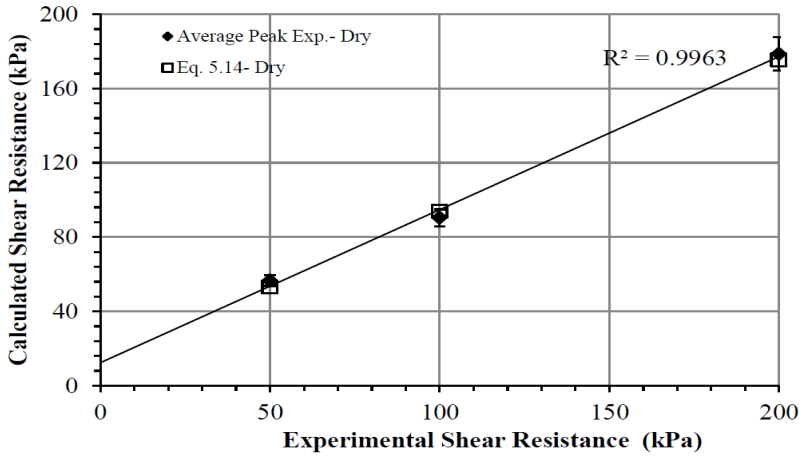

Figure 5.10: Evaluation of Eq. 5.14 against the experimental results for the dry sand at peak used in this study.

5.3.4 Evaluation of the reformulated shear strength equation against the experimental results for fully saturated and unsaturated conditions at peak

Figures 5.11a, b, c and d show the evaluation of Eq. 5.14 against the average experimental shear resistance at peak for the three normal stresses for fully saturated and unsaturated soils showing error bars for the repeat tests. Table 5.8, presented previously in Chapter 4 -Table 4.7, shows the variation of ϕ^* and c^* at peak for the dry, fully saturated and unsaturated cases which were used in the evaluation. The figures also show evaluation against Eq. 5.1 in which for Eq. 5.1 the average dry shear strength parameters shown in Table 5.8 were used and the results showed poor agreement. No attempt was carried to use the pair ($c = 13.45$ kPa, $\phi = 44.1^o$) in Eq. 5.1 as the higher values of ϕ^* and c^* ($\phi^* = 46.56^o$ and $c^* = 27.79$ kPa) already underestimated the experimental data (see Subsection 5.3.6 - Fig. 5.13a). For

Table 5.8: Variations of internal friction angle and cohesion at peak at different saturation conditions.

Case	s kPa	Average ϕ^* degrees	c^* kPa
Dry	—	$\phi = 39.15$	$c = 12.431$
Fully saturated	0	46.56	28.86
Unsaturated	2	51.04	27.79
	4	51.66	23.77
	6	50.27	27.34

Eq. 5.14, $\beta = 1$ was used. Equation 5.14 fitted well to the straight lines for the different suction profiles.

Figures 5.12a, b, c and d show the evaluation of Eqs. 5.14 and 5.1 in which the y-axis represents the average shear resistance and the x-axis represents the average applied suction at peak. The parameter $\beta = 1$ was used in the evaluation. The average ϕ^* and c^* values

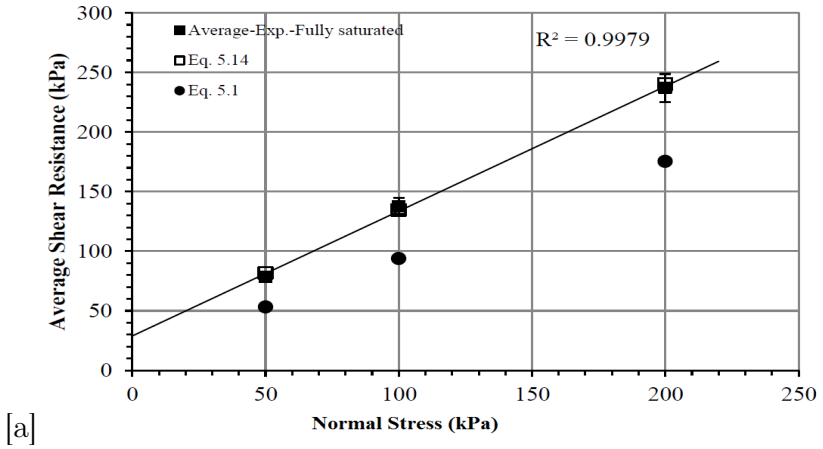

[a]

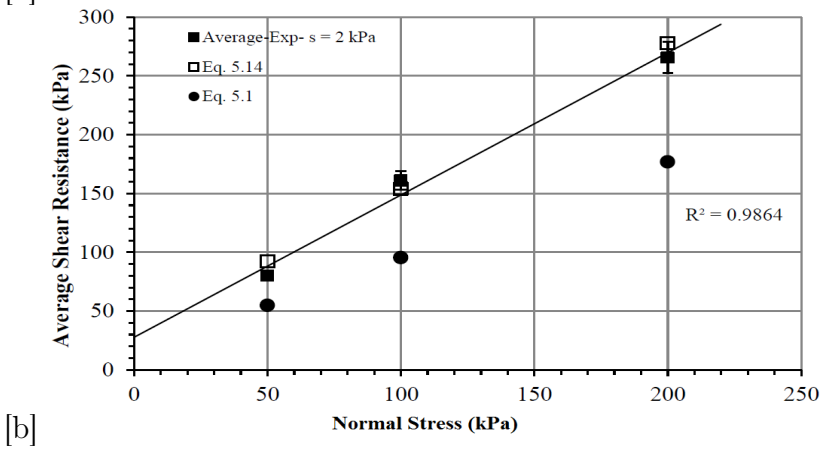

[b]

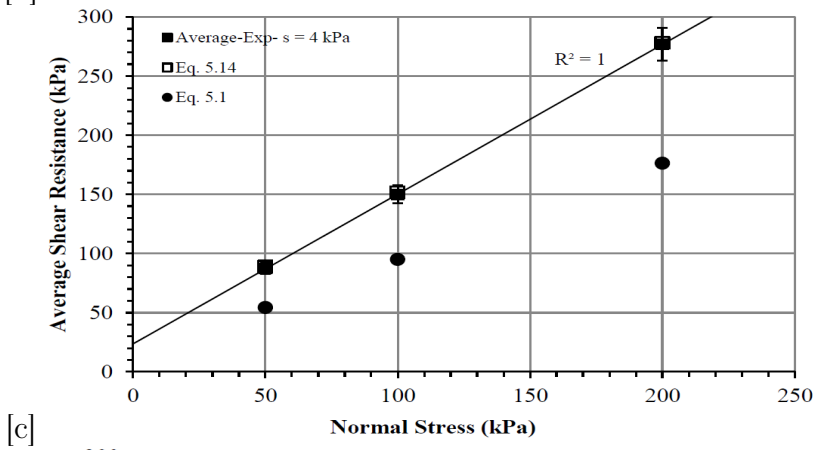

[c]

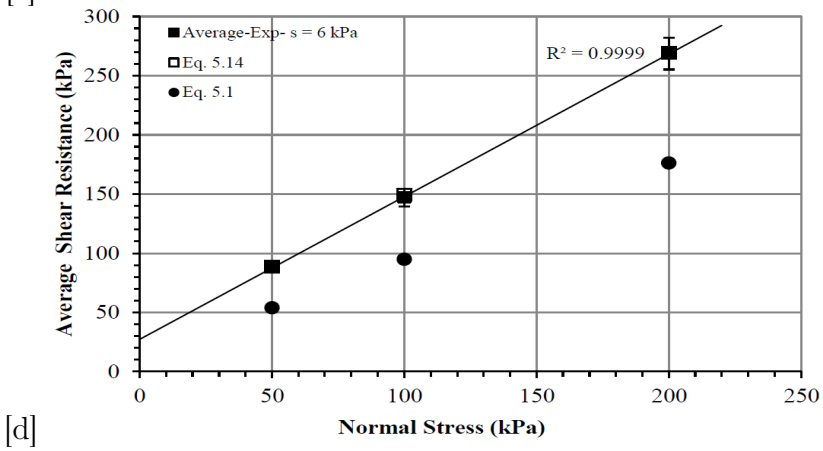

[d]

Figure 5.11: Evaluation of Eqs. 5.14 and 5.1 at different normal stresses at peak for (a) fully saturated case ($s = 0$ kPa) (b) $s = 2$ kPa (c) $s = 4$ kPa (d) $s = 6$ kPa.

shown in Table 5.8 were used for each suction. Equation 5.14 showed good agreement for the data except at $s = 2$ kPa for $\sigma = 50$ kPa.

5.3.5 Effect of the $s^*S_r^*$ term at peak on the shear strength of the unsaturated sand

Table 5.9 shows the small effect of term $(s^*S_r^*)$ on the shear resistance at peak of the unsaturated sand used. In Table 5.9, the 5^{th} column was determined by excluding the term $(s^*S_r^*)$ from Eq. 5.14 where s^* and S_r^* are the average peak values. The values of s^* at peak were obtained by capturing images for the water level in the burette (burette No.2- see Fig. 3.11a at different stages of the test and selecting the corresponding image at the peak), while S_r^* was calculated by knowing the amount of water expelled or imbibed by the sample at the peak. Here the volume of the sample and void ratio were calculated using the vertical LVDT reading at the peak. The values of c^* and ϕ^* shown in Table 5.8 at different suctions were used to calculated the shear resistance in columns 4 and 5 in Table 5.9. Table 5.9 shows how the shear resistance of the sand is significantly dominated by σ and the shear strength parameters c^* and ϕ^* but not the term $s^*S_r^*$.

Table 5.9: Effect of term $s^*S_r^*$ on the shear resistance at peak for sand used in this study.

σ kPa	s^* kPa	$S_r^*\%$	Eq. 5.14 with term $s^*S_r^*$ kPa	Eq. 5.14 without term $s^*S_r^*$ kPa
50	0	100	81.66	81.66
50	**2.14**	**98**	**92.22**	**89.62**
50	4	36	88.85	87
50	5.55	16	88.62	87.50
100	0	100	134.47	134.47
100	1.98	100	153.91	151.45
100	3.94	34	151.90	150.21
100	5.39	22	149.10	147.66
200	0	100	240.06	240.06
200	1.99	100	277.58	275.12
200	3.84	31	278.18	276.65
200	5.52	19	269.28	267.98

5.3.6 Effect of ϕ^* at peak on the shear strength of the unsaturated sand

Figures 5.13a, b and c show the effect of the internal friction angle at peak on the shear resistance for the unsaturated sand in which the dry and saturated internal friction angle values: 44.1^o and 46.56^o were used, respectively as well as the other values of the internal friction angle and cohesion for the unsaturated samples (see Table 5.8). It is clear that the shear resistance for the unsaturated sand is significantly affected by the internal friction angle. No attempt was carried out for the analyses shown in this section and Subsection 5.3.7 to use the pair ($c = 12.43$ kPa, $\phi = 39.15^o$) as the higher values of $c^* = 27.79$ kPa and $\phi^* = 46.56^o$ (see Fig. 5.13a) were already underestimated.

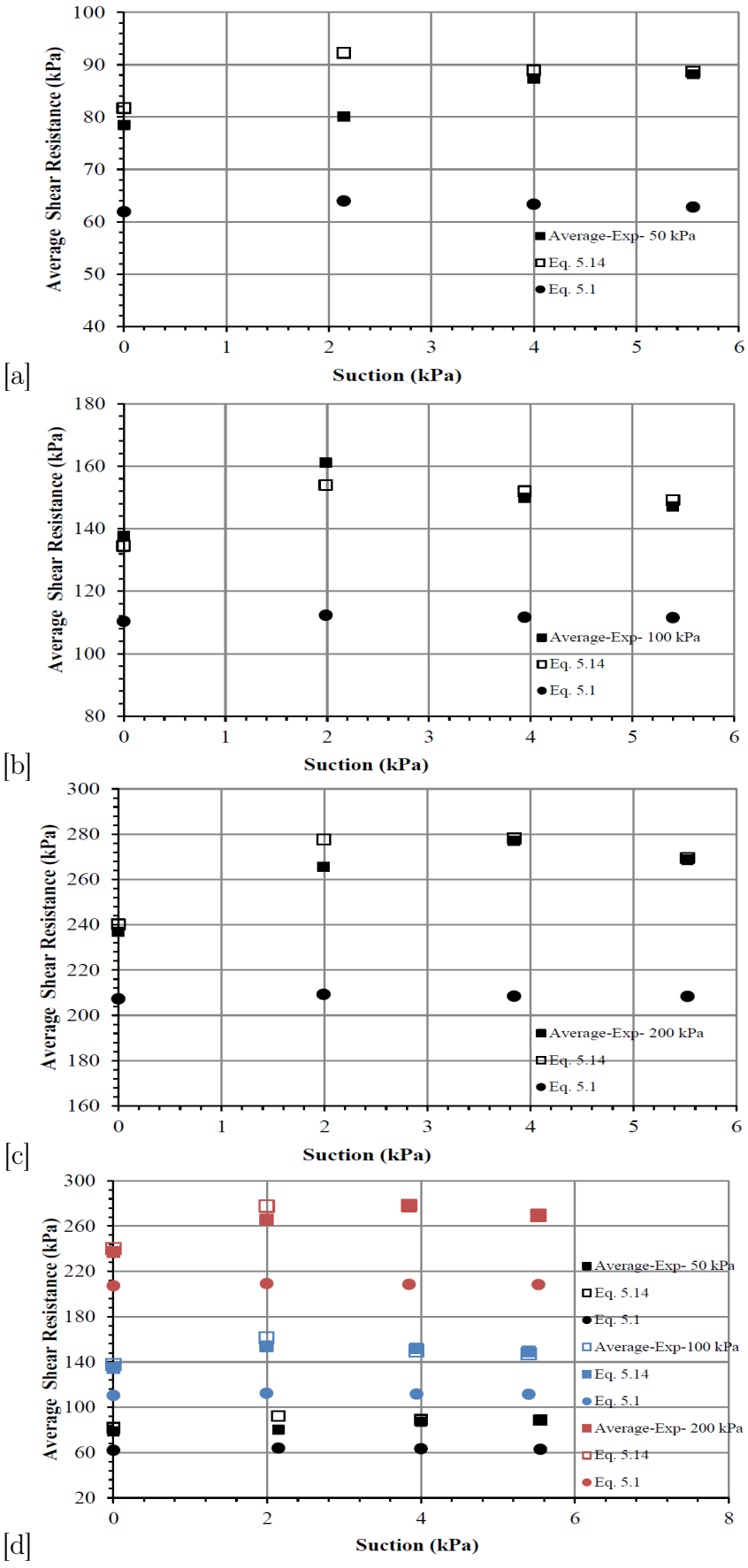

Figure 5.12: Evaluation for Eqs. 5.14 and 5.1 against the average experimental direct shear results at peak over a range of the applied suctions ($\beta = 1$) (a) $\sigma = 50$ kPa (b) $\sigma = 100$ kPa (c) $\sigma = 200$ kPa (d) all normal stresses σ.

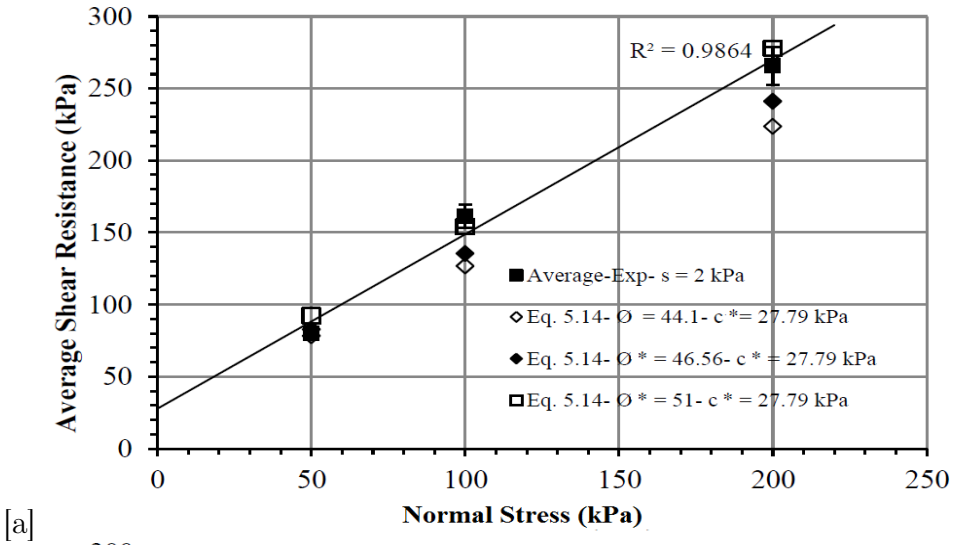

[a]

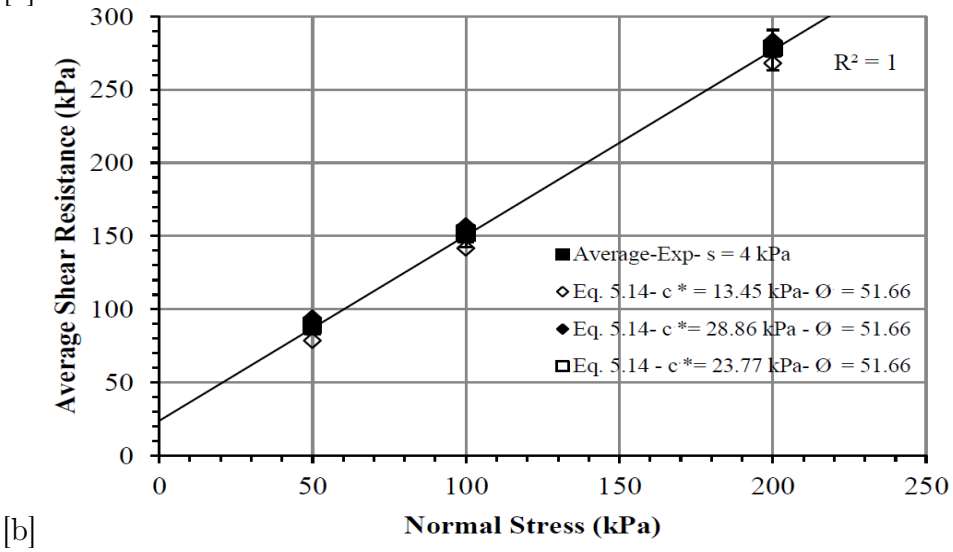

[b]

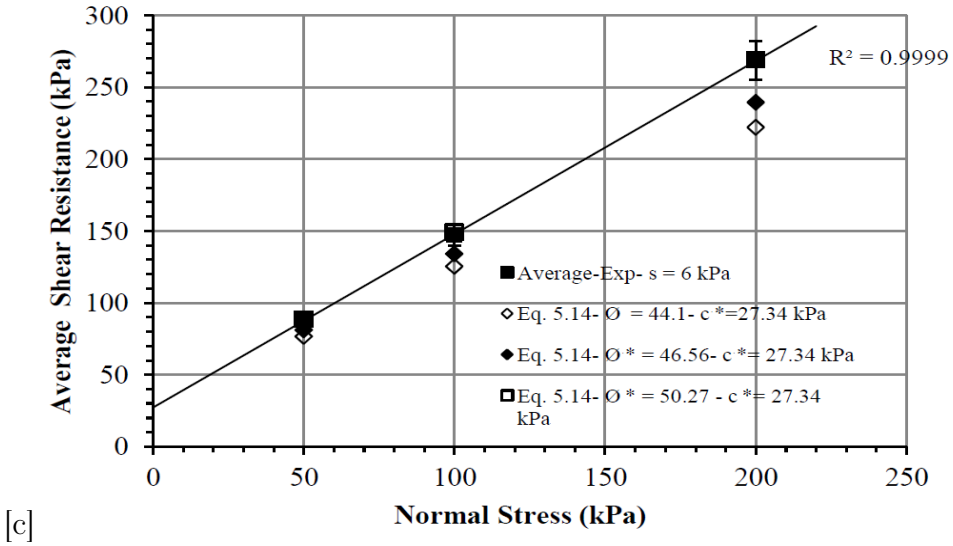

[c]

Figure 5.13: Effect of ϕ^* at peak on shear resistance of the unsaturated sand at constant c^* for (a) $s = 2$ kPa (b) $s = 4$ kPa (c) $s = 6$ kPa.

5.3.7 Effect of c^* value at peak on the shear strength of the unsaturated sand

Figures 5.14a, b and c shows the effect of c^* at peak on shear strength of the unsaturated sand. Three different cohesion values, see Table 5.8, were used according to the sample's condition (e.g. dry, saturated and unsaturated case), except for the dry case where the higher value 13.45 kPa was used. The internal friction values for the unsaturated samples shown in Table 5.8 were used. Unlike the effect of ϕ^*, the influence of c^* is less than that of the internal friction angle on the shear resistance.

5.3.8 Evaluation of the reformulated shear strength equation against the experimental results for fully saturated and unsaturated conditions at critical state

In this section, Eq. 5.14 is evaluated against the experimental results at critical state as well as the effect of the parameter β is investigated. Figures 5.15a, b and c show the shear resistance at critical state versus suction for three applied normal stresses: 50, 100 and 200 kPa using different β values. As before, the average values of the shear resistance of the three repeat tests at the same s and σ are used as well as the average cohesion and internal friction angle at critical state.

Once again, Eq. 5.14 shows good agreement with the experimental data except at $s = 2$ kPa - $\sigma = 50$ kPa. The high values of the shear resistance for the fully saturated case are attributed to the fact that most of the unsaturated samples at critical state showed a lower shear resistance than the saturated samples (e.g. see Figs. 4.3b and c). Here values of the shear resistance at critical state were selected at the end of the test. For cases when the oscillation happened at the end of the test, the value before the last oscillation was selected. For the unsaturated samples, the data are fitted using polynomial regression. In Figs. 5.15a, b and c for $\beta = 1$, the effect of the parameter β eliminated since it is a power of the degree of saturation (see Eq. 5.14), while any value of β less than one accentuates increasing S_r and vice versa. The importance of the parameter β can be observed more significantly for clay soils when a high range of suctions is applied. However, it is clear in Figs. 5.15a, b and c that the effect of β is small due to the small capillarity of the sand used and the small applied suctions as discussed previously. Therefore, the value of the parameter β in Eq. 5.14 was taken as unity in the numerical analysis presented in Chapter 6

.

5.4 Summary of the chapter

This chapter addressed the evaluation of an existing shear strength equation (Eq. 5.1) for unsaturated soils. The evaluation showed poor agreement with the experimental results. Following the evaluation, the equation was reformulated based on the experimental behaviours observed in the direct shear tests conducted in this study and incorporated the increase of the shear strength parameters. Also an existing degree of saturation equation, proposed by Stanier & Tarantino (2010), was reformulated to take into account the effect of air entry value.

The reformulated shear strength equation (Eq. 5.14) was evaluated using data of the direct shear tests conducted in this study. This was performed by using different values of

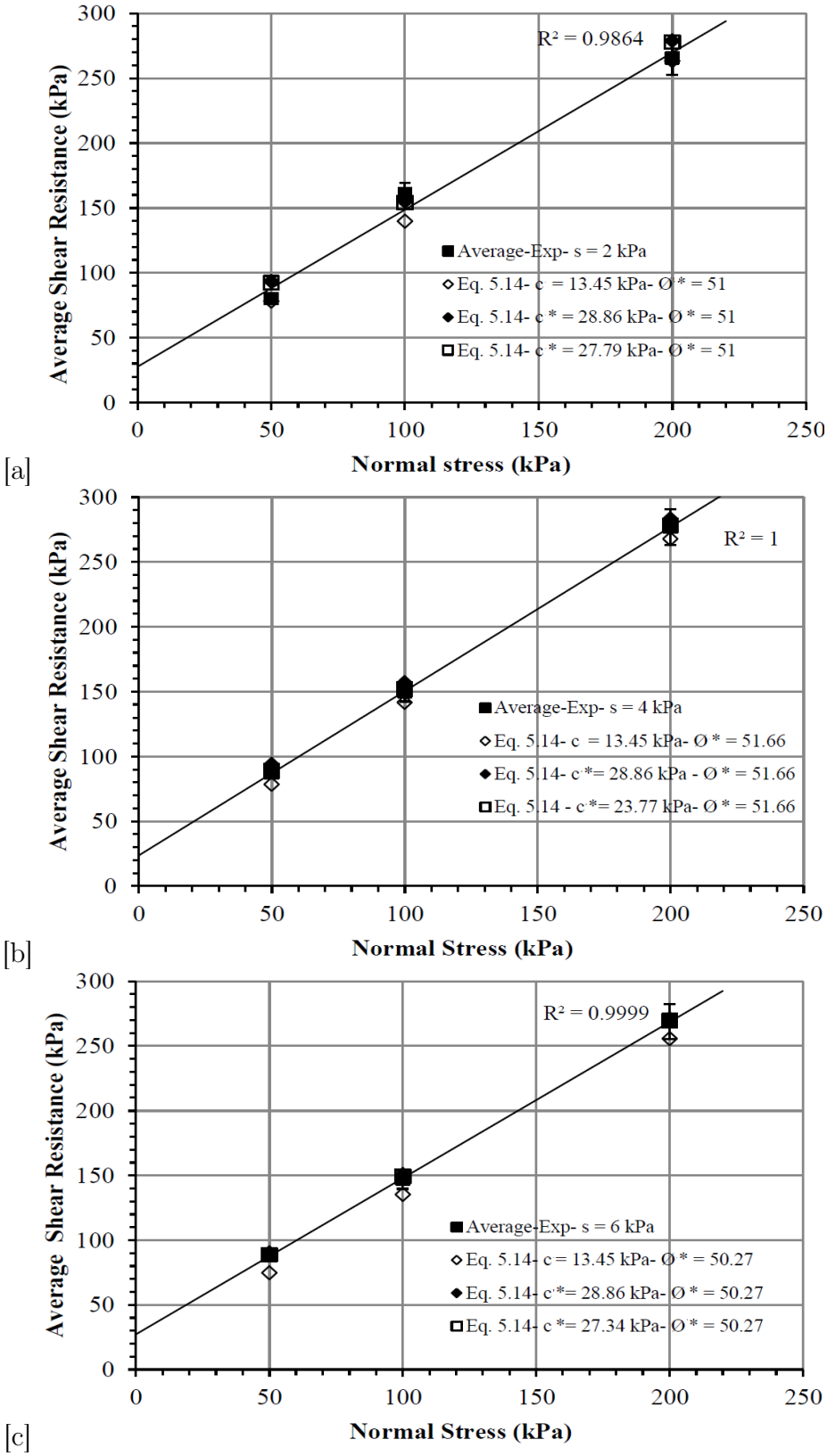

Figure 5.14: Effect of c^* at peak on shear resistance of the unsaturated sand at constant ϕ^* for (a) $s = 2$ kPa (b) $s = 4$ kPa (c) $s = 6$ kPa.

the internal friction angle and cohesion obtained for the dry, fully saturated and unsaturated cases at both peak and critical state. The evaluation of the reformulated equation fitted close

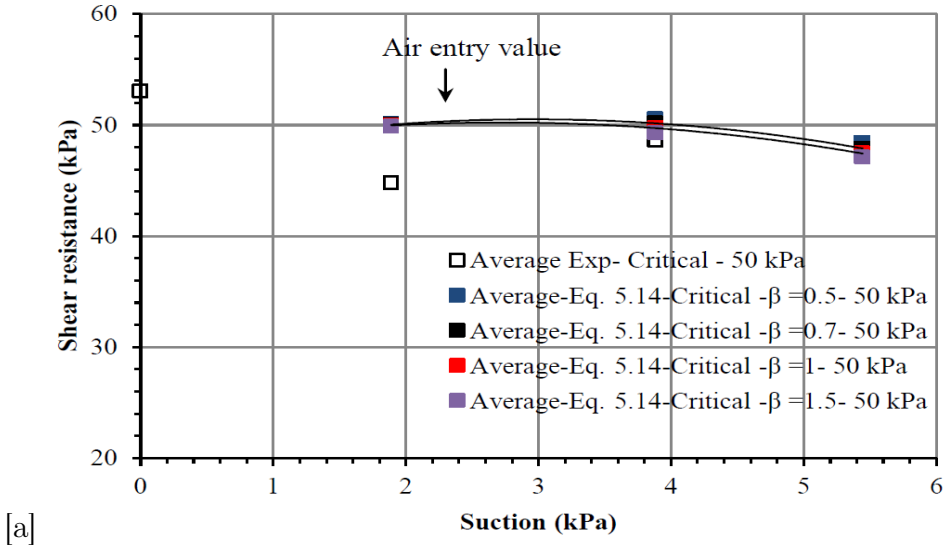

[a]

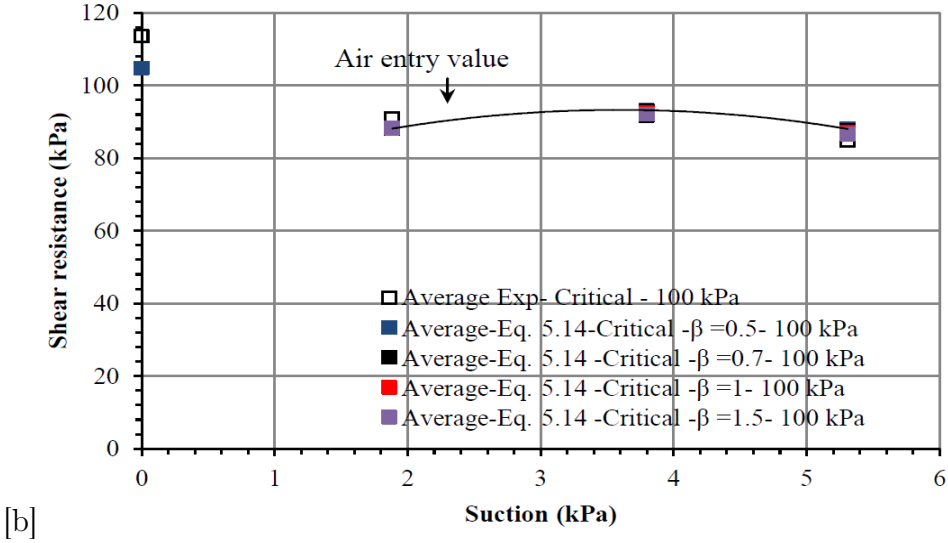

[b]

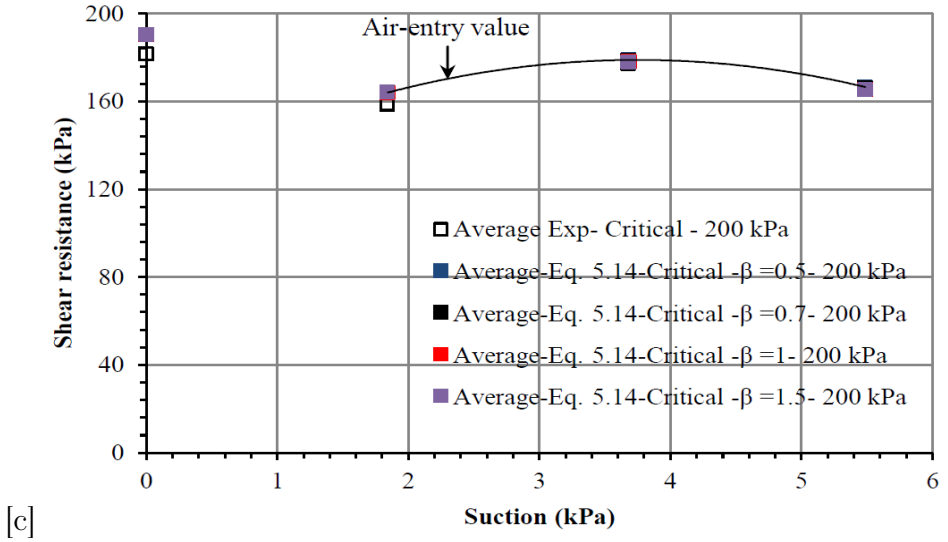

[c]

Figure 5.15: Evaluation of Eq. 5.14 at critical state with different β values for (a) $\sigma = 50$ kPa (b) $\sigma = 100$ kPa (c) $\sigma = 200$ kPa.

to the straight lines of the experimental data for different suctions, but it was necessary to separately measure ϕ^* and c^*. Prediction of these values themselves will be discussed in

Chapter 7. The effect of the increase of the internal friction angle and cohesion on the shear strength was also examined individually in this chapter. The examination showed that the effect of ϕ^* was more dominant on the shear strength than the effect of the c^*. The mutual effect of the $(s^* S_r^*)$ term exhibited an insignificant influence on the shear strength for the unsaturated samples. Also, the parameter β showed a small effect on strength for the saturated and unsaturated cases. Overall it is shown that the key effect of partial saturation on the tested sand is on the values of c^* and ϕ^*.

Following the evaluation of the reformulated shear strength equation, the next chapter addresses incorporation of the reformulated equations (Eqs. 5.9, 5.10 and 5.14) into the DLO procedure and use of the modified DLO method to conduct parametric studies on retaining wall and bearing capacity problems.

Chapter 6

Numerical Modelling

6.1 Introduction

This chapter addresses the extension of DLO to handle unsaturated conditions. This requires the derivation of unsaturated shear strength and self strip weight equations at different water table positions and slip line failure angles. Following the derivation, the equations are incorporated into an existing DLO Matlab code. The modified code, termed UNSAT-DLO, is then evaluated using a retaining wall case study. The code was then incorporated into a research version of the LimitState:GEO software and used to conduct parametric studies for earth pressure and bearing capacity problems.

A parametric study of passive earth pressure is carried out investigating the effect of the degree of saturation (by utilising different positions of the water table), the effect of the internal friction angle and the wall friction. The results are compared with a closed form version of the passive earth pressure equation using the Rankine method which was modified to take into account the effect of capillary rise.

A comparative study of the modified LimitState:GEO version against the experimental results of the bearing capacity test is presented studying the effect of the suction and degree of saturation on the strength for both surface and buried strip footings. The drying behaviour due to the applied load which was observed in the experimental bearing capacity tests was not investigated due to the complexity of interpreting such phenomenon using the conventional soil mechanics principles.

6.2 Incorporation of the unsaturated yield condition into DLO

The unsaturated yield equations discussed previously in Section 5.3 can be applied to the numerical DLO procedure. In order to compute the value of U in Eq. 2.40 for use in the DLO formulation in unsaturated soil, the following integration is required:

$$U_i = -\int_0^L s\ S_r^{\beta}.dl \tag{6.1}$$

where L and dl are defined in Fig. 2.28. However rather than using U directly in the DLO equations it will be used to compute an apparent cohesion $\hat{C} = U_i\ \tan\phi'$ to be used in the strength equations.

6.3 Integration of apparent cohesion force and strip weight equations

Shear forces developed along a discontinuity have a direct effect on the stability of the soil. Figure 6.1 shows the shear forces and strip weight above a discontinuity. The increase of strength, which will be termed "apparent cohesion" throughout this study, develops due to suction forces. In this study, the discontinuity was divided into three categories according

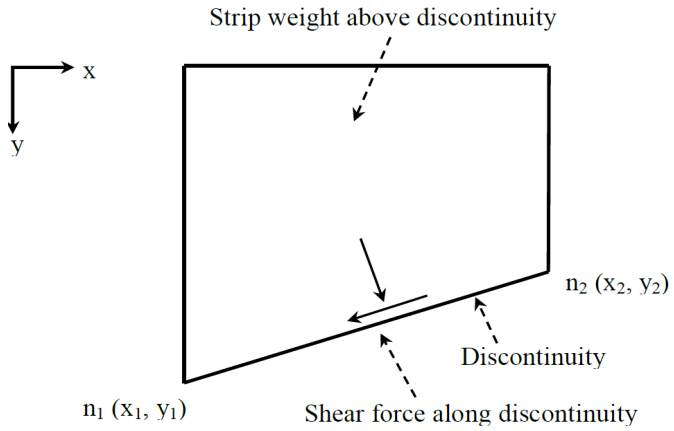

Figure 6.1: Shear force and strip weight for a block of soil.

to its inclination: inclined failure line ($\theta \neq 0$ and $\theta \neq 90$), horizontal failure line ($\theta = 0$) and vertical failure line ($\theta = 90$), where θ is the angle of discontinuity to the horizontal (see Fig. 6.2b). This is because for $\theta = 0$, a general equation of the apparent cohesion force (see Eq. 6.11) is divided by sin θ and this leads to infinity at $\theta = 0$. While for a case when the discontinuity happens at an angle of 90^o, sin θ is eliminated from the apparent cohesion equation and the strip weight above the discontinuity in this case is equal to zero.

6.3.1 Integration of apparent cohesion force equations along the discontinuity

To study all possible cases of the water table locations and the inclination angles, several sets of equations are integrated. First; equations for a case of a discontinuity fully above the water table. Second; equations for a discontinuity locates below the water table. Finally; equations when a discontinuity crosses the water table as shown in Fig. 6.2a.

6.3.1.1 Integration of apparent cohesion force equation along the discontinuity for $\theta \neq 0$ and $\neq 90$

1. When $y_1 \geq Y_w$, $y_2 > Y_w$:
   Redefining Eq. 5.5, showed previously in Chapter 5, in an (x, y) coordinate system where y is measured positive upwards from the domain base and the water table is a height Y_w above the origin, and the soil surface at y_{max} gives:

$$z = y_{max} - y = Y_w + H_w - y \tag{6.2}$$

   or

$$z - H_w = Y_w - y \tag{6.3}$$

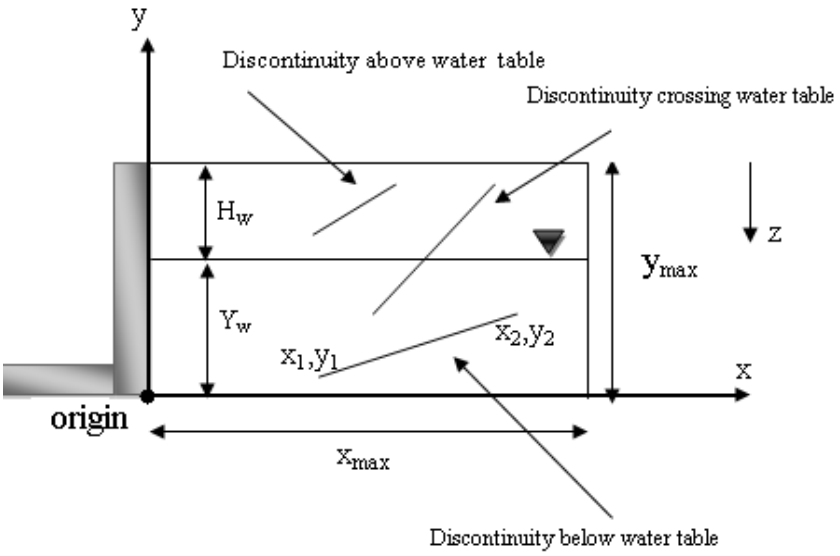

[a]

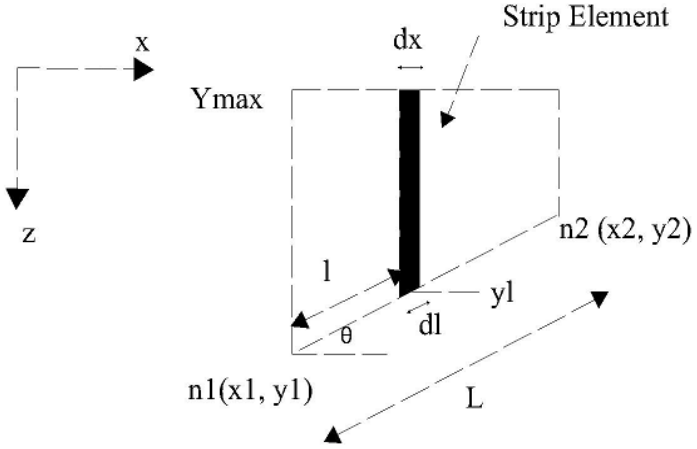

[b]

Figure 6.2: (a) Defining discontinuity for all possible cases (b) Strip weight above the discontinuity showing nodes and a strip element.

Hence:

$$S_r = e^{a\gamma_w(Y_w - y)} \tag{6.4}$$

$$s = -u_w = \gamma_w(y - Y_w) \tag{6.5}$$

The apparent cohesion force, when the discontinuity above the water table shown in Fig. 6.2a, can be derived by integrating the second term of Eq. 5.8 as follows:

$$U_i \tan\phi' = \hat{C} = \int_A^B s S_r^\beta \tan\phi' dl = \int_0^L \gamma_w(y - Y_w) e^{a\gamma_w Y_w} e^{-a\gamma_w y} \tan\phi' dl \tag{6.6}$$

where $\hat{C}$ is the apparent cohesion force and $\beta = 1$. Referring to Fig. 6.2b, (y) can be determined as $y = y_1 + l\sin\theta$, where θ is measured anti-clockwise from the horizontal, and l is measured from node (1) ($l_1 = 0$) to node (2) ($l_2 = L$). By substituting (y) in Eq. 6.6 and then integrating, the following can be obtained:

$$\hat{C} = \int_0^L \gamma_w(y_1 + l\sin\theta - Y_w) e^{a\gamma_w Y_w} e^{-a\gamma_w(y_1 + l\sin\theta)} \tan\phi' dl \tag{6.7}$$

$$\hat{C} = \int_0^L \gamma_w (l\sin\theta - (Y_w - y_1)) e^{a\gamma_w (Y_w - y_1)} e^{-a\gamma_w l \sin\theta} \tan\phi' dl \tag{6.8}$$

$$\hat{C} = \gamma_w \tan\phi' e^{a\gamma_w (Y_w - y_1)} \int_0^L (l\sin\theta - (Y_w - y_1)) e^{-a\gamma_w l \sin\theta} dl \tag{6.9}$$

$$\hat{C} = \frac{-\gamma_w \tan\phi' e^{a\gamma_w (Y_w - y_1)}}{(a\gamma_w)^2 \sin\theta} \left[e^{(-a\gamma_w l \sin\theta)} (a\gamma_w (l\sin\theta - (Y_w - y_1)) + 1) \right]_0^L \tag{6.10}$$

By substituting the boundary conditions, the following can be obtained:

$$\hat{C} = \frac{-\tan\phi' e^{a\gamma_w (Y_w - y_1)}}{(a)^2 \gamma_w \sin\theta} \left[e^{(-a\gamma_w L \sin\theta)} (a\gamma_w (L\sin\theta - (Y_w - y_1)) + 1) + (a\gamma_w (Y_w - y_1)) - 1 \right] \tag{6.11}$$

Equation 6.11 gives the apparent cohesion force along the discontinuity above the water table for the case of $\theta \neq \theta$ and $\theta \neq 90$. As the integration procedure is straightforward; therefore, only the final derived equations for the apparent cohesion force for the other cases are presented in this chapter. The full integration procedure for the other cases is shown in Appendix F.

2. When $y_1 < Y_w,\ y_2 \leq\ Y_w$:
   This is a fully saturated case, the discontinuity is fully below the water table. The effect of the degree of saturation (S_r) is eliminated in Eq. 6.6 since $S_r = 100\%$. The final apparent cohesion force equation is given by:

$$\hat{C} = \gamma_w \tan\phi' [\frac{L^2}{2} \sin\theta + L(y_1 - Y_w)] \tag{6.12}$$

3. When $y_1 < Y_w,\ y_2 > Y_w$:
   In this case, the discontinuity crosses the water table. The final form of the apparent cohesion force along the discontinuity is as follows:

$$\hat{C} = \gamma_w \tan\phi' \left[\frac{L_1^2}{2} \sin\theta + L_1\ (y_1 - Y_w) \right] - \frac{\tan\phi'}{(a)^2 \gamma_w \sin(\theta)} \left[(1 + a\gamma_w L_2 \sin(\theta)) e^{-a\gamma_w L_2 \sin(\theta)} - 1 \right] \tag{6.13}$$

where $L_1 = (Y_w - y_1)/\sin\theta$.

6.3.1.2 Integration of apparent cohesion equation along the discontinuity for $\theta = 0$

Two conditions exist for this case where the discontinuity is located above and below the water table.

1. When $(y_1 = y_2) > Y_w$:
   The apparent cohesion force equation for the case of the discontinuity above the water table for $\theta = 0$ is as follows:

$$\hat{C} = \gamma_w (y - Y_w) e^{a\gamma_w (Y_w - y)} \tan\phi' (x_2 - x_1) \tag{6.14}$$

   where $y = y_1 = y_2$.

2. When $(y_1 = y_2) \leq\ Y_w$:
   In this case, the apparent cohesion force equation for the discontinuity below the water table is given by:

$$\hat{C} = \gamma_w (y - Y_w) \tan\phi' (x_2 - x_1) \tag{6.15}$$

6.3.1.3 Integration of apparent cohesion equation along the discontinuity for $\theta = 90$

1. When $y_1 \geq Y_w,\ y_2 > Y_w$:
   The discontinuity is located above the water table and the equation is given by:

$$\hat{C} = -\frac{\tan\phi'}{(a)^2\gamma_w}\left[(1 - a\gamma_w Y_w + a\gamma_w y_2)e^{a\gamma_w(Y_w - y_2)} - (1 - a\gamma_w Y_w + a\gamma_w y_1)e^{a\gamma_w(Y_w - y_1)}\right] \tag{6.16}$$

2. When $y_1 < Y_w,\ y_2 \leq Y_w$:
   This is a saturated case and equation of the apparent cohesion force is given by:

$$\hat{C} = \gamma_w \tan\phi'[(\frac{y_2^2}{2} - Y_w y_2) - (\frac{y_1^2}{2} - Y_w y_1)] \tag{6.17}$$

3. When $y_1 < Y_w,\ y_2 > Y_w$:
   The apparent cohesion force equation for the case when the discontinuity crosses the water table is as follows:

$$\hat{C} = \gamma_w \tan\phi' \left[(\frac{Y_w^2}{2} - Y_w^2) - (\frac{y_1^2}{2} - Y_w y_1)] - \frac{\tan\phi'}{(a)^2 * \gamma_w}[(1 - a\gamma_w Y_w + a\gamma_w y_2)e^{a\gamma_w(Y_w - y_2)} - 1\right] \tag{6.18}$$

6.3.2 Integration of strip weight equations

6.3.2.1 Integration of strip weight equations for $\theta \neq 0$ and $\theta \neq 90$

1. When $y_1 \geq\ Y_w,\ y_2 > Y_w$:
   As for the case of the apparent cohesion integration, the integration procedure for the strip weight equations is given for only one case study and other cases are shown in Appendix G. Referring to Fig. 6.2b, the strip weight equation along the discontinuity can be obtained by double integration of the unit weight. For a non-vertical line, $a = y_1 + l\sin\theta$ and $b = y_{max}$. The integration is as follows:

$$W = \int_0^L \int_a^b (\gamma.dy)dl\cos\theta \tag{6.19}$$

   By substituting Eq. 5.7 in Eq. 6.19 and integrating, the following can be obtained:

$$W = \int_0^L \int_a^b (\rho_d + (\rho_{sat} - \rho_d)S_r).dy.dl\cos\theta \tag{6.20}$$

$$W = \int_0^L \int_a^b (\rho_d + (\rho_{sat} - \rho_d)S_r).dy.dl\cos\theta \tag{6.21}$$

$$W = \int_0^L \left[\rho_d y - \frac{(\rho_{sat} - \rho_d)}{a\gamma_w}e^{a\gamma_w Y_w}e^{-a\gamma_w y}\right]_a^b dl\cos\theta \tag{6.22}$$

$$W = \frac{1}{a\gamma_w}\int_0^L \left[a\gamma_w\rho_d y - (\rho_{sat} - \rho_d)e^{a\gamma_w Y_w}e^{-a\gamma_w y}\right]_{y_1 + l\sin\theta}^{y_{max}} dl\cos\theta \tag{6.23}$$

Substituting the boundary conditions of y gives:

$$W = \frac{1}{a\gamma_w}\int_0^L \left[a\gamma_w\rho_d y_{max} - (\rho_{sat}-\rho_d)e^{a\gamma_w Y_w}e^{-a\gamma_w y_{max}} - a\gamma_w\rho_d(y_1 + l\sin\theta)\right. \quad (6.24)$$
$$\left. + (\rho_{sat}-\rho_d)e^{a\gamma_w(Y_w-y_1)}e^{-a\gamma_w l\sin\theta}\right] dl\cos\theta$$

Integrating with respect to (L), then simplifying the equation gives:

$$W = \frac{1}{a\gamma_w}\left[(a\gamma_w\rho_d y_{max} - (\rho_{sat}-\rho_d)e^{a\gamma_w Y_w}e^{-a\gamma_w y_{max}} - a\gamma_w\rho_d y_1)l\right. \quad (6.25)$$
$$\left. -\frac{a\gamma_w\rho_d\sin\theta}{2}l^2 - \frac{(\rho_{sat}-\rho_d)}{a\gamma_w\sin\theta}e^{a\gamma_w(Y_w-y_1)}e^{-a\gamma_w l\sin\theta}\right]_0^L\cos\theta$$

By substituting the boundary conditions, the strip weight equation for the case when the discontinuity occurs above the water table is given by:

$$W = \frac{1}{a\gamma_w}\left[(a\gamma_w\rho_d(y_{max}-y_1) - (\rho_{sat}-\rho_d)e^{a\gamma_w(Y_w-y_{max})})L - \frac{a\gamma_w\rho_d\sin\theta}{2}L^2\right. \quad (6.26)$$
$$\left. -\frac{(\rho_{sat}-\rho_d)}{a\gamma_w\sin\theta}e^{a\gamma_w(Y_w-y_1)}e^{-a\gamma_w L\sin\theta} + \frac{(\rho_{sat}-\rho_d)}{a\gamma_w\sin\theta}e^{a\gamma_w(Y_w-y_1)}\right]\cos\theta$$

Simplification of the equation gives:

$$W = \frac{\cos\theta}{a\gamma_w}[(a\gamma_w\rho_d(y_{max}-y_1) - (\rho_{sat}-\rho_d)e^{a\gamma_w(Y_w-y_{max})})L \quad (6.27)$$
$$-\frac{a\gamma_w\rho_d\sin\theta}{2}L^2 - \frac{(\rho_{sat}-\rho_d)}{a\gamma_w\sin\theta}e^{a\gamma_w(Y_w-y_1)}(e^{-a\gamma_w L\sin\theta}-1)]$$

2. When the discontinuity is below the water table:

   (a) when $y_1 < Y_w,\ y_2 \le Y_w$ and $Y_w = y_{max}$:
   The strip weight equation for this case is given by:

$$W = [\rho_{sat}\ L(y_{max}-y_1) - \frac{L^2}{2}\ \rho_{sat}\sin\theta]\cos\theta \quad (6.28)$$

   (b) When $y_1 < Y_w,\ y_2 \le Y_w$ and $Y_w\ <\ y_{max}$:
   The strip weight equation for this case, which is separated into two parts as shown in Fig. 6.3a, is given by:

$$W = \left[\rho_{sat}\ L(Y_w-y_1) - \rho_{sat}\frac{L^2}{2}\sin\theta\right]\cos\theta \quad (6.29)$$
$$+\left[\rho_d\ (y_{max}-Y_w) - \frac{(\rho_{sat}-\rho_d)}{a\gamma_w}(e^{a\gamma_w(Y_w-y_{max})}-1)\right](x_2-x_1)$$

3. When $y_1 < Y_w,\ y_2 > Y_w$:
   For this case; for simplicity the discontinuity is divided into two parts, below and above

the water table as shown in Fig. 6.3b. The strip weight equation for this case is given by:

$$W = \frac{\cos\theta}{a\gamma_w}[(a\gamma_w\rho_d(y_{max} - Y_w) - (\rho_{sat} - \rho_d)e^{a\gamma_w(Y_w - y_{max})})L_2 - \frac{a\gamma_w\rho_d \sin\theta}{2}L_2^2 \quad (6.30)$$
$$-\frac{(\rho_{sat} - \rho_d)}{a\gamma_w \sin\theta}(e^{-a\gamma_w L_2 \sin\theta} - 1)] + \left[\rho_{sat}\ L_1(Y_w - y_1) - \frac{L_1^2}{2}\ \rho_{sat}\sin\theta\right]\cos\theta$$
$$+\frac{1}{a\gamma_w}\left[a\gamma_w\rho_d(y_{max} - Y_w) - (\rho_{sat} - \rho_d)(e^{a\gamma_w(Y_w - y_{max})} + 1)\right](L_1\cos\theta)$$

where $L_1 = (Y_w - y_1)/\sin(\theta)$ and $L_2 = (y_2 - Y_w)/\sin\theta$.

6.3.2.2 Integration of strip weight equations for $\theta = 0$

1. When $(y_1 = y_2) > Y_w$:
   The strip weight equation for this case is as follows:

$$W = \left[\rho_d\ (y_{max} - y_1) - \frac{(\rho_{sat} - \rho_d)}{a\gamma_w}e^{a\gamma_w(Y_w - y_{max})} + \frac{(\rho_{sat} - \rho_d)}{a\gamma_w}e^{a\gamma_w(Y_w - y_1)}\right](x_2 - x_1) \quad (6.31)$$

2. The discontinuity is below the water table:

   (a) When $(y_1 = y_2) \leq\ Y_w$ and $Y_w = y_{max}$:
   The strip weight equation for this case, based on Fig. 6.3c, can be given by:

$$W = \rho_{sat}(y_{max} - y_1)(x_2 - x_1) \quad (6.32)$$

   (b) When $(y_1 = y_2) \leq\ Y_w$ and $Y_w <\ y_{max}$:
   For this case, see Fig. 6.3d, the equation is as follows:

$$W = \rho_{sat}(Y_w - y_1)(x_2 - x_1) + \left[\rho_d\ (y_{max} - Y_w) - \frac{(\rho_{sat} - \rho_d)}{a\gamma_w}(e^{a\gamma_w(Y_w - y_{max})} + 1)\right](x_2 - x_1) \quad (6.33)$$

The above derived equations for the apparent cohesion force and the strip weight are first validated, shown in Appendix H, and then incorporated into an existing DLO Matlab code proposed by Smith & Gilbert (2007*a*). The UNSAT-DLO Matlab code is then validated against the existing DLO code and a hand calculation equation for a total passive earth pressure case study.

6.4 Validation of the UNSAT-DLO Matlab code

6.4.1 Retaining wall case study

A passive retaining wall problem (frictionless) of 1 m height was modelled, using the UNSAT-DLO code. The validation was carried out using different locations of the water table. The results of the UNSAT-DLO code were compared with results of the original (existing) DLO code and a hand calculation equation for a total passive earth pressure case study.

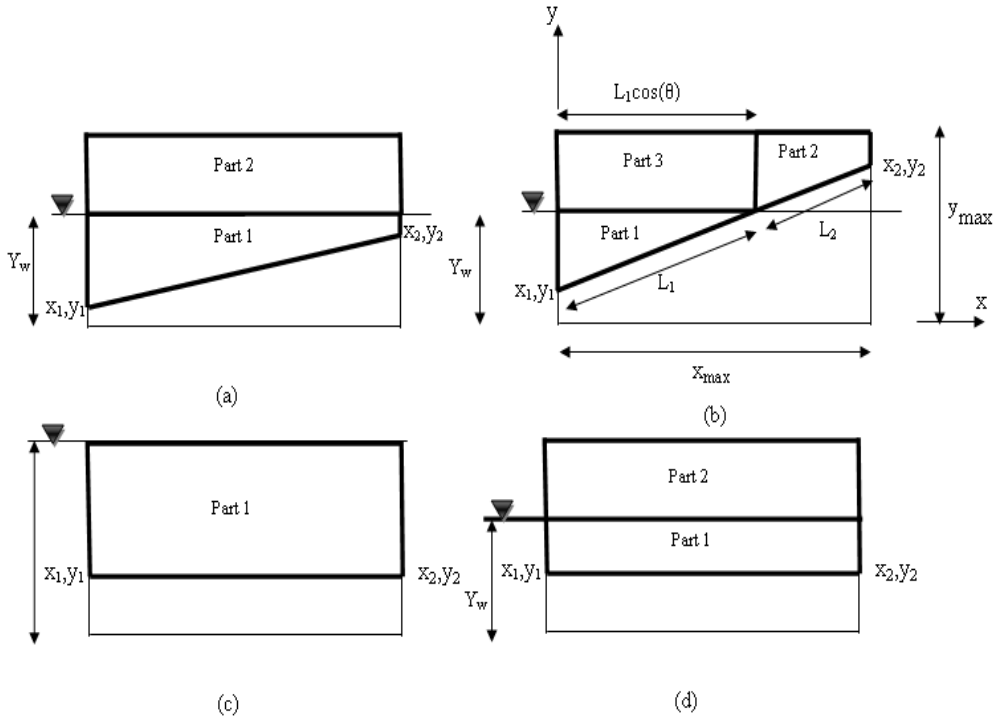

Figure 6.3: Strip weight block(s) for different cases of the discontinuity at various water table positions.

6.5 Validation of the UNSAT-DLO Matlab code

6.5.1 Retaining wall case study

A passive retaining wall problem (frictionless) of 1 m height was modelled, using the UNSAT-DLO code. The validation was carried out using different locations of the water table. The results of the UNSAT-DLO code were compared with results of the original (existing) DLO code and a hand calculation method. The hand calculation equation, derived based on the upper bound theorem (see Fig. 6.4), is given by:

$$F \times \delta - W_B \times \delta \times \tan(\alpha + \phi^{'}) = \hat{c} \times L \times \cos(\phi^{'}) \times \frac{\delta}{\cos(\alpha + \phi^{'})} \tag{6.34}$$

where F is collapse load (kN/m), δ is block displacement (m), W_B is weight of a block above the discontinuity (kN/m), α is angle between the vertical axis to the slip line (shown in Fig. 6.4a), $\phi^{'}$ is internal friction angle, $\hat{c}$ is apparent cohesion along the discontinuity (kN/m^2) and L is length of the discontinuity (m). Table 6.1 shows the parameters used in the validation for a simulated pyroclastic silty sand, after Stanier & Tarantino (2010).

Table 6.1: Parameters used in the USAT-DLO Code, after Stanier & Tarantino (2010).

ρ_d (kN/m^3)	ρ_{sat} (kN/m^3)	a (kPa^{-1})	$c^{'}$ (kN/m^2)	$\phi^{'}$ (degrees)	γ_w (kN/m^3)	y_{max}
8.8	15.2	0.017	0	36.9	9.81	1

Table 6.2 shows the collapse loads (total passive thrust) for various positions of the water table using different methods. The UNSAT-DLO code solution for a fully saturated

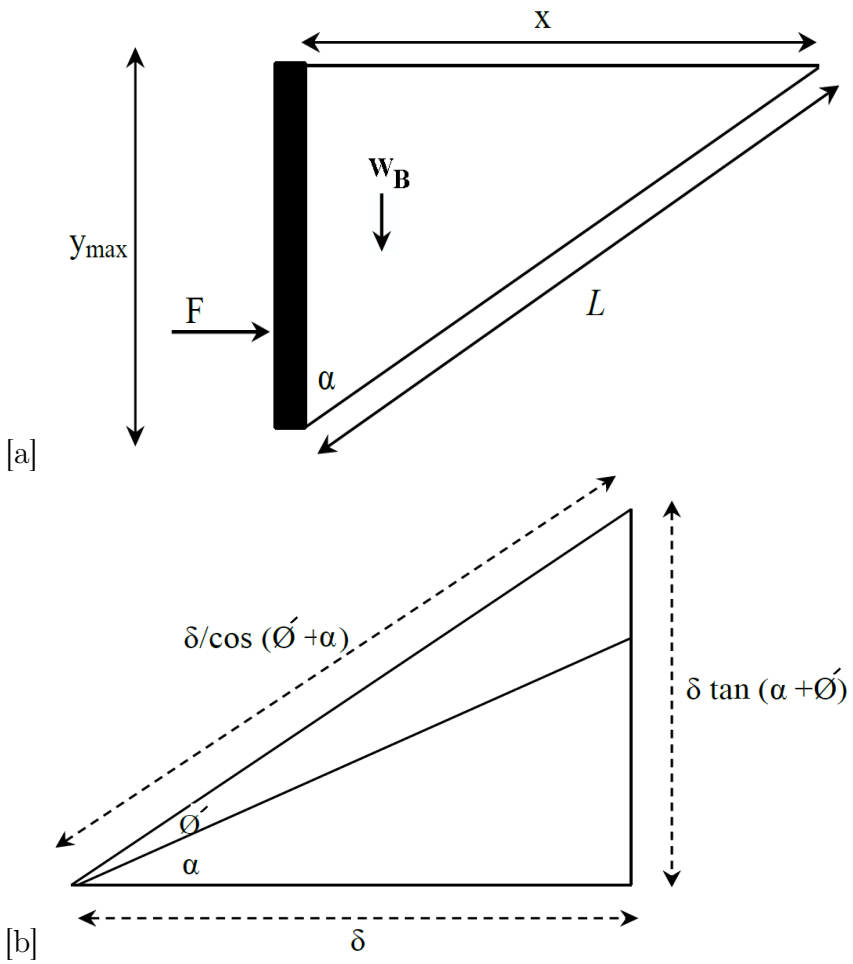

Figure 6.4: (a) Retaining wall case study (b) Hodograph

case should match with the original code result, named as ORG-DLO in Table 6.2, when using the buoyant unit weight of the soil. For the buoyant case shown in Table 6.2, the result obtained by the ORG-DLO code gives a collapse load equal to 18.9361 (kN/m), which is different from the UNSAT-DLO result (23.8411) (kN/m). The is because for the buoyant case, water pressure is implicity assumed on both sides of the wall (4.905) (kN/m). The ORG-DLO code solutions are obtained by substituting the apparent cohesion as a cohesion.

Further validations were performed on the derived apparent cohesion force and strip weight equations and the UNSAT-DLO code and are given in Appendix H. Once the UNSAT-DLO code was validated, the same equations were incorporated into a research version of the LimitState:GEO software. The UNSAT-DLO code was then cross checked against the modified LimitState:GEO software, see Appendix J. Following the validation, the modified LimitState:GEO software is utilised to perform parametric studies on the total passive earth pressure and bearing capacity problems.

6.6 Parametric study of total passive earth pressure

The passive earth pressure retaining wall problem has been investigated by many authors for both fully dry and saturated cases, e.g. Soubra & Macuh (2002) and Sokolovskii (2013). However, limited investigations of earth pressure have been carried out for unsaturated soils.

Table 6.2: Validation of UNSAT-DLO code using a retaining wall case study.

Y_w	StripWeight	ApparentCohesion	UNSAT-DLO	ORG-DLO	HandCal.	Buoyant
0	7.2655	3.297805	77.5198	77.5194	77.5194	–
0.1	7.3135	2.663883	72.7688	72.7687	72.7683	–
0.2	7.3613	2.010163	67.8572	67.8575	67.8572	–
0.3	7.4077	1.338624	62.7934	62.7935	62.7932	–
0.4	7.4516	0.651316	57.5858	57.5854	57.5853	–
0.5	7.4920	-0.04964	52.2438	52.2434	52.2428	–
0.6	7.5277	-0.76212	46.7755	46.7761	46.7751	–
0.7	7.5575	-1.48393	41.1911	41.1916	41.1910	–
0.8	7.5803	-2.21289	35.5005	35.5008	35.5003	–
0.9	7.5949	-2.94666	29.7173	29.7136	29.7134	–
0.9999	7.6	-3.68205	23.8470	23.8485	23.8467	–
1	7.6	-3.68275	23.8411	23.8429	23.8411	18.9361

Previous analyses of earth pressure assumed dry soil above the water table and this assumption neglected the effect of suction on the shear strength of the soil. This section, therefore, provides a study on passive earth pressure that is exerted by two different unsaturated soil types: a sandy soil and a silt loam. The effect of various positions of the water table, internal friction angle and unsaturated parameters (e.g. parameter a) have also been examined.

This analysis is limited only to the passive earth pressure due to the additional complexity of considering tensile failure between the wall and the soil for the active case in the modified LimitState:GEO software.

6.6.1 General description of the retaining wall problem

In this study, a non-dimensional analysis of the total passive earth pressure problem is addressed. As it is required to define a specific height for the problem in the LimitState:GEO software, a retaining wall of 1 m height with levelled backfill is modelled as shown in Fig. 6.5a with boundaries of the backfill of 1m height and 6.2 m length. As the results of this parametric study are normalized over the height of the wall, selection of an arbitrary height of the wall should not be an issue. Several trials were used to select appropriate boundary of the length to prevent restriction of the slip line mechanism. In the software, the output is given in terms of an adequacy factor, a factor by which the load should be increased or the material strengths should be decreased, to cause failure of the problem. Generally, an adequacy factor ≥ 1.0 means the problem is safe against the failure. In this analysis, the adequacy factor is applied on the load, therefore, a normal load of 1 kN/m is used as shown in Fig. 6.5a and b.

Three types of walls are modelled: a frictionless wall, a frictional wall with $\delta = \frac{2}{3}\phi'$ and a fully frictional wall $\delta = \phi'$ and they are named throughout the rest of the thesis as series FL, 0.67FW and FW, respectively. For series 0.67FW and FW, the depth of the soil is extended 0.8 m below the base of the wall to prevent restriction of the failure mechanism by the bottom boundary as shown in Fig. 6.5c.

In the analysis, the soil is assumed as a fully saturated below the capillary rise height and an average unit weight between dry and saturated unit weight is utilised above the capillary rise height. A separate dashed line as shown in Fig. 6.5a denotes the boundary of the capillary rise height. In this parametric study, the water table height Y_w measured from

the base of the wall (positive upwards), is varied from 1 m (fully saturated case at the soil surface) to -3 m below the base of the wall at intervals of 20 cm. This represents degree of saturation ranges from 100% to ≈ 0% for the sandy soil and 100% to 72% for the silt loam according to their SWCCs.

As the accuracy of the numerical results is significantly affected by the number of nodes, the same nodal spacing of 20 nodes/m (scale factor = 20) is utilised for all the series. The more nodes used, the more accurate results can be obtained as shown in Fig. 6.6. In this study, the difference between the scale factor of 20 and 30 was 0.272% which has an insignificant effect as the curve levelled off as shown in Fig. 6.6.

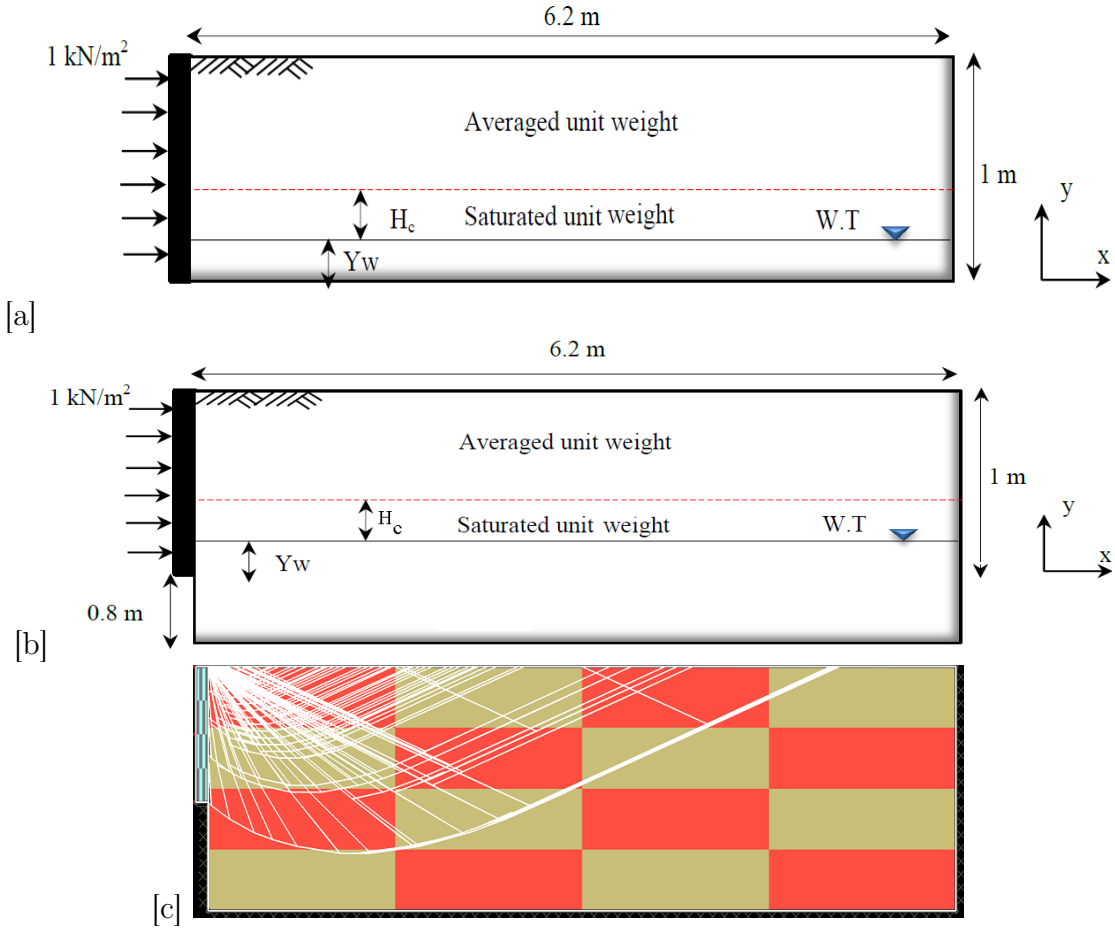

Figure 6.5: Modelling a retaining wall in the LimitState:GEO software (a) frictionless wall (b) frictional wall (c) failure mechanism extending the wall base for the sandy soil-series FW- $\phi^{'} = 45^{o}$, $c^{'} = 0$ kPa, $a = 0.1$, $Y_w = 0.5$ m and $s_o = 5$ kPa.

6.6.2 Selection of the simulated backfill materials

The suction properties of the two different types of soil, sandy soil and silt loam which were selected as simulated backfill materials, are shown in Table 6.3. Dry and saturated unit weight of the soils are assumed as 1.5 and 1.9 of unit weight of water. This is to keep the effect of unit weight constant while studying the effect of the degree of saturation. A range of design values of internal friction from 30^{o} to 45^{o} is utilised for this parametric study.

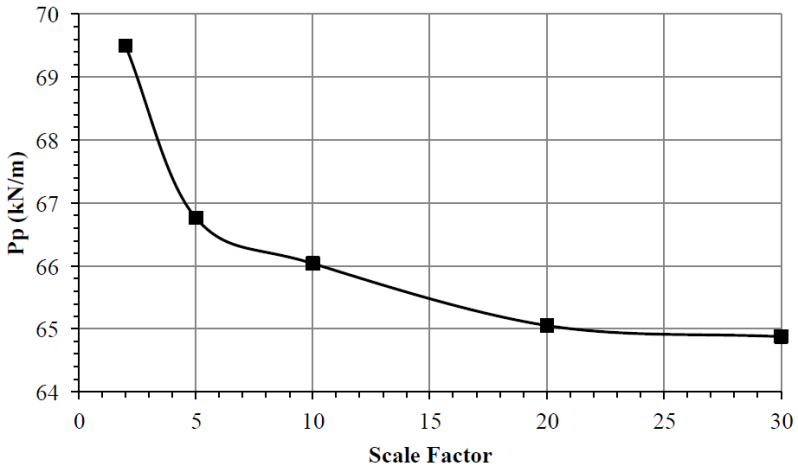

Figure 6.6: Selecting an adequate scale factor for the sandy soil at $Y_w = 0$, $\phi^{'} = 30^o$-series FW.

Table 6.3: Soil properties and unsaturated parameters of the two selected backfills.

	Material	Sandy Soil	Silt Loam
Soil properties	$c^{'}$ (kPa)	0	0
	γ_w (kN/m^3)	9.81	9.81
	γ_{sat} (kN/m^3)	18.639	18.639
	γ_{dry} (kN/m^3)	14.715	14.715
	$\gamma_{average}$ (kN/m^3)	16.677	16.677
Unsaturated parameters	a (kPa^{-1})	0.1	0.01
	s_o (kPa)	5	7
	H_c (m)	0.50968	0.71355

The parameter a and air entry suction s_o in Table 6.3 are obtained using best fit (using Eq. 5.10- Section 5.3) for the actual SWCCs obtained from work of Krishnapillai & Ravichandran (2012) for the two selected materials as shown in Fig. 6.7.

Both selected materials have almost the same s_o. This is to keep the effect of the air entry value of the soil constant in order to study the effect of parameter a independently. The effect of parameter a in Fig. 6.7 is quite clear in that two different SWCCs are produced with wider range of suction for smaller value of a. Accordingly, this has advantage of studying two different degrees of saturation at the same suction. Another reason for selecting these two materials is attributed to the fact that most of the backfill materials are coarse grained soils as they provide adequate drainage.

6.6.3 Results for the sandy soil backfill material

Figures 6.8a, b and c give an example of the design chart in which the x-axis represents normalized total passive thrust ($\frac{Pp}{H^2\ \gamma_w}$) and the y-axis represents normalized water table height ($\frac{Y_w}{s_o\ a\ H}$) for a range of internal friction angles for FL, 0.67FW and FW series. The results are compared with the Rankine method which takes into account capillary rise height. The total P_p equations for a frictionless wall, with a levelled backfill, using the Rankine method for the fully saturated and the case when water table is below the soil surface and

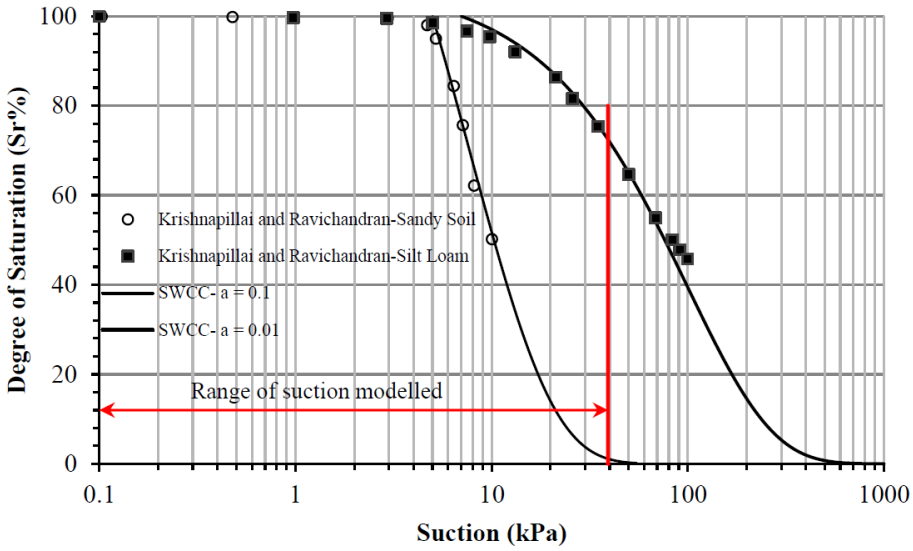

Figure 6.7: SWCC for the sandy soil and the silt loam, after Krishnapillai & Ravichandran (2012) with the fit using Eq. 5.10 and range of the suctions modelled.

capillary rise at the surface are given in Eqs. 6.35 and 6.36, respectively:

$$Pp = \frac{1}{2}\ k_p\ \gamma^{'}\ H^2 + \frac{1}{2}\ \gamma_w\ H_w^2 \tag{6.35}$$

$$P_p = (k_p - 1)\ \gamma_w\ y_1^2 + \frac{1}{2}\ y_1\ [k_p\ \gamma_{sat}\ y_1\ - (k_p - 1)\ \gamma_w\ y_1] + k_p\ \gamma_{sat}\ y_1\ H_w + \frac{1}{2}\ k_p\ \gamma^{'}\ H_w^2 + \frac{1}{2}\ \gamma_w\ H_w^2 \tag{6.36}$$

where k_p is passive earth pressure coefficient based on Eq. 6.37 for FL series or on Fig. 6.9d for all the series, $\gamma^{'}$ is buoyant unit weight (kN/m^3), H is height of the wall (m), γ_w is unit weight of water (kN/m^3), $H_w = (Y_w)$ is water table height (m) (positive upwards), y_1 is distance from the water table to the capillary rise line (H_c in Fig. 6.5a) and γ_{sat} is saturated unit weight (kN/m^3). The derivations of the preceding equations and for other cases are shown in Appendix L. The derivations are based on full continuity of water between the soil and the wall. A capillary rise height $y_1 = H_c = 0.50968$ m is assumed (same as for the sandy soil - shown in Table 6.3) to be compatible with the numerical results.

$$k_p = \frac{1 + \sin\phi^{'}}{1 - \sin\phi^{'}} \tag{6.37}$$

It can be seen from Figs. 6.8a, b and c that an increase of about 46.8%, 54.2% and 54.2% can be obtained for the case of $\phi^{'} = 30^o$ at Y_w = - 0.6m (corresponding to $\frac{Y_w}{s_o\ a\ H}$ = -1.2 in Figs. 6.8a, b and c) for the series FL, 0.67FW and FW when compared to their counterpart total passive thrust result using the Rankine method. The height Y_w = - 0.6 m corresponds to a maximum normalized Pp value, to a hydrostatic suction of 15.696 kPa (1.6×9.81) and degree of saturation of about 34% (see Fig. 6.7- SWCC for the sandy soil).

At depth Y_w = -3 m ($\frac{Y_w}{s_o\ a\ H}$ = -6 in the Figs. 6.8a, b and c), the $\frac{Pp}{H^2\ \gamma_w}$ for the unsaturated case at $\phi^{'} = 30^o$ is closer to the result of the Rankine method. No further drop of the water table beyond 3 m below the base of the wall is carried out as the overall trend of the curves is clear.

Sharper curves can been seen for the higher $\phi^{'}$ values at the same Y_w. For example, for series FL (Fig. 6.8a) at $\frac{Y_w}{s_o\ a\ H}$ = -1.2 for $\phi^{'} = 45^o$, higher total passive thrust can be seen

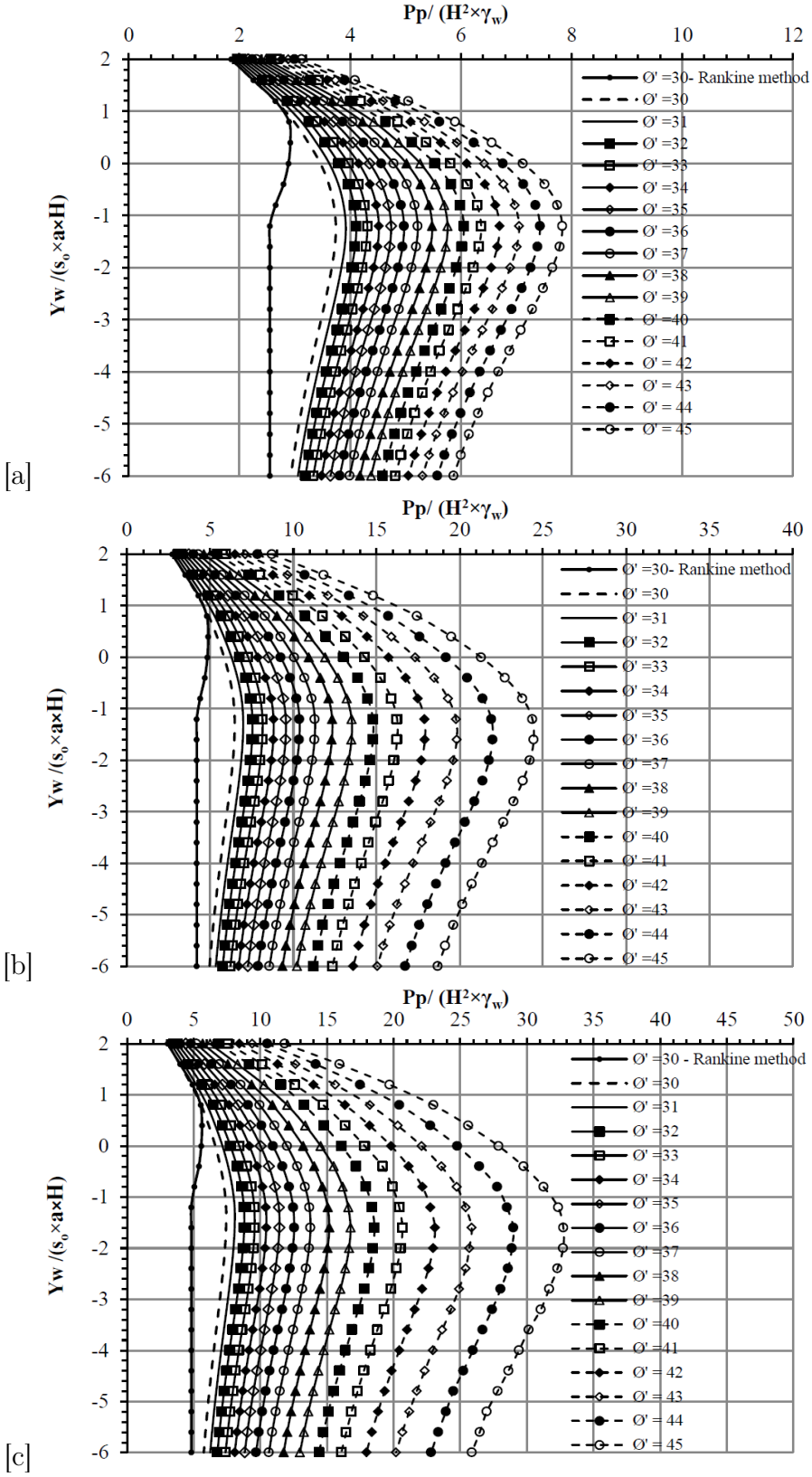

Figure 6.8: Normalized total passive thrust ($\frac{Pp}{H^2\ \gamma_w}$) against various normalized water table ($\frac{Y_w}{s_o\ a\ H}$) for variety of internal friction angle values for the sandy soil for (a) FL (b) 0.67FW (c) FW.

when compared to the case of $\phi^{'} = 40^{o}$ at the same Y_w. This increase is inherently due to the effect of $\phi^{'}$ in the term $(sS_r) \times \tan\phi^{'}$ (see Eq. 5.14).

Figures 6.9a, b and c reveal the $\frac{Pp}{H^2\ \gamma_w}$ versus k_p for a various water table positions at each $\frac{Y_w}{s_o\ a\ H}$ = 0.8 (40 cm) depth for series FL, 0.67FW and FW. Only the data for each $\frac{Y_w}{s_o\ a\ H}$ = 0.8 drop of the water table are selected to avoid congestion in Figs. 6.9a, b and c. The k_p values are obtained using Fig. 6.9d. Results for both the Rankine method at the fully saturated case and $Y_w = 1$ are matched together for all the series. However, an increase of about 43.2%, 55.6% and 56.4% in the $\frac{Pp}{H^2\ \gamma_w}$ at $\phi^{'} = 30^{o}$(corresponding to the begining of the curves) can be obtained for the Y_w = 1.00 m case compared to Y_w = 0.6 m for the series FL, 0.67FW and FW, respectively.

6.6.3.1 Effect of the wall friction on total passive thrust for the sandy soil

The effect of wall friction on the total passive earth thrust is presented in Figs. 6.10a, b, c and d. In Fig. 6.10a, the value of $\phi^{'}$ (= 30^{o}) was kept constant while varying the wall friction as well as in Fig. 6.10b ($\phi^{'} = 45^{o}$- constant). An increase of about 47.78% and 66.62%, for Fig. 6.10a, can be obtained when comparing the $\frac{Pp}{H^2\ \gamma_w}$ of the FL series with the 0.67FW and FW, respectively at $\frac{Y_w}{s_o\ a\ H}$ = 2. Comparison between the cases of 0.67FW and FW at normalized $\frac{Y_w}{s_o\ a\ H}$ = 2 shows an increase by a factor of 1.39 fold of the FW case over the 0.67FW case. Also Figs. 6.10a and b inherently include the effect of Y_w as well as the wall friction on the total passive earth thrust at the cases when the soil is not fully saturated ($\frac{Y_w}{s_o\ a\ H} \neq 2$). Figure 6.10b shows a higher difference (between the results of $\phi^{'} = 45^{o}$ with the counterpart Rankine method results at normalized Y_w = - 1.2) when compared to Fig. 6.10a due to the higher effect of the wall friction.

Figure 6.10c shows the effect of wall friction on the total passive thrust at Y_w = 0 m for various $\phi^{'}$ values. Frictional walls deliver higher total passive thrust when compared to its counterparts (e.g. Rankine method-Y_w = 0.00-FL and Y_w = 0.00-FL). Figure 6.10d represents the $\frac{Pp}{H^2\ \gamma_w}$ versus k_p in which a non-linear increase in the passive earth pressure can be seen. The fully frictional wall (Y_w = 0.00-FW) at $\phi^{'} = 42^{o}$ ($k_p \approx 17$) serves to provide approximately the same total passive thrust when compared to the case of Y_w = 0.00-0.67FW at $\phi^{'} = 45^{o}$. Once more, this is due to the effect of wall friction.

Figures 6.11a, b and c show failure mechanisms obtained by the modified LimitState:GEO software for the FL, 0.67FW and FW series at Y_w = -0.6 m and $\phi^{'} = 45^{o}$. The FW series reveals a wider and a deeper failure mechanism when compared to the other cases due to the effect of the wall friction.

6.6.4 Results for the silt loam backfill material

Figures 6.12a, b and c show the normalized total passive thrust results versus the normalized water table for the three series. The fully saturated case in Fig. 6.12a corresponds to the beginning of the curve, while the end of the curve represents 3 m drop of the water table below the base of the wall. This happens (curves do not start from the origin of the axes) because the water table is normalized by the small value of the parameter a (a = 0.01). A part from the sandy soil, the silt loam backfill material shows non-linear continuous increase in the total passive thrust even at Y_w = -3 m ($\frac{Y_w}{s_o\ a\ H}$ = -42.85 - end of the curves). This is because of the high degree of saturation at this depth. As stated before, S_r at Y_w = -3 m (corresponds to a hydrostatic suction of 4 $\times$9.81 = 39.24 kPa) for the silt loam is 72% which

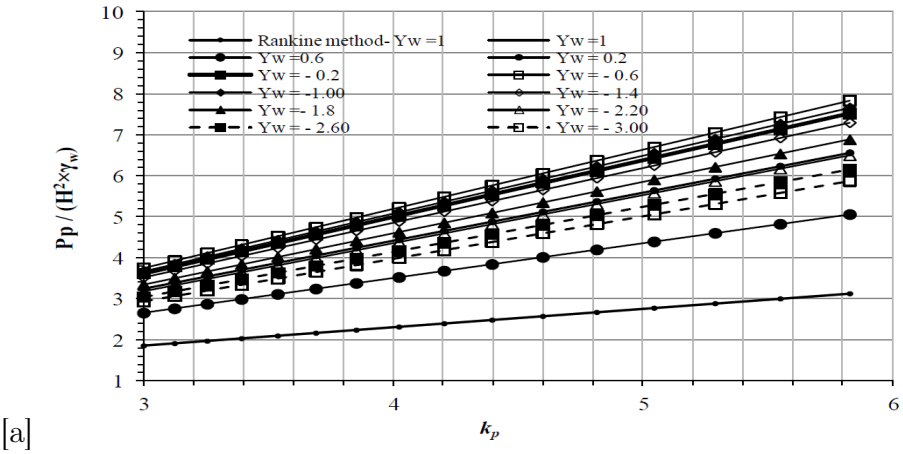

[a]

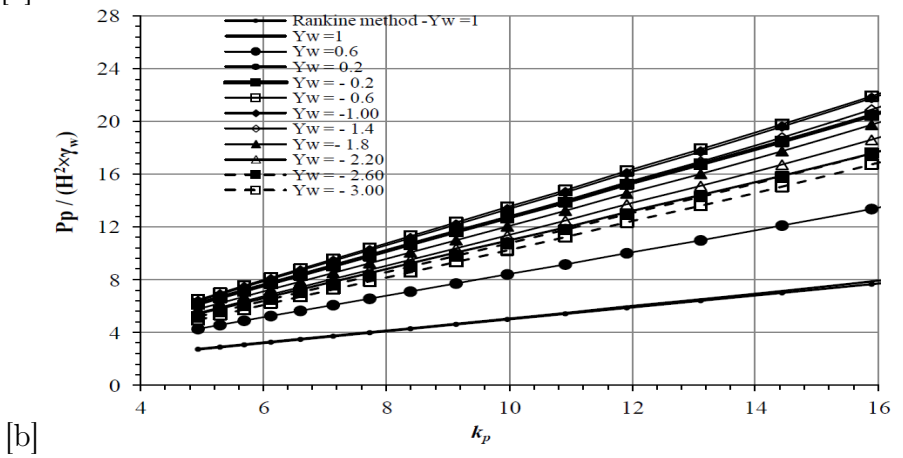

[b]

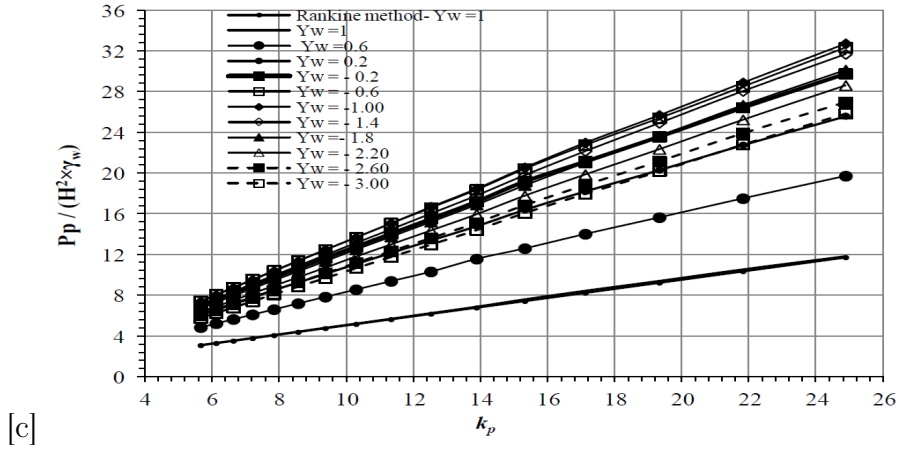

[c]

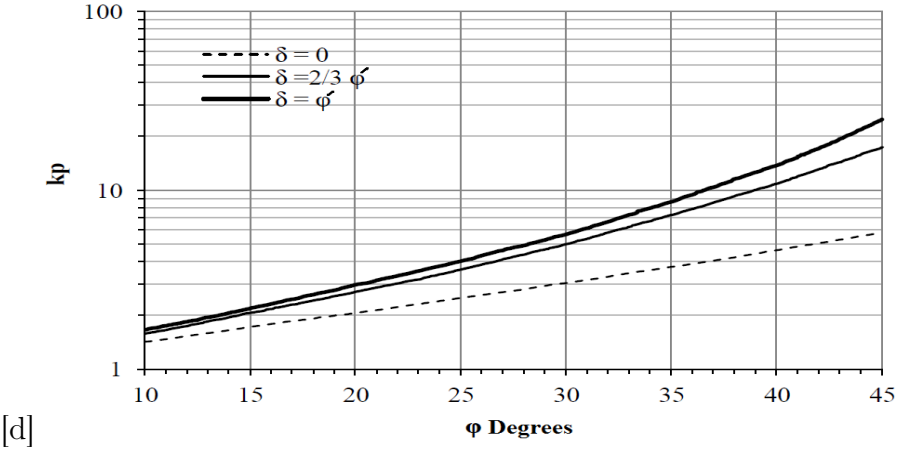

[d]

Figure 6.9: Normalized total Pp versus k_p for various Y_w positions for the sandy soil for (a) FL (b) 0.67FW (c) FW (d) k_p for various design values of ϕ' for all series based on EuroCode (2004)(Annex C).

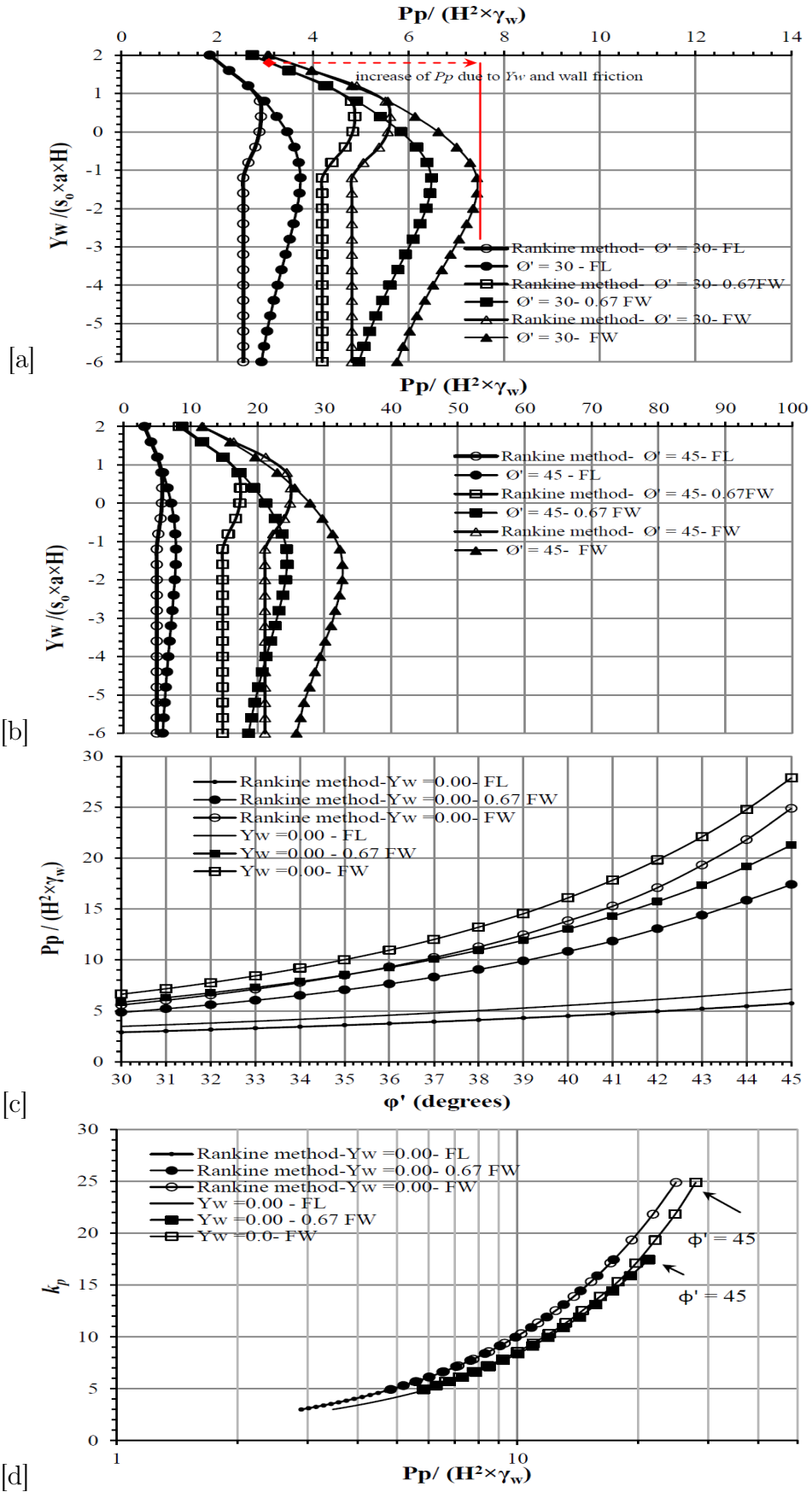

Figure 6.10: (a) Comparison between three different frictional walls for the sandy soil with the Rankine method at $\phi^{'} = 30^{o}$ (b) $\phi^{'} = 45^{o}$ (c) normalized total Pp versus $\phi^{'}$ for three different types of wall at $Y_w = 0$ (d) k_p versus normalized total passive thrust for three different types of wall at $Y_w = 0$.

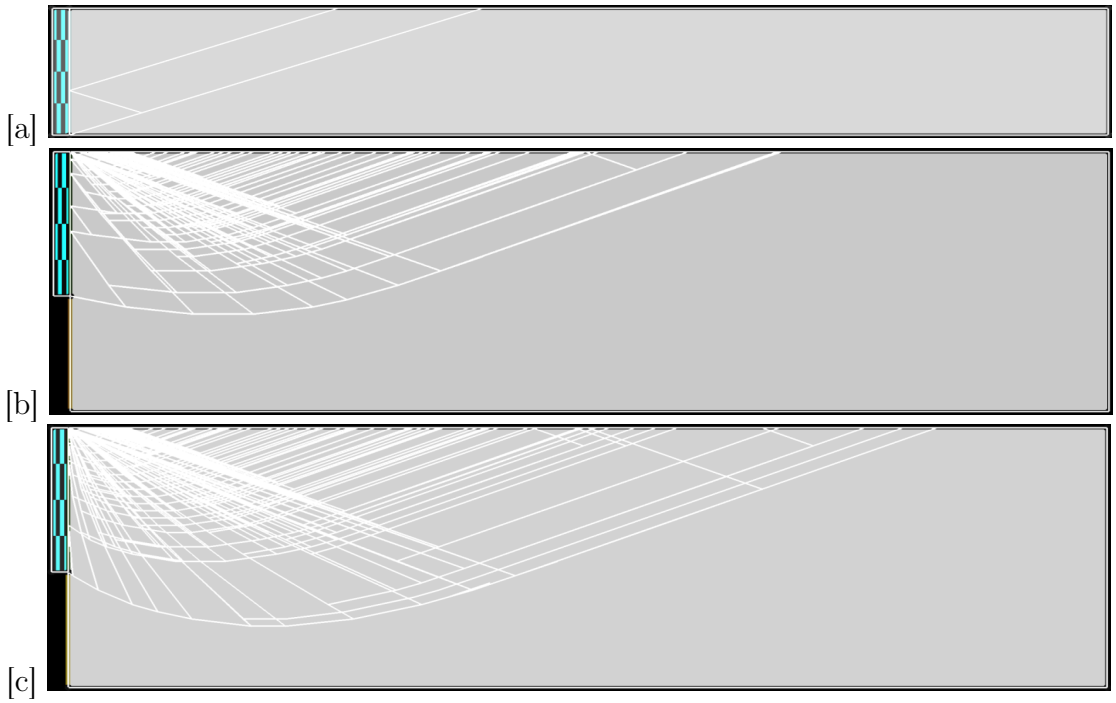

Figure 6.11: Failure mechanism obtained by the LimitState:GEO at Y_w = -0.6 m, $\phi^{'} = 45^o$ for the sandy soil (a) FL (b) 0.67FW (c) FW.

is quite high compared to the sandy soil ($S_r \approx 0$ %) at the same water table drop of 3 m below the base of the wall.

For the silt loam, the same capillary rise height of 0.71355 m shown in Table 6.3 was used for the Rankine equations. In Fig. 6.12a for the fully saturated case (beginning of the curves), a small difference for various values of $\phi^{'}$ can be seen which is attributed to the solo effect of the internal friction angle while the larger gap at $\frac{Y_w}{s_o\ a\ H}$ = -42.85 (end of the curves) is due to the effect of the internal friction angle and degree of saturation. At $\frac{Y_w}{s_o\ a\ H}$ = -42.85, an increase of the $\frac{Pp}{H^2\ \gamma_w}$ of 3.08, 3.33 and 2.26 fold can be obtained for the FL, 0.67FW and FW series, respectively when compared to their counterparts of the Rankine method at $\phi^{'}$ = 30^o.

For the fully saturated case in Figs. 6.13a, b and c, both the Rankine method and Y_w = 1 for all series matched. The coefficient of lateral earth pressure k_p is calculated based on Fig. 6.9d.

6.6.4.1 Effect of the wall friction on total passive thrust for the silt loam

Figures 6.14a, b, c and d show the effect of wall friction on the total passive earth pressure for the silt loam. In Fig. 6.14a, a significant increase in $\frac{Pp}{H^2\ \gamma_w}$ can be observed when comparing the FL, 0.67FW and FW series with the Rankine method at $\frac{Y_w}{s_o\ a\ H}$ = -42.85. As usual, the FW series serves to provide the higher total passive thrust then follows by the 0.67FW case. The interesting finding in Fig. 6.14a at Y_w = -3 m (normalized Y_w = - 42.857) is that the case of FL gives a normalized total passive thrust greater than the Rankine method by a factor of about 3.08. This is totally due to the effect of parameters a (the unsaturated case) which inherently contains the degree of saturation effect and hence the suction. This was not the case for the sandy soil (see Fig. 6.10a) in which an increase of just 1.14 fold at $\frac{Y_w}{s_o\ a\ H}$

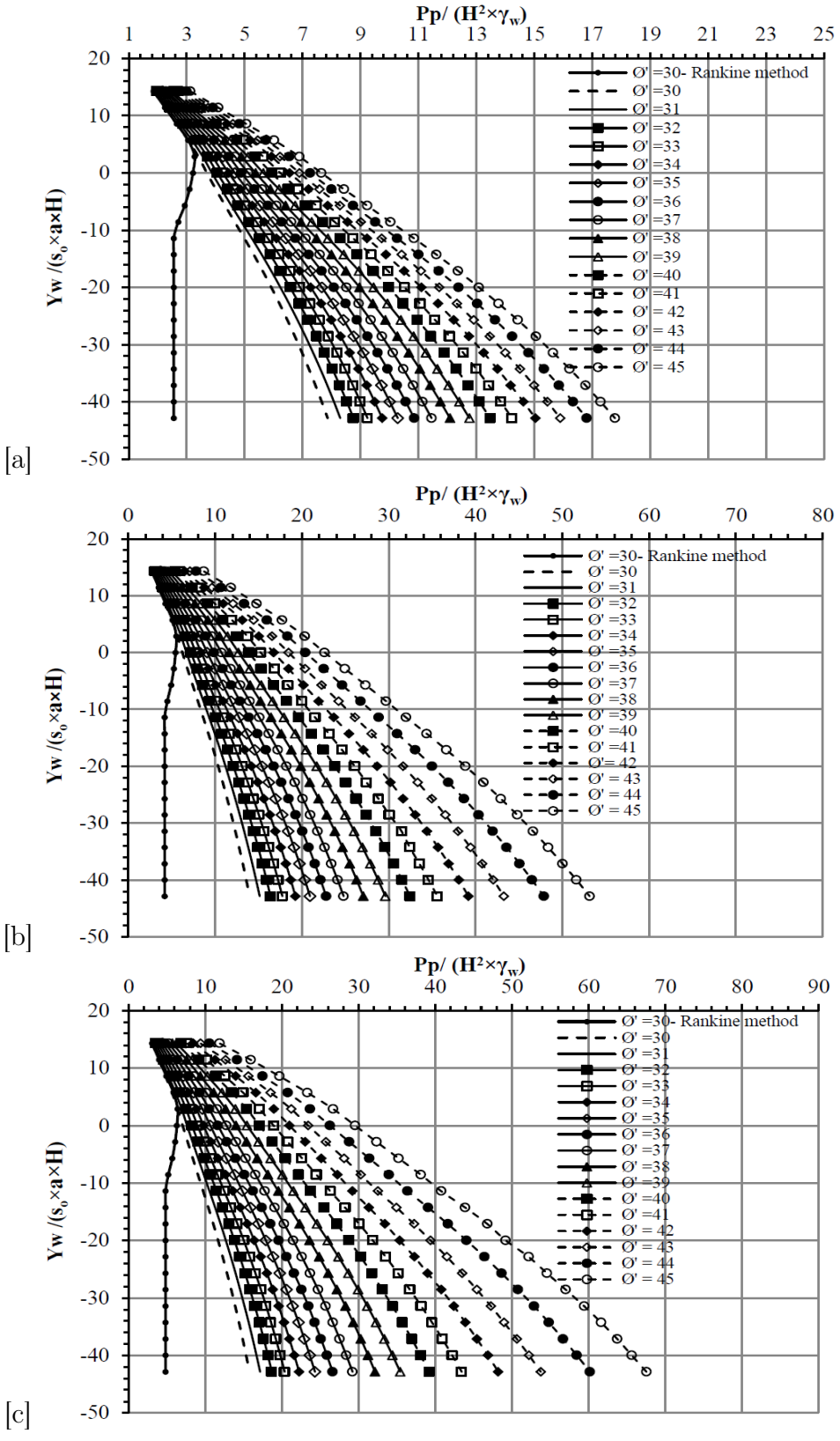

Figure 6.12: Normalized total passive thrust ($\frac{Pp}{H^2\ \gamma_w}$) various normalized water table ($\frac{Y_w}{s_o\ a\ H}$) for the silt loam at a variety of ϕ' for (a) FL (b) 0.67FW (c) FW.

= -6 in $\frac{Pp}{H^2\ \gamma_w}$ of the FL was achieved when compared the Rankine method results. The implication of Fig. 6.14b is that a higher difference between the result obtained by the DLO

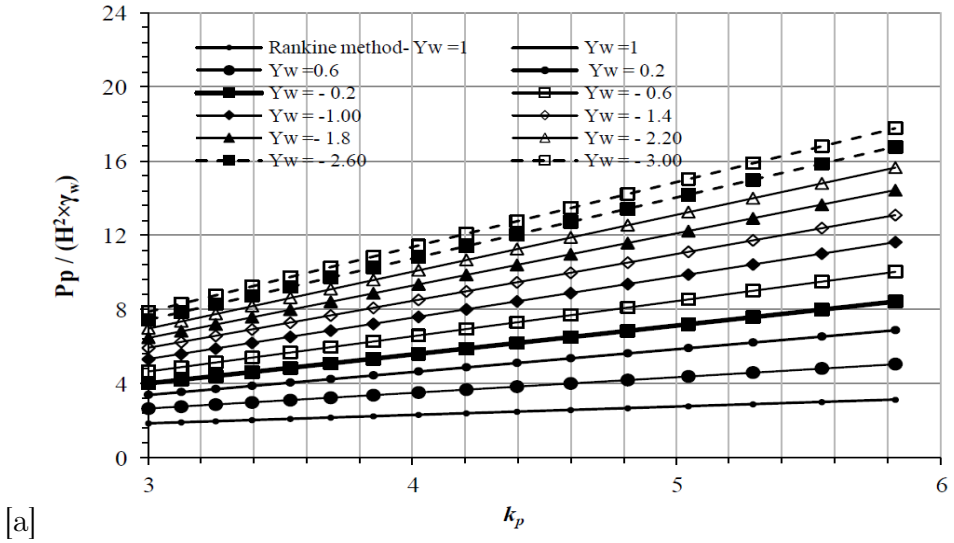

[a]

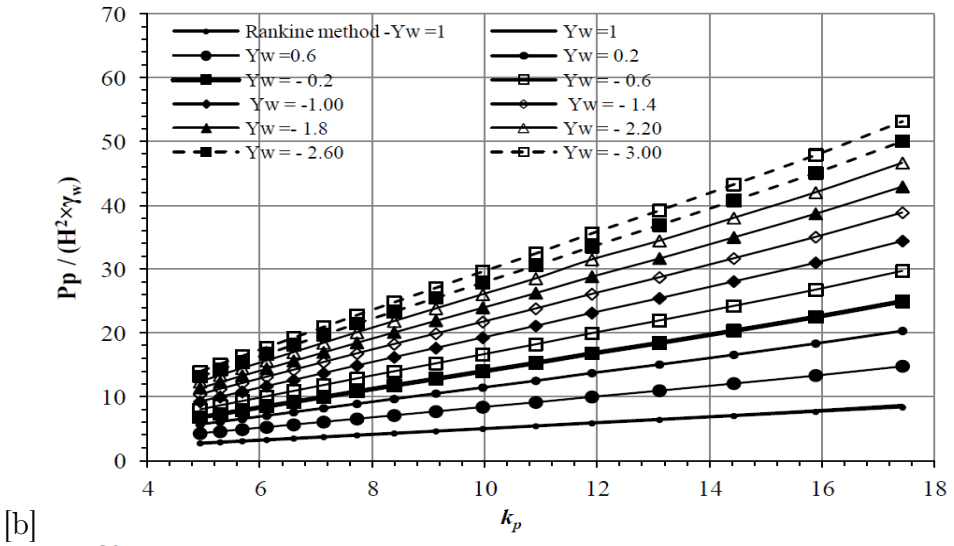

[b]

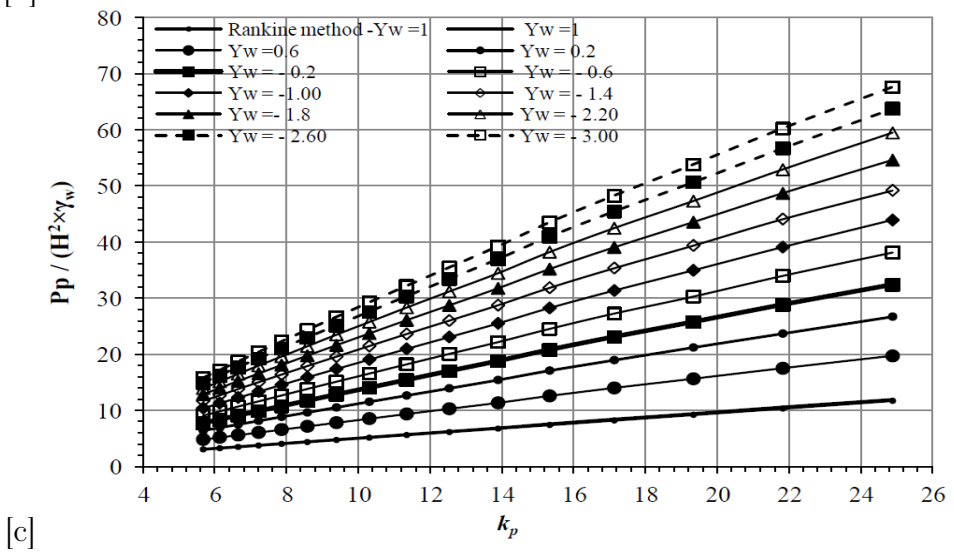

[c]

Figure 6.13: Normalized total Pp against various k_p for for the silt loam at a variety of $\phi^{'}$ values (a) FL (b) 0.67FW (c) FW.

method (e.g. $\phi^{'} = 45^{o}$-FW) with its counterpart by the Rankine method at the same Y_w can be obtained if it is compared to the same counterpart pair in Fig. 6.14a (the difference

between $\phi^{'} = 30^{o}$-FW with $\phi^{'} = 30^{o}$-Rankine-FW). This is attributed to the effect of the wall friction (higher $\phi^{'}$). In Fig. 6.14c, all cases of the Rankine method give less total passive thrust when compared to their counterparts (e.g. Rankine method- Y_w = 0.00-FL against Y_w = 0.00-FL). The same finding also is identical with that in Fig. 6.14d which is re-plotted in another manner. The failure mechanisms of the FL, 0.67FW and FW series for the silt loam soil at Y_w = -0.7 and $\phi^{'} = 45^{o}$ are shown in Figs. 6.15a, b and c. A wider and a deeper failure mechanism can be seen for the FW series.

6.6.4.2 Effect of the parameter *a* on total passive thrust

Figure 6.16a shows the effect of parameter (a) on the total passive earth pressure for the two simulated backfill materials. In Figs. 6.16a and b, a smaller value of parameter a gives a smaller and a narrower range of the total passive thrust (with depth). The passive thrust for the case when $a = 0.1$ kPa^{-1} (the sandy soil) delivers an increase to a specific water table position followed by a decrease when the water table drops further. However, a continuous increase of the passive thrust with normalized Y_w can be seen for the case of $a = 0.01$ kPa^{-1} (the silt loam). This can be attributed to the effect of the degree of saturation on the passive thrust in which for $a = 0.1$ kPa^{-1} only a small range of the suction needs to empty the voids from water (a sharp decrease in the degree of saturation can be observed based on the SWCC for the sandy soil- see Fig. 6.7). However, this is not the case for $a = 0.01$ kPa^{-1} as the soil is finer. Retaining water in the inter-aggregated voids extends suction range and hence increases the shear strength of the soil.

The maximum total passive thrust for the case a = 0.1- FL is obtained at about S_r = 34% which is close to the case of a = 0.01-FL at about S_r = 95%. In other words, at the same hydrostatic suction, it is the degree of saturation that dominates the total passive earth pressure of the soil. Figure 6.16b is a magnification of Fig. 6.16a which shows this more clearly.

In Fig. 6.16c, all cases of $a = 0.01$ kPa^{-1} provide a higher total passive thrust when compared to their counterparts of the case $a = 0.1$ kPa^{-1} at the same $\phi^{'}$. Figure 6.16d is re-plotted to show the same as Fig. 6.16c. Finally, Table 6.4 shows a comparison between the two selected backfill materials at three Y_w positions and $\phi^{'} = 30^{o}$ in which the effect of both unsaturated conditions and the wall friction are summarized.

Table 6.4: Comparison of $\frac{Pp}{H^2\ \gamma_w}$ for two selected backfill materials at $\phi^{'} = 30^{o}$ and three different Y_w positions.

row 1	Sandy Soil			Diff%		Silt Loam			Diff %		Diff %
	col 2	col 3	col 4			col 7	col 8	col 9			
Y_w m	FL	0.67FW	FW			FL	0.67FW	FW			
1	1.850	2.734	3.082	32.3[1]	11.3[2]	1.850	2.734	3.082	32.3[3]	11.3[4]	0[5]
-0.6	3.743	6.475	7.432	42.2	12.8	4.656	8.027	9.045	42	11.2	19.3
-3	2.928	4.965	5.761	41	13.8	7.866	13.979	15.758	43.7	11.3	64.5

1 percentage between col. 3 and 2 at row 4. *2* percentage between col. 4 and 3 at row 4.
3 percentage between col. 8 and 7 at row 4. *4* percentage between col. 9 and 8 at row 4.
5 percentage between col. 8 and 3 at row 4.

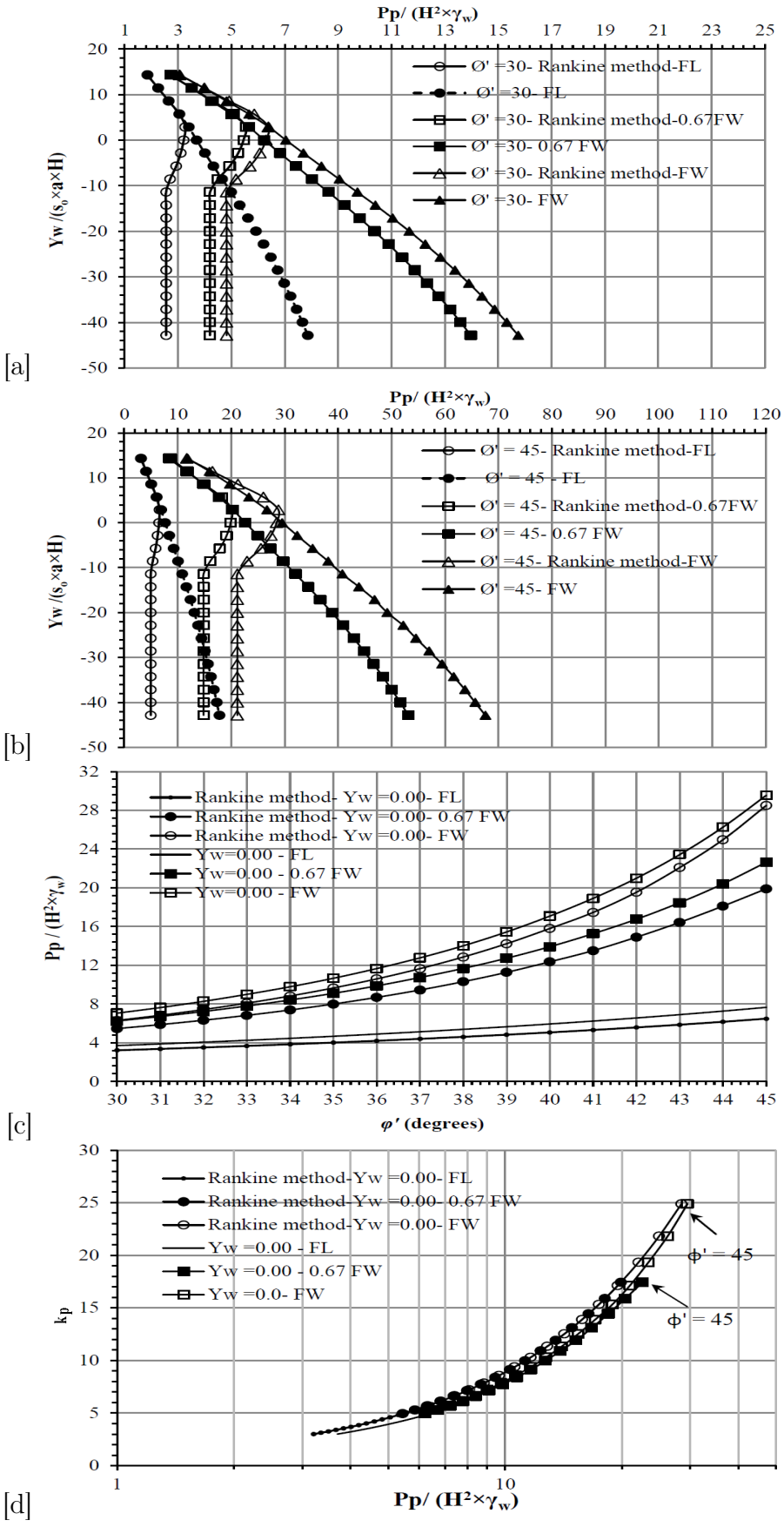

Figure 6.14: (a) Comparison between three different frictional walls for the silt loam with the Rankine method at $\phi^{'} = 30^{o}$ (b) $\phi^{'} = 45^{o}$ (c) $(\frac{Pp}{H^2\ \gamma_w})$ versus $\phi^{'}$ for three different types of wall at $Y_w = 0$ (d) k_p versus normalized total passive thrust for three different types of wall at $Y_w = 0$.

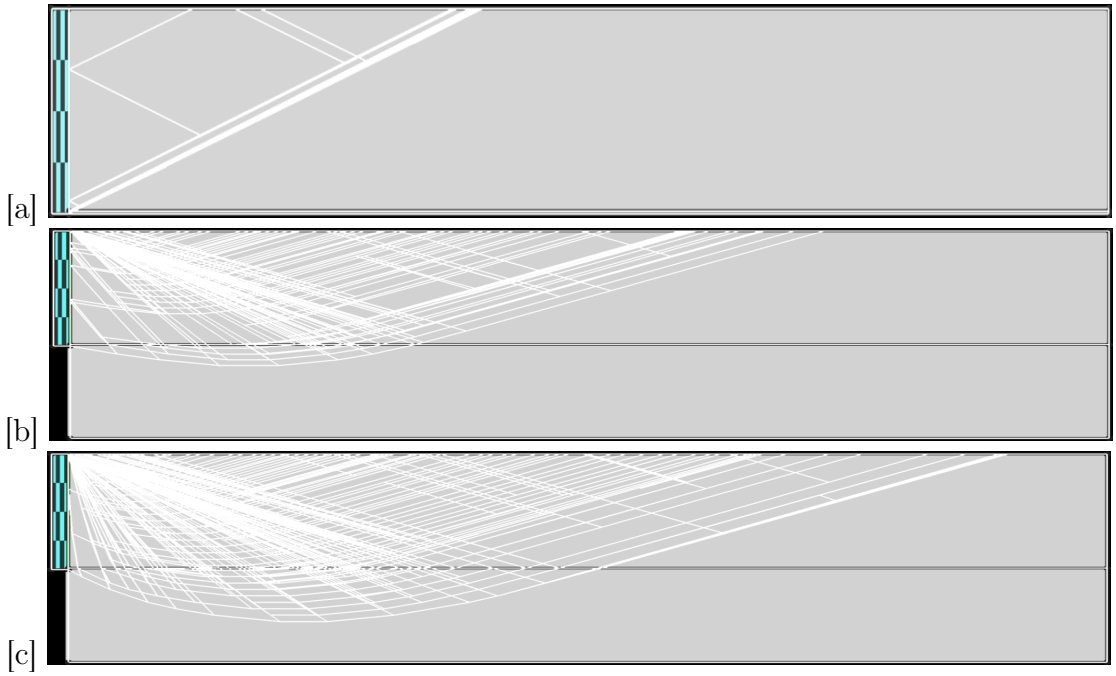

Figure 6.15: Failure mechanism obtained by the LimitState:GEO at Y_w = -0.7 m, $\phi^{'} = 45^o$ for the silt loam (a) FL (b) 0.67FW (c) FW.

6.6.5 Summary of total passive earth thrust study

The two selected backfill materials provided an opportunity to study the effect of two different SWCCs on the passive earth thrust through investigating the unsaturated parameter *a*. The results showed that an increase of the total passive thrust between (0 - 64.5%) for the case FL and 0.67FW at $\phi^{'} = 30^o$ for a range of Y_w = 1 m (fully saturated) and Y_w = -3 m (below the base of the wall) can be achieved due to the effect of parameter *a* (two different materials-see Table 6.4-last column). The variation of the water table position allows the soil to transit from fully saturated to fully dry cases for the sandy soil and to a zone of suction for the silt loam. For example, for the sandy soil, for the series FW at $\phi^{'} = 30^o$, an increase of about 86.9% in the normalized total passive thrust can be obtained when Y_w drops from 1 to -3 m. This is due to the effect of degree of saturation. Also the parametric study included the effect of both wall friction and internal friction angle. The higher internal friction angle and wall friction, the higher total passive thrust can be obtained.

6.7 Comparison of numerical analysis with the experimental bearing capacity results

This section compares the modified DLO approach with the experimental bearing capacity results for both the surface and buried strip footings. The analysis is conducted at different ranges of suction values and internal friction angles.

6.7.1 Footing placed on the surface

The surface footing was modeled using the modified DLO code for fully saturated and unsaturated conditions. The bearing capacity test was modeled in plane strain with a 0.025

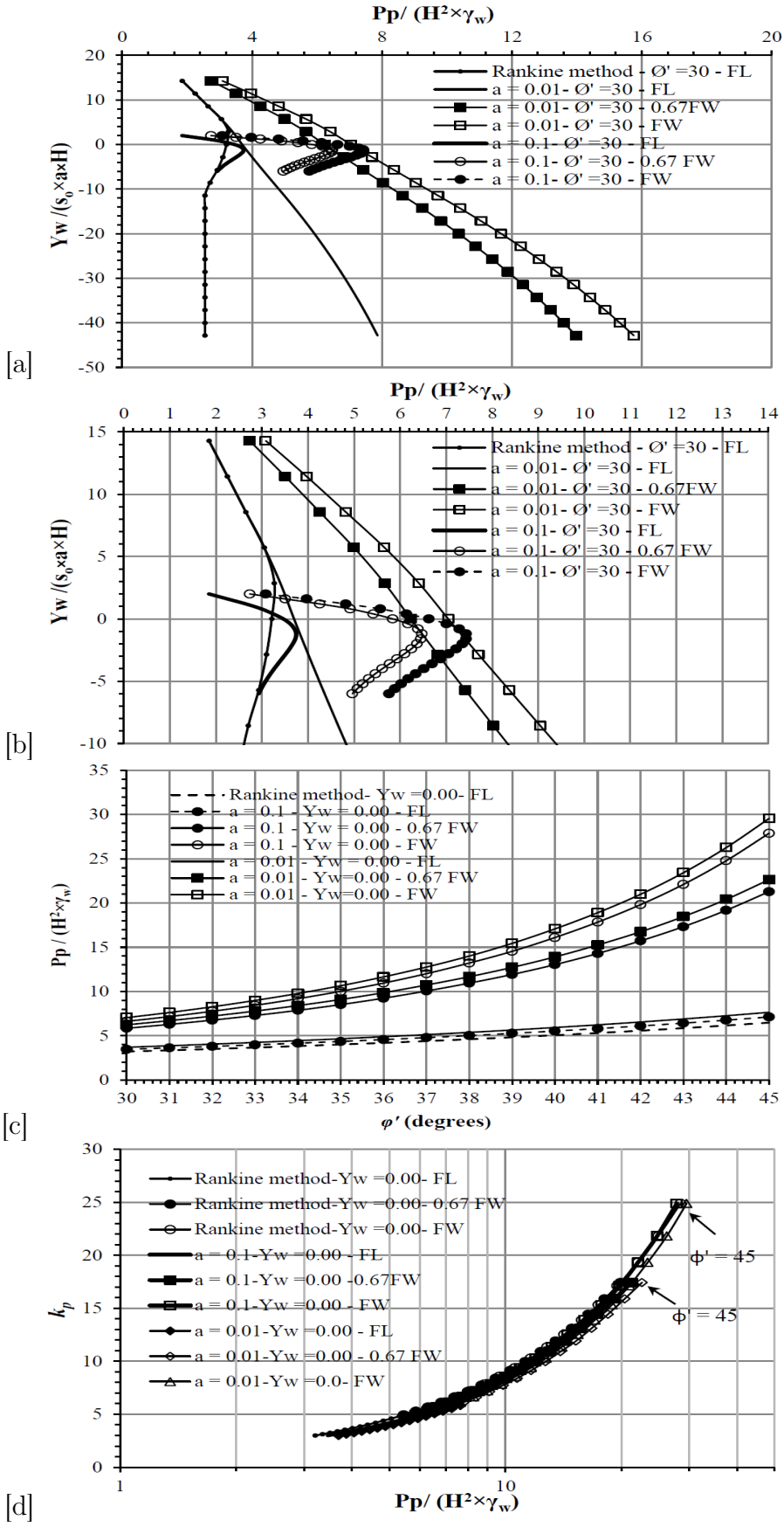

Figure 6.16: $(\frac{Pp}{H^2\ \gamma_w})$ at $\phi^{'} = 30^o$ for $a = 0.1$ kPa^{-1}(sandy soil) and $a = 0.01$ kPa $^{-1}$ (silt loam) against (a) normalized Y_w positions for the two different backfill materials (b) normalized Y_w positions (c) internal friction angle at $Y_w = 0.00$ m (d) passive earth pressure coeffiecient k_p at $Y_w = 0.00$ m.

m wide rigid footing centrally placed on the surface of a rectangular body of sand 0.6 m wide and 0.1 m deep (see Fig. 6.17). It was necessary only to model the top 0.1 m of the soil (the experimental depth of the soil was 0.3 m), since the failure mechanism did not exceed this depth. The x-boundary of the problem is extended to 0.6 m from 0.4 m (the experimental width) to prevent edge restrictions (where the failure mechanism hits the boundary edge) especially for high values of the internal friction angle. The soil-footing interface is modelled as 0.5 tan ϕ. This was in accordance to the results of the direct shear test at the interface (see Section 4.13) in which the mobilized ϕ ($= 21.59^o$) at the interface was approximately half of the ϕ obtained for the dry sand ($= 44.1^o$).

Figure 6.17 shows the modelling scenario. As before, soil below the capillary line was assumed to be fully saturated and an average unit weight of soil above the capillary line was assumed. Table 6.5 gives the unit weight properties, while Table 6.6 provides the required unsaturated parameters obtained to model the surface footing in the modified LimitState:GEO. The parameter a and s_o are determined using the best fit to the SWCC data, shown previously in Fig. 5.8. This gives $H_c = 0.2344$ m using Eq. 5.11 presented in Section 5.3.

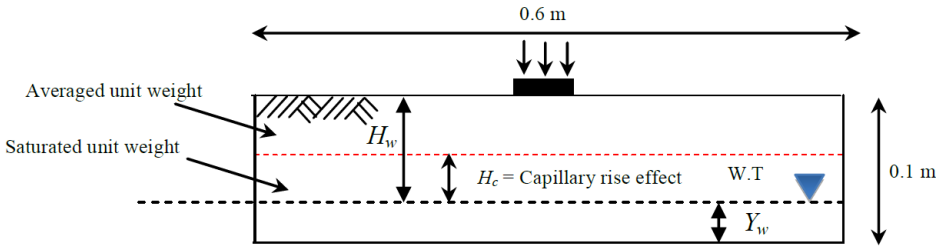

Figure 6.17: Modelling footing surface in the DLO method.

Table 6.5: Soil properties used in the DLO method.

Soil properties	
γ_d (kN/m^3)	15.3
γ_{sat} (kN/m^3)	19.33
γ_w (kN/m^3)	9.81
$\gamma_{average}$ (kN/m^3)	17.315

As stated previously in Chapter 4, at least four repeat experimental tests were conducted at the same nominal suction. Due to the difficulty in obtaining the same suction using the HCT for the experimental bearing capacity tests each time, slightly different applied suctions are produced in the laboratory. This is due to the difficulty in obtaining the same amount of water expelled from the samples each time. However, the applied suction (same suction) needed to be generalized in the DLO and this was performed by taking the average of the experimental applied suctions for the repeat tests (given in Table 6.6). The experimental obtained suction for the surface and buried footings are showed in Subsections 4.10.1 and 4.10.2. The average suction values were then used to determine the average degree of saturation in Table 6.6 based on the original SWCC.

Figure 6.18 shows the trial cases which were performed for selecting an adequate nodal spacing (scale factor) for $H_w = 0.387$ m ($s_{average} = 3.796$ kPa) at $\phi = 45^o$ with the other properties as given in Tables 6.5 and 6.6. The higher value of the $\phi = 45^o$ was used to represent a less conservative case (the highest difference can be obtained between two different

Table 6.6: Unsaturated DLO parameters for the surface footing using average s and S_r values.

H_w (m)	H_c (m)	a (kPa^{-1})	s_o (kPa)	$s_{average}$ (kPa)	$S_{r(average)}$ %
0.0	0.2344	0.7	2.3	0	100
0.22	0.2344	0.7	2.3	2.158	100
0.387	0.2344	0.7	2.3	3.796	35
0.558	0.2344	0.7	2.3	5.58	11.4

scale factors). The difference between a scale factor of 200 and 300 is about 3.3% which has an insignificant effect. The nodal spacing of B/6 (scale factor of 200) is; therefore, selected which also reduced the computational time. Where B is footing width.

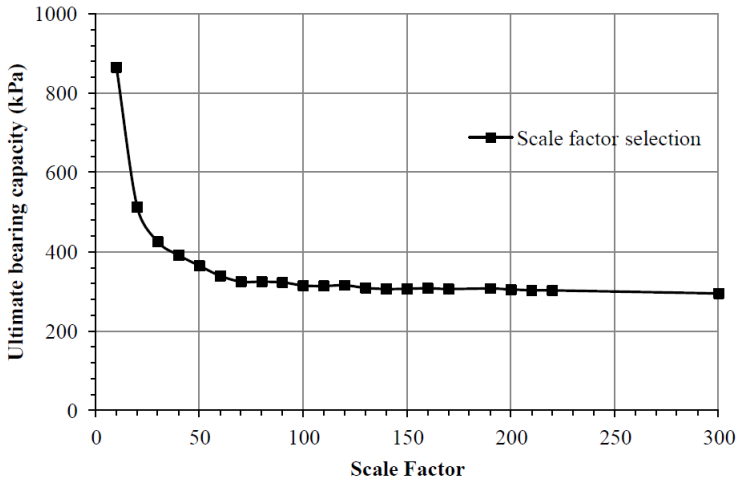

Figure 6.18: Selecting an adequate scale factor for the surface footing for $s = 3.796$ kPa at $\phi' = 45^o$.

6.7.1.1 Results for surface footing

A range of design values of the internal friction angle from 30^o to 45^o and the cohesion from 0 to 4 kPa are utilised for this comparison. This is based on the experimental direct shear results (presented in Chapter 4) in which both ϕ and c increased due to the effect of the unsaturated conditions.

Figures 6.19a, b, c and d show the ultimate experimental bearing capacity (q_{ult}) values (including repeat tests) for four average applied suction values compared with the modified DLO method results for the range of assumed friction angle and cohesion values. As a reminder for the reader, the experimental ultimate bearing capacity is defined as the maximum bearing capacity value at the peak or at the end of the test (when no distinguished peak can be picked) experienced by the soil. Series (S-I) and (S-II) in the legend of Figs. 6.19a and b represent the range of the experimental applied suctions (e.g. see Subsection 4.10.1.1 and 4.10.1.2) and so on.

The experimental ultimate bearing capacity values are plotted in Figs. 6.19a, b, c and d using the two different ϕ values 39.15^o and 44.1^o obtained previously for the dry sand using the direct shear test (see Table 4.1). The ultimate bearing capacity values in Fig. 6.19a for the fully saturated case are between 25-38 kPa, excluding the high values which are explained previously in Subsection 4.10.1.1- see Fig. 4.32. The mobilized ϕ obtained using

the direct shear test for the dry sand at low normal stresses (43.64^o), see Section 4.12, was close to the ϕ obtained for the dry sand at high normal stresses (44.1^o). This implies that the same range of ϕ may also mobilized in the bearing capacity test for the fully saturated case.

The conclusion from Figs. 6.19a, b, c and d is that there are possibilities of different values of both c between 0 to 4 kPa and ϕ in the range of 39.15^o and 44.1^o mobilized in the experimental bearing capacity test. The PIV analysis also confirmed this fact in which the unsaturated samples showed higher dilation rate (see Figs. 4.63). Note that at $\phi = 39.15^o$, the unsaturated samples seem to gain higher cohesion when compared to the saturated samples. Also, at $\phi = 39.15^o$ some of the experimental data show high ultimate bearing capacity values (higher than curve of $c = 4$ kPa), however, at $\phi = 44.1^o$, the data are fitted between $c = 0$ and 2 kPa.

The small values of cohesion from 0 - 4 kPa utilised in the numerical DLO matched the experimental bearing capacity data as the effect of any small change of cohesion in the bearing capacity equation is higher than that for the shear strength equation obtained from direct shear tests. In other words, cohesion is scaled up by bearing capacity factor Nc in the bearing capacity equation (see Eq. 2.34 - first term) which in turns increases the bearing capacity value by an amount well in excess of the increase of shear strength due to the cohesion intercept in the direct shear test using the Mohr-Coulomb failure envelope fit (see Eq. 2.19 - first term). This may support that such smaller values of cohesion, compared to that obtained from the direct shear tests for the saturated and unsaturated samples, are mobilized in the experimental bearing capacity tests. Also, the effect of small change in suction, for example, from 2 to 6 kPa, provided a significant increase in bearing capacity value of about 160 kPa at $c = 4$ kPa and $\phi = 45^o$ (see Figs. 6.19b and d). This is because any change of suction and degree of saturation (sS_r) in the numerical analysis in this study is modelled as an apparent cohesion increase (see Eq. 6.6) which in turns is added directly to the energy dissipation equation (see Eq. 2.40).

The failure mechanisms for the four applied suctions obtained using modified DLO are shown in Figs. 6.20a, b, c and d using $c = 0$ kPa and $\phi = 45^o$. The case of $s = 2.158$ kPa shows a deeper and a wider failure mechanism compared to the other cases. This was also consistent with the numerical obtained bearing capacity value for this case (higher bearing capacity obtained for this suction- see Fig. 6.21a). The failure mechanisms shown in Figs. 6.19a, b, c and d have a reasonable match to Figs. 4.63a, b, c, d and e obtained using the PIV analysis.

Figures 6.21a and b show the comparison of the modified DLO results versus the experimental ultimate bearing capacity for a range of the applied suctions. In the legend, the number (e.g. 1, 2,...n) after the ϕ value for the experimental data denotes test No.1, 2 and so on. For those experimental data located below the curve of $c = 0$ kPa, this can be attributed to the fact that a smaller ϕ than the fitted value of 44.1^o might be mobilized in the test. This will bring down the values obtained by DLO to match better the experimental data at smaller ϕ.

6.7.2 Footing placed 5 cm depth

The experimental results for the strip footing buried at 5 cm depth in the soil which were presented in Chapter 4 are compared against the DLO method in this section. Figure 6.22a shows the schematic diagram of the footing, while Fig. 6.22b shows the same footing but with the 5 cm of soil above the footing replaced by a surcharge. The surcharge value of

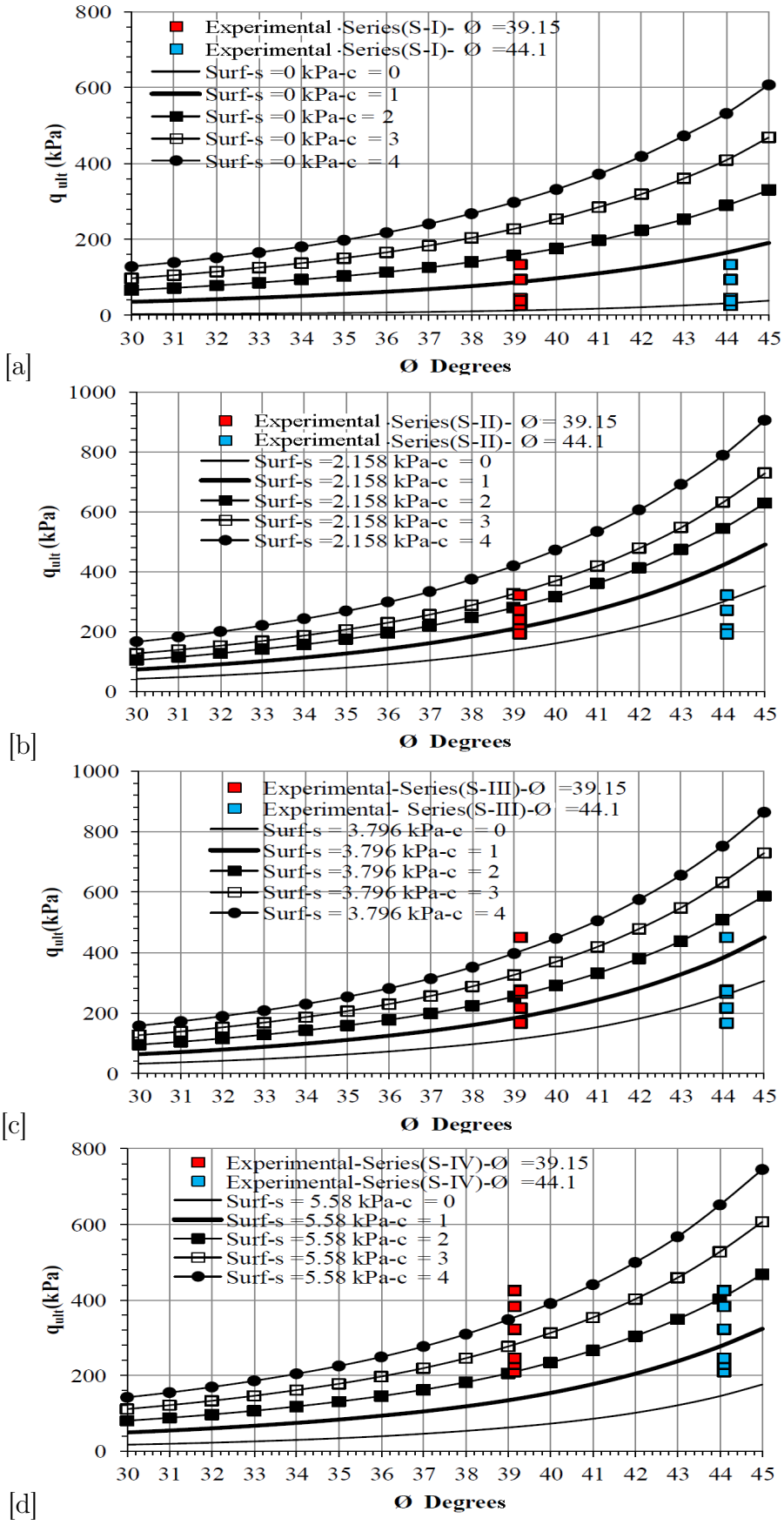

Figure 6.19: Comparison between the modified DLO method and the experimental peak bearing capacity for the surface footing for a range of assumed c and ϕ values for (a) $s = 0$ kPa (b) $s = 2.158$ kPa (c) $s = 3.796$ kPa (d) $s = 5.58$ kPa. Where s is nominal surface suction.

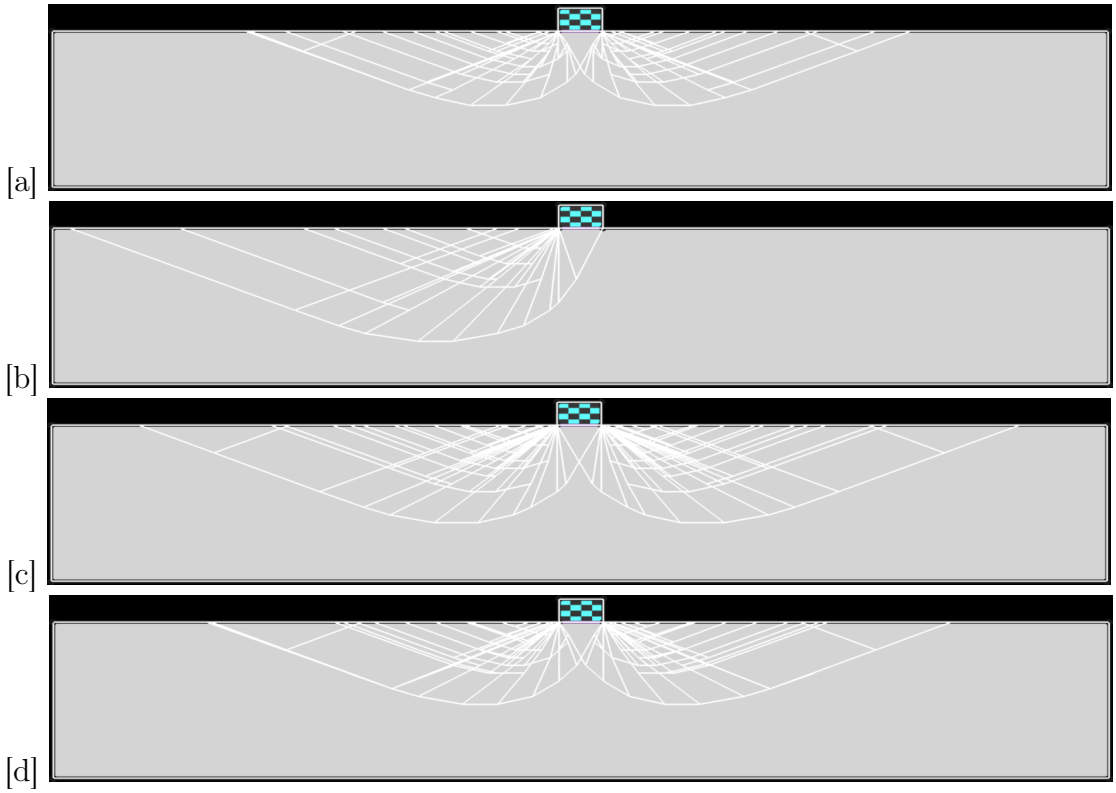

Figure 6.20: Failure mechanism using $c = 0$ kPa and $\phi = 45^o$ for the surface footing for (a) $s = 0$ kPa (b) $s = 2.158$ kPa (c) $s = 3.796$ kPa and (d) $s = 5.58$ kPa. Where s is nominal surface suction.

the soil above the footing for the average $s = 0$ and 1.788 kPa is equal to $q = \gamma^{'} \times D_f = (19.33 - 9.81) \times 0.05 = 0.476$ kPa. While for the average $s = 3.089$ and 5.274 kPa is equal to $q = \gamma \times D_f = 17.315 \times 0.05 = 0.8657$ kPa.

In this analysis, the averaged applied suction head for the repeat tests was taken as the distance from the water table to the footing base. This is to be consistent with the case of the surface footing. Once again, only 0.1 m depth below the footing is modelled. The x-boundary of the problem is extended to 0.4 m on both sides of the footing to prevent failure mechanism restriction at high internal friction angles (see Fig. 6.22b). As before, the nodal spacing of B/6 (scale factor of 200) is selected. Table 6.7 shows the unsaturated parameters used in the modelling of the strip footing buried at 5 cm depth and the other parameters are given in Table 6.5. H_w and H_c are defined previously in Fig. 6.17.

Table 6.7: Unsaturated DLO parameters for the buried footing using average s and S_r values.

H_w (m)	H_c (m)	a (kPa^{-1})	s_o (kPa)	$s_{average}$ (kPa)	$S_{r(average)}\%$
0.1	0.2344	0.7	2.3	0	100
0.182	0.2344	0.7	2.3	1.788	100
0.315	0.2344	0.7	2.3	3.089	57.53
0.537	0.2344	0.7	2.3	5.274	12.46

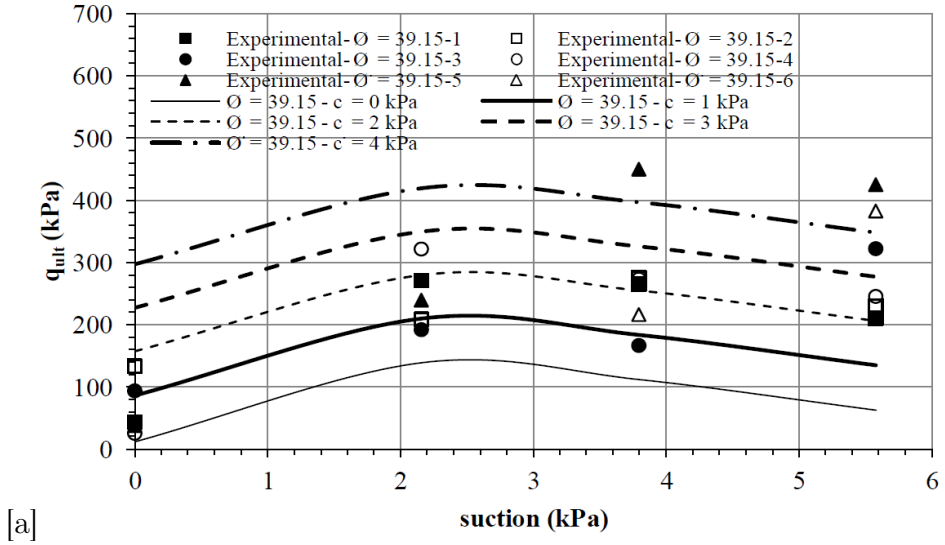

[a]

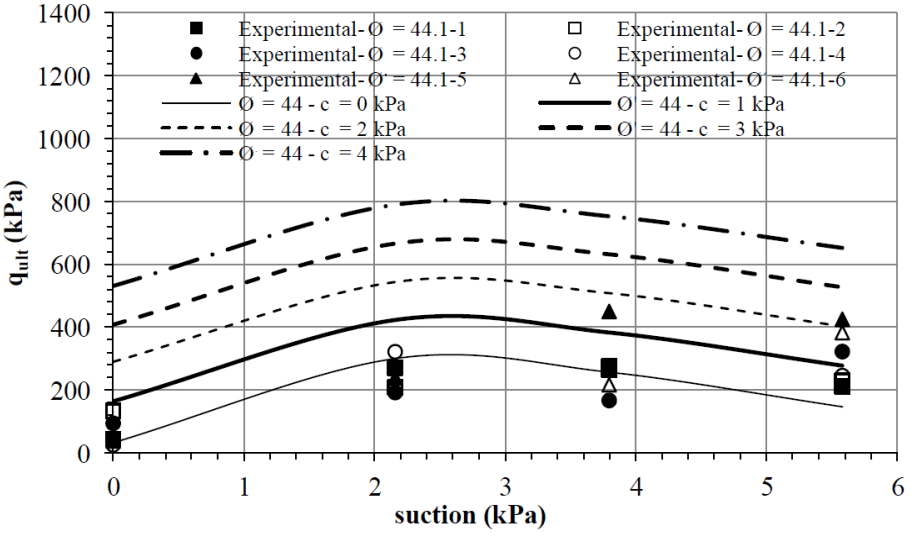

[b]

Figure 6.21: Comparison between the modified DLO method and the experimental peak bearing capacity for the surface footing for a range of assumed c values at (a) $\phi = 39.15^o$ (b) $\phi = 44.1^o$.

6.7.2.1 Verification of the replacement procedure

As a double check of the LimitState:GEO software using the replacement procedure, a fully saturated case study with $\phi = 30^o$ and $c = 0$ kPa is modelled for both cases shown in Fig. 6.22a and b. The bearing capacity values using the DLO method were 10.70 and 12.74 kN/m^2 for the cases in Fig. 6.22a and b, respectively. The is equivalent to a difference of 19.06%. The DLO result for the case in Fig. 6.22b was then compared to the ABC software. The difference between the numerical model case in Fig. 6.22b given by the LimitState:GEO software (12.74 kN/m^2) and the ABC software (12.19 kN/m^2) was 4.5% which can be considered insignificant.

6.7.2.2 Results for footing buried at 5 cm depth

Figures 6.23a, b, c and d show the modified DLO results against the experimental ultimate bearing capacity values (including repeat tests) for four different applied suctions (denoted (D-I), (D-II), (D-III) and (D-IV) in the figure legend - see subsection 4.10.2.1 and followed

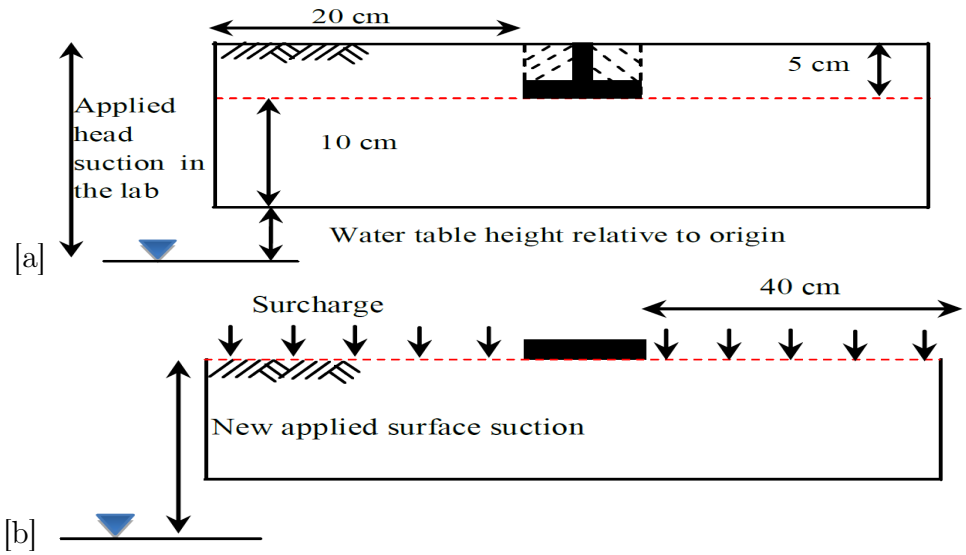

Figure 6.22: (a) Footing placed at 5 cm depth (b) Replacing soil above the footing by a surcharge.

subsections) and with a range of design values of the internal friction angle and cohesion. As before, the experimental ultimate bearing capacity values for the buried footing are plotted in the figures assuming either one of the two different ϕ values: 39.15^o and 44.1^o.

The implication of Fig. 6.23a, b, c and d is that a higher internal friction angle is more likely as the experimental data fitted reasonably at $\phi = 44.1^o$. Figures 6.24a, b, c and d show the failure mechanisms obtained for the four series using the modified DLO method. As for the surface footing case, the Series (D-II) shows a deeper and a wider failure mechanism than the other cases.

The comparison of the modified DLO solutions versus the experimental ultimate bearing capacity results for a range of the applied suctions is shown in Figs. 6.25a and b. Once more, some of the experimental results overestimated the numerical results for $\phi = 39.15^o$ and $c = 4$ kPa. Figure 6.25b, however, shows better fit of the experimental data at $\phi = 44.1^o$ with c value less than 3 kPa. Some of the data located below the case of $c = 0$ kPa would imply that a smaller ϕ than 44.1^o might be mobilized in the test.

6.7.3 Summary of the bearing capacity study

The direct shear results presented in Chapter 4 that included an increase of the internal friction angle and cohesion of the unsaturated sand were used as evidence to assume a range of cohesion and internal friction angle values in the numerical analysis. The results of the numerical study showed reasonable agreement for both the experimental data of the surface and buried footings and indicate a strong possibility that the shear strength parameters increased in the bearing capacity test due to unsaturated conditions.

6.8 Summary of the chapter

This chapter addressed the modification of an existing DLO Matlab code. The modified DLO code, UNSAT-DLO code, was then evaluated using a retaining wall case study and incorporated into a research version of the LimitState:GEO software. The modified Lim-

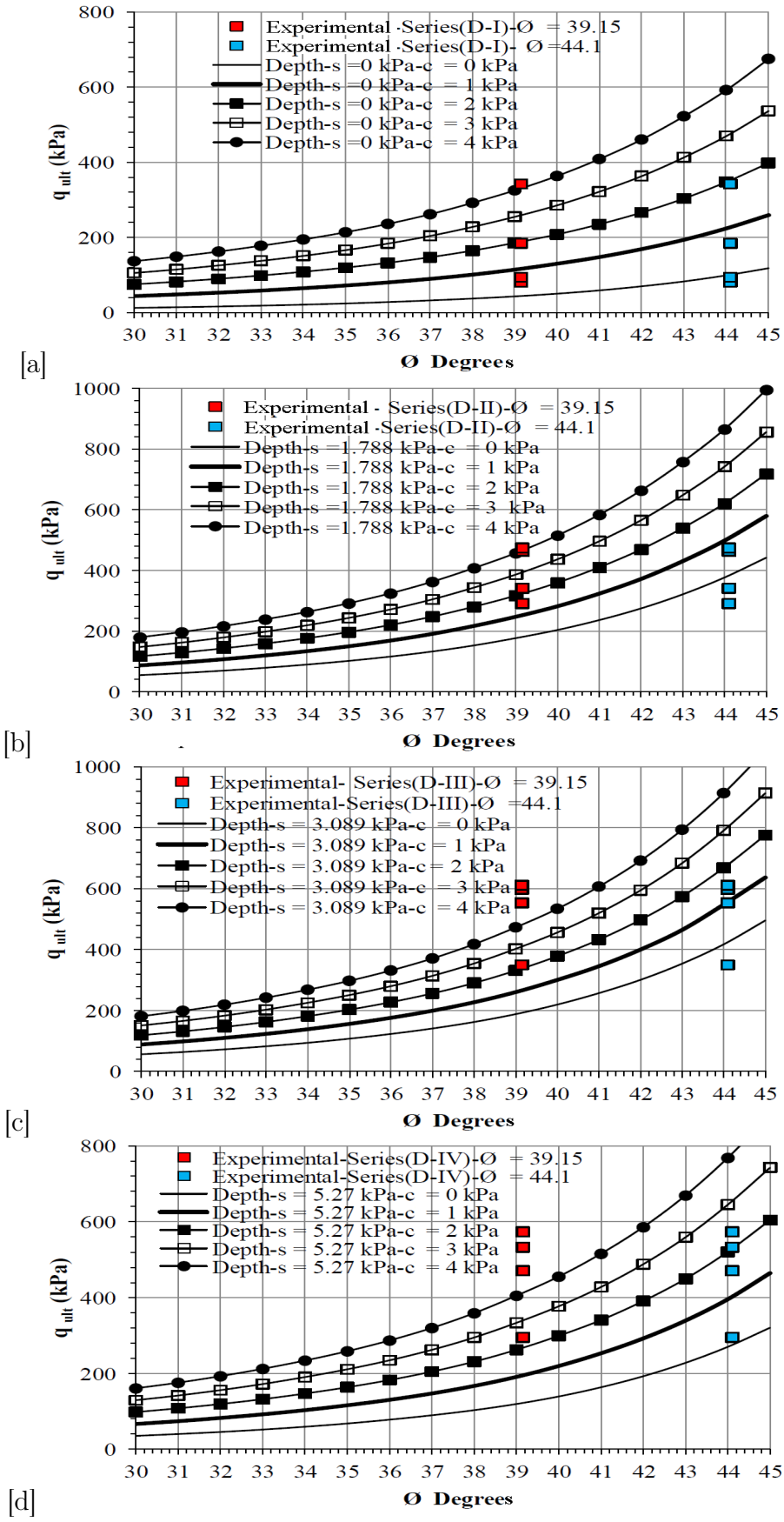

Figure 6.23: Comparison between the modified DLO method and the experimental peak bearing capacity for the buried footing for a range of assumed c and ϕ values for (a) $s = 0$ kPa (b) $s = 1.788$ kPa (c) $s = 3.089$ kPa (d) $s = 5.274$ kPa.

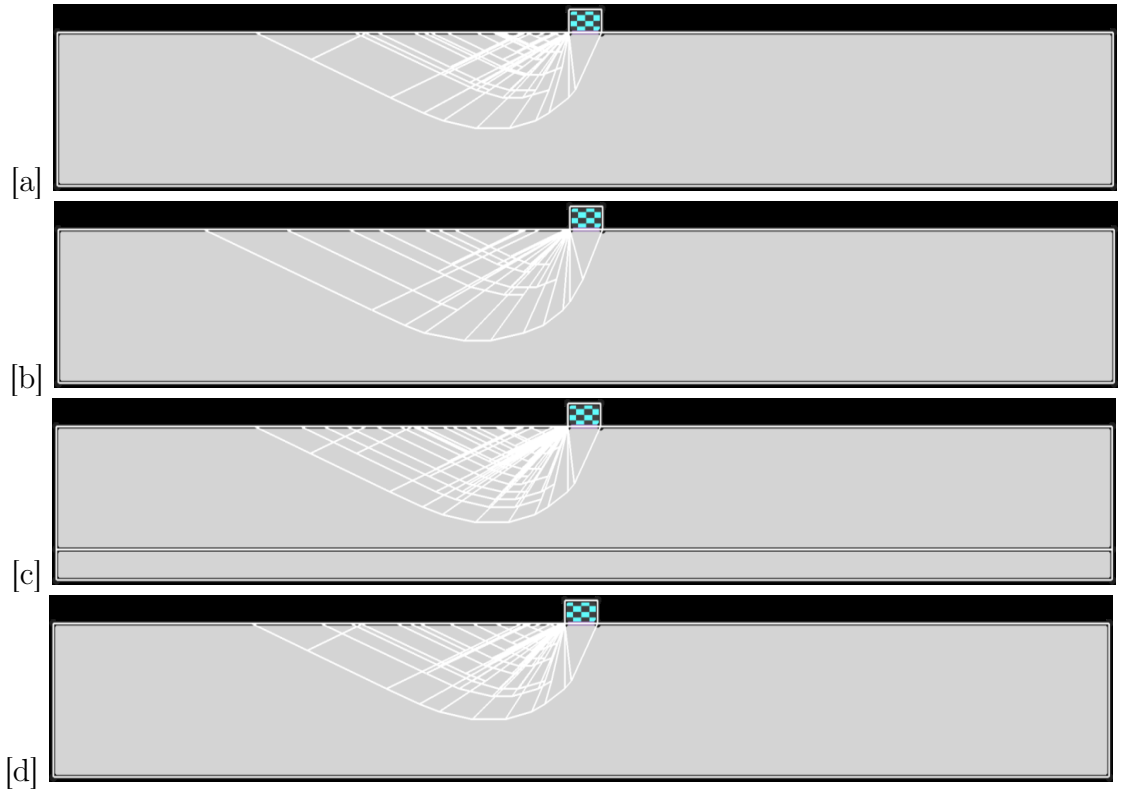

Figure 6.24: Failure mechanism using $c = 0$ kPa and $\phi = 45^o$ for the buried footing for (a) $s = 0$ kPa (D-I) (b) $s = 1.788$ kPa (D-II) (c) $s = 3.089$ kPa (D-III) and (d) $s = 5.274$ kPa (D-IV).

itState:GEO software was then used to conduct a parametric study on total passive earth pressure, for a sandy soil and a silt loam with walls with different interface frictions, and a comparative study for surface and buried footings. These were to examine the effect of the degree of saturation and suction on the strength.

The study of the passive earth pressure demonstrated the effect of unsaturated conditions on the total passive earth thrust. Also, the influence of the wall friction and the internal friction angle were examined. In general, results of the modified LimitState:GEO software showed an increase of the total passive earth pressure for partially saturated soils when compared to the Rankine method. An increase of 46.8% in normalized total passive thrust ($\frac{Pp}{H^2\ \gamma_w}$) for a frictionless wall (FL) at $\phi^{'} = 30^o$ and 0.6 m depth of water table below the base of the wall was achieved due to the effect of unsaturated conditions for the sandy soil when compared to its counterpart Rankine method result, while an increase by a factor of 3.08 for the silt loam at $Y_w = 3$ m below the base and $\phi^{'} = 30^o$ for the FL gained when compared to the counterpart Rankine method result.

The comparison of the modified LimitState:GEO software with the experimental bearing capacity study was performed by selecting different values of internal friction angle and cohesion. The bearing capacity for the unsaturated samples for the surface and buried footings increased by a factor of about 10 and 4.3 fold, respectively (typically the peak) at $\phi = 44.1^o$ and $c = 0$ kPa when compared to the fully saturated case. The effect of the suction on the failure mechanism was also examined and showed that a wider and a deeper failure mechanism can be obtained near the air entry value.

In general, the comparison showed reasonable agreement with the experimental data for both the surface and buried footings. The possibility of an increase of both the internal

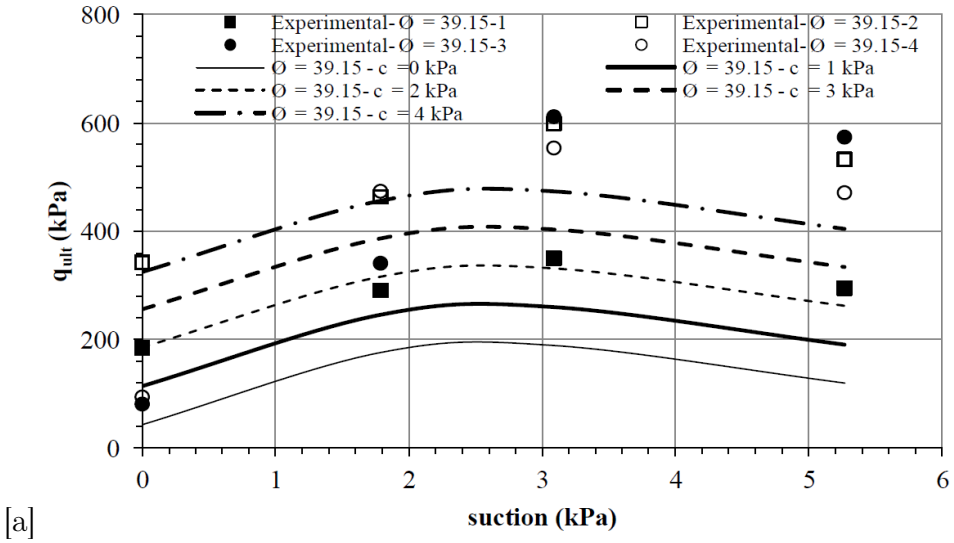

[a]

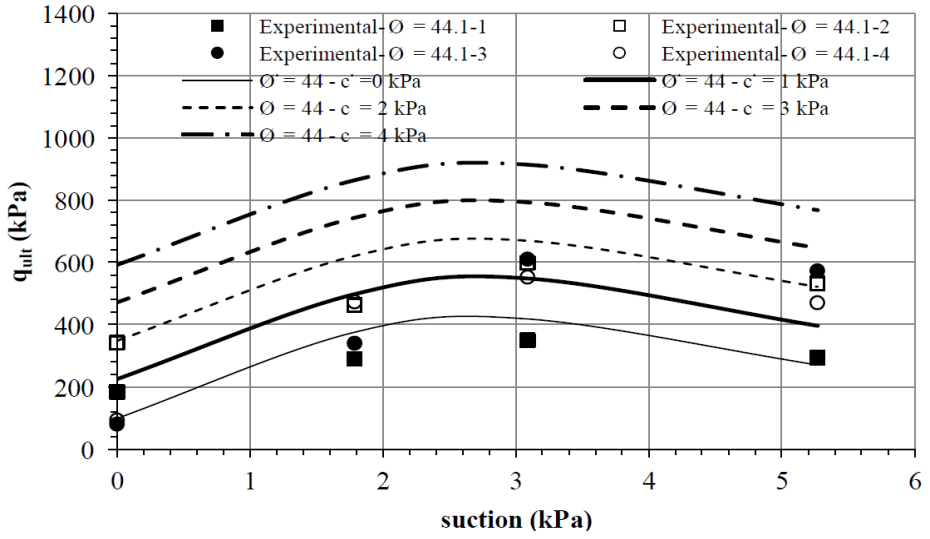

[b]

Figure 6.25: Comparison between the modified DLO method and the experimental peak bearing capacity for the buried footing for a range of assumed c values at (a) $\phi = 39.15^o$ (b) $\phi = 44.1^o$.

friction angle and the cohesion compared to the dry case is strongly indicated in the bearing capacity tests.

To summarize, the modified DLO approach showed the ability of the method to model any change of suction and degree of saturation on the shear strength of the unsaturated soils through determining the collapse load for a wide range of problems such as retaining walls and foundations.

Chapter 7

Discussion

7.1 Introduction

This chapter discusses the results of the experimental and numerical studies conducted in this research. The aim of the experimental tests was to develop a shear strength equation for unsaturated sand which is presented and discussed first in this chapter. Following this, the unexpected phenomena obtained in both direct shear and the bearing capacity tests are discussed. Finally, the numerical results undertaken in this research are reviewed.

7.2 Reformulated SWCC and shear strength equation

The SWCC equation which was proposed by Stanier & Tarantino (2010) (Eq. 5.6) was reformulated in this study by taking into consideration the effect of the air entry value. The equation was then compared with the experimental data using different types of soils within a range of suctions from zero to the residual suction. The reformulated SWCC equations (Eqs. 5.9 and 5.10) fitted the experimental data well (see Fig. 5.9).

This study also evaluated the shear strength equation which was proposed by Öberg & Sällfors (1997). The evaluation showed poor agreement with experimental results found in the literature for different types of soils and within a wide range of applied suctions. Reformulation of the Öberg & Sällfors (1997) equation was therefore proposed based on values of s, S_r, ϕ and c occurring at peak strength and termed s^*, S_r^*, ϕ^* and c^*. The reformulated shear strength equation showed good agreement with the experimental direct shear test results conducted in this study as shown in Subsections 5.3.3 and 5.3.4. However, it does depend on parameters being measured for different suction levels, with ϕ^* and c^* being dominant.

Figure 7.1 shows the average measured value of s^* at peak and the inferred value of $s^*S_r^*$ at different normal stresses. It is clear that there is no way that the strength increase for saturated and unsaturated samples can be attributed to the effect of the $s^*S_r^*$ term due to its small effect (maximum increase in strength due to $s^*S_r^*$ at $s^* = 2.14$ kPa and high degree of saturation ($S_r^* = 0.98$) is equal to 2.09 kPa $\times$ tanϕ^* using Eq. 5.14). This is equivalent to an increase of strength about 2.6 kPa well below that observed in the experiments.

Relating c^* and ϕ^* to changes in suction remains a challenge. The experimental data is discussed in more detail in the next section.

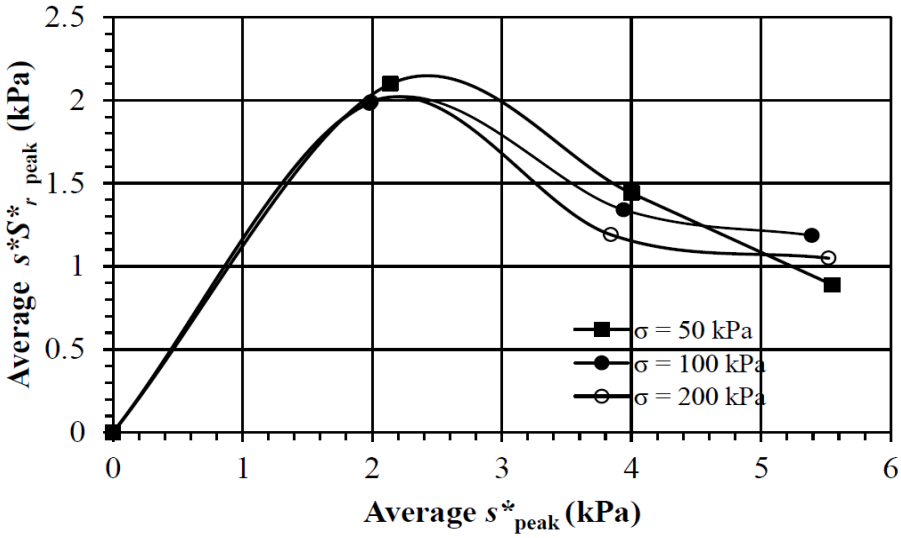

Figure 7.1: Average measured s^* and average $s^*S_r^*$ at peak for different normal stresses (the data were plotted based on Table 5.9).

7.3 Experimental observations

7.3.1 Increase of ϕ^* and c^* due to unsaturated conditions

The increase of ϕ^* and c^* observed for the saturated and unsaturated samples which was presented in Section 4.7 is re-plotted in Figs. 7.2a, b and c. The data are plotted based on Table 4.7 in which s in the figures presents the nominal applied suction value. Results for the repeat tests confirmed the increase of ϕ^*.

It is intriguing that the average cohesion intercept, c^* of the sand approximately doubles and that average ϕ^*_{peak} also increased by $\approx$ 2.5 degrees due to saturation and up to 7.5 degrees for partially saturated soil when compared with the dry conditions. As the former result not in accordance with expected behaviour, further tests were carried out where an initially dry sample was sheared to an initial horizontal displacement of about 3.2 mm and then saturated and shearing continued for both the drained condition and the case when the effluent port was closed during the test so as not to allow any water in or out of the specimen from the burette. The closed effluent port case was undertaken to double check the fully saturated condition (water expelled from the sample for the drained case during shearing led to a slight decrease of about 1% or less in the degree of saturation). The strength and dilatancy rate (see Figs. 4.18c and d) were observed to rise after saturation in line with the currently reported tests. These differences are challenging to explain using conventional theory.

Figure 7.2d shows the average shear resistance at peak versus the normal stress for the five applied suctions. Based on the direct shear results, all unsaturated results would have been expected to map closely onto the "dry" line in Fig. 7.2d. However it is clear that unsaturated conditions give rise to significant gain in strength. Significant increases in shear strength due to full and partial saturation were observed well in excess of that expected by the action of pore pressure or suction within a simple effective stress framework. The data presented here are a part of a technical note in preparation (presented in Appendix A).

The mechanisms of this effect cannot be related only to the effect of the suction in the effective stress equation (Eq. 5.14) even if it is assumed to act as if present in the entire pore

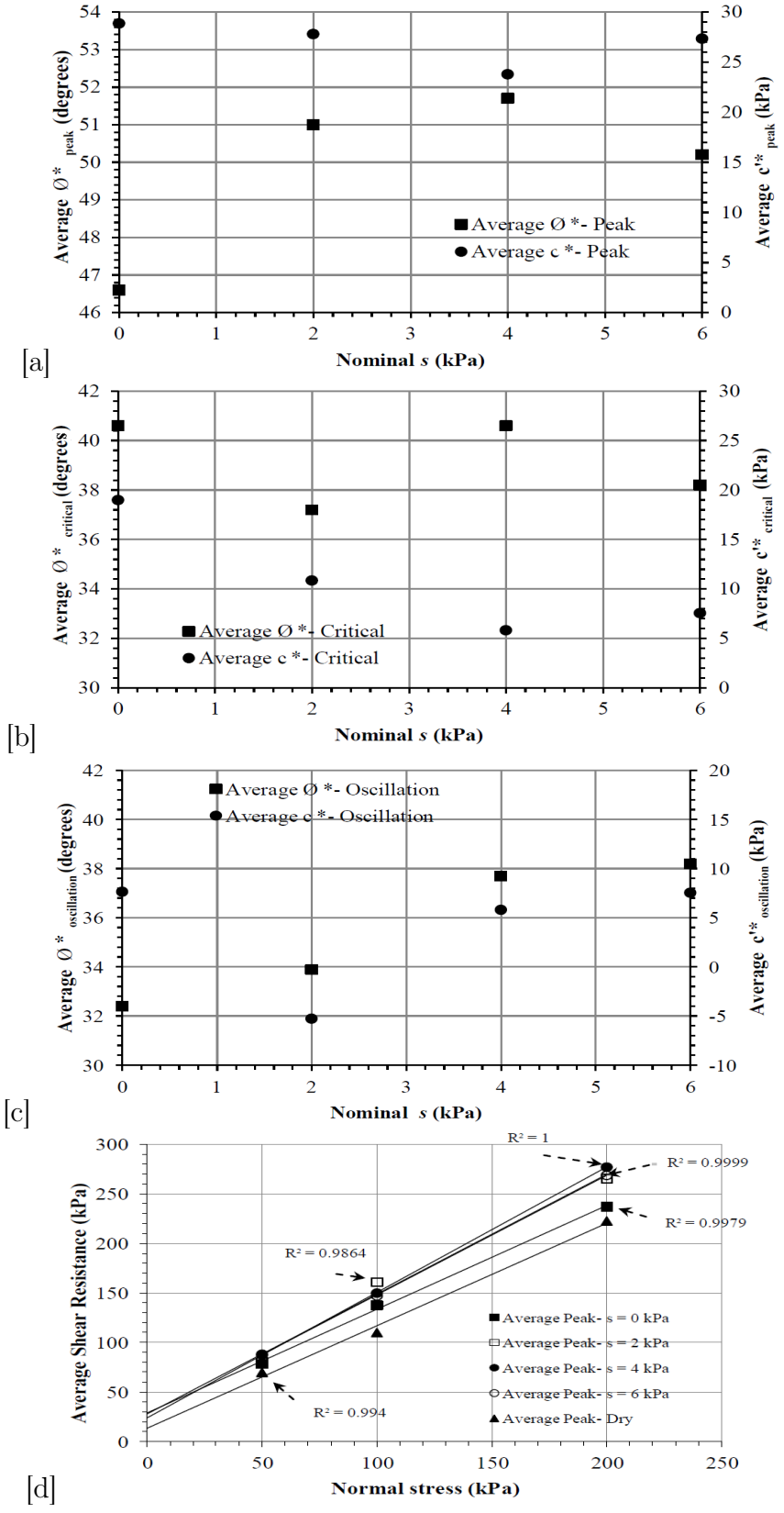

Figure 7.2: Increase of average ϕ^* and c^* due to unsaturated conditions at (a) Peak (b) Critical state (c) Oscillation (d) Average peak shear resistance versus normal stress for five applied suctions.

space. It is proposed that the increase of the shear strength parameters can be attributed to changes in soil fabric. Soil fabric is significantly affected by dilation, Bolton (1986). Dilation for dry soils is affected by several factors such as stress level, soil density and friction, Houlsby (1991). Soil fabric for unsaturated soils, on the other hand, is affected by the suction level, as shown by Simms & Yanful (2001) (who investigated a compacted glacial till), in addition to the three preceding factors stated by Houlsby (1991). This implies different soil structures at different applied suctions.

It is hypothesised that when soil desaturates (suction increases), the drying creates aggregations of the particles. On desaturation, air enters larger pore spaces (inter-aggregate pores) with water filling the smaller voids (intra-aggregate pores) and forming menisci around these aggregates, see Fig. 2.21a. The aggregate structure is then preserved during subsequent wetting and drying cycles, Murray et al. (2008).

The aggregation changes the soil fabric, as also observed by Toll & Ong (2003) and Fern et al. (2014), and hence there is a possibility of the dilation rate increase (as observed in sand tested in this study - see Figs. 4.12 to 4.14) which leads to increase shear strength (see Figs. 4.3 to 4.5). This leads to an increase in the internal friction angle and the cohesion of the soil. This is also obtained by Toll (2000) and Toll et al. (2008).

It is also hypothesised that the difference in the soil fabrics due to the different applied suctions led to a scatter in peak shear strength obtained for the sand used in this study (e.g. see Fig. 4.6a). This is attributed to the menisci arrangement between the particles. In other words, the way of arranging menisci between the particles at each applied suction (e.g. s = 2 kPa and s = 4 kPa) was not consistent and this significantly affects shear strength and this explains why differences in ϕ^* and c^* for the repeat tests were obtained (e.g. see Table 4.4 - s = 2 kPa- Test 1, 2 and 3).

7.3.2 Drying behaviour for unsaturated samples

The water level in the burette for both the direct shear (Table 4.3 and Figs. 4.33c and d) and the bearing capacity tests (Figs. 4.38a and b) was seen to rise in conjunction with normal load application. During shearing, the water level in the burette for the direct shear and bearing capacity tests also increased indicating continued water content loss from the samples. This was over and above any change in saturation that would arise due to volume change. There was insufficient time to investigate this fully, however, discussion of the phenomenon in the context of the SWCC is presented and a simple hypothesis to explain this behaviour is proposed. The data presented here are a part of a conference paper, Shwan (2016).

The samples' paths on the SWCC in Figs. 4.28 to 4.30, presented in Chapter 4, typically showed drying behaviour with only a few wetting cases. The wetting path A to B in Fig. 7.3 is the expected behaviour which is attributed to an increase of degree of saturation during shearing (due to decrease in void ratio) and hence in suction.

The drying path A to C in Fig. 7.3, on the other hand, would not be expected but this corresponds to the observed increase in water level in the burette during shearing. As water is expelled from the sample towards the burette during shearing (S_r decreases), the distance from the water level in the burette to the sample surface decreased (s decreases). This means both S_r and s decreased when water is expelled from the sample. A similar situation occurs when water is imbibed by the sample during shearing (both S_r and s increase). The drying behaviour appears to be associated with a decrease in suction. This is due to the constraints imposed by the HCT as used in this study, where a flow of water out of the

specimen produces a change in head (loss of suction).

In general, drying behaviour was observed for most samples in spite of whether the samples follow path A to C or A to E. These paths are described in more details below:

1. Scenario I- path A to C
   The drying behaviour on the SWCC for the direct shear results were analysed based on this scenario, Figs. 4.28 to 4.30, due to the assumed direct relationship between s and S_r.

2. Scenario II- path A to D
   If suction is assumed to be constant (omitting the water level change in the burette), the sample will follow path A to D. This scenario is unlikely to happen because suction will change with any change of degree of saturation.

3. Scenario III- path A to E
   This scenario is the most likely case to be followed by the sample during drying. Here, the actual measurement of the suction, for example using tensiometers placed into the sample, is required.

The importance of studying the drying behaviour on the SWCC for Scenario-III is highlighted to that such finding is not reported (to the knowledge of the researcher) in the literature yet and is worthy of further work.

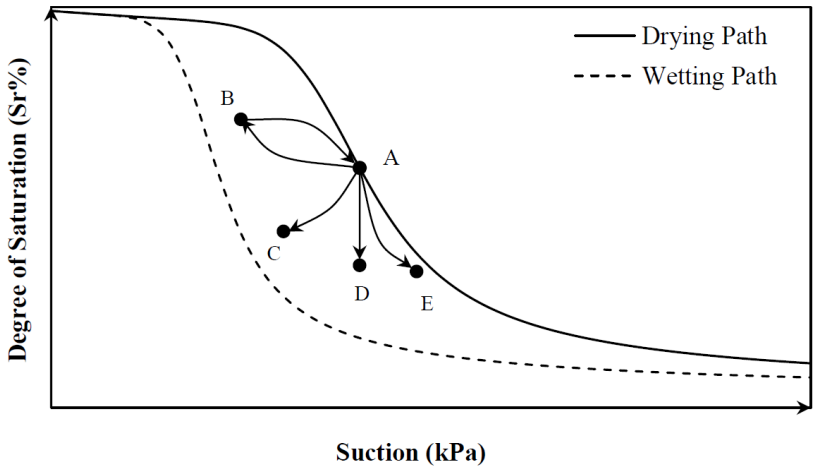

Figure 7.3: Typical SWCC showing scanning paths.

7.3.3 Wetting collapse at a high degree of saturation

This section presents discussion on the wetting collapse behaviour which was observed at a high degree of saturation ($s = 2$ kPa) for the unsaturated sand during shearing. The data presented here are a part of a conference paper (presented in Appendix E), Shwan (2015).

Wetting collapse was observed where the response was punctuated by a sudden loss of strength and volume followed by a rapid recovery of strength as presented previously in Section 4.8 (see Figs. 4.26a, b and c). After this, further repeated sudden losses of strength were observed but without a significant loss of volume. The sudden volume loss was most evident for the samples with the highest saturation. Dry and saturated samples generally displayed continuous oscillations in strength, with no collapse. Figures 7.4a, b and c show

the vertical displacement versus horizontal displacement for three repeat tests (1, 2 and 3) for $s = 2$ kPa. This suction is close to the air-entry value, 2.3 kPa, of the sand used (see Fig. 4.1). The sudden decrease in volume was a plastic deformation change as irreversible rearrangement of the particles happened.

This behaviour is attributed to (i): high degree of saturation and (ii): availability of the space between the particles. To further support the significance of the high degree of saturation on wetting collapse, Table 7.1 is presented here for all other repeat tests for $s = 2$ kPa and at $\sigma = 50$, 100 and 200 kPa.

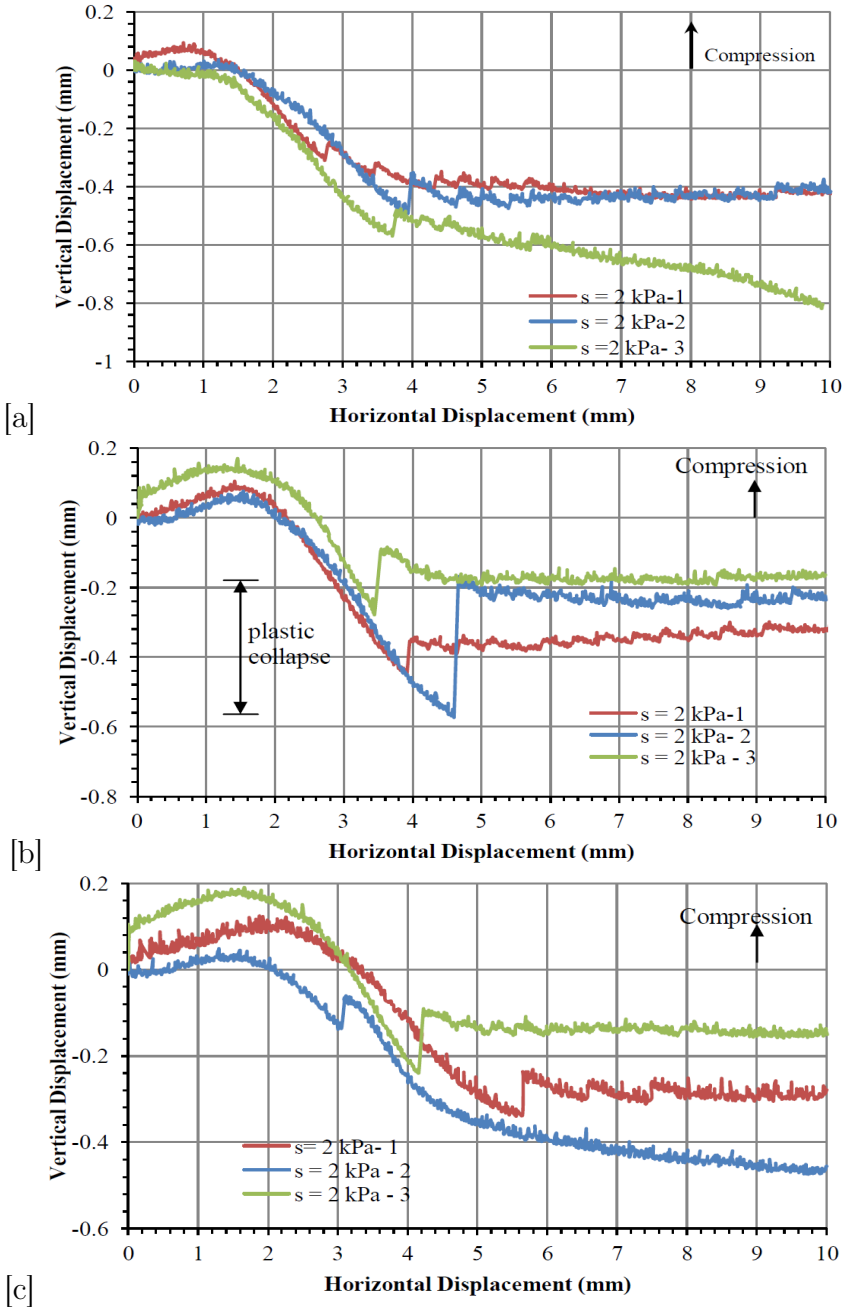

Figure 7.4: Vertical displacement versus horizontal displacement for $s = 2$ kPa for three repeat tests at (a) $\sigma = 50$ kPa (b) $\sigma = 100$ kPa (c) $\sigma = 200$ kPa.

For $s = 2$ kPa, the initial saturations S_{ri} were between (88.9 - 91.5)% for the three repeat tests, while an increase of the degree of saturation at the plastic collapse S_{rp} can

Table 7.1: Degree of saturation at initial and wetting collapse for $s = 2$ kPa.

σ kPa	S_{ri}	S_{rp}	Wetting Collapse %
50-1	91.5	100.4	16
50-2	90.4	96.2	24.3
50-3	89.9	91.6	15
100-1	90.8	101	21.1
100-2	90	96	67.7
100-3	88.9	106.8	65.2
200-1	90.2	111.2	26.9
200-2	89.8	100.1	45.4
200-3	89	113.8	61.7

be seen during the shearing. The S_{ri} value is calculated by knowing the amount of water expelled from the sample during application of the suction (before shearing), the volume of the sample (which is constant) and the initial void ratio ($e = 0.70$ - see Table 4.1). Values of S_{rp} were obtained by performing linear interpolation of the S_r values before and after the collapse. The values of S_r before and after collapse were obtained by knowing the amount of water expelled or imbibed by the sample during shearing. Here the volume of the sample and void ratio are calculated based on the vertical LVDT reading at the corresponding stage of shearing (before or after the collapse). However, this is an estimation of the volume and explains why some values of S_{rp} higher than 100% are obtained. In all cases, collapse happened at a time not coinciding with the time of capturing the water level in the burette by the camera, thus requiring interpolation. However, the errors are expected to be small since the maximum difference between S_r before and after the collapse was 1.5%. Results in Table 7.1 showed that up to 67% of the overall volume change during the test up to that point could be lost during the sudden change, typically post peak. In Table 7.1, the wetting collapse % was calculated as the percentage difference between the vertical displacement just before and after collapse. Note that the unsaturated samples prepared at $s = 4$ ($S_{ri} =$ 24-36%) and $s = 6$ kPa ($S_{ri} =$ 15-22%) did not show wetting collapse (see Figs. 4.12, 4.13 and 4.14) indicating the dominance of the high degree of saturation on this behaviour.

The degree of collapse highly depends on the availability of the space between the particles which is the second reason for this behaviour. In other words, wetting collapse is significantly affected by the interlocking position for the particles. The fully saturated samples (in spite of their high S_{ri}) did not show any wetting collapse. This is may be because of unavailability of air space between the particles (see Figs. 4.12, 4.13 and 4.14).

In conclusions, it is hypothesised that this behaviour was due to the high degree of saturation and the availability of the space between the particles.

7.3.4 Oscillatory behaviour

Oscillatory or stick-slip behaviour was observed where the response was punctuated by a sudden loss of strength (and volume at a high degree of saturation for $s = 2$ kPa for the direct shear tests) then followed by a rapid recovery. Dry samples displayed this behaviour almost continuously (e.g. see Fig. 4.3a). This was also most evident for the samples with highest saturation. A few cases at lower degree of saturation showed oscillation (e.g. see Fig. 4.5c - $s = 4$ kPa-3 and Fig. 4.43). For the direct shear samples at $s = 2$ kPa, a large reduction of shear strength at each oscillation was observed, however, with a longer interval

between one oscillation to another. The oscillatory behaviour was primarily a post-peak behaviour (see Figs. 4.3 to 4.5) where only a few cases were observed, especially for the unsaturated samples, in which the oscillation happened prior to the peak.

As the shear band is a localization of the deformation in a thin layer, its thickness depends on the particle size. For sandy soils, the shear band thickness is about 15 times the particle size, Vermeer (1990) (see Section 2.9). If it is the case, the shear band developed for the dry sand tested in this study is equal to $0.1875 \times 15 = 2.8125$ mm, where 0.1875 is the average particle size (see Table 4.1- Section 4.1). This rules out the oscillatory behaviour being due to any anomalies due to the height($= 47$ mm) of the direct shear box where the shear band might interact with HAED.

The sudden loss in strength was observed to be systematically related to the contraction, while the recovery was attributed to the dilation. The schematic diagram shown in Figs. 7.5a and b is a suggested explanation for the stick-slip phenomenon. As the sand tested in this study showed rounded to sub-rounded particles and was classified as a poorly graded sand (SP), the oscillation behaviour can be related to the shape of the particles. The uniform shaped particles slip over the crest of the adjacent particles into the next existing pore. The particle slip causes a loss in shear strength and a reduction in volume (contraction). The contraction size can be associated with the particle size (the bigger particles, the higher contraction can be observed due to bigger space between the particles). The recovery of the shear strength, on the other hand, is attributed to the climbing of the particles towards the crest of the next adjacent particle. This climbing behaviour is associated with an increase in volume (dilation). This phenomenon is related to particle size and normal stress, Duttine et al. (2008). The oscillatory behaviour was observed with shorter interval between one oscillation to another for the dry samples tested under $\sigma = 50$ kPa when compared to $\sigma = 100$ and 200 kPa, see Figs. 4.3a, 4.4a and 4.5c.

For the unsaturated samples prepared at high suction ($s = 4$ and 6 kPa), the oscillatory behaviour was suppressed (except for a few cases) due to the effect of the aggregation as shown in Fig. 7.5c. It is hypothesised that clustering of the particles changed the size, shape of the macro particles and voids between the particles. Thus a single particle no longer exists and cannot drop to the neighbouring pore. The assemblage of the particles continues climbing and hence higher dilative behaviour is observed until the critical state reaches.

In conclusion, the oscillation behaviour was an unstable behaviour for the rounded to sub-rounded particles for the poorly graded sand used in the current work in which this phenomenon is significantly related to the particle shape and normal stress.

7.4 Conceptual model based on the preceding experimental observations

To summarise, the effect of suction had a direct influence on the behaviour of the sand tested in this study. It is hypothesised that suction caused accumulations and aggregations of the particles by menisci which led to changes in the soil fabric. This led to an increase in the shear resistance and shear strength parameters of the sand.

The changes in soil fabric caused a distinct peak in shear strength during shearing for unsaturated samples in which this was not the case for the fully dry samples. A higher dilatancy rate was also observed for the unsaturated samples over the dry and fully saturated samples. Additionally, the dilative behaviour caused drying phenomenon for the unsaturated samples.

Suction had also a direct influence on the stability of the sand tested in this study. The oscillatory behaviour, for example, was suppressed for most of the unsaturated samples at low degrees of saturation due to the effect of the aggregation. The aggregation changed size, shape of the particles and voids between the particles. A drop of a single particle, therefore, eliminated (see Figs. 7.5a, b and c). Wetting collapse was not seen in the unsaturated samples due to the effect of suction and saturation (at low degrees of saturation) as higher strength was gained due to the effect of menisci. Generally, the small range of the nominal suction (0 - 6 kPa) had a significant effect on the hydro-mechanical behaviour of the sand used in this study.

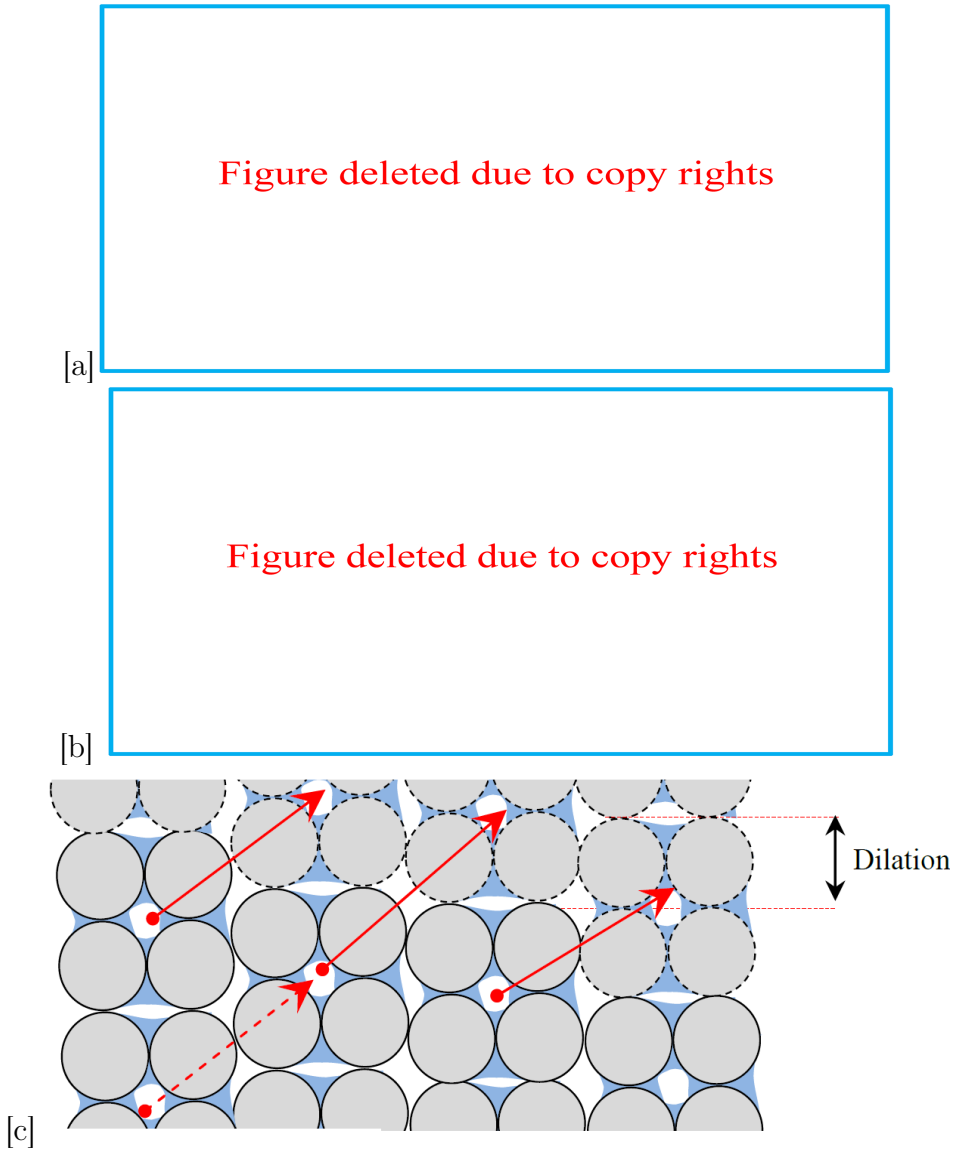

Figure 7.5: (a) Slip behaviour for the dry sand (b) Stick behaviour for the dry sand, after Duttine et al. (2008) (c) Oscillation suppression due to aggregation for unsaturated samples prepared at $s = 4$ and 6 kPa.

7.5 Numerical modelling

The extension of the DLO procedure to allow the modelling of partially saturated soils was described, and included the combined effects of suction and saturation, shown in Appendices F, G., H. and J. Once the modified version of the LimitState:GEO software was validated, the parametric studies listed below were carried out:

1. The total passive earth thrust was analysed using two simulated backfill materials, a sandy soil and a silt loam. The effects of suction, degree of saturation (by adjusting water table position), parameter a, internal friction angle and wall friction were examined. The numerical results showed that the suction and the distribution of the degree of saturation had a significant effect on the passive earth pressure. A non-linear relationship between the total passive earth thrust with the water table position was obtained due to the unsaturated conditions. For example; for the 0.67FW case at $\phi^{'} = 30^{o}$ for the sandy soil backfill material, an increase by a factor of about 2.37 in the normalized total passive earth thrust ($\frac{P_p}{H^2 \times \gamma_w}$) was observed (comparing cases when the water table was at the surface to that 0.6 m below the base of the wall) and increased by 1.82 (comparing cases when the water table was at the surface to that -3 m below the base of the wall). This implied the significant effect of (sS_r) on the passive thrust.

   A change of $\phi^{'}$ significantly affects the passive resistance of the retaining wall. A series of internal friction angle values were; therefore, utilised in the numerical analysis. The aim was to investigate the solo effect of any change of $\phi^{'}$ on the resistance, independent of the (sS_r) effect. For example for the sandy soil backfill material for the case of 0.67FW; if a drop of - 0.6 m of the water table below the base of the wall could cause an increase of $\phi^{'}$ from 30^{o} to 35^{o} due to aggregations, the normalized total passive earth thrust would then increase by a factor of 1.47 fold for $\phi^{'} = 35^{o}$ over the case of $\phi^{'} = 30^{o}$ at the same Y_w = - 0.6 m (constant values of the s and S_r).

2. The influence of partial saturation on the bearing capacity of the surface and buried strip foundations was investigated by performing a series of model tests using a range of suction profiles. A non-linear relationship for bearing capacity with water table depth was determined with bearing capacity initially increasing with increased suction in the soil around the foundation and then this increase levelled off as the saturation of the soil fell.

   The effect of suction and degree of saturation was studied numerically and was in reasonable agreement with the experimental results of the bearing capacity tests. For example, the numerical results of the surface footing for $\phi = 39^{o}$ and $c = 0$ kPa (see Fig. 6.21a) showed an increase in bearing capacity by a factor of 9.5 when the fully saturated case was compared to the case of the average suction of 3.796 kPa. This increase was in the range of the experimental gain in bearing capacity for the surface footing (4-10) fold. The numerical results for the buried footing exhibited 4.38 fold increase in bearing capacity when the fully saturated case was compared to the case of the averaged suction of 3.089 kPa at $\phi = 39^{o}$ (Fig. 6.25a). Once again, this coincided with the experimental increase range in bearing capacity for the buried footing (4-7) fold.

   The effects of internal friction angle and cohesion were studied and demonstrated the influence of the shear strength parameters on the stability of the footing. For example, the numerical bearing capacity of the surface footing increased by a factor of ≈ 2.19

fold (at averaged $s = 2.158$ kPa - see Fig. 6.19b) when ϕ was increased 5^o from 40^o to 45^o at $c = 0$ kPa. While, an increase in bearing capacity by a factor of ≈ 2.58 fold was obtained when $c^{'}$ was increased from 0 kPa to 4 kPa at the constant $\phi = 45^o$ and $s = 2.158$ kPa.

To summarize, the modified DLO method showed that even a small change in suction had a significant effect on passive earth pressure or bearing capacity problems. The DLO method is a promising tool to find the collapse load for a wide range of problems such as retaining walls or foundations under unsaturated conditions without the simplifications inherent in hand calculations or the complexity of the elasto-plastic finite element method.

It is noted, however, that the LimitState:GEO software was unable to directly account for any change in degree of saturation due to the drying behaviour which was observed for both the direct shear and bearing capacity tests. The additional complexity of modelling tension forces between the wall and the soil for the active case was also one of the limitations of the modified version of the software. The development of tension cracks which may partially destroy the tension forces between the wall and the soil gives an extra complexity.

7.6 Implications for engineering practice

While the sS_r term effects showed a small direct influence on the shear strength equation, this was shown numerically to still translate to a fairly large effect on the bearing capacity and passive pressure problems.

In addition, the increase of shear strength parameters observed in the direct shear test results, for a range of nominal suctions from 0 - 6 kPa, due to the inferred aggregation and hence the changes in soil fabric exhibited how the stability of problems was also influenced by these changes. The implication of this for engineering practice is important as a geotechnical structure's stability is further enhanced due to the strength imparted to them due to the soil fabric changes. In the numerical analysis, the changes in soil fabrics and their effect on the stability of the structures can be studied through utilising the actual unsaturated shear strength parameters ϕ^* and c^* obtained from the laboratory experiments, e.g. direct shear or triaxial tests.

The unsaturated shear strength parameters (ϕ^* and c^*), however, may not be available always and it may be possible to estimate them from the saturated shear strength parameters (ϕ and c) without conducting elaborate laboratory tests on unsaturated soils. This requires the development of a rational method for estimation the unsaturated shear strength parameters using either the saturated or dry shear strength parameters.

For the sand tested in this research, for example, the difference between saturated ϕ ($= 46.6^o$) and unsaturated ϕ^* ($= 51.7^o$) at peak was about 5^o. To put this into context, this was equivalent to an increase of 10.7% in ϕ. The c and c^* obtained from the direct shear test results for saturated and unsaturated samples, respectively showed almost the same increase.

However, this research has also demonstrated that there is a risk of wetting collapse on shearing for near saturated samples. The implication of such kind of the behaviour is important as many problems in the real life can be related to the wetting collapse. For example, foundation failure due to wetting, sinkholes due to water infiltration and rainfall induced landslides are essentially related to the wetting collapse issue. A disastrous landslide due to slope stability issues could cost loss of money and perhaps fatalities.

The water migration observed for the sand tested in the current work due to application of the normal stress and during shearing caused drying of the unsaturated samples. This

behaviour had a significant effect on the suction and may also on the shear strength. Once more, the implication of this behaviour is important to the engineering practice. The water movement due to application of the load by foundations, for example, would have an influence on the soil behaviour and requires further study. Another application which is related to the water movement can be addressed is, for example, evaporation of water for a soil above the zone of the capillary rise for an embankment. Also, any movement of water due to capillary effect for the soil above the water table within the embankment structure can bracket the water movement behaviour.

The evaporation causes significant loss in moisture and hence increase in suction. The numerical study of the retaining wall showed that up to 20% increase in total passive earth pressure could be achieved if a drying behaviour causes desaturation from a fully saturated case to a case of 2 kPa suction for the sandy soil. While, in the same range of the suction change, an increase by a factor of more than 4 fold in bearing capacity for the sand used in this study can be obtained. The implication of suction increase is important due to its considerable effect on the stability and safety factor of the structures.

Chapter 8

Conclusions and Recommendations for Future Work

This chapter reports the most important conclusions from the experimental and the numerical studies. Following the conclusions, recommendations for future work are presented.

8.1 Conclusions

1. Reformulation of the existing shear strength and SWCC equations:
   This aim of this study was to evaluate an existing shear strength equation proposed by Öberg & Sällfors (1997) for unsaturated soils. The evaluation showed poor agreement against the experimental results found in the literature as well as the results from direct shear tests of the unsaturated sand conducted in this study. A reformulation of the equation was therefore proposed in accordance to the behaviours observed in the direct shear tests performed in this study such as the increase of internal friction angle and cohesion. The reformulated equation showed an improved ability to predict shear strength, however, it did rely on some experimentally derived parameters. Additionally, the SWCC equation proposed by Stanier & Tarantino (2010) was reformulated and evaluated and showed a good ability to model SWCC. Following the evaluations of both reformulated equations, the shear strength and SWCC equations (Eqs. 5.9, 5.10 and 5.14) were then incorporated into the numerical DLO method.

2. The experimental study:

   (a) Design of the experimental rigs

      i. Design of the direct shear box
      A circular shear box was designed with the following features:
      (1) provision of a high air entry disk (HAED) of 1 bar in the bottom half of the shear box (see Fig. 3.4), (2) provision of the water reservoir underneath the HAED using grooves, (3) provision of two ports to allow saturation of the groove channel during test initialization and connection to a burette, (4) provision of a burette for applying and controlling suction (see Fig. 3.11a) and (5) provision of a camera installed in front of the burette to capture the water level in the burette. This also allowed monitoring of the water content of the sample and hence the degree of saturation at different stages during the test.

The box additionally allowed direct measurement of the SWCC for the fine sand within the suction range of 0 to 10 kPa.
The modified shear box performed well and 73 direct shear tests were undertaken.

ii. Modification of an existing bearing capacity rig
An existing bearing capacity rig was modified by providing the following additional features:
(1) a layer of porous plastic in the bottom of the rig covered by a thin layer of fraction F sand. This is to transmit the suction from a burette to the main sand body relatively quickly, (2) two layers of glass on both front and back faces of the container to minimize the friction between the soil and the rig walls, (3) a burette to apply the suction using the HCT, (4) a humidity and temperature meter on the wall of the rig, (5) perforated containers, each of 5 cm depth, in the soil to allow measurement of the water content at different depths after the test (see Fig. 3.5), (6) a camera in front of the rig to capture images every 1 minute for vector displacement analysis using PIV (see Fig. 3.11b). The modified box performed well and allowed control and measurement of suction during the tests.

(b) Results of the experimental tests

The direct shear results showed that changes in ϕ and c dominated the shear strength of the sand tested rather than the effect of the term (sS_r) which exhibited an insignificant direct effect on the strength. The direct shear results also showed several interesting behaviours as listed below:

i. Increase of shear strength parameters: c and ϕ
The value of c at peak for the unsaturated samples doubled when compared to the fully dry case with ϕ at peak also increasing by 7.6^o. For the fully saturated samples, c showed also an increase by two fold and with a 2.5^o increase in ϕ when compared to the fully dry case. As this behaviour was not consistent with the common findings in the basic soil mechanics, tests were carried out where the sample was saturated at a specific horizontal displacement through the shear test (see Figs. 4.18a and b). The strength and dilatancy were observed to rise after saturation. It is hypothesised that the increase of shear strength parameters was due to changes in soil fabric. Clusters or assemblages of particles, were held by menisci, increased dilation and frictional resistance during shearing and hence shear strength parameters.

ii. Drying behaviour during shearing
A sudden rise of the water level in the burette after application of normal load, observed for both the direct shear and the bearing capacity tests, was due to water migration. The water content loss continued during shearing due to the increase of the water level in the burette observed in the direct shear and bearing capacity tests. Samples taken after the tests for water content measurement confirmed the observed effect. This was above any change in saturation that would arise due to volume change. The study of the phenomenon in the context of the SWCC was investigated (Section 4.9) and it was shown that this behaviour was normal stress and void ratio dependant.

iii. Wetting collapse at a high degree of saturation

A sudden, large collapse behaviour of the unsaturated sand was observed at a high degree of saturation (s = 2 kPa). The response of this behaviour was punctuated by the sudden loss of strength and volume followed then by a rapid recovery of strength as explained previously in Subsection 7.3.2. After the collapse; further repeated sudden losses of strength were observed, but without significant loss of volume. Dry and saturated samples generally showed oscillations in strength, with no collapse. Results showed that up to 67.7% of the overall volume change during the test up to that point (see Table 7.1) could occur during the sudden change, typically post peak. This behaviour was attributed to an increase of degree of saturation (reduction in suction) and availability of space between the voids.

iv. Oscillatory behaviour
Oscillation in the measured shear resistance load was observed for the dry, saturated and unsaturated samples at high degrees of saturation (S_r = 88.9 - 91.5%) for the direct shear test. The unsaturated samples prepared at lower degrees of saturation (S_r = 24-36% and S_r = 15-22%) did not show this phenomenon. The period of oscillation decreased with suction increase. As the oscillatory behaviour was not consistent with the common principles of the soil mechanics, a programme of further tests was carried out to investigate further this behaviour and confirmed the effect. The tests investigated the effect of displacement rate, smoothness of the HAED (replaced by a piece of porous plastic and by the serrated plates), the geometry of the direct shear box (circular and square box) and the effect of the silicon grease (see Section 4.5). These tests confirmed also the oscillatory behaviour. The oscillation was a post-peak behaviour since it was observed after the peak for most of the tests (for tests where this behaviour happened).
To summarize, the so-called stick-slip behaviour which caused instability in shear strength for the poorly graded sand tested in this study was significantly attributed to the particle shape.

3. The numerical study
The DLO method was extended to account for the effects of partial saturation on strength by adopting the reformulated shear strength and SWCC equations. An existing DLO Matlab code and the commercial version of the LimitState:GEO software were modified to allow the modelling of partially saturated soils. The modified DLO Matlab code, called UNSAT-DLO, provided a reference for calibration against the modified version of the LimitState:GEO software. Following the modifications, presented in Appendices H and J, the modified LimitState:GEO software was utilised to carry out a parametric study on the passive earth pressure and a comparative study on the bearing capacity problem. The following conclusions were made:

(a) Total passive earth pressure study
This investigation was carried out using two simulated backfill materials: a sandy soil and a silt loam. The effect of wall friction and internal friction angle was also studied. Three types of the walls were modelled: a frictionless wall (FL), a frictional wall with $\delta = \frac{2}{3}\phi^{'}$ (0.67FW) and a fully frictional wall (FW). The numerical results were compared to a closed form solution based on the Rankine method which was modified to model fully saturated conditions but was also able to take into account the effect of capillary rise. A non-linear relationship between

the total passive earth thrust with the water table elevation was obtained for unsaturated conditions. For the sandy soil backfill material for example, for the 0.67FW case at $\phi^{'} = 30^{o}$, the normalized passive force ($\frac{P_p}{H^2 \times \gamma_w}$) increased by a factor of about 2.37 (comparing cases when the water table was at the surface to that 0.6 m below the base of the wall) and increased by 1.82 (comparing cases when the water table was at the surface to that -3 m below the base of the wall). This demonstrated the relatively significant effect of small changes in (sS_r) on the passive thrust.

The maximum passive earth pressure for the two simulated backfill materials was obtained at different positions of the water table due to the effect of the different values of the degree of saturation on the strength (see Fig. 6.16a). As expected, the silt loam backfill material showed higher total passive earth pressure than the sandy soil even at the same water table depth, Y_w, see Table 6.4. The frictional wall, FW case, exhibited higher total passive earth pressure when compared to cases of 0.67FW and FL for the same soil, see Table 6.4.

(b) Bearing capacity study

The modified DLO method was also used to model strip footings placed on the surface and buried at 5 cm depth. The numerical analysis results were compared with the laboratory model tests conducted in this study. These experimental tests provided the load-deflection data for a range of soil saturation scenarios and also soil displacement data using PIV. A non-linear relationship for bearing capacity with water table depth was determined with bearing capacity initially increasing with increased suction in the soil around the foundation and then this increase levelled off as the saturation of the soil fell (see Fig. 6.21). The modified DLO numerical models showed reasonable agreement with the experimental data that can be attributed to reduction in saturation with increase in suction.

The experimental results for the surface footing demonstrated 4 to 10 fold increase in bearing capacity at peak when the unsaturated cases were compared with the fully saturated samples (e.g. see Figs. 4.32 - $s = 0$ kPa-4 and Fig. 4.35). Similarly, the modified DLO result showed a 9.5 fold increase in bearing capacity for the surface footing when the averaged suction changed from 0 to 3.796 kPa for $\phi = 39.15^{o}$ and $c = 0$ kPa (see Fig. 6.21a). An increase of 4 to 7 fold in bearing capacity (typically at the end of the test) when comparing the fully saturated with the unsaturated samples was obtained for the experimental buried footing results. The modified DLO result for the buried footing exhibited a 4.38 fold increase in bearing capacity when the fully saturated case was compared to the unsaturated case at an averaged suction of 3.089 kPa at $\phi = 39.15^{o}$ and $c = 0$ kPa (Fig. 6.25a).

The implication of the above comparison is important as the modified DLO method showed ability of the approach to model the increase in bearing capacity due to reduction in saturation in which this increase coincided with the range of gain in bearing capacity for the experimental results.

In conclusion, the modified DLO approach showed the ability of the method to model both passive earth pressure and bearing capacity problems. The method exhibited that even a small change in suction had a significant effect on strength. The modified DLO method therefore seems promising, however, needs further calibration and it is likely to be conservative if dry strength parameters ϕ and c are used.

8.2 Recommendations and future work

1. Recommendations for the experimental work:
    (a) The increase of the internal friction angle behaviour for the unsaturated sand used in this research could be investigated further by studying the effect of the soil fabric on this increase using X-ray tomography method. Although suction was controlled in this study using the HCT, installing mini probes (tensiometers) to measure actual suctions in the direct shear test would be also useful to link the increase of the internal friction angle with any variation of the suction during shearing.
    (b) The high shear strength of the saturated samples was an unexpected result and could be investigated further using different experiments such as triaxial tests.
    (c) The oscillatory behaviour observed in this study for the dry, saturated and unsaturated samples prepared at high degrees of saturation was an unexpected and interesting phenomenon and is worthy of further work.
    (d) The drying behaviour observed in this study immediately after application of the normal load and during shearing can be investigated further. This could be studied by tracking water migration using X-ray tomography.

2. Recommendations for the numerical work:
    (a) The current derived formulations for the apparent cohesion did not account for residual saturation. These could be extended to model this also. Initial work is presented in Appendix I and validated in Appendix J (Section J.3) and can be usefully incorporated in the LimitState:GEO software.
    (b) Formulations of the strip weight above the discontinuity (based on Eq. 5.7-Section 5.3) were derived and validated in this study, see Appendices G and H. These formulations can be incorporated into the LimitState:GEO software to better account of the unsaturated unit weight above the water table.
    (c) The DLO method for the unsaturated problems was based on the assumption that the hydrostatic suction can be utilised along the soil profile. Inclusion of the influence of rainfall into the hydraulic model used with DLO would be useful as it has a direct effect on the suction value and then the stability of the problems.

References

Adrian, R. (1991), 'Particle-imaging technique for experimental fluid dynamics', *Annual Reviews in Fluid Mechanics* **23**, 261–304.

Aitchison, G. D. (1965), 'Moisture equilibria and moisture changes in soils beneath covered areas', *a symposium in print, Butterworths.* .

Alabdullah, J. (2010), Testing Unsaturated Soil for Plane Strain Conditions: A New Double-Wall Biaxial Device, PhD thesis, Faculty of Civil Engineering-Bauhaus-University Weimar.

Alonso, E. E., Gens, A. & Josa, A. (1990), 'A constitutive model for partially saturated soils', *Géotechnique* **40**(3), 405–430.

Alonso, E. E., Pereira, J. M., Vaunat, J. & Olivella, S. (2010), 'A microstructually based effective stress for unsaturated soils', *Géotechnique* **60**(12), 913–925.

ASTM-D4253 (1989), 'Standard test methods for maximum index density of soils using a vibratory table', *ASTM International* .

ASTM-D6836-02 (2008), 'Standard test methods for determination of the soil water char-characteristic curve for desorption using hanging column, pressure extractor, chilled mirror hygrometer, or centrifuge', *ASTM International* .

Aysen, A. (2002), *Soil mechanics: basic concepts and engineering applications*, CRC Press.

Balzano, B., Amabile, A., Urciuoli, G. & Tarantino, A. (2012), Effect of partial saturation on the stability of shallow foundations above the water table, in Unsaturated Soils: Research and Applications. Springer Berlin Heidelberg, pp. 247–253.

Barden, L., Madedor, A. & Sides, G. (1969), 'Volume change characteristics of unsaturated clay', *Journal of Soil Mechanics Foundations Div* **95**(1), 33–52.

Bardet, J. P. (1997), *Experimental soil mechanics.*, Upper Saddle River, NJ: Prentice Hall.

Biot, M. A. (1955), 'Theory of elasticity and consolidation for a porous anisotropic soil', *Journal of Applied Physics* **26**(2), 182–185.

Bishop, A. & Blight, G. (1963), 'Some aspects of effective stress in saturated and partly saturated soils', *Géotechnique* **13**(3), 177–179.

Bishop, A. & Gibson, R. (1964), 'The influence of the provisions for boundary drainage on strength and consolidation characteristics of soils measured in the triaxial apparatus', *ASTM International* pp. 273–328.

Bishop, A. W. (1960), 'The principle of effective stress', *Norwegian Geotechnical Institute, Oslo* **4**, 1–4.

Bishop, A. W., Alpan, I., Blight, G. E. & Donald, I. B. (1960), 'Factors controlling the strength of partly saturated cohesive soils', *ASCE International* pp. 503–532.

Bishop, A. W. & Donald, I. B. (1961), The experimental study of partly saturated soil in the triaxial apparatus, Proceedings of the 5th international conference on soil mechanics and foundation engineering, Paris, pp. 13–21.

Blanchfield, R. & Anderson, W. (2000), Wetting collapse in opencast coalmine backfill, Vol. 149, Proceedings of the Institution of Civil Engineers-Geotechnical Engineering, pp. 139–149.

Bolton, M. D. (1986), 'The strength and dilatancy of sands', *Géotechnique* **36**(1), 65–78.

Boso, M. (2005), Shear strength behaviour of a reconstituted partially saturated clayey silt, PhD thesis, University of Trento.

Buckingham, E. (1907), 'Studies on the movement of soil moisture', *Bull 38 USDA, Bureau of Soils, Washington DC* .

Buisson, M. & Wheeler, S. (2000), 'Inclusion of hydraulic hysteresis in a new elastoplastic framework for unsaturated soils', *Experimental evidence and theoretical approaches in unsaturated soils* pp. 109–119.

Bulut, R. & Leong, C. (2008), 'Indirect measurement of suction', *Geotechnical and geological engineering* **26**(6), 633–644.

Burland, J. (1964), 'Effective stresses in partly saturated soils', *Géotechnique* **14**(1), 64–68.

Burland, J. B. (1965), 'Correspondence', *Géotechnique* **15**(2), 211–214.

Carsuso, M. & Tarantino, A. (2004), 'A shear box for testing unsaturated soils at medium to high degrees of saturation', *Gétechnique* **54**(4), 281–284.

Casini, F., Minder, P. & Springman, S. M. (2011), Shear strength of an unsaturated silty sand, Proceeding of the 5th international conference of unsaturated soils, Barcelona, Spain, pp. 211–216.

Chandler, R. J., Crilley, M. S. & Montgomery-Smith, G. (1992), 'A low-cost method of assessing clay desiccation for low-rise buildings', *Proceeding of the ICE-Civil Engineering* **92**, 82–89.

Chen, W. F. (1975), *Limit Analysis and Soil Plasticity*, Developments in Geotechnical Engineering 7, Elsevier.

Chen, W. F. & Liu, X. (2012), *Limit analysis in soil mechanics*, Elsevier.

Childs, E. C. (1969), *An introduction to the physical basis of soil water phenomena*, John Wiley and Sons.

Chiu, C. F. & Ng, C. W. W. (2003), 'A state-dependent elasto-palstic model for saturated and unsaturated soils', *Géotechnique* **53**(9), 809–829.

Coleman, J. D. (1962), 'Stress strain relations for partly saturated soil', *Géotechnique* **12**(4), 348–350.

Connell, L. D. (1999), 'A quasilinear based procedure for saturated/unsaturaed water movement in soils', *Transport in porous media* **36**(1), 1–21.

Costa, Y. D., Cintra, J. C. & Zornberg, J. G. (2003), 'Influence of matric suction on the results of plate load tests performed on a lateritic soil deposit', *Geotechnical Testing Journal* **26**(2), 219–227.

Cox, D. W. (1978), Volume change of compacted clay fill, Proceedings from the Clay Fills Conference, held at the Institution of Civil Engineers, London, pp. 79–86.

Cui, Y. J. & Delage, P. (1996), 'Yielding and plastic behaviour of an unsaturated compacted silt.', *Géotechnique* **46**(2), 291–311.

Delage, P., Howat, M. D. & Cui, Y. J. (1998), 'The relationship between suction and swelling properties in a heavy compacted unsaturated clay', *Engineering Geology* **50**(1), 31–48.

Dineen, K. & Burland, J. B. (1995), A new approach to osmotically controlled oedometer testing., Vol. 2, Proceedings of the 1st International Conference on Unsaturated Soils, Paris.

Drucker, D., Prager, W. & Greenberg, H. (1952), 'Extended limit design theorems for continuous media', *Quarterly of Applied Mathematics* **9**, 381–389.

Duttine, A., Tatsuoka, F., Kongkitkul, W. & Hirakawa, D. (2008), 'Viscous behaviour of unbound granular materials in direct shear', *Soils and Foundations* **48**(3), 297–318.

Escario, V. (1980), Suction controlled penetration and shear tests, Proceeding of 4th International Conference on Expansive Soils, Denver, pp. 781–797.

Escario, V. & Saez, J. (1986), 'The shear strength of partly saturated soils', *Géotechnique* **36**(3), 453–456.

Fathi, M. O. & Vanapalli, S. K. (2006), Laboratory investigations for the measurement of the bearing capacity of an unsaturated coarse-grained soil, Proceedings of the 59th Canadian Geotechnical Conference. Vancouver, British Columbia, Canada, pp. 1–4.

Fern, J., Soga, K. & Robert, D. J. (2014), Shear strength and dilatancy of partially saturated sand in direct shear tests, TC105 ISSMGE International Symposium on Geomechanics From Micro to Macro, IS-Cambridge, Cambridge, pp. 1391–1396.

Feuerharmel, C., Bica, A., Gehling, W. & Flores, J. (2005), A study of the shear strength of two unsaturated colluvium soils, Proceedings of the International Symposium on Advanced Experimental Unsaturated Soil Mechanics, Trento, Italy, pp. 169–174.

Fisher, R. A. (1926), 'On the capillary forces in an ideal soil', *The Journal of Agricultural* **16**, 492–505.

Fredlund, D. G. (1981), Seepage in saturated soils, Proceedings of the 10th International Conference in Soil Mechanics, pp. 629–641.

Fredlund, D. G. & Morgenstem, N. R. (1977), 'Stress state varables for unsaturated soils', *Geotechnical and Geoenvironmental Engineering, ASCE 12919* .

Fredlund, D. G., Morgenstern, N. R. & Widger, R. A. (1978), 'The shear strength of unsaturated soils', *Canadian Geotechnical Journal* **15**(3), 313–321.

Fredlund, D. G. & Rahardjo, H. (1993), *Soil Mechanics for Unsaturated Soils*, John Wiley and Sons , New York.

Fredlund, D. G. & Xing, A. (1994), 'Equation for soil-water characteristic curve', *Canadian Geotechnical* **31**, 521–532.

Gan, J. K., Fredlund, D. G. & Rahardjo, H. (1988), 'Determination of the shear strength parameters of an unsaturated soil using the direct shear test', *Canadian Geotechnical Journal* **25**(3), 500–510.

Geiser, F., Laloui, L. & Vulliet, L. (2006), 'Elasto-plasticity of unsaturated soils: laboratory test results on a remoulded silt', *Soils and Foundations* **46**(5), 545–556.

Gens, A. (1995), Constitutive modelling: Application to compacted soils, Proceedings of the 1st International Conference on Unsaturated Soils, Paris,Balkema, pp. 1179–1200.

Gillbert, M., Smith, C., Haslam, I. & Pritchard, T. (2010), Application of discontinuity layout optimization to geotechnical engineering, *in* 'Proceedings of the 7th European Conference on Numerical Methods in Geotechnical Engineering', pp. 169–174.

Griffiths, D. (1990), 'Failure criteria interpretation based on mohr-coulomb friction', *Journal of Geotechnical Engineering* **116**(6), 986–999.

Guler, M., Edil, T. & Bosscher, P. (1999), 'Measurement of particle movement in granular soils using image analysis', *Journal of Computing in Civil Engineering* **13**(2), 116–122.

Haines, W. B. (1930), 'Studies in the physical properties of soil: V. the hysteresis effect in capillary properties, and the modes of moisture distribution associated therewith', *The Journal of Agricultural Science* **20**(1), 97–116.

Hamblin, A. P. (1981), 'Filter paper method for routine measurements of field water potencial', *Journal of Hydrology* **53**, 355–360.

Head, K. H. (1994), *Manual of soil laboratory testing*, Vol. 2, John Wiley Sons. Inc.

Hilf, W. J. (1956), An investigation of pore-water pressure in compacted cohesivve soils, PhD thesis, U.S. Department of the Interior, Bureau of Reclamation. PhD dissertation, Tech, Memo. No. 654.

Hillel, D. (1980), *Fundamentals of soil physics*, Academic Press, Inc.(London) Ltd.

Ho, D. Y. F. & Fredlund, D. G. (1982), 'A multistage triaxial test for unsaturated soils', *ASCE Journal* pp. 18–25.

Horn, H. M. & Deere, D. U. (1962), 'Frictional characteristics of minerals', *Géotechnique* **12**(4), 319–335.

Houlsby, G. (1991), How the dilatancy of soils affects their behaviour, Invited lecture delivered at the 10th European Conference on Soil Mechanics and Foundation Engineering, Florence, Italy, pp. 27–30.

Jardine, R. J., Gens, A., Hight, D. W. & Coop, M. R. (2004), Developments in understanding soil:advances in geotechnical engineering, The Skempton Conference, organised by the Institution of Civil Engineers and held at the Royal Geographical Society, London, UK, pp. 103–206.

Jennings, J. E. B. & Burland, J. B. (1962), 'Limitations to the use of effective stresses in partly saturated soils.', *Géotechnique* **12**(2), 125–144.

Kassif, G. & Ben Shalom, A. (1971), 'Experimental relationship between swell pressure and suction.', *Géotechnique* **21**(3), 245–255.

Khalili, N. & Khabbaz, M. H. (1998), 'A unique relationship for χ for the determination of', *Géotechnique* **48**(5), 681–687.

Kim, Y. T., Shin, H. & Park, D. K. (2011), 'Variation of shear strength for weathered granite soil with water content', *Journal of Korean Society of Hazard Mitigation* **11**(4), 157–162.

Krishnapillai, S. H. & Ravichandran, N. (2012), 'New soil-water characteristic curve and its performance in the finite-element simulation of unsaturated soils.', *International Journal of Geomechanics* **12**(3), 209–219.

Lagerwerff, J. V., G., O. & Eagle, H. E. (1961), 'Control of osmotic pressure of culture solutions with polyethylene glycol', *Science* **133**(3463), 1486–1487.

Leong, E. C., He, L. & Rahardjo, H. (2002), 'Factors affecting the filter paper method for total and matric suction measurements', *Geotechnical testing journal* **25**(3), 321–332.

Likos, W. J. & Lu, N. (2004), *Unsaturated soil mechanics*, John Wiley and Sons Ltd.

Likos, W. J., Wayllace, A., Godt, J. & Lu, N. (2010), 'Modified direct shear apparatus for unsaturated sands at low suction and stress', *ASTM Geotechnical Testing* **33**(4), 286–298.

LimitState:GEO (2013), *Limit State Manual*, http://www.limitstate.com.

Lings, M. L. & Dietz, M. (2004), 'An improved direct shear apparatus for sand', *Géotechnique* **54**(4), 245–256.

Liu, J. & Iskander, M. (2004), 'Adaptive cross correlation for imaging displacements in soils', *Journal of Computing in Civil Engineering* **18**(1), 46–57.

Liu, S. (2006), 'Simulating a direct shear box test by dem', *Canadian Geotechnical Journal* **43**(2), 155–168.

Lloret, A. & Alonso, E. (1980), 'Consolidation of unsaturated soils including swelling and collapse behaviour', *Géotechnique* **30**(4), 449–477.

Loukidis, D., Chakraborty, T. & Salgado, R. (2008), 'Bearing capacity of strip footings on purely frictional soil under eccentric and inclined loads', *Canadian Geotechnical Journal* **45**(6), 768–787.

Loukidis, D. & Salgado, R. (2009), 'Bearing capacity of strip and circular footings in sand using finite elements', *Computers and Geotechnics Journal* **36**, 871–879.

Lu, Z. H., Chen, Z. H., Fang, X. W., Guo, J. F. & Zhou, H. Q. (2006), 'Structural damage model of unsaturated expansive soil and its application in multi-field couple analysis on expansive soil slope', *Applied Mathmatics and Mechanics Journal* **27**, 891–900.

Lyamin, A., Sloan, S., Krabbenhoft, K. & Hjiaj, M. (2005), 'Lower bound limit analysis with adaptive remeshing', *International Journal for Numerical Methods in Engineering* **63**(14), 1961–1974.

Lysmer, J. (1970), 'Limit analysis of plane problems in soil mechanics', *Journal of the Soil Mechanics and Foundations Division ASCE* **96**(4), 1311–1334.

Makrodimopoulos, A. & Martin, C. (2006), 'Lower bound limit analysis of cohesive-frictional materials using second-order cone programming', *International Journal for Numerical Methods in Engineering* **6**(4), 604–634.

Marinho, W. A., Take, W. A. & Tarantino, A. (2008), 'Measurement of matric suction using tensiometric and axis translation techniques', *Geotechnical and Geological Engineering* **26**(6), 615–631.

Masson, S. & Martinez, J. (2001), 'Micromechanical analysis of the shear behavior of a granular material', *Journal of Engineering Mechanics* **127**(10), 1007–1016.

Maswoswe, J. (1985), Stress path for a compacted soil during collapse due to wetting, PhD thesis, Imperial College.

Matyas, E. L. & Radhakrishna, H. S. (1968), 'Volume change characteristics of partially saturated soils', *Géotechnique* **18**(4), 432–448.

Md. Noor, M. J. (2005), shear strength and volume change behaviour of unsaturated soils, PhD thesis, The university of Sheffield.

Mohamed, F. M., Vanapalli, S. K. & Saatcioglu, M. (2011), Bearing capacity and settlement behaviour of footings in an unsaturated sand, Proceedings of the 14th Pan-American Conference on Soil Mechanics and Geotechnical Engineering.

Murray, E. J. & Sivakumar, V. (2010), *Unsaturated Soils: a fundamental interpretation of soil behaviour*, John Wiley and Sons Ltd.

Murray, E., Murray, B. & Sivakumar, V. (2008), 'Discussion on meta-stable equilibrium in unsaturated soils. unsaturated soils', *Advances in Geo-Engineering* pp. 553–558.

Nabil, F. I. (1985), 'Allowable pressure from loading tests on kuwaiti soils', *Canadian Geotechnical Journal* **22**(2), 151–157.

Nam, S., Gutierrez, M., Diplas, P. & Petrie, J. (2011), 'Determination of the shear strength of unsaturated soils using the multistage direct shear test', *Engineering Geology* **122**(3), 272–280.

Ng, C. W. W., Cui, Y., Chen, R. & Delage, P. (2007), 'The axis-translation and osmotic techniques in shear testing of unsaturated soils', *Soils and Foundations* **47**(4), 678–684.

Ng, C. W. W. & Zhou, R. Z. B. (2005), Effect of soil suction on dilatancy of an unsaturated soil, Vol. 2, Proceedings of the 16th International Conference of Soil Mechanics and Geotechnical Engineering, Osaka, Japan, pp. 559–562.

Nicotera, M. V. (2000), Interpretation of shear response upon wetting of natural unsaturated pyroclastic soils, In experimental evidence and theoretical approaches in unsaturated soils, Rotterdam, A. A. Balkema, A. Tarantino and C. Mancuso eds, pp. 177–192.

Nishimura, T., Toyota, H., Vanapalli, S. K. & Oh, W. T. (2008), The shear strength behavior of a silty soil in the residual zone of unsaturation, Proceedings of the 12th International Conference of International Association for Computer Methods and Advanced in GeomeGeomechanics, pp. 2213–2221.

Nuth, M. (2009), Constitutive modelling of unsaturated soils with hydro-geomechanical couplings, PhD thesis, École Polytechnique Fédérale De Lausanne.

Nuth, M. & Laloui, L. (2008*a*), 'Advances in modelling hysteretic water retention curve in deformable soils', *Computers and Geotechnics Journal* **35**(6), 835–844.

Nuth, M. & Laloui, L. (2008*b*), 'Effective stress concept in unsaturated soils: clarification and validation of a unified framework', *International Journal for Numerical and Analytical Methods in Geomechanics* **32**(7), 771–801.

Öberg, A. L. & Sällfors, G. (1997), 'Determination of shear strength parameters of unsaturated silts and sands based on the water retention curve', *Geotechnical testing* **20**(1), 40–48.

Oh, W. T. & Vanapalli, S. K. (2011), 'Modelling the applied vertical stress and settlement relationship of shallow foundations in saturated and unsaturated sands', *Canadian Geotechnical Journal* **48**(3), 425–438.

Oh, W. T. & Vanapalli, S. K. (2012), 'Interpretation of the bearing capacity of unsaturated fine-grained soil using the modified effective and the modified total stress approaches', *International Journal of Geomechanics* **13**(6), 769–778.

Oloo, S. Y., Fredlund, D. & Gan, J. K. (1997), 'Bearing capacity of unpaved roads', *Canadian Geotechnical Journal* **34**(3), 398–407.

Olson, R. E. & Langfelder, L. J. (1965), 'Pore pressure in unsaturated soils', *Journal of Soil Mechanics and Foundations Division, ASCE* **91**, 127–150.

Ovesen, N. K. (1979), The scaling law relationship, Proceedings of the 7th European Conference of Soil Mechanics and Foundation Engineering, Brighton, pp. 319–323.

PIVlab1.32 (2012), 'Pivlab software', *http://pivlab.blogspot.co.uk* .

Powrie, W. (2013), *Soil mechanics: concepts and applications*, CRC Press.

Richards, L. A. (1928), 'The usefulness of capillary potential to soil moisture and plant investigators', *Journal of Agricultural Research* **37**(12), 719–742.

Richards, L. A. (1931), 'Capillary conduction of liquids through porous meduim', *Physics* **1**(5), 319–333.

Röhm, S. A. & Vilar, O. M. (1995), Shear strength of an unsaturated sandy soil, Proceedings of the 1st International Conference on Unsaturated Soils, Paris, pp. 189–193.

Romano, N., Hopmans, J. W. & Dane, J. H. (2002), 'Suction table', *Methods of Soil Analysis* pp. 692–698.

Romero, E. & Vaunat, J. (2000), Retention curves of deformable clays, Experimental evidence and theoretical approaches in unsaturated soils. Rotterdam, A. A. Balkema, A.

Sadek, S., Iskander, M. & Liu, J. (2005), 'Accuracy of digital image correlations for measuring deformations in transparent media', *Journal of Computing in Civil Engineering Geology* **19**(2), 219–222.

Sharma, R. S. & Mohamed, M. H. A. (2003), 'An experimental investigation of lnapl migration in an unsaturated/saturated sand', *Engineering Geology* **70**(3), 305–313.

Shwan, B. J. (2015), Wetting collapse at a high degree of saturation during shearing for unsaturated sand, Proceedings of the 6th Asia-Pacific Conference on Unsaturated Soils (AP-UNSAT 2015), China, pp. 253–256.

Shwan, B. J. (2016), Moisture migration during loading and shearing of unsaturated sand, Proceedings of the 3rd European Conference on Unsaturated Soils-(E-UNSAT 2016), Paris-In press.

Shwan, B. J. & Smith, C. C. (2014), Application of limit analysis in unsaturated soils: numerical and experimental study of bearing capacity, Vol. 2, In Unsaturated Soils: Research and Applications - Proceedings of the 6th International Conference on Unsaturated Soils, UNSAT 2014, Sydney, Australia, pp. 1757–1762.

Shwan, B. J. & Smith, C. C. (2015), Investigation of the shear strength of unsaturated sand using a modified direct shear apparatus, Proceedings of the XVI ECSMGE- Edinburgh, pp. 3353–3357.

Simms, P. H. & Yanful, E. K. (2001), 'Measurement and estimation of pore shrinkage and pore distribution in a clayey till during soil-water characteristic curve tests', *Canadian Geotechnical Journal* **38**(4), 741–754.

Sivakumar, V. (1993), A critical state framework for unsaturated soil, PhD thesis, University of Sheffield.

Skempton, A. W. (1960), Effective stress in soils, concrete and rocks, Thomas Telford Ltd, London, pp. 4–16.

Sloan, S. (1988), 'Lower bound limit analysis using finite elements and linear programming', *International Journal for Numerical and Analytical Methods in Geomechanics* **12**(1), 61–77.

Smith, C. C. & Gilbert, M. (2007*a*), Application of discontinuity layout optimization to plane plasticity problems, Vol. 463, Proceedings of the Royal Society of London: Physical and Engineering Sciences, pp. 2461–2484.

Smith, C. & Gilbert, M. (2007*b*), New upper bound solutions for layered soil bearing capacity problems using discontinuity layout optimazation, Proceedings of the 10th Australia New Zealand Conference on Geomechanics, Brisbane, pp. 250–255.

Sokolovskii, V. V. (2013), *Statics of soil media*, Elsevier.

Soubra, A. H. & Macuh, B. (2002), Active and passive earth pressure coefficients by a kinematical approach, Vol. 155, Proceedings of the ICE-Geotechnical Engineering, pp. 119–131.

Stanier, S. A. (2011), Modelling the Behaviour of Helical Screw Piles, PhD thesis, University of Sheffield.

Stanier, S. A. & Tarantino, A. (2010), Active earth force in 'cohesionless' unsaturated soils using bound theorems of plasticity, Vol. 2, In: Alonso, E.E., Gens, A. (Eds.), Proceedings of 5th International Conference on Unsaturated Soils , CRC Press, Barcelona, Spain, pp. 1081–1086.

Stanier, S. A. & Tarantino, A. (2013), 'An approach for predicting the stability of vertical cuts in cohesionless soils above the water table', *Engineering Geology* **158**(2013), 98–108.

Steensen-Bech, J. O., Foged, N. & Steenfelt, J. S. (1987), Capillary induced stresses-fact or fiction?, Proceedings of the 9th European Conference on Soil Mechanics and Foundation Engineering, Budapest, Hungary, pp. 83–89.

Suklje, L. & Sûklje, L. (1969), *Rheological aspects of Soil Mechanics*, New York, Wiley.

Sun, S. & Xu, H. (2007), Determining the shear strength of unsaturated silt, Springer Proceedings in Physics.

Tarantino, A. (2007), 'A possible critical state framework for unsaturated compacted clay', *Géotechnique* **57**(4), 385–389.

Tarantino, A., Gallipoli, D., Augarde, C. E., De Gennaro, V., Gomez, R., Laloui, L., Mancuso, C., El Mountassi, G., Munoz, J. J., J.-M. Pereira, J.-M., Peron, H., Pisoni, G., Romero, E., A. Raveendiraraj, A., Rojas, J. C., Toll, D. G. & S. Tombolato, S.and Wheleer, S. (2011), 'Benchmark of experimental techniques for measuring and controlling', *Géotechnique* **61**(4), 303–312.

Tarantino, A. & Tombolato, S. (2005), 'Coupling of hydraulic and mechanical behaviour in unsaturated compacted clay', *Géotechnique* **55**(4), 307–317.

Terzaghi, K. (1943), *Theoretical soil mechanics*, Wiley.

Terzaghi, K. V. (1936), The shearing resistance of saturated soils and the angle between the planes of shear, Vol. 1, Proceedings of the 1st International Conference on Soil Mechanics and Foundation Engineering, pp. 54–56.

Toll, D. G. (1990), 'A framework for unsaturated soil behaviour', *Géotechnique* **40**(1), 31–44.

Toll, D. G. (2000), The influence of fabric on the shear behavior of unsaturated compacted soils, number 99, In Advanced in Unsaturated Soils-American Society of Civil Engineers, Geotechnical Special Publication, pp. 222–234.

Toll, D, G. (2001), Rainfall-induced landslides in singapore, Vol. 149, Proceedings of the Institution of Civil Engineers: Geotechnical Engineering, pp. 211–216.

Toll, D. G. & Ong, B. H. (2003), 'Critical state parameters for an unsaturated residual sandy clay', *Géotechnique* **53**(1), 93–103.

Toll, D., Rahman, A. Z. & Gallipoli, D. (2008), *Critical State conditions for an unsaturated artificially bonded soil*, Taylor Francis, pp. 435–440.

Uchaipichat, A. & Man-Koksung, E. (2011), 'Variation of ultimate bearing capacity of unsaturated clay with suction', *Journal of Engineering Applied Sciences* **6**(12), 62–65.

Vaid, Y. & Negussey, D. (1988), 'Preparation of reconstituted sand specimens', *Advanced triaxial testing of soil and rock, ASTM STP* **977**, 405–417.

Van Genuchten, M. T. (1980), 'A closed-form equation for predicting the hydraulic conductivity of unsaturated soils', *Soil Science Society of America Journal* **44**, 892–898.

Vanapalli, S. K., Fredlund, D. G., Pufahl, D. E. & Clifton, A. W. (1996), 'Model for the prediction of shear strength with respect to soil suction', *Canadian Geotechnical Journal* **33**, 379–392.

Vanapalli, S. K. & Mohamed, F. M. (2007), Bearing capacity of model footings in unsaturated soils, *in* 'Experimental unsaturated soil mechanics', T. Schanz, ed., Springer, Berlin, pp. 483–493.

Vanapalli, S. K., Nicotera, M. V. & Sharma, S. (2008), 'Axis translation and negative water column techniques for suction control', *Geotechnical and geological engineering* **26**(6), 645–660.

Vanapalli, S. K., Wright, A. & Fredlund, D. G. (1998), Shear strength behavior of a silty soil over the suction range from 0 to 1000000 kpa, Proceedings of the 53th Canadian Geotechnical Conference, Montreal, Quebec, Canada, pp. 15–18.

Vasallo, R. & Mancuso, C. (2000), Soil behaviour in the small and the large strain range under controlled suction conditions, In experimental evidence and theoretical approaches in unsaturated soils, Rotterdam, A. A. Balkema, A. Tarantino and C. Mancuso eds, pp. 75–89.

Vermeer, P. A. (1990), 'The orientation of shear bands in biaxial tests', *Géotechnique* **40**(2), 223–236.

Vermeer, P. A. & Borst, D. (1984), 'Non-associated plasticity for soils', *concrete and rock* **29**(3).

Vesic, A. B. (1973), 'Analysis of ultimate loads of shallow foundations', *ASCE Journal* **99**, 45–73.

Wheeler, S. J. (1991), 'An alternative framework for unsaturated soil behaviour', *Géotechnique* **41**(2), 257–261.

Wheeler, S. J. (2006), Constitutive modelling of unsaturated soils, Proceedings of the 4th Keynote oral presentation International Conference on Unsaturated Soils (UNSAT06), Arizona, USA. Keynote oral presentation.

Wheeler, S. J. & Karube, D. (1995), Constitutive modelling., Vol. 3, Proceedings of the 1st International Conference on Unsaturated Soils, Paris, Belkema, Rotterdam, state of the art Report, pp. 1323–1356.

Wheeler, S. J. & Sivakumar, V. (1995), 'An elasto-plastic critical state framework for unsaturated soil', *Géotechnique* **45(1)**, 35–53.

White, D. (2002), An investigation into the behaviour of pressed-in piles, PhD thesis, University of Cambridge.

White, D. J., Take, W. A. & Bolton, M. (2003), 'Soil deformation measurement using particle image velocimetry (piv) and photogrammetry', *Géotechnique* **53**(7), 619–631.

Williams, J. & Shaykewich, C. F. (1969), 'An evaluation of polyethlene glycol peg 6000 and peg 20000 in osmotic control of soil water matric potential', *Canadian Geotechnical Journal* **102**(3), 394–398.

Xie, Z., Zeng, Q., Dai, Y. & Wang, B. (1998), 'Numerical simulation of an unsaturated flow equation', *Science in China Series D: Earth Sciences* **41**(4), 429–436.

Yoshida, T. (1994), Shear banding in sands observed in plane strain compression, Proceedings of Symposium on Localization and Bifurcation Theory for Soils and Rocks, Belkema, pp. 165–179.

Zhao, L. H., Luo, Q., Li, L., Yang, F. & Yang, X. L. (2009), The upper bound calculation of passive earth pressure based on shear strength theory of unsaturated soil, Proceedings of Slope Stability, Retaining Walls and Foundation, ASCE, pp. 151–157.

Appendix A

Increase of the Shear Strength Parameters for Unsaturated Sand

This Appendix contents a draft technical note to be submitted to the Géotechnique journal.

Abstract

A series of tests were conducted on dry, saturated and unsaturated sand using a direct shear box where suction was controlled using the hanging column technique (HCT). The experimental results showed that the shear resistance of unsaturated samples increased compared to the fully dry case as expected. Somewhat unexpectedly, both shear resistance parameters $\phi^{'}$ and $c^{'}$ of the saturated and unsaturated sand also increased. Tests where the sample was saturated part way through the shear box test confirmed the phenomena. It is hypothesised that this increase is due to soil aggregation that improved the soil fabric.

A.1 Introduction

Early works in field of unsaturated soil mechanics make the assumption that $c^{'}$ and $\phi^{'}$ are constant and independent of suction. However, a number of studies have reported an increase in internal friction angle for unsaturated soils such as an increase has been observed in clay and sandy soils by Wheeler & Sivakumar (1995) and Röhm & Vilar (1995). In terms of the former, an increase in internal friction angle of about 3.5 degrees in the range of suctions between 0 to 200 kPa for compacted Speswhite kaolin for triaxial compression tests was found. Röhm & Vilar (1995) established a maximum difference of friction angle of about 2.5 degrees for suction ranged between 0 to 400 kPa for a sandy soil. No explanation of this increase was given by the authors.

Toll (2000) studied the influence of fabric on the shear behaviour of clayey soils compacted dry of optimum and separated out the effect of net stress $(\sigma - u_a)$ and matric suction $(u_a - u_w)$. The internal friction angle with respect to the net stress ϕ^a was found to be greater than the saturated internal friction angle $\phi^{'}$ due to aggregation of the particles. Also the internal friction angle with respect to the matric suction ϕ^b was found to be less than $\phi^{'}$ and equal to zero when the soil approached dry condition.

Toll et al. (2008) conducted a series of triaxial tests on artificially bonded sand for unsaturated samples at constant water content while suction was applied using the axis

translation technique. The sample was prepared by mixing 87% sand and 13% kaolin and the mixture was fired in a furnace at 500^{o}C. Three radial net stresses: 50, 100 and 300 kPa and a range of suctions from 0 to 560 kPa were used. The data were presented at the critical state.

Three different internal friction angles were stated according to the water retention curve. For suctions less than the air entry value, ϕ^a and ϕ^b were found to be equal to $\phi^{'}$ ($\phi^a = \phi^b = \phi^{'}$). For the range between the air entry value and the residual suction, $\phi^a > \phi^{'}$and $\phi^b = \phi^{'}$ were observed. Finally at residual suction, ϕ^a remained constant and ϕ^b started to reduce. To put this in context, a difference of 4 degrees between ϕ^a and $\phi^{'}$ was observed. This behaviour was explained due to changes in fabric of the soil.

This aim of this work is to examine the change of friction angle and cohesion intercept with degree of saturation for a fine sand using drained direct shear test results. A simple hypothesis for increase of the shear strength parameters is also presented.

A.2 Experimental work

A.2.1 Soil properties

The soil used in this study was fine sand designated as Fraction D and available from the David Ball Group, UK. The physical properties and shear strength parameters for the sand are shown in Table E.1 with the particle size distribution curve shown in Fig. 1. The dry shear strength parameters c and ϕ are the average of the three conducted direct shear test results on the dry sand at three normal stresses of 50, 100 and 200 kPa using a shearing rate of 0.0096 mm/min. A maximum variation of 0.8 degree was observed in ϕ_{peak} between the three repeated tests.

Table A.1: Shear strength parameters and physical properties for the test sand.

Soil properties	
G_s	2.65
Coefficient of uniformity, cu	1.529
Coefficient of curvature, cv	1.095
Particle size range mm	0.075-0.3
e_{min}	0.54
e_{max}	0.87
γ_{dry} $(\frac{kN}{m^3})$	15.30
γ_{sat} $(\frac{kN}{m^3})$	19.33
Relative density %	52
c_{dry} (kPa)	13.5
$\phi_{peak-\ dry}$ - $\phi_{critical-\ dry}$-(degrees)	44.1- 43.6
Void ratio, e	0.7

A.2.2 Modified direct shear apparatus and sample preparation

A circular shear box of diameter 80 mm was designed with several additional modifications over standard laboratory shear boxes (see Fig. 2a). The modifications included provision of: (1) a high air entry disk (HAED) of 1 bar in the bottom half of the shear box, (2) a water

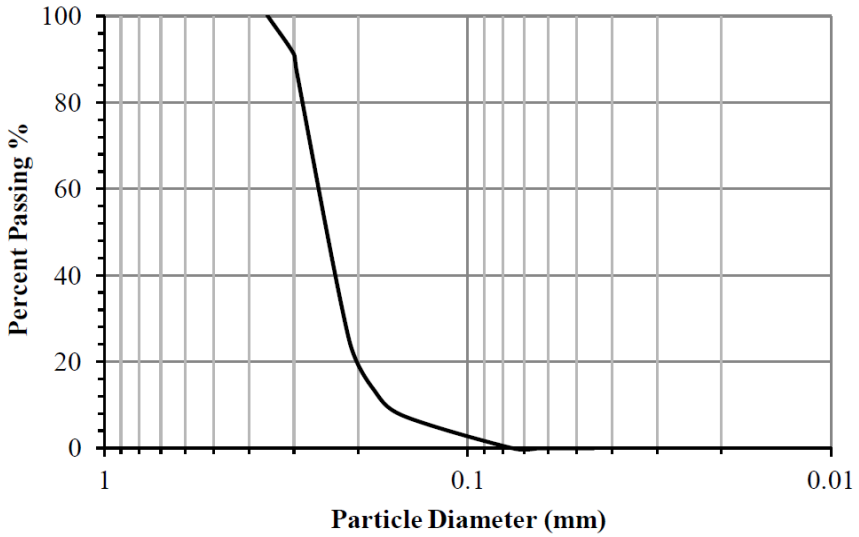

Figure A.1: Particle-size distribution curve for sand used.

reservoir underneath the HAED using grooved channels, (3) two ports to allow saturation of the grooved channels during test initialization and connection to a burette, (4) a burette for applying and controlling suction and (5) a camera installed in front of the burette to capture water level in the burette and hence water content of the sample at different stages of the test.

Following assemblage of the two halves of the box, the gap between them was sealed by a layer of silicon grease to prevent water leakage from the sample. The influent port was then connected to burette No.1 to flush de-aired water beneath the HAED for removing the air, while the effluent port was connected to burette No. 2. After the flushing procedure, the influent port was disconnected from burette No. 1 and closed. The amount of de-aired water required to saturate the sample was poured into the box, then a mass of dry soil (364 gm- provided a void ratio of 0.7 and dry unit weight of 15.3 kN/m^3) was then poured into the box using the water pluviation technique. The soil surface was levelled off and a grooved plate was placed. On top, a small normal stress of = 0.97 kPa (0.5 kg) was applied, the box was then covered by a piece of latex membrane to avoid evaporation prior and during the test. The small applied load was left for 1 hr.

The application of suction was achieved by lowering burette No.2 to the desired height. Nominal suction head was defined as the distance from water table in the burette to the surface of the sample. After successful application of the suction, the sample was left for at least 15 hrs for equalization purposes. In a constant temperature room (20^{o}C), vertical and horizontal LVDTs were then set up for the displacement measurements. The dry samples were prepared by pouring the soil at distance zero from the HAED to obtain the same unit weight and void ratio stated above. This was within 1% of the overall average dry unit weight of 15.3 kN/m^3 which corresponds to the void ratio 0.7.

A.2.3 Soil water characteristic curve (SWCC)

The box additionally allowed direct measurement of the soil water characteristic curve (SWCC) for the fine sand within the suction range of 0 to 10 kPa. Figure 2b shows the SWCC for the used sand obtained using the apparatus and compared with filter paper method. The experimental results were fitted using the Fredlund & Xing (1994) model for

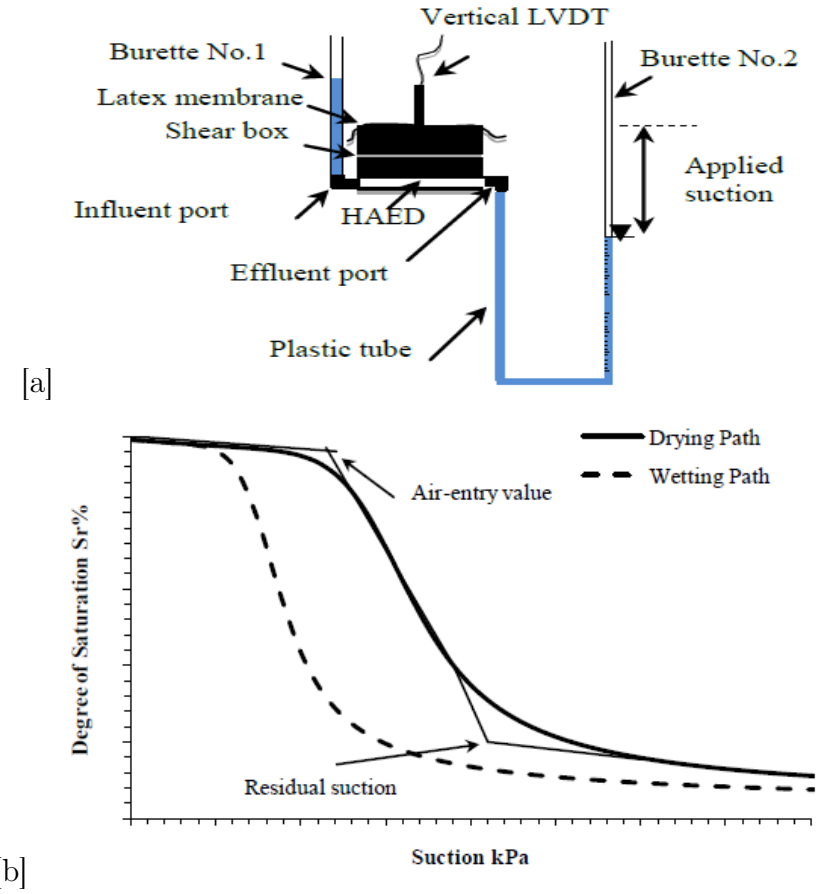

Figure A.2: (a) Modified direct shear box and suction application using HCT. (b) SWCC using two different methods.

both main drying and wetting curves.

A.3 Results

A.3.1 Unsaturated shear resistance and dilatancy behaviour

A series of drained tests were conducted at different vertical stresses of 50, 100 and 200 kPa and at a range of applied suctions (dry, 0, 2, 4 and 6 kPa) to cover the range between the air entry and residual suction. Figures 3a, b and e show the shear resistance versus horizontal displacement at different applied suctions and for σ = 50, 100 and 200 kPa, respectively. The shear resistance values are based on the corrected area of the samples. At each normal stress and suction three repeat tests were performed. Here only the data for the first repeat test (denoted as "1" in the figures legend) were presented. The shearing rate for the dry, saturated and unsaturated samples were 0.0096, 0.048 and 0.0096 mm/min, respectively. A higher shearing rate was used for the saturated sample compared to the unsaturated samples due to the higher effective permeability of the former. Three empty control tests (box is sheared without soil) were also conducted at two different shearing rates of 0.048 and 0.0096 mm/min. This was to study the effect of the grease used to seal the two halves of the box. As expected near zero shear resistance was recorded. The noise of the data acquisition measurement was 5 N maximum, equivalent to 0.987 kPa shear stress. All

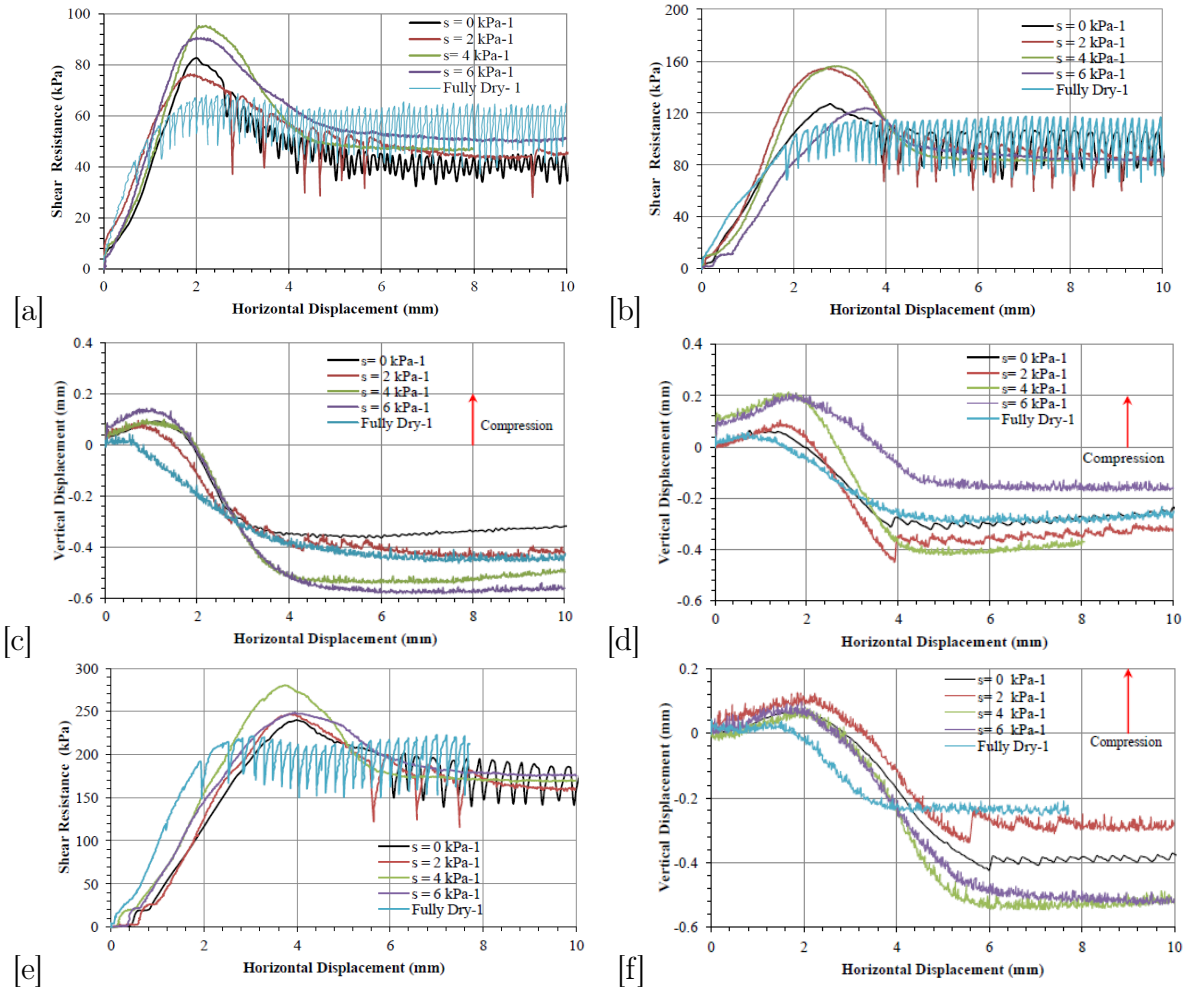

Figure A.3: Shear resistance versus horizontal displacement for different applied suctions at (a) $\sigma = 50$ kPa. (b) $\sigma = 100$ kPa. (e) $\sigma = 200$ kPa.Vertical displacement versus horizontal displacement at (c) $\sigma = 50$ kPa. (d) $\sigma = 100$ kPa. (f) $\sigma = 200$ kPa.

specimens exhibited peak strength behaviour, except the fully dry case, followed by a shear resistance reduction to critical state. There is significant increase in the shear resistance for the unsaturated cases when compared to the fully dry case. For example, the shear resistance at peak strength for $s = 4$ kPa and $\sigma = 50$ kPa increased about 1.42 fold when compared to the fully dry case. The other repeat tests (2 and 3 - not presented in this paper) demonstrated closely similar behaviour.

Figures 3c, d and f show vertical displacement versus horizontal displacement for test 1 at different applied suctions and three normal stresses of 50, 100 and 200 kPa, respectively. Figures 3c, d and f are plotted with the positive vertical displacement (compression) axis pointing upwards. All samples exhibited contractive behaviour initially, but then dilative behaviour as the horizontal displacement continued to increase until the critical void ratio was reached. At the critical void ratio, continued shearing of the soil took place at constant or steady volume. The maximum value of dilation correlated with the peak strength. However, samples displayed maximum dilation and peak strength at mid-range values of suctions (2-6 kPa). Generally; for all three normal stresses, the unsaturated samples showed higher dilation compared to the fully dry or saturated cases (see Figs. 3c, d and f).

The fully saturated samples showed high shear resistance at peak compared to the fully

dry case (see Figs. 3a, b and e). As this in not in accordance with expected behaviour, repeat tests were carried out including tests where the sample was saturated after a horizontal displacement of about 3.2 mm during a shear test for both a drained condition and a case when effluent port was closed during the test to not allow any water in or out of the specimen from the burette as shown in Figs. B.4a and b. The closed effluent port case was suggested to double check the fully saturated condition (water expelled out from the sample for the drained case during shearing led to a slight decrease of about 1% or less in degree of saturation). For both drained and closed effluent port tests, the HAED was replaced by a piece of porous plastic to speed up the saturation stage. Here the strength and dilatancy rate (see Figs. B.4c and d) were observed to rise after saturation in line with the currently reported tests. The explanation of the strength increase at the fully saturated case is difficult using the conventional soil mechanics theory.

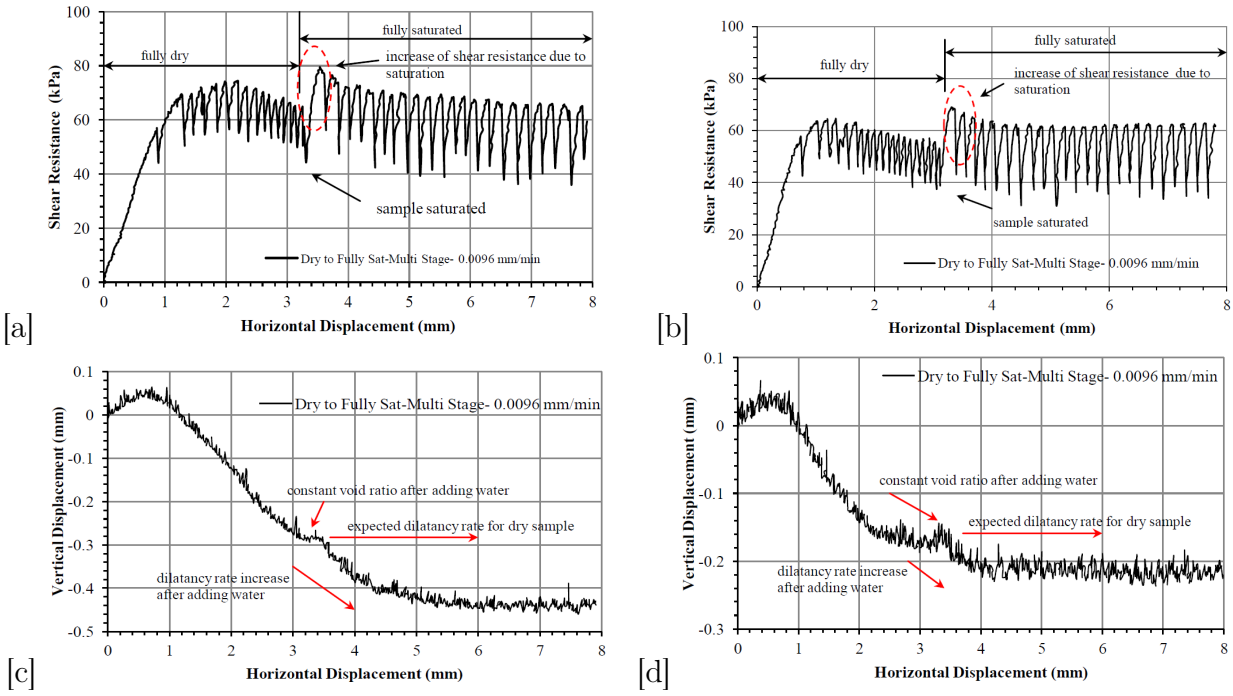

Figure A.4: Multi-stage test at displacement rate of 0.0096 mm/min and $\sigma = 50$ kPa (a) Shear resistance - drained condition. (b) Shear resistance-closed effluent port condition (c) Dilatancy - drained condition (d) Dilatancy- closed effluent port condition.

A.3.2 Increase of ϕ and c at peak for saturated and unsaturated sand

Figure B.5a shows the averaged shear resistance across the three repeat tests at peak versus net normal stress in which the variation of cohesion can be seen. The data are fitted using the least squares method. The importance of Fig. B.5a is that different ϕ_{Peak} values at different applied normal stresses can be seen.

It is intriguing that the cohesion intercept, c of the sand approximately doubles when comparing fully saturated and unsaturated cases with the dry condition. The ϕ_{peak} value increased 2.5^o (for saturated case) and 7.5^o (for unsaturated case - as a maximum increase at $s = 4$ kPa) when compared to the fully dry case. This gives a maximum increase of 5^o

in the average ϕ_{peak} between fully saturated and unsaturated samples. These differences are challenging to explain using conventional theory.

All unsaturated results would have been expected to map closely onto the "dry" line in Fig. B.5a. However it is clear that unsaturated conditions give rise to significant gain in strength. This behaviour cannot be attributed to the effect of the suction in the effective stress equation even if the suction is assumed to act as if present in the entire pore space. This can be demonstrated by adopting the following equation (proposed by Öberg & Sällfors (1997)).

$$\tau = c + (\sigma + s\ S_r)\ \tan\phi \tag{A.1}$$

Figure B.5 b shows the average measured value of s at peak and inferred value of sS_r at different normal stresses in which there is no way that the strength increase for saturated and unsaturated samples can be attributed to the effect of the sS_r term due to its small effect (maximum increase in strength due to sS_r at $s = 2.14$ kPa and high degree of saturation ($S_r = 0.98$) is equal to 2.09 kPa $\times$ tanϕ using Eq. A.1). This is equivalent to an increase of strength about 2.6 kPa.

It is hypothesised that the increase of shear strength parameters are due to the water-soil interaction in which menisci formation changes the soil fabric. As suggested by Fern et al. (2014) clusters or assemblages of particles are held together by menisci suction (see Fig. 5c). It is generally accepted that larger particles due to aggregation produce higher frictional resistance under shearing, (Murray & Sivakumar (2010)). The change of the soil fabric leads to increase the shear resistance and hence ϕ_{peak} and c.

A.4 Conclusions

Direct shear test results performed on dry, saturated and unsaturated sand samples using a direct shear box have been presented. In the light of the experimental data, the following conclusions can be made:

1. Significant increases in shear strength due to full and partial saturation were observed well in excess of that expected by the action of pore pressure or suction within a simple effective stress framework.

2. It is hypothesised that this behaviour is due to the change of the soil fabric due to particle aggregation. This change led to increase the dilatancy rate, shear resistance and hence the mobilized internal friction angle and cohesion of saturated and unsaturated sand.

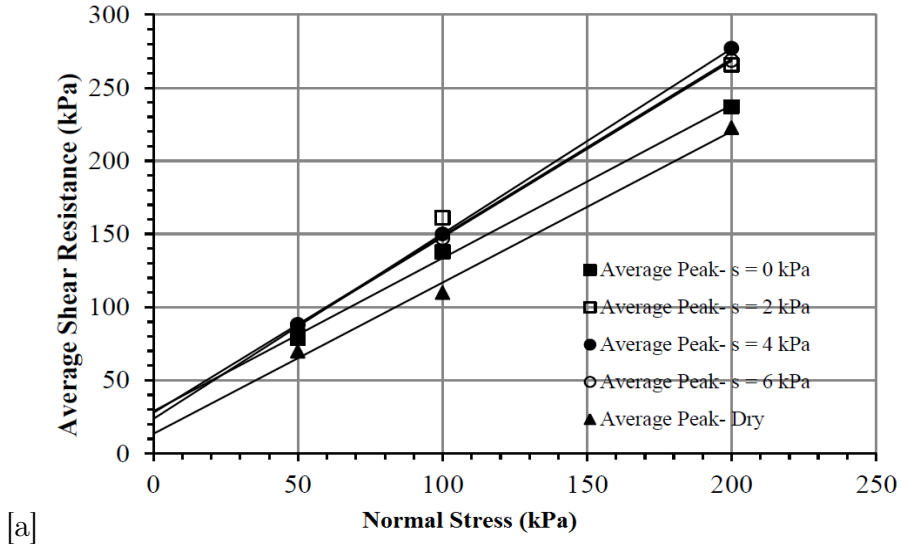

[a]

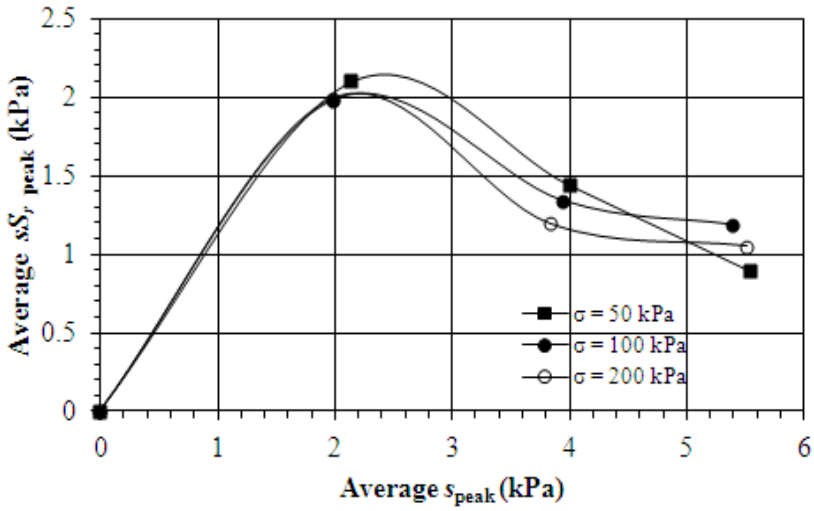

[b]

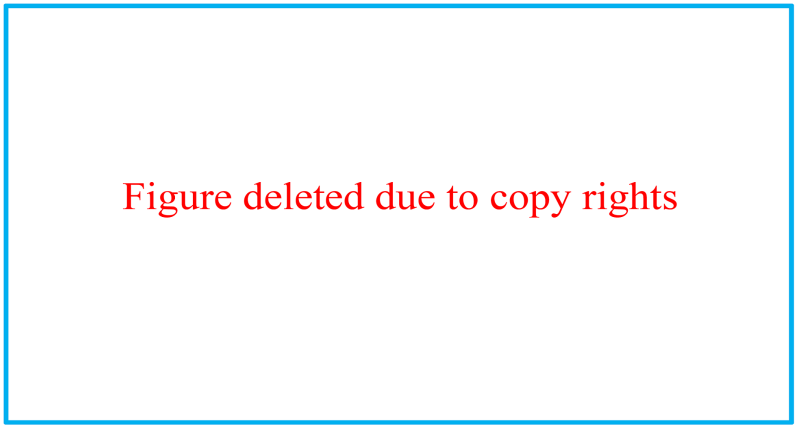

[c]

Figure A.5: (a) Average shear resistance versus net normal stress for dry, saturated and unsaturated samples at peak (b) Average measured s and average sS_r at peak for different normal stresses (c) Water-air menisci between two solid spheres (after Fisher (1926)).

Appendix B

Effect of Dilation on the Degree of Saturation during Shearing

This Appendix contents a draft technical note to be submitted to the Géotechnique journal.

Abstract

A series of direct shear tests were conducted on saturated and unsaturated sand where suction was controlled using the hanging column technique (HCT). Unsaturated samples showed higher dilative behaviour compared to the saturated sample and this volume change correlated with water migration into or out from the sample and with the change of suction. An increase of the degree of saturation (wetting behaviour) in a fully saturated case and in a case when a large reduction of volume (collapse) at a high degree of saturation was observed. Other cases when the collapse was small or samples were prepared at a higher suction (lower degree of saturation) showed drying behaviour. In contrast, the change of suction (even it is controlled using the HCT) was unexpected and suggests a reassessment of the HCT as a method of controlling suction. It is hypothesised that the change of soil suction and the drying and wetting behaviours are attributed to the dilative behaviour which changed the fabric of the soil.

B.1 Introduction

The theoretical developments in unsaturated soil mechanics are due to the applicability of controlling and measuring the suction in unsaturated soils confidentially. Several methods have been developed to control or measure the suction both in the laboratory and in the field such as axis translation technique, filter paper, tensiometer and hanging column technique (HCT).

A few studies can be found in the literature which used the HCT as a method of controlling suction such as these performed by Likos et al. (2010) and Sharma & Mohamed (2003). In terms of the former, they studied shear strength of saturated and unsaturated sand using the HCT in which no attempt was made to quantify the association between dilatancy, water flow and suction. While Sharma & Mohamed (2003) investigated migration of contaminants in unsaturated/saturated sand to obtain the SWCC. This study was limited to address the effect of the contaminants flow on the SWCC but not on the volume change and shear strength.

Although the HCT is a method of controlling suction, it has not been utilised broadly to study behaviours such as hydro-mechanical and water migration during shearing for sand. These behaviours are significantly affected by the dilatancy, and in saturated soils dilatancy has been fairly well studied and understood. In contrast, the understanding of principles of dilatancy in unsaturated soils are restricted due to the long experimental time and complexity Ng & Zhou (2005).

This study therefore sets an approach to use the HCT with a direct shear box which accounts for dilatancy-shear strength and dilatancy-water flow dependency. The relationship between the dilation, suction and degree of saturation throughout monitoring the level of the water table in a burette via a camera at different stages of the test is studied. The drying and wetting behaviours of the samples during shearing due to the changes in soil fabric at different degrees of saturation are also reported. The dilative behaviour observed for unsaturated samples which caused changes in the soil fabric suggests revision of the HCT as a method of controlling suction.

B.2 Experimental work

B.2.1 Material used

A fine sand designated as Fraction D and available from the David Ball Group, UK was utilised in this study with the physical and shear strength properties shown in Table B.1. The dry shear strength parameters $c^{'}$ and $\phi^{'}$ shown in Table B.1 are the average of the three direct shear test results conducted on the dry sand at three normal stresses of 50, 100 and 200 kPa. A shearing rate of 0.0096 mm/min was used.

Table B.1: Physical properties and shear strength parameters for the test sand.

Soil properties	
Physical properties	
G_s	2.65
Coefficient of uniformity, cu	1.529
Coefficient of curvature, cv	1.095
Particle size range mm	0.075-0.3
Void ratio, e	0.7
e_{min}	0.54
e_{max}	0.87
γ_{dry} $(\frac{kN}{m^3})$	15.30
γ_{sat} $(\frac{kN}{m^3})$	19.33
Relative density %	52
Shear strength parameters	
c_{dry} (kPa)	13.5
$\phi_{peak-\ dry}$ (degrees)	44.1

B.2.2 Suction application using the HCT

Figure B.1a shows the direct shear test with a burette (called No.2) for applying and controlling suction using the HCT and a camera installed in front of the burette to capture the

water level during the test (not shown in Fig. B.1a) and hence the water content of the sample at different stages of the test can be obtained accordingly. Further details about the direct shear box and the sample preparation are given by Shwan & Smith (2015).

After the successful flushing procedure and sample preparation, the application of suction was by lowering the burette No.2 to the desired depth. Nominal suction head was defined as the distance from water table in the burette to the surface of the sample. The sample was then left for at least 15 hrs for equalization purposes. Vertical and horizontal LVDTs were then set up for the displacement measurements. Figure B.1b shows soil water characteristic curve (SWCC) obtained for the sand used using the HCT (using the box) and filter paper method. The experimental results were fitted using the Fredlund & Xing (1994) model for both drying and main wetting curves.

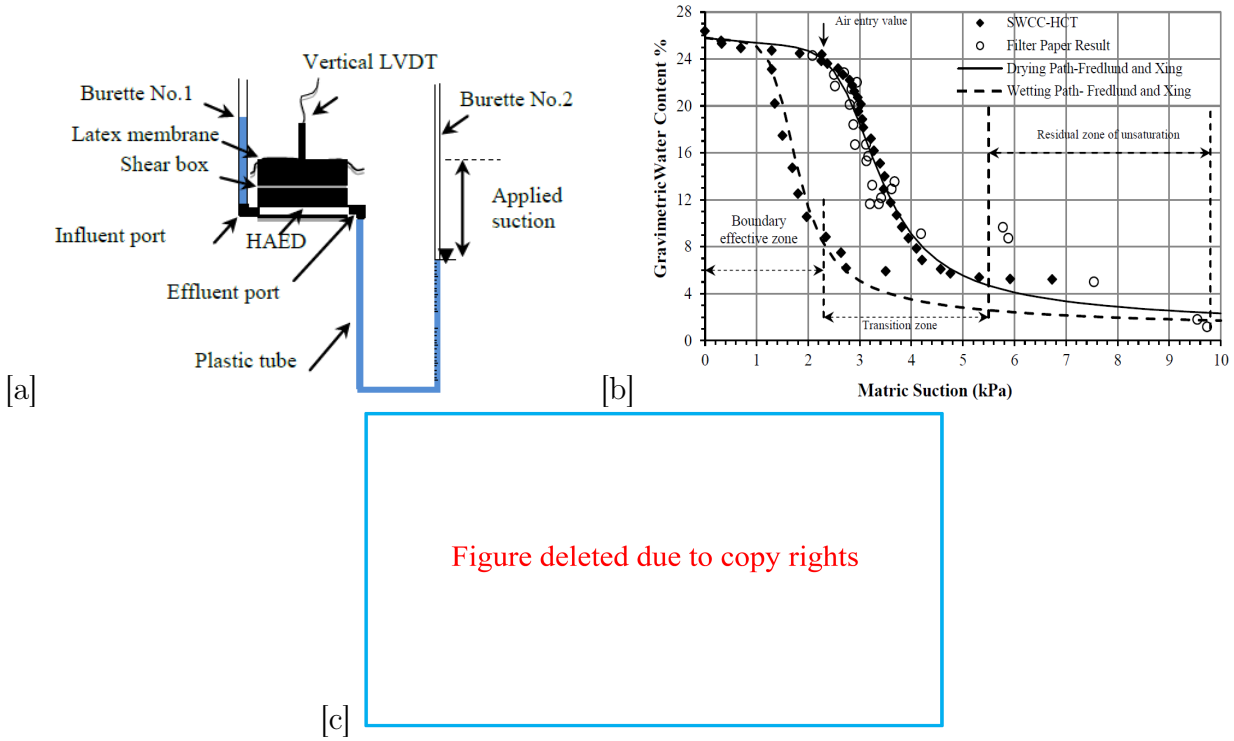

Figure B.1: (a) Modified direct shear box and suction application using HCT. (b) SWCC using two different methods. (c) Air-water interface at different suction, after Childs (1969).

B.3 Results

A series of drained direct shear tests were performed on saturated and unsaturated samples at different vertical stresses of 50 and 100 kPa. A range of initial applied suction, s as 0, 2 and 4 kPa were applied. The shearing rate for the saturated and unsaturated samples were 0.048 and 0.0096 mm/min, respectively. A higher shearing rate was used for the saturated sample compared to the unsaturated samples due to the higher effective permeability of the former. Figures B.2, B.3, B.4 and B.5 show results of the direct shear test for saturated and unsaturated samples. The specimen exhibited peak strength behaviour followed by a shear strength reduction to critical state (see Fig. B.2a). The shear strength values are based on the corrected area of the samples.

Figure B.2b shows degree of saturation, S_r, versus horizontal displacement. The initial

value of S_r (begining of the curves- see Fig. B.2b) is calculated by knowing the amount of water expelled from the sample during application of the suction (before shearing). The volume of the sample is constant and the initial void ratio is known ($e = 0.7$ - see Table 1). Values of S_r during shearing are obtained by knowing the amount of water expelled or imbibed by the sample during shearing. Here, the volume of the sample and void ratio are calculated based on the installed vertical LVDT (see Fig. B.1a) readings and corrected area at the corresponding stage of the shearing. This is an estimation of the volume especially for the case when a large plastic collapse occurred as it is assumed that this collapse (volume change) happened on the overall area of the sample not locally. The assumption interprets why values of S_r higher than 100% are obtained (Fig. B.4b).

Figure B.2c shows suction versus horizontal displacement during the shearing. The suction values were obtained by monitoring the water level in the burette via the installed camera. The camera was set up to take a picture of the burette every 10 and 30 minutes for the saturated and unsaturated samples, respectively. A smaller time of the image capturing was utilised for the saturated samples due to its higher shearing rate.

B.3.1 Effect of dilatancy and degree of saturation on the shear resistance of unsaturated sand

Figure B.2d shows vertical displacement versus horizontal displacement which is plotted with the positive vertical displacement (compression) axis pointing upwards. The sample exhibited contractive behaviour initially, but then dilation behaviour as horizontal displacement continued to increase until critical void ratio was reached. At the critical void ratio, continued shearing of the soil was taking place at constant or steady volume. The maximum rate of dilation correlated with the peak strength. Figures B.3, B.4 and B.5 are plotted in the same manner of Fig. B.2, however with different suction values and normal stresses. Generally, unsaturated samples exhibited higher dilative behaviour compared to fully saturated sample. This is in line with the results obtained by Cui & Delage (1996) for a compacted silt and for that obtained by Ng & Zhou (2005) for a coarse grained sand.

Based on Figs. B.2b, B.3b, B.4b and B.5b, two interesting scenarios of S_r change can be seen as follows:

1. An increase of S_r until the critical state
   An increase of the degree of saturation was observed which was the case for the fully saturated samples (Fig. B.2b) and the samples prepared at a high degree of saturation ($s = 2$ kPa) when a sudden large plastic collapse happened during the shearing (circled in Fig. B.4d). This suction ($s = 2$ kPa) is close to the air-entry value of the sand used in this study (see Fig. B.1b). The plastic collapse was an irreversible wetting deformation which happened due to high degree of saturation. This collapse is beyond of the scope of this paper and more details are given by Shwan (2015).

   The initial increase of S_r is due to bedding down of the particles as initially contractive behaviour happened (see Figs. B.2d). This is also the case for the second scenario (Fig. B.4d). After the peak, further wetting happened although the sample exhibited dilative behaviour. The continuous wetting trend at $s = 0$ kPa (Fig. B.2b) is attributable to the increase of the void ratio, due to the dilative behaviour, and to the free water. The sample dilated and absorbed water after the peak (position 3 to 2 in Fig. B.1c) since

water was interconnected between the voids and this caused suction increase as shown in Fig. 2c. The implication of the Figs B.2a, b, c and d is important as the suction is no longer constant (after the peak) due to the volume change or dilation. The result is identical for that shown in Figs. B.3, B.4 and B.5.

For the sample which exhibited a large plastic collapse (Fig. B.4b), the wetting trend was also observed due to irreversible decrease in void ratio at the collapse. Here the free extra water was expelled from the sample which led to decrease the suction after the peak (see Fig. B.4c).

2. An increase of S_r until the peak then followed by a decrease
   Samples prepared at a high degree of saturation ($s = 2$ kPa) with no or a small plastic collapse and prepared at lower degree of saturation (higher suction, $s = 4$ kPa - see Fig. B.5b) showed this trend.

The decrease of S_r (drying behaviour) after the peak can be attributed to the increase of void ratio (vertical displacement - see Figs. B.3d and B.5d) due to the higher dilative behaviour compared to the fully saturated case. Hence, the increase of void ratio due to dilation caused water movement to the smaller pores at the inter-particle contact points (water migration from position 4 to 5 in Fig. B.1c). The extra water then expelled from the sample leading to suction decrease (see Figs. B.3c and B.5c). The higher S_r at the same normal stress, the higher shear strength at the peak can be obtained (see Figs. B.4a and B.5a). This is because of the effect of S_r on the shear strength of the soil outweighed that of dilatancy. In other words, although higher dilatancy was observed for $s = 4$ kPa (Fig. B.5d) compared to the sample prepared at $s = 2$ kPa (Fig. B.4d), higher shear strength was obtained for the latter due to its higher degree of saturation.

The increase of void ratio which caused water migration highly affected the soil fabric. Suction was constant prior to peak, then followed by either an increase or decrease (water imbibed or expelled by the sample) due to change of the soil fabric. This is an interesting behaviour shows that how changes of the soil fabric affected the change in suction and consequently caused the drying and wetting behaviours for the sand. It is somewhat surprising that the suction change which caused due to the water migration led to a conclusion that the HCT which was used previously as a method of controlling suction may needs reconsideration. The reassessment is required as the effect of suction on the shear strength reached its maximum at peak then followed by a reduction after perturbation of the water menisci due to dilation.

It is hypothesised that the effect of the dilation which changed the soil fabric caused water migration. This migration and therefore suction change can be linked directly to the ultimate strength of the soil as it was a peak behaviour for almost all the samples (i.e see Figs. B.3a and c).

B.4 Conclusions

A series of drained direct shear tests on saturated and unsaturated samples were reported in which the effect of dilation on the soil fabric and then water migration were investigated. The following conclusions are made:

1. Unsaturated samples exhibited higher dilation compared to the saturated sample due to the effect of suction and the soil fabric changes.

2. An increase of the degree of saturation occurred prior to the peak for fully saturated sample and for samples prepared at a high degree of saturation when a large plastic collapse happened. On the other hand, a decrease of the degree of saturation was observed, for samples prepared at a high degree of saturation with small plastic collapse and at low degree of saturation, after the peak which coincided with the decrease in the suction head. These changes can be attributed to the effect of the change of air-water interface which affected by the change of the soil fabric due to dilation.

3. Although suction was controlled using the HCT, for all of the cases suction remained constant prior to the peak then followed by a change. This was attributed to the change of void ratio due to dilation in which water either imbibed or expelled from the sample. The change of suction set the necessity to reassess the principles of the HCT as a method of controlling suction.

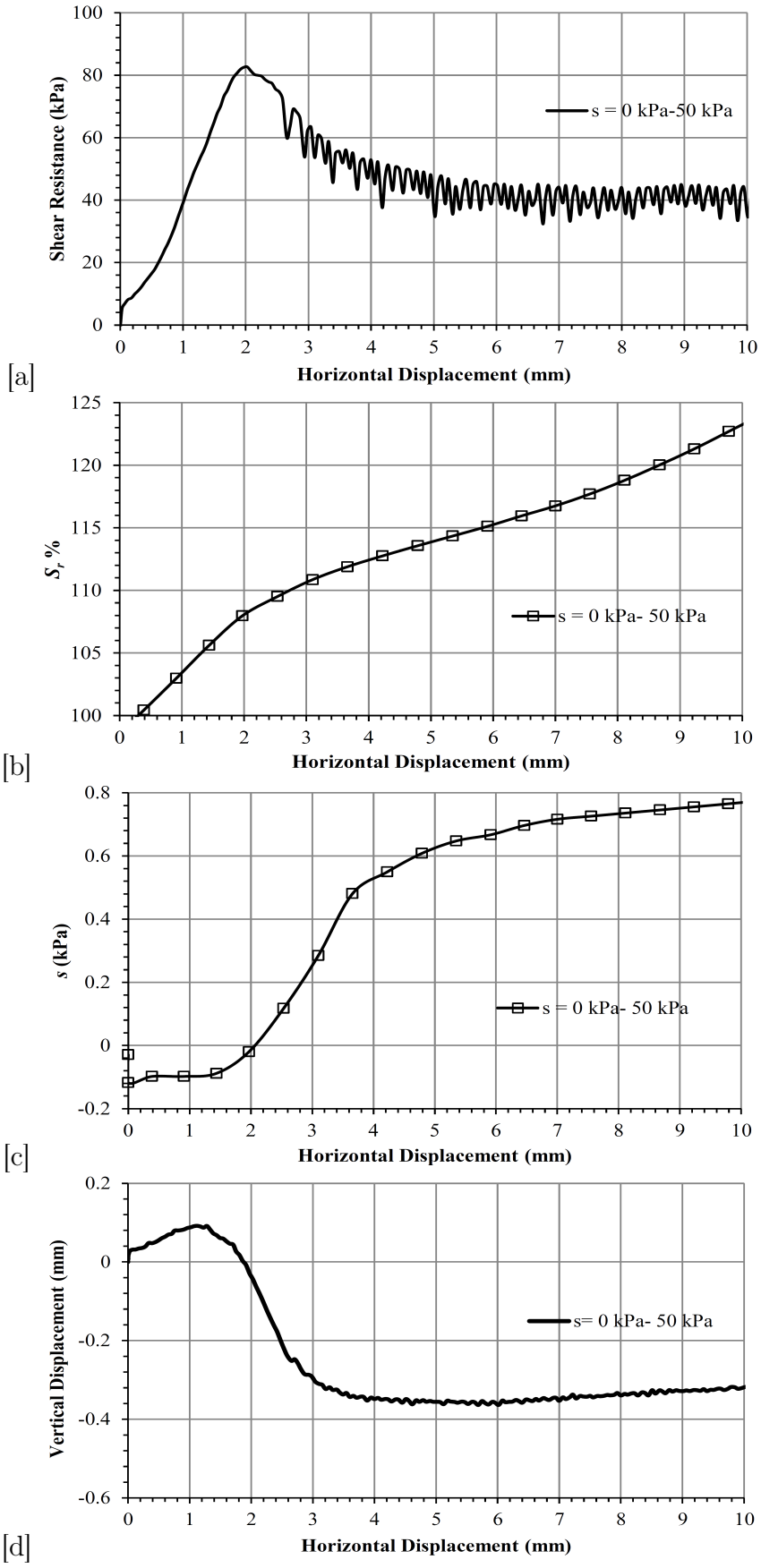

Figure B.2: Results of $s = 0$ kPa at $\sigma = 50$ kPa (a) shear resistance versus horizontal displacement (b) degree of saturation S_r versus horizontal displacement (c) suction, s versus horizontal displacement (d)vertical displacement versus horizontal displacement.

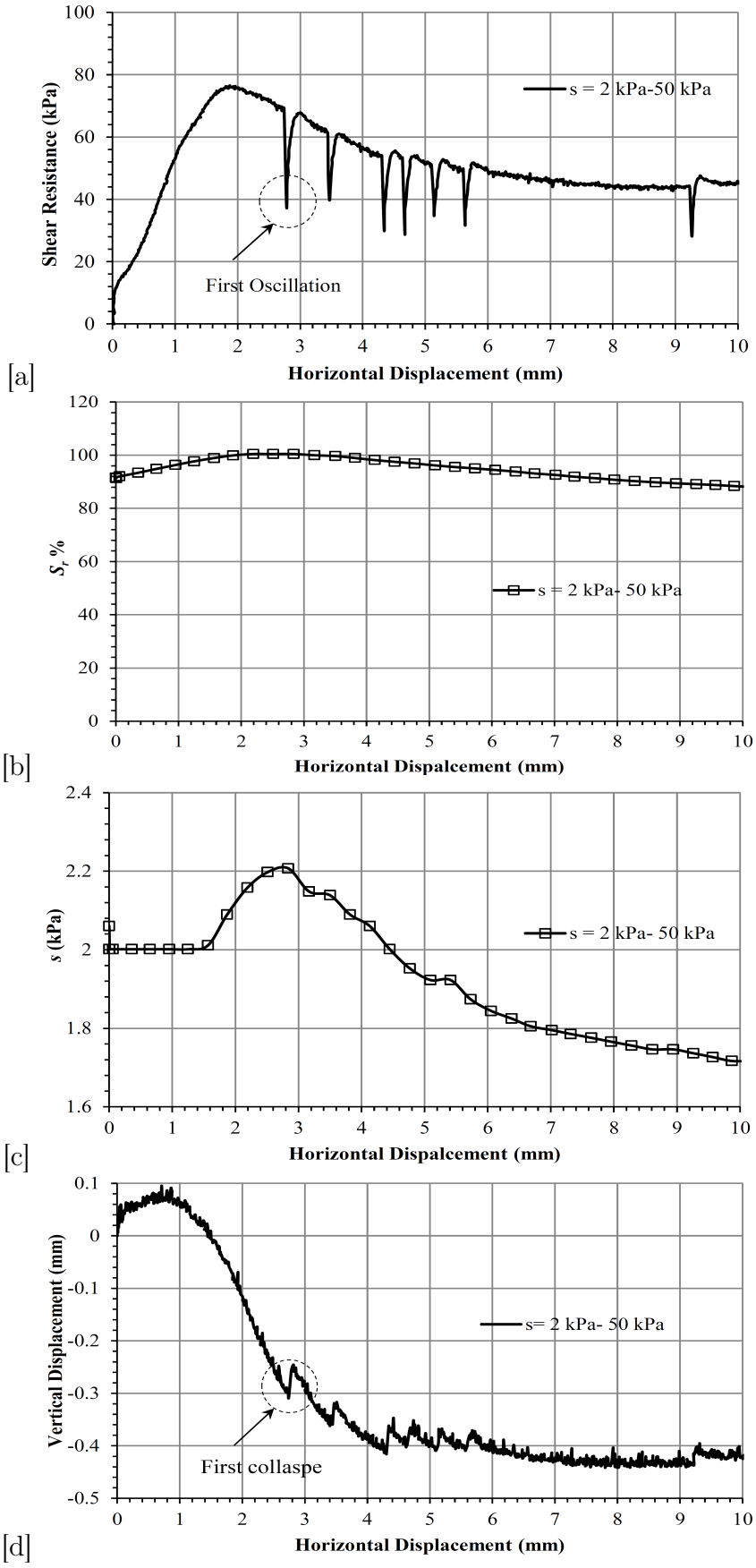

Figure B.3: Results of $s = 2$ kPa at $\sigma = 50$ kPa (a) shear resistance versus horizontal displacement (b) degree of saturation S_r versus horizontal displacement (c) suction, s versus horizontal displacement (d)vertical displacement versus horizontal displacement.

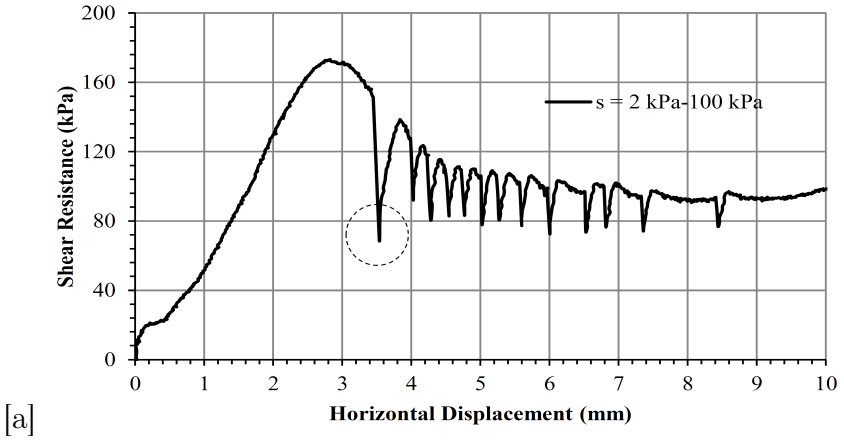

[a]

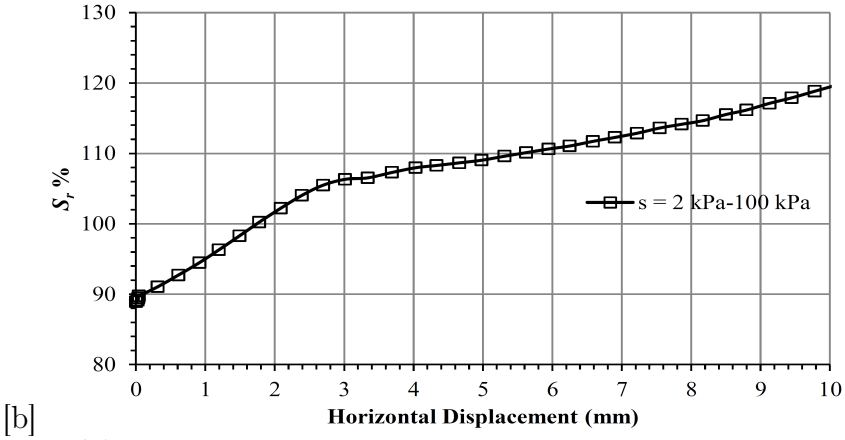

[b]

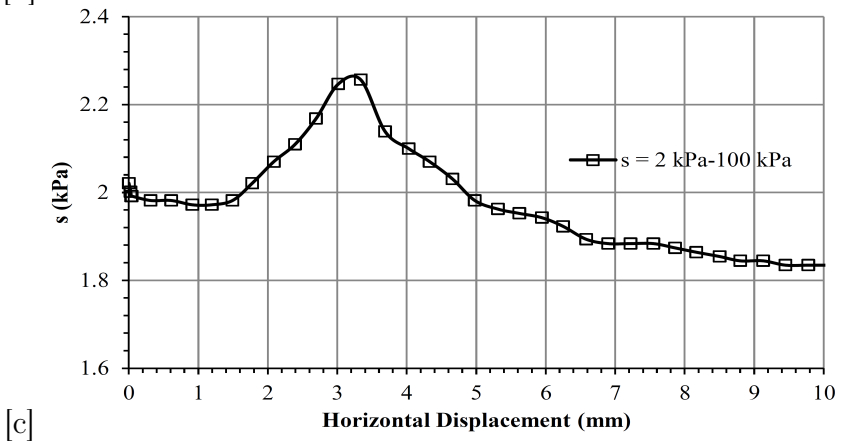

[c]

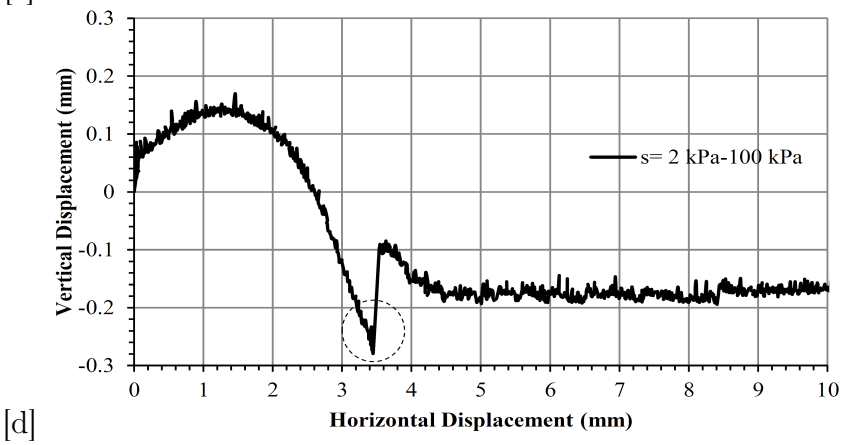

[d]

Figure B.4: Results of $s = 2$ kPa at $\sigma = 100$ kPa (a) shear resistance versus horizontal displacement (b) degree of saturation S_r versus horizontal displacement (c) suction, s versus horizontal displacement (d)vertical displacement versus horizontal displacement.

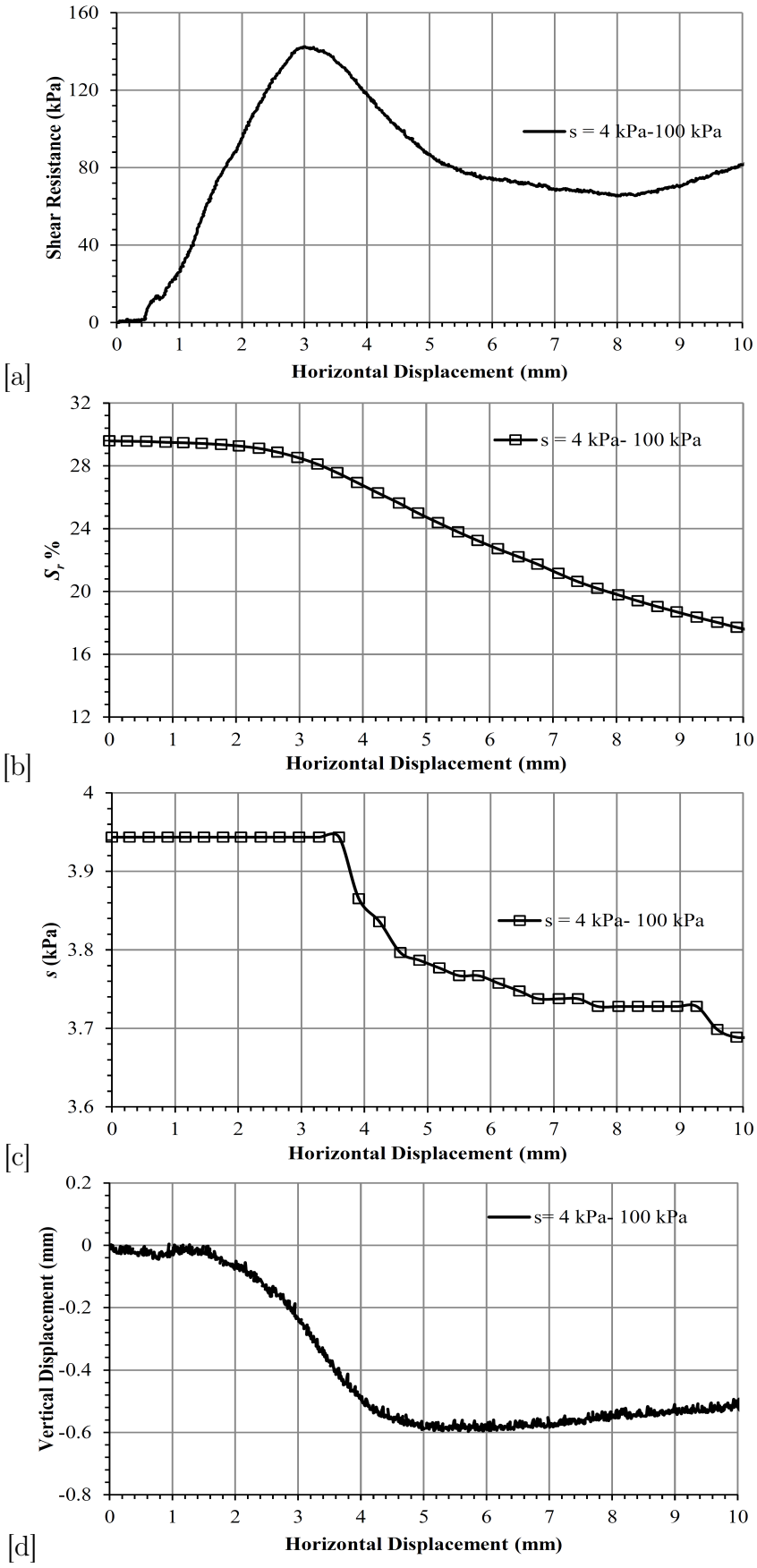

Figure B.5: Results of $s = 4$ kPa at $\sigma = 100$ kPa (a) shear resistance versus horizontal displacement (b) degree of saturation S_r versus horizontal displacement (c) suction, s versus horizontal displacement (d) vertical displacement versus horizontal displacement.

Appendix C

Application of Limit Analysis in Unsaturated Soils: Numerical and Experimental Study of Bearing Capacity

This Appendix contents a paper published in the proceedings of the International Conference on Unsaturated Soils: Research and Applications- UNSAT-2014.

Abstract

Computational limit analysis (CLA) is a tool that has found significant application in conventional geotechnical engineering. This paper presents work in progress that extends the CLA method, Discontinuity Layout Optimization (DLO), to account for the effects of partial saturation on strength, by adopting an effective stress equation that accounts for suction and degree of saturation. The analysis is then used to model a simple bearing capacity problem and is compared with laboratory model tests. These tests provided load-deflection data for a range of soil saturation scenarios and also soil displacement data using particle image velocimetry (PIV). The experimental results demonstrated that 3-fold changes in bearing capacity could be achieved across the modelled water levels. Comparison of the numerical and experimental data shows reasonable agreement indicating that the bearing capacity strength enhancement first rises as suctions in the soil increase but then subsequently diminish as the degree of saturation starts to fall.

C.1 Introduction

Significant efforts during the last two decades have led to the formulation of several theoretical frameworks and a number of constitutive models for understanding unsaturated soil mechanics, e.g Alonso et al. (1990), Wheeler (1991), Wheeler & Sivakumar (1995) and Tarantino (2007). In contrast, application of unsaturated soil mechanics theory to geotechnical analysis and design has been more limited. Typically work has

either involved the incorporation of unsaturated mechanics into numerical models (e.g. finite element, slip circle, finite difference), or into conventional hand type calculations (either using limit analysis or limit equilibrium methods). In terms of the latter, Zhao et al. (2009) proposed an approach to calculate passive earth pressure based on the upper bound theorem and the shear strength of unsaturated soils. More recently, Stanier & Tarantino (2010) proposed equations based on the lower and upper bound theorems for the active earth pressure exerted by partially saturated soils. Such studies are limited by the nature of what can be dealt with using hand calculations. However developments in computational limit analysis (CLA) (e.g. Lysmer (1970); Sloan (1988); Makrodimopoulos & Martin (2006), Smith & Gilbert (2007*a*)) have extended the scope of such analytical methods, so that they can deal with any geometry and loading configuration, and have been applied in many areas to ultimate limit state (ULS) design. The aim of this paper is to report current work investigating the application of the computational limit state analysis method to unsaturated geotechnical problems. Specifically the plane strain upper bound approach, Discontinuity Layout Optimization (DLO) described by Smith & Gilbert (2007*a*) is extended to model the effects of partial saturation and is compared against laboratory scale models tests of bearing capacity on a fine sand.

C.2 Theory

C.2.1 Discontinuity layout optimization

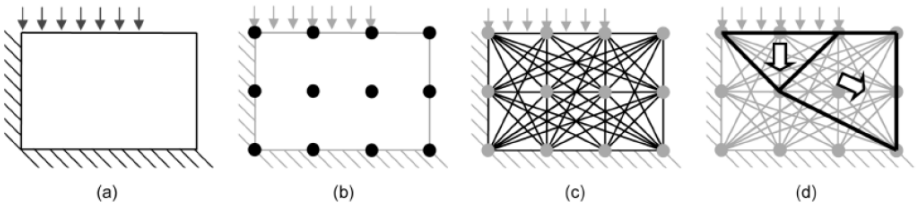

Figure C.1: Stages in the DLO procedure: (a) starting problem (surcharge applied to block of soil close to vertical cut); (b) discretization of soil using nodes; (c) interconnection of every nodes to every other node with potential discontinuities;(d)identification of critical subset of potential discontinuities using optimization (giving the layout of the slip-lines in the critical failure mechanism) (after Gillbert et al. (2010)).

A summary of the DLO procedure is given in Fig. C.1. The method is based on the discretization of the problem domain into nodes and on determining the optimal layout of discontinuities drawn from the set of all discontinuities connecting every node to every other node that make up the critical collapse mechanism. The accuracy of the model is a function of the number of nodes utilised.

C.2.2 Energy dissipation and work equation in DLO

Following (Smith & Gilbert (2007*a*), Smith & Gilbert (2007*a*)) in the presence of water, the rate of internal energy dissipation and work done against body forces for

the problem of a Mohr-Coulomb material with self-weight γ, cohesion c and angle of friction ϕ collapsing as a set of sliding blocks where each discontinuity (or interface) i between adjacent sliding blocks has relative shear and normal displacement jumps of s_i and n_i can be written as:

$$E = \sum_{i=1}^{m} (c_i \; l_i \; s_i \; + U_i \; n_i + W_i \; s_i \sin\theta_i + W_i \; n_i \cos\theta_i) \tag{C.1}$$

where m is the number of interfaces and U_i, and W_i are respectively the pore water force on, and weight of the strip of soil above interface i and l_i, θ_i are the length of interface i and the angle of interface i to the horizontal. For a limit analysis approach, $n_i = |s_i| \tan\phi'$.
The strip weight of the soil W above a discontinuity (see Fig. C.2) can be obtained by double integration of the unit weight over the strip area.
By matching the internal energy to the external work done, it is possible to determine the critical collapse load and mechanism. Further details may be found in Smith & Gilbert (2007*a*).

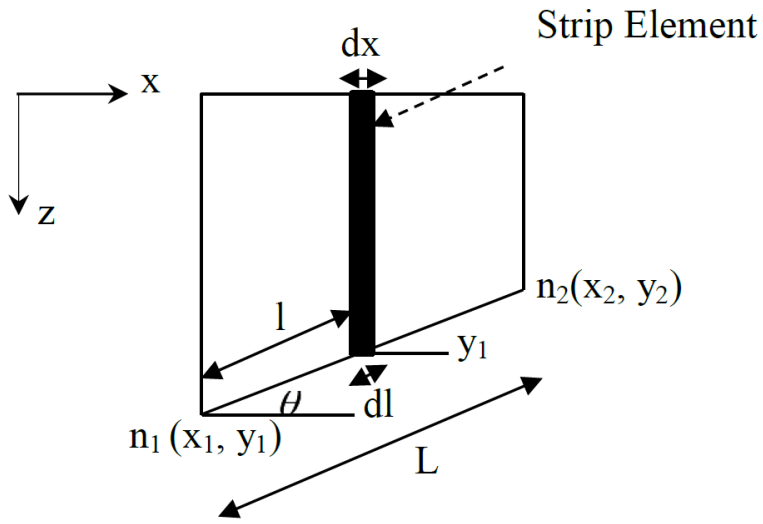

Figure C.2: Strip weight above the discontinuity showing nodes and strip element.

C.2.3 Modelling of suction and strength

Tarantino & Tombolato (2005) proposed a effective stress equation for the shear strength of compacted aggregated soils in partially saturated conditions as follows:

$$\tau = (\sigma \; + s \; S_r) \tan\phi' \tag{C.2}$$

where σ is the total normal stress, S_r is the effective degree of saturation and s is the hydrostatic suction.
The second term in the brackets in equation C.2 represents the effect of water pressure (suction) while also allowing for the reduced effective area of action due to the reduction of water content. A linear relationship with S_r is assumed here.

Stanier & Tarantino (2010) proposed equations for suction, degree of saturation and unit weight for unsaturated soil as follows:

$$s = \gamma_w \ (H_w - z) \tag{C.3}$$

$$S_r = e^{-as} \tag{C.4}$$

$$\gamma = \rho_d \ + \ (\rho_{sat} \ - \rho_d) \ S_r \tag{C.5}$$

where a is a fitting parameter (kPa^{-1}), γ_w is unit weight of the water (kN/m^3), z is vertical coordinate (positive downward) and H_w is water table depth (positive downward), γ is unit weight of the soil, ρ_d is dry density of the soil, and ρ_{sat} is saturated density of the soil. Equation C.3 assumes full water continuity within the soil.
In this paper, it is proposed that the preceding equations may be used to represent the unsaturated behaviour of fine sand. Implicit in this is the assumption that the water distribution is continuous and unaffected by deformation. Additionally variations of equations C.2 and C.4 are proposed which allow more flexible modelling of the unsaturated conditions as follows:

$$\tau = (\sigma \ + s \ S_r^{\alpha}) \tan \phi' \tag{C.6}$$

where α is a fitting parameter, and

$$S_r = 1.0, \ \ s \leq s_o \tag{C.7}$$

$$S_r = e^{-a \ (s - s_o)}, \ \ s > \ s_o \tag{C.8}$$

where s_o (kPa) is the air entry value of the soil and may be related to the depth to capillary rise (full saturation) H_c as follows:

$$H_c = H_w - \frac{s_o}{\gamma_w} \tag{C.9}$$

In order to compute the value of U in Eq. C.1 for use in the DLO formulation in a partially saturated soil, the following integration is required:

$$U = -\int_0^L s \ S_r^{\alpha} . \ dl \tag{C.10}$$

where L and dl are defined in Fig. C.2. The integration is straightforward but not included here due to space restrictions.

C.3 Bearing Capacity Problem Specification

To study the effect of partial saturation on bearing capacity, physical model tests were undertaken on a steel strip footing of width 25 mm, thickness 15 mm, and length 138 mm centrally placed on the surface of a 300 mm deep sample of fine sand of average particle size 0.18 mm. The sand was contained within a glass sided chamber of length 140 mm and width 400 mm.

Approximate plane strain conditions were maintained due to the reduced friction of the glass walls and the length/width ratio of the footing of 1:5. The footing/particle size ratio was ∼140 which should ensure particle size effects are negligible. The experimental data was compared with plane strain numerical model results.

C.4 Experiment

C.4.1 Material used and soil water characteristic curve (SWCC)

The soil used in this study was a commercial fine sand available from the David Ball Group, UK. Fig. C.3 shows the results from direct shear tests on the dry sand at the same density employed in the model tests. This density was dense of critical state, with dilative behaviour displayed in all tests. The corresponding shear strength parameters and physical properties are given in Table C.1.

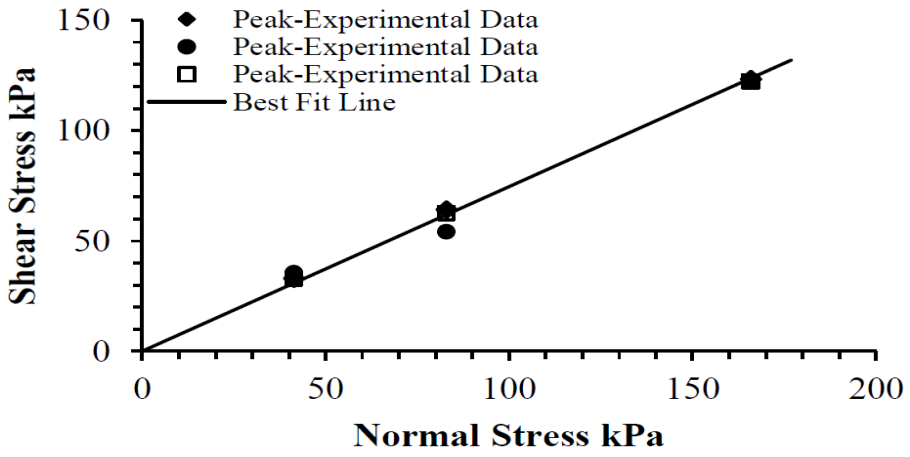

Figure C.3: Direct shear results for Fraction D fine sand at voids ratio 0.7.

The SWCC of the soil was obtained using two methods: the filter paper method and the hanging column technique (HCT). The test results are plotted in Figure C.4 together with a model fit using the Fredlund & Xing (1994) method. The data was also fitted to equations C.7 and C.8 and plotted in Figure C.5. It can be seen that a reasonable fit to the data is obtained over the range of suctions 0 - 5 kPa using a value of s_o = 2.3 kPa and a = 0.7.

Table C.1: Shear strength parameters and physical properties for the test sand.

c' kPa	ϕ'	G_s	γ_{dry} kN/ m^3	γ_{sat} kN/ m^3	particle size range
0	36.8	2.65	15.3	19.33	0.063-0.3

C.4.2 Sample preparation

Uniform, homogeneous and fully saturated samples of large size require a precise procedure for sample preparation. The sample was prepared by pouring oven dry fine sand (fraction D) below water level into the sample chamber at zero distance from the bottom of the box while maintaining the water level above the soil surface to avoid air entrapment. Due to the size of the test chamber, the specimen was poured in six equal layers of 50 mm thickness and the mass of each layer determined. These were within 1% of the overall average dry unit weight of 15.30 kN/m^3 which corresponds to a void ratio 0.699.

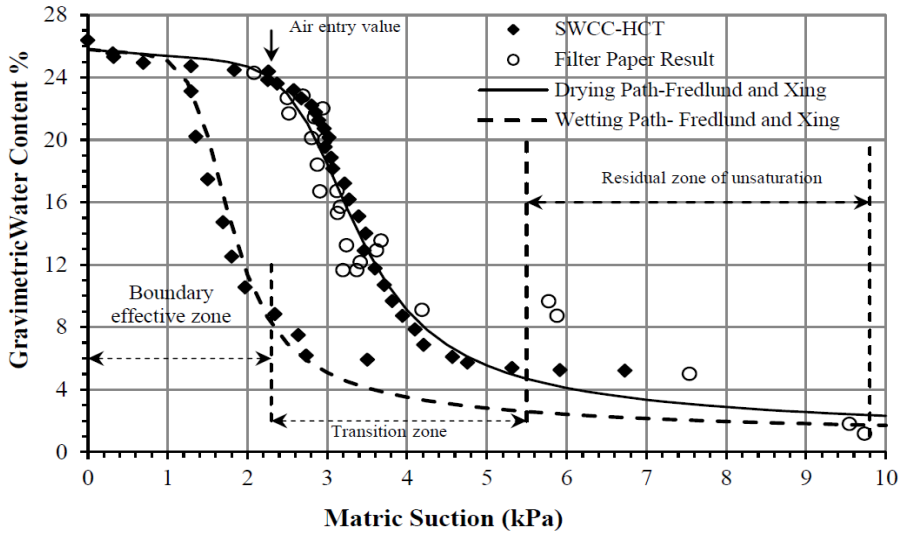

Figure C.4: Soil water characteristic using HCT and filter paper method.

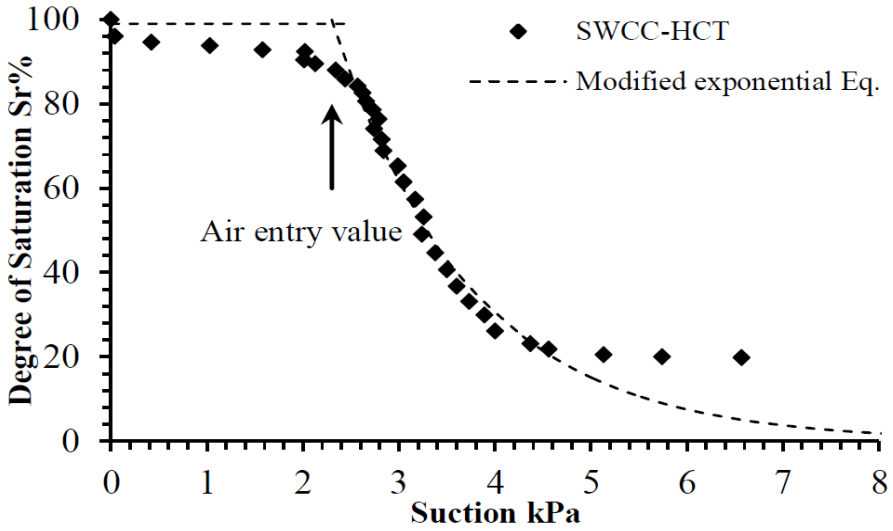

Figure C.5: Soil water characteristic for model sand and fit using equations C.7 and C.8.

C.4.3 Suction control

Suction and water pressure were controlled by means of a water tank and hanging water column (burette) connected to the sample chamber as shown in Fig. C.6. To allow smooth transmission of suction from the burette to the sand, a layer of porous plastic was placed in the bottom of the sample chamber covered by a thin layer of silt. During sample preparation, the water level in the tank, burette and soil chamber were maintained at the same level above the final soil surface by opening the connecting valves. After the sand had been poured the valve to the water tank was closed. A specific suction was applied by lowering the burette to the desired level. The system reached equilibrium after a period of time when the water level in the burette stabilized and matched the water table in the sample. The rig was then covered by a latex membrane to avoid evaporation of water from the sample during the test.

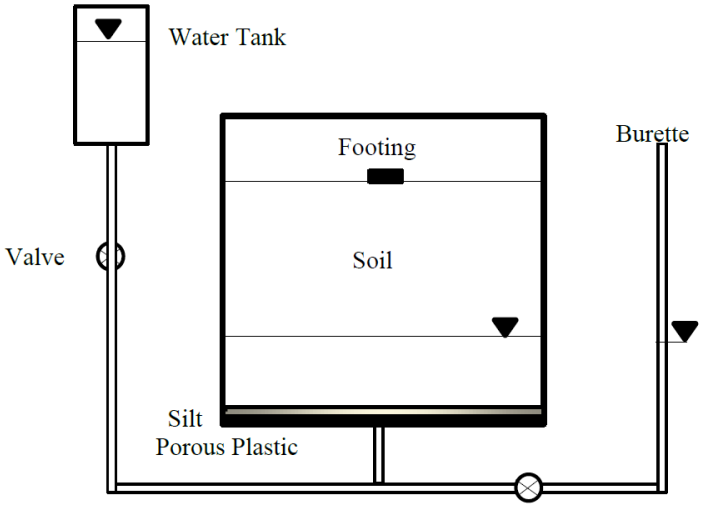

Figure C.6: Bearing capacity test rig.

C.4.4 Bearing capacity test

The model footing was displaced vertically using a loading piston at a constant displacement rate of 0.6 mm/min and the load monitored using a load cell. The test was terminated when the load reached approximate steady state. The model footing was free to rotate below the piston. Example plots of bearing capacity versus settlement are given in Fig. C.7 for four different suctions.

C.5 Numerical analysis

The suction model described in Section C.4.3 was incorporated into the DLO procedure and implemented into a research version of LimitState:GEO software (LimitState:GEO (2013)), using a value of $s_o = 2.3$ kPa.

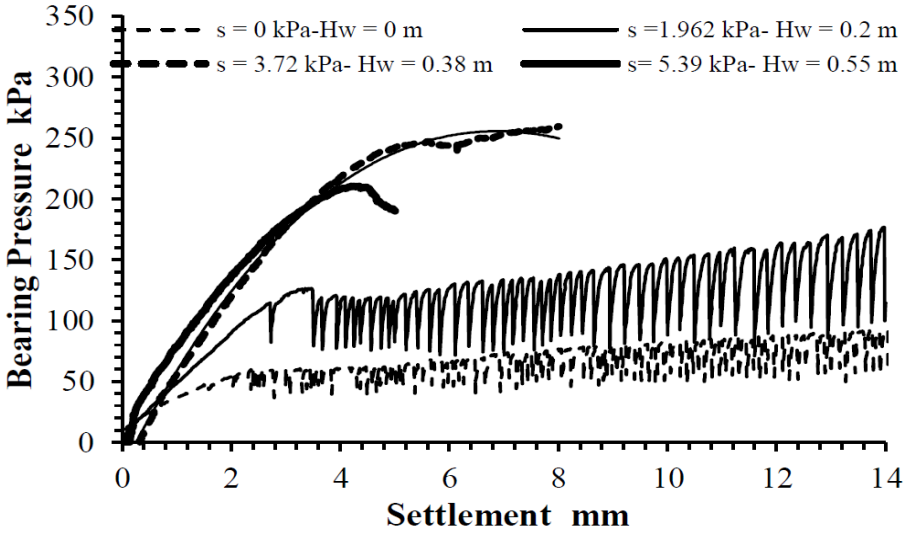

Figure C.7: Bearing capacity results for different values of H_w.

The bearing capacity test was modeled in plane strain using a 0.025 m wide rigid footing centrally placed on the surface of a rectangular body of sand 0.4 m wide and 0.1 m deep with the properties described in Table C.1. 2000 nodes were employed in the model to give a high level of accuracy. It was necessary only to model the top 100 mm of the soil, since the failure mechanism did not exceed this depth. Table C.2 shows the parameters used for the four modeled water table levels (where the soil surface is at height 0.0m). The average unit weight between dry and fully saturated cases was used for soil above water table.

Table C.2: parameters used in the DLO model.

H_w (m)	H_c (m)	s (kPa)	S_r %	sS_r (kPa)
0.00	0.00	0.00	100	0.00
0.2	0.0	1.962	100	1.962
0.38	0.146	3.72	36.8	1.36
0.55	0.316	5.39	11.4	0.61

An example DLO predicted mechanism for the footing for of $H_w = 0.2$ m is shown in Fig. C.8.

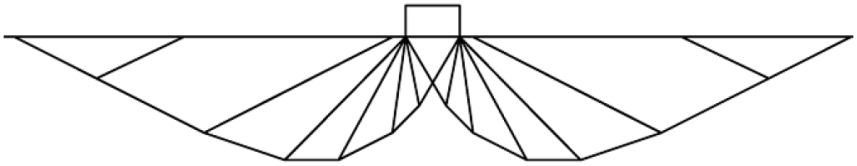

Figure C.8: Failure mechanism for the strip footing for H_w= 0.2 m obtained using DLO.

C.6 Results and Discussion

C.6.1 Peak load capacity

It can be seen from Figure C.7 that the bearing capacity for $H_w = 0.38$ m corresponding to an assumed surface suction of 3.8 kPa is about 3 times greater than for $H_w =$ 0 kPa (fully saturated model). Steensen-Bech et al. (1987), Nabil (1985) and Fathi & Vanapalli (2006) also observed similar differences for similar ranges of suctions in the partially saturated zone. The former stated that the bearing capacity of unsaturated soil is higher by a factor of 4 to 6 times compared to fully saturated soil. Nabil (1985) established a 3 to 5 times increase in bearing capacity, while Fathi & Vanapalli (2006) showed in their study a 5 to 7 times increase in bearing capacity.
Figure C.9 shows peak experimental bearing capacity values (including repeated tests) for different water table levels together with bearing capacity values predicted using the DLO procedure. It can be seen that the experimental results show a sharp increase from H_w from 0 to 0.2 m, but then the increase in capacity then levels out approximately above this level.

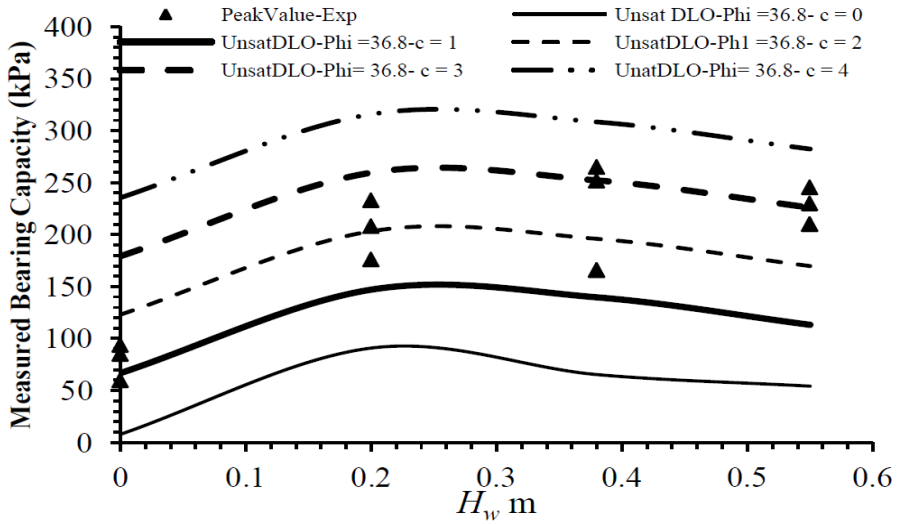

Figure C.9: Comparison of experimental results with DLO analysis for $\alpha = 1.0$.

From Figure C.9 it can be seen that the DLO results for $\phi^{'} = 36.8^{o}$, $c^{'} = 0$, and $\alpha = 1.0$, under predict the experimental results, though is able to qualitatively predict the general pattern. However it can be seen that the results for $\phi = 36.8^{o}$ and $c^{'} = 0$, $= 2$, $\alpha = 1.0$, give a better fit, while changing $\alpha = 0.8$ gives a further improved fit at higher values of H_w as shown in Fig. C.10.

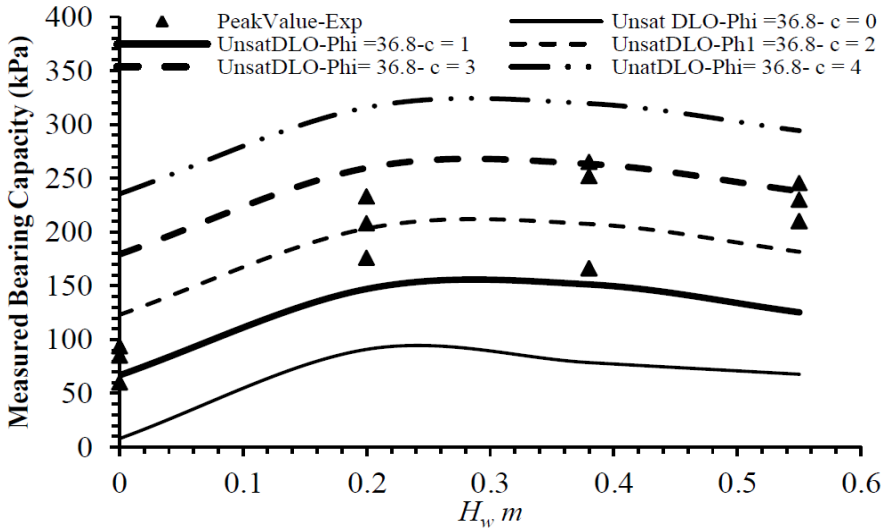

Figure C.10: Comparison of experimental results with DLO analysis for $\alpha = 0.8$.

The cautious interpretation at present is that the modeling of the effect of suction using equations C.6, C.7 and C.8 can allow for the changes in saturation in the effective stress and that the coefficient α may be less than 1.0 implying a non-linear relationship of strength with saturation. However the best fit does require an assumption of a small value of $c^{'}$ which is not evident from the shear box tests or anticipated for a fine sand. Further work is planned to investigate the experimental and theoretical issues that may affect the results obtained so far.

C.6.2 Failure mechanism

Particle image velocimetry (PIV) was used to obtain displacement data from sequences of digital images captured during the geotechnical model test. A Canon EOS 1100 camera was set up in front the bearing capacity rig to capture photos every 1 minute which were analysed using PIVlab software version 1.32, PIVlab1.32 (2012).
Figure C.11 shows preliminary results from the $H_w = 0.2$ m test showing the overall displacements between the start of the test and at settlement 11 mm. The failure mechanism can be clearly seen and has a reasonable match to Fig. C.8, however the image indicates that there is some compression/shear contraction of the soil itself during the whole loading sequence to that point which has extended the depth of deformation significantly. The mechanism has also clearly localized on the left hand side.

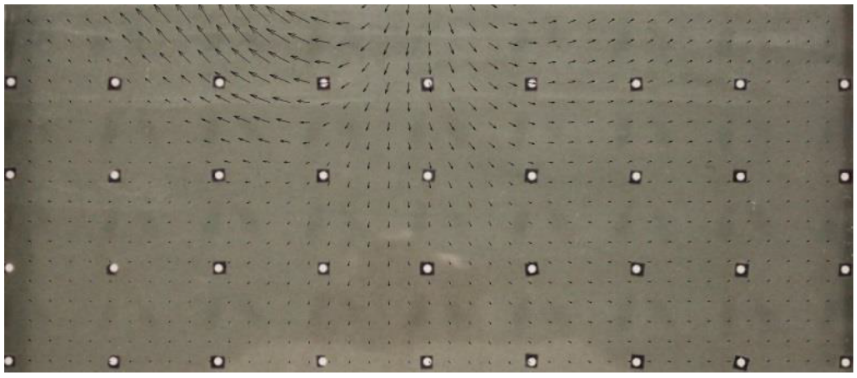

Figure C.11: Vector displacement for a strip footing for $H_w = 0.2$ m.

C.7 Conclusions

(a) A theoretical extension to the Discontinuity Layout Optimization (DLO) procedure to allow the modelling of partially saturated soils has been described, and includes the combined effects of suction and saturation.

(b) The influence of partial saturation on the bearing capacity of a surface strip foundation was investigated by performing a serious of model tests using a range of suction profiles. A non-linear relationship for bearing capacity with water table depth was determined with bearing capacity initially increasing with increased suction in the soil around the foundation and then this increase levelling off as the saturation of the soil falls.

(c) The DLO numerical models showed a good qualitative match with the experimental data that can be attributed to reduction in saturation with increase in suction, however some discrepancies remain which are the subjects of further investigation.

Appendix D

Investigation of the Shear Strength of Unsaturated Sand using a Modified Direct Shear Apparatus

This Appendix contents a paper published in the proceedings of the XVI ECSMGE Conference - Edinburgh-2015.

Abstract

This paper reports an investigation into the effect of stress state and matric suction on the unsaturated shear strength of a fine sand using a direct shear apparatus. The direct shear apparatus was adapted to enable application of a specified suction to the sand sample using the hanging column technique (HCT). This also allowed monitoring of the water content of the sample and hence the average degree of saturation at different stages during the test. This additionally allows direct measurement of the soil water characteristic curve (SWCC) for the fine sand within the suction range of 0 to 10 kPa. A modified effective stress equation is evaluated that accounts for applied stress, suction and degree of saturation and is calibrated against the experimental results. Somewhat unexpectedly the shear strength of the unsaturated sand was significantly affected by the degree of saturation far in excess of what would have been expected by simple account of suction and saturation used in the effective stress equation.

RÉSUMÉ Cet article pre'sente une enquête sur l'effet de l'état de stress et de la succion matricielle sur la résistance au cisaillement non sature'e de sable fin en utilisant un appareil de cisaillement direct modifie'. Appareil cisaillement direct a e'te' adapte' pour permettre l'application d'une aspiration spe'cifie' a' l'e'chantillon de sable a' l'aide de la technique de la colonne de suspension (HCT). Ce suivi a également permis de la teneur en eau de l'e'chantillon et donc le degre' moyen de saturation a' différents stades au cours de l'essai. Cela permet en outre AME-me- directe de la courbe de re'tention d'eau du sol (SWCC) pour le sable fin dans la plage d'aspiration de 0 a' 10 kPa. Une e'quation de contrainte effective modifie' est e'value'e qui repre'sente la contrainte applique'e, l'aspiration et le degre' de saturation et qui est e'talonne' par rapport a' des re'sultats expe'rimentaux. De manie're inattendue la re'sistance au cisaillement du

sable sature' a e'te' significativement affectée par le degré de saturation bien au-delà de ce qui aurait été prévu par simple compte de l'aspiration et de la saturation utilise'e dans l'e'quation de contrainte effective modifie'.

D.1 Introduction

The shear strength of unsaturated soil has been the subject of numerous experimental and theoretical investigations during the last few decades e.g. Bishop (1960), **?**, Escario & Saez (1986), Gan et al. (1988), Öberg & Sällfors (1997), Tarantino & Tombolato (2005) and Likos et al. (2010).
Bishop (1960) proposed a stress state variable for unsaturated soils as follows:

$$\sigma^{'} = (\sigma - u_a) \ + \chi \ (u_a - u_w) \tag{D.1}$$

where $\sigma^{'}$ is effective stress, σ is normal stress, u_a is pore air pressure, χ an effective stress parameter, attaining a value of 1 for saturated soils and zero for dry soils, and u_w is pore water pressure.
Based on Eq. D.1, the following shear strength equation can be formulated:

$$\tau_f = c^{'} + [(\sigma - u_a) + \chi \ (u_a - u_w)] \tan \phi^{'} \tag{D.2}$$

where τ_f is shear strength at failure kPa, $c^{'}$ is the effective cohesion intercept, $\phi^{'}$ and is the internal friction angle. Equation D.2 is based on Terzaghi's shear strength equation for the fully saturated case. It does however not overcome the disadvantages of the single stress state variable equation proposed by Bishop (1960), leading to equations based on two independent variables, suction and degree of saturation, being proposed. Tarantino & Tombolato (2005) proposed a modified effective stress equation for the shear strength of compacted aggregated soils in partially saturated conditions as follows:

$$\tau = (\sigma + s \ S_r) \tan \phi^{'} \tag{D.3}$$

where τ is shear strength, s is suction and S_r is the effective degree of saturation. The applicability of Eq. D.3 for sand has not been reported in the literature. The aim of this paper is therefore, to evaluate the applicability of Eq. D.3 for an unsaturated fine sand.

D.2 Proposed shear strength equation

To enable a more general interpretation of the experimental results, further modification was applied to Eq. D.3 as follows:

$$\tau = c^{'} + (\sigma + s^* \ S_r^*) \tan \phi^{'} \tag{D.4}$$

where $c^{'}$, s^*, S_r^* and $\phi^{'}$ are cohesion intercept, suction, degree of saturation and internal friction angle at peak strength. c$^{'}$ and $\phi^{'}$ are assumed to be functions of S_r^*. The superscript * denotes values derived from experiment.

D.3 Experimental

D.3.1 Soil properties and soil water characteristic curve (SWCC)

The soil used in this study was commercial fine sand (designated Fraction D by the supplier) available from the David Ball Group, UK and was used in all tests at an initial void ratio of 0.69. The physical properties for the sand are shown in Table D.1. The SWCC of the soil was obtained using two methods: the filter paper method and the hanging column technique (HCT). Results are shown in Figure D.1.

Table D.1: Physical properties for the test dry sand.

G_s	γ_{sat} kN/ m^3	γ_{dry} kN/ m^3	e	particle size range	Relative Density %
2.65	19.33	15.3	0.69	0.075-0.3	52

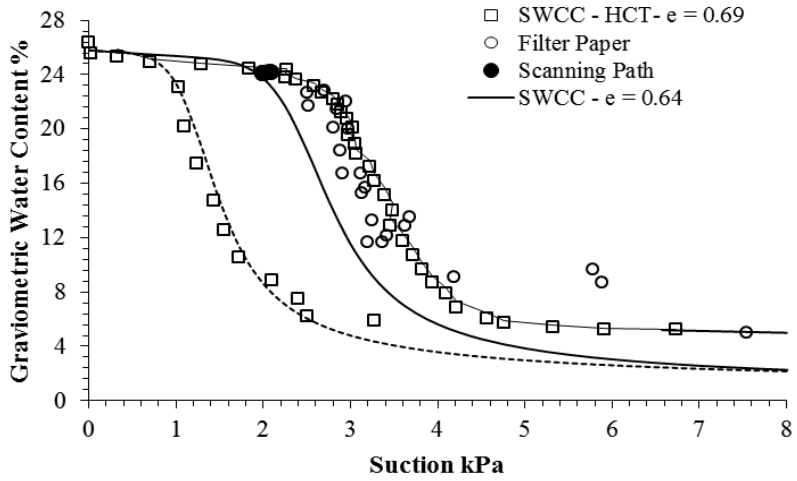

Figure D.1: SWCC using HCT and filter paper method.

The initial void ratio was e = 0.69 for the case when $s = 2$ kPa at $\sigma = 50$ kPa, however it decreased to 0.64 at peak strength due to shearing. The final state of the sample at peak strength can be determined from the scanning path. In Fig. D.1, the scanning path is determined by observing suction and the amount of water imbibed or expelled by the sample using a camera (see Section D 3.2). By knowing the corrected volume of the specimen (height of the sample and corrected area) and volume of solid (V_s), the void ratio of 0.64 was determined using e = V_v/V_s where V_v is the volume of voids. These values are then used directly in Eq. D.4. The same procedure was used at suction levels 4 and 6 kPa.

D.3.2 Modification of the direct shear apparatus, sample preparation and suction application

A circular direct shear box (80 mm in diameter), constructed of Perspex, was designed with the following additional features over standard laboratory shear boxes: (i) a high air entry disk (HAED) of 1 bar in the bottom half of the shear box, (ii) grooves at

the bottom half of the shear box to form a water reservoir underneath the HAED, (iii) influent and effluent ports in the bottom half of the box to allow saturation of the groove channel during test initialization and connection to a burette and (iv) a burette to allow application of a hanging water column for applying and controlling suction as shown in Fig. D.2.

Prior to sample preparation, an O-ring was placed around the saturated HAED which

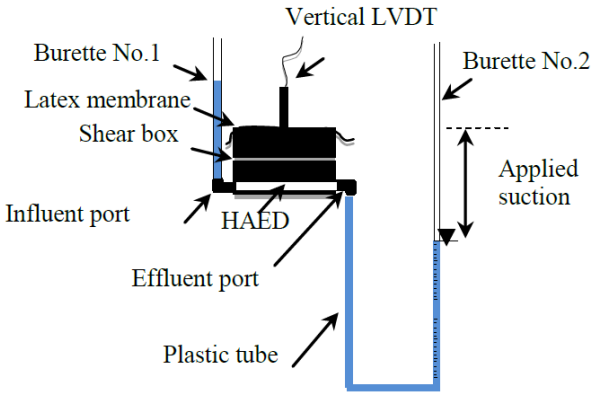

Figure D.2: Modified direct shear box and suction application using HCT.

was then pushed into the bottom half of the shear box. The two halves of the box were fixed together by screws. The gap between the two halves was sealed by a layer of silicon grease to prevent water leakage from the sample. A burette was then connected to the influent port (named as burette No. 1- see Fig. D.2) to flush water beneath the HAED for removing the air, while the effluent port was connected to another burette (named as burette No. 2). After the flushing procedure, the influent port was disconnected from burette No. 1 and closed. The amount of water required to saturate the sample (calculated by mass of dry soil prior to sample preparation) was poured in the box, a mass of dry soil (364 gm) to target a void ratio of 0.69 and dry unit weight of 15.3 kN/m^3, was then poured into the box using the water pluviation technique. With this technique, an initially saturated sample can be obtained, and no precise drop height is required leading to less effort and time com-paring to air pluviation Vaid & Negussey (1988). After pouring, the soil surface was levelled off and then the box was covered by a piece of latex membrane to avoid evaporation prior and during the test. Suction was applied by lowering the burette (No.2) to the desired height. Nominal suction head was defined as the distance from water table in the burette to the surface of the sample. After successful application of the suction, the sample was left for at least 15 hours for equalization purposes. Vertical and horizontal LVDTs were then set up and a small normal stress (from the loading plate) of ∼1 kPa (0.5 kg) was placed on the sample and left for 1 hour. Finally, a Canon EOD1100 camera was utilised to monitor the water level in the burette at 30 minute intervals during the test. This allows suction and hence degree of saturation of the sample to be calculated accordingly.

D.4 Results and discussion

D.4.1 Direct shear test results

A series of unsaturated drained tests were conducted at different vertical stresses and at a range of applied suctions (dry, 0, 2, 4 and 6 kPa). Figure D.3 presents the shear resistance versus horizontal displacement results conducted at the different applied suctions and at normal stresses of 50 kPa. The shear resistance values are based on the corrected area of the samples. All specimens exhibited peak strength behaviour, except the fully dry case, followed by a shear resistance reduction to critical state. There is significant increase in the shear resistance for the unsaturated cases when compared to the fully dry case. For example, the shear resistance at peak strength for $s = 4$ kPa increased about 1.4 fold when compared to the fully dry case. The shearing rate for the dry, saturated and unsaturated samples were 0.0096, 0.048 and 0.0096 mm/min, respectively. Three repeat tests for each case were conducted and demonstrated closely similar behaviour.

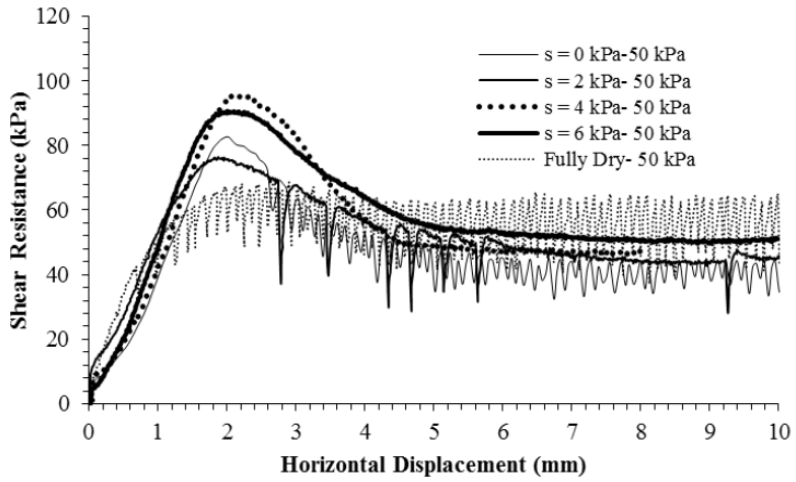

Figure D.3: Shear resistance versus horizontal displacement at $\sigma = 50$ kPa.

A higher shearing rate was used for the saturated sample compared to the unsaturated samples due to higher effective permeability of the former.
Three empty control tests (box is sheared without soil) were conducted at two different shearing rates of 0.048 and 0.0096 mm/min. As expected zero shear resistance was recorded. The noise of the data acquisition measurement was at maximum as 5 N, equivalent to 0.987 kPa shear stress.

D.4.2 Evaluation of equation D.4

Figure D.4 shows the average shear resistance at peak versus normal stress for the five conducted applied suctions. The average peak values of $\phi^{'}$and $c^{'}$ are summarized in Table D.2 and were obtained from three repeated direct shear tests conducted at the same applied suction and three applied normal stresses.

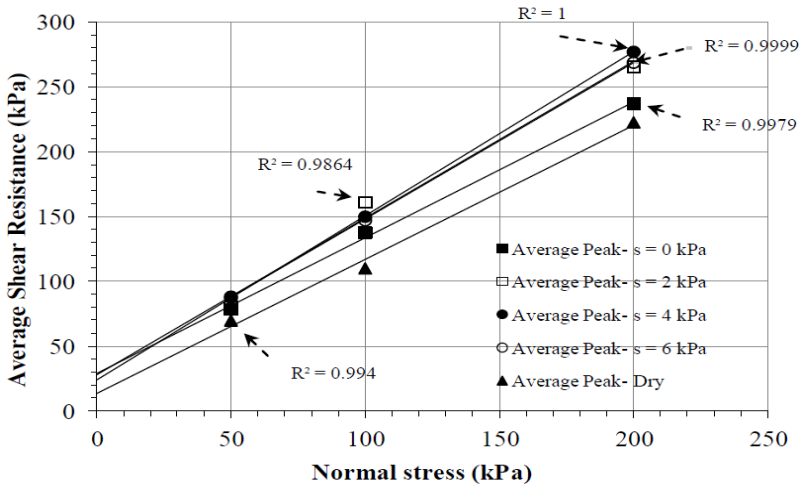

Figure D.4: Averaged shear resistance versus normal stress for fully dry, saturated and unsaturated cases.

Table D.2: variations of internal friction angle at peak and cohesion at different saturation conditions.

Case	s kPa	Average $\phi^{'}$ degrees	Average $c^{'}$ kPa
Dry	—	44.1	13.45
Fully saturated	0	46.56	28.86
Unsaturated	2	51.04	27.79
	4	51.66	23.77
	6	50.27	27.34

It is intriguing that the cohesion intercept, $c^{'}$ of the sand approximately doubles and that $\phi^{'}_{peak}$ also increased by $\sim$ 2.5 degrees due to saturation and up to $\sim$ 7.5 degrees for partially saturated soil when compared with the dry conditions. As this in not in accordance with expected behaviour, repeat tests were carried out including tests where the sample was saturated half way through a shear test. Here the strength was observed to rise after saturation in line with the currently reported tests. These differences are challenging to explain using conventional theory.

Table D.3 shows values of average s^* and S^*_r at peak as well as the effect of the term s^*Sr^*on Eq. D.4. It is clear from Table D.3 that the effect of s^*Sr^* is marginal on shear resistance for the sand in this study and it is the significant apparent change in cohesion $c^{'}$ and $\phi^{'}$ that affects the shear resistance. Values of s^* at peak were obtained by capturing images for the water level in the burette (burette No.2- see Fig. D.2) at different stages of the test and selecting the corresponding image at peak, while S^*_r is calculated by knowing the amount of water expelled or imbibed by the sample at peak. Here the volume of the sample and void ratio are calculated using the vertical LVDT reading at the peak.

Based on Table D.3, all unsaturated results would have been expected to map closely onto the dry line in Fig D.4. However it is clear that unsaturated conditions give rise to significant gain in strength. The reasons for this are under further investigation and cannot be attributed to the effect of the suction in the effective stress equation (Eq. D.4) even if it is assumed to act as if present in the entire pore space.

An increase of internal friction angle has been observed in clay soils by other researchers

such as Wheeler & Sivakumar (1995) and Röhm & Vilar (1995). In terms of the former, an increase in internal friction angle about 3.5 degree in range of suctions between 0 to 200 kPa for compacted Speswhite kaolin for triaxial compression tests was found. While Röhm & Vilar (1995) established a maximum difference of friction angle about 2.5 degrees for suction ranged between 0 to 400 kPa for sandy soil.

Table D.3: Shear resistance values obtained using Eq. D.4 with and without $s^*S_r^*$ term.

σ kPa	s^* kPa	S_r^*	Eq. D.4 with term $s^*S_r^*$	Eq. D.4 without term $s^*S_r^*$
50	0	1	81.66	81.66
50	2.14	0.98	92.22	89.62
50	4	0.36	88.85	87
50	5.55	0.16	88.62	87.50
100	0	1	134.47	134.47
100	1.98	1	153.91	151.45
100	3.94	0.34	151.90	150.21
100	5.39	0.22	149.10	147.66
200	0	1	240.06	240.06
200	1.99	1	277.58	275.12
200	3.84	0.31	278.18	276.65
200	5.52	0.19	269.28	267.98

D.5 Conclusions

(a) A series of shear tests undertaken on unsaturated sand using a shear apparatus has been reported.

(b) Significant increases in shear strength due to full and partial saturation were observed well in excess of that expected by the action of pore pressure or suction within a simple effective stress framework.

(c) The mechanisms of this effect are not clear at present and are under further investigation.

Appendix E

Wetting Collapse at a High Degree of Saturation during Shearing for Unsaturated Sand

This Appendix contents a paper published in the proceedings of the 6^{th} Asia-Pacific Conference on Unsaturated Soils: AP-UNSAT-2015.

Abstract

Wetting collapse at a high degree of saturation was investigated by performing a series of drained unsaturated direct shear tests on the fine sand. The degree of saturation of the sample at different stages during the test was monitored. Wetting collapse was observed where the response is punctuated by a sudden loss of strength and volume followed by rapid recovery of strength. After this, further repeated sudden losses of strength were observed but without significant loss of volume. The sudden volume loss was most evident for the samples with highest saturation. Dry and saturated samples generally displayed continuous oscillations in strength, with no collapse. Results showed that up to 67% of the volume change could be lost during the sudden change, typically post peak. It is hypothesised that this behaviour is due to increase of the degree of saturation (reduction in suction) and the availability of the space between the voids.

E.1 Introduction

Wetting collapse is a sudden, large deformation behaviour of unsaturated soils Nuth (2009) and it highly depends on the applied mechanical stress and the stress history Buisson & Wheeler (2000). This behaviour is caused by the reduction in suction upon inundation Matyas & Radhakrishna (1968), Escario & Saez (1986), Cox (1978), Lloret & Alonso (1980), Maswoswe (1985) and Blanchfield & Anderson (2000). Near the saturation, a large reduction in volume can occur and this is the case for clay soils Alonso et al. (1990) and for coarse-grained soil Blanchfield & Anderson (2000).
When the granular soils are compacted well, collapse will be limited due to small space accessibility.
This work is, therefore, devoted to the behaviour of the wetting collapse for the unsaturated

sand at a high degree of saturation by performing a series of drained-constant rate of strain direct shear tests at different normal stresses and applied suctions. The factors affecting this behaviour are explained and therefore, a simple hypothesis is proposed.

E.2 Experimental work

E.2.1 Soil properties

The soil used in this study was fine sand designated as Fraction D available from the David Ball Group, UK. The physical properties and the shear strength parameters for the sand are shown in Table E.1.

Table E.1: Physical properties and the shear strength parameters for the test sand.

Physical properties	
G_s	2.65
γ_{dry} $(\frac{kN}{m^3})$	15.30
γ_{sat} $(\frac{kN}{m^3})$	19.33
Void ratio, e	0.699
Coefficient of uniformity, cu	1.529
Coefficient of curvature, cv	1.095
Particle size range mm	0.075-0.3
e_{min}	0.5382
e_{max}	0.8717
Relative density %	52
Shear strength parameters	
c_{dry} (kPa)	13.45
$\phi_{peak-\ dry}$ (degrees)	44.1

E.2.2 Modified direct shear apparatus

A circular direct shear box with a diameter of 80 mm was designed with the following additional features over standard laboratory shear boxes: (i) a high air entry disk (HAED) of 1 bar in the bottom half of the shear box, (ii) grooves at the bottom half of the shear box to form a water reservoir underneath the HAED, (iii) influent and effluent ports in the bottom half of the box to allow saturation of the groove channel during test initialization and connection to a burette (iv) a burette to allow application of a hanging water column for applying and controlling suction. (v) a camera installed in front of the burette to capture the water level in the burette at different stages during the test. The degree of saturation, therefore, can be calculated accordingly. The sample preparation and suction application using the hanging column technique (HCT) are given by Shwan & Smith (2015).

E.3 Results

A series of drained unsaturated direct shear tests were conducted at different vertical stresses of 50, 100 and 200 kPa and at a range of applied suctions, s (dry, 0, 2, 4 and 6 kPa). At each normal stress and applied suction, three repeat tests were conducted and named as 1,

2 and 3, respectively within the Figs.'s legend. Figures E.1a, b and e show shear resistance versus horizontal displacement for first repeat test for the three applied normal stresses. The shearing rate of the dry, saturated and unsaturated samples were 0.0096, 0.048 and 0.0096 mm/min, respectively.
Unsaturated samples exhibit higher shear resistance compared to the dry and fully saturated cases. Fully dry, saturated and samples of s = 2 kPa show a sudden loss of strength (oscillation - circled in Figs. E.1a, b and e) then followed by rapid recovery. Other repeat tests (test 2 and 3) demonstrated closely similar behaviour. Figure E.1f shows the corresponding vertical displacement versus horizontal displacement of the different applied suctions for σ = 50 kPa-1 where collapse behaviour happened only for the case when s = 2 kPa (circled in Fig. E.1f). The collapse behaviour was observed for the other repeat tests (1, 2 and 3) at the different applied normal stresses at s = 2 kPa as shown in Figs. E.1c, d and g (the Figs. presented in this manner in order to be easier for the reader to match the first oscillation with the first collapse). The s = 2 kPa is close to the air-entry value of the sand used (2.3 kPa). More details about the soil water characteristic curve (SWCC) of the sand is given by Shwan & Smith (2014).

E.4 Wetting collapse at high degree of saturation

Referring back to Figs. E.1c, d and g for all cases at s = 2 kPa, collapse coincides with the first oscillation of the shear resistance (i.e. see Fig. E.1a, oscillation happened at horizontal displacement = 2.74 mm for s = 2 kPa-1 which coincides with collapse at the same horizontal displacement for s = 2 kPa-1 in Fig. E.1c - circulated in the Figs.). This sudden decrease in volume is a wetting plastic deformation change as an irreversible rearrangement of the particles happened.
A huge volume change occurred at a high degree of saturation or near fully saturated case. The hypotheses to explain this behaviour is due, firstly increase of degree of saturation and hence decrease of effective stress and secondly due to availability of the space between the particles. Further details are discussed below.
To further support the first reason of the wetting collapse, Table E.2 is presented. For s = 2 kPa, the initial S_{ri} were between (88.9 - 91.5) % for the three repeat tests. S_{ri} value is calculated by knowing the amount of water expelled from the sample during application of the suction (before shearing). Here the volume of the sample is constant and the initial void ratio is known (e = 0.699 - see Table E.1). An increase of the degree of saturation at the plastic collapse S_{rp} can be seen during the shearing (see Table E.2). Values of S_{rp} are obtained by performing linear interpolation of the two S_r values before and after the collapse (see Fig. E.1h). The values of the S_r before and after the collapse were obtained by knowing the amount of water expelled or imbibed by the sample during the shearing. Here the volume of the sample and void ratio are calculated based on one installed vertical LVDT reading at the corresponding stage of the shearing (before of after the collapse). This is an estimation of the volume and interprets why values of S_{rp} higher than 100% are obtained (see Table E.2). Note that for all the cases, the collapse happened at a time not in a match with the time of capturing the water level in the burette by the camera. This is why the interpolation was performed. The errors are expected to be small by using the interpolation for the S_{rp} as the maximum difference between S_r before and after the collapse was 1.5%.
Table E.2 shows that up to 67.7% of the volume change (wetting collapse %) could be lost during the sudden change, typically post peak. The wetting collapse % in Table E.2 was calculated as a percentage between the vertical displacement just before and at the collapse.

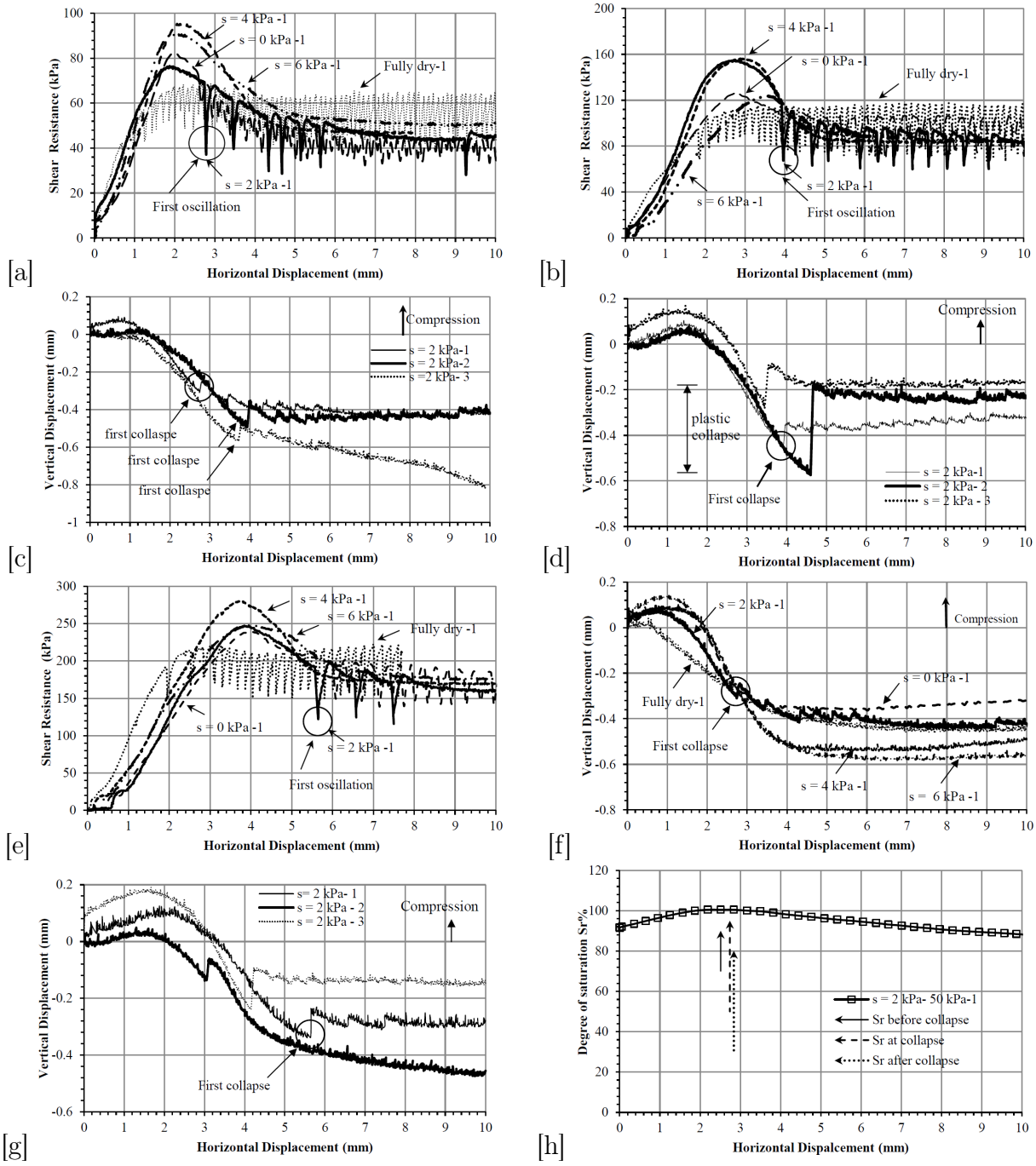

Figure E.1: Shear resistance versus horizontal displacement for (a) $\sigma = 50$ kPa-1. (b) $\sigma = 100$ kPa-1. Vertical displacement versus horizontal displacement at $s = 2$ kPa for three repeat tests at (c) $\sigma = 50$ kPa (d) $\sigma = 100$ kPa (e) Shear resistance versus horizontal displacement for $\sigma = 200$ kPa-1. Vertical displacement versus horizontal displacement at (f) different applied suction and $\sigma = 50$ kPa-1 (g) $s = 2$ kPa and $\sigma = 200$ kPa for three repeat tests (h) degree of saturation versus horizontal displacement for $s = 2$ kPa and $\sigma = 50$ kPa-1.

Unsaturated samples prepared at $s = 4$ (S_{ri} = 24-36)% and $s = 6$ kPa (S_{ri} = 15-22)% did not show wetting collapse (see Fig. E.1f) indicating the dominance of the high degree of saturation on this behaviour.

Table E.2: Degree of saturation at initial and at the wetting collapse for $s = 2$ kPa.

σ kPa	S_{ri}%	S_{rp}%	Wetting Collapse %
50-1	91.5	100.4	16
50-2	90.4	96.2	24.3
50-3	89.9	91.6	15
100-1	90.8	101	21.1
100-2	90	96	67.7
100-3	88.9	106.8	65.2
200-1	90.2	111.2	26.9
200-2	89.8	100.1	45.4
200-3	89	113.8	61.7

The degree of collapse highly depends on the availability of the space between the particles which is the second reason of this behaviour. In other words, the collapse is significantly affected by the interlocking position for the particles. Fully saturated samples (in spite of their high S_{ri}) did not show any wetting collapse (see Fig. E.1f - $s = 0$ kPa-1) because of unavailability of the space between the particles.
The wetting collapse is, therefore, a function of both high degree of saturation and availability of the air between the particles.

E.5 Conclusions

The wetting collapse of the unsaturated sand was investigated by performing a series of the drained constant rate of strain direct shear tests while monitoring the degree of saturation via a camera. The following conclusions are demonstrated:

1. The wetting collapse occurred at a high degree of saturation at suction near the air entry value of the sand used in this study.
2. The wetting collapse is an irrecoverable plastic deformation in which huge reduction in volume change can be observed. This behaviour has nothing to do with the ultimate resistance of the soil as it is post-peak behaviour.
3. It is hypothesised of the wetting collapse is due to the high degree of saturation and the availability of the space between the particles.

Appendix F

Integration of apparent cohesion force equations along a discontinuity

This appendix addresses integrations of the apparent cohesion force along a discontinuity. Different positions of water table were selected to cover cases of fully dry, saturated and unsaturated conditions. The derived equations were then incorporated into an existing DLO Matlab code and validated. The validation is shown in Appendix H. Once the validations were satisfied, the UNSAT-DLO code was incorporated into a research version of the LimitState:GEO software and then validated again. The validation of the LimitState:GEO software is given in Appendix J.

F.1 Integration of apparent cohesion force along the discontinuity

To study all possible cases of water table locations and failure angles, three sets of the equations were established. First; equations for the case of a discontinuity above the water table. Second; a set of equations for a discontinuity below the water table, which were also provided to perform validation against equations above the water table. Third; equations for when a discontinuity crosses the water table (part of the discontinuity is below the water table and the rest is above the water table) as shown in Fig. F.1a. It is possible that a discontinuity occurs at different angles (e.g $\theta = 0$, $\theta = 90$ or at inclined angles) as shown in Fig. F.1a. Therefore, all possible cases for derivation of the apparent cohesion force equations were taken into consideration.

F.1.1 Integration of apparent cohesion force along the discontinuity for $\theta \neq 0$ and $\theta \neq 90$

1. When $y_1 \geq Y_w,\ y_2 >$Y$_w$:
   Redefining Eq. 5.5, showed previously in chapter 5, in an (x, y) coordinate system where y is measured positive upwards and the water table is a height Y_w above the origin, and the soil surface at y_{max} gives:

$$z = y_{max} - y = Y_w + H_w - y \tag{F.1}$$

   or

$$z - H_w = Y_w - y \tag{F.2}$$

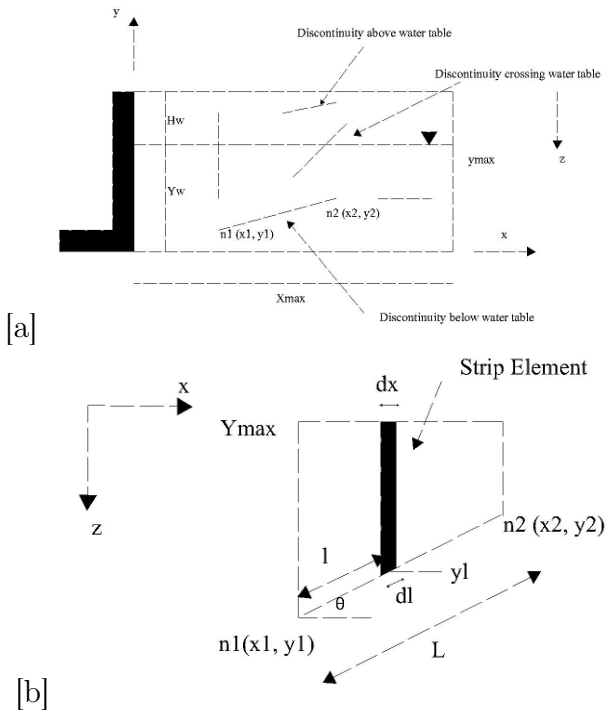

Figure F.1: (a) Defining the boundary of the problem showing discontinuities for all possible cases(b) Strip weight above the discontinuity with nodes and strip element.

Hence:

$$S_r = e^{a\gamma_w(Y_w - y)} \tag{F.3}$$

$$s = -u_w = \gamma_w(y - Y_w) \tag{F.4}$$

where s is suction under hydrostatic condition. In this case when the discontinuity is above the water table, shown in Fig. F.1 a, the apparent cohesion force can be derived by integrating the second term of Eq. 5.8 as follows:

$$\hat{C}\tan\phi^{'} = \int_A^B sS_r \tan\phi' dl = \int_0^L \gamma_w(y - Y_w)e^{a\gamma_w Y_w}e^{-a\gamma_w y}\tan\phi' dl \tag{F.5}$$

where $\beta = 1$ in Eq. 5.8 (validated in Subsection 5.3.8 in Chapter 5). Referring to Fig. F.1b, (y) can be determined as $y = y_1 + l\sin\theta$, where θ is measured anti-clockwise from the horizontal, and l is measured from node (1) ($l_1 = 0$) to node (2) ($l_2 = L$) and then by substituting (y) in Eq. F.5, the following equation can be obtained:

$$\hat{C} = \int_0^L \gamma_w(y_1 + l\sin\theta - Y_w)e^{a\gamma_w Y_w}e^{-a\gamma_w(y_1 + l\sin\theta)}\tan\phi' dl \tag{F.6}$$

$$\hat{C} = \int_0^L \gamma_w(l\sin\theta - (Y_w - y_1))e^{a\gamma_w(Y_w - y_1)}e^{-a\gamma_w l\sin\theta}\tan\phi' dl \tag{F.7}$$

$$\hat{C} = \gamma_w \tan\phi' e^{a\gamma_w(Y_w - y_1)} \int_0^L (l\sin\theta - (Y_w - y_1))e^{-a\gamma_w l\sin\theta} dl \tag{F.8}$$

$$\hat{C} = \frac{-\gamma_w \tan\phi' e^{a\gamma_w(Y_w - y_1)}}{(a\gamma_w)^2\sin\theta}\left[e^{(-a\gamma_w l\sin\theta)}(a\gamma_w(l\sin\theta - (Y_w - y_1)) + 1)\right]_0^L \tag{F.9}$$

By substituting the boundary conditions, the following can be obtained:

$$\hat{C} = \frac{-\tan\phi' e^{a\gamma_w(Y_w - y_1)}}{(a)^2\gamma_w \sin\theta}\left[e^{(-a\gamma_w L\sin\theta)}(a\gamma_w(L\sin\theta - (Y_w - y_1)) + 1) + (a\gamma_w(Y_w - y_1)) - 1\right] \tag{F.10}$$

Equation F.10 gives the apparent cohesion force along the discontinuity, above the water table, for the case when $\theta \neq \theta$ and $\theta \neq 90$.

2. When $y_1 < Y_w,\ y_2 \leq Y_w$:
In this case, the discontinuity is located below the water table (soil is fully saturated) and the effect of the degree of saturation (S_r) will be eliminated (since $S_r = 100\%$) in Eq. F.5. The apparent cohesion force along the discontinuity, therefore, can be obtained as follows:

$$\hat{C} = \int_A^B s\tan\phi'\ dl = \int_0^L \gamma_w(y - Y_w)\ \tan\phi'\ dl \tag{F.11}$$

By integrating and substituting the boundary conditions, the following can be obtained:

$$\hat{C} = \int_0^L \gamma_w(y_1 + l\sin\theta - Y_w)\tan\phi'\ dl = \gamma_w \tan\phi'[\frac{L^2}{2}\sin\theta + L(y_1 - Y_w)] \tag{F.12}$$

3. When $y_1 < Y_w,\ y_2 > Y_w$:
In this case, the discontinuity crosses the water table. For simplicity, the apparent cohesion force can be separated into two parts; above and below the water table. Derivation of the apparent cohesion force for this case is not quite different from the cases when the discontinuity is above or below the water table. However, there is a small change regarding the boundary conditions. Boundary conditions for the first part below the water table begin from 0 to L_1. The final form of the apparent cohesion force along the discontinuity for the part below the water table is shown in Eq. F.13 (which is same as Eq. F.12, however, with replacing L to L_1).

$$\hat{C} = \gamma_w \tan\phi'\left[\frac{L_1^2}{2}\sin\theta + L_1(y_1 - Y_w)\right] \tag{F.13}$$

where $L_1 = (Y_w - y_1)/\sin(\theta)$.
Boundary conditions for the second part of the discontinuity, which is above the water table, start from 0 to L_2. Therefore, the integration for this part is given by:

$$\hat{C} = \int_0^{L_2} \gamma_w(y - Y_w)e^{a\gamma_w Y_w}e^{-a\gamma_w y}\ \tan\phi' dl \tag{F.14}$$

where $y = Y_w + l\sin(\theta)$ and $L_2 = (y_2 - Y_w)/\sin(\theta)$. By substituting the boundary conditions, following can be obtained:

$$\hat{C} = \int_0^{L_2} \gamma_w(Y_w + l\sin(\theta) - Y_w)e^{a\gamma_w Y_w}e^{-a\gamma_w(Y_w + l\sin(\theta))}\tan\phi' dl \tag{F.15}$$

More simplifications of the integration give:

$$\hat{C} = \int_0^{L_2} \gamma_w l\sin(\theta)e^{-a\gamma_w l\sin(\theta)}\tan\phi' dl \tag{F.16}$$

Integrating with respect to L and then substituting the boundary conditions gives:

$$\hat{C} = -\frac{\tan\phi'}{(a)^2\gamma_w \sin(\theta)}[(1 + a\gamma_w l\sin(\theta))e^{-a\gamma_w l\sin(\theta)}]_0^{L_2} \tag{F.17}$$

$$\hat{C} = -\frac{\tan\phi'}{(a)^2\gamma_w \sin(\theta)}\left[(1 + a\gamma_w L_2\sin(\theta))e^{-a\gamma_w L_2\sin(\theta)} - 1\right] \tag{F.18}$$

Combination of Eqs. F.13 and F.18 provides the apparent cohesion force equation for the case of the discontinuity crossing the water table as follows:

$$\hat{C} = \gamma_w \tan\phi'\left[\frac{L_1^2}{2}\sin\theta + L_1\ (y_1 - Y_w)\right] - \frac{\tan\phi'}{(a)^2\gamma_w \sin(\theta)}\left[(1 + a\gamma_w L_2\sin(\theta))e^{-a\gamma_w L_2\sin(\theta)} - 1\right] \tag{F.19}$$

F.1.2 Integration of apparent cohesion along the discontinuity for $\theta = 0$

In this case, two conditions are exist. Firstly, the discontinuity occurs above the water table. secondly, the discontinuity occurs below the water table.

1. When $(y_1 = y_2) > Y_w$:
   For $\theta = 0$, the apparent cohesion force equation above the water table can be obtained as:

$$\hat{C} = \int_{x_1}^{x_2} \gamma_w(y - Y_w)e^{a\gamma_w Y_w}e^{-a\gamma_w y}\ \tan\phi' dx \tag{F.20}$$

$$\hat{C} = \gamma_w(y - Y_w)e^{a\gamma_w Y_w}e^{-a\gamma_w y}\tan\phi' x]_{x_1}^{x_2} \tag{F.21}$$

$$\hat{C} = \gamma_w(y - Y_w)e^{a\gamma_w (Y_w - y)}\tan\phi'(x_2 - x_1) \tag{F.22}$$

   where $y = y_1 = y_2$.

2. When $(y_1 = y_2) \leq\ Y_w$:
   In this case, the apparent cohesion force along the discontinuity is given by:

$$\hat{C} = \int_A^B s\tan\phi' dx = \int_{x_1}^{x_2} \gamma_w(y\_Y_w)\tan\phi' dx \tag{F.23}$$

$$\hat{C} = \gamma_w(y - Y_w)\tan\phi'(x_2 - x_1) \tag{F.24}$$

F.1.3 Integration of apparent cohesion along the discontinuity for $\theta = 90$

1. When $y_1 \geq Y_w,\ y_2 > Y_w$:
   The discontinuity is located above the water table and the integration is from y_1 to y_2 as follows:

$$\hat{C} = \int_{y_1}^{y2} \gamma_w(y - Y_w)e^{a\gamma_w Y_w}e^{(-a\gamma_w y)}\tan\phi' dy \tag{F.25}$$

$$\hat{C} = -\frac{\tan\phi'}{(a)^2\gamma_w}\left[(1 - a\gamma_w Y_w + a\gamma_w y_2)e^{a\gamma_w (Y_w - y_2)} - (1 - a\gamma_w Y_w + a\gamma_w y_1)e^{a\gamma_w (Y_w - y_1)}\right] \tag{F.26}$$

2. When $y_1 < Y_w,\ y_2 \leq Y_w$:
   This is a saturated condition and the apparent cohesion force is given by:

$$\hat{C} = \int_{y_1}^{y_2} \gamma_w (y - Y_w) \tan\phi' dy \tag{F.27}$$

$$\hat{C} = \gamma_w \tan\phi' [(\frac{y_2^2}{2} - Y_w y_2) - (\frac{y_1^2}{2} - Y_w y_1)] \tag{F.28}$$

3. When $y_1 < Y_w,\ y_2 > Y_w$:
   As stated before, in this case the apparent cohesion force equation can be separated into two parts, below and above the water table. The first part of the equation, which is under the water table, is same as Eq. F.28. The integration limits run from y_2 to Y_w and; therefore, the apparent cohesion force is as follows:

$$\hat{C} = \gamma_w \tan\phi' [(\frac{Y_w^2}{2} - Y_w^2) - (\frac{y_1^2}{2} - Y_w y_1)] \tag{F.29}$$

   The apparent cohesion force equation for the second part of the equation, part above the water table, is given by:

$$\hat{C} = \int_{Y_w}^{y_2} \gamma_w (y - Y_w) e^{a\gamma_w Y_w} e^{(-a\gamma_w y)} \tan\phi' dy \tag{F.30}$$

$$\hat{C} = -\frac{\tan\phi'}{(a)^2 * \gamma_w} [(1 - a\gamma_w Y_w + a\gamma_w y_2) e^{a\gamma_w (Y_w - y_2)} - (1 - a\gamma_w Y_w + a\gamma_w Y_w) e^{a\gamma_w (Y_w - Y_w)}] \tag{F.31}$$

$$\hat{C} = -\frac{\tan\phi'}{(a)^2 \gamma_w} [(1 - a\gamma_w Y_w + a\gamma_w y_2) e^{a\gamma_w (Y_w - y_2)} - 1] \tag{F.32}$$

   By adding Eqs. F.29 and F.32, the final form of the apparent cohesion force is as follows:

$$\hat{C} = \gamma_w \tan\phi' \left[(\frac{Y_w^2}{2} - Y_w^2) - (\frac{y_1^2}{2} - Y_w y_1)] - \frac{\tan\phi'}{(a)^2 \gamma_w} [(1 - a\gamma_w Y_w + a\gamma_w y_2) e^{a\gamma_w (Y_w - y_2)} - 1 \right] \tag{F.33}$$

Appendix G

Integration of strip weight equations above a discontinuity

G.1 Integration of strip weight equation above a discontinuity for $\theta \neq 0$ and $\theta \neq 90$

1. When $y_1 \geq Y_w,\ y_2 > Y_w$:
   Referring to Fig. F.1b, to obtain a strip weight equation along the discontinuity, the double integration of the unit weight is required. For a non-vertical line, $a = y_1 + l\sin\theta$ and $b = y_{max}$, and the integration is as shown below:

$$W = \int_0^L \int_a^b (\gamma.dy)dl\cos\theta \tag{G.1}$$

   By substituting Eq. 5.7 in Eq. G.1 and then integrating, the following can be obtained:

$$W = \int_0^L \int_a^b (\rho_d + (\rho_{sat} - \rho_d)S_r).dy.dl\cos\theta \tag{G.2}$$

$$W = \int_0^L \int_a^b (\rho_d + (\rho_{sat} - \rho_d)S_r).dy.dl\cos\theta \tag{G.3}$$

$$W = \int_0^L \left[\rho_d y - \frac{(\rho_{sat} - \rho_d)}{a\gamma_w} e^{a\gamma_w Y_w} e^{-a\gamma_w y}\right]_a^b dl\cos\theta \tag{G.4}$$

$$W = \frac{1}{a\gamma_w}\int_0^L \left[a\gamma_w\rho_d y - (\rho_{sat} - \rho_d)e^{a\gamma_w Y_w}e^{-a\gamma_w y}\right]_{y_1 + l\sin\theta}^{y_{max}} dl\cos\theta \tag{G.5}$$

   Substituting the boundary conditions of y gives:

$$W = \frac{1}{a\gamma_w}\int_0^L \big[a\gamma_w\rho_d y_{max} - (\rho_{sat} - \rho_d)e^{a\gamma_w Y_w}e^{-a\gamma_w y_{max}} - a\gamma_w\rho_d(y_1 + l\sin\theta) + (\rho_{sat} - \rho_d)e^{a\gamma_w(Y_w - y_1)}e^{-a\gamma_w l\sin\theta}\big]\, dl\cos\theta \tag{G.6}$$

   Integrating with respect to (L), then simplifying the equation gives:

$$W = \frac{1}{a\gamma_w}\left[(a\gamma_w\rho_d y_{max} - (\rho_{sat} - \rho_d)e^{a\gamma_w Y_w}e^{-a\gamma_w y_{max}} - a\gamma_w\rho_d y_1)l - \frac{a\gamma_w\rho_d\sin\theta}{2}l^2 - \frac{(\rho_{sat} - \rho_d)}{a\gamma_w\sin\theta}e^{a\gamma_w(Y_w - y_1)}e^{-a\gamma_w l\sin\theta}\right]_0^L \cos\theta \tag{G.7}$$

Then by substituting the boundary conditions, the strip weight equation for the case when the discontinuity occurs above the water table is given by:

$$W = \frac{1}{a\gamma_w}\Bigg[(a\gamma_w\rho_d(y_{max}-y_1)-(\rho_{sat}-\rho_d)e^{a\gamma_w(Y_w-y_{max})})L-\frac{a\gamma_w\rho_d\sin\theta}{2}L^2 \\ -\frac{(\rho_{sat}-\rho_d)}{a\gamma_w\sin\theta}e^{a\gamma_w(Y_w-y_1)}e^{-a\gamma_w L\sin\theta}+\frac{(\rho_{sat}-\rho_d)}{a\gamma_w\sin\theta}e^{a\gamma_w(Y_w-y_1)}\Big]\cos\theta \tag{G.8}$$

More simplification of the equation gives:

$$W = \frac{\cos\theta}{a\gamma_w}\Big[(a\gamma_w\rho_d(y_{max}-y_1)-(\rho_{sat}-\rho_d)e^{a\gamma_w(Y_w-y_{max})})L \\ -\frac{a\gamma_w\rho_d\sin\theta}{2}L^2-\frac{(\rho_{sat}-\rho_d)}{a\gamma_w\sin\theta}e^{a\gamma_w(Y_w-y_1)}(e^{-a\gamma_w L\sin\theta}-1) \tag{G.9}$$

2. When the discontinuity is below the water table:
   (a) when $y_1 < Y_w,\ y_2 \le Y_w$ and $Y_w = y_{max}$:
   The strip weight equation for this case is given by:

$$W = \int_0^L\int_a^b(\rho_d+(\rho_{sat}-\rho_d))\,dy\,dl\cos\theta \tag{G.10}$$

$$W = \int_0^L[\rho_d y+(\rho_{sat}-\rho_d)y]_{y_1+l\sin\theta}^{y_{max}}\,dl\cos\theta \tag{G.11}$$

   By substituting the boundary conditions for (y) and simplifying the equation, the following can be obtained:

$$W = \int_0^L[\rho_d y_{max}+(\rho_{sat}-\rho_d)y_{max}-\rho_d(y_1+l\sin\theta)-(\rho_{sat}-\rho_d)(y_1+l\sin\theta)]\,dl\cos\theta \tag{G.12}$$

   Integrating with respect to (L) then substituting the boundary conditions and simplifying the equation gives:

$$W = [\rho_{sat}\ L(y_{max}-y_1)-\frac{L^2}{2}\ \rho_{sat}\sin\theta]\cos\theta \tag{G.13}$$

   (b) When $y_1 < Y_w,\ y_2 \le Y_w$ and $Y_w < y_{max}$:

   For this case; the strip weight equation, which is separated into two parts as shown in Fig. G.1a, is given by:

$$W = \int_0^L\int_{y_1+l\sin\theta}^{Y_w}(\rho_{sat})dydl\cos\theta+\int_{x_1}^{x_2}\int_{Y_w}^{y_{max}}(\rho_d+(\rho_{sat}-\rho_d)S_r).dy.dx \tag{G.14}$$

   By integrating and substituting the boundary conditions, the final form of the strip weight equation for this case can be given by:

$$W = \left[\rho_{sat}\ L(Y_w-y_1)-\rho_{sat}\frac{L^2}{2}\sin\theta\right]\cos\theta \\ +\left[\rho_d\ (y_{max}-Y_w)-\frac{(\rho_{sat}-\rho_d)}{a\gamma_w}(e^{a\gamma_w(Y_w-y_{max})}-1)\right](x_2-x_1) \tag{G.15}$$

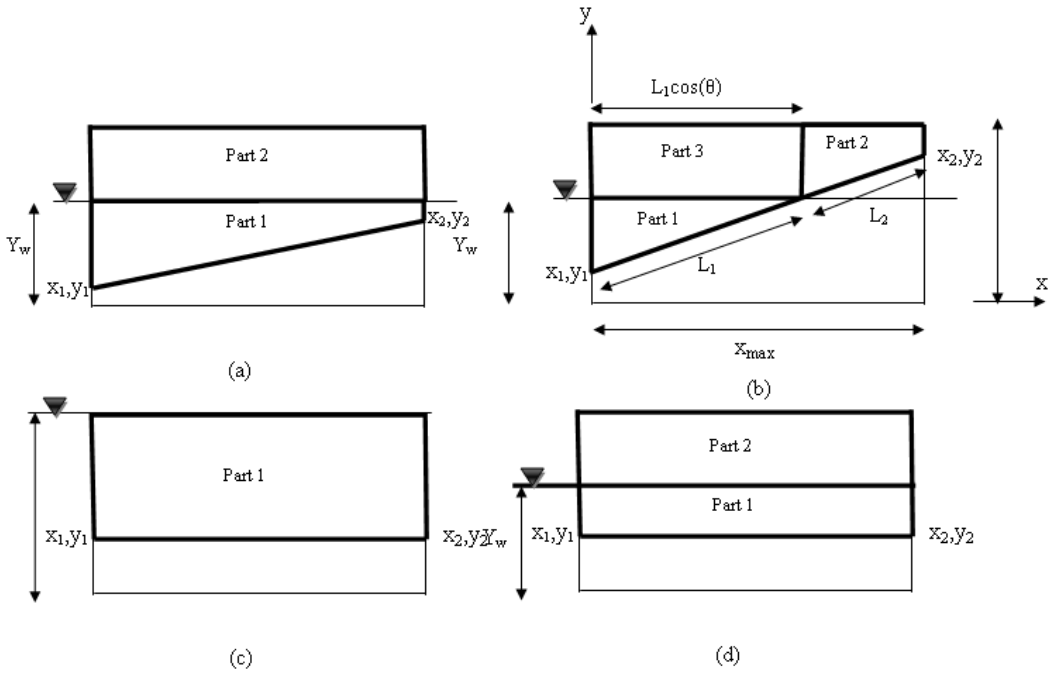

Figure G.1: Strip weight block(s) for different cases of the discontinuity at various positions for the water table.

3. When $y_1 < Y_w,\ y_2 > Y_w$:
   For this case, for simplicity the discontinuity is divided into two parts, below and above the water table. The strip weight equation for part 1, shown in Fig. G.1b below the water table, is same as Eq. G.13, however the integration limits are changed from y_{max} to Y_w and L to L_1. Therefore the strip weight equation for this part is given by:

$$W = \left[\rho_{sat}\ L_1(Y_w - y_1) - \frac{L_1^2}{2}\ \rho_{sat}\ \sin\theta\right]\cos\theta \tag{G.16}$$

   where $L_1 = (Y_w - y_1)/\sin(\theta)$.

   For part 2 shown in Fig. G.1b, above the water table, the integration of the strip weight equation is as follows:

$$W = \int_0^{L_2}\int_{Y_w + l\sin(\theta)}^{y_{max}} (\rho_d + (\rho_{sat} - \rho_d)S_r).dy.dl\cos\theta \tag{G.17}$$

$$W = \int_{Y_w}^{L_2}\left[\rho_d y - \frac{(\rho_{sat} - \rho_d)}{a\gamma_w} e^{a\gamma_w Y_w} e^{-a\gamma_w y}\right]_{Y_w + l\sin(\theta)}^{y_{max}} dl\cos\theta \tag{G.18}$$

$$W = \frac{1}{a\gamma_w}\int_0^{L_2}\left[a\gamma_w\rho_d y - (\rho_{sat} - \rho_d)e^{a\gamma_w Y_w}e^{-a\gamma_w y}\right]_{Y_w + l\sin\theta}^{y_{max}} dl\cos\theta \tag{G.19}$$

   By substituting the boundary conditions of (y), the following is obtained:

$$W = \frac{1}{a\gamma_w}\int_0^{L_2}\Big[a\gamma_w\rho_d y_{max} - (\rho_{sat} - \rho_d)e^{a\gamma_w Y_w}e^{-a\gamma_w y_{max}} - a\gamma_w\rho_d(Y_w + l\sin\theta) + (\rho_{sat} - \rho_d)e^{a\gamma_w(Y_w)}e^{-a\gamma_w(Y_w + l\sin\theta)}\Big]\, dl\cos\theta \tag{G.20}$$

Integrating with respect to (L) then simplifying the equation gives:

$$W = \frac{\cos\theta}{a\gamma_w}[(a\gamma_w\rho_d(y_{max} - Y_w) - (\rho_{sat} - \rho_d)e^{a\gamma_w(Y_w - y_{max})})l - \frac{a\gamma_w\rho_d \sin\theta}{2}l^2 - \frac{(\rho_{sat} - \rho_d)}{a\gamma_w \sin\theta}e^{-a\gamma_w l \sin\theta}]_0^{L_2} \tag{G.21}$$

By substituting the boundary conditions, the equation for the strip weight for the second part along the discontinuity is as follows:

$$W = \frac{\cos\theta}{a\gamma_w}[(a\gamma_w\rho_d(y_{max} - Y_w) - (\rho_{sat} - \rho_d)e^{a\gamma_w(Y_w - y_{max})})L_2 - \frac{a\gamma_w\rho_d \sin\theta}{2}L_2^2 - \frac{(\rho_{sat} - \rho_d)}{a\gamma_w \sin\theta}(e^{-a\gamma_w L_2 \sin\theta} - 1)] \tag{G.22}$$

where $L_2 = (y_2 - Y_w)/\sin\theta$.
For part 3 in Fig. G.1b, the strip weight equation is given by:

$$W = \int_{x_1}^{x_1 + L_1\cos\theta} \int_{Y_w}^{y_{max}} (\rho_d + (\rho_{sat} - \rho_d)S_r).dy.dx \tag{G.23}$$

$$W = \frac{1}{a\gamma_w}\int_{x_1}^{x_1 + L_1\cos\theta} \left[a\gamma_w\rho_d y_{max} - (\rho_{sat} - \rho_d)e^{a\gamma_w Y_w}e^{-a\gamma_w y_{max}} - a\gamma_w\rho_d Y_w + (\rho_{sat} - \rho_d)e^{a\gamma_w Y_w}e^{-a\gamma_w Y_w}\right] dx \tag{G.24}$$

By integrating with respect to (x) and substituting the boundary conditions, the following equation can be obtained for part 3:

$$W = \frac{1}{a\gamma_w}\left[a\gamma_w\rho_d(y_{max} - Y_w) - (\rho_{sat} - \rho_d)(e^{a\gamma_w(Y_w - y_{max})} + 1)\right](L_1\cos\theta) \tag{G.25}$$

By adding Eqs. G.16, G.22 and G.25 for parts 1, 2 and 3, respectively, the final equation of the strip weight is as follows:

$$W = \frac{\cos\theta}{a\gamma_w}[(a\gamma_w\rho_d(y_{max} - Y_w) - (\rho_{sat} - \rho_d)e^{a\gamma_w(Y_w - y_{max})})L_2 - \frac{a\gamma_w\rho_d \sin\theta}{2}L_2^2 - \frac{(\rho_{sat} - \rho_d)}{a\gamma_w \sin\theta}(e^{-a\gamma_w L_2 \sin\theta} - 1)] + \left[\rho_{sat}\ L_1(Y_w - y_1) - \frac{L_1^2}{2}\ \rho_{sat}\sin\theta\right]\cos\theta + \frac{1}{a\gamma_w}\left[a\gamma_w\rho_d(y_{max} - Y_w) - (\rho_{sat} - \rho_d)(e^{a\gamma_w(Y_w - y_{max})} + 1)\right](L_1\cos\theta) \tag{G.26}$$

G.2 Integration of strip weight equation above a discontinuity for $\theta = 0$

1. When $(y_1 = y_2) > Y_w$:
The strip weight equation for $\theta = 0$ can be integrated as:

$$W = \int_{x_1}^{x_2}\int_{y_1}^{y_{max}} \rho_d + (\rho_{sat} - \rho_d)\ S_r.dy.dx \tag{G.27}$$

$$W = \int_{x_1}^{x_2} \left[\rho_d \; y - \frac{(\rho_{sat} - \rho_d)}{a\gamma_w} e^{a\gamma_w Y_w} e^{-a\gamma_w y} \right]_{y_1}^{y_{max}} dx \tag{G.28}$$

$$W = \int_{x_1}^{x2} \left(\rho_d \; y_{max} - \frac{(\rho_{sat} - \rho_d)}{a\gamma_w} e^{a\gamma_w Y_w} e^{-a\gamma_w y_{max}} - \rho_d \; y_1 + \frac{(\rho_{sat} - \rho_d)}{a\gamma_w} e^{a\gamma_w Y_w} e^{-a\gamma_w y_1} \right) dx \tag{G.29}$$

By integrating with respect to (x) and substituting the boundary conditions of (x), the following can be obtained:

$$W = \left[\rho_d \; (y_{max} - y_1) - \frac{(\rho_{sat} - \rho_d)}{a\gamma_w} e^{a\gamma_w (Y_w - y_{max})} + \frac{(\rho_{sat} - \rho_d)}{a\gamma_w} e^{a\gamma_w (Y_w - y_1)} \right] (x_2 - x_1) \tag{G.30}$$

2. The discontinuity is below the water table:

   (a) When $(y_1 = y_2) \leq \; Y_w$ and $\; Y_w = y_{max}$:
   Referring to Fig. G.1c, the strip weight equation for this case can be given by:

$$W = \int_{x_1}^{x_2} \int_{y_1}^{y_{max}} (\rho_d + (\rho_{sat} - \rho_d)).dy.dx \tag{G.31}$$

$$W = \int_{x_1}^{x2} \left[\rho_{sat} (y_{max} - y_1) \right] dx \tag{G.32}$$

$$W = \rho_{sat} (y_{max} - y_1)(x_2 - x_1) \tag{G.33}$$

   (b) When $(y_1 = y_2) \leq \; Y_w$ and $Y_w < \; y_{max}$:
   In this case; the equation is separated into two parts as shown in Fig. G.1d, part below the water table and part above the water table. The integration is as follows:

$$W = \int_{x_1}^{x_2} \int_{y_1}^{Y_w} \rho_{sat}.dy.dx + \int_{x_1}^{x_2} \int_{Y_w}^{y_{max}} \rho_d + (\rho_{sat} - \rho_d) S_r.dy.dx \tag{G.34}$$

   After integrating and substituting the integration limits, the following can be obtained:

$$W = \rho_{sat} (Y_w - y_1)(x_2 - x_1) + \left[\rho_d \; (y_{max} - Y_w) - \frac{(\rho_{sat} - \rho_d)}{a\gamma_w} (e^{a\gamma_w (Y_w - y_{max})} + 1) \right] (x_2 - x_1) \tag{G.35}$$

Appendix H

Validation of the derived apparent cohesion force and strip weight equations

This appendix addresses validation of the derived equations for the apparent cohesion force and strip weight.

H.1 Validation of the derived apparent cohesion force equations

For the apparent cohesion force equations, showed in Appendix F, a case study with a set of parameters is suggested for the validation. Figure H.1 shows a discontinuity above the water table (ensuring an unsaturated case) with arbitrarily assumed dimensions. In Fig. H.1, Y_w is water table height from the origin, x_1, x_2, y_1, y_2 are nodal coordinates (shown in Fig. F.1b) and y_{max} is height of the soil from the origin to the surface. For the assumed dimensions in Fig. H.1, the discontinuity is orientated at an angle of $\theta = 68.198^o$.

(a) Discontinuity above and under the water table:

- The apparent cohesion force equation for the case above the water table (e.g. Eq. F.10) should match the apparent cohesion force equation for the case under the water table (e.g. Eq. F.12) at a small value of parameter (a) (e.g. 10^{-6}), since (a) is the power of the exponent. At the small value of (a), the degree of saturation term (S_r) in Eq. F.10 will eliminate, since ($e^{10^{-6}} = 1$). As a result, the apparent cohesion force equation for the case above the water table matches with the apparent cohesion force equation for the case below the water table. At $a = 10^{-6}$, Eqs. F.10 and F.12 give $\hat{C} = 4.41902665$ and $\hat{C} = 4.41905245$, respectively.
- For a case $\theta = 0$, the apparent cohesion force equation (Eq. F.22) gives $\hat{C} = 0.29462196$ and Eq. F.24 gives $\hat{C} = 0.29462225$ when $a = 10^{-6}$. Also, for a case of $\theta = 90$, Eqs. F.26 and F.28 give $\hat{C} = 4.41933380$ and 4.41929440, respectively.
  For the case $\theta = 0$, length of the discontinuity ($L = 0.4$ m) and $y_1 = y_2 = 0.2$ m (assumed) were used, while for the case when $\theta = 90$, $x_1 = x_2 = 1$ m (assumed)

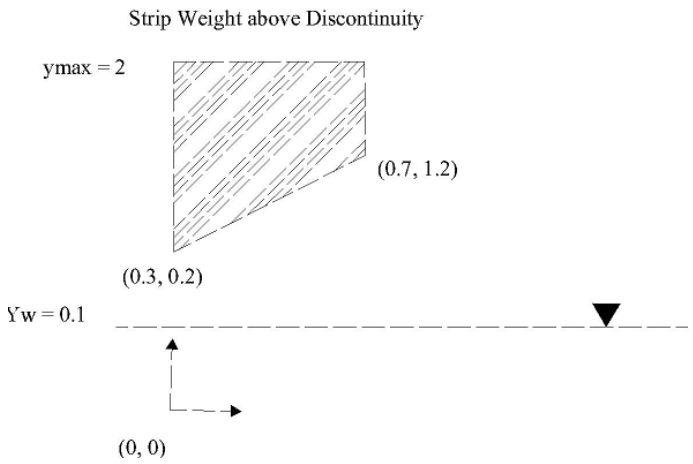

Figure H.1: Assumed dimensions for the apparent cohesion force equations validation.

and $L = 1$ m were utilised.

- For a dry case, the apparent cohesion force equations above the water table (Eqs. F.10, F.22 and F.26) should be zero. To validate the equations for the dry case, a high value of the parameter (a) can be assumed (e.g. $a = 200$) until $\hat{C} = 0$, since ($e^{200} = 0$). In this case, $Y_w = 0.2$ m , $y_1 = 0.6$ m, $y_2 = 1.2$ m and $L = 0.721$ m were used and this gives an angle of failure equal to $\theta = 56.309^o$.

(b) Discontinuity crossing the water table:

- Validation of the equations for the case where the discontinuity crosses the water table is shown in Table H.1. In this case, the parameters used were $a = 0.017$, $x_1 = 0$, $x_2 = 1$, $y_1 = 0$, $y_2 = 1$ and $\theta = 45^o$. Equation F.19 should match with Eq. F.10 when the water table is at the origin ($Y_w = 0$) and should also match Eq. F.12 for a case when the water table is at the surface (fully saturated case $Y_w = 1$). The same method was followed to validate Eq. F.33 with their counterpart equations shown in Table H.1.

Table H.1: Apparent cohesion force equations validation for the discontinuity crossing the water table.

	$0 \neq \theta \neq 90$			$\theta = 90$		
Y_w (m)	Eq. F.10	Eq. F.12	Eq. F.19	Eq. F.22	Eq. F.24	Eq. F.33
0	4.6638	-	4.6638	3.2978	-	3.2978
1	-	-5.2082	-5.2082	-	-3.6828	-3.6828

H.2 Validation of the derived strip weight equations

There are different possibilities of the failure mechanism in which a discontinuity can be happened (e.g. $\theta = 0$, $\theta = 60$). At each possible case, weight of soil above the discontinuity is different. To validate the strip weight equations, the equations were showed in Appendix G, the same set of the parameters shown in Fig H.1 were used with a few required additional parameters as: ρ_{sat}= 15.2 kN/m^3, ρ_{dry}= 8.8 kN/m^3 and y_{max}= 2 m.

(a) Discontinuity above and below the water table:

- The strip weight equations for the case when the discontinuity is above the water table should coincide with those where the discontinuity is below the water table at a very small value of the parameter (a). At a very small value of a ($=10^{-6}$), both Eqs. G.9 and G.13 give W = 7.90396373 and 7.90399999, respectively.
- For $\theta = 0$, both Eqs. G.30 and G.33 give W = 10.94395479 and 10.94399999, respectively when $a = 10^{-6}$. For the case when $\theta = 0$, $L = 0.4$ m and $y_1 = y_2 = 0.2$ m(assumed) were used.
- For the dry case, validation of the strip weight equations was also satisfied at a high value of $a = 200$. Equations G.9 and G.30 gave (NaN) and 4.92800000, respectively since the latter does not depend on parameter a. In this case, $Y_w = 0.2$, $y_1 = 0.6$ and $L = 0.721$ were used and the discontinuity acts at an angle of $\theta = 56.309^o$.

(b) Discontinuity crossing water table:

- Validation of the strip weight equations for this case, where the discontinuity crosses the water table, is shown in Table H.2. Here, $a = 0.017$, $x_1 = 0$ m, $x_2 = 1$ m, $y_1 = 0$, $y_2 = 1$ m, $y_{max} = 1$ m and $\theta = 45^o$ were used. For the case when $\theta \neq 0$ and $\theta \neq 90$, Eq. G.9 (the discontinuity above the water table) should match Eq. G.25 when using Y_w as a small value (Y_w= 0.00001 m). Also, Eq. G.13 (valid for the case under the water table) should match with Eq. G.25 when Y_w is close to the surface (Y_w= 0.9999 m). Equation G.13 should match Eq. G.16 when $Y_w = 1.9999$ m (in this case $y_{max} = 2$ m was used to obtain the condition $Y_w < y_{max}$). For $\theta = 0$, $y_1 = y_2 = 1$ and $y_{max} = 2$ were used. Equation G.35 matches with Eq. G.30 when $Y_w = 0.00001$ m and with Eq. G.33 when Y_w= 1.9999 m.

Table H.2: Strip weight equations validation for the discontinuity crossing the water table.

	$0 \neq \theta \neq 90$				$\theta = 0$		
Y_w (m)	Eq. G.9	Eq. G.13	Eq. G.16	Eq.G.25	Eq. G.30	Eq.G.33	Eq.G.35
0.00001	7.2655	—	—	7.2655	14.6948	—	14.6948
0.9999	—	7.6000	—	7.6000	—	—	—
1.9999	—	22.7999	22.7999	—	—	15.200	15.200

H.3 A Retaining wall case study

H.3.1 Validation of (1×1) domain square dimension problem using the UNSAT-DLO code

To validate the derived equations for both the apparent cohesion force and strip weight in the UNSAT-DLO code, a (1×1) domain square dimension was selected. In this study, the height of a retaining wall was selected as the height of the domain square dimension ($H = 1$ m). Different locations of the water table were selected along the height of the retaining wall to ensure all possible cases (unsaturated and fully saturated). Table H.3 shows parameters used in the validation. Table H.4 shows the collapse loads obtained

at different positions of the water table along the height of the wall. To validate the collapse loads obtained using the UNSAT-DLO code (named Unsaturated Soln in Table H.4), a hand calculation solution (based on upper bound theorem) was used. The UNSAT-DLO code solution for a fully saturated case should match with the original DLO code result, named as ORG Code in Table H.4 which is proposed by Smith & Gilbert (2007*a*), when using the buoyant unit weight of the soil. The collapse load equation for the hand calculation, derived based on Figs. H.2a and b, is given by:

$$F \times \delta - W_B \times \delta \times \tan(\alpha + \phi^{'}) = \hat{c} \times L \times \cos(\phi) \times \frac{\delta}{\cos(\alpha + \phi^{'})} \tag{H.1}$$

where F is collapse load (kN/m), δ is block displacement, W_B is weight of a block above the discontinuity (kN/m), α is angle between the vertical axis to the slip line (shown in Fig. H.2a), $\phi^{'}$ is internal friction angle, $\hat{c}$ is apparent cohesion along the discontinuity and L is length of the discontinuity. For the buoyant case shown in Table H.4, the obtained collapse load is equal to 18.9361 (kN/m), which is different from the Unsaturated Soln (23.8411) (kN/m). The is because for the buoyant case, the water pressure behind the wall (4.905) (kN/m) is not included in the calculation. For larger dimensions of the wall, the difference is larger. A general equation that covers this difference, even for larger dimensions of the wall, is give by:

$$D = \frac{n}{2} \times \gamma_w \times \frac{n}{n} \tag{H.2}$$

where D is difference between the Unsaturated Soln result (for the case of the fully saturated) and the original DLO code (the buoyant case), n is number of nodes along the height of the wall and γ_w is the unit weight of water (kN/m^3). The ORG Code solutions are obtained by substituting the apparent cohesion as a cohesion and the strip weight above the discontinuity was multiplied by 2 (to obtain the unit weight of the soil).

Table H.3: Used parameters in the validation.

ρ_d (kN/m^3)	ρ_{sat} (kN/m^3)	a (kPa^{-1})	$c^{'}$ (kN/m^2)	$\phi^{'}$ (degrees)	γ_w (kN/m^3)	y_{max} (m)
8.8	15.2	0.017	0	36.9	9.81	1

H.4 Validation of (2×2) domain square dimension problem using the UNSAT-DLO code

This case study was used as a double check of the derived equations for the apparent cohesion and the strip weight equations. A (2×2) domain square dimension (height of the wall H = 2 m) was used. Table H.5 shows the collapse load results obtained using the UNSAT-DLO code, the ORG Code and the hand calculation equation. The same parameters given in Table H.3 were used. For the solutions obtained using the ORG Code, the first set of the apparent cohesion and the strip weight values were used to obtain the collapse load and then the second set of the values (e.g. see Table H.5-$Y_w = 0$). Then an average between the two solutions was taken. For the (2×2) domain square dimension, there are two values of the apparent cohesion and the strip weight

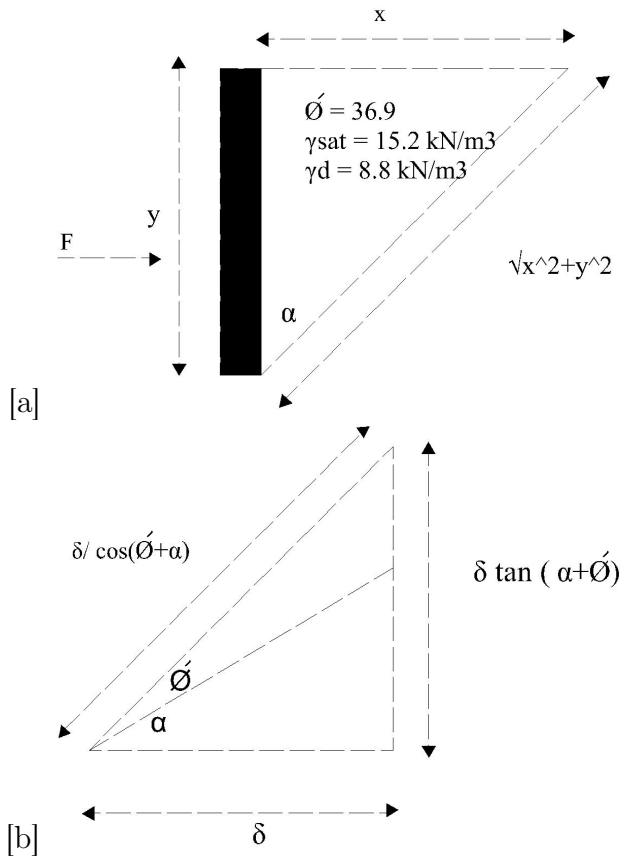

Figure H.2: (a) Retaining wall (b) Hodograph

since the height of the problem is divided in the DLO code into two unit lengths. For a (3×3) domain square dimension, there are three values of the apparent cohesion and the strip weight and so on.

H.4.1 Further check for the UNSAT-DLO code

Further check of the UNSAT-DLO code was performed by using different heights of the wall. The same solution should be obtained when doubling the domain square dimension of the problem (height) and with dividing each of these parameters ρ_d, ρ_{sat} and γ_w by n. Table H.6 shows the collapse load solutions obtained by the UNSAT-DLO code for different dimensions of the wall with the water table at the base of the wall.

Table H.4: Validation of (1×1) domain square dimension problem.

Y_w(m)	Strip Weight	Apparent Cohesion	Unsaturated Soln	ORG Code	Hand Calculation	Buoyant
0	7.2655	3.297805	77.5198	77.5194	77.5194	–
0.1	7.3135	2.663883	72.7688	72.7687	72.7683	–
0.2	7.3613	2.010163	67.8572	67.8575	67.8572	–
0.3	7.4077	1.338624	62.7934	62.7935	62.7932	–
0.4	7.4516	0.651316	57.5858	57.5854	57.5853	–
0.5	7.4920	-0.04964	52.2438	52.2434	52.2428	–
0.6	7.5277	-0.76212	46.7755	46.7761	46.7751	–
0.7	7.5575	-1.48393	41.1911	41.1916	41.1910	–
0.8	7.5803	-2.21289	35.5005	35.5008	35.5003	–
0.9	7.5949	-2.94666	29.7173	29.7136	29.7134	–
0.9999	7.6	-3.68205	23.8470	23.8485	23.8467	–
1	7.6	-3.68275	23.8411	23.8429	23.8411	18.9361

Table H.5: Validation of (2×2) domain square dimension problem.

Y_w(m)	Strip Weight	Apparent Cohesion	Unsaturated Soln	ORG Code	Hand Calculation	Buoyant
0	21.0548&6.8254	3.297805&8.5332	145.4294	145.4286	145.4282	–
0.5	21.7152&7.0363	-0.04964&6.1546	125.5215	125.5194	125.5096	–
1	22.2948&7.2655	-3.68275&3.2978	102.3060	102.306	102.3058	–
1.25	22.5119&7.3847	-5.52420&1.6764	89.5910	89.5904	89.5902	–
1.5	22.6702&7.4920	-7.3655&-0.04964	76.2094	76.2104	76.2070	–
1.75	22.7671&7.5699	-9.2069&-1.8476	62.2155	-1.67e+003	62.2156	–
1.8	22.7789&7.5803	-9.5752&-2.2128	59.3496	-ve	59.3500	–
1.9	22.7942&7.5949	-10.3118&-2.9098	53.5612	-ve	53.5555	–
1.9999	22.8&7.6	-11.0476&-3.5547	47.6880	-ve	48.19869	–
2	22.8&7.6	-11.04762&-3.6827	47.6821	-ve	47.6822	37.8722

Table H.6: Further check for UNSAT-DLO code for different domain square dimension problems for Y_w= 0 m.

Saturated density of soil	Dry density of soil	Unit weight of water	Domain square ($n \times n$)	Collapse Load
ρ_{sat}	ρ_d	γ_w	1×1	77.5198
$\rho_{sat/2}$	$\rho_{d/2}$	$\gamma_w/2$	2×2	77.5199
$\rho_{sat/3}$	$\rho_{d/3}$	$\gamma_w/3$	3×3	77.5197
$\rho_{sat/4}$	$\rho_{d/4}$	$\gamma_w/4$	4×4	77.6126
$\rho_{sat/5}$	$\rho_{d/5}$	$\gamma_w/5$	5×5	77.5201

Appendix I

Integration of apparent cohesion equations at the residual saturation

I.1 Introduction

The proposed SWCC equation, proposed by Stanier & Tarantino (2010) shown in Chapter 5 (Eq. 5.6), was formulated to match better with the experimental SWCC for the sand tested in this study (Eq. 5.10). The reformulation of the SWCC equation showed a reasonable match up to a residual suction of 5 kPa (see Fig. 5.8). However, beyond the residual suction the equation showed poor agreement with the experimental results of the SWCC.
For better match beyond the residual saturation, Eq. 5.10 was further reformulated as follows:

$$S_r = S_o + (1 - S_o)e^{a\gamma_w(y_c - y)} \tag{I.1}$$

where S_o is the residual saturation and y_c $(= H_c)$ is capillary rise height and y is distance from the base (origin) to the soil surface.
In this appendix, integration of the apparent cohesion force equations at the residual saturation is presented.

I.1.1 Discontinuity above the water table

The integration is given by:

$$\hat{C} = \int_o^L sS_r \tan\phi' dy \tag{I.2}$$

By substituting s and S_r equations, Eqs. 5.5 and I.1, the following can be obtained:

$$\hat{C} = \tan\phi' \int_o^L \gamma_w(y_1 + l\sin\theta - Y_w)[S_o + (1 - S_o)e^{a\gamma_w(y_c - y_1 - l\sin\theta)}]\, dl \tag{I.3}$$

where $y = y_1 + l\sin\theta$ and more simplification of the integration gives:

$$\hat{C} = \tan\phi'\, \gamma_w[\int_o^L S_o\,(y_1 + l\sin\theta - Y_w)\, dl + \int_o^L (1 - S_o)\,(y_1 + l\sin\theta - Y_w)\, e^{a\gamma_w(y_c - y_1 - l\sin\theta)}\, dl] \tag{I.4}$$

$$\hat{C} = \gamma_w \tan\phi' \left([\frac{1}{2} S_o\, l\, (2y_1 + l\sin\theta - 2Y_w)]_0^L + [(1-S_o)\, \frac{-(a\gamma_w\, l\sin\theta + 1)}{(a\gamma_w)^2 \sin\theta}\, e^{a\gamma_w(y_c - y_1 - l\sin\theta)}\,]_0^L\right) \tag{I.5}$$

By substituting the boundary conditions, the apparent cohesion force equation is as follows:

$$\hat{C} = \gamma_w \tan\phi' \left([\frac{1}{2} S_o\, L\, (2y_1 + L\sin\theta - 2Y_w)] \; - \right.$$

$$\left.[(1\text{-}S_o)\, \frac{(a\gamma_w\, L\sin\theta + 1)}{(a\gamma_w)^2 \sin\theta}\, e^{a\gamma_w(y_c - y_1 - L\sin\theta)}\,] + [(1 - S_o)\, \frac{e^{a\gamma_w(y_c - y_1)}}{(a\gamma_w)^2\, \sin\theta}]\right) \tag{I.6}$$

I.1.2 Discontinuity below the water table

For this case, the integration is same as Eq. F.12.

I.1.3 Discontinuity crosses the water table

The integration in this case is given by:

$$\hat{C} = \tan\phi'\, \gamma_w \left[\int_o^{L1} (y - Y_w) dl + \int_o^{L2} (y - Y_w)[S_o + (1 - S_o) e^{a\gamma_w(y_c - y)}\, dl]\right] \tag{I.7}$$

where for the first part of the integration $y = y_1 + l\sin\theta$ and for the second part $y = Y_w + l\sin\theta$. By substituting y in Eq. I.7, the following can be obtained:

$$\hat{C} = \tan\phi'\, \gamma_w \left[\int_o^{L1} (y_1 + l\sin\theta - Y_w)\, dl + \int_o^{L2} (l\sin\theta)[S_o + (1 - S_o) e^{a\gamma_w(y_c - Y_w - l\ \sin\theta)}\, dl]\right] \tag{I.8}$$

Integration of Eq. I.8 gives:

$$\hat{C} = \tan\phi'\, \gamma_w [[(\frac{l}{2}\sin\theta\ + l(y_1 - Y_w)]_0^{L_1} + [(S_o\ \frac{l^2}{2}\sin\theta)]_0^{L2} + \tag{I.9}$$
$$[(1 - S_o) \frac{-(a\ \gamma_w\ l\sin\ \theta + 1)}{(a\gamma_w)^2 \sin\theta} e^{a\gamma_w(y_c - Y_w - l\sin\theta)}]_0^{L_2}]$$

$$\hat{C} = \tan\phi'\, \gamma_w [(\frac{L_1^2}{2}\sin\theta\ + L_1(y_1 - Y_w)) + [(S_o\ \frac{L_2^2}{2}\sin\theta)] + \tag{I.10}$$
$$(1 - S_o)[\frac{-(a\ \gamma_w\ L_2 \sin\ \theta + 1)}{(a\gamma_w)^2 \sin\theta} e^{a\gamma_w(y_c - Y_w - L_2\sin\theta)} + \frac{e^{a\gamma_w(y_c - Y_w)}}{(a\gamma_w)^2 \sin\theta}]]$$

Appendix J

Validation of the UNSAT-DLO code against the modified LimitState:GEO software

Although the UNSAT-DLO code was validated using different case studies for a retaining wall with different heights as showed previously in Appendix H, the code was validated again once it was incorporated into the commercial LimitState:GEO software. This appendix therefore addresses the validations for the modified version of the LimitState:GEO software that takes into consideration the effect of unsaturated conditions.

J.1 Validation of the UNSAT-DLO code against the modified LimitState:GEO software

The modified LimitState:GEO software was evaluated against the UNSAT-DLO code using a retaining wall case study. Two different heights of the wall as 1 and 2 m (domain square ranges of 1×1 and 2×2 m) and different water table positions were used in the validation. The parameters showed in Table H.3 in appendix H were used for the validation. Figures J.1a and b show results of the modified LimitState:GEO and the UNSAT-DLO code in which good agreement can be seen. Where the legend "LS-GEO" in the figures denotes to modified LimitState:GEO result. In spite of the good agreement between the modified LimitState:GEO and the UNSAT-DLO code results, further checks were performed as shown in the next sections.

J.2 Validation of the water pressure along the discontinuity

A retaining wall of height 1 m was used to perform this validation. High numbers of nodes along the slip line were used (baseline nodal spacing = 0.1 m). The water pressure along the slip line was validated against values obtained by the (sS_r) term. The (sS_r) values were obtained using Eqs. 5.5 and 5.10 showed in Chapter 5. Several values of the capillary rise height H_c as 0, 0.1, 0.5, 0.9 and 1 m were assumed arbitrarily in order

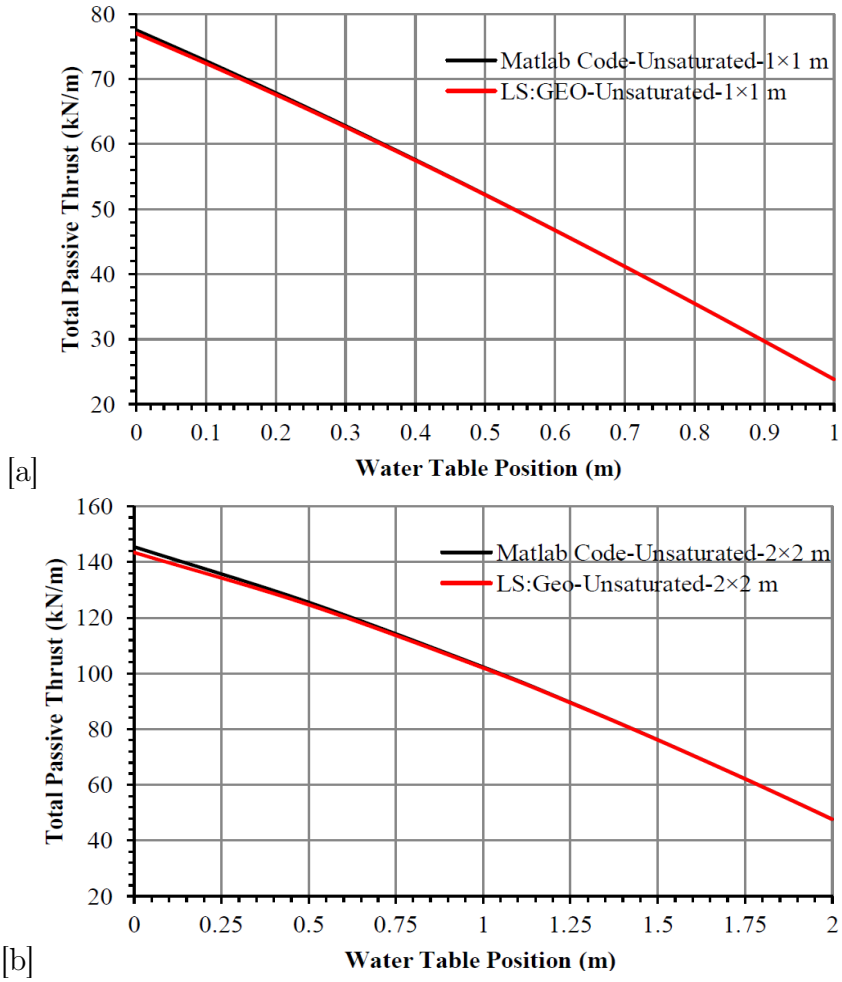

Figure J.1: Validation of the modified LimitState:GEO software against the UNSAT-DLO code for a retaining wall height (a) 1 m (domain square = 1×1 m) (b) 2 m (domain square = 2×2 m).

to perform the validation. The water table position $Y_w = 0$ m (base of the wall) was used to ensure an unsaturated case. The parameters showed previously in Table H.3 - (Appendix H) were used. Figures J.2a, b, c, d and e show the water pressure along the slip line for both the term sS_r and the one obtained by the modified LimitState:GEO. The results show good agreement for all the cases.

J.3 Validation of the modified LimitState:GEO software at residual saturation

The new equations for the derived apparent cohesion forces, presented in Appendix I, were incorporated in the LimitState:GEO software to model a retaining wall case study of 1 m height. These equations were validated using two walls placed in both sides of the geometry as shown in Fig. J.3. This is to move the wall horizontally and; therefore, it would be easier to calculate the shear force along the horizontal base of the soil. On the left hand side of the wall, a permanent load of 1 kN was applied while 2 kN load was applied on the right hand side of the wall. For cases when the wall was unstable (high water table i.e. $Y_w = 0.5$ m), the value of 10 kN was used instead of 2 kN. For

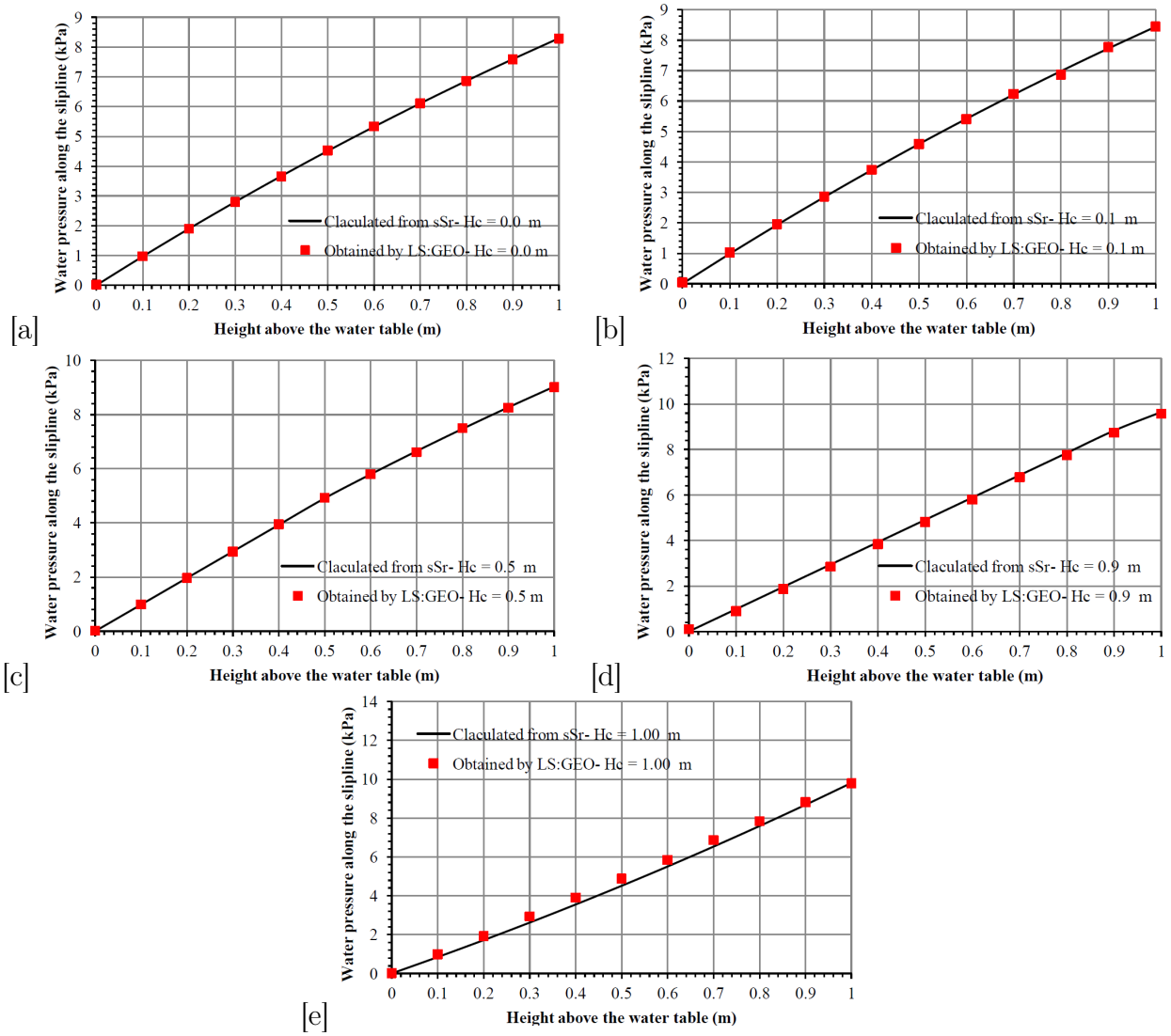

Figure J.2: Water pressure along the slip line obtained by the (sS_r) term and modified LimitState:GEO software for (a) $H_c = 0$ m (b) $H_c = 0.1$ m (c) $H_c = 0.5$ m (d) $H_c = 0.9$ m (e) $H_c = 1$ m.

this validation, the fraction D soil was used as a backfill material with the properties shown in Table J.1. The value of $S_o = 0.19898$ at the residual saturation was obtained from the actual SWCC for fraction D. Different positions of the water table, Y_w, were

Table J.1: Used parameters in modified LimitState:GEO at residual saturation.

γ_{sat} (kN/m^3)	γ_{dry} (kN/m^3)	$c^{'}$ (kN/m^2)	$\phi^{'}$ (degrees)	a (kPa^{-1})	s_o (kPa)	y (m)
19.33	15.2	0	36.8	0.7	2.3	0

selected as shown in Table J.2. The model results, then, were validated against the hand calculation method based on Eq. J.1.

$$T = (\sigma \times l \times \tan\phi^{'} + \hat{C}) \times l \tag{J.1}$$

where T is shear force (kN), σ is normal stress (kN/m^2), l is width of the soil (m) and $\hat{C}$ is the apparent (artificial) cohesion (kN/m^2) given by Eqs. J.2 and J.3 for the

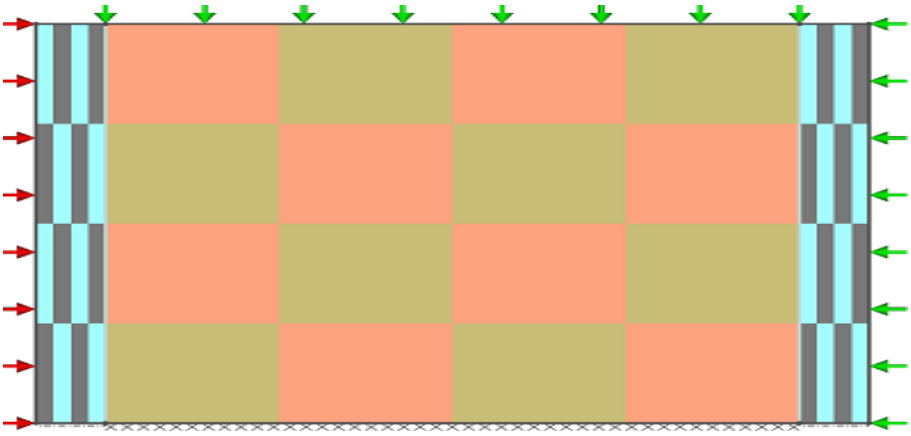

Figure J.3: Validation of the apparent cohesion force equations at residual saturation using a retaining wall case study (height = 1 m) in the modified LimitState:GEO software.

horizontal discontinuity ($\theta = 0$) for cases when the discontinuity is below and above the capillary rise height, respectively. Here $\theta = 0$, since the wall was forced to move horizontally.

For the discontinuity below the capillary rise height:

$$\hat{C} = \gamma_w \tan\phi^{'} \ (y - y_c) \ (x_2 - x_1) \tag{J.2}$$

For the discontinuity above the capillary rise height:

$$\hat{C} = \gamma_w \tan\phi^{'} \ (y - Y_w) \ (x_2 - x_1)[S_o + (1 - S_o) \ e^{a\gamma_{w(y_c - y)}}] \tag{J.3}$$

The validation of the modified LimitState:GEO software with the hand calculation results showed a good agreement as can be seen in the last two columns in Table J.2. Note that the value y_c was calculated based on the Eq. 5.11. Further validation of the pore water pressure at the base of the wall with the hand calculation is shown in Fig. J.4.

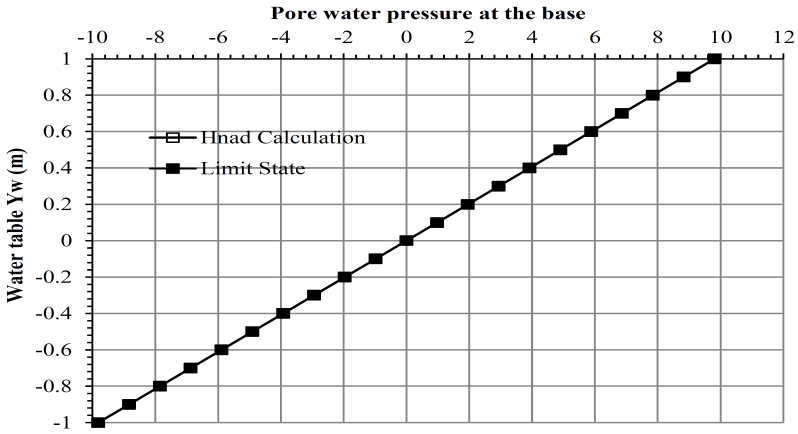

Figure J.4: Water pressure at the base of the wall (horizontal discontinuity) versus water table position.

Table J.2: Validation of the modified LimitState:GEO against the hand calculation method at residual saturation.

y_c	Y_w m	$\hat{C}$	s kPa	S_r	sS_r	T Hand Calculation (Eq. J.1)	LS:GEO
1.2344	1.0	-7.3388	0	1	0	4.03	4.03
1.1344	0.9	-6.6049	0.981	1	0.981	4.766	4.77
1.0344	0.8	-5.8710	1.962	1	1.962	5.499	5.5
0.9344	0.7	-5.1371	2.943	0.7096	2.088	6.23	6.23
0.8344	0.6	-4.4032	3.924	0.4559	1.7892	6.967	6.97
0.7344	0.5	-3.6694	4.905	0.3283	1.6103	7.70	7.70
0.6344	0.4	**-2.9355**	5.886	0.2640	1.5542	**8.435**	**8.44**
0.5344	0.3	-2.2016	6.867	0.2317	1.5913	9.169	9.17
0.4344	0.2	-1.4677	7.848	0.2154	1.6909	9.90	9.90
0.3344	0.1	-0.7338	8.829	0.2072	1.8300	10.637	10.64
0.2344	0	0	9.81	0.2031	1.9929	11.37	11.37
0.1344	-0.1	0.7338	10.79	0.2010	2.1698	12.10	12.1
0.0344	-0.2	1.4677	11.77	0.2000	2.3548	12.838	12.84
-0.0655	-0.3	1.5624	12.75	0.1995	2.5443	12.93	12.93
-0.1655	-0.4	1.3385	13.73	0.1992	2.7364	12.709	12.71
-0.2655	-0.5	1.2047	14.71	0.1991	2.9299	12.57	12.57
-0.3655	-0.6	1.1627	15.69	0.1990	3.1242	12.53	12.53
-0.4655	-0.7	1.1904	16.67	0.1990	3.3189	12.56	12.56
-0.5655	-0.8	1.2649	17.65	0.1989	3.5138	12.636	12.64
-0.6655	-0.9	1.3690	18.63	0.1989	3.7089	12.74	12.74
-0.7655	-1	1.4909	19.62	0.1989	3.9040	12.86	12.86

J.4 Example verification

This example shows the procedure of calculation the shear force along the discontinuity using the hand calculation method (Eq. J.1) for the retaining wall case study explained in the previous section (see Table J.2).
For the case of Y_w = 0.4 m, the value of $\hat{C}$ = - 2.9355 was obtained (see Table J.2) with l = 1.00 m (horizontal distance of the domain square 1×1) and with other used properties shown in Table J.1, the shear force is giving by:

$$T = [\sigma \times l \times \tan\phi' + \hat{C}] \times l = [15.2 \times 1 \times 1 \times \tan(36.8) + (-2.9355)] \times 1 = 8.4355 \text{ kN/m}$$

where $\sigma = \gamma_{dry} \times 1 = 15.2$ kN/m^2. The result of 8.44 kN/m was obtained by the modified LimitState:GEO software (last column in Table J.2 - bold number) with a difference of 0.005.

J.5 Validation of the modified LimitState:GEO with a Rankine analysis for a fully saturated case

In this section, the modified LimitState:GEO software was validated against a Rankine analysis at the fully saturated case for a passive earth pressure case study. The prop-

erties showed previously in Table J.1 was used here for the height of the wall $H = 1$ m. Equation J.4 was used to calculate total passive earth thrust using a Rankine analysis.

$$P_p = \frac{1}{2}\ k_p\ \gamma^{'}\ H^2 + 2c^{'}\ \sqrt{k_p}\ H + \frac{1}{2}\ \gamma_w\ H_w^2 \tag{J.4}$$

where P_p is the total passive earth trust (kN/m), $\gamma^{'}$ is the buoyant unit weight (kN/m^3), $c^{'}$ is the cohesion (kN/m^2), γ_w is the unit weight of water (kN/m^3), H_w is the water table height and k_p is the passive lateral earth pressure coefficient and its given by:

$$k_p = \frac{1 + \sin\phi^{'}}{1 - \sin\phi^{'}} \tag{J.5}$$

The total passive thrust $P_p = 23.849$ kN/m was obtained using $k_p = 3.98$ ($\phi^{'} = 36.8^o$), $\gamma^{'}$ = (19.33-9.81) = 9.49 kN/m^3, $H = 1$ m, $c^{'} = 0$ kPa, $\gamma_w = 9.81$ kN/m^3 and $H_w = 1$ m (fully saturated case). The same result was obtained using the modified LimitState:GEO software.

J.6 Further validation for the modified LimitState:GEO software

J.6.1 Validation of the modified LimitState:GEO software at different heights of the wall

For further check the modified LimitState:GEO software, different heights of the wall as 1, 2, 3 and 4 m were used. $Y_w = 0$ m (water table at the base of the wall) was selected to ensure an unsaturated case. For this validation, an arbitrary set of parameters were used as shown in Table J.3 (different parameter values were selected to verify the case study using various values). Here γ_{dry} and γ_{sat} were taken as 1.5 $\times$ γ_w and 1.9 $\times$ γ_w, respectively and an average unit weight of the soil between dry and saturated unit weight was assumed above the capillary rise height.

For this validation, the same solution should be obtained when the height of the wall is doubled and γ_{sat}, $\gamma_{average}$ and γ_w are divided by the height of the wall. In other words, the unit weights should be scaled down by the height of the wall in the software (e.g. dividing by 3 when using $H = 3$ m). And also a new capillary rise height value should be used which is given as:

$$H_c = H_w\ + \frac{H \times s_o}{\gamma_w} \tag{J.6}$$

Table J.4 shows almost the same results obtained by the modified LimitState:GEO software for the different heights of the wall.

In conclusion, the validations performed for the modified LimitState:GEO software showed good agreement using various case studies.

Table J.3: Used parameters in modified LimitState:GEO software.

Soil Properties	Values
γ_{sat} kN/m^3	18.639
γ_{dry} kN/m^3	14.715
$\gamma_{average}$ kN/m^3	16.667
γ_w kN/m^3	9.81
$c^{'}$ kN/m^2	0
$\phi^{'}$	30^o
H_c	0.50968
s_o kPa	5
Y_w	0.0

Table J.4: Further check for the modified LimitState:GEO software at different heights of the wall.

Wall height (H) m	γ_{sat} kN/m^3	$\gamma_{average}$ kN/m^3	γ_w kN/m^2	H_c m	P_p kN/m
1	18.639	16.667	9.81	0.50968	57.54896
2	9.3195	8.3335	4.905	1.01936	57.54254
3	6.213	5.5556	3.27	1.52904	57.26137
4	4.6597	4.16675	2.4525	2.03872	57.27454

Appendix K

General calibration procedure for load cells and LVDTs

K.1 Introduction

This appendix describes the general calibration procedures for the LVDTs and load cells used in this study. Prior to the calibration, the apparatus that was used for the load cell calibration was warmed up for 30 minutes (see Fig. K.2a). A digital voltmeter device was then utilised to calibrate against the fixed supply to set the transducer input voltage (5V or 10V) prior to the calibration.
The LVDTs, used for the direct shear and the bearing capacity tests, were calibrated using several complete cycles of displacement to determine suitable calibration equations. The same procedure was used for the load cells. Data were acquired via data logger using LabVIEW software. For each application of displacement and pressure, readings of the load cell and LVDTs (more than 20 readings) were taken and the average of the reading was used. This is to minimize the noise of the load cell and LVDTs readings. If the data were unsatisfactory, the calibration was repeated.

K.2 Calibrations of LVDTs and load cell for the direct shear apparatus

Table K.1 shows serial numbers and other specifications for the LVDTs and load cell used for the direct shear apparatus. Figures K.1a, b, c and d show the calibration lines for the LVDTs and the load cell.

Table K.1: Specifications for the LVDTs and load cell for the direct shear apparatus.

Apparatus	**Serial No.**	**Input (v)**	**Capacity**
LVDT 1	HS 25/5764	10 v AC or DC, full bridge, 350 omega	0-25 mm
LVDT 2	HS 25/6018	10 v AC or DC,full bridge, 350 omega	0-25 mm
Load cell	68027	2mv/v	3500 N

Due to restrictions with the shear box container, the load cell was set to measure in the tension direction in this study (see Fig. K.4). For this reason, tension calibration on the load cell was performed. Although, the difference between compression and tension

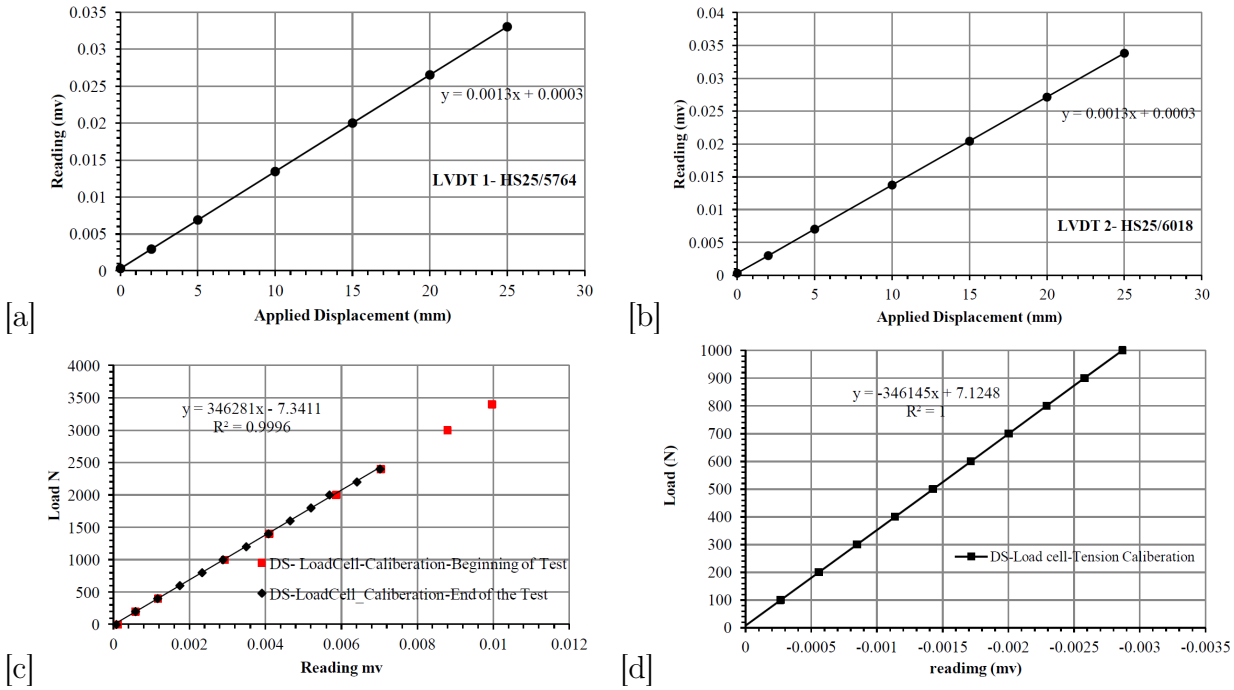

Figure K.1: Calibration line for the direct shear device of (a) LVDT 1 and (b) LVDT 2. Calibration line of load cell for the direct shear device for (c) compression (d) tension.

output of the load cell was recorded by the manufacturer as negligible, the tension calibration was conducted and the results showed no difference between the compression and tension calibrations. As a double check, the regression parameters for the tension calibration were used in the LabVIEW software and the load cell was subjected to a compression load as shown in Fig. K.2a. The outcome of readings for different applied loads coincided with the actual applied loads and showed no difference between the compression and tension loads of the load cell. Figure K.4 shows a consolidation apparatus which was used for the tension calibration of the load cell.

K.3 Calibrations of the LVDT and load cell for the bearing capacity apparatus

The bearing capacity load cell with a capacity of 2500 N (Serial No. 1128) which is shown in Fig. K.2c was used in this study. An LVDT with 50 mm displacement capacity (serial No. HS50 50617552) was used. Figures K.3a and b show the calibration lines for both the LVDT and load cell that used for the bearing capacity rig.

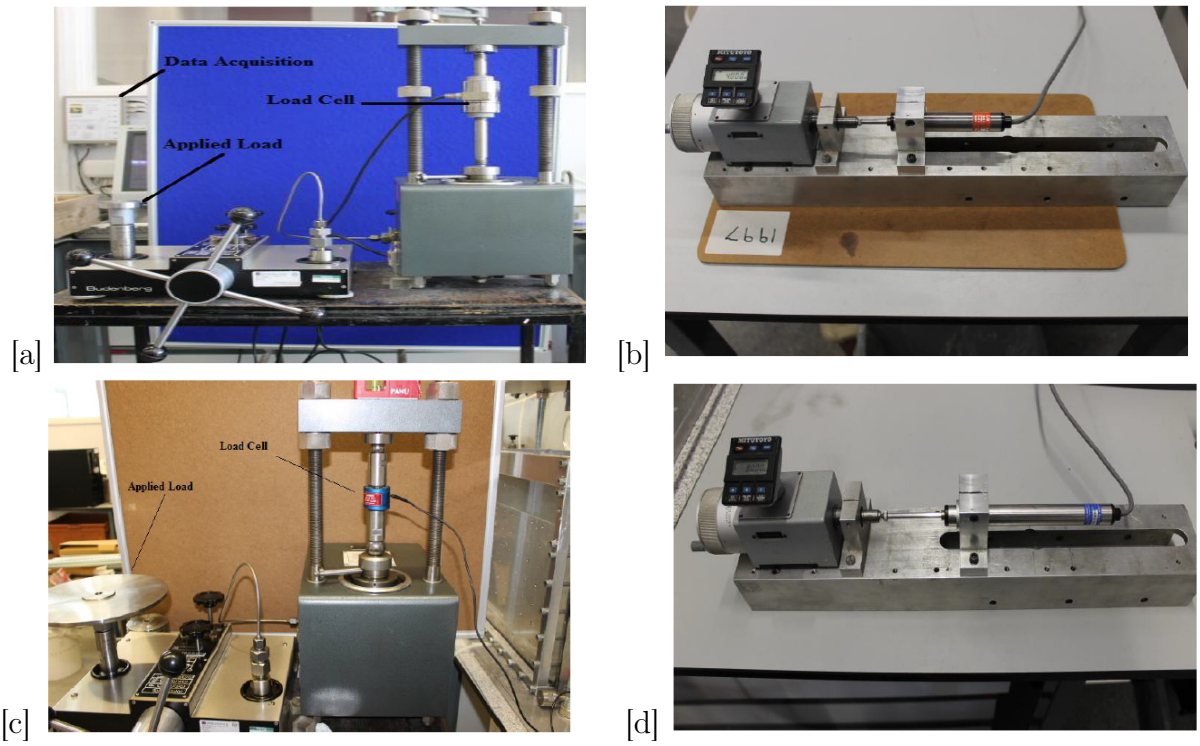

Figure K.2: (a) load cell calibration of the direct shear device (b) micrometre rig used of the LVDTs calibration for the direct shear device (c) load cell calibration of the bearing capacity rig (d) micrometre rig used of the LVDT calibration for the bearing capacity test.

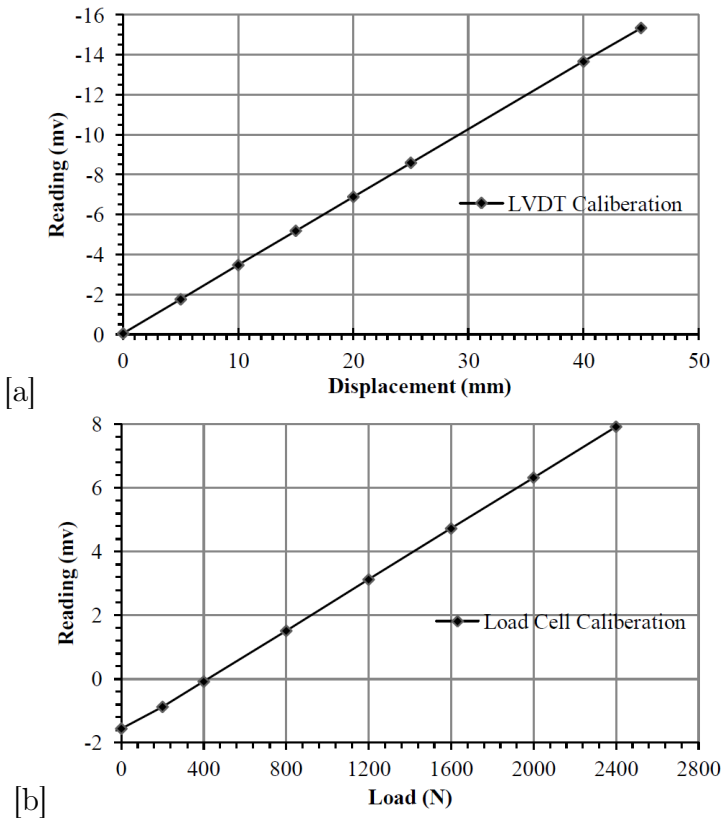

Figure K.3: Calibration line for the bearing capacity test for the (a) LVDT (b) load cell.

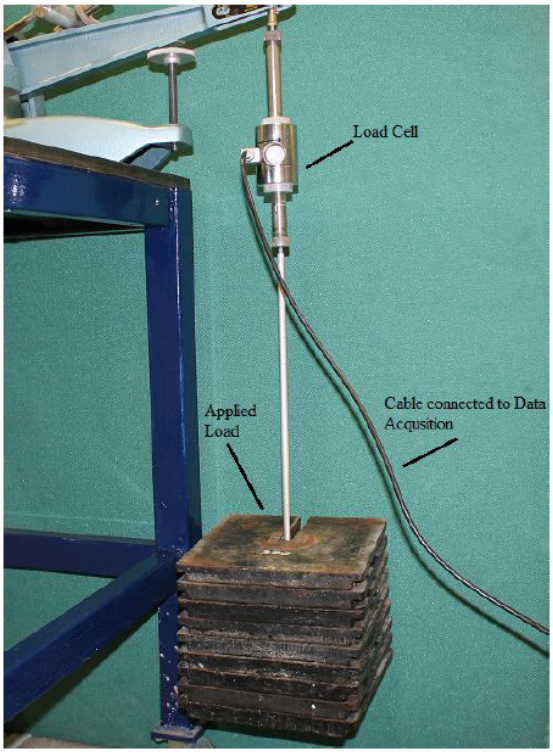

Figure K.4: Tension calibration for the load cell used for the direct shear apparatus.

Appendix L

Rankine equations for total passive earth thrusts

This appendix addresses Rankine earth pressure equations for fully saturated and unsaturated cases. The unsaturated equations take into consideration the effect of capillary rise.

L.1 Total passive earth thrust equations

For cohesionless soil, total passive earth thrust can be calculated as:

(a) Fully saturated case:

$$P_p = \frac{1}{2}\, k_p\, \gamma^{'}\, H^2 + \frac{1}{2}\, \gamma_w\, H_w^2 \tag{L.1}$$

$$k_p = \frac{1+\sin\phi^{'}}{1-\sin\phi^{'}} \tag{L.2}$$

where P_p = total passive earth thrust (kN/m), k_p is passive earth pressure coefficient based on Eq. L.2 for frictionless wall, $\gamma^{'}$ is buoyant unit weight (kN/m^3), H is height of the wall (m), γ_w is unit weight of water (kN/m^3), H_w is water table height (m) (positive upwards) and $\phi^{'}$ is the internal friction angle.

(b) Unsaturated case - when the water table is between the soil surface and the base of the wall:
For total passive earth pressure calculations in the rest of this appendix, full continuity of water between the soil and the wall was assumed for cases when the water table is below the surface and the capillary rise has an effect on the wall.

i. When the capillary rise line is at the surface:
Figure L.1 shows a retaining wall case with the water table below the soil surface and the capillary rise to the surface, as well as the total passive thrust induced on the wall. Table L.1 shows the effective and total horizontal stresses for points 1, 2 and 3 shown in Fig. L.1. For simplicity, the total passive thrust for each term is calculated individually as:

- For Term 1:

$$P_{p1} = (k_p - 1)\, \gamma_w\, y_1^2 \tag{L.3}$$

- For Term 2

$$P_{p2} = \frac{1}{2}\ y_1\ [k_p\ \gamma_{sat}\ y_1\ -(k_p-1)\ \gamma_w\ y_1] \tag{L.4}$$

- For Term 3

$$P_{p3} = k_p\ \gamma_{sat}\ y_1\ H_w \tag{L.5}$$

- For Term 4

$$P_{p4} = \frac{1}{2}\ k_p\ \gamma^{'}\ H_w^2 \tag{L.6}$$

- For Term 5

$$P_{p5} = \frac{1}{2}\ \gamma_w\ H_w^2 \tag{L.7}$$

The total passive earth thrust for all the terms, therefore, is given by:

$$P_p = (k_p{-}1)\ \gamma_w\ y_1^2{+}\frac{1}{2}\ y_1\ [k_p\ \gamma_{sat}\ y_1\ {-}(k_p{-}1)\ \gamma_w\ y_1]{+}k_p\ \gamma_{sat}\ y_1\ H_w{+}\frac{1}{2}\ k_p\ \gamma^{'}\ H_w^2{+}\frac{1}{2}\ \gamma_w\ H_w^2 \tag{L.8}$$

where y_1 is distance from the water table to the capillary rise line and γ_{sat} is saturated unit weight (kN/m^3).

Table L.1: Calculation of the total horizontal stresses for a case when the water table locates below the surface and the capillary rise line at the surface.

Point	σ_v	u_c [1]	$\sigma_v^{'}$	$\sigma_h^{'}$	$\sigma_h = \sigma_h^{'} + u_w$
1	0	$-\gamma_w\ y_1$	$\gamma_w\ y_1$	$k_p\ \gamma_w\ y_1$	$(k_p-1)\ \gamma_w\ y_1$
2	$\gamma_{sat}\ y_1$	0	$\gamma_{sat}\ y_1$	$k_p\gamma_{sat}\ y_1$	$k_p\gamma_{sat}\ y_1$
3	$\gamma_{sat}(y_1+H_w)$	$u_w = \gamma_w\ H_w$	$\gamma_{sat}\ y_1 + \gamma^{'}\ H_w$	$k_p(\gamma_{sat}\ y_1 + \gamma^{'}\ H_w)$	$k_p(\gamma_{sat}\ y_1 + \gamma^{'}\ H_w){+}\gamma_w H_w$

[1] where u_c is the capillary rise pressure.

ii. When the water table is located between the surface and the base of the wall and the capillary rise line is located below the surface:
The effective and total horizontal stresses for this case is shown in Table L.2. Figure L.2 shows the total passive thrust for each term. Average unit weight, γ_{ave}, above the capillary rise line was used and h_1 defined as a distance from the capillary rise line to the surface. It was assumed that the pore pressure was zero above the capillary rise zone. Total passive thrust for each term is as follows:

- For Term 1

$$P_{p1} = \frac{1}{2}k_p\ \gamma_{ave}\ h_1^2 \tag{L.9}$$

- For Term 2

$$P_{p2} = [k_p\ \gamma_{ave}\ h_1\ + (k_p-1)\ \gamma_w\ y_1]\ y_1 \tag{L.10}$$

- For Term 3

$$P_{p3} = \frac{1}{2}[k_p\ \gamma_{sat}\ y_1\ -(k_p-1)\ \gamma_w\ y_1]\ y_1 \tag{L.11}$$

Table L.2: Calculation of the total horizontal stresses for a case when the water table below the surface and up to the base of the wall and the capillary rise line below the surface.

Point	σ_v	u_c [1]	$\sigma_v^{'}$	$\sigma_h^{'}$	$\sigma_h = \sigma_h^{'} + u_w$
1	0	0	0	0	0
2	$\gamma_{ave}\ h_1$	-$\gamma_w\ y_1$	$\gamma_{ave}\ h_1 + \gamma_w\ y_1$	$k_p(\gamma_{ave}\ h_1 + \gamma_w\ y_1)$	$k_p\gamma_{ave}\ h_1 + (k_p - 1)\gamma_w\ y_1$
3	$\gamma_{ave}\ h_1 + \gamma_{sat}\ y_1$	0	$\gamma_{ave}\ h_1 + \gamma_{sat}\ y_1$	$k_p\big(\gamma_{ave}\ h_1 + \gamma_{sat}\ y_1\big)$	$k_p\big(\gamma_{ave}\ h_1 + \gamma_{sat}\ y_1\big)$
4	A^1	$A^2 = u_w$	A^3	A^4	A^5

1 where u_c is the capillary rise pressure. $A^1 = \gamma_{ave}\ h_1 + \gamma_{sat}\ (y_1 + H_w)$.
$A^2 = \gamma_w\ H_w$. $A^3 = \gamma_{ave}\ h_1 + \gamma_{sat}\ y_1 + \gamma^{'} H_w$. $A^4 = k_p\big(\gamma_{ave}\ h_1 + \gamma_{sat}\ y_1 + \gamma^{'} H_w\big)$.
$A^5 = k_p\big(\gamma_{ave}\ h_1 + \gamma_{sat}\ y_1 + \gamma^{'} H_w\big) + \gamma_w H_w$.

- For Term 4

$$P_{p4} = [k_p\ \gamma_{ave}\ h_1\ + k_p\ \gamma_{sat}\ y_1]\ H_w \tag{L.12}$$

- For Term 5

$$P_{p5} = \frac{1}{2}\ [k_p \gamma^{'}\ H_w^2] \tag{L.13}$$

- For Term 6

$$P_{p6} = \frac{1}{2}\ \gamma_w\ H_w^2 \tag{L.14}$$

The total passive earth thrust for all the terms, therefore, is given by:

$$\begin{aligned} P_p = \frac{1}{2} k_p\ \gamma_{ave}\ h_1^2 + [k_p\ \gamma_{ave}\ h_1\ + (k_p - 1)\ \gamma_w\ y_1]\ y_1 \\ + \frac{1}{2}[k_p\ \gamma_{sat}\ y_1 - (k_p - 1)\ \gamma_w\ y_1]\ y_1 + [k_p\ \gamma_{ave}\ h_1\ + k_p\ \gamma_{sat}\ y_1]\ H_w \\ + \frac{1}{2}\ [k_p \gamma^{'}\ H_w^2] + \frac{1}{2}\ \gamma_w\ H_w^2 \end{aligned} \tag{L.15}$$

where $y_1 = H - H_w - h_1$.

(c) Unsaturated case - when the water table is located below the wall base and the capillary rise line is above the wall base:
The effective and total horizontal stresses for this case is shown in Table L.3. Total passive thrust for each term shown in Fig. L.3 is as follows:

Table L.3: Calculation of the total horizontal stresses for a case when the water table locates below the base and the capillary rise has an effect on the wall.

Point	σ_v	u_c [1]	$\sigma_v^{'}$	$\sigma_h^{'}$	$\sigma_h = \sigma_h^{'} + u_w$
1	0	0	0	0	0
2	$\gamma_{ave}\ h_1$	-$\gamma_w\ y_1$	$\gamma_{ave}\ h_1 + \gamma_w\ y_1$	$k_p(\gamma_{ave}\ h_1 + \gamma_w\ y_1)$	$k_p\gamma_{ave}\ h_1 + (k_p - 1)\gamma_w\ y_1$
3	A^1	A^2	A^3	A^4	A^5

1 where u_c is the capillary rise pressure. $A^1 = \gamma_{ave}\ h_1 + \gamma_{sat}\ y_2$.
$A^2 = -\gamma_w\ H_w$. $A^3 = \gamma_{ave}\ h_1 + \gamma_{sat}\ y_2 + \gamma_w\ H_w$. $A^4 = k_p(\gamma_{ave}\ h_1 + \gamma_{sat}\ y_2 + \gamma_w\ H_w)$.
$A^5 = k_p(\gamma_{ave}\ h_1 + \gamma_{sat}\ y_2) + (k_p - 1)\ \gamma_w\ H_w$.

- For Term 1

$$P_{p1} = \frac{1}{2} k_p \ \gamma_{ave} \ h_1^2 \tag{L.16}$$

- For Term 2

$$P_{p2} = [k_p \ \gamma_{ave} \ h_1 \ + (k_p - 1) \ \gamma_w \ y_1] \ y_2 \tag{L.17}$$

- For Term 3

$$P_{p3} = \frac{1}{2} [k_p \ \gamma_{sat} \ y_2 \ - (k_p - 1) \ \gamma_w \ H_w - (k_p - 1) \ \gamma_w \ y_1] \ y_2 \tag{L.18}$$

The total passive earth thrust for all the terms, therefore, is given by:

$$P_p = \frac{1}{2} k_p \ \gamma_{ave} \ h_1^2 + [k_p \ \gamma_{ave} \ h_1 \ + (k_p - 1) \ \gamma_w \ y_1] \ y_2 \tag{L.19}$$
$$+ \frac{1}{2} [k_p \ \gamma_{sat} \ y_2 \ - (k_p - 1) \ \gamma_w \ H_w - (k_p - 1) \ \gamma_w \ y_1] \ y_2$$

where $y_2 = y_1 - H_w$ and H_w has a negative value.
When capillary rise line is located below the base of the wall, $y_2 = 0$. So, terms 2 and 3 in Eq. L.19 are equal to zero (no effect of the capillary rise on the wall) and total passive thrust is given by:

$$P_p = \frac{1}{2} k_p \ \gamma_{ave} \ h_1^2 \tag{L.20}$$

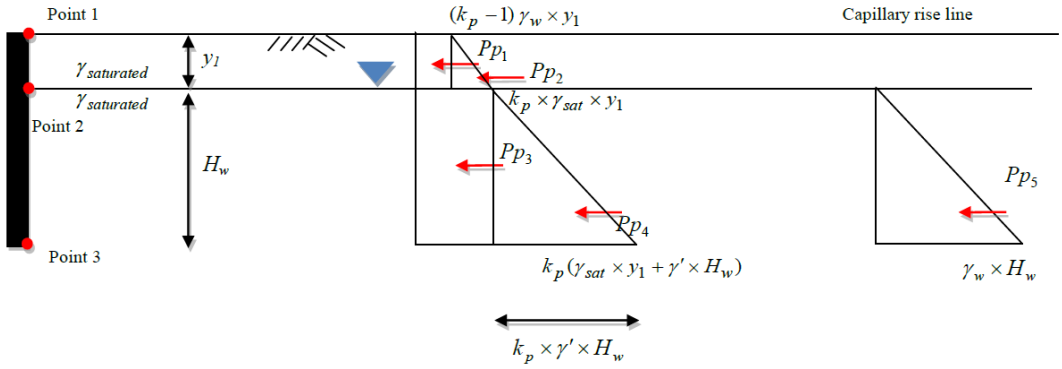

Figure L.1: Total horizontal passive stresses with the capillary rise pressures for the case when the water table locates below the surface and the capillary rise line at the surface.

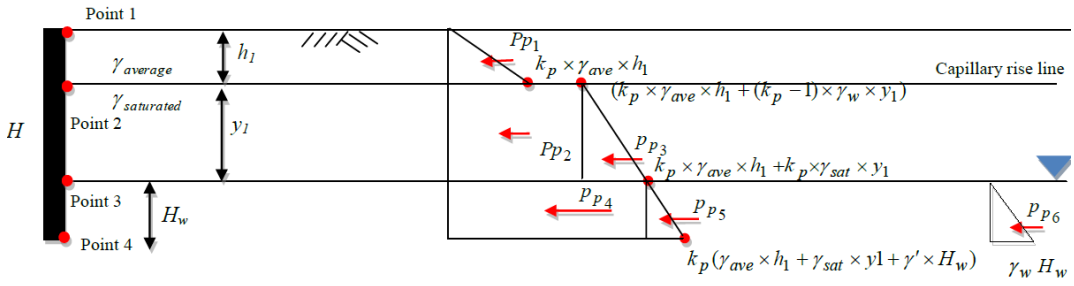

Figure L.2: Total horizontal passive stresses with the capillary rise pressures for the case when the water table and capillary rise line locate below the surface up to the base of the wall.

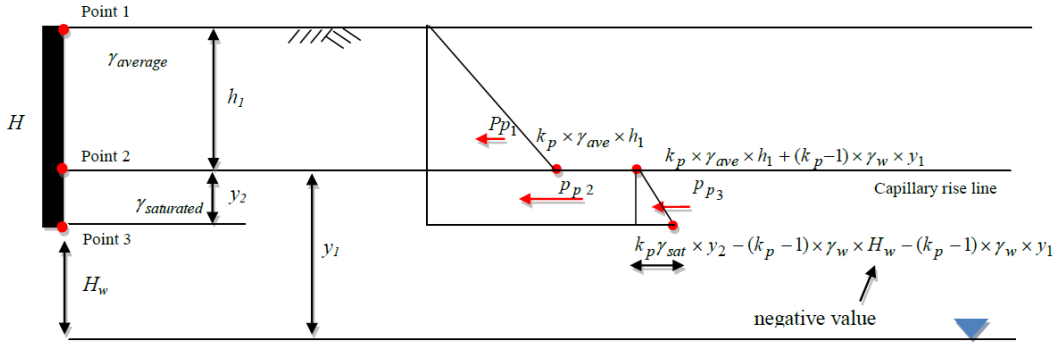

Figure L.3: Total horizontal passive stresses with the capillary rise pressures for the case when the water table below the base (capillary rise has effect on the wall).

Appendix M

Calculation procedure for determination of the SWCC using the HCT

M.1 Calculation procedure

To obtain the SWCC using the HCT, the direct shear box with a diameter of 80.03 mm and a height of 48 mm was used. The initial saturated mass of the sample of 467 gm was used to obtain the void ratio ($e = 0.70$). The amount of water extracted from the sample after each lowering of the burette was measured and then the weight of the sample was adjusted accordingly. Equation M.1 was used to calculate the unit weight of the sample after each lowering of the burette. Here, the volume (and hence void ratio) of the sample was assumed to be constant and then Eq. M.2 was used to calculate the corresponding degree of saturation. Values of $G_s = 2.65$ and $\gamma_w = 9.81$ kN/m^3 were used. The gravimetric water content was then calculated using Eq. M.3. Tables M.1 and M.2 show data for the main drying and wetting curves of the SWCC, respectively. The SWCC was, therefore, plotted using the last two columns in Tables M.1 and M.2 for the main drying and wetting curves, respectively.

$$\gamma_t = \frac{W_t}{V_t} \tag{M.1}$$

$$S_r = \frac{\gamma_t\ (1+e) - G_s\ \gamma_w}{e\ \gamma_w} \tag{M.2}$$

$$w = \frac{S_r\ e}{G_s} \tag{M.3}$$

Table M.1: Calculation procedure for determination the main drying curve of the SWCC using the HCT.

Cumulative expelled water (kg)$\times 10^{-3}$	Total weight (kg)	γ_t (kN/m^3)	S_r%	w%	s (kPa)
0	0.467	19.21	100	26.37	0
0.956	0.466	19.17	95.97	25.31	0.32
2.379	0.464	19.11	94.52	24.93	0.69
3.158	0.464	19.08	93.73	24.72	1.29
4.114	0.462	19.04	92.75	24.46	1.83
4.470	0.462	19.03	92.39	24.37	2.26
6.494	0.461	18.95	90.33	23.82	2.25
7.316	0.459	18.91	89.49	23.60	2.37
8.873	0.458	18.84	87.91	23.18	2.58
10.875	0.456	18.76	85.86	22.65	2.67
12.587	0.454	18.69	84.12	22.19	2.80
14.166	0.453	18.63	82.51	21.769	2.85
16.057	0.451	18.55	80.58	21.259	2.89
18.081	0.449	18.47	78.52	20.72	2.96
20.216	0.447	18.38	76.34	20.14	3.02
22.440	0.445	18.29	74.07	19.54	2.97
24.953	0.442	18.18	71.51	18.86	3.05
27.622	0.439	18.07	68.79	18.14	3.07
31.113	0.436	17.93	65.23	17.20	3.21
34.918	0.432	17.77	61.35	16.18	3.27
38.920	0.428	17.61	57.28	15.11	3.39
43.012	0.424	17.44	53.11	14.00	3.48
47.104	0.419	17.27	48.94	12.90	3.46
51.352	0.415	17.10	44.61	11.76	3.60
55.355	0.411	16.93	40.53	10.68	3.72
59.136	0.408	16.78	36.67	9.67	3.81
62.672	0.404	16.63	33.07	8.72	3.94
65.874	0.401	16.50	29.80	7.86	4.10
69.544	0.397	16.35	26.06	6.87	4.21
72.480	0.394	16.23	23.07	6.08	4.57
73.814	0.393	16.17	21.71	5.72	4.75
75.060	0.392	16.12	20.44	5.39	5.31
75.593	0.391	16.10	19.89	5.25	5.91
75.727	0.391	16.09	19.76	5.21	6.73

Table M.2: Calculation procedure for determination the main wetting curve of the SWCC using the HCT.

Cumulative added water (kg)$\times 10^{-3}$	Total weight (kg)	γ_t (kN/m^3)	S_r%	w%	s (kPa)
0	0.391	16.09	19.76	5.21	6.73
2.600	0.394	16.21	22.41	5.91	3.50
3.603	0.395	16.25	23.43	6.18	2.74
8.495	0.400	16.45	28.42	7.49	2.64
13.499	0.405	16.65	33.52	8.84	2.34
19.838	0.411	16.91	39.98	10.55	1.97
27.199	0.419	17.22	47.48	12.53	1.81
35.339	0.427	17.55	55.78	14.71	1.70
45.570	0.437	17.97	66.21	17.46	1.50
55.755	0.447	18.39	76.59	20.20	1.35
66.564	0.458	18.84	87.61	23.11	1.29
75.616	0.467	19.21	96.83	25.54	0.31